
Probing Nuclear Structure Relevant for Neutrinoless Double-Beta Decay with Nuclear Resonance Fluorescence

**Kernstrukturuntersuchungen mit Bezug zum neutrinolosen doppelten
Betazerfall mit der Kernresonanzfluoreszenzmethode**

Zur Erlangung des Grades eines Doktors der Naturwissenschaften (Dr. rer. nat.)
genehmigte Dissertation im Fachbereich Physik von Udo Friman-Gayer aus
Miltenberg, BY, DE

Tag der Einreichung: 19. November, 2019, Tag der Prüfung: 16. Dezember, 2019

1. Gutachten: Prof. Dr. Dr. h.c. mult. Norbert Pietralla

2. Gutachten: Prof. Dr. Wilfried Nörtershäuser

Darmstadt – D 17



TECHNISCHE
UNIVERSITÄT
DARMSTADT

Physics Department
Institut für Kernphysik
Pietralla Group

Probing Nuclear Structure Relevant for Neutrinoless Double-Beta Decay with
Nuclear Resonance Fluorescence

Kernstrukturuntersuchungen mit Bezug zum neutrinolosen doppelten Betazerfall
mit der Kernresonanzfluoreszenzmethode

Doctoral thesis in Physics by Udo Friman-Gayer

1. Review: Prof. Dr. Dr. h.c. mult. Norbert Pietralla

2. Review: Prof. Dr. Wilfried Nörtershäuser

Date of submission: 19. November, 2019

Date of thesis defense: 16. Dezember, 2019

Darmstadt – D 17

Bitte zitieren Sie dieses Dokument als:

URN: urn:nbn:de:tuda-tuprints-113857

URL: <https://tuprints.ulb.tu-darmstadt.de/id/eprint/11385>

Dieses Dokument wird bereitgestellt von tuprints,

E-Publishing-Service der TU Darmstadt

<http://tuprints.ulb.tu-darmstadt.de>

tuprints@ulb.tu-darmstadt.de

This work is licensed under a Creative Commons “Attribution-NonCommercial-
NoDerivatives 4.0 International” license.

<https://creativecommons.org/licenses/by-nc-nd/4.0/deed.en>



Erklärungen laut Promotionsordnung

§8 Abs. 1 lit. c PromO

Ich versichere hiermit, dass die elektronische Version meiner Dissertation mit der schriftlichen Version übereinstimmt.

§8 Abs. 1 lit. d PromO

Ich versichere hiermit, dass zu einem vorherigen Zeitpunkt noch keine Promotion versucht wurde. In diesem Fall sind nähere Angaben über Zeitpunkt, Hochschule, Dissertationsthema und Ergebnis dieses Versuchs mitzuteilen.

§9 Abs. 1 PromO

Ich versichere hiermit, dass die vorliegende Dissertation selbstständig und nur unter Verwendung der angegebenen Quellen verfasst wurde.

§9 Abs. 2 PromO

Die Arbeit hat bisher noch nicht zu Prüfungszwecken gedient.

Darmstadt, den 19. November, 2019

U. Friman-Gayer

Table of Contents

Table of Contents	5
Nomenclature	9
1. Introduction	33
1.1. Neutrinoless Double-Beta Decay and Nuclear Structure	33
1.1.1. A Simple Model: Hypothetical $0\nu\beta\beta$ Decay of the Dineutron	37
1.2. Current State of Nuclear Structure Input	51
1.3. Outline	57
2. Background	59
2.1. Nuclear Resonance Fluorescence	59
2.1.1. General Properties	59
2.1.2. Formalism	63
2.2. Nuclear Structure Models	67
2.2.1. Shell Model	67
2.2.2. Interacting Boson Model	71
2.3. Scissors Mode	78

3. Experiments	83
3.1. High-Intensity γ -ray Source (HI γ S)	83
3.2. Experimental Setups	87
3.3. Experiments on ^{82}Kr and ^{82}Se	87
3.4. Experiments on ^{150}Nd and ^{150}Sm	92
4. Analysis	93
4.1. General	93
4.1.1. Propagation of Uncertainty	93
4.1.2. Parameter Estimation	95
4.1.3. Systematic Uncertainty	97
4.1.4. Spectrum	97
4.1.5. Numerical Evaluation and Visualization	98
4.2. Simulation of the Experimental Setup	98
4.3. Spectrum Decomposition	100
4.3.1. Original Spectrum	101
4.3.2. Detector Response	101
4.3.3. Pileup	101
4.4. Sensitivity Limit	105
4.4.1. Definition	105
4.4.2. Spectroscopic Sensitivity Limit	106
4.5. Calibrations	108
4.5.1. Energy Calibration and Binning	108
4.5.2. Efficiency Calibration	114
4.5.3. Width Calibration	120

4.5.4. Photon Flux Calibration	121
4.6. Derived Quantities	134
4.6.1. Quantum Numbers and Multipole Mixing Ratio	137
4.6.2. Branching Ratio	139
4.6.3. Cross section	140
5. Results	143
6. Discussion	153
6.1. ^{82}Se and ^{82}Kr	153
6.2. ^{150}Nd and ^{150}Sm	156
7. Summary and Outlook	159
A. Spectroscopic Sensitivity Limit	161
A.1. Evaluation for Theuerkauf Lineshape Model	167
B. Schematic Detector Setups	171
C. List of Gamma Energies	175
D. Spectra	185
Bibliography	351
Acknowledgements	371
Academic CV	375

Nomenclature

This section contains a list of all symbols and indices which are used in this work. The nomenclature complies with the following general rules:

- Operator- and operator-like symbols are typed in bold characters.
- Operator-like quantities are displayed with a caret, i.e. $\hat{\mathbf{t}}$.
- Lowercase operator symbols denote single-particle operators. An uppercase symbol denotes the corresponding manybody operator, which is a sum of the single-particle operators, e.g. $\hat{\mathbf{T}} = \sum_{a=1}^A \hat{\mathbf{t}}_a$. The nomenclature contains only the lowercase symbols.
- The eigenvalues of operator-like quantities are denoted with the same symbol as the operator, but without the caret and as regular text. For example, the eigenvalue equation for the operator $\hat{\mathbf{t}}_z$ is: $\hat{\mathbf{t}}_z |t_z\rangle = t_z |t_z\rangle$. One exception of this rule is the definition $l_z \equiv m_l$ of the magnetic quantum number for the eigenvalues of angular momentum operators for historical reasons and better readability.
- The absolute value $|\mathbf{r}|$ of a boldface symbol is displayed as regular text ($|\mathbf{r}| \equiv r$).
- The components of up-to three-dimensional operator- and vector-like symbols are denoted by the indices x , y and z as regular text. For example, a three-dimensional vector \mathbf{r} has the components r_x , r_y , and r_z . The components of vectors with arbitrary (n_x) dimensions are denoted by numbers starting from 1, i.e. $\mathbf{X} = (X_1, X_2, \dots, X_{n_x})^T$.

- Raising and lowering operators are denoted by an additional '+' and '-' sign, respectively, for example \hat{t}^+ and \hat{t}^- .
- General indices for a set of values, for example i for the set of states of a nucleus, are taken from the Latin or Greek alphabet. Additional indices are added as they follow in the respective alphabet, for example i is followed by j, k, \dots . The set itself is denoted by an uppercase letter, for example: $k \in K$.
- The average/expectation value of a quantity is denoted in angular brackets, i.e. $\langle X \rangle$ is the average value of X .
- Nuclear reactions are denoted as '(in, out)', where 'in' is the incoming projectile and 'out' a set of ejectiles, in accordance with the Evaluated Nuclear Structure Data File (ENSDF) manual [1].
- Particles are denoted by the symbols recommended by the Particle Data Group (PDG) [2]. In particular, the word 'photon' and the symbol γ will be used. The word 'gamma ray' was avoided, if possible, due to its conflicting definitions in the literature.

$2\nu\beta\beta$	Two-neutrino double beta
α_j	Expansion parameter for the representation of a nucleon-nucleon pair with $J = 0$ and $M_J = 0$ in terms of shell-model orbitals.
$e_{x/y/z}$	Unit vector in x -, y - or z direction.
$j_\gamma(E_\gamma, \mathbf{r}, t)$	Photon flux density, i.e. directional number of photons per area and time unit with an energy E_γ at a space point \mathbf{r} .
\mathbf{P}	Vector of parameters.
r_a	Single-particle position operator.
r_{ab}	Distance vector of two particles a and b .
X	Vector of input quantities.
Y	Vector of output quantities.

$\dot{A}(t)$	Time-dependent activity of a radioactive source in decays per time interval.
$\frac{dI_{i \rightarrow j \rightarrow k}}{d\Omega}$	Energy-integrated differential cross section for the absorption of a photon by a nucleus in the state i to an excited state j , and the subsequent decay to a state k .
$\hat{A}^\dagger(jj'; J, M_J)$	Operator which creates a pair of nucleons from orbitals j and j' with a total angular momentum J and a z projection M_J .
$\hat{a}_i^\dagger, \hat{a}_i$	Creation/annihilation operator for a fermion in the state i .
\hat{D}^\dagger	Operator which creates a pair of nucleons with $J = 2$ and a z projection M_J in a given valence space.
$\hat{d}_\mu, \hat{d}_\mu^\dagger$	Annihilation/creation operator for a d boson state with a z component μ .
\hat{f}	Single-particle F -spin operator.
\hat{H}	Hamilton operator.
\hat{k}_a	Single-particle kinetic energy operator $\hat{k}_a = \hat{p}_a^2/2m_a$.
\hat{l}	Orbital angular momentum operator.
$\hat{O}^{(0\nu)}$	Operator for neutrinoless double-beta decay.
$\hat{O}_F^{(0\nu)}$	Fermi-part of the operator for neutrinoless double-beta decay.
$\hat{O}_{GT}^{(0\nu)}$	Gamow-Teller part of the operator for neutrinoless double-beta decay.
\hat{P}_ν	Valence-space projection operator.
\hat{Q}^χ	Quadrupole operator in the IBM with the parameter χ .
\hat{Q}_ν	Complement of the valence-space projection operator, i.e. $\hat{Q}_\nu = 1 - \hat{P}_\nu$.

\hat{s}, \hat{s}^\dagger	s -boson annihilation/creation operator.
\hat{S}^\dagger	Operator which creates a pair of nucleons with $J = 0$ and $M_J = 0$ in a given valence space.
\hat{s}_a	Single-particle spin operator.
\hat{t}	Single-particle isospin operator. The $t_z = 1/2$ and $t_z = -1/2$ eigenstates of this operator are the proton and the neutron, respectively.
\hat{U}_a	Mean-field potential energy of particle a .
\hat{V}_{ab}^{2N}	General two-body potential between particles a and b .
\hat{d}_μ	Modified annihilation operator for a d boson state with a z component μ ($\hat{d}_\mu = (-1)^\mu \hat{d}_{-\mu}$).
\hbar	Reduced Planck constant ($6.582119596 \times 10^{-16}$ eVs [3]).
$\langle m_\nu \rangle$	Effective light neutrino mass in $0\nu\beta\beta$ decay.
$\langle W_{i \rightarrow j \rightarrow k} \epsilon_d(E_\gamma) \rangle$	Abbreviation for the energy-dependent solid-angle integral over the product of the angular distribution of an NRF cascade $i \rightarrow j \rightarrow k$ and the full-energy peak efficiency of a detector d . This integral appears in the expression for the number of NRF events which are counted by a detector.
$\langle X \rangle_t$	Time average of a quantity X .
$\mathcal{O}(x)$	'Big O notation' or 'Landau symbol' which indicates the limiting behavior of a function when x is 'small' according to some criterium.
$\mathfrak{B}(\sigma L; i \rightarrow j)$	Lower limit for the reduced transition probability $B(\sigma L; i \rightarrow j)$. In principle, all branching transitions of an excited state need to be known in order to determine the 'true' reduced transition probabilities. This notation indicates that some of them may not have been observed.

\mathfrak{P}	Projection operator onto states with good seniority.
$\text{Ci}(x)$	Cosine integral $\text{Ci}(x) = -\int_x^\infty \frac{\cos(t)}{t} dt$.
$\text{sc}_\pm(X)$	Upper ('+') and lower ('-') limit of the shortest coverage interval of the quantity X .
$\text{Si}(x)$	Sine integral $\text{Si}(x) = \int_0^x \frac{\sin(t)}{t} dt$.
$dA_{i \rightarrow k, d}/dt$	Count rate of events corresponding to a transition from a state i to a state j observed by a detector d .
g_V/g_A	Ratio of the vector- and axial-vector coupling constants of the weak interaction (the experimental value of the inverse ratio is $g_A/g_V = 1.27641(45)_{\text{stat.}}(33)_{\text{syst.}}$ [4]).
$\overline{N}(E_m)$	Original energy spectrum before the application of the detector response. See also the definition of $N(E_m)$.
A	Mass number ($A = N + Z$).
$A(E_\gamma)$	Number of events contained in a lineshape with the centroid energy E_γ .
$a_{0 \rightarrow j \rightarrow k, dd'}$	Asymmetry of the number of counted events associated with a transition from a state j to a state k between two detectors d and d' .
$A_{i \rightarrow k, d}$	Number of events corresponding to a transition from a state i to a state j observed by a detector d .
a_{nn}	Neutron-neutron s-wave scattering length.
a_{pp}	Proton-proton s-wave scattering length.
$B_Z^A(X)$	Binding energy of the nucleus ${}^A_Z X$.
$B(E, \mathbf{p}_B)$	Normalized probability distribution of the continuous background in a spectrum, which may depend on a vector of parameters \mathbf{p}_B .

c	Speed of light ($c = 2.99792458 \times 10^8 \text{ ms}^{-1}$ [3]).
$D(E_m, E_n)$	Detector response matrix which connects the energy bin E_n of the original spectrum to the energy bin E_m of the detected spectrum.
D_X	Set of all detectors in a setup X .
E_γ	Energy of a photon.
E_{beam}	Nominal beam energy of the HIγS beam, which can be seen as the centroid of the approximately Gaussian beam profile.
e_π, e_ν	Charges of proton- and neutron bosons in the $E2$ operator of the IBM-2.
E_i	Excitation energy of state i .
E_m	Energy of the m -th bin.
ee	even-even
eo, oe	even-odd, odd-even
$f(\mathbf{X}, \mathbf{P})$	Arbitrary function f of a vector of input quantities \mathbf{X} and parameters \mathbf{P} .
F_{max}	Maximum projection of the F -spin for a given number of proton- and neutron bosons: $F_{\text{max}} = 1/2(N_{\nu,s} + N_{\nu,d} + N_{\pi,s} + N_{\pi,d})$.
g_π, g_ν	Proton- and neutron g factors in the $M1$ operator of the IBM-2.
g_l^π, g_l^ν	Orbital g factors in the $M1$ operator for protons and neutrons. Their bare values are given by $g_l^\pi = 1$ and $g_l^\nu = 0$ (see, e.g., Sec. V.B.III in [5]).
g_s^π, g_s^ν	Spin- g factors in the $M1$ operator for protons and neutrons with their bare values $g_s^\pi = 5.5856946893(16)$ and $g_s^\nu = -3.382608545(90)$ [6].

$G_{0\nu}$	Integrated kinematical/phase space factor in $0\nu\beta\beta$ decay.
$g_X(\xi)$	Probability distribution function of the vector X . The symbol ξ denotes a vector of variables for all possible values of X .
$g_{i\rightarrow j}$	Ratio of the number of J_z substates of the initial and final state for a transition from state i to j ('spin factor' J_{j+1}/J_{i+1}).
$H(r, \langle E \rangle)$	Neutrino potential in the Fermi- and Gamow-Teller part of the $0\nu\beta\beta$ decay operator, which depends on the distance r between two nucleons and the average energy difference $\langle E \rangle$ between an excited state of the intermediate nucleus and the mean value of the initial and final state of the $0\nu\beta\beta$ decay.
$I_{\text{rel}}(E_\gamma)$	Relative intensity of a photon with the energy E_γ which is emitted by a radioactive source. $I_{\text{rel}} = 1$ means that each decay of the source creates exactly one photon of this energy.
$I_{i\rightarrow j\rightarrow k}$	Total cross section for the absorption of a photon by a nucleus in the state i to an excited state j , and the subsequent decay to a state k .
$I_{i\rightarrow j}$	Total cross section for the absorption of a photon by a nucleus in the state i to an excited state j .
L_C	Threshold for a 95% confidence for the absence of activity.
$L_{i\rightarrow j}$	Multipole order of an EM transition between states i and j ($L \in \mathbb{N}$). The index for the corresponding transition is dropped if the initial and final state are clear from the context.
L_k^α	Associated/generalized Laguerre polynomial.
M	Total mass of a system of particles.
$M(\overset{A}{Z}X), M(Z, A)$	Mass of the nucleus $\overset{A}{Z}X$.
$M(E_m, E_n)$	Pileup matrix which connects the energy bin E_n of the original spectrum to the energy bin E_m of the pileup spectrum.

$M^{(0\nu)}$	Nuclear matrix element for neutrinoless double-beta decay.
m_e	Electron mass $(9.1093837015(28) \times 10^{-31} \text{ kg [6]})$.
m_l	z projection of the orbital angular momentum operator ('magnetic quantum number').
m_n	Neutron mass $(1.00866491582(49) \text{ u [7]})$.
m_p	Proton mass $(1.00782503224(09) \text{ u [7]})$.
$N(E_m)$	Content of the bin of the spectrum N with the centroid energy E_m . May also be denoted as N_m for brevity or to emphasize that a channel-energy mapping does not exist. In particular, the bare letter N denotes an actually observed spectrum. When N is split up into different contributions, subscripts, superscripts, or diacritics are used in this work.
N	Neutron number or principal quantum number of the harmonic oscillator.
$N(\mu, \sigma)$	Normal distribution with mean value μ and standard deviation σ .
$n^{2S+1}l_J$	Spectroscopic notation, which contains the radial (n), total spin (S), angular momentum (l) and total angular momentum (J) quantum number of a manybody state.
$N^{(0)}(E_m)$	Energy spectrum that would be detected if every single event could be resolved. Corresponds to 'zero-order pileup'.
$N^{(p)}(E_m)$	p -th order pileup correction to the spectrum $N^{(0)}(E_m)$ with $p \geq 1$.
$N_\gamma(E_\gamma)$	Number of photons with an energy E_γ .
N_γ	Total number of photons which hit the target.
$N_{\text{fit}}(E_m)$	Fit function which is assumed to describe the shape of the spectrum $N(E_m)$.

N_B	Number of background events.
N_D	Threshold for a 95% confidence for the presence of activity OR number of nucleon-nucleon pairs with $J = 2$ and a z component M_J .
N_d	Number of d bosons.
N_m	See $N(E_m)$.
N_R	Number of randomly sampled values.
N_S	Number of events caused by artificial activity OR number of nucleon-nucleon pairs with $J = 0$ and $M_J = 0$.
N_s	Number of bins of spectrum s OR number of s bosons.
N_T	Normalization factor of the Theuerkauf line shape model.
N_t	Number of target nuclei.
$n_t(\mathbf{r})$	Number of target nuclei per unit volume at a point \mathbf{r} .
$N_{B,\Sigma}$	Total number of background events in a spectrum.
N_{nl}	Normalization constant of the harmonic oscillator wave function.
oo	odd-odd
$P(E, \mathbf{p}_P)$	Normalized probability distribution ('line shape') of a peak, which may depend on a vector of parameters \mathbf{p}_P .
$P_\gamma(E_\gamma)$	Polarization factor which depends on the beam energy ($P_\gamma \in [-1, 1]$).
P_ν	Legendre polynomial of degree ν .
P_ν^μ	Unnormalized Legendre polynomial of degree ν and order μ .
$P_T(E_m, \mu, \sigma, t_l, t_r)$	Theuerkauf model for the line shape.

$Q_{\beta\beta}$	Q value of a neutrinoless or a two-neutrino double-beta decay. $Q_{0\nu\beta\beta} \approx Q_{2\nu\beta\beta}$ for negligible neutrino masses.
$R_{nl}(r)$	Radial part of the harmonic oscillator wave function.
t_{dead}	Dead time of a detector.
t_{live}	Live time of a detector.
t_{start}	Point in time when an experimental run starts.
t_{stop}	Point in time when an experimental run stops.
t_l	Left-tail parameter of the Theuerkauf line-shape model.
t_r	Right-tail parameter of the Theuerkauf line-shape model.
$T_{1/2}$	Half life of a decay process ($T_{1/2} = \ln(2)\tau$).
$V_T(\theta)$	Factorized part of the transversal inelastic electron scattering cross section which almost only depends on the scattering angle if the electron energy is much larger than the excitation energy of the nucleus.
$W_{i \rightarrow j \rightarrow k, \text{polarized}}(\theta, \varphi)$	Term which is added to (or subtracted from, depending on the EM character) the unpolarized angular distribution $W_{i \rightarrow j \rightarrow k, \text{unpolarized}}(\theta)$ to take into account the excitation from i to j by a completely polarized photon beam.
$W_{i \rightarrow j \rightarrow k, \text{unpolarized}}(\theta)$	Angular distribution of the emitted photon in the transition from state j to k during the two-step cascade between states i, j and k . The index 'unpolarized' indicates that the excitation is assumed to be caused by an unpolarized photon beam. Normalized to 4π .

$W_{i \rightarrow j \rightarrow k}(\theta, \varphi, \delta_{i \rightarrow j}, \delta_{j \rightarrow k}, P_\gamma)$	Angular distribution of the emitted photon in the transition from state j to k during the two-step cascade between states i, j and k . It depends on the angular momentum- and parity quantum numbers of the involved states and the multipole mixing ratios $\delta_{i \rightarrow j}$ and $\delta_{j \rightarrow k}$. The excitation is assumed to be caused by a photon beam which has an energy-dependent polarization P_γ . Normalized to 4π .
X_{rand}	Random value drawn from the probability distribution g_X of the quantity X .
$y^{(i)}$	Auxiliary, energy-dependent quantity in the integrated phase space factor.
$Y_{lm_l}(\theta, \varphi)$	Spherical harmonics.
Z	Proton number.
$0\nu\beta\beta$	Neutrinoless double-beta
\mathbb{N}	Set of positive integer numbers including zero.
$\beta_{jj'}$	Expansion parameter for the representation of a nucleon-nucleon pair with $J = 2$ and a z component M_J in terms of shell-model orbitals.
\hat{n}_d	Single- d boson number operator.
CCD	Charge-coupled device
COM	Center of mass
DIN	Deutsches Institut für Normung
ENSDF	Evaluated Nuclear Structure Data File
EW	Electroweak
exp	experimental

F	Fermi
FEP	Full-energy peak
FFT	Fast Fourier transform
FWHM	Full width at half maximum
GEANT4	Geometry and Tracking 4. Software framework for the simulation of the passage of particles through matter [8–10].
GT	Gamow-Teller
HI γ S	High-Intensity γ -ray Source
HO	Harmonic oscillator
HPGe	High-purity Germanium
IBM	Interacting boson model
IBM-2	Proton-neutron version of the interacting boson model
INT	Intrinsic
LCB	Laser Compton backscattering
MC	Monte Carlo
n	Radial quantum number of the harmonic oscillator i.e. number of nodes of the radial wave function OR index for an arbitrary nucleon, i.e. $n \in \{\nu, \pi\}$.
NME	Nuclear matrix element
NRF	Nuclear resonance fluorescence
ODR	Orthogonal distance regression

PDF	Probability distribution function
PDG	Particle Data Group
PVC	Polyvinyl chloride
resi	residual
sc	Scissors mode
SM	(Nuclear) Shell model
stat.	Statistical contribution to the total uncertainty.
syst.	Systematic contribution to the total uncertainty.
theo.	Theory contribution to the total uncertainty.
u	Atomic mass unit (931.49410242(28) MeV c ⁻² . [6])
$B(\sigma L; i \rightarrow j)$	Reduced transition probability for the σL transition from state i to j . This quantity is given in units of eV fm ^(2L+1) in the SI [3] system of units. For conversion to the commonly used cgs [11] system of units, use the relations $e_{\text{cgs}}^2 = 1.4399764 \text{ MeVfm}$ and $\mu_{N,\text{cgs}} = 0.10515446 \text{ efm}$.
α	Fine-structure constant (0.0072973525693(11) $\approx 1/137$ [6]).
$\beta\beta$	Double beta
χ^2	Chi square statistic. Measure for the agreement between a model and measured data.
χ	Spin part of the total wave function.
χ_{red}^2	Reduced chi square.
χ_{π}, χ_{ν}	Strength of the term in the proton- or neutron-quadrupole operator which controls the γ -softness.

$d\Omega$	Solid angle element. In spherical coordinates: $d\Omega = \sin(\theta)d\theta d\varphi$.
ΔE	General notation for an energy difference.
$\Delta E_N(E_m)$	Width of a single bin of spectrum N . In the case of equidistant binning, the dependence on the centroid energy E_m is omitted.
$\Delta N(E_m)$	Residual of the bin with centroid energy E_m after subtracting a fit function $N_{\text{fit}}(E_m)$ from a spectrum $N(E_m)$.
ΔT	'Shaping time' of a trapezoidal filter.
$\delta(x)$	Delta function.
δ_p	Pairing energy in the semiempirical mass formula.
$\delta_{L,i \rightarrow j}$	Multipole mixing ratio in the convention of Krane, Steffen and Wheeler [12]: Ratio of the reduced transition widths of EM character and multipole order σL and $\sigma'(L + 1)$ with $\sigma \neq \sigma'$ for a transition from state i to state j .
$\epsilon(E_\gamma, \mathbf{r})$	Energy-dependent full-energy peak efficiency for the detection of photons from an isotropic source at \mathbf{r} . The parameter \mathbf{r} may be omitted if the origin of the photons is clear.
ϵ_{int}	Intrinsic detection efficiency of a detector.
ϵ_d	Single- d boson energy in the IBM-2 Hamiltonian.
$\gamma\gamma$	Double gamma
Γ	Gamma function.
γ_1	Auxiliary, Z -dependent quantity in the integrated phase space factor.
Γ_i	Total width of a state i .

$\Gamma_{i \rightarrow j}$	Partial transition width from the state i to the state j . For the EM process of NRF, the detailed balance theorem holds (chapter X.2.E in [13]) and implies that $\Gamma_{i \rightarrow j} = \Gamma_{j \rightarrow i}$.
$\hat{\sigma}_a$	Single-particle Pauli matrix, which is related to the single-particle spin operator via $\hat{s}_a = \hbar/2 \hat{\sigma}_a$.
κ	Strength of the quadrupole-quadrupole interaction in the IBM-2 Hamiltonian.
λ	Overall strength of the Majorana operator in the IBM-2 Hamiltonian.
λ	Reduced wave length, i.e. de-Broglie wave length of a particle divided by 2π . If indexed with a transition label, i.e. $\lambda_{i \rightarrow j} \equiv \lambda_{j \rightarrow i}$, it denotes the reduced wave length which corresponds to the energy difference of the excited states.
$\langle \Phi(E_\gamma) \rangle_t$	Energy-dependent time-averaged photon flux.
μ	Mean value of a quantity OR the reduced mass of a system of particles.
$\mu(E_\gamma)$	Energy-dependent mass attenuation coefficient of a material.
ν	Symbol for the neutron OR a parameter of the quantum-mechanical harmonic oscillator wave function, which can be interpreted as the inverse squared length scale of the oscillator OR the seniority quantum number.
ω	Oscillator frequency multiplied by 2π .
Φ	Basis states which do not have to be eigenstates of the full Hamiltonian of a system.
$\Phi_\gamma(E_\gamma, t)$	Energy- and time-dependent photon flux on target, i.e. number of photons with an energy E_γ which hit the target per time interval at a time t .

π	Symbol for the proton.
π_i	Parity quantum number of state i .
Ψ	Eigenstates of the full Hamiltonian for a given system.
$\psi_{nlm_l}(r, \theta, \varphi)$	Harmonic oscillator wave function.
$\langle \sigma_N \rangle$	Standard deviation of the bin contents of spectrum N in an energy range where the expectation value for each bin is approximately equal.
ρ	Density of a material.
σL	Notation for an electromagnetic transition of character $\sigma \in \{E, M\}$ and multipole order $L \in \mathbb{N}$.
σ	Electromagnetic character. Either E for 'electric' or M for 'magnetic'.
$\sigma(E)$	Energy-dependent width of a peak with a centroid energy E and a normal-distributed line shape.
$\sigma_f(\mathbf{X}, \mathbf{P})$	Uncertainty of the function value $f(\mathbf{X}, \mathbf{P})$
$\sigma_N(E_m)$	Uncertainty of the bin of the spectrum N with the centroid energy E_m
σ_X	Uncertainty of the quantity X . Depending on the context, this symbol either denotes the 68.27% shortest coverage interval or the standard deviation.
$\sigma_{i \rightarrow j}(E_\gamma)$	Cross section for the absorption of a photon with an energy E_γ by a nucleus in a state i , leaving it in a state j .
$\sigma_{X,\pm}$	Upper ('+') and lower ('-') limit of the uncertainty of the quantity X .
τ	Lifetime of excited nuclear states or, in general, the inverse of the decay parameter of an exponential function.

θ	Polar angle in spherical coordinates.
φ	Azimuthal angle in spherical coordinates.
ξ	Isospin part of the total wave function.
$\xi_{1,2,3}$	Strength of the different terms in the Majorana operator in the IBM-2 Hamiltonian.
$\frac{d\epsilon}{d\Omega'}(E_\gamma, \theta', \varphi', \mathbf{r})$	Energy-dependent full-energy peak efficiency for the detection of photons, emitted by a source at \mathbf{r} in a direction given by θ' and φ' .
0	Index for the ground state of a nucleus.
$[\hat{\mathbf{a}}^\dagger \hat{\mathbf{b}}^\dagger \dots]_i$	Coupling of a set of single-particle creation operators $\hat{\mathbf{a}}^\dagger, \hat{\mathbf{b}}^\dagger, \dots$ to a creation operator for a multi-particle state with a set of quantum numbers summarized by the index i .
a, b, \dots	Indices for single particles in an A -body system, i.e. $1 \leq a, b, \dots \leq A$.
i, j, \dots	Indices for states of a nucleus, both excited states and the ground state.
m, n, \dots	Indices for the bins of a spectrum.

Abstract

Neutrinoless double-beta ($0\nu\beta\beta$) decay is a hypothetical second-order process of the weak interaction, which, if observed, would reveal neutrinos as the first example of so-called Majorana particles which are their own antiparticles. Furthermore, since the decay rate for $0\nu\beta\beta$ decay is directly related to the effective mass of the electron neutrino, it would allow for a direct determination of the neutrino mass. However, an obstacle for the planning of future $0\nu\beta\beta$ -decay searches and for a quantitative extraction of the neutrino mass are currently the poorly constrained nuclear matrix elements which mediate the decay process. These matrix elements have to be supplied by nuclear theory, which is challenged with the phenomena of nuclear shape evolution and shape coexistence that prevail in regions of the nuclear chart where most $0\nu\beta\beta$ decay candidates are located. A major problem is the lack of sensitive experimental data, which are required to fix the parameters of effective theories.

Based on a previous successful study, the nuclear structure of the candidate pairs $^{82}\text{Se}/^{82}\text{Kr}$ and $^{150}\text{Nd}/^{150}\text{Sm}$ was investigated in this work using the method of nuclear resonance fluorescence. The observables of interest were the decay channels of a low-lying collective nuclear excitation, the scissors mode, which are expected to be highly sensitive to the location of the candidate pairs in the phase diagram of nuclear shapes. The scissors mode can be studied selectively and with a high degree of model independence with the chosen method. The experiments were performed at the High-Intensity Gamma-Ray Source which currently provides the most intense, linearly polarized, quasi-monochromatic photon beam at the energies of interest. Using the high sensitivity of the polarized beam, magnetic dipole excitations, which are the manifestations of the scissors mode in even-even nuclei, were identified and their decay behavior was characterized. A known drawback of

experiments with monoenergetic photon beams, namely the lack of a photon-flux calibration, was solved in the present work without any additional instrumentation by calibrating the flux on the nonresonant scattering of photons on the targets. For this purpose, a detailed Monte-Carlo particle simulation application was developed.

For all nuclei of interest, decay branches on the order of few percent could either be observed, or constrained to such small values. Two effective nuclear models, the shell model and the interacting boson model, which are also frequently used to predict $0\nu\beta\beta$ decay matrix elements, were used for a preliminary interpretation of the data. For the nucleus ^{82}Se , the shell model gave a good description of the energies of excited 1^+ states and the total observed strength. The good agreement allowed for an interpretation of the structure of the wave functions of the scissors mode candidates, which advised against a simple relation between the measured quantities and the shape coexistence in that nucleus. For the higher-mass isotopes, a careful parameter adjustment in the framework of the interacting boson model was able to reproduce the entire low-energy structure of ^{150}Nd and, with minor exceptions also of ^{150}Sm . The new parameter sets in this model were used together with our collaborator to update previous predictions of nuclear matrix elements for $0\nu\beta\beta$ decay.

Note that the analysis of the data on the $A = 150$ nuclei was done by Jörn Kleemann. This work presents only his main results.

Zusammenfassung

Der neutrinolose doppelte Betazerfall ($0\nu\beta\beta$ -Zerfall) ist ein hypothetischer Prozess zweiter Ordnung in der schwachen Wechselwirkung, der, im Falle einer experimentellen Beobachtung, Neutrinos als das erste Beispiel von sogenannten Majorana-Teilchen identifizieren würde, welche ihre eigenen Antiteilchen sind. Außerdem würde es eine direkte Bestimmung der Neutrinomasse ermöglichen, da die Zerfallsrate für den $0\nu\beta\beta$ -Zerfall im direkten Zusammenhang mit der effektiven Masse des Elektron-Neutrinos steht. Ein Hindernis für die Planung von zukünftigen Experimenten, die nach dem $0\nu\beta\beta$ -Zerfall suchen, und für eine quantitative Bestimmung der Neutrinomasse sind momentan die nicht ausreichend eingeschränkten Kern-Matrixelemente die dem Zerfallsprozess innewohnen. Diese Matrixelemente müssen von der Kernstrukturtheorie bereitgestellt werden, die vor dem Problem der Beschreibung von Phänomenen wie der Entwicklung von Kerngestalten und der Koexistenz von Kerngestalten steht, welche in Regionen der Nuklidkarte vorherrschen, in denen auch die Kandidatenpaare für den $0\nu\beta\beta$ -Zerfall zu finden sind. Ein Hauptproblem ist der Mangel an aussagekräftigen experimentellen Daten, die benötigt werden um die freien Parameter von effektiven Theorien einzuschränken.

Basierend auf einer vorherigen Studie wurde die Kernstruktur der Kandidatenpaare $^{82}\text{Se}/^{82}\text{Kr}$ und $^{150}\text{Nd}/^{150}\text{Sm}$ in dieser Arbeit mit der Methode der Kernresonanzfluoreszenz untersucht. Zerfallskanäle einer niedrigliegenden, kollektiven Kernanregung, der Scherenmode, waren die wichtigen Observablen, denn sie sind erwartungsgemäß höchst sensitiv auf die Lage der Kandidatenpaare im Phasendiagramm der Kerngestalten. Mit der gewählten Methode kann die Scherenmode selektiv und mit einem hohen Grad an Modellunabhängigkeit untersucht werden. Die Experimente wurde an der High-Intensity Gamma-Ray Source durchgeführt,

die momentan im interessanten Energiebereich die intensivsten linear polarisierten quasi-monochromatischen Photonenstrahlen zur Verfügung stellt. Durch die hohe Sensitivität des polarisierten Strahls konnten magnetische Dipolübergänge, als welche sich die Scherenmode in gerade-gerade - Kernen manifestiert, identifiziert und ihr Zerfallsverhalten charakterisiert werden. Ein bekannter Nachteil von Messungen mit monoenergetischen Photonenstrahlen, der Mangel an Möglichkeiten zur Kalibrierung des Photonenflusses, wurde in der vorliegenden Arbeit dadurch umgangen, dass, ohne Zuhilfenahme weiterer Messaufbauten, der Photonenfluss anhand der nichtresonanten Streuung von Gammastrahlung an der Probe kalibriert wurde. Zu diesem Zweck wurde eine detaillierte Monte-Carlo Simulationsanwendung entwickelt.

Für alle betrachteten Kerne konnten Zerfallskanäle in der Größenordnung von wenigen Prozenten entweder beobachtet, oder auf solch kleine Werte eingeschränkt werden. Zwei effektive Kernmodelle, das Schalenmodell und das Modell wechselwirkender Valenzbosonen, die auch häufig benutzt werden um $0\nu\beta\beta$ - Zerfallsmatrixelemente vorherzusagen, wurden für eine vorläufige Interpretation der Daten benutzt. Das Schalenmodell lieferte eine gute Beschreibung der Anregungsenergien von 1^+ -Zuständen und der gesamten beobachteten Stärke für den Kern ^{82}Se . Die gute Übereinstimmung erlaubte eine Interpretation der Struktur der Wellenfunktionen der mutmaßlichen Scherenmodenfragmente, die jedoch gegen einen einfachen Zusammenhang zwischen den Messgrößen und der Koexistenz von Kerngestalten in diesem Kern spricht. Bei den Isotopen mit höherer Masse konnte eine sorgfältige Anpassung der Parameter des Modells wechselwirkender Valenzbosonen die gesamte Niederenergie-Kernstruktur von ^{150}Nd und, mit Abstrichen, auch die von ^{150}Sm reproduzieren. Die neuen Parametersätze für dieses Modell wurden in Zusammenarbeit mit unserer Kollaborateurin benutzt, um bisherige Vorhersagen von Kernmatrixelementen für den $0\nu\beta\beta$ -Zerfall auf den neusten Stand zu bringen.

Es wird angemerkt, dass die Analyse der Daten für die Kerne mit der Massenzahl 150 von Jörn Kleemann durchgeführt wurde. In dieser Arbeit werden lediglich seine Hauptergebnisse aufgeführt.

Epigraph

Aber noch schlimmer wurde es, wenn er auf die Wissenschaft zu sprechen kam, - an die er nicht glaubte. Er glaube nicht an sie, sagte er, denn es stehe dem Menschen völlig frei, an sie zu glauben oder nicht. Sie sei ein Glaube, wie jeder andere, nur schlechter und dümmer als jeder andere, und das Wort "Wissenschaft" selbst sei der Ausdruck des stupidesten Realismus, der sich nicht schäme, die mehr als fragwürdigen Spiegelungen der Objekte im menschlichen Intellekt für bare Münze zu nehmen oder auszugeben und die geist- und trostloseste Dogmatik daraus zu bereiten, die der Menschheit je zugemutet worden sei. Ob etwa nicht der Begriff einer an und für sich existierenden Sinnenwelt der lächerlichste aller Selbstwidersprüche sei? Aber die moderne Naturwissenschaft als Dogma lebe einzig und allein von der metaphysischen Voraussetzung, daß die Erkenntnisformen unserer Organisation, Raum, Zeit und Kausalität, in denen die Erscheinungswelt sich abspiele, reale Verhältnisse seien, die unabhängig von unserer Erkenntnis existierten. Diese monistische Behauptung sei die nackteste Unverschämtheit, die man dem Geiste je geboten.

Polemik der Figur Leo Naphta in
T. Mann, "Der Zauberberg", 1. Auflage, Fischer E-Books (2009)

1. Introduction

1.1. Neutrinoless Double-Beta Decay and Nuclear Structure

Recently, the experimental observations of two-neutrino double-beta ($2\nu\beta\beta$) decay [14] and double-gamma ($\gamma\gamma$) decay [15–17] have been complemented by two more nuclear decays which are mediated by the electroweak (EW) interaction at second order: the competitive version of $\gamma\gamma$ decay [18] and the two-neutrino double electron capture ($2\nu\text{ECEC}$) decay [19]. From the point of view of nuclear structure physics, the transition rates of these decays provide a quasi¹ model-independent access to nuclear matrix elements with the schematic structure [see, e.g. [21] ($2\nu\beta\beta$) [18] ($\gamma\gamma$), [22] ($2\nu\text{ECEC}$)],

$$\sum_n w_n(E_f - E_n, E_n - E_i, \dots) \langle f | \hat{O} | n \rangle \langle n | \hat{O}' | i \rangle, \quad (1.1)$$

which is unsurprisingly very similar to the expressions found in textbook-second-order perturbation theory (see, e.g., chapter XVI in [23]). In Eq. (1.1), the transition rate between the initial (i) and the final (f) state of the nuclear system is given by a sum over transition matrix elements of operators \hat{O} and \hat{O}' to intermediate states (n). The symbols w_n denote weighting factors which depend on the energy differences between the nuclear states and potentially also other variables. Accessing matrix elements like $\langle f | \hat{O} | n \rangle$ by direct reactions is challenging, and

¹There are non-negligible discrepancies between predictions of the phase-space factors in the EW theory (for $\beta\beta$ decay, see, e.g., [20]). But generally, the nuclear matrix elements are by far the most uncertain parameters. For $0\nu\beta\beta$ decay, this will be discussed below.

probably also model-dependent to a higher degree (see, e.g., the proposed experimental study of $\beta\beta$ -decay-analog matrix elements by double charge exchange reactions by the NUMEN project [24] and a related theoretical investigation [25]).

While the aforementioned decay processes are in agreement with the Standard Model of particle physics [26], the motivation for this work is the lepton-number violating process of neutrinoless double-beta ($0\nu\beta\beta$) decay. Recent review articles about the topic, on which the following introduction of $0\nu\beta\beta$ decay will be based, have been published by Vergados, Ejiri, and Šimković [27] (theory), and Avignone, Elliott, and Engel [28] (theory and experiment).

After a first theoretical study by Goepfert-Mayer on the possibility of a double-beta ($\beta\beta$) decay process [29], Racah proposed a 'neutrino capture after beta decay' [27] version as a test [30] of Majorana's theory of the neutrino [31]. The latter, as an alternative to the Dirac-Fermi theory of the neutrino [32], assumed that it was its own antiparticle. This would facilitate a 'true' (in addition to the sequential version of Racah [30]) $0\nu\beta\beta$ process as proposed later by Furry [33], based on [29]. Explicitly, the $\beta\beta$ -decay processes with and without emission of an electron antineutrino are denoted as [27]:

$${}^A_Z X \rightarrow {}^A_{Z+2} X' + 2e^- + 2\bar{\nu}_e \quad (1.2)$$

$${}^A_Z X \rightarrow {}^A_{Z+2} X' + 2e^- \quad (1.3)$$

In the neutrinoless version [Eq. (1.3)], the two neutrinos form a virtual connection in the Feynman diagram of the process, but do not appear as real particles (Fig. 2 in [28]).

In principle, $\beta\beta$ decay is possible for any situation where the binding energy $B({}^A_{Z+2} X'')$ of the nucleus ${}^A_{Z+2} X''$ is larger than the one of the nucleus ${}^A_Z X'$. From the experimental point of view, a situation is preferred where the two-step transition between these nuclei via single β decays is energetically forbidden, i.e.:

$$B({}^A_{Z+1} X) < B({}^A_Z X') < B({}^A_{Z+2} X'') \quad (1.4)$$

For a chain of even-even (ee), odd-odd (oo), or even-odd/odd-even (eo , oe) isobars, $B({}^A_Z X)$ is approximately proportional to $-Z^2$ in proximity of the valley of stability according to the semiempirical mass formula (see, e.g., Sec. 3.3. in [34] or [35]). Therefore, it is much more likely that Eq. (1.4) is fulfilled for a sequence of

ee/oo isobars, where the odd-even staggering due to the nuclear pairing force is superimposed on the Z dependence.

In this case, the half-life for $0\nu\beta\beta$ decay from a 0^+ ground state of an ee nucleus to a 0^+ state of the daughter nucleus is given by [27]².

$$\left[T_{1/2}^{(0\nu)}\right]^{-1} = G_{0\nu}(Q_{\beta\beta}, Z) \left|\frac{\langle m_\nu \rangle}{m_e}\right|^2 |M^{(0\nu)}|^2 \quad (1.5)$$

In Eq. (1.5), the symbol $G_{0\nu}$ denotes the integrated phase space factor, which takes into account the residual interaction of the two emitted electrons with the Coulomb field of the daughter nucleus. It depends on the proton number Z of the daughter nucleus and the Q value of the decay, $Q_{\beta\beta}$. For the assumed decay between 0^+ states, the two electrons are in an $s_{1/2}$ state, which makes the final result particularly simple³. In close analogy to the so-called Fermi theory [32] of single β decay, $G_{0\nu}$ can be approximated as [Eqs. (3.5.17a - 3.5.21) for light neutrinos using the 'Fermi factor' from (3.1.25, 3.1.26) [36]]:

$$\begin{aligned} G_{0\nu} \propto & \int d(\mathbf{p}_{e^-}^{(1)} \cdot \mathbf{p}_{e^-}^{(2)}) dE_{e^-}^{(1)} dE_{e^-}^{(2)} \times \delta \left\{ E_{e^-}^{(1)} + E_{e^-}^{(2)} - \overbrace{\left[M \left(\begin{smallmatrix} A \\ Z-2X \end{smallmatrix} \right) - M \left(\begin{smallmatrix} A \\ ZX'' \end{smallmatrix} \right) \right]}^{Q_{\beta\beta}} c^2 \right\} \\ & \times p_{e^-}^{(1)} p_{e^-}^{(2)} \left(2p_{e^-}^{(1)} R \right)^{2(\gamma_1-1)} \left(2p_{e^-}^{(2)} R \right)^{2(\gamma_1-1)} \\ & \times \frac{|\Gamma[\gamma_1 + iy^{(1)}]|^2 |\Gamma[\gamma_1 + iy^{(2)}]|^2}{\Gamma(2\gamma_1 + 1)^4} e^{\pi y^{(1)}} e^{\pi y^{(2)}} \end{aligned} \quad (1.6)$$

²Equation (1.5) assumes the annihilation of two left-handed light Majorana neutrinos, which is regarded as the 'most popular' mechanism by the authors of [27]. Other possibilities, like the exchange of right-handed or heavy neutrinos, some of which are not sensitive to the neutrino mass, are discussed in [27] as well. Nevertheless, all of them require nuclear structure input.

³The restriction to $0^+ \rightarrow 0^+$ transitions is a valid approximation for light neutrinos, which can be seen, e.g., by comparing the expressions for $0^+ \rightarrow 0^+$ and $0^+ \rightarrow 2^+$ transitions in [36]

$$\gamma_1 \equiv \sqrt{1 - (\alpha Z)^2} \quad (1.7)$$

$$y^{(i)} \equiv \alpha Z \frac{E_{e^-}^{(i)}}{p_{e^-}^{(i)} c} \quad (1.8)$$

In Eq. (1.6), $p_{e^-}^{(i)}$ and $E_{e^-}^{(i)}$ denote the linear momentum and the total energy of the i -th electron that is emitted in the decay. The symbol $M(\frac{A}{Z}X)$ denotes the mass of the nucleus $\frac{A}{Z}X$. For $0\nu\beta\beta$ decay, the difference of the rest energies of mother ($\frac{A}{Z-2}X$) and daughter ($\frac{A}{Z}X''$) nucleus, obtained from the rest masses by multiplication with the squared speed of light c , is equal to $Q_{\beta\beta}$ [indicated by a brace in Eq. (1.6)]. The symbol $\Gamma(z)$ denotes the gamma function. The integration contains a delta function δ , which ensures the conservation of energy. The symbol R denotes the radius of the daughter nucleus, which is assumed to be spherical with a well-defined boundary in this approximation [32], and the auxiliary symbols γ_1 and $y^{(i)}$ are defined by Eqs. (1.7) and (1.8). In the latter two equations, α denotes the fine-structure constant. For medium-mass and rare-earth nuclei, the factor γ_1 is on the order of unity, therefore the energy- and Z dependence of Eq. (1.6) is dominated by the exponential terms. Consequently, $G_{0\nu}$ is expected to vary strongly with Z , and also at low Q values which are on the order of the rest energy of the electron $m_e c^2$. This behavior is confirmed by realistic calculations with different levels of approximative character[20, 37]⁴. The discrepancy of different predictions is mostly less than 30% [20, 38], depending on the nucleus of interest. This gives an estimate of the accuracy of $G_{0\nu}$.

The second factor in Eq. (1.3) contains the ratio of the effective light neutrino mass in $0\nu\beta\beta$ decay [27],

$$\langle m_\nu \rangle = \sum_{k=1}^3 [U_{ek}^{(11)}]^2 m_k, \quad (1.9)$$

and the electron mass. In Eq. (1.9), the quantities $U^{(11)ek}$ are matrix elements of the experimentally well-investigated [2] Pontecorvo-Maki-Nakagawa-Sakata matrix, which connect the light neutrino mass eigenstates m_k to the flavor eigenstate ' e '

⁴The authors of Ref. [20] claim a more precise calculation than [37]. Nevertheless, [37] is mentioned here as well, since the publication contains predictions for a larger set of nuclei and phase space factors for decays to excited states.

of the electron neutrino [39]. Of course, an observation of $0\nu\beta\beta$ decay alone would have a enormous impact on contemporary physics. In addition, the factor $\langle m_\nu \rangle / m_e$ adds the hope that a measurement of $T_{1/2}^{(0\nu)}$ can be used to fix the currently unknown neutrino mass scale [27]. Due to the high interest in beyond-standard model physics, many groups around the world are searching for signals from $0\nu\beta\beta$ decay, using experimental setups with ever-increasing scale and finesse. For an overview of present and future efforts, see, e.g., a recent review article by Dolinski, Poon, and Rodejohann [40]. The currently highest lower limits at a 90% confidence level for several $0\nu\beta\beta$ -decay candidates are shown in Fig. 1.1.

The last factor in Eq. (1.3) is the nuclear matrix element (NME) $M^{(0\nu)}$, whose general structure was discussed at the beginning of this section (Eq. (1.1)). Since the most 'straightforward' access to $M^{(0\nu)}$ would be via the $0\nu\beta\beta$ decay itself (if $\langle m_{\beta\beta} \rangle$ was known) the NMEs have to be provided by nuclear theory at the moment, despite the ongoing experimental efforts on analog reactions (see, e.g., [24]). The NME is the quantity that connects the aforementioned exciting beyond-standard model physics to the main objective of this work, i.e. the nuclear structure of $0\nu\beta\beta$ decay candidates. In Sec. 1.1.1, a simplified model will be used to illustrate the influence of nuclear structure on $M^{(0\nu)}$. In Sec. 1.2, a summary of state-of-the-art realistic calculations for $M^{(0\nu)}$ will be presented.

1.1.1. A Simple Model: Hypothetical $0\nu\beta\beta$ Decay of the Dineutron

The main aspects of the interplay between nuclear structure - in particular quadrupole deformation - and $0\nu\beta\beta$ -decay will be illustrated by a simple model in this section⁵. It is mainly based on chapters 3, 4 and 13 of the textbook by Talmi [59].

The smallest system in which a $0\nu\beta\beta$ decay could occur is a two-nucleon system of protons (π) with an isospin quantum number of $t_z = +1/2$, and neutrons (ν) with $t_z = -1/2$. The corresponding two-nucleon systems are the $T_z = -1$ (dineutron),

⁵This section was motivated by the search of the author for a simple explanation of commonly quoted properties of the NMEs like 'the matrix element is large if the overlap of the wave functions of the initial and final state is large'. After finding Eqs. (34-36) in [28] and realizing that the approximated operator for $0\nu\beta\beta$ decay is actually relatively simple, it was decided to attempt a simple calculation from which this section originates. The reader may feel free to skip it.

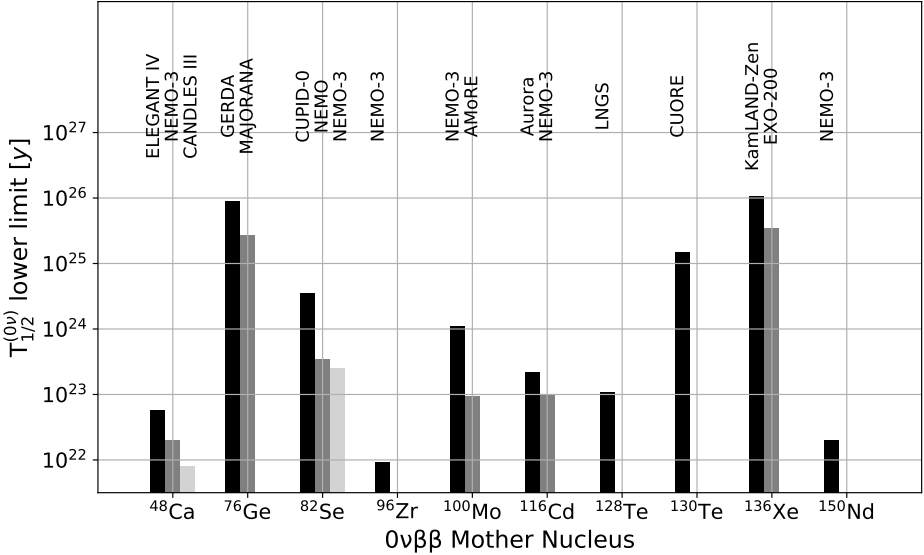


Figure 1.1.: Experimental limits (90% confidence interval) for the $0\nu\beta\beta$ -decay half life of different mother nuclei. For each mother nucleus, up to three bars indicate the current half-life limits. The experimental collaborations which published the results are indicated by labels on top of the bars. The limits are from [41–43] (^{48}Ca), [44, 45] (^{76}Ge), [46–48] (^{82}Se), [49] (^{96}Zr), [50, 51] (^{100}Mo), [52, 53] (^{116}Cd), [54] (^{128}Te), [55] (^{130}Te), [56, 57] (^{136}Xe), and [58] (^{150}Nd).

$T = 0$ (deuteron), and $T_z = 1$ (diproton) eigenstates of the total isopin operator \hat{T} . In the following, consider the hypothetical situation where both the diproton and the dineutron are more strongly bound than the deuteron. Furthermore, the diproton is assumed to be more strongly bound than the dineutron to facilitate a $\beta\beta$ decay ⁶.

⁶In reality, of course, the situation is quite adverse: The proton-neutron system (the deuteron) is

Defintion of Operators

For the two-nucleon system, the intrinsic quadrupole moment of a state i , which will be used as a measure of the quadrupole deformation in this section⁷, is given by (see, e.g., Appendix 'Electromagnetic Transitions and Moments' in [66]):

$$Q = \langle i | \sqrt{\frac{16\pi}{5}} [e_1 r_1^2 Y_{20}(\theta_1, \varphi_1) + e_2 r_2^2 Y_{20}(\theta_2, \varphi_2)] | i \rangle \quad (1.10)$$

In Eq. (1.10), $a = 1, 2$ are the single-particle indices. The quantities e_a actually denote the electric charges of the particles. To be able to assign a quadrupole moment to the nuclear matter distribution instead of the charge distribution (otherwise, the dineutron would always have a deformation of zero in this model), $e_\pi = e_\nu = 1$ will be used. The symbols r_a denote the single-particle position operators, which depend, in particular, on the polar- θ_a and the azimuthal angle φ_a in spherical coordinates. Both are arguments of the spherical harmonic Y_{20} .

In the two-nucleon system, the Fermi (F) and Gamow-Teller (GT) parts of the $0\nu\beta\beta$ decay operator, which are expected to be the dominant contributions, are approximately given by (Eqs. (34) and (35) in [28]):

$$\hat{O}_F^{(0\nu)} = H(r_{12}, \langle E \rangle) \hat{\tau}_1^+ \hat{\tau}_2^+ \quad (1.11)$$

$$\hat{O}_{GT}^{(0\nu)} = H(r_{12}, \langle E \rangle) (\hat{\sigma}_1 \cdot \hat{\sigma}_2) \hat{\tau}_1^+ \hat{\tau}_2^+ \quad (1.12)$$

In Eqs. (1.11) and (1.12), the symbols $\hat{\tau}_a^+$ denote the single-particle isospin raising operators, which convert neutrons into protons. The symbol $(\hat{\sigma}_1 \cdot \hat{\sigma}_2)$ denotes a scalar product of the two single-particle pauli matrices, which are proportional

indeed weakly bound with an energy of about 2.22 MeV [7]. On the other hand, the relatively large measured absolute values of the s-wave scattering lengths for the neutron-neutron (discrepant values of $a_{nn} = -18.63 \pm 0.10_{\text{stat.}} \pm 0.44_{\text{sys.}} \pm 0.30_{\text{theo.}}$ fm [60] and $a_{nn} = -16.06 \pm 0.35$ fm [61] coexist at the moment) and the proton-proton ($a_{pp} = -7.8063 \pm 0.0026$ fm [62]) system suggest that both systems are very weakly unbound. Due to the repulsive Coulomb interaction in the diproton, it can be expected to be less strongly bound than the dineutron. A recent theoretical investigation [63] even suggests that experimental results for a_{nn} can not exclude a very weakly bound system, since the experimental techniques are not sensitive to the sign of the scattering length.

⁷The deformation parameter β_2 from the collective model [64], which is often used to quantify the quadrupole deformation of a nucleus, is approximately proportional to the quadrupole moment at typical deformations of nuclei (see, e.g., the discussion of Eq. (6.9) in [65]).

to the spin operators $\hat{s}_a = \hbar/2\hat{\sigma}_a$. In the definition of \hat{s} , the symbol \hbar denotes the reduced Planck constant. The function $H(r_{ab}, \langle E \rangle)$, which appears in both operators, is the neutrino potential. It is approximately given by [Eq. (36) in [28]]:

$$\begin{aligned}
 H(r_{12}, \langle E \rangle) &\approx \frac{2R}{\pi r_{12}} \int_0^\infty d(qc) \frac{\sin(qr_{12}/\hbar)}{qc + \langle \Delta E \rangle} \\
 &= \frac{R}{\pi r_{12}} \{2\text{Ci}(\langle \Delta E \rangle r_{12}/\hbar c) \sin(\langle \Delta E \rangle r_{12}/\hbar c) \\
 &\quad + \cos(\langle \Delta E \rangle r_{12}/\hbar c) [\pi - \text{Si}(\langle \Delta E \rangle r_{12}/\hbar c)]\}
 \end{aligned} \tag{1.13}$$

$$\langle \Delta E \rangle \equiv \langle E \rangle - (E_i + E_f)/2 \tag{1.14}$$

In Eq. (1.13), r_{ab} denotes the distance between two nucleons a and b . The quantity $\langle \Delta E \rangle$, defined in Eq. (1.14), is the difference between the average energy $\langle E \rangle$ of excited states in the intermediate nucleus ${}^A_{Z+1}X'$ and the mean value of the energies of the initial (E_i) and final (E_f) state of the $0\nu\beta\beta$ decay of the nuclei A_ZX and ${}^A_{Z+2}X''$, respectively. Actually, a sum over all intermediate state of the nucleus ${}^A_{Z+1}X'$ would have to be performed (Eq. (24) in [28]), but their energies are often replaced by an effective value $\langle E \rangle$. This is the so-called closure approximation [see, e.g., Eq. (25) in [28] and [67, 68] for recent theoretical investigations]. The neutrino potential has been multiplied by the nuclear radius R to make it dimensionless. In the second equality of Eq. (1.13), the integration over the momentum variable qc has been executed, resulting in an expression that includes the sine- and cosine integrals $\text{Si}(x)$ and $\text{Ci}(x)$.

While the neutrino potential in Eq. (1.13) depends on the distance of the nucleons r_{12} , the quadrupole moment in Eq. (1.10) requires the knowledge of the single-nucleon wave functions. A model for which the transition between both representations of the same total wave function is very simple is the harmonic oscillator (HO). The Hamiltonian for the two-nucleon system is given by [see, e.g.,

Eq. (13.1) in [59]]:

$$\hat{H}_{\text{HO}} = \underbrace{\frac{1}{2m_1}\hat{p}_1^2 + \frac{1}{2}m_1\omega^2\mathbf{r}_1^2}_{\hat{H}_{\text{HO},1}} + \underbrace{\frac{1}{2m_2}\hat{p}_2^2 + \frac{1}{2}m_2\omega^2\mathbf{r}_2^2}_{\hat{H}_{\text{HO},2}} \quad (1.15)$$

In Eq. (1.15), \hat{p}_a denotes the momentum operator for particle a , and m_a its mass. In the scope of this problem, the masses of the proton and the neutron will be assumed to be equal: $m_p = m_n \equiv m$, in particular also $m_1 = m_2 = m$. Both quantities appear in the single-particle kinetic energy operator \hat{k}_a , whose definition is indicated by the innermost braces. The symbol ω denotes the oscillator frequency, multiplied by 2π . Equation (1.15) is the form of \hat{H}_{HO} where the independence of the motion of the two particles is most evident, because it is a sum of two single-particle Hamiltonians, as indicated by the outermost braces. An equivalent formulation of the problem in terms of an independent motion of the center-of-mass (COM) and the intrinsic (INT) two-nucleon system is possible [see, e.g., Eqs. (13.2) and (13.3) in [59]]:

$$\hat{H}_{\text{HO}} = \underbrace{\frac{1}{4M}\hat{P}^2 + \frac{1}{2}M\omega^2\mathbf{R}^2}_{\hat{H}_{\text{HO,COM}}} + \underbrace{\frac{1}{2\mu}\hat{p}_{12}^2 + \frac{1}{2}\mu\omega^2\mathbf{r}_{12}^2}_{\hat{H}_{\text{HO,INT}}} \quad (1.16)$$

In Eq. (1.16), the symbols \hat{P} and \mathbf{R} denote the momentum operator and the position of the center-of-mass, respectively. The symbols \hat{p}_{12} and \mathbf{r}_{12} denote the relative momentum operator and the distance vector between the two particles, respectively. The symbols $M = 2m$ and $\mu = m/2$ denote the total- and the reduced mass of the system. Two braces indicate the independent center-of-mass- and intrinsic parts of the Hamiltonian.

Wave Functions

For any of the independent systems, the eigenstates of the Hamiltonian are given by [see, e.g., Eq. (3.7) and (4.3) in [59]]:

$$\begin{aligned}\psi_{nlm_l}(r, \theta, \varphi) &= \frac{1}{r} R_{nl}(r) Y_{lm_l}(\theta, \varphi) \\ &= N_{nl} r^l \exp(-\nu r^2) L_{n-1}^{l+1/2}(2\nu r^2) Y_{lm_l}(\theta, \varphi).\end{aligned}\quad (1.17)$$

In Eq. (1.17), the vector \mathbf{r} and its components r , θ and φ may be replaced by \mathbf{r}_1 , \mathbf{r}_2 , \mathbf{r}_{12} , or \mathbf{R} from Eqs. (1.15) and (1.16). The wave function ψ_{nlm_l} depends on the angular momentum quantum number l , its projection on the z axis m_l , and the number of nodes n of the radial wave function R_{nl} . The radial wave function includes a normalization factor N_{nl} [Eq. (4.3) in [59]] and the associated Laguerre polynomials L_k^α . To simplify the notation, the quantity

$$\nu = \frac{\mu\omega}{2\hbar}\quad (1.18)$$

has been introduced, which can be interpreted as half the squared oscillator length. In Eq. (1.18), the symbol μ may be replaced by any of m , μ , and M which corresponds to the choice of the position vector. The angular part of the wave function is given by the 3D spherical harmonics Y , which depend on the quantum numbers l and m_l . The eigenvalues of the harmonic oscillator are [Eq. (4.5) in [59]]:

$$E_{nl} = \left[2(n-1) + l + \frac{3}{2} \right] \hbar\omega = \left(N + \frac{3}{2} \right) \hbar\omega\quad (1.19)$$

In Eq. (1.19), the principal quantum number N has been introduced.

It is now assumed that the spatial dynamics of both the dineutron and the diproton are given by Eqs. (1.15) and (1.16). Furthermore, it is implicitly assumed that the energetic prerequisites for $0\nu\beta\beta$ decay [Eq. (1.4)] are fulfilled⁸. The aim is to study the impact of nuclear structure on $0\nu\beta\beta$ decay by calculating nuclear matrix elements between initial and final two-nucleon states. The lowest-lying states of $\hat{H}_{\text{HO,INT}}$ in Eq. (1.16) for the $T_z = \pm 1$ systems are given by 1^1s_0 and the triplet 2^3p_0 ,

⁸This can be achieved, for example, by introducing artificial, isovector terms in the Hamiltonian that depend on powers of T_z .

2^3p_1 , and 2^3p_2 in the spectroscopic notation $n^{2S+1}l_J$. Using the symbols ψ_{nlm_l} for the spatial-, χ_{SS_z} for the spin-, and ξ_{TT_z} for the isospin wave function, their total wave functions Ψ are given by (only the $J = 0$ states are shown):

$$|\Psi(1^1s_0)\rangle = \psi_{100}(\mathbf{R})\psi_{100}(\mathbf{r}_{12}) \times \chi_{00} \times \xi_{1(\pm 1)} \quad (1.20)$$

$$\begin{aligned} |\Psi(2^3p_0)\rangle &= \frac{1}{\sqrt{3}}\psi_{100}(\mathbf{R})\psi_{211}(\mathbf{r}_{12}) \times \chi_{1(-1)} \times \xi_{1(\pm 1)} \quad (1.21) \\ &\quad - \frac{1}{\sqrt{3}}\psi_{100}(\mathbf{R})\psi_{210}(\mathbf{r}_{12}) \times \chi_{10} \times \xi_{1(\pm 1)} \\ &\quad + \frac{1}{\sqrt{3}}\psi_{100}(\mathbf{R})\psi_{21(-1)}(\mathbf{r}_{12}) \times \chi_{11} \times \xi_{1(\pm 1)} \end{aligned}$$

In Eqs. (1.20) and (1.21), it was assumed that the center-of-mass motion remains in the $1s$ state. The numerical factors and phases in Eq. (1.21) are the usual Clebsch-Gordan coefficients (see, e.g., chapter 44 in [2] for tabulated values) for the coupling of angular momentum $l = 1$ and spin $S = 1$ to $J = 0$. The spatial wave functions for the $1s$ and $2p$ states can be expanded in single-particle wave functions [compare Eq. (13.10) and (13.11) in [59]]:

$$\psi_{100}(\mathbf{R})\psi_{100}(\mathbf{r}_{12}) = \psi_{100}(\mathbf{r}_1)\psi_{100}(\mathbf{r}_2) \quad (1.22)$$

$$\psi_{100}(\mathbf{R})\psi_{21m_l}(\mathbf{r}_{12}) = \frac{1}{\sqrt{2}} [\psi_{100}(\mathbf{r}_1)\psi_{21m_l}(\mathbf{r}_2) - \psi_{21m_l}(\mathbf{r}_1)\psi_{100}(\mathbf{r}_2)] \quad (1.23)$$

The '-' sign on the right-hand side of Eq. (1.23) is required since the wave function on the left-hand side is antisymmetric.

Quadrupole Deformation

For the calculation of the quadrupole moments of the $1s$ and $2p$ states, it is evident from the definition in Eq. (1.10) that only the spatial part of the wave functions plays a role. Furthermore, since the quadrupole operator is separable in the same way as ψ_{nlm_l} , the matrix element is a product of integrals over the radial part (r_a^2) and the angular part Y_{20} . For a single harmonic-oscillator wave function, the

integral over the radial part only depends on the principal quantum number [Eq. (4.10) in [59]]:

$$\langle \psi_{nlm_l} | r_a^2 | \psi_{nlm_l} \rangle = \frac{1}{2\nu} \left(N + \frac{3}{2} \right). \quad (1.24)$$

Note that Eq. (1.24) defines the mean square radius. As already implied by Eq. (1.24) for the angular part, any J_z substate can be selected due to the Wigner-Eckart theorem for spherical tensor operators [see, e.g., chapter 8 of [59], in particular Eqs. (8.4) and (8.15)], and the matrix elements evaluate to:

$$\langle \psi_{nlm_l} | Y_{20} | \psi_{nlm_l} \rangle = (2l+1) \sqrt{\frac{5}{4\pi}} \begin{pmatrix} l & 2 & l \\ 0 & 0 & 0 \end{pmatrix}^2. \quad (1.25)$$

Eq. (1.25) contains a Wigner 3- j symbol, which vanishes for $l = 0$ and evaluates to $\sqrt{2/15}$ for $l = 1$. Consequently, the quadrupole moments of the physical states in Eqs. (1.20)/(1.22) and (1.21)/(1.23) are (using the shorter, basis-independent notation $\psi_{nlm_l}(\mathbf{r}_1)\psi_{n'l'm'_l}(\mathbf{r}_2) \rightarrow \langle \psi_{nlm} | \langle \psi_{n'l'm'_l} |, | \psi_{nlm} \rangle | \psi_{n'l'm'_l} \rangle$):

$$Q(1^1s_0) \propto \langle \psi_{100} | Y_{20} | \psi_{100} \rangle = 0 \quad (1.26)$$

$$\begin{aligned} Q(2^3p_0) \propto & \left(\langle \psi_{100} | \langle \psi_{211} | - \langle \psi_{211} | \langle \psi_{100} | - \langle \psi_{100} | \langle \psi_{210} | + \langle \psi_{210} | \langle \psi_{100} | \right. \\ & + \langle \psi_{100} | \langle \psi_{21(-1)} | - \langle \psi_{21(-1)} | \langle \psi_{100} | \\ & \times (\mathbf{r}_1^2 Y_{20}(\theta_1, \varphi_1) + \mathbf{r}_2^2 Y_{20}(\theta_2, \varphi_2)) \\ & \times (| \psi_{100} \rangle | \psi_{211} \rangle - | \psi_{211} \rangle | \psi_{100} \rangle - | \psi_{100} \rangle | \psi_{210} \rangle + | \psi_{210} \rangle | \psi_{100} \rangle \\ & \left. + | \psi_{100} \rangle | \psi_{21(-1)} \rangle - | \psi_{21(-1)} \rangle | \psi_{100} \rangle \right) \\ \propto & 2 \int d\Omega (Y_{11} Y_{20} Y_{11} + Y_{10} Y_{20} Y_{10} + Y_{1(-1)} Y_{20} Y_{1(-1)}) \\ & > 0 \end{aligned} \quad (1.27)$$

In the second step of Eq. (1.27), vanishing off-diagonal matrix elements have been neglected, and the equivalent integrations over Ω_1 and Ω_2 have been summed. Equations (1.26) and (1.27) show that the restriction to the first two states of the system was sufficient to study the influence of quadrupole deformation on the NME, since the s state is spherical and the p state has a finite quadrupole moment.

Nuclear Matrix Elements

For a qualitative analysis of the NMEs the isospin-, spin-, and spatial part (in this order) can be considered separately due to the absence of couplings between the subspaces in the $0\nu\beta\beta$ -decay operators [Eqs. (1.20) and (1.21)]. Firstly, the isospin part can be neglected, since its action is always the same, turning the $\nu\nu$ system into a $\pi\pi$ system:

$$\hat{\tau}_1^+ \hat{\tau}_2^+ |1, -1\rangle \propto |1, +1\rangle \quad (1.28)$$

Concerning the spin-part of the wave function, only the Gamow-Teller part of the $0\nu\beta\beta$ -decay operator [Eq. (1.12)] contains a spin-dependent factor $\hat{\sigma}_1 \hat{\sigma}_2$. The wave functions χ_{SS_z} are eigenfunctions of this operator, which can be seen by rewriting it in the following way:

$$\begin{aligned} (\hat{\sigma}_1 \hat{\sigma}_2) |\chi_{SS_z}\rangle &= 4\hbar^2 (\hat{s}_1 \hat{s}_2) |\chi_{SS_z}\rangle = \\ 2\hbar^2 (\hat{S}^2 - \hat{s}_1^2 - \hat{s}_2^2) |\chi_{SS_z}\rangle &= \begin{cases} -3\hbar^2, & S = 0 \\ 1\hbar^2, & S = 1 \end{cases} \end{aligned} \quad (1.29)$$

In the last equality of Eq. (1.29), the eigenvalues for the two possibilities of parallel ($S = 1$) and antiparallel ($S = 0$) spins have been evaluated. This means that neither the Fermi- (a simple identity operator), nor the Gamow-Teller part of the $0\nu\beta\beta$ -decay operator connect states with different spin alignments, in particular not the $1s$ and $2p$ states. Note that this is a consequence of the extremely simple LS coupling in the two-body system that was considered here, where a given value of J can be traced back unambiguously to L and S . Nevertheless, it can be anticipated for systems with more than two particles that transitions between states with a large number of $S = 0$ -nucleon pairs, i.e. in particular ground states of even-even nuclei (see also Sec. 2.2.2), are enhanced.

At last, consider the spatial part of the NME. Obviously, the neutrino potential in Eq. (1.13) only depends on the distance r_{12} of two nucleons. Therefore, it can immediately be concluded from the orthogonality of the spherical harmonics [see,

e.g., chapter 3 in [59]):

$$\int_0^{2\pi} d\varphi \int_0^\pi d\theta Y_{lm}^* Y_{l'm'} = \delta_{ll'} \delta_{mm'}, \quad (1.30)$$

that matrix elements between different l vanish. Since the type of deformation is encoded in the contributions of different spherical harmonics to a given state, this means that $0\nu\beta\beta$ decay favors transitions between similar shapes. This makes the process susceptible to phenomena like shape-phase transitions along a chain of nuclei [69] and shape coexistence [70, 71] within a single nucleus, both of which will be discussed in Sec. 1.2.

While the spherical harmonics are related to the type of deformation, the radial wave functions can be a measure of the degree of deformation. For the harmonic oscillator wave functions, this can be seen from the mean square radius in Eq. (1.24), which increases monotonously with the principal quantum number. The distance dependence of the neutrino potential $H(r_{12}, \langle\Delta E\rangle)$ in Eq. (1.13) is shown in part (a) of Fig. 1.2 for realistic values of $\langle\Delta E\rangle$. Since it is nonnegative for all values of r_{12} , $H(r_{12})$ can be interpreted as an (unnormalized) weighting factor in integrals of the type

$$N_{nl}N_{n'l'} \int_0^r dr_{12} R_{nl} H_{12} R_{n'l'}, \quad (1.31)$$

which favors small distances between nucleons. The lower three panels of Fig. 1.2 show the normalized radial probability density $N_{nl}^2 R_{nl}^2 r^{-2}$ for different low-lying eigenstates of the two-body system. In addition, the value of the integral in Eq. (1.31) is shown, which is asymptotic for $r \rightarrow \infty$ due to the exponential decay of the integrand [see Eq. (1.17)]. It can be seen that the radial integrals in the NMEs for $0\nu\beta\beta$ decay are largest for small nuclear deformations, i.e. configurations for which the average distance between nucleons is minimized. The factor $\langle\Delta E\rangle$ has a significant, but uniform impact on all the integrals.

Based on the findings in the previous paragraphs, a simple study of the effects of shape evolution [69] can be performed: Assume that both the ground states of the dineutron $\Psi_{\nu\nu}^{(0)}$ and the diproton $\Psi_{\pi\pi}^{(0)}$ are superpositions of the two lowest-lying

$J = 0$ states 1^1s_0 and 2^3p_0 ⁹:

$$|\Psi_{nn}^{(0)}\rangle = \sqrt{1-\beta_{nn}}|1^1s_0\rangle + \sqrt{\beta_{nn}}|2^3p_0\rangle \quad (1.32)$$

$$0 \leq \beta_{nn} \leq 1 \quad (1.33)$$

In Eq. (1.32), the index nn may stand for either $\nu\nu$ or $\pi\pi$. A parameter β_{nn} , suggestively named like the nuclear deformation parameter, has been introduced to control the mixing of the $1s$ and $2p$ states. According to Eqs. (1.26) and (1.27), the admixture of a $2p$ component in the ground state introduces a finite quadrupole deformation:

$$Q(\Psi_{nn}^{(0)}) \propto \beta_{nn} \quad (1.34)$$

The NME for $0\nu\beta\beta$ -decay between the states in Eq. (1.32) consists of matrix elements of the type:

$$\begin{aligned} M^{(0\nu)} &= \langle \Psi_{\pi\pi}^{(0)}(\beta_{\pi\pi}) | \hat{\mathcal{O}}^{(0\nu)} | \Psi_{\nu\nu}^{(0)}(\beta_{\nu\nu}) \rangle = \quad (1.35) \\ &= \left[\sqrt{1-\beta_{\pi\pi}} \langle 1^1s_0 | + \sqrt{\beta_{\pi\pi}} \langle 2^3p_0 | \right] \hat{\mathcal{O}}^{(0\nu)} \left[\sqrt{1-\beta_{\nu\nu}} | 1^1s_0 \rangle + \sqrt{\beta_{\nu\nu}} | 2^3p_0 \rangle \right] = \\ &= \sqrt{1-\beta_{\pi\pi}} \sqrt{1-\beta_{\nu\nu}} \langle 1^1s_0 | \hat{\mathcal{O}}^{(0\nu)} | 1^1s_0 \rangle \\ &+ \sqrt{1-\beta_{\pi\pi}} \sqrt{\beta_{\nu\nu}} \langle 1^1s_0 | \hat{\mathcal{O}}^{(0\nu)} | 2^3p_0 \rangle \\ &+ \sqrt{\beta_{\pi\pi}} \sqrt{1-\beta_{\nu\nu}} \langle 2^3p_0 | \hat{\mathcal{O}}^{(0\nu)} | 1^1s_0 \rangle \\ &+ \sqrt{\beta_{\pi\pi}} \sqrt{\beta_{\nu\nu}} \langle 2^3p_0 | \hat{\mathcal{O}}^{(0\nu)} | 2^3p_0 \rangle = \\ &= \sqrt{1-\beta_{\pi\pi}} \sqrt{1-\beta_{\nu\nu}} \langle 1^1s_0 | \hat{\mathcal{O}}^{(0\nu)} | 1^1s_0 \rangle + \sqrt{\beta_{\pi\pi} \beta_{\nu\nu}} \langle 2^3p_0 | \hat{\mathcal{O}}^{(0\nu)} | 2^3p_0 \rangle. \end{aligned}$$

The last equality in Eq. (1.35) follows from the fact that the off-diagonal matrix elements vanish due to Eqs. (1.29) and (1.30). The symbol $\hat{\mathcal{O}}^{(0\nu)}$ may stand for the Fermi- or the Gamow-Teller part of the complete $0\nu\beta\beta$ -decay operator [Eq. (33) [28]]:

$$\hat{\mathcal{O}}_{\text{F+GT}}^{(0\nu)} = \hat{\mathcal{O}}_{\text{GT}}^{(0\nu)} - \left(\frac{g_V}{g_A} \right)^2 \hat{\mathcal{O}}_{\text{F}}^{(0\nu)} \quad (1.36)$$

⁹An operator that mixes states of equal J must be introduced in the Hamiltonian to create such a situation. For example, in Sec. 7.1 of Casten's textbook [65] where the deformed (Nilsson) shell model is introduced, an anisotropic oscillator potential [Eq. (7.2) therein] can be used for this purpose.

In Eq. (1.36), the Fermi part is scaled by the squared ratio of the vector- and axial-vector coupling constants g_V/g_A of the weak interaction, which has a numerical value of about $(g_V/g_A)^2 \approx 0.61$ [4].

The dependence of the matrix elements in Eq. (1.35) for $\hat{O}^{(0\nu)} = (g_V/g_A)^2 \hat{O}_F^{(0\nu)}$ and $\hat{O}^{(0\nu)} = \hat{O}_{GT}^{(0\nu)}$ on the mixing parameters $\beta_{\nu\nu}$ and $\beta_{\pi\pi}$ is shown in part (a) and (b) of Fig. 1.2, respectively. Due to the scaling by the eigenvalues of the operator $(\hat{\sigma}_1 \hat{\sigma}_2)$ [Eq. (1.29)] and the factor $(g_V/g_A)^2$ in front of the Fermi part, the Gamow-Teller matrix elements show a much larger variation over the parameter space. The opposite signs of the $1s$ - and $1p$ matrix elements in Eq. (1.35), which are a consequence of the different spin alignments, cause a cancellation of the matrix elements for strongly mixed configurations. The absolute values of the NMEs are largest for similar, pure configurations of the mother- and daughter nucleus. In part (c) of Fig. 1.3, the NME, i.e. the squared absolute value of the sum of part (a) and (b) is shown. Its general dependence on $\beta_{\nu\nu}$ and $\beta_{\pi\pi}$ is similar to the dominating Gamow-Teller component. The accelerated change of the NME towards pure configurations and $\beta_{\nu\nu} \approx \beta_{\pi\pi}$ suggests that the NMEs will be highly sensitive to shape evolution, which may occur suddenly or gradually via first- or second-order phase transitions [72, 73].

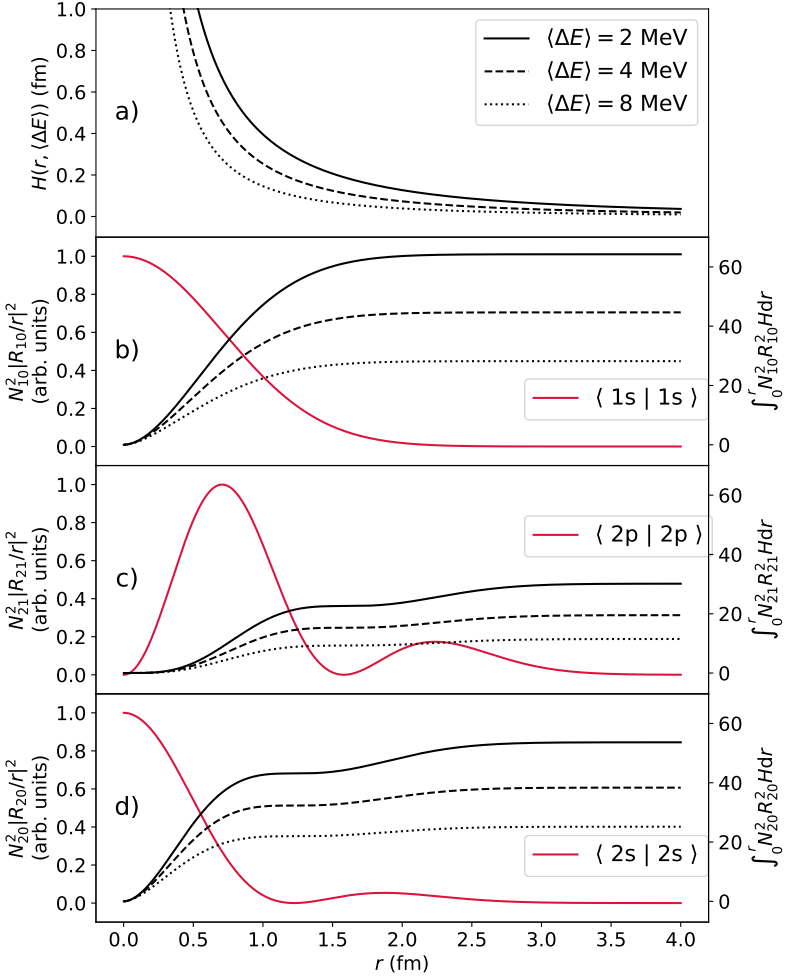


Figure 1.2.: (a): Distance dependence of the neutrino potential H in the $0\nu\beta\beta$ -decay operator for different values of $\langle\Delta E\rangle$ and $R = 1$ fm [Eqs. (1.11) - (1.14)]. (b – d): Probability density of the nucleon-nucleon distance r for a $1s$ -, $2p$ -, and $2s$ harmonic oscillator wave function with $\nu = 1$ fm in red (left ordinate), and the corresponding radial integral over the neutrino potential [Eq. (1.31)] in the same line styles as part (a) [right ordinate with identical scale for (b – d)].

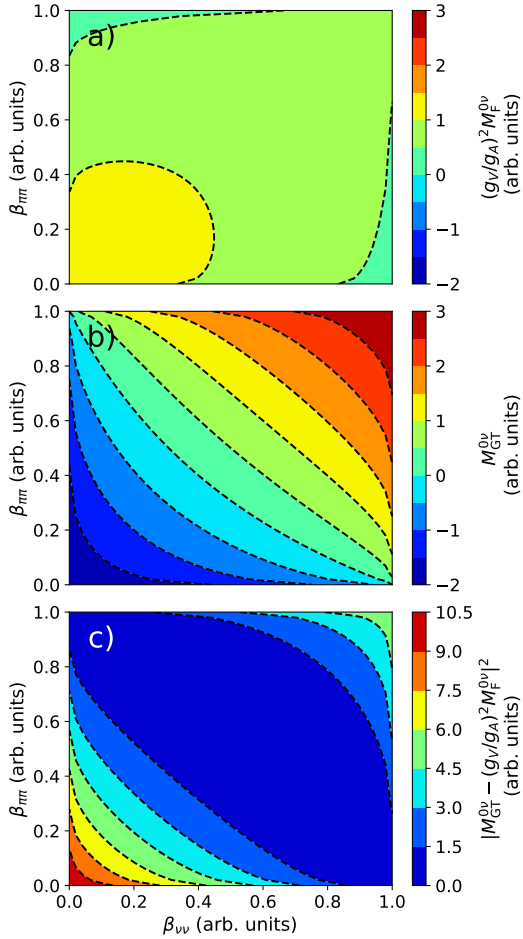


Figure 1.3.: Dependence of matrix elements of the Fermi- (a) and Gamow-Teller part (b) of the NME on the mixing parameters $\beta_{\nu\nu}$ and $\beta_{\pi\pi}$ in the two-nucleon model of Sec. 1.1.1. The former is multiplied by a factor of $(g_v/g_A)^2$ according to Eq. (1.36). To obtain parts (a) and (b), Eq. (1.35) was evaluated for $0 \leq \beta_{\nu\nu}, \beta_{\pi\pi} \leq 1$. The distance of the contour lines is the same for (a) and (b). Part (c) shows the squared absolute value of the total NME. The parameters $\beta_{\nu\nu}$ and $\beta_{\pi\pi}$ are correlated with the $2p$ admixture, i.e. proportional to the quadrupole deformation.

1.2. Current State of Nuclear Structure Input

Section 1.1 ended with the problem of the determination of the NME $M^{(0\nu)}$ from nuclear theory. Using a simple model, general properties of the NME were studied in Sec. 1.1.1. It turns out that these properties are reproduced by microscopic models for actual $0\nu\beta\beta$ -decay candidates. As an example, compare a calculation of the nuclear structure impact of deformation on the $0\nu\beta\beta$ decay between ^{150}Nd and ^{150}Sm within the framework of energy-density functional theory by Rodríguez and Martínez-Pinedo [74] (see also [75]) in Fig. 1.4 to the schematic calculation in Fig. 1.3. The preference for decay between similarly deformed, in particular weakly deformed, structures is apparent.

With the deformation parameters of Fig. 1.4 fixed by their experimental values, the authors of Ref. [74] also give predictions for the $0\nu\beta\beta$ -decay NME. Since their calculation implicitly contained more parameters and model assumptions (see, e.g. [76, 77] about the density functional that was used in [74]), the question about the accuracy and precision of theoretical NMEs arises. Obviously, there are no measurements to validate the calculated NMEs. Therefore, an estimate of the predictive power must be obtained by comparing the predictions of different models. The top part of Fig. 1.5 shows a compilation of predicted NMEs by various effective theories of nuclear structure from a review article by Engel and Menéndez [21]. From this comparison, it can be seen that the uncertainty of the NMEs is much larger than the one of the phase space factors (see Sec. 1.1). To obtain the bottom part of Fig. 1.5, Eq. (1.5) was solved for the product $T_{1/2}^{(0\nu)}| \langle m_\nu \rangle |^2$ to give an estimate of the impact of the NMEs on actually observable quantities. The predictions, which have an impact on the planning of future $0\nu\beta\beta$ searches and the extraction of meaningful information about the neutrino (Sec. 2.3 in [21]), vary by more than an order of magnitude at first glance. However, the predictions by different models are obviously correlated. It is evident that they could be brought into better agreement, at lowest order, by a simple multiplication with a constant factor. This is due to known deficiencies of the models, like the restriction to a valence space in the shell model and IBM, or the overestimation of pairing correlations in quasiparticle models (see Sec. 3.6 in [21]). Nevertheless, a systematic uncertainty inherent in all models is the general overprediction of weak decay rates. This problem, the so-called 'quenching' of the bare axial-vector coupling constant g_A (see Sec. 4 in [21]), was identified by comparison to experimental data on β - and

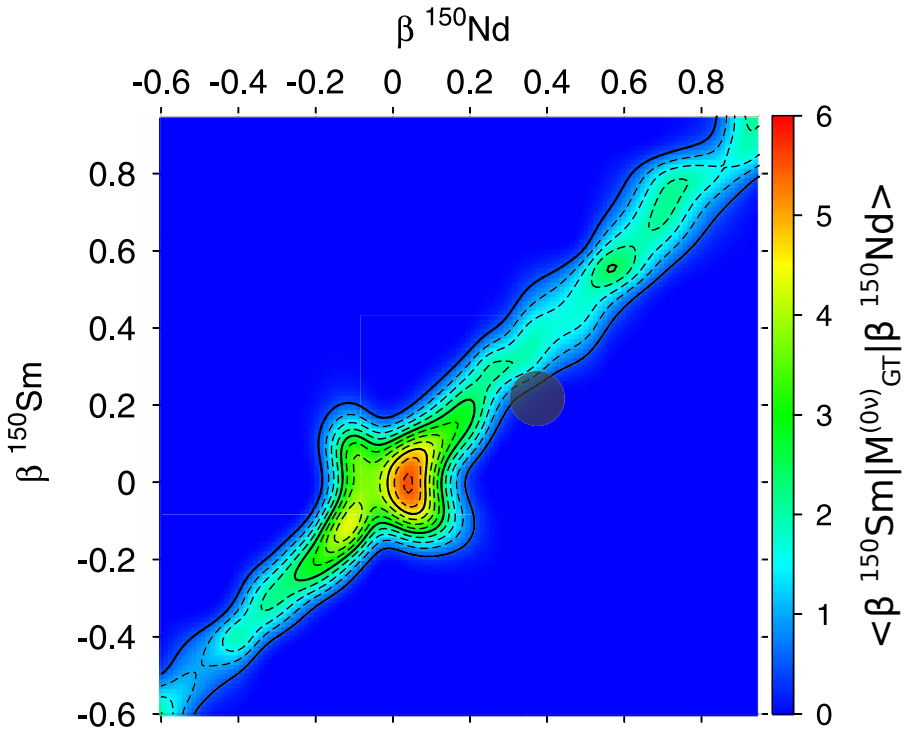


Figure 1.4.: Strength of the Gamow-Teller part of the $0\nu\beta\beta$ -decay operator as a function of the deformation (measured by the usual deformation parameter β) of the initial and final states of the nuclei ^{150}Nd and ^{150}Sm . Result of a realistic theoretical calculation within the framework of energy density functional theory. The right-hand ordinate indicates symbolically the matrix element whose absolute magnitude is indicated by the color code. A dark dot in the figure indicates the most probable deformations of both isotopes as returned by the model. Reprinted and modified figure with permission from [74] Copyright (2010) by the American Physical Society.

$2\nu\beta\beta$ decay (see Sec. 3.1 and 4 in [21]). The observed quenching of $M1$ strength for electromagnetic transitions of nuclei (see, e.g., Sec. V.C.2 in [5] or Sec. V.D.1 in [89]) has the same origin, summarized as 'quenching of spin matrix elements' in a review article by Towner [90]. From a microscopic point of view, quenching is caused mainly by the renormalization of transition operators (see also Secs. 2.3 and 2.2.2) and meson-exchange/two-body currents between nucleons [90].

Modern ab-initio theory (see, e.g., a review article by Epelbaum, Hammer, and Meißner [91]) does not suffer from the quenching problem [92], and calculations have been performed for nuclei as heavy as ^{100}Sn (ibid., and [93]). The many-body methods are, however, restricted to nuclei in proximity of shell closures at the moment [94, 95]. Except for ^{48}Ca , for which an ab-initio description is possible [96, 97], the isotopes of interest for $0\nu\beta\beta$ decay studies are at least 6 nucleons/nucleon holes away from doubly magic nuclei, as can be seen in Fig. 1.6. In addition, many of them are located in regions of the chart of nuclides where collective behavior and phase transitions between spherical and deformed shapes are expected to occur (black ellipses in Fig. 1.6). For the description of these phenomena, effective models are invaluable [73] (in particular Sec. III therein), but they require precise and unambiguous experimental data to constrain their free parameters and benchmark their predictions (see Sec. VI.C in [28]). For example, there has recently been a lot of $0\nu\beta\beta$ -decay related experimental effort to study the low-energy structure of $^{76}\text{Ge}/^{76}\text{Se}$ [102–106]¹⁰, since germanium is one of the most promising materials for $0\nu\beta\beta$ -decay detection (see Fig. 1.1).

The present work concentrates on the $0\nu\beta\beta$ -decay candidate pairs $^{82}\text{Se}/^{82}\text{Kr}$ and $^{150}\text{Nd}/^{150}\text{Sm}$. The former is motivated by recent progress [68] in the framework of the nuclear shell model towards large-scale calculations based on realistic interactions [101], and beyond the closure approximation (see Sec. 1.1.1). Furthermore, due to pioneering work in the operation of cryogenic calorimeters [107], the CUPID-0 collaboration was able to improve the half-life limit for the $0\nu\beta\beta$ decay of ^{82}Se by one order of magnitude [46] compared to previous results [47]. Note that CUPID-0 is a prototype for the planned large-scale CUPID experiment, which aims to be competitive with highest currently reported limits for other isotopes [108, 109]. The motivation for the investigation of the pair $^{150}\text{Nd}/^{150}\text{Sm}$ is its favorable $0\nu\beta\beta$ half-life, which is predicted to be about an order of magnitude lower than the ones for ^{76}Ge and ^{136}Xe (see Fig. 1.5), which hold the current

¹⁰The five publications are taken from the most recent of them, i.e. [106].

records for half-life upper limits (see Fig. 1.1). It should be noted that several of the calculations presented in Fig. 1.5 do not take into account an additional decay branch to the 0_2^+ state of ^{150}Sm , which is predicted [110] to lead to a further significant reduction of the half-life. From the structural point of view, the stable even-even Nd and Sm isotopes are collective nuclei in the vicinity of a shape phase transition, which are known to be described well by the interacting boson model [111]. In particular, ^{150}Nd is a textbook realization [112] of the $X(5)$ critical-point symmetry [113] for the transition between spherical and rotational nuclei.

Leading experts in the field, in a workshop on "Nuclear matrix elements for neutrinoless double beta decay" in 2005 [114] (see also Sec. VI.C in [28]), recommended to perform charge exchange- [24, 115], nucleon transfer- [116]¹¹, muon capture- [117] and neutrino-nucleus scattering [118] experiments. These reactions, in combination with β^- , $2\nu\beta\beta^-$, and $2\nu\text{ECEC}$ decay studies, were found to be the most sensitive to $0\nu\beta\beta$ -decay related matrix elements. The authors of [114] also emphasize the importance of deformation for $0\nu\beta\beta$ decay, which was discussed above. In the present work, it was decided to employ the nuclear resonance fluorescence method (see Sec. 2.1) to study the structure of $^{82}\text{Se}/^{82}\text{Kr}$ and $^{150}\text{Nd}/^{150}\text{Sm}$. Compared to the experimental methods mentioned above, the involved matrix elements are less closely related to $0\nu\beta\beta$ decay. However, the experiments are more straightforward, and observables of interest can be extracted with a high degree of model independence. The focus was on decay channels of a low-lying collective dipole excitation, the so-called scissors mode, which are sensitive to the deformation and the coexistence of shapes in an atomic nucleus (see Sec. 2.3). The experimental study of this work is based on pioneering work by Beller *et al.* [110].

¹¹The given review article by Wimmer is more focused on experiments with radioactive beams. See also references therein.

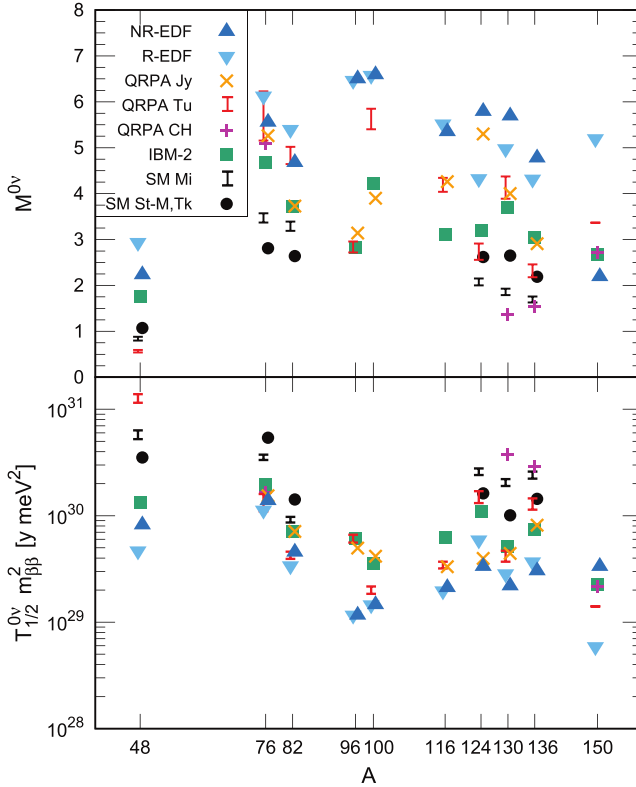


Figure 1.5.: (Top) Predictions of NMEs $M^{0\nu}$ for the $0\nu\beta\beta$ decay of different isotopes. The displayed calculations were performed in nonrelativistic ('NR-EDF' [78]) and relativistic ('R-EDF' [79, 80]) energy density functional theory, quasiparticle random-phase approximation ('QRPA Jy' [81], 'QRPA Tu' [82, 83], 'QRPA CH' [84]), the interacting boson model ('IBM-2' [85]), and the shell model ('SM Mi' [86], 'SM St-M, Tk' [87, 88]). All predictions used a bare g_A . Some of them have given uncertainty estimates from a variation of the interaction. (Bottom) Corresponding predictions of the product of the $0\nu\beta\beta$ decay half life $T_{1/2}^{0\nu}$ and the unknown effective neutrino mass $m_{\beta\beta}$. Figure from [21] (Fig. 5 therein). Reproduced with permission of IOP Publishing in the format Thesis/Dissertation via Copyright Clearance Center.

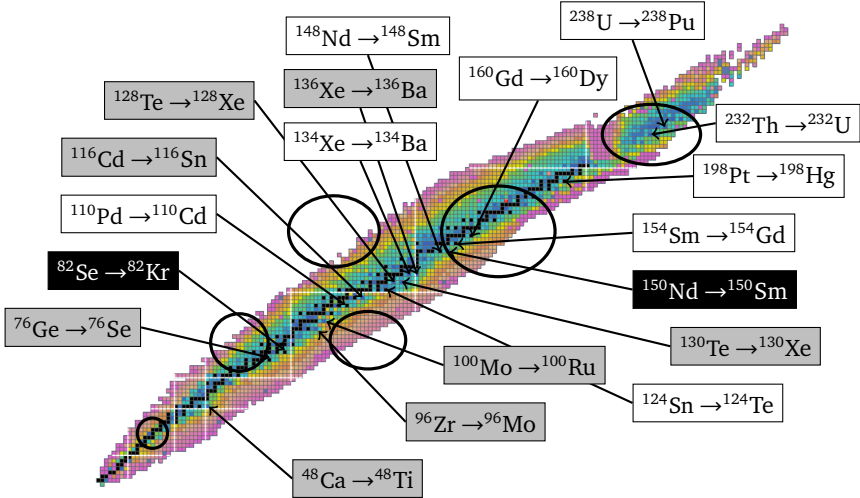


Figure 1.6.: Candidates for $0\nu\beta\beta$ decay on the chart of nuclides. The chart, which was taken from [98] and modified, shows all known isotopes with the neutron number on the abscissa and the proton number on the ordinate. Different colors correspond to different ranges of the isotopic lifetimes. Stable nuclei are shown in black. For better orientation, the classical magic numbers at 8, 20, 28, 50, 82, and 126 [99, 100] are indicated by white lines. Midshell regions, where nuclei are expected to be deformed in their ground states, are indicated by black circles in analogy to Fig. 2.1 in the nuclear structure textbook of Casten [65]. Compared to the latter figure, another circle has been added in the pf shell ($Z \geq 28$ and $28 \leq N \leq 50$) to indicate the region where the phenomena of shape coexistence and triaxial deformation appear [101]. The set of $0\nu\beta\beta$ decay candidates is from [85]. For pairs of isotopes that are shown in gray or black, dedicated experiments in search for their $0\nu\beta\beta$ decay have been or are still ongoing. The black-labeled isotopes are the main objective of this work.

1.3. Outline

The present work is structured as follows:

This introduction is followed by an overview of the relevant formalism (Sec. 2). 'Formalism' includes a discussion of the experimental method of nuclear resonance fluorescence (Sec. 2.1), the theoretical frameworks of the shell- and the interacting boson model (Secs. 2.2.1 and 2.2.2), and the nuclear structure phenomenon of interest (Sec. 2.3).

The following section (Sec. 3) describes the High-Intensity γ -Ray Source, where all experiments of this work were performed (Sec. 3.1), the experimental setups (Sec. 3.2), and the dedicated experiments (Secs. 3.3 and 3.4).

In the 'Analysis' section (Sec. 4), the processing of the experimental data (spectra) is described. The section starts with general information about the treatment of uncertainty and parameter estimation (Sec. 4.1). After that, the Monte-Carlo simulation framework which was used for the analysis is introduced (Sec. 4.2). The remaining sections give a detailed description and examples for all relevant analysis steps.

Results for the observed transitions of $^{82}\text{Se}/^{82}\text{Kr}$ and $^{150}\text{Nd}/^{150}\text{Sm}$ are presented in Sec. 5.

A discussion of selected results can be found in Sec. 6. In particular, the origin of the observed magnetic dipole strength in the $A = 82$ nuclei will be discussed. Furthermore, updated predictions of NMEs for the $0\nu\beta\beta$ decay of ^{150}Nd , based on the improved data, will be given (Sec. 6.2).

The main body of this work concludes with a summary and an outlook (Sec. 7).

2. Background

This section introduces the experimental technique of nuclear resonance fluorescence (NRF) that was used to study the low-energy nuclear structure of the $0\nu\beta\beta$ decay candidates. Furthermore, two theoretical models will be discussed which were used to interpret the experimental results. At last, the nuclear scissors mode will be introduced with a focus on its relation to nuclear shapes.

2.1. Nuclear Resonance Fluorescence

The most recent review article about NRF and the application to nuclear structure studies, which was used as a guideline for this section, was published by Kneissl, Pitz, and Zilges [119]. A historical review article on the topic, which is more focused on the technique itself, was published by Metzger [120].

2.1.1. General Properties

Resonance fluorescence, in particular N-RF $[(\gamma, \gamma')]$, is the interaction of a system with discrete bound states (the nucleus) and the quantized EM radiation field (see, e.g. [121], in particular chapter V, §20 therein). In other terms, it is the resonant absorption of a real photon by a nucleus, which leaves the nucleus in an excited state, and the subsequent emission of potentially multiple photons in the de-excitation process [119].

The mechanism has the advantage that the (nuclear) transition matrix elements between bound states can be clearly separated from the well-known EM part of

the reaction [see Eq. (2.4), or chapter V, §20 in [121] for a detailed derivation], facilitating a model-independent determination of the former. In this sense, the extraction of certain matrix elements is more straightforward over a large range of excitation energies and target proton numbers than for EM-mediated processes which involve the Coulomb scattering of charged elementary ([122], in particular chapter 4.2 therein) or nuclear [123] particles, since they eventually need to take into account the distortion of the projectile's wave function by the target (see, e.g. [124] for electron scattering or [125] for high-energy heavy-ion scattering).

Another advantage for the present study is the high selectivity of NRF to electric (E1) and magnetic (M1) dipole excitations. This can be anticipated from single-particle ('Weisskopf') estimates (chapter XII.6.A in [13]) for the EM transition rates between SM states, which decrease by orders of magnitude when the multipole order L increases¹. The suppression of magnetic character compared to electric character, which is also predicted by these estimates, is balanced by the collectiveness of the M1 scissors mode [89] which is of main interest in this work.

To demonstrate the main disadvantage of the NRF method, it is instructive to compare the relative magnitude of the energy-'integrated' cross sections for elastic photon scattering [Eq. (2.4) with $i = k$] and inelastic electron scattering [(e, e')] for low momentum transfer [Eq. (4-15a) in [122]], given a particular reduced M1 transition width $B(M1)$ [Eq. (2.6)] to an excited state at a typical energy for a fragment of the scissors mode [89] of $E_j = 3$ MeV. Neglecting all factors which are on the order of unity for a favorable choice of the target nucleus and experimental kinematics, i.e. branching ratios, J - and L -dependent factors, and recoil corrections, the energy-integrated cross sections are approximately:

$$\frac{dI}{d\Omega_{(\gamma, \gamma')}} \approx \frac{8\pi}{\lambda_{i \rightarrow j}^3} B(M1)W(\theta, \varphi) \approx 10^{-6} \text{ fm}^{-1} \times B(M1)W(\theta, \varphi) \quad (2.1)$$

$$\begin{aligned} \frac{d\sigma}{d\Omega_{(e, e')}} &= \int_{E_j - \Delta E/2}^{E_j + \Delta E/2} \frac{d\sigma}{d\Omega dE}(E) dE \approx \frac{d\sigma}{d\Omega dE}(E_0) \Delta E \\ &\approx \frac{\alpha^2}{\hbar c} B(M1) \Delta E V_T(\theta) \approx 10^{-13} \text{ fm}^{-1} \times B(M1) V_T(\theta) \end{aligned} \quad (2.2)$$

¹The lowest multipole order $L = 0$, however, is forbidden for transitions involving a single real photon, because due to their masslessness, the angular momentum of photons must always be a nonzero integer number (see, e.g. appendix 1 in [121]).

In Eq. (2.2), the symbol $V_T(\theta)$ denotes a scattering-angle dependent function which is on the same order of magnitude as $W(\theta, \varphi)$ (Eq. (2.11)) for certain scattering angles. It is assumed that the cross section is approximately constant over the integration range ΔE . Setting $\Delta E = 1$ eV, which is a typical width of a Doppler-broadened nuclear resonance [120] and definitely fulfils the aforementioned assumption, a numerical value for comparison with the NRF value is obtained. Equations (2.1) and (2.2) suggest that, given particle beams with similar intensities, the reaction rate in NRF should be orders of magnitude higher than in (e, e') . However, this naive estimate neglects that NRF is a resonant process, i.e. only photons with an energy in the range of the resonance can excite it. Typical photon beam performances (particles per time and energy interval) at 3 MeV are on the order of $10^2 \text{ s}^{-1} \text{ eV}^{-1}$ [126] for bremsstrahlung-generated photons and $10^4 \text{ s}^{-1} \text{ eV}^{-1}$ [127] for laser Compton-backscattered (LCB) photons. On the other hand, electrons with any energy larger than the resonance energy can in principle excite it. Therefore, a typical electron beam current of $20 \mu\text{A}$ and a spectral width of few keV [126], i.e. a particle current of 10^{14} s^{-1} , more than compensates the difference between Eqs. (2.1) and (2.2). Similar arguments can be applied for the scattering of nuclear particles. These instrumental restrictions must be overcome by increased target masses (possible due to the strong penetration power of gamma-rays [128]) and measuring times, which restrict NRF to stable, and sufficiently abundant isotopes [119].

Depending on the observable of interest, NRF experiments are also complicated by the large photonic background that is caused by nonresonant atomic scattering processes on the target or the beamline (see also Sec. 4.2 for a more detailed discussion). At energies of few MeV of the present experiment, the Compton effect is the dominant source of nonresonant background (see, e.g., chapter 2.III in [129], in particular Fig. 2.18). The cross section for Compton scattering, evaluated at a scattering angle of 90° for simplicity and integrated over the energy in analogy to Eq. (2.2), is given by (ibid.):

$$\frac{d\sigma}{d\Omega_{\text{Compton}}}(90^\circ) \approx \frac{1}{2} Z \alpha^2 \left(\frac{\hbar c}{m_e c^2} \right)^2 \frac{x^2 + x + 1}{(x + 1)^3} \Delta E \approx 10^{-3} \text{ eVfm}^2 \times Z \quad (2.3)$$

In Eq. (2.3), the symbol x is an abbreviation for the ratio of the initial photon energy, and the electron rest energy, i.e. $x = E_j/m_e c^2$. Considering that typical values of $B(M1)$ in Eqs. (2.1) and (2.2) for low-lying collective $M1$ strength are

on the order of $1 \mu_{\text{N}}^2 \equiv 1.6 \times 10^4 \text{ eVfm}^3$ [89], NRF still seems to dominate. But again, any photon in the beam spectrum can be Compton-scattered, so indeed the number of nonresonantly scattered photons will dominate the event rate in an NRF experiment with currently available beams. This is different for the scattering of massive, charged, and comparably highly energetic particles, where the main sources of background are not alternative scattering processes, but radiative corrections, especially for the light electrons (chapter 1.2 in [122])².

At last, an important difference to the aforementioned techniques is that NRF does not measure the excitation directly. A photoabsorption cross section derived from an NRF experiment will only resemble the 'true' cross section if all branching transitions to lower-lying excited states are known or can be excluded [see Eq. (2.4)]. Especially in recent discussions about low-lying electric dipole strength, this was identified as a serious issue [130]. The direct branching transitions are expected at lower energies where the intensity of the nonresonant background increases approximately exponentially (see spectra of this work in Sec. D), which prevents a firm constraint of single channels even if the ground-state transitions can be identified unambiguously [131]. A model-independent way to overcome this problem is the usage of the NRF-based self-absorption technique (for an introduction to the technique, see [120], for experimental applications see, e.g. [132, 133]). Ultimately, the model-independence of NRF can be sacrificed to take into account unobserved branching transitions by various assumptions which are summarized in [134].

For the present study, the comparably straightforward access to branching ratios and multipole mixing ratios [see Eq. (2.10)] and the selectivity to dipole excitations were seen as important advantages of NRF. Since several NRF cross sections of low-lying dipole excited states were already known from previous studies [135–137], the limited access to absolute cross sections in experiments with quasi-monochromatic photons could be partially compensated. Furthermore, a recently developed model-dependent method for the relative and absolute calibration of the beam photon flux was successfully applied (see Sec. 4.5.4). An access to absolute photoabsorption cross sections was found to be of minor importance, since the information about the relevant structure is contained in the branching ratios. Thus,

²For completeness, it should also be mentioned that the possibility of a coincident detection of different particle types, which of course complicates the experiment, is an invaluable technique to reduce experimental background.

the investment into large amounts of enriched materials and weeks of experiments for an NRF experiment were found to be worthwhile.

2.1.2. Formalism

In the following, consider the process in which a real photon is resonantly absorbed by a nucleus which is in an intrinsic state i (most probably the ground state, denoted as '0'). The absorption leaves the nucleus in an excited state j , from which it decays to a lower-lying state k via emission of another photon. Although it is emphasized here that 'another' photon is emitted, the process is often denoted as 'photon scattering' [119] in analogy to actual scattering experiments. The energy-integrated differential cross section for this process is [119]³:

$$\frac{dI_{i \rightarrow j \rightarrow k}}{d\Omega} d\Omega = \pi^2 \underbrace{\left(\frac{\hbar c}{E_j - E_i} \right)^2}_{\lambda_{i \rightarrow j}^2} \underbrace{\frac{2J_j + 1}{2J_i + 1}}_{g_{i \rightarrow j}} \underbrace{\Gamma_{i \rightarrow j} \frac{\Gamma_{j \rightarrow k}}{\Gamma_j}}_{\text{br.}} \frac{W_{i \rightarrow j \rightarrow k}(\theta, \varphi, \delta_{i \rightarrow j}, \delta_{j \rightarrow k}, P_\gamma)}{4\pi} d\Omega. \quad (2.4)$$

In Eq. (2.4), the excitation energies and angular momentum quantum numbers of the states of the nucleus are denoted as E_i and J_i , respectively. The quantities $\Gamma_{i \rightarrow j}$ and $\Gamma_{j \rightarrow k}$ denote the partial transition widths for the excitation- ($i \rightarrow j$) and the decay transition ($j \rightarrow k$), respectively, whose relation to the total width Γ_j of the state j will be discussed below. The symbol $W_{i \rightarrow j \rightarrow k}(\theta, \phi, \delta_{i \rightarrow j}, \delta_{j \rightarrow k}, P_\gamma)$ denotes the angular distribution of the emitted photon in the transition from state j to k for the given sequence of states, which also depends on the multipole mixing ratios $\delta_{i \rightarrow j}$ and $\delta_{j \rightarrow k}$ of the excitation ($i \rightarrow j$) and the decay ($j \rightarrow k$), and the polarization P_γ of the photon used for the excitation (see below)⁴. It is normalized to 4π and can be integrated out trivially in Eq. (2.4), resulting in the total cross section $I_{i \rightarrow j \rightarrow k}$ for the process, which is indicated by the lowermost brace. The next-to lowest

³Ref. [119] explicitly gives the cross section for the excitation from the ground state ($i \equiv 0$), but this assumption is not necessary (see, e.g. chapter V, §17 and §20 in [121]).

⁴The dependence of the angular distribution on the multipole mixing ratios and the polarization of the beam will often not be shown explicitly in other sections for the sake of brevity.

brace indicates the definition of the total cross section $I_{i \rightarrow j}$ for photoabsorption from state i to j which differs from $I_{i \rightarrow j \rightarrow k}$ by the branching ratio (br.) $\Gamma_{j \rightarrow k}/\Gamma_j$ for the subsequent decay to the state k . Equation (2.4) can be simplified further by introducing the definition of the reduced wavelength $\lambda_{i \rightarrow j}$ of the excitation photon, and the 'spin factor' [119] $g_{i \rightarrow j}$ which takes into account combinatorially the J_z substates of the initial and final states in the excitation transition.

The total transition width Γ_j is related to the lifetime τ_j of the state j via [119]:

$$\Gamma_j = \frac{\hbar}{\tau_j}. \quad (2.5)$$

It is the sum of partial transition widths for all possible decay channels [119]:

$$\Gamma_j = \sum_{k \in K} \Gamma_{j \rightarrow k} = \sum_{k \in K} \sum_{L=|J_j - J_k|}^{J_j + J_k} \Gamma_{j \rightarrow k, \sigma L} \quad (2.6)$$

In Eq. (2.6), K is assumed to be the set of all lower-lying states which can be populated from state j . If all partial widths $\Gamma_{j \rightarrow k}$ are assumed to be due to EM transitions⁵, they can be further decomposed into partial widths $\Gamma_{j \rightarrow k, \sigma L}$ for the different multipole orders $L_{i \rightarrow j}$ ⁶ and corresponding EM characters σ . According to the EM selection rules [Eq. (2.12) and (2.15) in chapter XII.2.B [13]], the following combinations of σ and L are allowed for a given transition from j to k :

$$|J_j - J_k| \leq L_{j \rightarrow k} \leq J_j + J_k \quad (2.7)$$

$$\sigma_{j \rightarrow k} = \begin{cases} E, & \pi_j \pi_k = (-1)^{(L+1)} \\ M, & \pi_j \pi_k = (-1)^L \end{cases}. \quad (2.8)$$

⁵Since the beam energies of the present experiment are much lower than the particle separation thresholds of the nuclei of interest [138, 139], decays of photoexcited states by particle emission can be neglected. On the other hand, even the lowest beam energy of 2.4 MeV is high enough that the alternative process of the emission of a conversion electron from a dipole-excited state is negligible. This can be seen from estimates similar to the Weisskopf estimates from Sec. 2.1.1 (chapter XII.5.A in [13]).

⁶The index of L , which indicates the corresponding transition, will only be used if the initial and final state are not clear from the context.

The first selection rule, Eq. (2.7), which corresponds to the conservation of angular momentum, limits the possible values for the momentum transferred by/to a photon. The second selection rule, Eq. (2.8), determines the EM character based on the parity quantum numbers π_j and π_k of the initial and final states of the transition.

The partial transitions widths are related to the nuclear matrix elements of EM transition operators [119]:

$$\Gamma_{j \rightarrow k, \sigma L} = 8\pi \frac{L+1}{L[(2L+1)!!]^2} \lambda_{j \rightarrow k}^{-(2L+1)} g_{k \rightarrow j} \underbrace{\frac{1}{2J_j+1} |\langle \Psi_k || \hat{\mathbf{O}}_{\sigma L} || \Psi_j \rangle|^2}_{\substack{B(\sigma L; j \rightarrow k) \\ B(\sigma L; k \rightarrow j)}} \quad (2.9)$$

In Eq. (2.9), the reduced probability $B(\sigma L; j \rightarrow k)$ for the transition $j \rightarrow k$, which is indicated by the inner braces, has already been expanded to show its relationship to the reduced matrix element of the EM multipole operator $\hat{\mathbf{O}}_{\sigma L}$ (see, e.g., the appendix 'Electromagnetic Transitions and Moments' in [66] where also explicit expressions for the EM operators can be found). From the definition of the reduced probability for decay [$B(\sigma L; j \rightarrow k)$] it can be seen that it differs from the one for excitation [$B(\sigma L; k \rightarrow j)$] by the factor $g_{k \rightarrow j}$. The definition of the latter is indicated by the outer braces in Eq. (2.9).

As indicated by the triangle inequality for L in Eq. (2.7), a transition between two states may include multiple multipolarities. The relative magnitude of one multipole order (σL) and the next-higher one [$\sigma' L' = \sigma'(L+1)$] with different EM character ($\sigma' \neq \sigma$) is quantified by the multipole mixing ratio (here in the convention of Krane, Steffen and Wheeler [12]):

$$\delta_{L,i \rightarrow j}^2 = \frac{\Gamma_{i \rightarrow j, \sigma'(L+1)}}{\Gamma_{i \rightarrow j, \sigma L}} = \frac{L(L+2)}{(L+1)^2(2L+3)^2} \lambda_{i \rightarrow j}^{-2} \frac{B[\sigma'(L+1)]}{B(\sigma L)} \quad (2.10)$$

The angular distribution for the two-step process in Eq. (2.4) can be expanded in terms of Legendre polynomials P_ν and unnormalized associated Legendre polyno-

mials P_ν^μ [119]⁷:

$$\begin{aligned}
 W_{i \rightarrow j \rightarrow k}(\theta, \varphi, \delta_{i \rightarrow j}, \delta_{j \rightarrow k}, P_\gamma) &= W_{i \rightarrow j \rightarrow k, \text{unpolarized}}(\theta, \delta_{i \rightarrow j}, \delta_{j \rightarrow k}) \\
 &\quad (\pm)_{L'_{i \rightarrow j}} P_\gamma(E_\gamma) W_{i \rightarrow j \rightarrow k, \text{polarized}}(\theta, \varphi, \delta_{i \rightarrow j}, \delta_{j \rightarrow k}) \\
 &= \sum_{\nu \in \{0, 2, 4\}} A_\nu \left(J_i J_j L_{i \rightarrow j} L'_{i \rightarrow j} \delta_{L, i \rightarrow j} \right) \\
 &\quad \times A'_\nu \left(J_k J_j L_{k \rightarrow j} L'_{k \rightarrow j} \delta_{L, k \rightarrow j} \right) \\
 &\quad \times P_\nu[\cos(\theta)] \quad (2.11) \\
 (\pm)_{L'_{i \rightarrow j}} P_\gamma(E_\gamma) \sum_{\nu \in \{2, 4\}} &A'_\nu \left(J_i J_j L_{i \rightarrow j} L'_{i \rightarrow j} \delta_{L, i \rightarrow j} \right) \\
 &\quad \times A'_\nu \left(J_k J_j L_{k \rightarrow j} L'_{k \rightarrow j} \delta_{L, k \rightarrow j} \right) \\
 &\quad \times P_\nu^{(2)}[\cos(\theta)] \cos(2\varphi)
 \end{aligned}$$

Eq. (2.11) consists of two terms. The first term, $W_{\text{unpolarized}}(\theta)$ denotes the angular distribution for the excitation by an unpolarized photon beam. It depends on the polar angle θ with respect to the direction of propagation of the incoming photon beam. The second term, $W_{\text{polarized}}(\theta, \varphi)$ affects the angular distribution for a nonzero polarization of the beam, quantified by the photon-beam energy (E_γ)-dependent polarization factor P_γ with $|P_\gamma| \leq 1$. It introduces a dependence on the azimuthal angle φ , which is the angle with respect to the electric field vector \vec{E} of the photon beam, i.e. the polarization axis. The symbol $(\pm)_{L'_{i \rightarrow j}}$ indicates that the sign of the polarization term is positive (negative) for an electric (magnetic) character of the alternative multipolarity of the excitation transition $i \rightarrow j$. The expansion coefficients A_ν and A'_ν , which depend on the sequence of angular momenta and

⁷Kneissl, Pitz and Zilges [119] assume that no larger momentum transfer than $L = 2$ occurs. This also imposes the restriction that no more than 2 multipoles may be mixed in a single transition. In accordance with the expected dominance of low multipoles (see Sec. 2.1.1), and since only dipole- and quadrupole transitions are relevant in this work, the same equations are given here. The most general formalism can be found in [12].

the corresponding EM multipoles, can be found in [12].

2.2. Nuclear Structure Models

This section introduces the nuclear shell model (SM) and the proton-neutron version of the the interacting boson model (IBM, or IBM-2 for the π - ν version), both of which were employed in this work to describe the structure of the $0\nu\beta\beta$ -decay candidate pairs $^{82}\text{Se}/^{82}\text{Kr}$ and $^{150}\text{Nd}/^{150}\text{Sm}$. A review article on the SM was published by Caurier, Martínez-Pinedo, Nowacki, Poves, and Zuker [5], while for the IBM, the textbook by Iachello and Arima [140] is usually cited. The models will be motivated as subsequent approximations of the full A -body problem.

2.2.1. Shell Model

The introduction of the SM approximation follows a recent review article by Coraggio, Covello, Gargano, Itaco, and Kuo [141] (in particular Sec. 3 therein), which is more specialized than [5]. It starts from a general Hamiltonian H of the A -body system:

$$\hat{H} = \sum_a \underbrace{\frac{\hat{P}_a^2}{2m}}_{\hat{k}_a} + \sum_{a<b} \hat{V}_{ab}^{2N}. \quad (2.12)$$

Equation (2.12) contains single-particle kinetic energy terms \hat{k}_a , and a two-body potential \hat{V}_{ab}^{2N} .

⁸As in Ref. [141], three-nucleon and higher-order interactions have been neglected here. They can be taken into account approximately by using phenomenological effective one- and two-body interactions, (see, e.g., Sec. 5.3.4 in [141]). In any case, the impact on excitation energies is expected to be small for three-nucleon forces (ibid.) compared to the impact on binding energies, while higher-order forces are not even expected to influence the latter significantly (see, e.g., the derivation of $4N$ forces in χ EFT [142] and a recent numerical investigation [143]).

Now, a one-body operator \hat{U} is introduced by inserting a zero in Eq. (2.12) [Eq. (9) in [141]]:

$$\hat{H} = \underbrace{\sum_a \hat{k}_a + \hat{U}_a}_{\hat{H}_{\text{mean}}} + \underbrace{\sum_{a<b} \hat{V}_{ab}^{2N} - \sum_a \hat{U}_a}_{\hat{H}_{\text{resi}}}. \quad (2.13)$$

The assumption behind \hat{U} is that, due to the nature of the nucleon-nucleon force⁹, all nucleons experience an effective mean-field \hat{H}_{mean} in which they move independently from each other. Residual nucleon-nucleon correlations are taken into account by \hat{H}_{resi} , which is assumed to be a comparably small perturbation. The eigenstates of \hat{H}_{mean} , defined by

$$\hat{H}_{\text{mean}}|\Phi_i\rangle = E_{\text{mean},i}|\Phi_i\rangle, \quad (2.14)$$

can be used as basis states to expand the solutions of the A -body system:

$$\hat{H}|\Psi_i\rangle = E_i|\Psi_i\rangle, \quad (2.15)$$

$$|\Psi_i\rangle = \sum_j \langle\Phi_j|\Psi_i\rangle|\Phi_j\rangle. \quad (2.16)$$

In Eqs. (2.14) and (2.15), the symbols E_i denote the energy eigenvalues of the eigenstates of the mean-field (Φ_i) and the total (Ψ_i) Hamiltonian.

Another assumption of the shell model is that the eigenstates of \hat{H}_{mean} can be grouped in sets ('shells'/orbitals') which are separated by their excitation energies from each other. As long as the excitation energies are small compared to the separation energy between different shells, the most strongly bound A_c nucleons will remain in the A_c lowest orbitals and can be treated as an inert core. Therefore, the A -body problem in the full space can be reduced to an $A - A_c = A_v$ problem in the 'valence' space using the projection operator \hat{P}_v [Eq. (12) in [141]]:

$$\hat{P}_v = \sum_{i \in V} |\Phi_{v,i}\rangle \langle\Phi_{v,i}|. \quad (2.17)$$

⁹See, e.g., phenomenological introductions to the SM by Casten in Sec. II.3 of [65] or Otsuka in Sec. 4.1 of [144]

In Eq. (2.17), the symbol V denotes the set of valence-space basis states $\Phi_{v,i}$. They are defined as [Eq. (10) in [141]]:

$$\Phi_{v,i} = \left[\hat{a}_{v,1}^\dagger \hat{a}_{v,2}^\dagger \dots \hat{a}_{v,A_v}^\dagger \right] |c\rangle \quad (2.18)$$

In Eq. (2.18), the symbols $\hat{a}_{v,j}^\dagger$ denote creation operators for single-particle states in the valence space, which are coupled to produce a basis state with the label 'i' (where i is assumed to contain all quantum numbers necessary to identify the state), and applied to the core state c . The complement of \hat{P}_v is given by $\hat{Q}_v = 1 - \hat{P}_v$. With these definitions, the eigenvalue equation in the valence space is given by [Eq. (16) in [141]]:

$$\underbrace{\left(\hat{P}_v \hat{H} \hat{P}_v + \hat{P}_v \hat{H} \hat{Q}_v \frac{1}{E_i - \hat{Q}_v \hat{H} \hat{Q}_v} \hat{Q}_v \hat{H} \hat{P}_v \right)}_{\hat{H}_{\text{eff}}} \hat{P}_v |\Psi_i\rangle = E_i \hat{P}_v |\Psi_i\rangle. \quad (2.19)$$

Equation (2.19) contains the definition of the effective valence-space Hamiltonian \hat{H}_{eff} . The second term of \hat{H}_{eff} can be interpreted as corrections due to correlations with basis states outside the valence space. An expansion of the denominator in this term, i.e.

$$\frac{1}{1 - \hat{Q}_v \hat{H} \hat{Q}_v / E_i} = 1 + \hat{Q}_v \hat{H} \hat{Q}_v / E_i + \left(\hat{Q}_v \hat{H} \hat{Q}_v / E_i \right)^2 + \dots, \quad (2.20)$$

shows that this term introduces higher-order multi-nucleon correlations to compensate for the reduction of the model space, even if the original \hat{H} contains only terms up to a certain order. Therefore, the transition to the valence-space problem is an actual simplification of the A -body problem only if the aforementioned assumptions are valid, i.e. the expansion in Eq. (2.20) can be truncated at some point¹⁰.

In analogy to Eq. (2.20), any transition operator must also be transformed for the application in the valence space (Sec. II.A in [5]). In a first-order approximation, this can be taken into account by using effective coupling constants

¹⁰In this context, the author of the present work would like to cite Talmi: "No clear demonstration was ever given that the shell model is a good approximation nor a characterization of properties of the interactions for which this is the case. Today, as in 1949, the best proof for the validity of the shell model is the good agreement of its predictions with experiment." (Introductory chapter of [59]. Talmi refers to the 'year of birth' of the shell model in 1949 [99, 100].)

(electric charges, g factors, ...). In particular for $M1$ strength, the observation that experimental transition strengths are systematically lower than predictions with bare coupling constants in the shell model is known as 'quenching' of $M1$ and GT strength (see, e.g., Sec. V.C.2 in [5] for a discussion of the problem, [92] for a recently proposed solution).

In practice, the original phenomenological proposal by Goeppert Mayer [99] and Haxel, Jensen and Suess [100] for \hat{U} [5],

$$\hat{U} = V(r) + c_{ll}\hat{l}^2 + c_{ls}\hat{l} \cdot \hat{s}, \quad (2.21)$$

can be used, which successfully describes the 'magic numbers' in nuclei. Equation (2.21) contains a potential with a dependence on the distance r from the origin. The most simple form of $V(r)$ is a harmonic oscillator ($V(r) \propto r^2$), which can be significantly improved by using phenomenologically or microscopically motivated potentials (see, e.g. [145], in particular Sec. 4.2). In addition to the dependence on r , Eq. (2.21) contains terms which are proportional to the 'll'- \hat{l}^2 and 'ls-coupling' $\hat{l} \cdot \hat{s}$ via the respective parameters c_{ll} and c_{ls} .

For the effective Hamiltonian, procedures exist to construct it from the underlying nucleon-nucleon potential [141]. The difficulty of such approaches lies in the appearance of the eigenvalues of the A -body problem E_i on both sides of Eq. (2.19) (see, e.g., the discussion of Eq. (22) in [141]). An alternative is to treat matrix elements of the form

$$\langle c | \hat{a}_{v,i} \hat{H} \hat{a}_{v,j}^\dagger | c \rangle \quad (2.22)$$

$$\langle c | \hat{a}_{v,i} \hat{a}_{v,i} \hat{H} \hat{a}_{v,k}^\dagger \hat{a}_{v,k}^\dagger | c \rangle \quad (2.23)$$

as free parameters, which can be fit to experimental data in a finite valence space. Equations (2.22) and (2.23) give examples for one- and two-body matrix elements. The pure fitting procedure has been successfully applied in the sd shell (Sec. 4.7 in [145]), for example.

The present work uses the JUN45 interaction for the $f_5p g_9$ space by Honma, Otsuka, Mizusaki and Hjorth-Jensen [101] to investigate the structure of ^{82}Kr and ^{82}Se . This interaction was constructed using a mixture of both approaches, where some parameters are fit to data and others are fixed by a realistic nucleon-nucleon interaction.

Presently, shell-model calculations for nuclei as heavy as the neutron-deficient mercury isotopes [146], and as far away from shell closures as ^{166}Er [147] are feasible in the framework of the Monte-Carlo shell model [148]. However, an interpretation of the results for the nuclei ^{150}Nd and ^{150}Sm is given in the framework of the IBM (see Sec. 2.2.2) in the present work, which is much less computationally demanding.

2.2.2. Interacting Boson Model

The introduction of the interacting boson model [140] follows a book chapter by Otsuka in [144], which is based on articles by Otsuka, Arima, and Iachello [149], and Iachello and Talmi [150]. As in that chapter, the introduction will sketch the mapping procedure from the shell model to the IBM oblivious to the distinction between the two types of nucleons without loss of generality. This approximation is the so-called IBM-1. At the end of this section, a distinction will be made between protons and neutrons to be able to describe mixed-symmetric states.

It is well known that nucleons of the same type, interacting via the nucleon-nucleon interaction and subjected to the Pauli principle, experience an effective, strong pairing interaction [151]. The simple semiempirical mass formula (see, e.g., Sec. 3.3 in [34] or [35]) gives the following estimate for the pairing energy of two neutrons or protons:

$$\delta_p \approx a_p A^{-3/4} \approx 34 \text{ MeV} A^{-3/4} \quad (2.24)$$

In Eq. (2.24), the numerical value of the parameter a_p was taken from the text below Eq. (3.29) in [34]. Comparing the excitation energies of low-lying states of rare-earth nuclei like ^{150}Nd and ^{150}Sm [139] to $\delta_p \approx 800 \text{ keV}$ suggests that pairs of equal nucleons can be used as elementary degrees of freedom, if only a description of those states is desired. This results in a strong reduction of the size of the model space.

Consequently, an operator \hat{A}^\dagger is introduced which creates a pair two equal nucleons in the j - and j' orbitals of the valence space with a total angular momentum J and a z component M_J [Eq. (4.3) in [144]]:

$$\hat{A}^\dagger(jj'; J, M_J) \equiv \frac{1}{\sqrt{1 + \delta_{jj'}}} \left[\hat{\mathbf{a}}_j^\dagger \hat{\mathbf{a}}_{j'}^\dagger \right]_{M_J}^{(J)} \quad (2.25)$$

From symmetry arguments for deformed nuclei (Sec. 4.3 in [64]), the properties of the residual interaction in a shell-model valence space (Sec. 4.4 in [65] or Sec. 6.6 'Features of Quadrupole Modes in Spherical Nuclei' in [64]), empirical studies [152], or simply from the success of the following truncation of the IBM [140], it is anticipated that the low-lying level scheme of medium-heavy to heavy nuclei away from shell closures is dominated by quadrupole-collective excitations. It is therefore a valid approximation to consider only pairs of nucleons coupled to $J = 0$ ('S pairs') and $J = 2$ ('D pairs') [Eqs. (4.1) and (4.2) in [144]]:

$$\hat{S}^\dagger = \sum_j \alpha_j \hat{A}^\dagger(jj; 0, 0) \quad (2.26)$$

$$\hat{D}_{M_J}^\dagger = \sum_{jj'} \beta_{jj'} \hat{A}^\dagger(jj; 2, M_J). \quad (2.27)$$

Equations (2.26) and (2.27) contain some degrees of freedom: the expansion parameters α_j and $\beta_{jj'}$. Before their impact is discussed, it should be noted that states of N_S S pairs and N_D D pairs generated by acting naively with the operators in Eqs. (2.26) and (2.27) on the inert core [Eq. (4.4) in [144]]

$$(\hat{S}^\dagger)^{N_S} [(\hat{D}^\dagger)^{(N_D)}]_{M_J}^{(J)} |c\rangle \quad (2.28)$$

are not orthogonal in general. The reason is that there may be several ways to achieve the coupling of D pairs to J and M_J (see, e.g., chapter 15 in [59] about multinucleon states). To resolve this ambiguity consistently within the IBM picture, the basis states are constructed as eigenstates of the pairing interaction [Eqs. (4.5)-(4.8) in [144], see also Sec. 19 in [59]]. They can then be distinguished by the so-called seniority quantum number ν , which indicates the number of nucleons that are not coupled to $J = 0$. With the projection operator \mathfrak{P} onto states with seniority $\nu = 2N_D$, the basis states are given by [Eq. (4.9) in [144]]:

$$|N_S, N_D, J, M_J, \Xi\rangle \propto \mathfrak{P} (\hat{S}^\dagger)^{N_S} [(\hat{D}^\dagger)^{N_D}]_{M_J}^{(J)} |c\rangle. \quad (2.29)$$

In Eq. (2.29), the symbol Ξ denotes a set of additional quantum numbers to distinguish between degenerate $\nu = 2N_D$ states. Given the proper orthogonalization, the states of Eq. (2.29) can be shown [149] to behave like a system of bosons with

spin $j = 0$ (s -boson) and $j = 2$ (d -boson). With the definition of the s - and d -boson annihilation/creation operators \hat{s}/\hat{s}^\dagger and $\hat{d}_\mu/\hat{d}_\mu^\dagger$ and the respective boson numbers N_s and N_d , Eq. (2.29) can be mapped to boson states [Eq. (4.10a) in [144]]:

$$|N_s, N_d, J, M_J, \Xi\rangle \propto (\hat{s}^\dagger)^{N_s} \left[(\hat{d}^\dagger)^{N_d} \right]_{M_J}^{(J)} |c\rangle. \quad (2.30)$$

In the following, a redefinition of the d -boson annihilation operator will be used [see, e.g., Eq. (2.79) in [144]]:

$$\hat{\tilde{d}}_\mu = (-1)^\mu \hat{d}_{-\mu} \quad (2.31)$$

In contrast to \hat{d}_μ , the operator $\hat{\tilde{d}}_\mu$ defined by Eq. (2.31) has the necessary symmetry properties to use the usual angular momentum coupling via Clebsch-Gordan coefficients (see, e.g., Sec. 2.5.1 in [144]). Furthermore, since the d -boson operators can be interpreted as 5-component vectors, a scalar product ‘.’ will be used to simplify sums of the type $\sum_\mu \hat{d}_\mu^\dagger \hat{\tilde{d}}_\mu$.

Now that the transition from the fermionic to the bosonic problem has been sketched, the impact of the parameters α_j and $\beta_{jj'}$ in Eqs. (2.26) and (2.27) can be discussed: In analogy to the matrix elements of the one-body operator \hat{U} in the motivation of the shell model [Eq. (2.13)], it is assumed that the α_j and $\beta_{jj'}$ can be chosen such that the residual interaction between many-boson states is a comparably small perturbation (for the general procedure, see [153])¹¹.

Given a shell-model operator \hat{O} , the matrix elements of the derived IBM operator \hat{O}_{IBM} can be obtained from the following requirement [Eq. (4.22) in [144]]:

$$\langle N_S, N_D, J, M_J, \Xi | \hat{O} | N_S, N_D, J', M_{J'}, \Xi \rangle \approx \langle N_s, N_d, J, M_J, \Xi | \hat{O}_{\text{IBM}} | N_d, N_d, J', M_{J'}, \Xi' \rangle \quad (2.32)$$

In analogy to the transition from the full space to the shell-model valence space [Eq. (2.20)], the restriction to S - and D -pair states may introduce higher-order multi-boson correlations. Alternatively, the matrix elements can also be obtained

¹¹In the words of Otsuka: "The first Ansatz for the microscopic foundation of the IBM is that the low-lying quadrupole collective states are dominated by the SD states in eq. (4.9) with appropriately chosen amplitudes α_j and $\beta_{jj'}$ " [Sec. 4.4 in [144]. Otsuka refers to Eq. (4.9) therein, which is equivalent to Eq. (2.29) in this work.]

by fitting experimental data, as outlined in Eqs. (2.22) and (2.23) for the shell model.

In practice, however, it was found that combinations of the Casimir operators of the six-dimensional group $U(6)$ with the 36 generators [Eq. (2.77) in [144]]:

$$\hat{s}^\dagger \hat{s}, \quad \hat{s}^\dagger \hat{d}_\mu, \quad \hat{d}_\mu^\dagger \hat{s}, \quad \hat{d}_\mu^\dagger \hat{d}_\nu, \quad (2.33)$$

are sufficient to describe the three most commonly encountered collective phenomena in even-even nuclei: the vibrator, rigid rotor, and γ -soft rotor [69]. In particular, the ideal limits of the three phenomena are represented by the three dynamical symmetries $U(5)$, $SU(3)$, and $O(6)$ of the $U(6)$ group. They are often visualized in the so-called symmetry triangle by Casten [69], which is shown in Fig. 2.1¹². It depicts the parameter space of the IBM in a 2D triangle with the dynamical symmetries and their geometrical interpretations at the edges. Two analytical solutions of the Bohr Hamiltonian are also indicated, the so-called critical point symmetries $E(5)$ [154] and $X(5)$ [113]. They describe the phase transitional points between the vibrator and the γ -soft rotor and between the vibrator and the rigid rotor.

The procedure described above can be performed for neutrons and protons separately (see, e.g., Sec. 4.6 in [144]) since neutron-proton pairing is expected to be suppressed, in particular for isospin-asymmetric nuclei [155]. This results in the definition of neutron- and proton-boson operators which are identified by an additional index ν or π compared to Eq. (2.33) (e.g. \hat{s}_ν^\dagger , $\hat{d}_{\pi,\mu}^\dagger$). With the requirement of particle number conservation for neutron- and proton bosons, respectively, the so-called IBM-2 has the group structure $U(6) \times U(6)$ with $2 \times 36 = 72$ generators (Sec. 2.8.1 in [144]). In particular, the IBM-2 retains the dynamical symmetries and the eigenstates of the IBM-1. IBM-2 states can be characterized by the F -spin quantum number, which is the bosonic analog of the isospin quantum number (Sec. 4.11 in [144]). Explicitly, the neutron- and the proton boson are the $f_z = -1/2$ and

¹²Note that there also exists a version of the symmetry triangle which differentiates between the prolate- and the less commonly encountered oblate ground-state deformation in the $SU(3)$ limit [Fig. 1 b) in [69]].

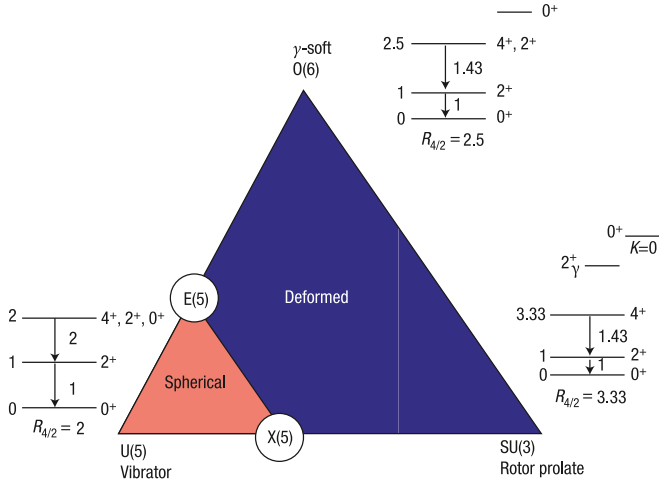


Figure 2.1.: Visualization of the parameter space between the three commonly encountered collective behaviors of nuclei in the so-called symmetry triangle by Casten [69]. The three ideal limits of the vibrator, prolate rotor, and γ -soft rotor are shown in the corners of the triangle together with their interpretation as the dynamical symmetries of the IBM-1 [140]. For each limit, a typical low-energy level scheme, including angular momentum and parity quantum numbers, relative excitation energies and transition strengths, and the $R_{4/2}$ ratio is shown. The symmetry triangle also includes the two critical point symmetries $E(5)$ [154] and $X(5)$ [113], which are analytical solutions of the Bohr Hamiltonian at the phase transition from spherical to deformed shapes. Reprinted by permission from Springer Nature Customer Service Center GmbH: Nature Physics [69] Copyright (2010).

$f_z = 1/2$ eigenstates of the F -spin operator. Many-boson states with the property

$$\hat{F}^2 |N_{\nu,s}, N_{\nu,d}, N_{\pi,s}, N_{\pi,d}, J, M_J, \Xi\rangle = F_{\max}(F_{\max} + 1) |N_{\nu,s}, N_{\nu,d}, N_{\pi,s}, N_{\pi,d}, J, M_J, \Xi\rangle$$

$$F_{\max} = \frac{1}{2} (N_{\nu,s} + N_{\nu,d} + N_{\pi,s} + N_{\pi,d}) \quad (2.34)$$

are called fully symmetric states and represent eigenstates of the IBM-1. In Eq. (2.34), the symbols N_s and N_d as well as the notation for the many-boson states in Eq. (2.30) has been generalized in an obvious way to distinguish neutron- and proton bosons. The quantity F_{\max} is the maximum possible projection of the F -spin for a given number of neutron- and proton bosons. IBM-2 states with $F < F_{\max}$ are called mixed-symmetric and not part of the IBM-1 basis. A prominent example for such a state, the scissors mode, will be introduced in Sec. 2.3.

Practical calculations in the IBM-1 (IBM-2) often do not employ all of the 36 (72) generating bilinear operators: a small subset is usually sufficient (see, e.g., Sec. 1.2 in [144] and [69]) to reproduce the structure of collective nuclei in the parameter space given by the symmetry triangle (Fig. 2.1). Consequently, instead of the full IBM-2 Hamiltonian (see, e.g., [140] or [156]), this work used the following subset of all available operators at lowest order, which is given, for example, by Eq. (5.5) in [150]:

$$\hat{H} = \epsilon_d (\hat{n}_{d_\pi} + \hat{n}_{d_v}) + \kappa (\hat{Q}_\pi^{\chi_\pi} \cdot \hat{Q}_v^{\chi_v}) + \lambda \hat{M}_{\pi v}. \quad (2.35)$$

The Hamiltonian in Eq. (2.35), whose parameterization has been changed compared to Eq. (5.5) in [150], consists of mainly three parts, which can be derived microscopically [150], but are motivated phenomenologically here. Each term has at least one parameter, which can also be derived from first principles (see above). However, in most cases, the parameters of Eq. (2.35) are adapted to experimental data within sensible limits (see, e.g., Sec. 3.4 and 3.7 in [144]). The first term, with the single- d boson energy ϵ , contains the number operators for neutron- and proton d bosons [Eq. (2.89) in [144]]:

$$\hat{n}_d = \hat{d}^\dagger \cdot \hat{d} \quad (2.36)$$

If the strength of the quadrupole-quadrupole interaction is negligible ($\kappa = 0$) in Eq. (2.35), the term in Eq. (2.36) creates an equidistant quadrupole-phonon like spectrum of excited states, which is expected to be found in an ideal vibrator [69]. The second term in Eq. (2.35) is interpreted as a quadrupole-quadrupole interaction between neutron- and proton valence bosons, and a microscopic motivation for it is given in Secs. 4.2 and 4.3 of [144]: In the single-nucleon picture, a pair of one neutron and one proton is expected to be spatially correlated due to the short-range character of the nucleon-nucleon interaction and the absence of the Pauli principle. As a consequence, the quadrupole moments of the neutron- and

proton distributions in the nucleus will adapt to each other. The IBM accounts for this fact by using the $\hat{Q}_\pi^{\chi_\pi} \cdot \hat{Q}_\nu^{\chi_\nu}$ term with the quadrupole operators $\hat{Q}_n^{\chi_n}$ defined by [Eq. (4.18) in [150]]:

$$\hat{Q}_n^{\chi_n} = \left(\hat{d}_n^\dagger \hat{s}_n + \hat{s}_n^\dagger \hat{d}_n \right) + \chi \left[\hat{d}_n^\dagger \hat{d}_n^\dagger \right]^{(2)} \quad (2.37)$$

For $\epsilon = 0$ and $\chi = -\sqrt{7}/2$ in Eq. (2.35), the second term in Eq. (2.35) creates a rotor-like spectrum of excited states with a scaling of the energies proportional to $J(J+1)$ [69]. The control parameter χ determines the γ -softness of the nucleus and leads to the limit of a γ -soft rotor for $\epsilon_d = 0$ and $\chi = 0$ in Eq. (2.35). In principle, the first two terms are therefore enough to traverse the symmetry triangle (Fig. 2.1) and describe states with $F = F_{\max}$.

The last term in Eq. (2.35), the so-called Majorana operator, distinguishes between IBM-2 states with different F spin. It is defined as [Eq. (5.6) in [150]]:

$$\hat{M}_{\pi\nu} = \xi_1 \left[\hat{d}_\pi^\dagger \hat{d}_\nu^\dagger \right]^{(1)} \cdot \left[\hat{d}_\pi \hat{d}_\nu \right]^{(1)} \quad (2.38)$$

$$+ \xi_3 \left[\hat{d}_\pi^\dagger \hat{d}_\nu^\dagger \right]^{(3)} \cdot \left[\hat{d}_\pi \hat{d}_\nu \right]^{(3)} \\ + \xi_2 \left(\hat{d}_\pi^\dagger \hat{s}_\nu^\dagger - \hat{d}_\nu^\dagger \hat{s}_\pi^\dagger \right) \cdot \left(\hat{d}_\pi \hat{s}_\nu - \hat{d}_\nu \hat{s}_\pi \right). \quad (2.39)$$

In addition to the global parameter λ it contains the parameters ξ_1 , ξ_2 , and ξ_3 to regulate the strengths of its three terms. In the literature, it is often emphasized that the Majorana operator is at least partially phenomenological (compare Sec. V.A in [150], Sec. 4.12 in [144], Sec. 3.2.3 in [157]), but its usual effect in the IBM-2 of shifting mixed-symmetric states to higher energies implies a relation to the symmetry energy of nuclear matter [158]. Obviously, in order to gain information about all parameters of the IBM-2 Hamiltonian in Eq. (2.35), experiments on mixed symmetry states are a valuable tool (see, e.g., [159] for vibrational nuclei, and [89] with a focus on deformed nuclei).

At last, the transition operators for magnetic dipole- and electric quadrupole transitions are given by [Eq. (5.8) and (4.17)/(4.18) in [150]]:

$$\hat{O}_{M1}^{\text{IBM}} = g_\pi \hat{L}_\pi + g_\nu \hat{L}_\nu \quad (2.40)$$

$$\hat{O}_{E2}^{\text{IBM}} = e_\pi \hat{Q}_\pi^{\chi_\pi} + e_\nu \hat{Q}_\nu^{\chi_\nu}. \quad (2.41)$$

The $M1$ operator [Eq. (2.40)] contains the proton- and neutron-boson g factors g_π and g_ν and the angular momentum operators [defined, e.g., near Eq. (2.11) in [150]]:

$$\hat{L} = \sqrt{10} [\hat{\mathbf{d}}^\dagger \hat{\mathbf{d}}]^{(1)}. \quad (2.42)$$

Note that the $M1$ operator does not distinguish between orbital and spin strength [compare to the single-nucleon $M1$ operator in Eq. (2.43)], since the nucleon pairing procedure [Eqs. (2.26) and (2.27)] eliminated the possibility of single-nucleon spin-flip transitions. The $E2$ operator [Eq. (2.41)] contains the quadrupole operators defined in Eq. (2.37), whose relative strength is given by the boson charges e_π and e_ν . Similar to the parameters of the Hamiltonian [Eq. (2.35)], the effective g factors and boson charges for a particular model space can be derived by renormalization of the bare g factors/charges or fixed by experimental data. In the present work, the so-called 'consistent-Q formalism' was used [160, 161], meaning that the same values of χ_π and χ_ν were used in the quadrupole operators of the Hamiltonian [Eqs. (2.35) and (2.37)] and the $E2$ transition operator [Eq. (2.41)].

2.3. Scissors Mode

In this section, the nuclear scissors mode will be introduced. The introduction is based on a review article by Heyde, von Neumann-Cosel and Richter [89].

Start by defining the (fermionic) magnetic dipole operator [Eq. (7) in [89]]:

$$\hat{O}_{M1} = \sqrt{\frac{3}{4\pi}} \sum_{a=1}^A (g_l^{(a)} \hat{l}_a + g_s^{(a)} \hat{s}_a) \mu_N \quad (2.43)$$

In Eq. (2.43), the symbols $g_l^{(a)}$ and $g_s^{(a)}$ denote the orbital- and spin- g factors, which are different for protons and neutrons and may be 'quenched' in a restricted model space (see Sec. 1.2). Equation (2.43) indicates that there are two mechanisms to

generate $M1$ strength, i.e. so-called spin-flip transitions (\hat{s}) and the orbital motion of nucleons (\hat{l}), both of which may be collective (see, e.g., Sec. I.A in [89]).

The phenomenon of interest in the present work, the nuclear scissors mode, is an orbital, collective magnetic dipole resonance in medium-heavy and heavy nuclei (see, e.g., Secs. I.A and I.B in [89]). Its orbital character can be inferred by using experimental probes like inelastic proton scattering which are only sensitive to one of the two contributions in Eq. (2.43) (see, e.g., Fig. 5 in [89]). The collective nature of the scissors mode can be seen from its comparably large excitation strength on the order of $1\mu_N^2$ (Sec. III.A.1.a in [89]), and its correlation with the nuclear quadrupole deformation (see, e.g., Sec. III.A.1.f in [89]) and the low-lying $E2$ strength [162]. Note here that electromagnetic probes like electron scattering and NRF have been invaluable (see, e.g., Sec. III.A.1.c in [89]) for the establishment of the $M1$ character of the scissors mode. Due to the collective nature of the scissors mode, the mean excitation energy $\langle E_{sc} \rangle$ of the 1^+ states, which are the manifestations of the scissors mode in even-even nuclei, show a rather smooth dependence on the mass number A and the deformation parameter β (Sec. III.1.a (ii) in [89], see also the footnote):

$$\langle E_{sc} \rangle \approx 62 \times A^{-1/3} \beta \text{ MeV} \quad (2.44)$$

The name 'scissors mode' originates from its interpretation as a rotational oscillation of the valence protons against the valence neutrons in a quadrupole-deformed nucleus (see, e.g., Sec. II.A.2.a in [89]). This interpretation of the scissors mode in geometrical model is depicted in Fig. 2.2. In the framework of the IBM, the counterpropagation of the proton- and neutron bodies is manifested in the mixed-symmetric character of the excited 1^+ states, which emerge naturally in the IBM-2 (see, e.g., Sec. II.A.2.b in [89]).

In the present work, the scissors mode is investigated due to its sensitivity to nuclear shape evolution: The study of decay branchings of low-lying dipole-excited states as a measure for shape coexistence was originally proposed by Rusev *et al.* [163], who used a calculation in a deformed mean-field model to interpret their observed branching from an excited $J = 1$ state to the 0_2^+ state of ^{100}Mo . The first observation of a decay from a scissors mode 1^+ state to an excited 0_2^+ state with a small branching ratio of $\Gamma_{1^+ \rightarrow 0_2^+} / \Gamma_{1^+} = 0.027(1)$ was reported by Beller *et al.* [110] for the nucleus ^{154}Gd . Since the IBM-2 is both well suited for the study of the

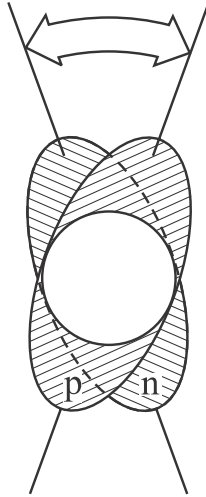


Figure 2.2.: Interpretation of the scissors mode in the geometrical model as a counterpropagation of the valence proton and -neutron bodies of a quadrupole-deformed nucleus. Reprinted with permission from [89] Copyright (2010) by the American Physical Society.

scissors mode (see, e.g., Sec. III.A.2.b in [89]) and the shape evolution [69] of heavy nuclei, it was the model of choice for the authors, who were able to readjust the model parameters with an unprecedented precision. With the new constraints, they updated their predictions of NMEs for the $0\nu\beta\beta$ decay from ^{154}Sm to ^{154}Gd , and found a strong increase of the predicted matrix element to the 0_2^+ state. From a calculation in the framework of energy density functional theory [75], the authors found that this increase of the matrix element was indeed a result of the rapid shape evolution in this region of the nuclear chart.

Systematic investigations of the decay behavior of the scissors mode in the IBM using, for example, the simple Hamiltonian given by Eq. (2.35) to traverse the entire symmetry triangle of nuclear shapes (see Fig. 2.1) predict a generic decay behavior (see, e.g., [164], in particular Abb. 3.4 therein, or [165]): Towards the limit of the ideal vibrator (the $U(5)$ limit of the IBM), low-lying 1^+ states are

interpreted as two-phonon mixed-symmetry states [Eq. (25) in [159]], which are expected to decay primarily to their symmetric counterparts (Sec. 2.6 in [159]). Towards the limit of the ideal rigid rotor (the $SU(3)$ limit of the IBM), the decay of the scissors mode to the 0_2^+ state, which is a member of another rotational band, is exactly forbidden (see, e.g. Sec. 2.7.4.2 in [144]). As one moves away from these ideal limits, the decay behavior of the scissors mode is expected to evolve accordingly.

Consequently, the scissors mode, whose properties can be studied with a high precision and quasi model-independently in NRF (see Sec. (2.1.1)), is expected to give a robust estimate of the degree of shape coexistence within a given nucleus. Furthermore, being a mixed-symmetry state, it provides access to the parameters of the Majorana operator, i.e. the proton-neutron interaction. Last but not least, a recent study by Beck *et al.* [166] opened up a path for a local determination of the effective boson charges in the IBM-2 quadrupole operator [Eq. (2.41)] by observing a nonzero $E2$ admixture to the $1^+ \rightarrow 2_1^+$ transition.

3. Experiments

This section describes the facility where all of the experiments of the present study were performed in Sec. 3.1. After that, the experimental setups are described in Sec. 3.2. Specific information about the experiments on $^{82}\text{Kr}/^{82}\text{Se}$ and $^{150}\text{Nd}/^{150}\text{Sm}$ will be given in Secs. 3.3 and 3.4, respectively. All subsequent sections will assume a right-handed coordinate system in which the beam propagates in the positive z direction and the positive y direction is assumed to point upwards (see Figs. B.1 and B.2). Information about the experiments is available in the general electronic logbook of the γ^3 collaboration [167]. A precise 3D reconstruction of the geometry around the beam line in the upstream target room (Sec. 3.1), in particular also of the experimental setups, was created as a part of this thesis (see Sec. 4.2).

3.1. High-Intensity γ -ray Source (HI γ S)

The experiments were performed at the High-Intensity Gamma-Ray Source (HI γ S) of the Triangle Universities Nuclear Laboratory at Duke University, NC, USA. A review article about HI γ S, on which the following introductory paragraph is based, was published by Weller *et al.* [168].

The facility generates a quasi-monochromatic, almost 100% linearly polarized photon beam by the Compton-backscattering of laser photons from a free-electron laser on an ultrarelativistic electron beam. In the collision with the beam, the energy of the laser photons on the order of 1 eV is increased by at least a factor of 10^6 , creating a highly energetic photon beam. This beam escapes the free-electron laser cavity and is transported downstream by about 60 m, where it is shaped by a variable-size lead collimator. In the present experiments, a collimator

diameter of 0.75 in or 1.0 in was used. Tens of centimeters after the collimation, the beam enters an evacuated¹ beam pipe made of polymethyl methacrylate (PMMA, 'plexiglass') and propagates into the so-called upstream target room. In this room, two setups were mounted in a row which are described in Sec. 3.2. Due to the low attenuation of the photon beam in the targets (see Sec. 4.6), the two samples can be irradiated simultaneously. About 50 cm downstream from the second setup, the photon beam exits the evacuated beam pipe and travels on into another experimental hall called the 'gamma vault' under normal atmosphere. The photon beam is stopped more than 10 meters downstream of the second target.

For beam diagnostics, a charge-coupled device (CCD) camera [169] is available, which can be moved into the optical axis to take a 2D image of the intensity distribution of the beam. Its location is about 1.5 m downstream from the second target position. Figures 3.1 and 3.2 show two such images of the beam². In the latter image, an alignment target was placed at the target position of the first setup to check the alignment of the beam with the target. Furthermore, a High-purity Germanium (HPGe) detector ('zero-degree detector') was available, which can be moved into a position about 1 m downstream from the second target position to record the energy spectrum of the beam. This measurement and the reconstruction of the beam spectrum is described in Sec. 4.5.4.

At nominal energies of about 3 MeV, the photon beam can be expected to be 100% linearly polarized in the x direction. For these polarization and energy settings, the HI γ S is expected to provide a collimated photon flux of about 10^7 s^{-1} to 10^8 s^{-1} [127]³ In the $^{82}\text{Kr}/^{82}\text{Se}$ experiment, the standard deviation of the approximately Gaussian beam profile increased linearly with the nominal energy E_{beam} from 30 keV at $E_{\text{beam}} = 2.4 \text{ MeV}$ to 60 keV at $E_{\text{beam}} = 4.1 \text{ MeV}$

¹For an estimate of the quality of this vacuum, see Sec. 4.5.4.

²In fact, the exemplary beam images in Figs. 3.1 and 3.2 are from a more recent campaign. However, the same instrumentation and alignment targets were used in the experiments of the present work.

³This value depends on the type of mirrors in the free-electron laser cavity and on their quality, since they degrade significantly within weeks from the constant irradiation.

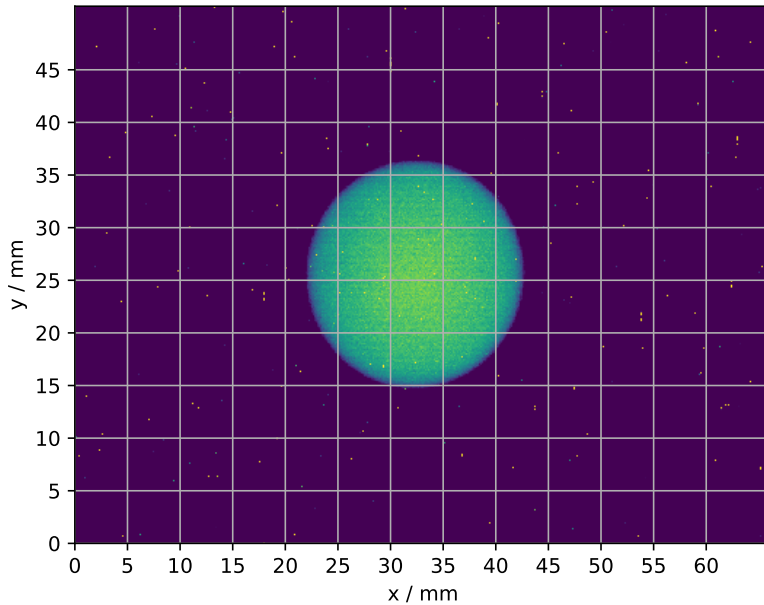


Figure 3.1.: Two dimensional intensity profile of the HI γ S beam as recorded by a CCD camera downstream from the zero-degree detector. The camera image consists of 752×580 quadratic pixels with side length 0.088 mm. No material was in the way of the beam when this image was taken. The intensity is indicated by a color scheme which goes from purple (low intensity) to yellow (high intensity). However, the exact relation between the actual beam intensity and the intensity of the image is unclear.

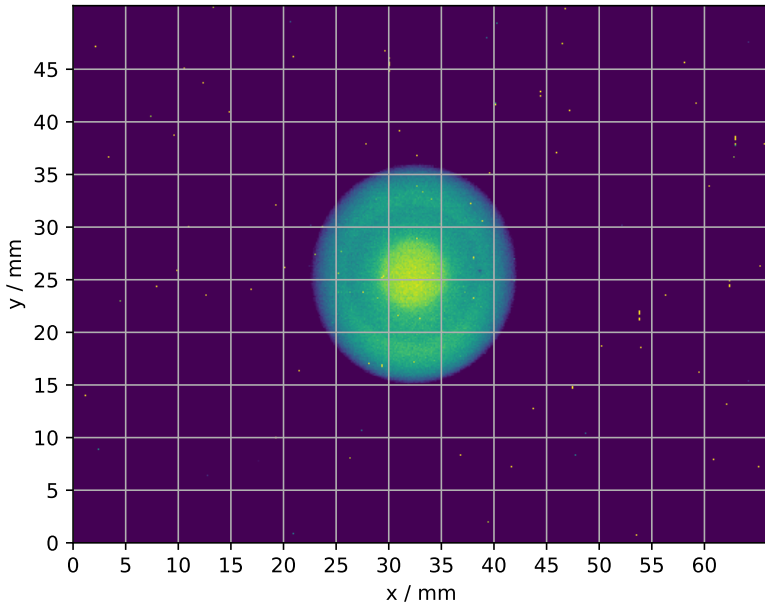


Figure 3.2.: Two dimensional intensity profile of the $\text{HI}\gamma\text{S}$ beam. In this measurement, an alignment target was mounted at the target position of the γ^3 setup. Its visible ring shape actually has an outer diameter of 10 mm, but it appears larger on the camera because the beam is divergent and distorted by the target itself. See also Fig. 3.1.

3.2. Experimental Setups

The two experimental setups which were used in the present study will be denoted as the γ^3 setup [170] and the 'polarimetry setup' in the following. Only the ^{82}Kr target was mounted in the second setup, all other isotopes were at the γ^3 target position.

The γ^3 setup is a dedicated setup for γ - γ coincidence measurements [170]. It features four HPGe detectors and four Lanthanum Bromide detectors in its most common configuration. For the present analyses, only the high-resolution spectra of the HPGe detectors were used. Denoting the detector positions by their polar angles θ and their azimuthal angles φ as (θ, φ) , the HPGe detectors were mounted at $(90^\circ, 0^\circ)$, $(90^\circ, 90^\circ)$, $(135^\circ, 45^\circ)$, and $(135^\circ, 135^\circ)$ or equivalent angles, i.e. $\varphi \pm 90^\circ$, in all experiments.

The polarimetry setup consisted of four HPGe detectors in a cross configuration $(90^\circ, 0^\circ)$, $(90^\circ, 90^\circ)$, $(90^\circ, 180^\circ)$, and $(90^\circ, 270^\circ)$. This configuration increased the sensitivity to parities of excited states, but without detectors at backward angles, a distinction between dipole- and quadrupole-excited states was not possible (see Sec. 4.6.1).

For the readout of all detector signals, an analog data acquisition system in combination with the GENIE software [171] was used.

The detectors were mounted at distances of 60 cm to 120 cm (measured from the detector face to the target position) and shielded by different amounts of lead and copper filters. Both setups were shielded from each other by walls of lead and concrete bricks, in particular to avoid small-angle scattering of photons from the first target into the detectors of the second setup. Long measurements with radioactive sources confirmed the impenetrability of these walls at the energies of the present experiment.

3.3. Experiments on ^{82}Kr and ^{82}Se

For the isotopes ^{82}Se and ^{82}Kr , little information about dipole-excited states in the energy range below the neutron separation threshold existed [138]. For ^{82}Se ,

a diploma thesis by Werner [137] was available to the author, in which an NRF experiment with bremsstrahlung at an end point energy of 3.2 MeV was performed. Therefore, the purpose of this experiment, which was performed simultaneously with ^{82}Se in the γ^3 - and ^{82}Kr in the polarimetry setup, was to scan the energy range where the scissors mode is expected. According to Eq. (2.44), it was decided to cover a range from $E_{\text{beam}} = 2.4\text{ MeV}$ to $E_{\text{beam}} = 4.1\text{ MeV}$. An overview of all experimental runs, including calibration and background measurements, can be seen in Tab. 3.1. Single runs for scanning had a duration on the order of 3 h. However, enough time was allocated in advance to perform a high-precision measurement of the decay behavior of newly observed 1^+ states. As can be seen from the run overview, the experiment first focused on the known 1^+ state of ^{82}Se at 2981 keV. However, when excited 1^+ states of both ^{82}Kr and ^{82}Se were found at a beam energy of 3.80 MeV, it was decided to measure their decay simultaneously.

The ^{82}Se target consisted of 1.99845(7) g of selenium in the chemical compound SeO_2 . It was enriched to 99.930(5)%⁴ in the isotope ^{82}Se . The target powder was contained in a cylindrical container made of polyvinyl chloride (PVC). Due to the chlorine and carbon content of the PVC material, several NRF transitions from isotopes ^{13}C ⁵ [173] ^{35}Cl [174] and ^{37}Cl [175] were observed in the spectra of the present experiment (see Sec. C).

The ^{82}Kr target consisted of 1.50218(11) g of pure krypton gas. It was enriched to 99.9450(5)% in the the isotope ^{82}Kr . The gas was contained in a stainless steel sphere, similar to Ref. [176], but with a larger inner radius of 9.0(2) mm. Due to the iron content of the gas sphere, NRF transitions from the isotope ^{56}Fe [177] were observed. Since the exact composition of the steel sphere was unknown (stainless steel may also contain significant amounts of chromium), measurements with an identical, empty target were performed whenever a potential transition of ^{82}Kr was observed, to make sure that it was not caused by a contaminant in the target container.

⁴Uncertainty estimated from the last digit given by the manufacturer.

⁵Note that the more abundant isotope of carbon, ^{12}C , does not have excited states below 4440 keV [172].

Table 3.1.: Run plan of the $^{82}\text{Kr}/^{82}\text{Se}$ experiment based on the electronic logbook [167]. The order of the runs corresponds to the actual history of the experiment. Some very short runs, which were aborted due to various reasons, are not listed here. This is why the run numbers are not continuous. Lines without run numbers indicate modifications of the experimental setup which happened in between two runs. The notation 'empty target' indicates that an identical, but empty, target container was placed at the target position. Runs without a beam energy correspond to measurements with the given radioactive sources at the target positions. Footnotes to the respective beam energies indicate when the beam profile was measured using the zero-degree detector. This was always done for about 30 min immediately before the actual run.

Run Number	E_{beam} (MeV)	γ^3	Polarimetry	Real Time ⁶ (s)
707	2.98 ⁷	^{82}Se	^{82}Kr	13461
708	2.98	^{82}Se	^{82}Kr	14384
709	2.98	^{82}Se	^{82}Kr	7764
710	2.40 ⁷	^{82}Se	^{82}Kr	5554
	Changed shielding between setups. Shielded ^{56}Co source inside safe.			
711	2.40	^{82}Se	^{82}Kr	2172
712	2.40	^{82}Se	^{82}Kr	1820
713	2.50 ⁷	^{82}Se	^{82}Kr	6280
714	2.65 ⁷	^{82}Se	^{82}Kr	6865
715	2.65	^{82}Se	^{82}Kr	7679
716	2.80 ⁷	^{82}Se	^{82}Kr	10859
717	2.98	^{82}Se	^{82}Kr	24800
718	3.10 ⁷	^{82}Se	^{82}Kr	6918
719	3.10	^{82}Se	^{82}Kr	9100

⁶Read off from the spectra of the arbitrarily selected HPGe 1 created by the GENIE [171] data acquisition system. The real times of other channels always agreed within few seconds.

⁷Beam profile was measured using the zero-degree detector before this run.

Table 3.1.: (Continued).

	Changed shielding upstream of γ^3 setup.			
720	2.50	^{82}Se	^{82}Kr	8491
721	2.98 ⁷	$^{82}\text{Se} + ^{152}\text{Sm}$	^{82}Kr	8129
722		Natural background measurement		40924
	Changed shielding upstream of γ^3 setup.			
723		^{56}Co	^{152}Eu	11994
724		^{152}Eu	^{56}Co	10760
725		Natural background measurement		49207
726		^{56}Co	^{60}Co	18976
	Changed distance of HPGe 1.			
727		^{152}Eu	^{56}Co	11736
728 ⁸		Natural background measurement		35665
729 ⁸	2.98 ⁷	^{82}Se	^{82}Kr	6505
730	2.98	^{82}Se	^{82}Kr	11825
731	2.98	^{82}Se	^{82}Kr	51798
732 ⁸	2.98	^{82}Se	^{82}Kr	31285
733	2.98	^{82}Se	^{82}Kr	18676
734 ⁸		^{56}Co	^{152}Eu	7254
735 ⁸		Natural background measurement		42634
736 ⁸		^{152}Eu	^{56}Co	7254
737 ⁹		^{22}Na	^{60}Co	9601
738		^{22}Na	^{60}Co	7907
739		^{60}Co	^{22}Na	5853
740		^{56}Co	^{152}Na	3532
741		^{152}Eu	^{56}Co	44162
742		Natural background measurement		8849
	Adjusted target position in both setups.			
743	3.20	^{82}Se	^{82}Kr	2224
	Changed distance of HPGe 7.			
744	3.20 ⁷	^{82}Se	^{82}Kr	12554
	Shielded ^{56}Co source inside safe.			

⁸No spectra of HPGe 3 for this run.

⁹Beamline not evacuated. In all runs labeled with this footnote, this was unintentional.

Table 3.1.: (Continued).

745	3.35 ⁷	⁸² Se	⁸² Kr	18009
746	3.50 ⁷	⁸² Se	⁸² Kr	13180
747 ¹⁰	3.65 ⁷	⁸² Se	⁸² Kr	1755
	Changed distance of HPGe 7.			
	Changed shielding in polarimetry setup.			
748	3.65	⁸² Se	⁸² Kr	21955
	Changed distance of HPGe 6 and 8.			
	Changed shielding in both setups.			
749 ⁹	3.65	⁸² Se	empty target	7999
750	3.80 ⁷	⁸² Se	⁸² Kr	8269
751	3.80	⁸² Se	empty target	10430
752 ¹⁰	3.95 ⁷	⁸² Se	⁸² Kr	2687
753 ⁸	3.95	⁸² Se	⁸² Kr	16118
754 ⁸	3.95	empty target	empty target	10419
755	4.10 ⁷	⁸² Se	⁸² Kr	14023
756	4.10	⁸² Se	empty target	8441
757	3.82 ⁷	⁸² Se	⁸² Kr	10026
758	3.82	⁸² Se	⁸² Kr	19173
759	3.82	⁸² Se	⁸² Kr	20037
760	3.82	⁸² Se	⁸² Kr	28873
	Changed shielding between both setups.			
762 ¹¹		⁶⁰ Co	²² Na	18311
763 ^{8,9}		⁵⁶ Co	⁶⁰ Co	39686
764 ^{8,12}		¹⁵² Eu	⁶⁰ Co	39686
766 ⁸		⁵⁶ Co	⁶⁰ Co	6150
767 ⁸	Natural background measurement			47053
768		¹⁵² Eu	⁶⁰ Co	12232
769		⁵⁶ Co		1497
770			⁵⁶ Co	2036

¹⁰Beam profile measurement.

¹¹No shielding around both target positions. The shielding had to be removed in order to place the target correctly. After the target placement, it was forgotten to reattach it.

¹²No shielding around γ^3 target position. The shielding had to be removed in order to place the target correctly. After the target placement, it was forgotten to reattach it.

3.4. Experiments on ^{150}Nd and ^{150}Sm

For the isotopes ^{150}Nd and ^{150}Sm , NRF data from bremsstrahlung experiments already existed [135, 136]. However, the bremsstrahlung experiments, which were not sensitive to the parities of dipole-excited states, could only report strong dipole-excited states in the energy range of the scissors mode (see Sec. 2.3). The present experiments focused on the strongest known transitions of both isotopes at 2994 keV (^{150}Nd) and 3082 keV (^{150}Sm) for a precise determination of their decay behavior. The experimental data were analyzed and prepared by Jörn Kleemann. This thesis presents a summary of his work in the present sections and in Sec. 6.2. A detailed description of both experiments can be found in the BSc (^{150}Sm) [178] and MSc theses (^{150}Nd) [179] of Jörn Kleemann. For ^{150}Sm , it turned out that the parity quantum number of the excited state at 3082 keV, which had been assigned by Ziegler *et al.* using the model-dependent Alaga rule [see, e.g., Eq. (6.19) in [65]], was incorrect. However, another 1^+ state was located within the energy range of the beam profile and this one's decay behavior could be studied.

4. Analysis

4.1. General

In this section, the general methodology of the analysis is introduced, loosely following the notation of Sec. 4 in [180]. Several sections discuss a functional relation between vectors of input quantities \mathbf{X} and output quantities \mathbf{Y} with n_X and n_Y dimensions:

$$\mathbf{Y} = f(\mathbf{X}, \mathbf{P}). \quad (4.1)$$

In Eq. (4.1), the symbol f denotes an arbitrary function of the input quantities and a vector of additional parameters \mathbf{P} . Any component of \mathbf{X} and \mathbf{Y} may be distributed according to a probability distribution function (PDF). The corresponding PDF for \mathbf{X} is denoted as $g_X(\xi)$, where ξ is a vector of variables for all possible values of \mathbf{X} . A random value drawn from the PDF g_X is denoted as \mathbf{X}_{rand} . It is assumed that the components of \mathbf{X} are independent, which means that a respective PDF $g_{X_i}(\xi_i)$ for each X_i exists. Furthermore, it is assumed that 'uncertainties' σ_{X_i} of the quantities X_i can be quantified, which are discussed in more detail in Sec. 4.1.1.

4.1.1. Propagation of Uncertainty

For the propagation of uncertainty, a method recommended in Supplement 1 [180] to the 'Guide to the Expression of Uncertainty in Measurement' [181] was used. To approximate the PDF g_Y , a number of N_R random vectors \mathbf{X}_{rand} is sampled from g_X . The function f is evaluated for each \mathbf{X}_{rand} , resulting in a set of values \mathbf{Y}_{rand} which is distributed according to g_Y in the limit $N_R \rightarrow \infty$.

Final results for Y_i are given in the form

$$\text{mode}(Y_i)_{-[\text{mode}(Y_i)-\text{sc}_-(Y_i)]}^{+[\text{sc}_+(Y_i)-\text{mode}(Y_i)]} \quad (4.2)$$

where $\text{mode}(Y_i)$ denotes the mode, and sc_\pm denote the upper ('+') and lower ('-') limit of the 68.3%¹ shortest coverage interval (Sec. 3, in particular 3.16 in [180]) of the approximated distribution. If the shortest coverage interval is symmetric, a quantity may also be given in the short form:

$$\text{mode}(Y_i)[\text{sc}_+(Y_i) - \text{mode}(Y_i)] = \text{mode}(Y_i)[\text{mode}(Y_i) - \text{sc}_-(Y_i)] \quad (4.3)$$

The number inside the brackets of Eq. (4.3) is given without a decimal point. This means that the last digit of the uncertainty is assumed to correspond to the last digit of the mode, i.e. for example, $12.3(23) \equiv 12.3_{-2.3}^{+2.3}$.

In this work, the mode is determined by the following procedure: A first approximation of g_Y is obtained by sorting the values $Y_{i,\text{rand}}$ into a histogram with $\left[\sqrt{N_R}\right]$ equidistant bins². The mode is assumed to be the centroid of the bin with the highest content. Since the histogramming method is highly sensitive to statistical fluctuations and outliers, the smooth probability distribution of Y_{rand} is approximated by a Gaussian kernel-density estimator [183], using Scott's rule (ibid., in particular Sec. 6.5.1). Scott's rule is a standard choice for the bandwidth of the smoothing kernel which is used, for example, by the python scientific computing library SciPy [184]. Using the first approximation of the mode from the histogram as a starting point, it is then determined as the maximum of the estimated probability distribution.

The probability distributions of the input quantities X_i are assumed to be Poissonian (chapter 3.II.B in [129]) if the uncertainty is dominated by counting statistics (for example peak areas in raw spectra returned by the fit algorithm of hdtv). If a symmetric uncertainty σ_{X_i} of a value $\langle X_i \rangle$ is given³, for example as the output of an algorithm or in a data sheet, the quantity is assumed to follow a normal distribution

¹This number was chosen in analogy to a normal-distributed quantity, where approximately 68.3% of the distribution are contained in a 2σ interval around the mode/mean value.

²This is a rule of thumb for the optimum number of histogram bins, and often used as a standard choice, for example by the data analysis framework ROOT [182].

³The notation for the uncertainty and the value itself are intentionally suggesting a standard deviation and a mean value.

$N(\langle X_i \rangle, \sigma_{X_i})$. If a quantity with a lower ($\sigma_{X_i,-}$) and upper ($\sigma_{X_i,+}$) uncertainty limit is given, it is modeled by the PDF

$$g_{X_i}(\xi_i) = \begin{cases} N(\xi_i, \langle X_i \rangle, \sigma_{X_i,-}) & \xi_i \leq \langle X_i \rangle \\ N(\xi_i, \langle X_i \rangle, \sigma_{X_i,+}) & \xi_i > \langle X_i \rangle \end{cases}. \quad (4.4)$$

The PDF in Eq. (4.4) is discontinuous at its mode $\xi_i = \langle X_i \rangle$, which, in general, is not equal to its mean value.

For the present calculations, $N_R = 10^6$ was chosen, because repeated Monte Carlo (MC) evaluations of the same output quantity yielded stable results for the mode and the shortest coverage interval with systematic uncertainties lower than $< 1\%$.

4.1.2. Parameter Estimation

Equation (4.1) can also be interpreted in the sense that tuples of measured values (X_i, Y_i) exist, i.e. $n_X = n_Y$, and the goal is to estimate the parameters \mathbf{P} of a mathematical model f that is assumed to describe ('fit') the data. In the most general case, the uncertainties of the X_i and Y_i are on the same order of magnitude. In this case, the optimum values of \mathbf{P} were determined using orthogonal distance regression (ODR, see, e.g., [185]⁴), which is one possible generalization of ordinary least-squares fitting:

$$\min_{\mathbf{P}, \delta} \sum_{i=1}^{n_X} w_{Y_i}^2 \left\{ [f(X_i + \delta_i, \mathbf{P}) - Y_i]^2 + w_{X_i}^2 \delta_i^2 \right\}. \quad (4.5)$$

In Eq. (4.5), the vectors \mathbf{w}_X and \mathbf{w}_Y contain weighting factors for each data point in the X - and Y dimension. The vector δ contains n_X additional artificial parameters, which take into account the deviation of the fitted function in the X dimension. In this work, $\mathbf{w}_{X_i} = \sigma_{X_i}^{-2}$ and $\mathbf{w}_{Y_i} = \sigma_{Y_i}^{-2}$ were used.

The uncertainties of the parameters \mathbf{P} were determined by an MC method in close analogy to Sec. 4.1.1: The minimization of Eq. (4.5) was repeated N_R times using

⁴Equation (4.5) is an intermediate step between Eq. (1.7) and Eq. (ODR) in [185] which includes the weighting factors w , but only scalar values of X_i and Y_i . The notation has been adapted.

randomly sampled values \mathbf{X}_{rand} and \mathbf{Y}_{rand} and the same weighting factors, resulting in a set of values \mathbf{P}_{rand} . The mode and shortest coverage interval for \mathbf{P} were then evaluated as described in Sec. 4.1.1. In a similar way, the total uncertainty of the 'predicted' function value $f(\mathbf{X}, \mathbf{P})$ for a fixed \mathbf{X} can be evaluated by evaluating f with the N_R sets of parameters. The generalized uncertainty band of f will be denoted as $\sigma_f(\mathbf{X}, \mathbf{P})$. An advantage of the aforementioned procedure is that correlations between the fit parameters are implicitly taken into account, which is especially important for evaluating σ_f .

It was applied, for example, for the energy calibration (Sec. 4.5.1). Figure 4.3, which shows the fit residuals in the X - and Y dimension, illustrates the interplay between σ_X and σ_Y . There is one calibration point at 2448 keV [186], which is well-known in the literature, but has poor statistics in this run. Without taking into account the peak-fit uncertainty, it would have strongly increased the calibration uncertainty. In many other cases, the uncertainty in one dimension was much larger than the other, and a 1D fit was performed, minimizing the chi square (χ^2) statistic (see below).

If an evaluation of the function f was computationally too expensive, the aforementioned MC method could not be applied. This was the case, for example, for the determination of $\delta_{L,i \rightarrow j}$ (see Sec. 4.6.1), where each evaluation of f for a given $\delta_{L,i \rightarrow f}$ required a full MC particle simulation. Since all of the computationally demanding fits in this work only had a single parameter, its value was determined by evaluating f on a 1D grid of values for $\mathbf{P} \equiv P$ and minimizing the reduced chi-square (χ_{red}^2) statistic (see, e.g., Sec. 39.3.2.3 in [2]):

$$\chi_{\text{red}}^2 = \frac{1}{n_X - n_P} \underbrace{\sum_{i=1}^{n_X} \frac{[Y_i - f(X_i, P)]^2}{\sigma_{Y_i}^2}}_{\chi^2}. \quad (4.6)$$

For simplicity, Eq. (4.6) is shown for a 1D problem ($n_P = 1$). The definition of χ^2 is indicated by a brace below Eq. (4.6). With the χ^2 statistic, a confidence interval for \mathbf{P} can be obtained by taking all sets of parameters for which the following inequality is fulfilled [Eq. (39.29) in [2]]:

$$\chi^2 \lesssim \min_P(\chi^2) + 1. \quad (4.7)$$

4.1.3. Systematic Uncertainty

Some parts of the analysis contain inherent systematic uncertainties, which are difficult to quantify. If a situation was encountered where a parameter estimation obviously yielded too small uncertainties, and the presence of systematic uncertainties could not be excluded, the procedure recommended by the Particle Data Group (PDG) ([2], in particular Sec. 5.2.2) for dealing with underestimated uncertainties is used: First, χ_{red}^2 [Eq. (4.6)] is calculated using the optimum parameters and compared to the expected value of 1. If χ_{red}^2 is larger than 1, indicating the presence of systematic uncertainties, then σ_f is scaled by a factor $\sqrt{\chi_{\text{red}}^2}$. As the authors of [2] emphasize, this method was not used to fix extremely large χ_{red}^2 , which would indicate an insufficient model or systematic uncertainties strong enough to make the measurement meaningless.

The method of the PDG was applied in the analysis steps listed below. For each point, a short justification is given where the systematic uncertainties are identified.

- For the fits of the energy calibration (see Sec. 4.5.1), where nonlinear effects may be superimposed on the assumed linear energy calibration. This is discussed in Sec. 9.4 of [187] [in particular, see Fig. 9.5 (a)].
- For the calculation of the weighted average of photon energies observed in multiple detectors (see Sec. 4.5.1). Some of the energy calibrations had to be extrapolated in cases where no high-energy calibration points were available. As another safeguard against the aforementioned nonlinear effects, the PDG procedure was applied again.
- For the fits of MC simulations to data (see Sec. 4.5.2 and 4.5.4). These simulations are based on phenomenological models of the underlying microscopic processes and an approximation of the actual experimental geometry.

4.1.4. Spectrum

The raw data from the DAQ are available as pulse-height spectra, whose processing will be one of the main subjects of this chapter. To be able to perform mathematical operations on a spectrum, the following definition will be used throughout this work:

Definition 4.1. Identify the bins of a one-dimensional spectrum by their discrete centroid energy values E_m , where m is an integer label (the ADC channel) with the possible values $1 \leq m \leq N_s$. Assuming that the symbol N denotes the spectrum itself, then $N(E_m)$ or N_m denotes the content of the bin with centroid energy E_m . The width of a single bin of the spectrum N is denoted as $\Delta E_N(E_m)$.

4.1.5. Numerical Evaluation and Visualization

For numerical calculations in this work, the python libraries NumPy [188, 189] and SciPy [184], and the C++ data analysis framework ROOT [182] were used. All data were visualized using the python library Matplotlib [190]. Some schematic plots used the TikZ library for LaTeX [191].

4.2. Simulation of the Experimental Setup

An about 7 m-long part of the beam line at HI γ S [168] was implemented in the MC particle simulation framework GEANT4 [8–10], as a part of the so-called 'utr' code [192]. Even though its original field of application was high-energy physics, the GEANT4 framework is now routinely applied in the analysis of low-energy NRF experiments by groups all over the world, for example in Cologne [193], Darmstadt [194], Dresden [195], Durham [196], Istanbul [197], and Tokai [198]⁵.

The virtually reconstructed setup was used in several steps of the analysis to take into account geometric effects, and, in particular, to inter- and extrapolate properties of the detectors which would otherwise be challenging to determine. Presumably, the simulation contains all structural elements of the beam line which are relevant for the present NRF experiment. The geometry extends from the collimator room, where the photon beam exits the evacuated beam line, to the zero-degree detector, after which it propagates unhindered into another experimental

⁵The given publications are, to the knowledge of the author, the latest NRF-based publications which make use of the GEANT4 framework and have a first author from the respective location. They are sorted alphabetically by the location. The representative publications for Cologne and Durham do not mention GEANT4 explicitly, but as a co-author of [193] and close collaborator of the Durham group, the author of this work can confirm that GEANT4 was used.

hall. It includes the two experimental setups and various shielding components. Due care has been exercised in the implementation of the targets and the detectors, which are based on technical drawings and data sheets, since they represent the main interaction points of the photons.

GEANT4 provides (phenomenological) models for a multitude of interaction processes of particles with matter. The choice which models and particles to include in a simulation is left to the user. Since the photon beam energies of the present experiment were below the neutron separation thresholds of most commonly used materials and, in particular, the targets, only photons and electrons/positrons, which may be created as secondary particles, were simulated. For photons, models for Rayleigh scattering, the photoelectric effect, Compton scattering, and the conversion of polarized particles (see, e.g., Sec. 2.III in [129]) from the so-called 'Livermore' package of low-energy EM physics models were used. The aforementioned interaction processes are the most probable ones for photons at the energies of the present experiment (see, e.g., Sec. 2.III in [129]). Recently, the Delbrück scattering process was added to GEANT4 by Omer and Hajima [199]. Elastic, or coherent, scattering processes like Rayleigh- and Delbrück scattering are a potential source of systematic errors in NRF experiments. Especially when single ground-state transitions cannot be resolved any more in the range of the beam profile [133], they can mimic the elastic NRF process and lead to an overestimation of the actual NRF cross section. However, even in long-term simulations of the present experimental setup, no elastically scattered photons from either of the two processes were detected. In any case, the level density of the isotopes of interest was low enough, so that a discrimination of NRF photons would have been straightforward.

The NRF process itself is not included in the standard packages of GEANT4, probably because the data are too sparse⁶. It was not needed for the present analysis, since all other relevant processes could be simulated, and therefore it was possible to disentangle the different contributions to the observed spectrum (see Sec. 4.3 and 4.5.4). In addition, the low cross section of NRF would have required simulation times which are orders of magnitude larger (see the discussion in Secs. 2.1.1 and 4.5.4). However, the present analysis required a simulation of the angular distributions of the resonantly scattered photons. This functionality

⁶The author of this work became aware too late of the excellent GEANT4 extension which has been developed by Lakshmanan *et al.* [200] and extensively tested [201].

was implemented as a part of this work. Using an accept-reject sampling algorithm (see, e.g., chapter 2 in [202]), the 'utr' code generates primary particles with an arbitrary angular distribution in an arbitrarily oriented coordinate system.

For electrons/positrons, models for quasi-continuous energy loss by bremsstrahlung, ionization and multiple scattering were used and complemented by a model for the annihilation of positrons (see, e.g., Sec. 2.II in [129]), all of them from the same Livermore package.

In all simulations, primary photons with a well-defined energy and momentum direction were released into the virtual geometry and their interactions were simulated by GEANT4. For each particle, the energy depositions inside the detector crystals were accumulated and stored to obtain energy spectra in analogy to the experiment. This procedure assumes a pileup-free (see, e.g., Sec. 17.V in [129]) detection system. However, pileup can be taken into account by post-processing the simulated spectra (see Sec. 4.3.3) in the present case. The number of simulated primary particles was always chosen large enough, so that the influence of the statistical uncertainty which is introduced by the Monte Carlo method was negligible compared to all other involved uncertainties.

4.3. Spectrum Decomposition

This subsection describes the different contributions to the energy spectra of photons⁷ which were detected during the experiments. Furthermore, the influence of the detector response on the original photon spectrum will be discussed. The combined knowledge of photon sources and detector properties was used in the analysis to extract information like the original beam spectrum or the photon flux from the measured spectra.

⁷Due to the properties of the beam and the detectors, almost exclusively photons were detected in the experiments of this work. Therefore, the word 'photons' will be used as a substitute for 'particles' in this section.

4.3.1. Original Spectrum

In the experiments of this work, the original spectrum \bar{N} is composed of contributions by actual NRF photons from the target (\bar{N}_{nrf}), nonresonantly scattered photons from anywhere on the beamline (\bar{N}_{nr}) (see, e.g., Sec. 4.III in [129]), ambient background (\bar{N}_{bg}) (Sec. 20.I in [129]), energy deposition by cosmic radiation (\bar{N}_{cr}) (ibid.), and electronic noise (\bar{N}_{en}) (for the specific case of HPGe detectors, see chapter 12.III in [129]):

$$\bar{N} = \bar{N}_{\text{nrf}} + \bar{N}_{\text{nr}} + \bar{N}_{\text{bg}} + \bar{N}_{\text{cr}} + \bar{N}_{\text{en}}. \quad (4.8)$$

4.3.2. Detector Response

Assuming that an original spectrum \bar{N} of particles impinges on a detector, then the detected spectrum $N^{(0)}$ is obtained by a matrix-vector multiplication of $\bar{N}(E_m)$ with the detector response matrix $D(E_m, E_n)$:

$$N^{(0)}(E_m) = \sum_{n=1}^{N_s} D(E_m, E_n) \bar{N}(E_n). \quad (4.9)$$

The response matrix D defined for the purpose of this work contains all physical effects that take place inside a detector volume and create a finite energy deposition in the volume. It assumes that the detector can resolve every single photon event and therefore neglects signal pileup, which is indicated by the (0) superscript (see below). The diagonal matrix elements $D(E_m, E_m)$ give the intrinsic efficiency ϵ_{int} of a detector for photons with an energy E_m . For a detector with a perfect energy resolution, the matrix elements $D(E_m > E_n, E_n)$ are exactly zero. Due to a finite resolution, there can also be detected events with a larger energy than the maximum energy of the original spectrum.

4.3.3. Pileup

At higher count rates, pileup effects (see, e.g., Sec. 17.V in [129]) can occur when multiple electronic signals of the detector are counted as one because they are too

close in time to each other. The top part of Fig. 4.1 shows two artificial electronic

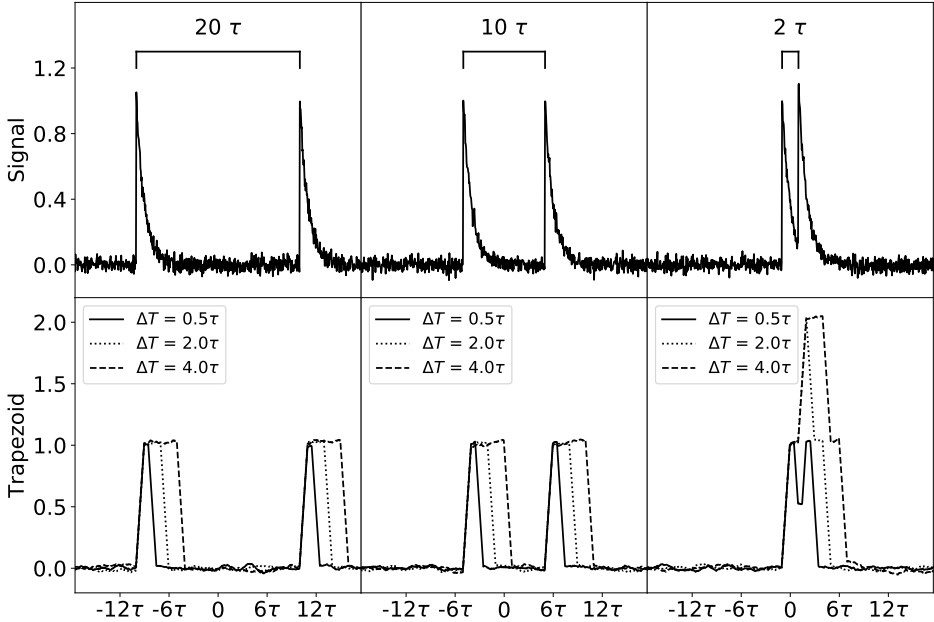


Figure 4.1.: Schematic illustration of the emergence of pileup in signal processing. Each panel in the top row shows two artificial exponentially decaying raw signals with a decay constant τ . From left to right, the distance between the two signals decreases leading to pileup in the third panel. The bottom row shows the signal after processing by trapezoidal filters with three different settings of the shaping time ΔT . Only the most narrow trapezoid is able, at the expense of an inferior energy resolution, to resolve the double signal.

pulses which have a much larger (exponential) decay time than their rise time. This behavior is typical for HPGe detectors (see, e.g., Sec. 12.III.C.2 [129]). Besides the normal-distributed artificial noise which was imposed on the spectrum, the two pulses have identical properties. In the lower part, a trapezoidal filter [203] which is commonly used in digital signal processing, has been applied to the signals. The

filter function in the aforementioned publication has two parameters, the decay time τ which has to be matched to the decay time of the signal, and the 'shaping time' ΔT that determines the width of the trapezoid. The latter parameter is used to improve the energy resolution by sampling a larger part of the decay curve, at the expense of pileup and increased dead time. From left to right, as the pulses get closer to each other, not all filters are able to separate the two signals any more and will report a single signal with about twice the height of a single pulse. The spectrum N , which is actually observed in the experiment, will be composed of the spectrum $N^{(0)}$ from Eq. (4.9) plus all pileup components $N^{(p)}$, where p denotes the order of the pileup (two signals merged into one would be first order pileup, and so on):

$$N(E_m) = N^{(0)}(E_m) + \sum_{p=1}^{\infty} N^{(p)}(E_m) \quad (4.10)$$

Pileup can be taken into account in a similar matrix-vector multiplication as the detector response (Eq. (4.9)). The formalism was introduced by Cano-Ott et al. [204] and specialized for the present type of experiments by Angell [205]. The relation between the spectrum $N^{(0)}$, and its first-order pileup component $N^{(1)}$ is given by [Eq. (1) and (3) in [205]]:

$$N^{(1)}(E_m) = \sum_{n=1}^{N_s} M(E_m, E_n) N^{(0)}(E_n) \quad (4.11)$$

In this equation, the pileup matrix M has been introduced, which connects the bin E_n of the spectrum with the bin $E_m > E_n$ of the first-order pileup spectrum. The pileup matrix can be written as [Eq. (3) in [205]]:

$$M(E_m, E_n) = \sum_{o=1}^{N_s} P(E_o) P(E_o, E_n, E_m) \quad (4.12)$$

In the sum in Eq. (4.12), two expressions for probabilities appear: The symbol $P(E_m)$ denotes the probability of measuring an event with the energy E_m , which is approximately proportional to the bin content of the spectrum $N^{(0)}$:

$$P(E_m) \approx c_{N^{(0)}} N^{(0)}(E_m) \quad (4.13)$$

The proportionality via the normalization constant $c_{N^{(0)}} = (\sum_m N^{(0)}(E_m))^{-1}$ is only approximate, because the spectrum $N^{(0)}$ is a statistical sample of the underlying probability distribution. The symbol $P(E_o, E_n, E_m)$ denotes the probability of two signals with energies E_o and E_n summing up to an energy E_m . In general, it depends on the shape of the signal pulses and the pulse sequence, but in the following it will be argued that $P(E_o, E_n, E_m)$ can be approximated by:

$$P(E_o, E_n, E_m) \approx \delta[(E_o + E_n) - E_m] \quad (4.14)$$

Equation (4.14) means that if two signals with energies E_o and E_n pile up, then they will always pile up to their sum energy. Due to the characteristics of the HI γ S beam, this is highly probable: With the chosen quasi-continuous wave operation mode, the beam time structure consists of 'micropulses with sub-ns durations at 5.5796 Hz' [127]. Comparing the micropulse duration to the typical decay time of an HPGe detector signal of about $\tau = 10^5$ ns [see, e.g. Sec. 4 in [187], in particular Fig. 4.7 a)], it becomes clear that if pileup within a single micropulse occurs, it will almost certainly lead to the sum energy of both photons being recorded.

Since the approximation of Eq. (4.14) is well justified in this case, the pileup matrix [Eq. (4.12)] can be simplified:

$$M(E_m, E_n) \stackrel{\text{Eq. (4.14)}}{=} \sum_{o=1}^{N_s} P(E_o) \delta[(E_n + E_o) - E_m] = P(E_m - E_n) \quad (4.15)$$

Inserting Eq. (4.15) into the definition of the pileup matrix [Eq. (4.11)] yields:

$$N^{(1)}(E_m) = \sum_{n=1}^{N_s} P(E_m - E_n) N^{(0)}(E_n) \quad (4.16)$$

$$\stackrel{\text{Eq. (4.13)}}{\approx} c_{N^{(0)}} \sum_{n=1}^{N_s} N^{(0)}(E_m - E_n) N^{(0)}(E_n) = c_{N^{(0)}} N^{(0)} * N^{(0)}$$

The last equality in Eq. (4.16) shows that the first-order pileup spectrum can be obtained from the pileup-free spectrum by a mathematical convolution of $N^{(0)}$ with itself. For this, the spectrum needs to be zero-padded, i.e.:

$$N(E_{m < 1}) \equiv N(E_{m > N_s}) \equiv 0 \quad (4.17)$$

The convolution method, which can be implemented efficiently using the FFT algorithm, can be used to impose pileup on simulated spectra by post processing (see Sec. 4.5.4, note that the simulated spectra are pile-up free by design)⁸. Higher-order pileup contributions with $p \geq 1$ can be obtained from the recursive formula:

$$N^{(p)} = c_{N^{(0)}} N^{(p-1)} * N^{(0)} \quad (4.18)$$

4.4. Sensitivity Limit

Due to the different interaction processes of photons with matter (see Sec. 4.2), the spectra of this work are composed of a continuous background on which quasi-discrete lines can be identified (see, e.g., the spectra of the present work in Sec. D). A quantitative criterium for the statistical significance of such a line, which has been used consistently for all subsequent analysis steps, will be given in this section.

4.4.1. Definition

In Sec. 3.VI of his textbook, Knoll [129] derives sensitivity limits under the assumption that the probability distributions of all measured quantities are normal, i.e. first-order ('Gaussian') propagation of uncertainty can be applied. In the derivation, it is assumed that two measurements are performed in which a total number of events is counted in a detector. The first one is a background measurement, and the second one is a measurement with potentially present artificial radioactivity. In the background measurement, N_B events are measured, while in the second measurement $N = N_B + N_S$ events are counted, which correspond to the sum of the background events and the artificial activity. In a situation where the determination of a sensitivity limit is necessary, it can be assumed that $N_S \ll N_B$ and $N_B \approx N$. Given an estimate for the standard deviation σ_{N_B} of N_B

⁸The raw output of the Monte-Carlo simulations in this work contained the energy depositions by every single primary particle. Therefore, instead of using the convolution of Eq. (4.16), the p -th order pile up contribution was obtained by adding up p subsequent energy depositions by different primary particles in the same detector crystal. This reduced the total number of events by a factor of p .

from the background measurement, the probability that statistical fluctuations of the background activity are falsely interpreted as artificial activity in the second experiment is less than 5%, if a threshold L_C is set to [Eq. (3.61) in [129]]:

$$L_C \approx 2.326 \times \sigma_{N_B} = 2.326 \times \frac{\sigma_{N_S}}{\sqrt{2}} \approx 1.645 \times \sigma_{N_S}. \quad (4.19)$$

In the second equality of Eq. (4.19), the relation between the standard deviations σ_{N_B} and σ_{N_S} [Eq. (3.60) in [129]] was inserted. If the randomness of σ_{N_B} is caused by counting statistics only, the probability distribution for N_B is Poissonian (see Sec. 3.II and 3.VI in [129]), and $\sigma_{N_B} = \sqrt{N_B}$.

The probability that excess counts have been caused by statistical fluctuations of the background is lower than 5% if the threshold N_D is determined by the 'Currie equation' [[206] or Eq. (3.67) in [129]]:

$$N_D \approx 4.653 \times \sigma_{N_B} + 2.706 \approx 3.290 \times \sigma_{N_S} + 2.706 \quad (4.20)$$

Equations (4.19) and (4.20) are therefore 95% confidence limits for the absence and the presence of artificial radioactivity.

4.4.2. Spectroscopic Sensitivity Limit

Compared to the counting experiments discussed in Sec. 4.4.1, spectroscopy provides additional information about the energy of the radiation. The goal is to detect photons with quasi-discrete energies on a continuous background. The discrete energies are blurred by the finite detector resolution into a line shape ('peak') that extends over multiple bins of the spectrum. Now the question arises how to determine σ_{N_B} , σ_{N_S} , or N_B in Eqs. (4.19) and (4.20). A commonly quoted rule of thumb is to take N_B to be the 'area below the peak'. But this rule is not well-defined and can be exaggerated ad absurdum if one considers that the frequently assumed Gaussian shape of peaks has an infinite range.

Assuming that the line shape is normal distributed and its location known, the German Institute for Standardization (DIN) gives a definition of N_B . It is recommended

to determine the area below the peak as [207]:

$$N_B(E_0) \approx \int_{E_0 - c_{\text{DIN}} \text{FWHM}/2}^{E_0 + c_{\text{DIN}} \text{FWHM}/2} N_{B,\Sigma} B(E) dE. \quad (4.21)$$

In Eq. (4.21), the symbol $B(E)$ denotes the normalized probability distribution of the background spectrum, which is proportional to the actual spectrum via the total number of background events $N_{B,\Sigma}$. Since $B(E)$ is smooth, but the measured spectrum contains statistical fluctuations, Eq. (4.21) is approximate. A parameter c_{DIN} times the full width at half maximum (FWHM) of the expected line shape is the integration range. If the location of the peak is known, $c_{\text{DIN}} \approx 1.2$ is recommended. The parameter E_0 should be chosen to 'cover the line shape as symmetrically as possible' (translated from [207]).

The method of determining a detection limit followed by spectrum analysis programs like tv [208, 209] and hdtv [210, 211] is to perform a simultaneous weighted fit of a background- and a line shape model. This has the advantage that the uncertainties of the bin contents are automatically taken into account and manifest in the fit uncertainty of $N_{B,\Sigma}$ and N_S . The disadvantage of fitting is the increased computational effort.

In Sec. A, an analytical expression for the spectroscopic sensitivity limit is derived from few assumptions about the background and the line shape model. For a narrow normal-distributed line shape with standard deviation (detector resolution) $\sigma(E)$ on a constant background, the factor σ_{N_S} in Eq. (4.19) and (4.20) is:

$$\sigma_{N_S}(E) = \langle \sigma_{N_B}(E) \rangle \sqrt{2\sqrt{\pi} \frac{\sigma(E)}{\Delta E_N}} \approx 1.88 \times \langle \sigma_{N_B}(E) \rangle \sqrt{\frac{\sigma(E)}{\Delta E_N}}. \quad (4.22)$$

In Eq. (4.22), $\langle \sigma_{N_B}(E) \rangle$ denotes the average standard deviation of the number of events in a single background bin with a width of ΔE_N in the energy region of interest.

In practice, the sensitivity limit was determined by the following procedure: The quasi-continuous background in the spectra was interpolated at manually identified points by a cubic spline [211] to obtain a smooth approximation of $N_{B,\Sigma} B(E)$ [Eq. (4.21)]. A running average of $N_{B,\Sigma} B(E)$ ($\langle N_B \rangle$) was calculated by (FFT)

convolving it with a 4-bin wide rectangular function. This range is large enough to reduce statistical fluctuations of single bins, but small enough to be able to consider the background as constant. From $\langle N_B \rangle$, $\langle \sigma_{N_B} \rangle$ in Eq. (4.22) was obtained. Using a width calibration (see Sec. 4.5.3), σ_{N_S} was obtained, which can be used to calculate the energy-dependent values of L_C and N_D in Eqs. (4.19) and (4.20). In all spectra of Sec. D, the spline interpolation of the background is shown as a dashed line. The ratios $(N_S - \langle N_B \rangle) / L_C$ and $(N_S - \langle N_B \rangle) / N_D$ are shown in comparison to the residuals of the background interpolation and enable a straightforward identification of statistically significant lines. The quantity $N_S(E)$ was determined in a similar way as $N_{B,\Sigma}B(E)$, using the original spectrum instead of the smooth background interpolation.

4.5. Calibrations

This section introduces the necessary calibrations for the extraction of nuclear properties from experimental observables.

4.5.1. Energy Calibration and Binning

An energy calibration is a mapping of the pulse-height spectra in units of ADC channels m to photon-energy spectra in units of E_m . The energy calibration is based on known photon energies from ambient background, radioactive calibration sources, or NRF reactions.

Recoil Correction

The energy E_γ of the observed photons is only equal to the energy difference ΔE between excited states up to the recoil energy transferred to the nucleus due to conservation of momentum in the absorption/emission process [120]. The recoil correction is on the order of $E_\gamma^2 / M(Z,A)c^2$ [120], where $M(Z,A)$ denotes the mass of the nucleus. For an $A = 82$ nucleus at an excitation energy of 3 MeV, this correction is on the order of 0.1 keV and therefore significant at the precision level of the present experiment (see below).

The recoil corrections can be derived in relativistic dynamics from the conservation of 4-momentum. Since the kinetic energy of the recoiling nucleus is much larger than the binding energy of an atom in condensed matter, which is typically on the order of few eV (see, e.g., chapter 20 in [212]), the atomic environment of the nucleus can be neglected. For the emission of a photonray from a nucleus at rest, which is the case for a radioactive source, the following relation holds:

$$\Delta E = M(Z,A)c^2 \left(\sqrt{1 - \frac{2E_\gamma}{M(Z,A)c^2}} - 1 \right). \quad (4.23)$$

For an elastic NRF process, i.e. the absorption and subsequent transition directly back to the ground state, the relation is approximately given by [Eq. (4.1) in [213]]:

$$\Delta E = E_\gamma \left\{ 1 + \frac{1}{2} \left[1 - 2 \cos(\theta) \frac{E_\gamma}{M(Z,A)c^2} \right] + \mathcal{O} \left[\left(\frac{E_\gamma}{M(Z,A)c^2} \right)^2 \right] \right\}. \quad (4.24)$$

In Eq. (4.24), the symbol θ denotes the angle between the incoming and the outgoing photon.

Energy Calibration

One of the available calibration sources, ^{56}Co , emits photons with energies that cover almost the entire energy range of the present experiment [177]. However, a run-by-run calibration using ambient background and known NRF transitions (if available) was preferred to the calibration runs with the ^{56}Co source, which were done mainly before and after the experiment.

The need for a continuous readjustment of the energy calibration arose because, during the more than three-week long experiment, the electronics showed considerable (nonlinear) drifts. This can be seen in Fig. 4.2, which shows the time-dependent centroid position of some background photons in units of ADC channels. First of all, Fig. 4.2 shows that the order of magnitude of the drifts varies by about two orders of magnitude for different detectors. HPGe 4 was the detector with the most extreme absolute drifts. Considering that the ADCs have $2^{14} = 16384$

channels, and the amplification was set to cover an energy range of roughly 5 MeV, this would mean that peak positions changed by up to 30 keV throughout the entire experiment. However, at least the relative position of the peaks is visibly stable for HPGe 4, which means that the drifts can be corrected approximately by multiplication with a constant factor. HPGe 1, on the other hand, exhibits comparably small, but nonlinear drifts. Obviously, the time dependence of the shifts of the two detectors in Fig. 4.2 is correlated, which is an indication that the problem was caused by the multichannel ADC or the crate to which both detectors were attached.

For HPGe detectors, the relation between E_m and m is usually linear with small quadratic corrections (chapter 7.4 in [187]). Indeed, it was found for all detectors in this work that the following relation was the best tradeoff between a good fit of the calibration data and a robust extrapolation (see, e.g., the discussion in chapter 9.4 in [187] about linearity):

$$E_m = p_0 + p_1 m + p_2 m^2. \quad (4.25)$$

Figure 4.3 shows an example for an energy calibration of a single detector in a target run. At this beam energy, a transition of ^{37}Cl was available as a high-energy calibration point in addition to the ambient background.

For the determination of energies of unknown transitions, a weighted average over all detectors of a setup was calculated, resulting in uncertainties on the sub-keV level in most cases. Newly observed transitions with an energy E_γ were associated with transitions between two nuclear states E_i and E_j with $E_j > E_i$ using the Ritz variation principle [216] with the boundary condition [similar to Eq. (18) in [131]]:

$$\left| (E_j - E_i) - E_\gamma \right| \leq \sqrt{\sigma_{E_j}^2 + \sigma_{E_i}^2} + \sigma_{E_\gamma} + \frac{E_\gamma^2}{M(Z, A)c^2} \quad (4.26)$$

The requirement in Eq. (4.26) is that the difference between $E_j - E_i$ and E_γ is smaller than the combined uncertainties of both quantities plus a recoil factor (see Sec. 4.5.1). For simplicity, only the first-order term of the recoil correction was taken.

Binning

A nonlinear energy calibration, as given by Eq. (4.25), will result in a spectrum with non-equidistant centroid energies. However, some analysis steps perform a fast Fourier transform (FFT) of the spectrum (see, e.g., Sec. 4.4), which is defined for equally spaced intervals (see Sec. 6.2 in [217]). To be able to apply the FFT and simplify other procedures as well, an equidistant binning of the spectra was restored using the 'relocation' algorithm proposed by Tsai, Mucciolo and Helene [218]. This algorithm redistributes the observed events into new bins based on a quasi-continuous interpolation of the original spectrum via an MC method. It ensures that the statistical properties of the spectrum are not changed in the process.

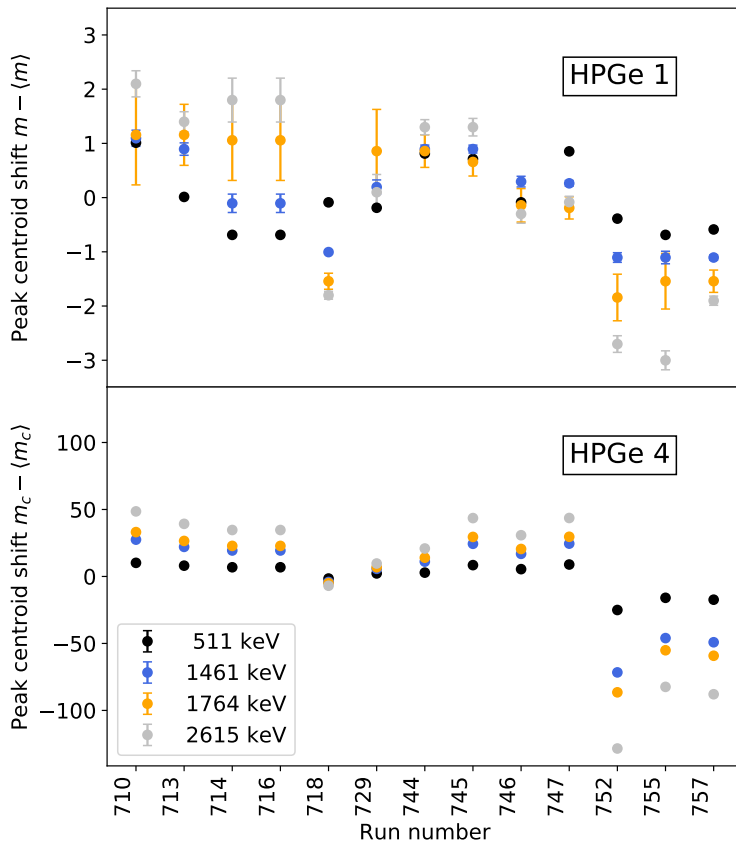


Figure 4.2.: Deviation of the centroid channel m_c from its unweighted time average $\langle m_c \rangle$, shown for four characteristic background lines at 511 keV ($e^- - e^+$ annihilation [2]), 1461 keV (^{40}K decay [214]), 1764 keV (^{214}Bi decay [186]), and 2615 keV (^{208}Bi decay [215]) for HPGe 1 (top) and HPGe 4 (bottom). The abscissa indicates the numbers of 13 runs, which correspond to different energy settings in the ^{82}Se experiment (see also Tab. 3.1).

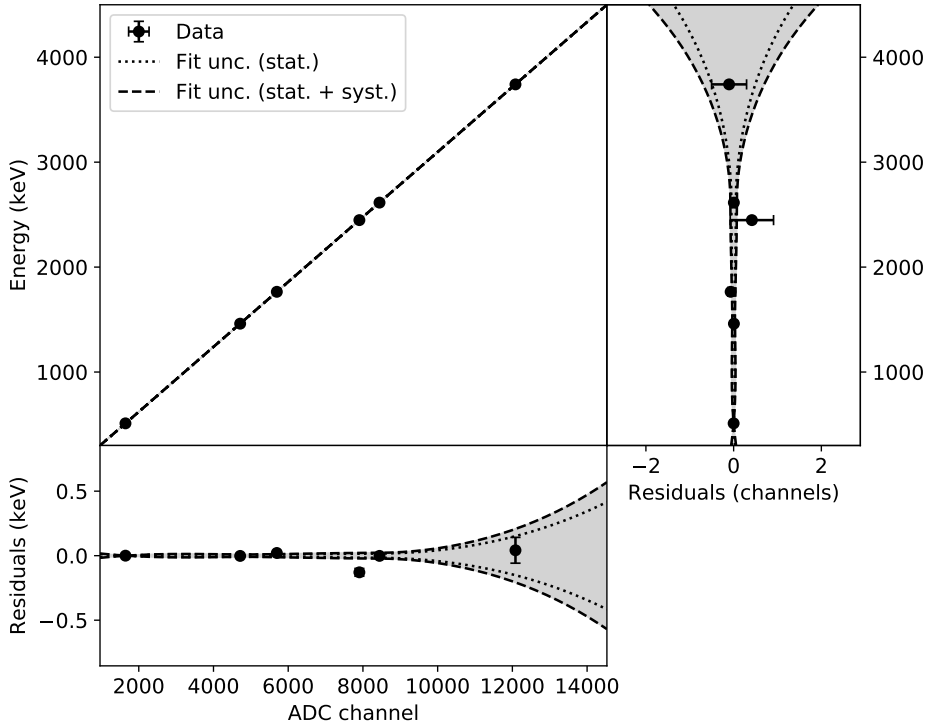


Figure 4.3.: Energy calibration of HPGe 3 at a beam energy of 3820 keV, using photons at 511 keV (e^-e^+ annihilation [2]), 1461 keV (^{40}K decay [214]), 1764 keV and 2448 keV (^{214}Bi decay [186]), 2615 keV (^{208}Bi [215]), and 3741 keV (^{37}Cl NRF [175]). A quadratic model [Eq. (4.25)] was fit to the experimental data. The uncertainty returned by the weighted fit, denoted as statistical ('stat'), is shown as a dotted line. Systematic uncertainties ('syst') have been taken into account by the procedure described in Sec. 4.1.3. The uncertainty band which includes both contributions is shown in gray with a dashed boundary. The figure shows the quadratic fit to the data (*top left*), and the projection of the fit residuals on the energy (*top right*) and channel (*bottom left*) axis.

4.5.2. Efficiency Calibration

Several steps of the analysis require knowledge of the energy-dependent photopeak- or full-energy peak (FEP) efficiency $\epsilon(E_\gamma, \mathbf{r})$ of the detectors, which is interpreted in this section as:

$$\epsilon(E_\gamma, \mathbf{r}) = \frac{\# \gamma \text{ rays with an energy } E_\gamma \text{ from the source at } \mathbf{r} \text{ counted by a detector}}{\# \gamma \text{ rays with an energy } E_\gamma \text{ emitted by an isotropic source at } \mathbf{r}} \quad (4.27)$$

Both in the numerator and denominator of Eq. (4.27), E_γ is assumed to take into account limitations like the finite resolution of the detector. In the numerator, 'number of γ rays ... from the source' implies that they can be separated from other photons with the same energy. The parameter \mathbf{r} will be dropped if it is clear from the context where the source was located.

In Sec. 4.6, the 'differential efficiency' will be used:

$$\frac{d\epsilon}{d\Omega'}(E_\gamma, \theta', \varphi', \mathbf{r}) = \frac{\# \gamma \text{ rays with an energy } E_\gamma, \text{ emitted by a source at } \mathbf{r} \text{ in a direction given by } \theta' \text{ and } \varphi' \text{ counted by a detector}}{\# \gamma \text{ rays with an energy } E_\gamma, \text{ emitted by a source at } \mathbf{r} \text{ in a direction given by } \theta' \text{ and } \varphi'} \quad (4.28)$$

The quantity in Eq. (4.28) describes the full-energy peak efficiency of a detector with respect to a beam of particles emitted from a point \mathbf{r} into a solid-angle element Ω' . Eq. (4.27) can be obtained from Eq. (4.28) by integrating the latter over the entire solid angle.

In the present work, the efficiency from Eq. (4.27) with respect to the two target positions was determined experimentally at a set of discrete energies $E_{\gamma,i}$ using radioactive ^{56}Co - [177] and ^{152}Eu [219] sources. Both sources emit photons with well-known relative intensities $I_{\text{rel}}(E_\gamma)$. The energy range covered by the ^{56}Co and ^{152}Eu sources extends from 300 keV to about 3600 keV, which fits the range of the present experiment relatively well. Information about the sources can be found in Tab. 4.1. For the ^{152}Eu source, the activity $\dot{A}(t)$ was known with a comparably high precision [167], while \dot{A} for the newly produced ^{56}Co source was unknown at that time. It was estimated by comparison to the ^{152}Eu source (see Tab. 4.1).

Table 4.1.: Information about the radioactive sources which were used for efficiency calibrations and coarse energy calibrations in this work.

Isotope	$T_{1/2}$	Activity (Bq)	Reference
^{56}Co	77.236(26) d	$1.405(21) \times 10^5$ ⁹	[177]
^{152}Eu	13.517(14) y	$3.5213(4) \times 10^4$ ¹⁰	[219]

Compared to the dimensions of the setup, the sources were approximately point-like. In the calibration runs, they were placed at the respective target positions in the γ^3 setup and the polarimetry setup. To be as close as possible to the actual experimental conditions, the beamline was also evacuated in these runs. From the observed number of counts $A(E_\gamma)$ at a certain photon energy, the experimental efficiency at this energy (ϵ_{exp}) was determined as:

$$\epsilon_{\text{exp}}(E_\gamma) = A(E_\gamma) \frac{\ln(2)}{T_{1/2} \dot{A}(t_{\text{start}}) I_{\text{rel}}(E_\gamma)} \left(1 + \frac{t_{\text{dead}}}{t_{\text{stop}} - t_{\text{start}} - t_{\text{dead}}} \right) \times \left\{ \exp \left[-\frac{\ln(2)}{T_{1/2}} t_{\text{start}} \right] - \exp \left[-\frac{\ln(2)}{T_{1/2}} t_{\text{stop}} \right] \right\}^{-1}. \quad (4.29)$$

Equation (4.29) was 'derived' from Eq. (4.27) using $A(E_\gamma)$ for the numerator and the integral over the radioactive decay law (see, e.g., Sec. 1.I.A in [129]) for the denominator. The symbols t_{start} and t_{stop} denote the points in time which mark the beginning and the end of the efficiency measurement. In the decay law, the half life $T_{1/2}$ of the radioactive source material is contained. Since the signal processing takes a certain amount of time, data can not be recorded during the full time interval $t_{\text{stop}} - t_{\text{start}}$. This dead time t_{dead} is taken into account by a correction factor (see, e.g., Sec. 4.VII in [129]). For later use, note that the difference between the real time and the dead time is called the 'live time' (t_{live}).

⁹Determined relative to the known activity of the ^{152}Eu source. Explicitly, runs 740 and 741 from November 27 and 28, 2016, (see Tab. 3.1) were compared using all four HPGe detectors of the γ^3 setup.

¹⁰Measured in January 2007. The label on the radioactive source said '0.9517 μCi ', so the uncertainty was estimated to be on the order of the last digit. See also the electronic logbook [167].

For an interpolation of the experimental efficiencies, there is the choice between parametric phenomenological models, like the ones given by Knoll [129] [Eq. (12.32)] and Jäckel, Westmeier, and Patzelt [220], or realistic simulations. By design, the parametric models are superior for this purpose. However, since they are generally based on exponential functions, corresponding to the characteristic energy-dependence of the photon-matter interaction (see, e.g., [128]), they may strongly diverge from the real underlying functional relation if extrapolated even moderately beyond the data range. For the present experiment, the extrapolated range was about 20% larger than the one covered by radioactive source data, which called at least for a comparison to simulations. In any case, other analysis steps depend on simulated quantities which implicitly contain the efficiency, so the efficiency simulations can be seen as a validation.

Explicitly, the energy dependence $\epsilon(E_\gamma)$ was simulated at discrete energy steps in GEANT4 using a point-like, isotropic, monoenergetic photon source at the target position. The simulated efficiency $\epsilon_{\text{sim}}(E_\gamma)$ was determined by comparing the number of events where the complete energy of a photon was deposited in a single detector crystal to the total number of simulated photons. For an interpolation of the simulated values, the simple function

$$\epsilon_{\text{sim}} = \left(a_1 E + \frac{a_2}{E} \right) \exp \left(a_3 E + \frac{a_4}{E} \right) \quad (4.30)$$

was fit to ϵ_{sim} via the four parameters $a_1 - a_4$. The fit residuals were on the order of magnitude of the statistical fluctuations of the simulation, i.e. negligible.

On an absolute level, no simulated efficiency deviated from the data by more than a factor of 50%. The largest contribution to this deviation is probably insufficient knowledge of the geometry (in particular the interior of the detectors and the parts closest to the target), since the photon interaction models of GEANT4 have been shown to be more precise (see, e.g., [221] for a pure benchmark study, and [201] for a dedicated NRF application). In order to test the energy dependence $\epsilon_{\text{sim}}(E_\gamma)$ and to correct for the aforementioned factor, the simulations were fit to the ^{56}Co -

and ^{152}Eu data by minimization of the quantity [see Eq. (4.6)]:

$$\chi_{\text{red}}^2 = \frac{1}{N_{56\text{Co}} + N_{152\text{Eu}} - 2} \quad (4.31)$$

$$\times \left\{ \sum_{i=1}^{N_{56\text{Co}}} \frac{[p_{56\text{Co}} \epsilon_{56\text{Co,exp}}(E_{56\text{Co},i}) - p_{\text{sim}} \epsilon_{\text{sim}}(E_{56\text{Co},i})]^2}{[p_{56\text{Co}} \sigma_{\epsilon_{56\text{Co,exp}}}(E_{56\text{Co},i})]^2} + \sum_{i=1}^{N_{152\text{Eu}}} \frac{[\epsilon_{152\text{Eu,exp}}(E_{152\text{Eu},i}) - p_{\text{sim}} \epsilon_{\text{sim}}(E_{152\text{Eu},i})]^2}{\sigma_{\epsilon_{152\text{Eu,exp}}}^2(E_{152\text{Eu},i})} \right\}.$$

In Eq. (4.31), N_{AX} denotes the number of transitions of the source nucleus AX which were used for the efficiency calibration. The reduced χ_{red}^2 is minimized via the two parameters p_{sim} and $p_{56\text{Co}}$, which represent a correction factor of the simulated efficiency and a scaling factor due to the unknown activity of the ^{56}Co source, respectively¹¹.

As an example, an efficiency calibration of HPGe 8 is shown in Fig. 4.4. It can be seen that the energy dependence of the efficiency is reproduced well by GEANT4. Therefore, an extrapolation of the simulation to about 4.2 MeV was considered to be reliable. For the detector in Fig. 4.4, the largest contribution to Eq. 4.31 was the transition of ^{152}Eu at 344.2785(12) keV. At such low energies, the impact of uncertainties in the experimental geometry is expected to be largest, which can be seen from a simple estimate: Consider the impact of the attenuation of photons in the filters in front of the detectors. After travelling a distance z inside a material, the initial photon intensity N_γ will be attenuated by a factor [Eq. (1) in Sec. 2 of [128]]:

$$\frac{N_\gamma(E_\gamma, z)}{N_\gamma(E_\gamma, z = 0)} = \exp[-\mu(E_\gamma) \rho z] \quad (4.32)$$

In Eq. (4.32), the symbol ρ denotes the density of the material (which is assumed to be homogenous for simplicity here) and $\mu(E_\gamma)$ denotes the energy-dependent

¹¹Note that the uncertainties $\sigma_{\epsilon_{56\text{Co,exp}}}$ need to be scaled consistently when the experimental values of the efficiency $\epsilon_{56\text{Co,exp}}$ are multiplied by $p_{56\text{Co}}$. In the present work, it was also tried to scale the simulated efficiency in the ^{56}Co sum in Eq. (4.31) by two parameters, i.e. $p'_{56\text{Co}} p_{\text{sim}} \epsilon_{\text{sim}}$, but the present formulation was found to be numerically more stable.

mass attenuation coefficient of the material. The latter quantity is well-known for many materials [128]. Assuming that the uncertainty of the geometry is manifested in the uncertainty σ_z of the z -dimension, and neglecting all other uncertainties, one obtains by Gaussian propagation of uncertainty from Eq. (4.32):

$$\sigma_{N_\gamma(\Delta z)/N_\gamma(0)} \approx \left| \sigma_z \mu(E_\gamma) \exp[-\mu(E_\gamma)z] \right|. \quad (4.33)$$

For typical thicknesses of the lead filters, the proportionality factor between $\sigma_{N_\gamma(\Delta z)/N_\gamma(0)}$ and σ_z , i.e. the left- and right-hand side of Eq. (4.33), decreases by an order of magnitude between 0.3 MeV and 3 MeV. The procedure from Sec. 4.1.3 was used to take into account such systematic uncertainties. If the scaling factor due to the systematic uncertainty became too large, the low-energy calibration points were sometimes omitted, since most transitions of interest were expected at higher energies [138].

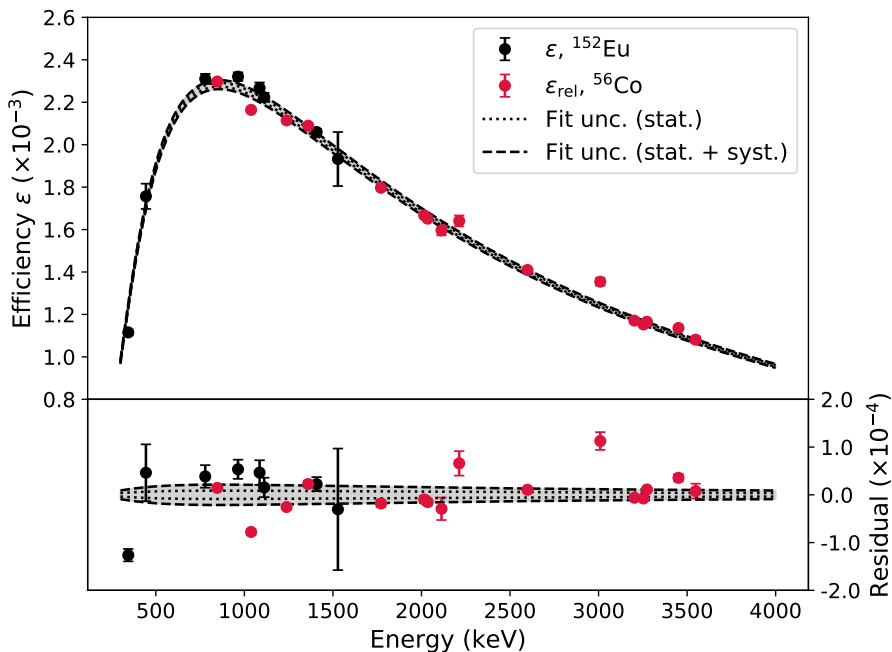


Figure 4.4.: Efficiency calibration of HPGe 8 using source measurements with a ^{152}Eu source (run 740, see Tab. 3.1) and ^{56}Co (run 741). (*Top*) Absolute efficiency data in black and the scaled relative efficiency data in red. A simulated energy dependence of the efficiency has been scaled to the data. The statistical ('stat.') uncertainty and the combination of statistical and systematic uncertainty ('syst.') of the fit are indicated by dotted and dashed lines, respectively (see also Fig. 4.3). (*Bottom*) Residuals of the fit together with the two uncertainty bands.

4.5.3. Width Calibration

In order to determine a sensitivity limit (see Sec. 4.4) or to identify multiplets of peaks, the expected line shape in a detector and its energy dependence must be known. For HPGe detectors, the line shape can be described by a normal distribution in a first approximation, due to the statistical character of the photon-energy measurement (see, e.g. Sec. 6.1 in [187] and Sec. A.1 for a discussion of corrections to the normal-distributed line shape). The line shape can therefore be characterized by a single energy-dependent parameter, the standard deviation of the normal distribution ('peak width'/energy resolution') $\sigma(E)$. If a constant electronic noise (e) is assumed to affect the resolution, in addition to the statistical processes of charge production and charge collection (cp), the energy dependence $\sigma(E)$ is expected to be given by [Eq. (6.11) in [187], referred to as the model of Debertin and Helmer due to Eq. (5.2) in [222]]:

$$\sigma(E) = \sqrt{p_e + p_{cp}E} \quad (4.34)$$

Equation (4.34) contains two parameters to describe the three aforementioned contributions to the width¹². It was found that it described the energy-dependent resolution of all detectors reasonably well.

Figure 4.5 shows an example of a width calibration for HPGe 1. Not all observed photons can be used for a width calibration. Most notably the electron-positron annihilation photon at 511 keV [2] is broadened compared to the nuclear transitions, since the e^+/e^- system may have a nonzero center-of-mass momentum before the annihilation (see, e.g., Sec. 1.2.2 and 7.5.4 in [187]). The same argument holds for the peak at 1022 keV, which is the result of pileup of two annihilation photons (see Sec. 4.3.3). Lastly, the widths of some background transitions were found to be systematically larger than the expected square-root behavior and assumed to be doublets. Such cases were always found at energies below 1 MeV, where the number of background photons, and therefore the probability for multiplets, increases strongly (see Tab. C.3).

¹²Charge production and charge collection are assumed to have the same energy dependence in Eq. (4.34). Gilmore [187] suggests, from empirical studies, that the process of charge collection introduces an energy dependence proportional to E [Eq. (6.10) therein]. However, this was not found to be necessary in the present work.

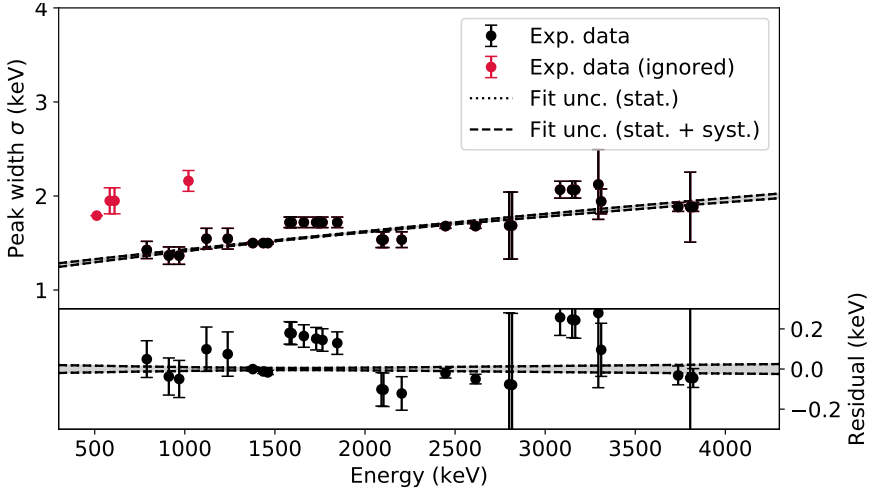


Figure 4.5.: (Top) Width calibration of HPGe 1 at a beam energy of 3820 keV. The experimental data points which are shown in red instead of black were not considered for the fit because they were found to deviate systematically from the underlying square-root dependence of Eq. (4.34). Similar to Fig. 4.3, the statistical uncertainty and the combination of statistical and systematic uncertainty are shown. In this case, as in most width calibrations, the value of χ_{red}^2 was very close to one, indicating the absence of systematic uncertainties. For this reason, the two uncertainty bands cannot be distinguished here. (Bottom) Residuals of the fit together with the two uncertainty bands. Only the data which were used for the fit are shown.

4.5.4. Photon Flux Calibration

The photon flux $\Phi(E_\gamma, t)$, i.e. the number of photons with an energy E_γ which hit target per time interval at a time t , is defined as the double differential of the total

number of photons N_γ ¹³:

$$\Phi(E_\gamma, t) \equiv \frac{dN_\gamma}{dEdt'}(E_\gamma, t). \quad (4.35)$$

In the present work, knowledge of the quantity dN_γ/dE is necessary for the determination of absolute NRF cross sections [Eq. (2.4)] and derived quantities (see Sec. 2.1.2). In experiments with bremsstrahlung-generated photons, flux calibration targets with few well-known resonances are used to calibrate dN_γ/dE at discrete energies (see, e.g., Sec. 'Photon Scattering Set-ups' in [119]). Since the bremsstrahlung spectrum created by a charged-particle beam is well known (see, e.g., [223] for analytical expressions and [224] for a recent validation, or [225] for a validation of Monte-Carlo simulations), it is possible to interpolate dN_γ/dE at intermediate energies.

The present experiments with quasi-monoenergetic photon beams would require large sets of calibration targets with well-known resonances at each beam energy, which is impractical. Furthermore, the energy dependence of the flux distribution (the 'beam profile') is not known a priori. In this section, the reconstruction of the photon flux by Monte-Carlo simulations will be described¹⁴. The determination of the energy dependence dN_γ/dE in arbitrary units and the total number of photons N_γ will be performed separately.

Similar calibrations of the photon flux have been applied in recent studies (see, e.g., [131, 197]) which could rely on known cross sections from NRF studies with bremsstrahlung. The reliability of the simulations was found to be sufficient by Savran and Isaak [194] to propose the application of the method for relative flux normalization. The present work represents one of the first (see also [227, 228]) largely 'blind' (i.e. without calibration to known resonances) analyses of this kind, since it could only be constrained by a single data point [137].

¹³See also Sec. 4.6 for the assumptions that lead to the given definition of Φ .

¹⁴To circumvent the extensive use of Monte-Carlo simulations, it was originally planned to perform experiments on ⁸²Kr and ⁸²Se with bremsstrahlung at the Darmstadt High-Intensity Photon Setup [226] at the S-DALINAC [126] to determine absolute NRF cross sections. However, due to technical problems with the accelerator, the experiments could not be performed in time.

Reconstruction of the Beam Profile

As indicated in Sec. 3.1, the profile of the $\text{HI}\gamma\text{S}$ beam was recorded before each run using a zero-degree HPGe detector¹⁵. For these measurements, the beam intensity was reduced by a variable-size copper attenuator which was located about 30 m upstream of the target [168]. Due to the large distance and the small variation of the attenuation coefficient of copper within the range of the beam profile [128], the distortion of the momentum- and energy distribution of the beam is negligible. The attenuation was chosen strong enough to keep the dead time of the zero-degree detector below 10% of the total measuring time. Therefore, pileup effects (see Sec. 4.3.3) were neglected in the reconstruction of the beam profile. Such a reconstruction is necessary, since the spectrum recorded by the detector will be affected by its response function (see Sec. 4.3.2).

The response matrix [Eq. (4.9)] of the zero-degree detector was obtained from simulations of the setup (see Sec. 4.2). Explicitly, lines $(D(E_m, E_n) \forall E_n)$ of the response matrix were obtained by simulating the passage of a monoenergetic photon beam with a circular cross section through the entire setup. The beam diameter was chosen to be 10% larger than the collimator diameter to simulate scattering on the collimator as well. It was assumed that the intensity distribution of the beam is uniform over its cross section and that the initial momentum vectors of the photons are parallel to the beam axis (see Secs. 4.6 and below for a discussion of these two assumptions, respectively). Simulations were performed in energy steps of 100 keV. For intermediate energies, the closest simulated energy spectrum, shifted by the energy difference¹⁶, was used. In principle, the original spectrum can be obtained by inverting the response matrix in Eq. (4.9). However, a straightforward inversion may lead to the appearance of unphysical negative bin contents in \bar{N} due to statistical and systematic (energy calibration) uncertainties (see, e.g., Sec. 4.1.1 in [229]). Therefore, the relevant bins of \bar{N} were interpreted as parameters with the constraint $\bar{N}(E_m) \geq 0$, and a least-squares fit was performed. This corresponds to the so-called Gold deconvolution [230, 231] (for implementation details, see [232]). Another degree of freedom in the fit was the

¹⁵Note that, the NRF targets were still mounted during these beam profile measurements in order to save time. This was also taken into account in the simulations of the response matrix of the zero-degree detector.

¹⁶Note that this shift would prevent the reconstruction of fixed-energy structures, like background photons. In this case, however, the photon beam was by far the dominant part of the spectrum.

point where the beam hits the zero-degree detector. It is obviously inefficient to hit the center of the detector where the copper cold finger is located. Therefore, it was displaced from the beam axis by an amount Δr which is only known up to ± 5 mm. Response matrices for different Δr were tried, and the optimum fit was determined to be the one with the lowest χ^2 which did not produce a pronounced left tail in the reconstructed spectrum. The latter requirement, which was checked visually, prevents overfitting of the data. It is based on systematic experimental [233] and theoretical [234] studies of the HI γ S beam. The statistical uncertainty of the reconstruction procedure was determined with the Monte-Carlo parameter estimation method described in Sec. 4.1.2, by varying the bin contents of the measured spectrum and the simulated response matrix within their statistical uncertainty.

An example for a reconstructed spectrum is shown in Fig. 4.6. Due to the good agreement of the simulated response with the experimental data, even far beyond the fitted range, the enhancement factors for systematic uncertainties were always close to 1 for the beam profile reconstruction¹⁷.

Absolute Gamma-ray Flux

The determination of the absolute photon flux in this work relies on the nonresonant scattering of photons off the target and the surrounding material. A preliminary version of this calibration, which used a different parameterization, is described in [165]. The appeal of this approach is that the cross sections of such processes are well known (see, e.g., [121]) and orders of magnitude larger than the NRF cross section (see Sec. 2.1.1). Due to the availability of precise Monte-Carlo particle simulation frameworks, multiple scattering processes and geometrical effects can be taken into account in a straightforward way (see Sec. 4.2). Since the low-energy part of the experimental spectra is completely dominated by these nonresonantly scattered photons (see Sec. D), it is sufficient to consider only this

¹⁷For an even better control of the systematic uncertainties in the reconstruction of the beam profile, the author would like to point the reader's attention to the 'ab-initio' method developed by Sun, Wu, Rusev, and Tonchev [235], which relies on a simulation of the complete beam line at HI γ S.

range [194]¹⁸. In particular, this implies that the necessary simulation times are considerably reduced. A drawback of using the nonresonant scattering is that it may happen anywhere on the beam line, i.e. a precise knowledge of the geometry and the properties of the detectors is required. For example, compare the results of the beam profile reconstruction in this section and the efficiency calibration (Sec. 4.5.2): In the former beam-on-detector experiment, almost no distortion of the beam by other parts of the setup is expected, therefore systematic uncertainties are at a minimum (see Fig. 4.6). On the other hand, attenuation in insufficiently well-known parts of the geometry contributed significantly in the latter case (see Fig. 4.4).

Based on the aforementioned arguments, the following procedure was applied to simulate the low-energy background: The nonresonant background was simulated by propagating a photon beam through the virtual geometry, similar to Sec. 4.5.4, but with the realistic energy distribution of the photon beam which was obtained there. As in the previous section, the radius of the beam was chosen to be slightly larger than the collimator radius. Using a number of $N_{\gamma,\text{sim}}$ primary photons, the simulation recorded the spectra $\bar{N}_{\text{sim},d}^{(0)}(E_m)$ of each detector d . As mentioned in Sec. 4.3.3, the simulated spectra are a priori pile-up free, therefore the notation with a bar diacritic. Furthermore, the number of photons $N_{\gamma,\text{sim},\text{target}}$ which hit the γ^3 target without undergoing any scattering process, i.e. which would be available for NRF reactions, was determined. This was done by another simulation (with a perfectly monoenergetic beam for simplicity) where the number of photons which reached the target without energy loss was counted.

From the appearance of a peak at about 1022 keV (i.e. twice the energy of the dominant annihilation photons at 511 keV) in all of the experimental spectra (see Sec. D), it can be concluded that there was a non-negligible impact of at least first-order pileup. Therefore, the experimental spectrum N_d ¹⁹ is described by the

¹⁸However, the fit range also should have a low-energy cutoff, since x-ray lines of some materials, in particular lead, appear below about 100 keV (see, e.g., [236]). Furthermore, electronic noise contributes at even lower energies, if it is not cut off by a threshold.

¹⁹It is assumed in this section that the off-beam background has been subtracted from N_d . In practice, this was done by scaling a background measurement to the experimental run via the ratio of live times.

simulated spectrum $N_{\text{sim},d}^{(0)}$ plus the pile-up contributions:

$$N_d(E_m) = p_t \frac{t_{\text{live},d}}{t_{\text{stop}} - t_{\text{start}}} \left[p_{d,0} N_{\text{sim},d}^{(0)}(E_m) + \sum_{p=1}^{\infty} p_{d,p} N_{\text{sim},d}^{(p)}(E_m) \right]. \quad (4.36)$$

Equation (4.36) contains an overall normalization parameter p_t which takes into account the different 'live times' of the simulation and the experiment. The sum inside the brackets contains all orders of pileup which contribute according to their relative weights:

$$\sum_{p=0}^{\infty} p_{d,p} = 1. \quad (4.37)$$

Note that the pile-up parameters are different for each detector since they have different properties and shielding. In practice, it was found that already the second-order pileup was negligible (see Fig. 4 in [165]), so Eq. (4.36) was simplified to:

$$N_d(E_m) \approx p_t \frac{t_{\text{live},d}}{t_{\text{stop}} - t_{\text{start}}} \left[p_{d,0} N_{\text{sim},d}^{(0)}(E_m) + p_{d,1} N_{\text{sim},d}^{(1)}(E_m) \right] \quad (4.38)$$

$$\stackrel{\text{Eq. (4.37)}}{=} p_t \frac{t_{\text{live},d}}{t_{\text{stop}} - t_{\text{start}}} \left[p_{d,0} N_{\text{sim},d}^{(0)}(E_m) + (1 - p_{d,0}) N_{\text{sim},d}^{(1)}(E_m) \right].$$

With the restriction $0 \leq p_{d,0} \leq 1$, a simultaneous fit was performed for all detectors of the γ^3 (D_{γ^3}) - and the polarimetry setup (D_{pol}) to minimize the quantity:

$$\chi^2 = \sum_{d \in D_{\gamma^3}} \sum_{m \in M} \frac{\left\{ N_d(E_m) - p_t \frac{t_{\text{live},d}}{t_{\text{stop}} - t_{\text{start}}} \left[p_{d,0} N_{\text{sim},d}^{(0)}(E_m) + (1 - p_{d,0}) N_{\text{sim},d}^{(1)}(E_m) \right] \right\}^2}{\sigma_{N_d}^2(E_m)} \quad (4.39)$$

$$+ \sum_{d \in D_{\text{pol}}} \sum_{m \in M} \frac{\left\{ N_d(E_m) - p_t p_a \frac{t_{\text{live},d}}{t_{\text{stop}} - t_{\text{start}}} \left[p_{d,0} N_{\text{sim},d}^{(0)}(E_m) + (1 - p_{d,0}) N_{\text{sim},d}^{(1)}(E_m) \right] \right\}^2}{\sigma_{N_d}^2(E_m)}.$$

In Eq. (4.39), the set M symbolizes the fit range of low-energy bins. Here, $0.1 \text{ MeV} \leq m \leq 1.0 \text{ MeV} \setminus 0.50 \text{ MeV} \geq m \leq 0.52 \text{ MeV}$ was used. Note that the

denominators in Eq. (4.39) do not contain the systematic uncertainty of the simulation, which is expected to dominate this kind of simulation. From the parameters p_i , the original number of photons which hit the target can be reconstructed for each detector separately:

$$N_{\gamma,d} = p_t p_a \left[p_{d,0} + (1 - p_{d,0}) \frac{\sum_{m=0}^{N_s} N_{\text{sim},d}^{(0)}(E_m)}{\sum_{m=0}^{N_s} N_{\text{sim},d}^{(1)}(E_m)} \right] N_{\gamma,\text{sim,target}} \quad (4.40)$$

In Eq. (4.40), the relative contribution of the first-order pileup (i.e. the term proportional to $(1 - p_{d,0})$) is scaled by the ratio of counts in the simulated spectra $N_{\text{sim},d}^{(0)}$ and $N_{\text{sim},d}^{(1)}$, since they may have a different normalization. In this work, the first-order pileup was obtained by adding two subsequent events of the simulation, i.e. the ratio is exactly 2.

The peak at 511 keV was excluded from the fit for the following reason: It is exclusively created by the pair production process and has a strong influence on the overall magnitude of the parameters due to its high count-rate. However, the cross section of this process at the energies of the present experiment is less well constrained than the other electromagnetic processes (see, e.g. a review article by Hubbell [237] or a recent investigation [238]). Therefore, it was preferred to fit only the continuous part of the low-energy background, which contains contributions by all nonresonant processes.

An additional parameter p_a was introduced in Eq. (4.39) as a global scale of the photon flux at the target in the polarimetry setup. Although the simulation takes into account effects like the attenuation of the photon beam in the first target and the different shapes/compositions of the targets, the fitted values were on the order of $p_a \approx 0.5$ and were found to improve the results considerably. A possible reason for the necessity of the correction factor is that the HI γ S beam actually has a non-negligible transversal divergence, which is increased by small-angle scattering on the γ^3 target. The impact of the divergence can be estimated from the projected image of an alignment target at the γ^3 setup, which is shown in Fig. 3.2. In the projection, its radius appears to be about $r_{\text{apparent}} \approx 14$ mm, while its actual radius was $r_{\text{target}} = 10$ mm. The distance from the γ^3 target to the polarimetry target position is about $\Delta z_{\text{pol}} \approx 1.5$ m, while the distance to the BGO camera is about $\Delta z_{\text{BGO}} \approx 2.5$ m. From the latter, an average relative beam divergence of

$(r_{\text{apparent}} - r_{\text{target}}) r_{\text{target}}^{-1} \Delta z_{\text{BGO}}^{-1} \approx 0.16 \text{ m}^{-1}$ is estimated. Consequently, a beam which completely covered the γ^3 target will have spread out to 1.24 times its size at the time it hits the second target, i.e. more than 50% of the photons which propagated through the γ^3 target will miss. This estimate is in good agreement with the observed magnitude of the parameter p_a .

Since a precise measurement of the level of the vacuum inside the beam pipe was not possible at the time of the experiment, this parameter was, a priori, unconstrained in the simulation. It is known (see, e.g., Sec. 3.2.1 in [229], in particular Fig. 3.6) that nonresonant scattering off the air in the beam pipe can lead to a significant increase of the nonresonant background. Due to the preference of the dominant Compton scattering process (see Sec. 2.1.1) for small forward angles at the energies of the present experiment (see, e.g. Fig. 2.19 in [129]), scattered photons from further upstream are expected to distort especially the high-energy part of the spectrum (see also Sec. 3.3). Nevertheless, simulations with different levels of the vacuum in the beam pipe, quantified by the ratio $\rho_{\text{air,pipe}}/\rho_{\text{air},0}$ of the density of air inside the beam pipe ('pipe') and at standard conditions ('0'), were performed as a cross check.

As an example, the result of a simultaneous fit of the low-energy background, in particular the impact of the vacuum, will be discussed in the following for the runs at a beam energy of 2.98 MeV. Figures 4.7 and 4.8 show the experimental and simulated spectra after the χ^2 minimization of Eq. (4.39). For Fig. 4.7, a simulated ratio of $\rho_{\text{air,pipe}}/\rho_{\text{air},0} = 1/10$ was used, while the air was assumed to have standard density ($\rho_{\text{air,pipe}}/\rho_{\text{air},0} = 1$) in the simulation for Fig. 4.8. At first glance, it appears that the inferior vacuum does not affect the fits very much. The largest impact can be seen for HPGe 4. This is expected, because it is the only one of the 7 detectors which was mounted at a backward angle, and therefore exposes a larger cross section of its crystal to small-angle scattered photons. Furthermore, together with the non-functional HPGe 3 in this run, it serves as an additional passive shielding for the detectors at $\theta = 90^\circ$.

More generally, it can be seen from Figs. 4.7 and 4.8 that there are significant discrepancies between the simulation and the experimental data, especially for HPGe 6 and HPGe 9. The fit yielded extremely large values of $\chi_{\text{red}}^2 \approx 10^4$ because of the non-quantifiable systematic uncertainty of the simulation. Therefore, both figures show the quantity $\chi_{\text{red,rel}}^2$, which has been normalized to the largest value

$\chi_{\text{red,max}}^2$ for each setup. The values of $\chi_{\text{red,max}}^2$ were in the same order of magnitude for both setups.

Using Eq. (4.40), the number of incident photons was reconstructed for each detector separately. The results are shown in Fig. 4.9 for three different values of $\rho_{\text{air,pipe}}/\rho_{\text{air},0}$. While the fits looked very similar for different vacuum levels, a systematic difference between the reconstructed N_γ is obvious. This indicates that an increase of $\rho_{\text{air,pipe}}/\rho_{\text{air},0}$ mainly causes an overall increase of the nonresonant background count rate at low energies, which can be compensated by the parameter p_t . As a logical consequence of this, the values of $\chi_{\text{red,rel}}^2$ for each detector, shown in the bottom part of Fig. 4.9, are independent of this parameter. It was found that already an assumed vacuum level of one tenth of the density at standard conditions reduced the background significantly. The reduction by another order of magnitude changed the values of N_γ only slightly compared to the overall discrepancy between different detectors. Based on this study of the effects of the vacuum, all simulations for other beam energies were performed with a value of $\rho_{\text{air,pipe}}/\rho_{\text{air},0} = 1/10$, since they also showed the best extrapolation behavior towards higher energies (see, e.g., Fig. 5 in [165]²⁰). The systematic uncertainty of N_γ was estimated as the standard deviation of all values $N_{\gamma,d}$ for a given setup, neglecting the small difference between $\rho_{\text{air,pipe}}/\rho_{\text{air},0} = 1/10$ and $\rho_{\text{air,pipe}}/\rho_{\text{air},0} = 1/100$. For all beam energies, this resulted in a relative uncertainty estimate on the order of 20%-30%, which is practically independent of the measuring time differences between different beam energy settings, since the statistical uncertainty of the low-energy background is always negligible.

²⁰In the publication, it is claimed that the density of the air was 'about two orders of magnitude' [165] lower than the density at standard conditions. This estimate was based on simulations for $\rho_{\text{air,pipe}}/\rho_{\text{air},0} = 1, 1/100$ and $1/1000$ because the authors were more optimistic about the vacuum level.

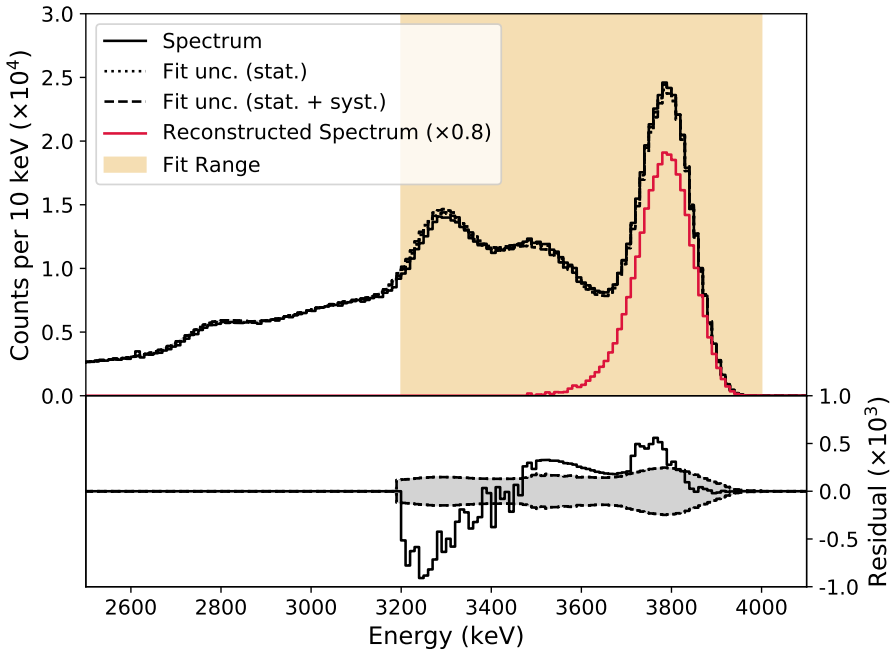


Figure 4.6.: Reconstruction of the incident beam spectrum by fitting a simulated detector response. (*Top*) The experimental spectrum which was recorded by the zero-degree detector and the reconstructed spectrum are shown in black and red, respectively. For better visibility, the latter was scaled by a factor of 0.8. The fitted range is indicated by a shaded area. Similar to Fig. 4.3, the statistical uncertainty and the combination of statistical and systematic uncertainty are shown. In this case, as in most beam profile reconstructions, the value of χ^2_{red} was very close to one, indicating the absence of systematic uncertainties. For this reason, the two uncertainty bands cannot be distinguished here. (*Bottom*) Residuals of the fit together with the two uncertainty bands. Only the data which were used for the fit are shown.

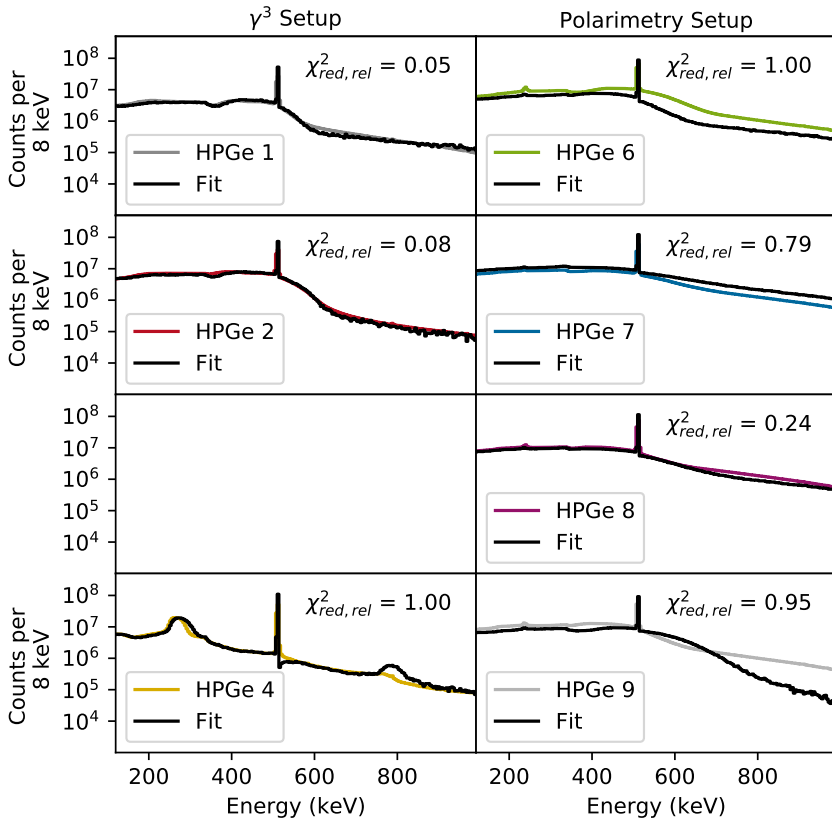


Figure 4.7.: Simultaneous fit of simulated background spectra (black) to experimental spectra (other colors). Except for a small excluded region around the 511 keV photons, the plotted range is equal to the fit range. The spectra of the γ^3 setup are shown on the left-hand side, the ones of the polarimetry setup are on the right-hand side. Each of the spectra has the same abscissa and ordinate. Note that HPGe 3 was not used in these runs. For each setup, the reduced chi-squares statistics have been normalized to the detector with the largest value. For the simulations shown here, it was assumed that the density of air in the beam pipe was $1/10$ of the density at standard conditions.

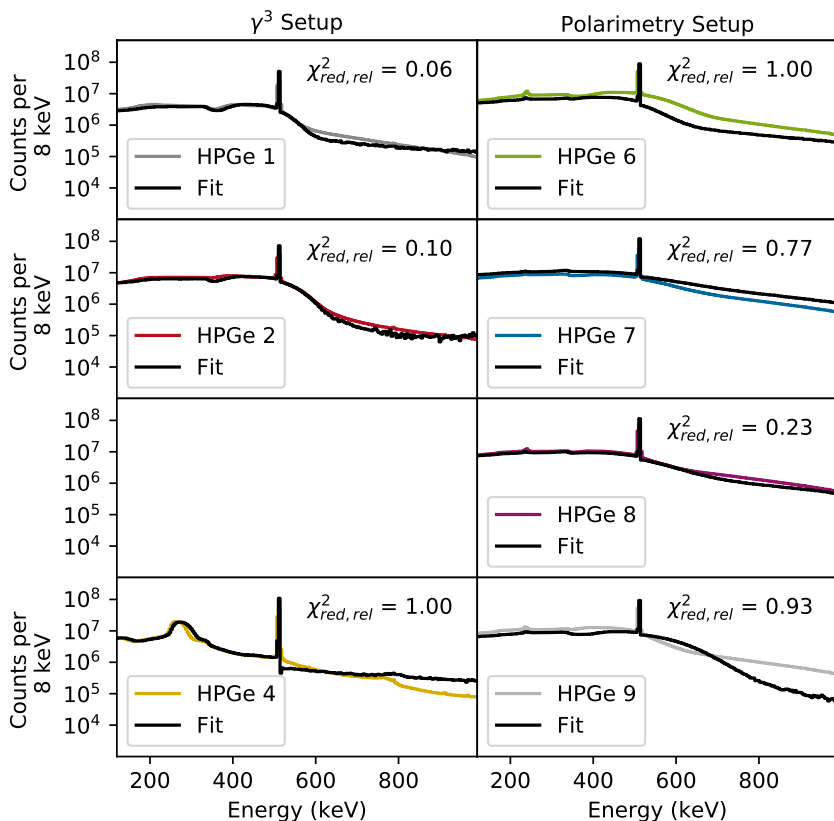


Figure 4.8.: Simultaneous fit of simulated background spectra (black) to experimental spectra (other colors). Except for a small excluded region around the 511 keV photons, the plotted range is equal to the fit range. The spectra of the γ^3 setup are shown on the left-hand side, the ones of the polarimetry setup are on the right-hand side. Each of the spectra has the same abscissa and ordinate. Note that HPGe 3 was not used in these runs. For each setup, the reduced chi-squares statistics have been normalized to the detector with the largest value. For the simulations shown here, it was assumed that the density of air in the beam pipe was equal to the density at standard conditions.

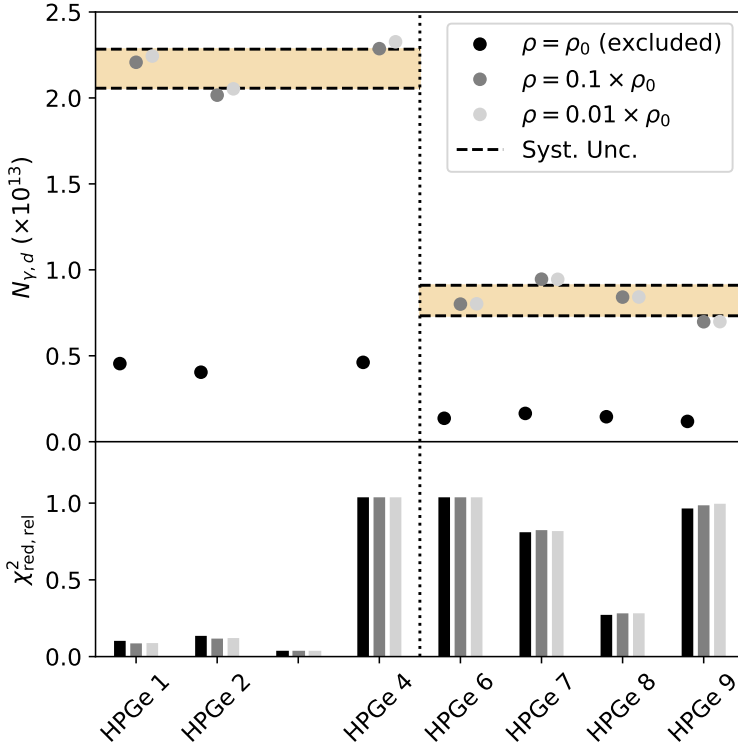


Figure 4.9.: (Top) Total number of photons ($N_{\gamma,d}$) which hit the γ^3 (left)- and the polarimetry (right) target in the runs at a beam energy of 2.98 MeV, reconstructed from a simultaneous fit of simulations to the low-energy part of the experimental spectra (see Figs. 4.7 and 4.8). $N_{\gamma,d}$ was obtained separately for each detector d using Eq. (4.40) and for three different assumptions for the density (ρ) of the air in the beam pipe with respect to the density at standard conditions (ρ_0). Note that HPGe 3 was not used in these runs. From the discrepancy of the values for $N_{\gamma,d}$ for different detectors (excluding $\rho = \rho_0$), the systematic uncertainty (dashed lines) was estimated. (Bottom) Reduced χ^2 statistics of the fits. For each setup, the χ^2_{red} were normalized to the largest value (HPGe 4 and HPGe 6 in this case). The colors of the bars correspond to the three different values of ρ .

4.6. Derived Quantities

The methodology of Sec. 4.1 and the calibrations of Sec. 4.5 are used in this section to derive properties of the nuclei of interest from the observed transitions in the spectra. In this introductory paragraph, the relation between the number of detected NRF reactions and the NRF cross section [Eq. (2.4)] will be discussed, which depends on several geometric factors²¹. Since only level sequences of the type $0 \rightarrow j \rightarrow k$ (i.e. excitation from the ground state to a state i followed by a transition to a state k) were considered in the present work, the calculations do not show higher-order cascades.

Start by defining the photon flux density $\mathbf{j}_\gamma(E_\gamma, \mathbf{r}, t)$ in analogy to fluid mechanics (chapter I, §1 in [240]), which describes the directional number of photons per area and time unit with an energy E_γ at a space point \mathbf{r} . Since the transversal divergence of the beam is negligible on the order of magnitude of the target size (see Sec. 4.5.4), it is assumed to be parallel to the unit vector in z direction, i.e. $\mathbf{j}_\gamma = j_\gamma(E_\gamma, \mathbf{r}, t)\mathbf{e}_z$. The z dependence of j_γ is given by the differential equation²²:

$$\frac{dj_\gamma(E_\gamma, \mathbf{r}, t)}{dz} = -[\mu(E_\gamma) + \sigma_{0 \rightarrow j}(E_\gamma)]n_t(\mathbf{r})j_\gamma(E_\gamma, \mathbf{r}, t) \quad (4.41)$$

In Eq. (4.41), the symbol $\sigma_{0 \rightarrow j}(E_\gamma) = dI_{0 \rightarrow j}/dE_\gamma$ [see Eq. (2.4)] denotes the cross section for the resonant absorption of photons [Eqs. (3-11) in [120]], and $n_t(\mathbf{r})$ denotes the number of target nuclei per unit volume at a point \mathbf{r} . Using the definition of j_γ , the count rate $dA_{j \rightarrow k, d}/dt$ in a detector d for a transition $j \rightarrow k$, associated with the NRF cascade $0 \rightarrow j \rightarrow k$, is given by:

$$\begin{aligned} \frac{dA_{j \rightarrow k, d}}{dt} = \int_0^\infty dE_\gamma \int d\Omega' \int d^3\mathbf{r} \frac{W_{0 \rightarrow j \rightarrow k}(\theta', \varphi', P_\gamma)}{4\pi} \frac{d\epsilon_d}{d\Omega'}(E_\gamma, \theta', \varphi', \mathbf{r}) \\ \times \sigma_{0 \rightarrow j}(E_\gamma) \frac{\Gamma_{j \rightarrow k}}{\Gamma_j} n_t(\mathbf{r}) j_\gamma(E_\gamma, \mathbf{r}, t) \end{aligned} \quad (4.42)$$

²¹The heuristic derivation discussed here will start from a more general expression than other dissertations which are referenced in this work [164, 213, 239], because the non-cylindrically symmetric ⁸²Kr target was used.

²²Heuristically reconstructed from Secs. 2.4 and 2.5 in [120] and Sec. 5 in [239].

In Eq. (4.42), $\int d^3\mathbf{r}$ symbolizes an integration over the entire three-dimensional space to take into account the spatial extent of the target. For each position \mathbf{r} in the target, another integral over the entire solid angle Ω' is executed to take into account the angular distribution and the solid-angle dependent detection efficiency $d\epsilon/d\Omega$ [Eq. (4.28)]. The fact that the decay transition is observed is taken into account by a multiplication of the cross section with the branching ratio $\Gamma_{j\rightarrow k}/\Gamma_j$.

If the target has a homogenous density distribution, i.e. $n_t(\mathbf{r}) \equiv n_t$, Eq. (4.41) can be solved analytically, and the target shape can be taken into account by restricting the integration in Eq. (4.42) to the target volume V_t :

$$\begin{aligned} \frac{dA_{j\rightarrow k,d}}{dt} = & \int_0^\infty dE_\gamma \int d\Omega' \int_{V_t} d^3\mathbf{r} \frac{W_{0\rightarrow j\rightarrow k}(\theta', \varphi', P_\gamma)}{4\pi} \frac{d\epsilon_d}{d\Omega'}(E_\gamma, \theta', \varphi', \mathbf{r}) \quad (4.43) \\ & \times \sigma_{0\rightarrow j}(E_\gamma) \frac{\Gamma_{j\rightarrow k}}{\Gamma_j} n_t j_\gamma(E_\gamma, x, y, z_0, t) \\ & \times \exp\{-[\mu(E_\gamma) + \sigma_{0\rightarrow j}(E_\gamma)]n_t z\} \end{aligned}$$

The factor $j_\gamma(E_\gamma, x, y, z_0, t)$ in Equation (4.43) is determined by the initial condition for the flux density at $z_0(x, y)$, which is assumed to be the x - and y -dependent entry point of the beam into the target on the z axis. In the present work, it was assumed that the transversal intensity distribution of the beam is homogenous. For a precision determination of cross sections, this assumption introduces a systematic error, since the intensity of the HI γ S beam decreases significantly as one goes away from the optical axis. This was extensively investigated by Sun and Wu [234]. From Fig. 5 therein, a full width at half maximum of the intensity distribution of about 50 mm is expected²³. Since the present work was focused mostly on branching ratios, which are independent of the absolute photon flux (see Sec. 4.6.2), and the reconstruction of the photon flux has a large systematic uncertainty anyway (see Sec. 4.5.4), the approximation of the actual spatial distribution by its average value has a negligible impact. Therefore, the following equations use:

$$j_\gamma(E_\gamma, x, y, z < z_0, t) \approx \Phi(E_\gamma, t) \quad \forall x, y \quad (4.44)$$

²³Compare also Figs. 3.1 and 3.2, but consider that there is no guarantee that the color intensity is proportional to the beam intensity, and that the beam profile is distorted by the target in the latter figure.

The spatially uniform photon flux Φ was defined in Eq. (4.35).

For a sufficiently thin target or low density, the attenuation by nonresonant processes and the self-absorption effect [μ and $\sigma_{0 \rightarrow j}$ in the exponential term in Eq. (4.43)] can be neglected. If the maximum spatial extent and the density of the ^{82}Kr target are estimated to be 1.8 cm and 0.5 g cm^{-3} (see Sec. 3.3), the photon flux is non-resonantly attenuated by less than 4% at 3 MeV [128]. Furthermore, even the largest values $\Gamma_{0 \rightarrow j}$ measured in this work were on the order of 0.1 eV, which leads to a maximum self-absorption effect on the order of 10%²⁴. Therefore, the following volume integral can be simplified considerably:

$$\int_{V_t} d^3\mathbf{r} n_t \exp\{-[\mu(E_\gamma) + \sigma_{0 \rightarrow j}(E_\gamma)]n_t z\} \approx \int_{V_t} d^3\mathbf{r} n_t = N_t \quad (4.45)$$

In Eq. (4.45), the quantity N_t denotes the total number of target nuclei.

The approximation in Eq. (4.45) can only be applied to Eq. (4.43) in a straightforward way, if the position-dependence of $d\epsilon_d/d\Omega$ is negligible. This was verified by comparing Monte-Carlo simulations (see Sec. 4.2) with a point-like source and others where photons were emitted from realistic ^{82}Kr and ^{82}Se targets²⁵. Quantities of interest like the full-energy peak efficiency or the asymmetry were only influenced on a level of less than 1% by the shape of the target.

Using the two approximations $j(E_\gamma, x, y, z_0, t) \approx \Phi(E_\gamma, t)$ and $(\mu + \sigma_{0 \rightarrow j}) \ll n_t \Delta z$, the count rate is given by:

$$\begin{aligned} \frac{dA_{j \rightarrow k, d}}{dt} = & \int_0^\infty dE_\gamma \int d\Omega' \frac{W_{0 \rightarrow j \rightarrow k}(\theta', \varphi', P_\gamma)}{4\pi} \frac{d\epsilon_d}{d\Omega'}(E_\gamma, \theta', \varphi', \mathbf{r} = 0) \\ & \times \sigma_{0 \rightarrow j}(E_\gamma) \frac{\Gamma_{j \rightarrow k}}{\Gamma_j} N_t \Phi(E_\gamma, t) \end{aligned} \quad (4.46)$$

In Eq. (4.46), the notation $\mathbf{r} = 0$ symbolizes that ϵ_d is evaluated at the target position. As a last simplification, the energy dependence of the HI γ S beam profile

²⁴Calculated in the formalism of [120] and Sec. 5 in [239] using a Debye temperature for elemental krypton from [241].

²⁵For a simple and fast geometrical estimate, analytical formulas for the solid angle of a disk-shaped detector surface with respect to a point in space are given in [242].

(see, e.g. Fig. 4.6) and the detection efficiency (see, e.g., Fig. 4.4) can be neglected compared to the width of a Doppler-broadened (see Sec. 2.2 in [120]) NRF resonance on the order of ≈ 1 eV.

$$\begin{aligned} \frac{dA_{j \rightarrow k, d}}{dt} &= \int d\Omega' \frac{W_{0 \rightarrow j \rightarrow k}(\theta', \varphi', P_\gamma)}{4\pi} \frac{d\epsilon_d}{d\Omega'}(E_{\gamma, j}, \theta', \varphi', \mathbf{r} = 0) \\ &\quad \times I_{0 \rightarrow j \rightarrow k} N_t \Phi(E_{\gamma, j}, t) \\ &= \langle W_{0 \rightarrow j \rightarrow k} \epsilon_d(E_{\gamma, j}) \rangle I_{0 \rightarrow j \rightarrow k} N_t \Phi(E_{\gamma, j}, t) \end{aligned} \quad (4.47)$$

To obtain Eq. (4.47) from Eq. (4.46), the photon flux and the efficiency were evaluated at the resonance photon energy $E_{\gamma, j}$ and the energy integral over the NRF cross section yielded the energy-integrated cross section from Eq. (2.4). In the last equality of Eq. (4.47), the notation $\langle W_{0 \rightarrow j \rightarrow k} \epsilon_d(E_\gamma) \rangle$ was introduced for the solid-angle integral over the product $W\epsilon$. Due to the good agreement of the efficiency simulations with source measurements (see Sec. 4.5.2, in particular Fig. 4.4), this quantity was also obtained from Monte-Carlo simulations. It was assumed that the scaling factors p_{sim} in Eq. (4.31), which were needed to reproduce the absolute detection efficiencies, can be applied to $\langle W_{0 \rightarrow j \rightarrow k} \epsilon_d(E_\gamma) \rangle$ as well. Furthermore, the linear polarization was assumed to be $P_\gamma(E_\gamma) = 1$ at all energies (see, e.g., [168, 234]). At last, the time dependence of the photon flux can be integrated out, since only time-integrated quantities were considered. Note that the finite dead time of detector d leads to an effectively reduced photon flux, which is taken into account here by multiplying the time-averaged photon flux $\langle \Phi(E_\gamma) \rangle_t$ with the live time $t_{\text{live}, d}$. Therefore, the total number of counted events is:

$$A_{j \rightarrow k, d} = \left\langle \frac{dA_{j \rightarrow k, d}}{dt} \right\rangle_t t_{\text{live}, d}. \quad (4.48)$$

4.6.1. Quantum Numbers and Multipole Mixing Ratio

In order to determine angular momentum- and parity quantum numbers of excited states and the multipole mixing ratios of the decay transitions, the dependence of the photons' angular distribution [Eq. (2.11)] on these quantities was used. The experimental method proposed by Pietralla et al. [243] for parity measurements

with polarized photon beams, which can be straightforwardly generalized to the measurement of multipole mixing ratios (see, e.g. [244]), was used. It is based on a determination of the asymmetry $a_{0 \rightarrow j \rightarrow k, dd'}$ of the number of counted events associated with a transition from state j to state k between two detectors d and d' . In the literature (see, e.g., Sec. 'Parity Assignments, Polarization Observables' in [119], and the two aforementioned publications), the proportionality

$$\frac{A_{j \rightarrow k, d}}{\int d\Omega \epsilon_d(E_{\gamma, j}, \theta, \varphi)} \propto \int_{\Omega_d} d\Omega W_{0 \rightarrow j \rightarrow k}(\theta, \phi, \delta_{0 \rightarrow j}, \delta_{j \rightarrow k}) \quad (4.49)$$

is often assumed. In Eq. (4.49), \int_{Ω_d} symbolizes an integration over the solid angle covered by the detector d . However, for the close geometry of the present experiments and the expected strong solid-angle dependence of the gamma-ray angular distributions, neglecting the solid-angle dependence of the full-energy peak efficiency (see, e.g., [245]) is not a good approximation.

Since the geometrical effects were taken into account by Monte-Carlo simulations in the present work (see Sec. 4.6), a different definition of the asymmetry was used:

$$a_{0 \rightarrow j \rightarrow k, dd'} = \frac{A_{j \rightarrow k, d} - A_{j \rightarrow k, d'}}{A_{j \rightarrow k, d} + A_{j \rightarrow k, d'}} \quad (4.50)$$

$$\text{Eqs. (4.47), (4.48)} \quad \frac{\langle W_{0 \rightarrow j \rightarrow k} \epsilon_d(E_{\gamma, j}) \rangle t_{\text{live}, d} - \langle W_{0 \rightarrow j \rightarrow k} \epsilon_{d'}(E_{\gamma, j}) \rangle t_{\text{live}, d'}}{\langle W_{0 \rightarrow j \rightarrow k} \epsilon_d(E_{\gamma, j}) \rangle t_{\text{live}, d} + \langle W_{0 \rightarrow j \rightarrow k} \epsilon_{d'}(E_{\gamma, j}) \rangle t_{\text{live}, d'}}. \quad (4.51)$$

Equations (4.50) and (4.51) connect the experimentally observable peak areas to properties of excited states. In practice, J_j , π_j , and $\delta_{j \rightarrow k}$ were assumed to be parameters of a χ^2 minimization:

$$\chi^2 = \sum_{d \in D} \sum_{d' \in D > d} \frac{\left(a_{0 \rightarrow j \rightarrow k, dd'}^{\text{sim}} - a_{0 \rightarrow j \rightarrow k, dd'} \right)^2}{\sigma_{a_{0 \rightarrow j \rightarrow k, dd'}}^2} \quad (4.52)$$

In Eq. (4.52), the symbol a^{sim} indicates the simulated asymmetry, using the definition of Eq. (4.51). For the quantities J_j and π_i , the most probable combinations 1^\pm and 2^+ were tried. For the continuous quantity $\delta_{j \rightarrow k}$, simulations were performed

on a variable grid of values in the interval $[-2, 2]$ (including $\delta_{j \rightarrow k} = 0$), where it is expected to vary most strongly (see, e.g., Fig. 4 in [244]) due to the equal contributions of both multipolarities. Simulations for values outside of this interval were performed on a more coarse grid until a further increase of δ did not change the expected asymmetry any more.

An example for the determination of the total angular momentum and parity of the excited state of ^{82}Se at 2981 keV is shown in Fig. 3 of [165]. Even if systematic uncertainties of the simulations on the order of 10% are assumed, the results for the γ^3 setup are unambiguous. The polarimetry setup was not sensitive enough to the distinction between $J_f = 1$ and $J_f = 2$ states, even for the ones with the largest statistics. An example for a determination of the multipole mixing ratio is shown in Fig. 4.10. In this figure, the determination of δ for the transition from the 1_2^+ state of ^{82}Kr to the 2_2^+ state is shown, which indicates a strong admixture of $E2$ strength to that transition.

4.6.2. Branching Ratio

The extraction of precise branching ratios to low-lying excited states, or at least firm constraints for their magnitude, were a major goal of the present study, since they are sensitive to the evolution of nuclear shapes and their coexistence (see Secs. 1.2 and 2.3). They are determined from the ratios of count rates for decays of the state j , which was excited from the ground state, to lower-lying states k . These count rates are corrected for different angular distributions and detection probabilities of the transitions $j \rightarrow k$ and $j \rightarrow k'$. Explicitly, ratios of partial transition widths were obtained from Eqs. (4.47) and (4.48) in the present work. It will be assumed in the following that the reference transition is the ground-state transition $0 \rightarrow j \rightarrow 0$, and that $k > 0 \forall k \in K$. Since there was no case in which the ground-state transition was not observed, this was always possible. First, Eq. (4.47) is solved for $I_{0 \rightarrow j \rightarrow k}$, and then the ratios of two different energy-integrated cross sections are calculated for the same detector:

$$\frac{I_{0 \rightarrow j \rightarrow k}}{I_{0 \rightarrow j \rightarrow 0}} = \frac{\langle W_{0 \rightarrow j \rightarrow 0} \epsilon_d(E_{\gamma, j \rightarrow 0}) \rangle A_{j \rightarrow k, d}}{\langle W_{0 \rightarrow j \rightarrow k} \epsilon_d(E_{\gamma, j \rightarrow k}) \rangle A_{j \rightarrow 0, d}} \stackrel{\text{Eq. (2.4)}}{=} \frac{\Gamma_{j \rightarrow k}}{\Gamma_{j \rightarrow 0}} \quad (4.53)$$

A high degree of model-independence is reached due to the cancellation of the photon flux, similar to Sec. 4.6.1. Ratios of $\Gamma_{j \rightarrow k}/\Gamma_{j \rightarrow 0}$ were determined for all observed branching transitions $j \rightarrow k$ of a detector. After that, an uncertainty-weighted average value $\langle \Gamma_{j \rightarrow k}/\Gamma_{j \rightarrow 0} \rangle$ of all detectors was calculated. From these, an upper limit for the actual branching ratios was obtained as:

$$\frac{\Gamma_{j \rightarrow k}}{\Gamma'_j} < \frac{\langle \Gamma_{j \rightarrow k}/\Gamma_{j \rightarrow 0} \rangle}{1 + \sum_{k' \in K} \langle \Gamma_{j \rightarrow k'}/\Gamma_{j \rightarrow 0} \rangle} \quad (4.54)$$

As indicated, Eq. (4.54) is an upper limit, since there may be other decay channels of the state j , i.e. the true value of Γ_j may be larger.

Due to the exponentially increasing nonresonant background towards lower energies (see Sec. D), a firm model-independent constraint of Γ_j with the present technique is challenging [131] and was not attempted here. Nevertheless, upper limits for branching transitions to low-lying excited states of interest were determined by replacing $A_{j \rightarrow k,d}$ in Eq. (4.53) by the corresponding sensitivity limit L_C from Eq. (4.19) at the energy where the branching transition would be expected. For the determination of upper limits, lowest-order multipolarities were assumed to dominate.

If multiple values for the multipole mixing ratio were available, the one closest to zero was chosen. Note that this does not have a large impact on the branching ratio, since the existence of multiple values implies that their angular distributions were similar.

4.6.3. Cross section

Cross sections for NRF transitions were determined in the present work by solving Eq. (4.47) for $I_{0 \rightarrow j \rightarrow k}$ for each detector and using the information from Secs. 4.6.1 and 4.6.2. The final results given in Sec. 5 represent a weighted average of the cross sections measured in different detectors, potentially scaled due to systematic uncertainties (see Sec. 4.1.3).

From the quantity $I_{0 \rightarrow j \rightarrow k}$, transition widths, and ultimately reduced transition strengths were determined using Eq. (2.4) with the assumption that the observed branching transitions represent all branching transitions of the state of interest.

Since the reduced transitions strengths are only a lower limit of the true transition strengths $B(\sigma L; k \rightarrow j)$, they are denoted as $\mathfrak{B}(\sigma L; k \rightarrow j)$ similar to Ref. [131].

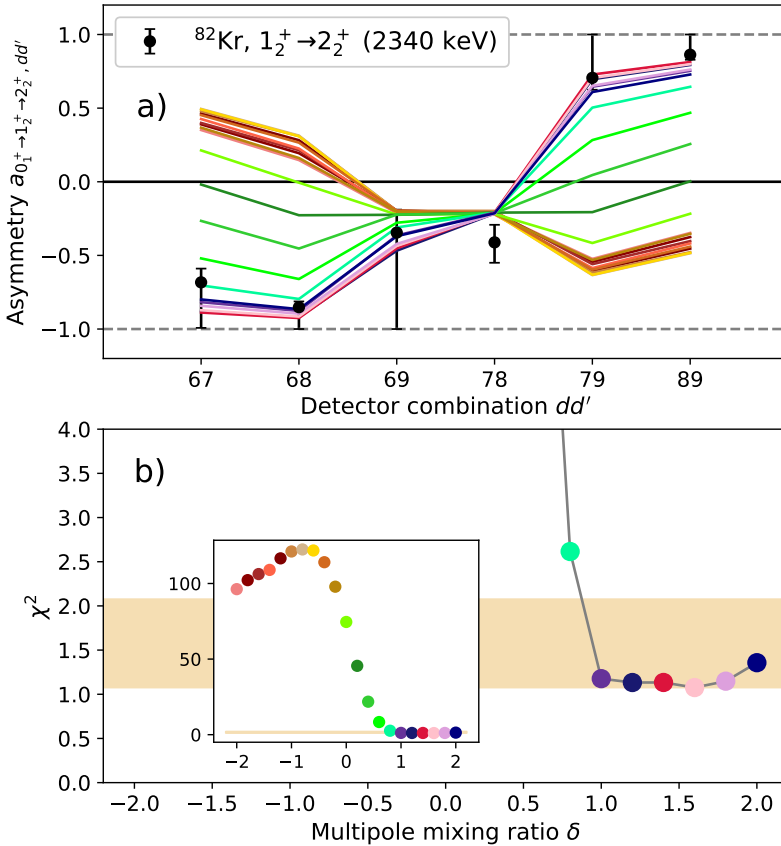


Figure 4.10.: Determination of the multipole mixing ratio δ for the decay of the 1_2^+ state of ^{82}Kr at 3815 keV to the 2_2^+ state at 1475 keV [138]. (a) Asymmetry of the $1_2^+ \rightarrow 2_2^+$ transition for different detector combinations dd' , which are indicated on the x axis ('67' means $d = 6, d' = 7$. See also Fig. B.2). The experimental values are shown as black dots with error bars. A set of simulated asymmetries for various assumptions for δ is shown in various colors. (b) Value of χ^2 for the different values of δ . The inset plot shows all data points in the same colors as in (a), while the containing panel shows a zoom into the minimum. The region between the minimum χ^2_{\min} and $\chi^2_{\min} + 1$ is highlighted.

5. Results

The excited states of ^{82}Kr and ^{82}Se , whose decay behavior was characterized in the present work, are shown in Tabs. 5.1 and 5.2. In the following, the content of the different columns in the two tables will be described and references to relevant section of this work will be given.

In general, a transition was considered to be 'observed', if the number of events N_S surpassed the sensitivity limit N_D given by Eq. (4.20) in at least one detector. Due to the focus of this work on branchings to low-lying excited states (see Sec. 2.3), upper limits for transitions (i.e. branching ratios and reduced transition strengths) to the known [138] 0_2^+ , 2_1^+ , and 2_2^+ states are given for both isotopes, if the transitions were not observed. No transitions to higher-lying excited states were observed. The upper limits were calculated using the threshold L_C from Eq. (4.19) and assuming a dominance of the lowest-order multipolarity.

All values given in Tabs. 5.1 and 5.2 are rounded according to recommendations by the PDG (Sec. 5.3 in [2]). For values with an asymmetric shortest-coverage interval, the larger of both limits determines the rounding digits, i.e. $1.000^{+0.456}_{-0.012}$ appears as $1.0^{+0.5}_0$. An exception to this rule are values where one of the limits was infinity. In these cases, the larger of the most probable value and the finite limit determined the rounding digits. This is why values like $-2^{+0}_{-\infty}$ appear.

In the first column, the energy E_j of the excited state is given. Excitation energies were determined from the energy calibration described in Sec. 4.5.1. If a level energy reported in the ENSDF [138] was in agreement with the present study [see Eq. (4.26)], but had a lower uncertainty, then the literature value is given.

The second column gives the level energy difference $E_j - E_k$, which was determined from the known excitation energies of the initial and final states E_j and E_k of the

decay transition. The Ritz variation principle [Eq. (4.26)], was the criterium for assigning an observed photon to an energy difference between the states j and k .

The third column gives the total angular momentum- (J_j) and parity (π_j) quantum numbers of the excited states, which were determined from an analysis of angular distributions in Sec. 4.6.1. Since the polarimetry setup was optimized for parity measurements, it was not always possible to distinguish between dipole- and quadrupole excitations. Therefore, the alternative assignment of $J^\pi = 2^+$ is indicated for 1^+ states. Due to the expected two-fold dominance of the E1- over the M2 character (see Sec. 2.1.1), the alternative 2^- -assignment is not shown for 1^- states in accordance with the literature [119].

The fourth column gives the total angular momentum- (J_k) and parity (π_k) quantum numbers of the final states of the transition. They are well known [138] for the transitions of interest.

The fifth column gives the branching ratio $\Gamma_{j \rightarrow k}/\Gamma_j$, which was determined in Sec. 4.6.2. Note that the quantity Γ_j includes only the observed transitions. Due to the chosen definition of the branching ratio [Eq. (4.54)] and the Monte-Carlo method for the propagation of uncertainty (see Sec. 4.1.1), the most probable values for $\Gamma_{j \rightarrow k}/\Gamma_j$ usually did not add up to 1. This property was artificially restored by adapting the value of the smallest branching ratio, which was always possible within the given uncertainty limits.

The sixth column gives the elastic NRF cross section $I_{0 \rightarrow j \rightarrow 0}$ for an excited state j as determined in Sec. 4.6.3. Note that there was no case where only inelastic transitions from an excited states were observed. Due to the dominance of the systematic uncertainty of the absolute photon flux calibration (see Sec. 4.5.4), which has an unknown probability distribution, the shortest coverage interval was assumed to be symmetric. For the case of ^{82}Se , note that the cross section for the state at 2981 keV was lower than the one measured by Werner [137] by a factor of $c_{\text{VW}} = 0.55(9)$. The elastic cross sections of all observed dipole-excited states, together with the sensitivity limit N_D [Eq. (4.20)], are shown in Fig. 5.1 for ^{82}Kr and in Fig. 5.2 for ^{82}Se .

The seventh column gives the multipole mixing ratio $\delta_{j \rightarrow k}$ for the transition between states j and k which was determined via a χ^2 minimization described in Sec. 4.6.1.

Alternative intervals may be given for $\delta_{j \rightarrow k}$ since the χ^2 statistic can have several minima.

The eighth column gives a lower limit for the reduced excitation strength [$\mathfrak{B}(\sigma L; k \rightarrow j) < B(\sigma L; k \rightarrow j)$] of the transition $k \rightarrow j$ as defined in Sec. 4.6.3. In general, only the strength of the dominant multipole is shown. If the absolute value of the mode of $\delta_{j \rightarrow k}$ was larger than 1, then the higher-order multipole was considered the dominant one, because its associated partial transition width is larger [see Eq. (2.10)]. The electromagnetic character and the multipole order is indicated by the unit of $\mathfrak{B}(\sigma L; k \rightarrow j)$.

Table 5.1.: Properties of excited states of ^{82}Kr which were determined in the present work. A detailed description of the displayed quantities can be found in Sec. 5. For better readability, to avoid repetition, or in cases where a quantity is not defined for the given transition, entries of the table may be empty.

E_j (keV)	$E_j - E_k$ (keV)	$J_j^{\pi_j}$	$J_k^{\pi_k}$	$\Gamma_{j \rightarrow k} / \Gamma$	$I_{0 \rightarrow i \rightarrow 0}$ (eVb)	$\delta_{j \rightarrow k}$	$\mathfrak{B}(\sigma L; k \rightarrow j)$
3254.37(24)		1^-	0_1^+	1	7.4(17)		$0.0068^{+0.016}_{-0.016} \text{e}^2 \text{fm}^2$
	2477.84(24)		2_1^+	< 1.8			$< 0.00010 \text{e}^2 \text{fm}^2$
	1779.46(24)		2_2^+	< 2.7			$< 0.0004 \text{e}^2 \text{fm}^2$
	1766.66(25)		0_2^+	< 3.4			$< 0.0025 \text{e}^2 \text{fm}^2$
3770.4(8)		$(1, 2)^+$	0_1^+	1	3.4(6)		$0.020^{+0.035}_{-0.035} \mu_N^2$
	2993.9(8)		2_1^+	< 1.4			$< 0.0025 \mu_N^2$
	2295.5(8)		2_2^+	< 2.3			$< 0.009 \mu_N^2$
	2282.7(8)		0_2^+	< 2.3			$< 0.05 \mu_N^2$
3815.25(7) ¹		$(1, 2)^+$	0_1^+	$0.68^{+0.02}_{-0.07}$	45(4)		$0.078^{+0.015}_{-0.011} \mu_N^2$
	3038.72(7)		2_1^+	$0.078^{+0.017}_{-0.015}$		$0.10^{+0.23}_{-0.10}$	$0.013^{+0.005}_{-0.003} \mu_N^2$
						-2^{+0}_{-0}	$20^{+\infty}_{-0} \text{e}^2 \text{fm}^4$
	2340.35(7)		2_2^+	$0.242^{+0.035}_{-0.029}$		$0.8^{+\infty}_{-0}$	$< 0.06 \mu_N^2$
	2327.55(9)		0_2^+	< 0.05			$< 0.028 \mu_N^2$
3918.7(5)		1^-	0_1^+	1	5.4(14)		$0.00034^{+0.00009}_{-0.00009} \text{e}^2 \text{fm}^2$
	3142.1(5)		2_1^+	< 0.7			$< 0.000019 \text{e}^2 \text{fm}^2$

¹Level energy from [138].

Table 5.1.: (Continued).

2443.8(5)	2_2^+		< 1.1		$< 0.00006 e^2 \text{fm}^2$
2431.0(5)	0_2^+		< 0.8		$< 0.00026 e^2 \text{fm}^2$
3958.05(14) ¹	0_1^+	(1,2) ⁺	1	60(12)	$0.33^{+0.07}_{-0.07} \mu_N^2$
3181.52(14)	2_1^+		< 0.29		$< 0.008 \mu_N^2$
2483.15(14)	2_2^+		< 0.5		$< 0.029 \mu_N^2$
2470.35(15)	0_2^+		< 0.5		$< 0.15 \mu_N^2$
4055.8(5)	0_1^+	(1,2) ⁺	1	8.5(13)	$0.046^{+0.07}_{-0.07} \mu_N^2$
3279.2(5)	2_1^+		< 0.8		$< 0.0032 \mu_N^2$
2580.9(5)	2_2^+		< 1.0		$< 0.008 \mu_N^2$
2568.1(5)	0_2^+		< 1.0		$< 0.04 \mu_N^2$

Table 5.2.: Properties of excited states of ^{82}Se which were determined in the present work. A detailed description of the displayed quantities can be found in Sec. 5. See also the caption of Tab. 5.1.

E_j (keV)	$E_j - E_k$ (keV)	$J_j^{\pi_j}$	$J_k^{\pi_k}$	$\Gamma_{j \rightarrow k}/\Gamma$	$I_{0 \rightarrow i \rightarrow 0}$ (eVb)	$\delta_{j \rightarrow k}$	$\mathfrak{B}(\sigma L; k \rightarrow j)$
2980.56(10)		1^+	0_1^+	$0.413^{+0.004}_{-0.026}$	8.1(13)		$0.134^{+0.025}_{-0.023} \mu_N^2$
	2325.87(9)		2_1^+	$0.587^{+0.007}_{-0.035}$		$0.10^{+0.05}_{-0.06}$	$0.078^{+0.018}_{-0.011} \mu_N^2$
	1570.34(20)		0_2^+	< 0.015			$< 0.009 \mu_N^2$
	1249.05(14)		2_2^+	< 0.04			$< 0.008 \mu_N^2$
3034.1(4)		2^+	0_1^+	1	1.00(20)		$12.0^{+2.0}_{-2.6} \text{e}^2 \text{fm}^2$
	2379.4(4)		2_1^+	< 0.31			$< 0.0021 \mu_N^2$
	1623.9(4)		0_2^+	< 2.0			$< 110 \text{e}^2 \text{fm}^4$
	1302.6(4)		2_2^+	< 0.8			$< 0.0033 \mu_N^2$
3244.64(14)		1^+	0_1^+	1	11.3(21)		$0.0102^{+0.0020}_{-0.0018} \mu_N^2$
	2589.93(21)		2_1^+	< 0.26			$< 0.0018 \mu_N^2$
	1834.42(22)		0_2^+	< 0.4			$< 0.04 \mu_N^2$
	1513.13(17)		2_2^+	< 0.7			$< 0.023 \mu_N^2$
3342.89(17)		1^-	0_1^+	$0.66^{+0.02}_{-0.04}$	17.4(32)		$0.026^{+0.004}_{-0.006} \text{e}^2 \text{fm}^2$
	2688.17(16)		2_1^+	$0.341^{+0.014}_{-0.031}$		$0^{+0.10}_{-0.20}$	$0.00041^{+0.00007}_{-0.00009} \text{e}^2 \text{fm}^2$
	1932.67(24)		0_2^+	< 0.04			$< 0.00007 \text{e}^2 \text{fm}^2$
	1611.38(20)		2_2^+	< 0.05			$< 0.00006 \text{e}^2 \text{fm}^2$
3632.0(4)		1^+	0_1^+	1	2.7(5)		$0.016^{+0.004}_{-0.003} \mu_N^2$

Table 5.2.: (Continued).

2977.3(4)	2_1^+	< 0.8	$< 0.0011 \mu_N^2$
2221.8(4)	0_2^+	< 1.5	$< 0.023 \mu_N^2$
1900.5(4)	2_2^+	< 1.7	$< 0.009 \mu_N^2$
3806.63(18)	1^-	$0.465^{+0.015}_{-0.033}$	$0.00135^{+0.00024}_{-0.00023} \text{e}^2 \text{fm}^2$
3151.50(10)	2_1^+	$0.535^{+0.020}_{-0.031}$	$0.00059^{+0.00008}_{-0.00010} \text{e}^2 \text{fm}^2$
	2_1^+		$5300^{+1200}_{-1000} \mu_N^2 \text{fm}^2$
2396.41(24)	0_2^+	< 0.04	$< 0.0001 \text{e}^2 \text{fm}^2$
2075.12(20)	2_2^+	< 0.05	$< 0.00004 \text{e}^2 \text{fm}^2$
3823.90(26)	1^+	$0.651^{+0.005}_{-0.010}$	$0.46^{+0.04}_{-0.06} \mu_N^2$
3168.66(8)	2_1^+	$0.262^{+0.008}_{-0.006}$	$0.064^{+0.007}_{-0.007} \mu_N^2$
2413.68(31)	0_2^+	< 0.017	$< 0.010 \mu_N^2$
2091.79(12)	2_2^+	$0.087^{+0.007}_{-0.005}$	$0.061^{+0.011}_{-0.007} \mu_N^2$
4061.9(5)	1^-	$0.444^{+0.012}_{-0.030}$	$219^{+34}_{-28} \text{e}^2 \text{fm}^4$
3407.13(24)	2_1^+	$0.556^{+0.018}_{-0.029}$	$0.0042^{+0.0008}_{-0.0006} \text{e}^2 \text{fm}^2$
2651.7(5)	0_2^+	< 0.031	$0.00177^{+0.00034}_{-0.00027} \text{e}^2 \text{fm}^2$
2330.4(5)	2_2^+	< 0.035	$< 0.00025 \text{e}^2 \text{fm}^2$
	2_2^+		$< 0.00009 \text{e}^2 \text{fm}^2$

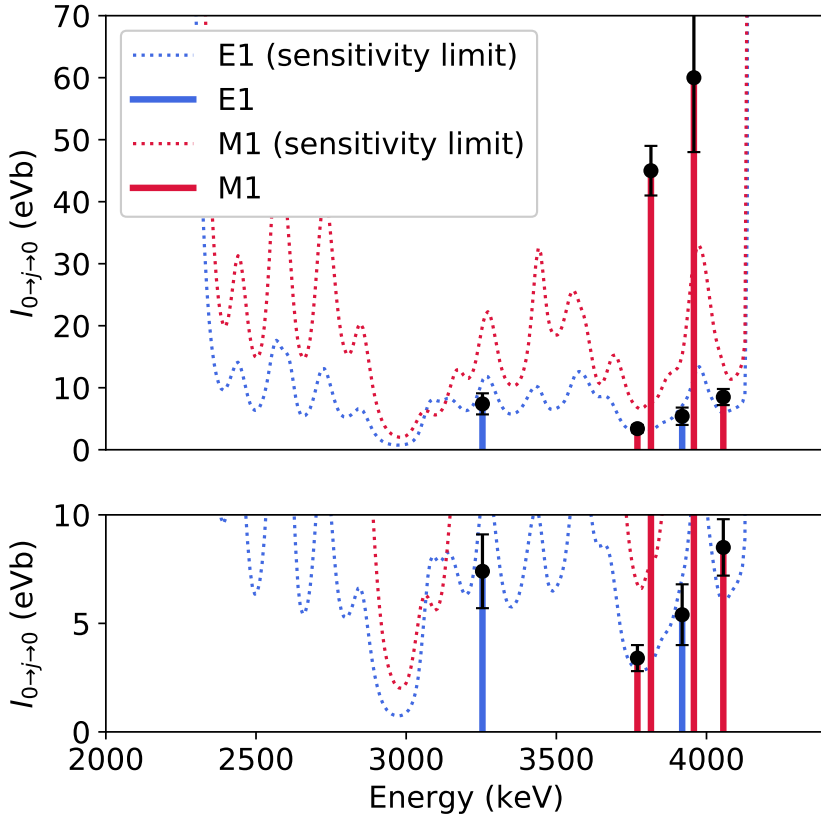


Figure 5.1.: Elastic cross sections $I_{0 \rightarrow j \rightarrow 0}$ for dipole-excited states of ^{82}Kr , which were determined in the present work. The sensitivity limits N_D from Eq. (4.20) for M1 and E1 strength are indicated by dotted lines. The lower part of this figure shows a zoom into the region of low cross sections for better visibility. In cases where it was unclear whether the observed states had dipole- or quadrupole character, the lower multipole order was assumed.

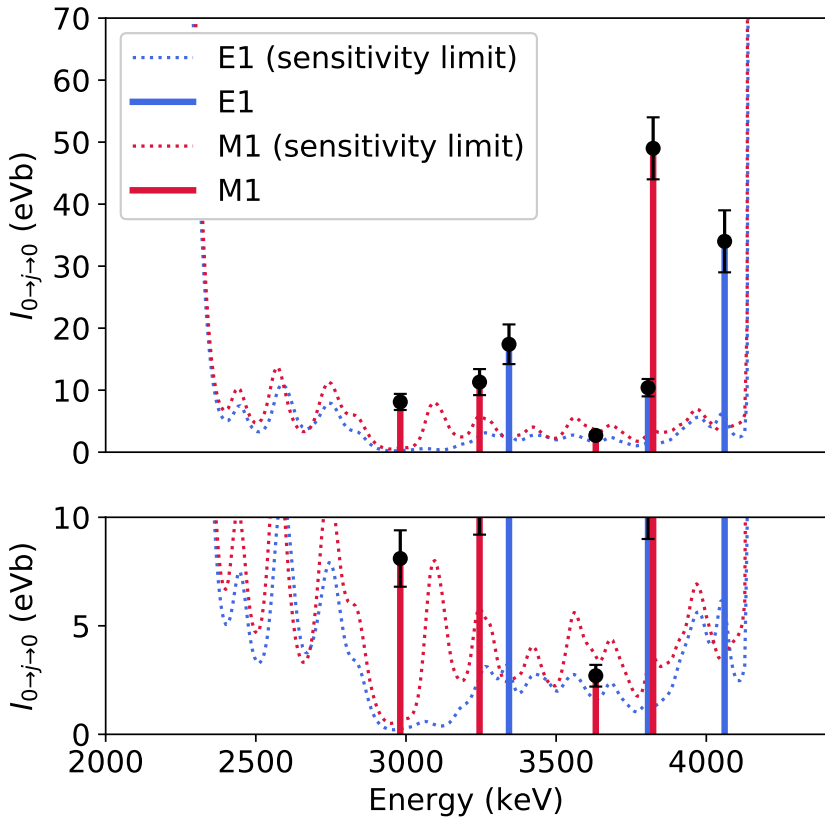


Figure 5.2.: Elastic cross sections $I_{0 \rightarrow j \rightarrow 0}$ for dipole-excited states of ^{82}Se , which were determined in the present work. See also Fig. 5.2.

6. Discussion

In this section, the results of the present work, which are tabulated and visualized in Sec. 5, will be discussed. For the experiment on $^{82}\text{Kr}/^{82}\text{Se}$, the origin of the observed magnetic dipole strength will be the main point of interest. For the experiment on $^{150}\text{Nd}/^{150}\text{Sm}$, updated calculations in the framework of the IBM-2, which include the new results, will be presented. Based on these results, predictions for $0\nu\beta\beta$ -decay matrix elements are given.

6.1. ^{82}Se and ^{82}Kr

In the present work, precise data on the decay behavior of newly observed 1^+ states of ^{82}Kr and ^{82}Se were obtained. No branching transition to a 0_2^+ state could be observed. However, the corresponding branching ratios were constrained to less than 2%, a value which is competitive with the study of Beller et al. [110] on ^{154}Gd .

Obviously, the interpretation that ^{82}Kr and ^{82}Se are close to the $SU(3)$ limit of the IBM-2 according to their decay behavior (see Sec. 2.3) cannot be true if one considers, for example, their small deformation parameters of $\beta(^{82}\text{Kr}) = 0.203(3)$ and $\beta(^{82}\text{Se}) = 0.1920(15)$ [138], respectively. It is more likely that the assumptions which go into the IBM-2 see Sec. 2.2.2 do not hold any more at these low mass numbers. The interpretation of a single origin of the observed $M1$ strength is further challenged by the fact that the excited states of ^{82}Se at 2981 keV and 3824 keV exhibit a very different decay behavior.

The observed discrepancies may be explained by an admixture of spin- $M1$ strength to the low-lying 1^+ states of both isotopes, because the ground-state decays of the spin-flip one-particle one-hole excitations are not as inhibited as the ground-state transitions of two-phonon mixed-symmetry states (see Sec. 2.3). To clarify the 'purity' of the observed $M1$ strength, a shell model calculation was performed for ^{82}Se . The calculation used the JUN45 effective interaction proposed by Honma et al. [101], which was found to give a satisfactory description of collective phenomena like triaxiality and shape coexistence within the model space denoted as $f_5p g_9$ by the authors. Note that the same interaction was also used by Sen'kov, Horoi and Brown [68] for the calculation of $0\nu\beta\beta$ -decay matrix elements of ^{82}Se . Using the shell-model code NuShellX@MSU [246], it was possible to perform a calculation of the first ten 1^+ states, with all 26 valence nucleons (6 protons, 20 neutrons) of ^{82}Se with respect to the ^{58}Ni core, in a reasonable time. For ^{82}Kr , the more even ratio between the number of valence protons and -neutrons circumvents the Pauli principle and leads to a strong increase of the basis size. Calculations for this isotope were tried with different truncation schemes, but no conclusive result could be obtained. Two calculations were performed for ^{82}Se , one with the bare orbital g factors $g_l^\pi = 1$ and $g_l^\nu = 0$, and another one where both were set to zero to obtain only orbital $M1$ strength.

The results of both calculations are compared to the experimentally observed values of $\mathfrak{B}(M1; 0 \rightarrow j)$ in Fig. 6.1. The energies of the low-lying 1^+ states are reproduced well. Considering the excitation strengths, the lowest lying state at 2981 keV is also in good agreement with the calculation, in particular if one considers that no quenching factor was used. At higher energies, the shell model predicts a larger fragmentation than exhibited by the experimental data. However, the total calculated strength of $0.69 \mu_N^2$ within the plotted energy range is in very good agreement with the summed $M1$ strength of the data of $0.62(6) \mu_N^2$.

As expected, the contribution of spin- $M1$ strength to the total strength is predicted to be almost 50% even at the lowest energy of 2981 keV. From this analysis, it can be concluded that for ^{82}Se , the simple IBM-2 picture is not applicable, and further microscopic calculations are necessary to clarify the situation. The same can be expected for ^{82}Kr .

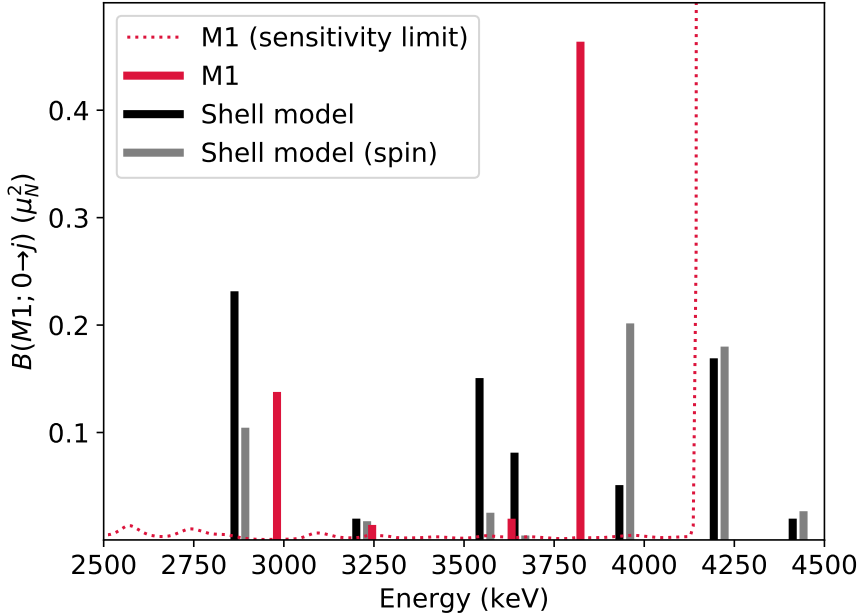


Figure 6.1.: Reduced magnetic dipole strength $B(M1; 0 \rightarrow j)$ for the excitation from the ground state of ^{82}Se in the energy range of the present experiment. The experimental values (which are actually lower limits $\mathfrak{B}(M1)$ for the transition strengths) of this work are shown in red, together with the same sensitivity limit as in Fig. 5.2, which was converted from a limit for elastic cross sections by neglecting branching transitions. The black bars show a shell model calculation (see Sec. 6.1) of the same quantity. Another shell model calculation in which the orbital part of the $M1$ operator was artificially set to zero is shown in gray. Both calculations returned the same energy values, but the gray bars were shifted by 30 keV to the right for better visibility.

6.2. ^{150}Nd and ^{150}Sm

In the theses of Jörn Kleemann [178, 179], branching ratios of the strongest scissors mode fragments of ^{150}Sm and ^{150}Nd in the energy range of the beam could be measured down to a few percent, similar to the $^{82}\text{Kr}/^{82}\text{Se}$ experiment. Probably due to the location of both $A = 150$ nuclei in proximity of a shape phase transition, decays to the 0_2^+ states could be observed.

The newly found experimental data were used to constrain parameters of the IBM-2 Hamiltonian given by Eq. (2.35). A sizable change is expected, especially for ^{150}Sm , since the parity of the most strongly excited state in the energy range of the experiment at 3082 keV was reassigned unambiguously to 1^- . An intelligent χ^2 minimization procedure was applied using different criteria to prevent overfitting the data. The procedure is described in detail in Sec. 7 of [179]. Fig. 6.2 shows the result of such a minimization procedure in comparison the the experimental level scheme and transition strengths of ^{150}Nd . From the comparison, it can be concluded that the IBM-2 gives a very good description of the textbook-X(5) nucleus ^{150}Nd [112]. Parameter variations for ^{150}Sm showed larger deviations from the experimental level scheme (see Sec. 7.4 in [179]). In particular, there were problems with the calculation producing mixed-symmetry states at unexpectedly low excitations energies.

Nevertheless, the present parameter sets were used to recalculate $0\nu\beta\beta$ decay matrix elements in collaboration with J. Kotila from the university of Jyväskylä. Using the formalism for $0\nu\beta\beta$ decay derived in [247] and applied in [85, 248], the results shown in Fig. 6.3 were obtained [249] for the nuclear matrix element. The impact of taking into account more precise data for the scissors mode is qualitatively the same as for the case of ^{154}Gd [110]. While the predicted matrix element to the ground state remains approximately the same, the increased sensitivity to shape coexistence effects increases the matrix element to the excited 0^+ state. Qualitatively, the enhancement is not as strong as in ^{154}Gd , probably because ^{150}Nd in particular was already described well by the IBM-2 parameterization of the previous analysis on which the predictions in [248] were based.

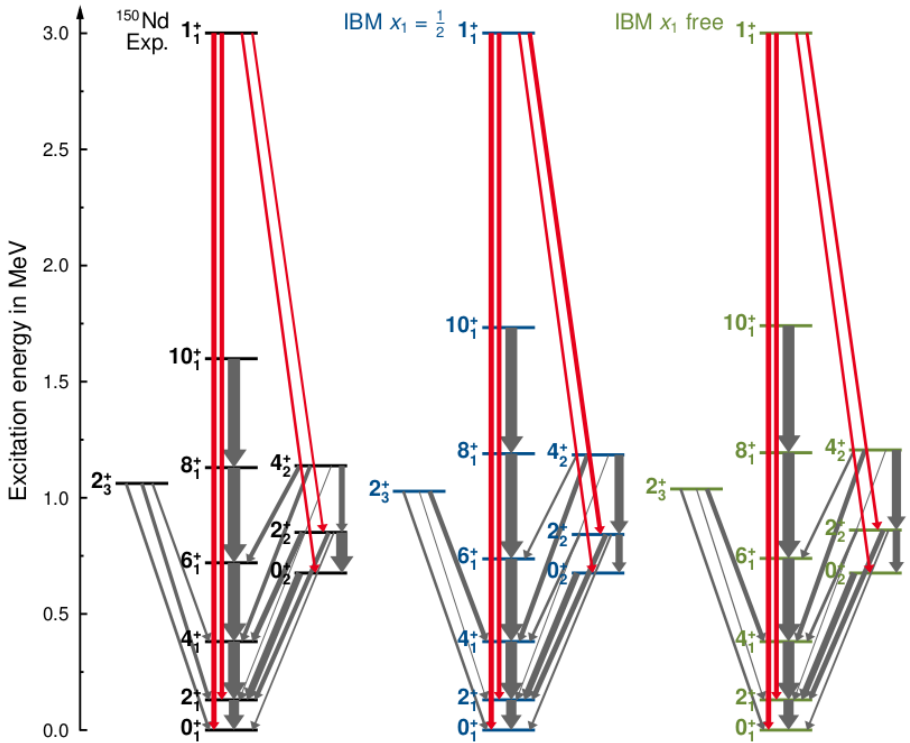


Figure 6.2.: *Left*: Low-lying level scheme of ^{150}Nd , which includes all excited states and transition strengths which were used for a minimization of the parameters of the IBM-2 in [179]. The thickness of the arrows is proportional to the $M1$ (red) and $E2$ (gray) transition strengths in Weisskopf units. *Middle*: The same level scheme, as obtained from a minimization of the parameters of the IBM-2 Hamiltonian. The label $x_1 = 1/2$ indicates, in the parameterization of [179], that the parameters ξ_1 and ξ_3 were constrained to be equal. *Right*: For this calculation, both ξ_1 and ξ_3 were allowed to vary independently from each other to further improve the description of the experimental data. Figure from [179].

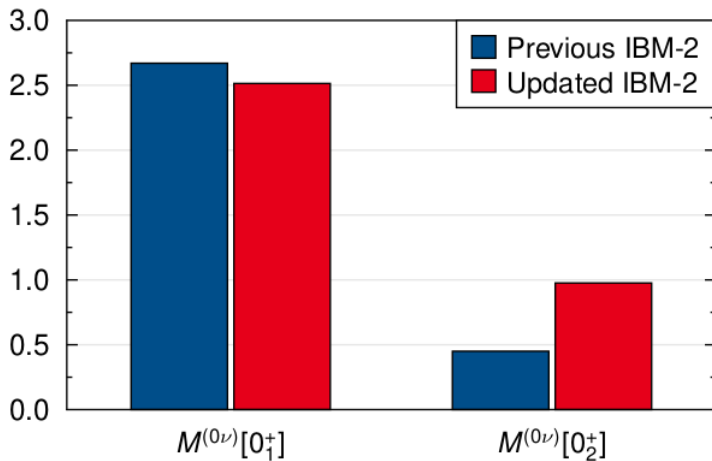


Figure 6.3.: Predictions for the nuclear matrix elements $M^{(0\nu)}$ for the $0\nu\beta\beta$ decay of ^{150}Nd to the ground state and the first excited 0^+ state of ^{150}Sm in the framework of the IBM-2 [249]. The calculation labeled 'previous' used the same parameters as in Ref. [248], while the 'updated' calculation used the parameters from the study in [179].

7. Summary and Outlook

In the present work, the decay characteristics of the nuclear scissors mode of $0\nu\beta\beta$ -decay candidate isotopes were studied. Exotic decay branches of the scissors mode are expected to be sensitive to phenomena like nuclear shape evolution along a chain of isotopes and shape coexistence within a certain nucleus, which strongly influence the nuclear matrix elements in $0\nu\beta\beta$ -decay rate calculations. Explicitly, the isotope pairs $^{82}\text{Se}/^{82}\text{Kr}$ and $^{150}\text{Nd}/^{150}\text{Sm}$ were of interest, since they are promising candidates for future $0\nu\beta\beta$ decay searches.

The method of choice was NRF with quasi-monoenergetic, linearly polarized photon beams, since it allows to investigate dipole-excited states with a high sensitivity and model-independence. Branching ratios and multipole mixing ratios of transitions to lower-lying excited states were measured with high precision or firmly constrained. Cross sections for excited states, if not known beforehand, were determined from Monte-Carlo simulations of the nonresonant background in the spectra.

The data on the $A = 82$ nuclei were interpreted in the framework of the nuclear shell model, which was in good agreement with the total observed strength and the location of the resonances. This shell-model analysis suggested a more complicated origin of the low-lying $M1$ strength than a pure scissors-like motion.

For the $A = 150$ nuclei, more precise parameter sets for the framework of the interacting boson model could be determined from the new data by a careful adjustment procedure. The updated parameters were used, in collaboration with a theorist, to improve predictions of the $0\nu\beta\beta$ decay between ^{150}Nd and ^{150}Sm . The new calculations expected a significantly larger branching ratio of this exotic decay to an excited state of ^{150}Sm .

For future experiments, the problem of the photon-flux calibration should definitely be addressed, even if it occurred in this work only because a follow-up measurement could not be performed. For the calibration on the non-resonantly scattered photon spectrum, it would have been helpful to mount a scattering target with a well-defined shape and composition. Also, it was noticed that it is very helpful to have at least one detector in each setup at a backward angle for a simple determination of angular momentum quantum numbers.

The data on the $A = 82$ nuclei are now ready for more involved analyses in the nuclear shell model, which could not be performed in the present work due to restricted computing power. Furthermore, an investigation of their structure in the framework of energy density functional theory (see Fig. 1.4) would be helpful to understand the interplay of different shapes in these nuclei, which can be rather complicated in this region of the nuclear chart.

For the $A = 150$ nuclei, a controlled addition of higher-order terms to the IBM-2 Hamiltonian might be beneficial to fix unexpectedly small values for the mixed-symmetry states in ^{150}Sm , which are a by-product of the parameter estimation. Furthermore, considering the recent success of the Monte-Carlo shell model [146, 147], calculations for the $A = 150$ pair may already or soon be feasible and overcome the limitations of the IBM-2.

At last, it was proposed to the author by P. von Neumann-Cosel at a conference that another experimental probe, like inelastic proton scattering, could be used to distinguish spin- and orbital magnetic dipole strength in the nuclei ^{82}Se and ^{82}Kr (see, e.g., Sec. III.A in [89], in particular Fig. 5). It should be noted in general, that the fascinating and complicated problem of nuclear shape evolution must be tackled by various probes, otherwise many misinterpretations can be made.

A. Spectroscopic Sensitivity Limit

In Sec. 4.4, it was mentioned that the general method of determining a sensitivity limit in spectroscopic experiments, implemented by spectrum analysis programs like tv [208, 209] and hdtv [210, 211], is to perform a least-squares fit of a two-component function

$$N_{\text{fit}}(E_m) = N_{B,\Sigma}B(E_m, \{p_B\}) + N_S P(E_m, \{p_P\}), \quad (\text{A.1})$$

weighted by the uncertainties σ_N of the spectrum bins, to a part of the spectrum. In Eq. (A.1), $B(E_m, \{p_B\})$ is a model for the energy dependence of the continuous background, while $P(E_m, \{p_P\})$ describes the line shape. Both functions have the number of events associated with the background ($N_{B,\Sigma}$) and the peak (N_S) as a scaling factor. Furthermore, both have additional sets of parameters p_B and p_P , which are fixed by experimental constraints. For any set of valid parameters p , the functions $B(E_m)$ and $P(E_m)$ are assumed to be normalized:

$$\frac{1}{\Delta E_N} \int_{E_1}^{E_{N_s}} P(E) dE \rightarrow \sum_{m=1}^{N_s} P(E_m) \equiv 1. \quad (\text{A.2})$$

$$\frac{1}{\Delta E_N} \int_{E_1}^{E_{N_s}} B(E) dE \rightarrow \sum_{m=1}^{N_s} B(E_m) \equiv 1. \quad (\text{A.3})$$

Equations (A.2) and (A.3) are only valid if the bin limits are equidistant, at least locally. However, an equidistant binning can always be obtained by rebinning the spectrum. Therefore, the validity of these equalities will be assumed in the following discussion.

In the following, well-founded assumptions will be made to simplify the general fitting procedure and derive a definition of the 'area below the peak' which can be computed efficiently. Start by making the following assumptions which hold in the vicinity of the peak:

- The background function is constant:

$$N_{B,\Sigma}B(E_m, \{p_B\}) \equiv \tilde{N}_{B,\Sigma} \quad (\text{A.4})$$

In Eq. (A.4), the proportionality constant has been absorbed into the parameter $N_{B,\Sigma}$. This is certainly valid for measurements with high-resolution HPGe detectors. For example, in the spectrum of the $^{82}\text{Kr}/^{82}\text{Se}$ experiment of this work at a beam energy of 3.95 MeV, the background decreased exponentially with a decay constant of about $\lambda \approx 10^{-3} \text{ keV}^{-1}$. This causes a relative change of the background from the low- to the high-energy side of a peak with a width of 5 keV by only a few per mille.

- The set of parameters $\{p_P\}$ of the peak function can be determined from experimental constraints, and the only parameter left is N_S :

$$N_S P(E_m, \{p_P\}) \equiv N_S P(E_m) \quad (\text{A.5})$$

In the current experiment, this could be achieved by fixing the standard deviation (σ) parameter of a Gaussian line shape with a width calibration, and the mean value (μ) by the known or expected energy of a transition.

- The line shape is narrow, i.e. there exists a range $[E_{m_1}, E_{m_2}]$ with $m_2 > m_1$ so that:

$$\begin{aligned} \sum_{m=m_1}^{m_2} P(E_m, \{p_P\}) &\approx 1 \\ \sum_{m=m_1}^{m_2} 1 &\ll N_S \\ N(E_{m_1-1}) &\approx N(E_{m_2+1}) \end{aligned} \quad (\text{A.6})$$

The first and the second condition state that the majority of the peak area should be contained in a small range of bins compared to the total spectrum size. The third condition repeats the requirement from above that the

background function is assumed to be constant.

- The peak is much smaller than the background, even within the narrow range given in the previous assumption, i.e.:

$$N_{B,\Sigma}B(E_m, \{p_B\}) \gg N_S P(E_m, \{p_P\}) \quad \forall E_m \in [E_{m_1}, E_{m_2}]. \quad (\text{A.7})$$

This assumption makes the determination of a sensitivity limit necessary in the first place.

With these assumptions, the function

$$N_{\text{fit}}(E_m) = \tilde{N}_{B,\Sigma} + N_S P(E_m) \quad (\text{A.8})$$

has become linear with two parameters $\tilde{N}_{B,\Sigma}$ and N_S . The fit of the model from Eq. (A.8) to the spectrum N in an energy range $[E_{m_1}, E_{m_2}]$ aims to minimize the squared deviation of the fit function and the data ('least-squares fit'):

$$\operatorname{argmin}_{\tilde{N}_{B,\Sigma}, N_S} \left\{ \sum_{m=m_1}^{m_2} [N(E_m) - N_{\text{fit}}(E_m)]^2 \right\}. \quad (\text{A.9})$$

Note that no weighting with the uncertainties $\sigma_N(E_m)$ needs to be applied due to the assumption of a constant, dominating background, which makes the uncertainties of all bins approximately equal.

In the case of a linear model, the minimization problem can be solved analytically ([250], see also [251]). It will be assumed in the following that the fit succeeded. For the residuals $\Delta N(E_m)$, defined by:

$$\Delta N(E_m) = N(E_m) - N_{\text{fit}}(E_m), \quad (\text{A.10})$$

a successful fit means that their sum is approximately equal to zero:

$$\sum_{m=m_1}^{m_2} \Delta N(E_m) \approx 0 \quad (\text{A.11})$$

The standard deviation of the fit parameter N_S can then be expressed as (Eq. (39)

in Sec. 2.2 of [250]):

$$\sigma_{N_S} = \sqrt{\frac{s_{yy} - N_S s_{xy}}{(m_2 - m_1 - 2)s_{xx}}} \quad (\text{A.12})$$

In Eq. (A.12), the symbols s_{ij} are defined as:

$$s_{xx} = \sum_{m=m_1}^{m_2} [P(E_m) - \langle P \rangle]^2 \quad (\text{A.13})$$

$$s_{yy} = \sum_{m=m_1}^{m_2} [N(E_m) - \langle N \rangle]^2 \quad (\text{A.14})$$

$$s_{xy} = \sum_{m=m_1}^{m_2} [P(E_m) - \langle P \rangle][N(E_m) - \langle N \rangle] \quad (\text{A.15})$$

The notation with angle brackets for an energy-dependent quantity in Eq. (A.13) denotes its average value:

$$\langle N \rangle \equiv \frac{1}{m_2 - m_1} \sum_{m=m_1}^{m_2} N(E_m). \quad (\text{A.16})$$

For the quantities $N(E_m)$ and $P(E_m)$, the average values are:

$$\begin{aligned} \langle N \rangle &= \frac{1}{m_2 - m_1} \sum_{m=m_1}^{m_2} N(E_m) \\ &\stackrel{\text{Eq. (A.10)}}{=} \frac{1}{m_2 - m_1} \sum_{m=m_1}^{m_2} \tilde{N}_{B,\Sigma} + N_S P(E_m) + \Delta N(E_m) \end{aligned} \quad (\text{A.17})$$

$$\begin{aligned} &\stackrel{\text{Eq. (A.11)}}{=} \tilde{N}_{B,\Sigma} + N_S \langle P \rangle \\ \langle P \rangle &\equiv \frac{1}{m_2 - m_1} \sum_{m=m_1}^{m_2} P(E_m). \end{aligned} \quad (\text{A.18})$$

In the first step of Eq. (A.17), the definition of the residuals has been inserted. In the second step, the fact that the sum over all residuals vanishes [Eq. (A.11)] was

used. Equation (A.17) anticipates the definition of $\langle P \rangle$ in Eq. (A.18) which can not be simplified further without assuming a specific line-shape model.

In Eq. (A.12), another simplification can be introduced by comparing the magnitude of the quantities s_{yy} and $N_S s_{xy}$ in the numerator. As a consequence of the third assumption [Eq. (A.6)], a fit range $[E_{m_1-\Delta m}, E_{m_2+\Delta m}]$ can be chosen with $1 \leq m_1 - \Delta m \ll m_1$ and $m_2 \ll m_2 + \Delta m \leq N_S$, such that:

$$\begin{aligned} \sum_{m=m_1-\Delta m}^{m=m_2+\Delta m} N_S P(E_m) &= \underbrace{\sum_{m=m_1-\Delta m}^{m_1-1} N_S P(E_m)}_{\approx 0} + \sum_{m=m_2+1}^{m_2+\Delta m} N_S P(E_m) + \underbrace{\sum_{m=m_1}^{m_2} N_S P(E_m)}_{\approx N_S} \\ &\approx \sum_{m=m_1}^{m_2} N_S P(E_m) \ll \sum_{m=m_1-\Delta m}^{m_2+\Delta m} \Delta N(E_m). \end{aligned} \quad (\text{A.19})$$

From this inequality, it follows that

$$\begin{aligned} N_S s_{xy} &= \sum_{m=m_1-\Delta m}^{m_2+\Delta m} N_S [P(E_m) - \langle P \rangle] \underbrace{[N(E_m) - \langle N \rangle]}_{\approx \Delta N(E_m)} \\ &\ll \sum_{m=m_1-\Delta m}^{m_2+\Delta m} \Delta N(E_m)^2 \approx s_{yy}. \end{aligned} \quad (\text{A.20})$$

Therefore, the term $N_S s_{xy}$ will be neglected in the following. Furthermore,

$$\sum_{m=m_1-\Delta m}^{m_2+\Delta m} N_S^2 [P(E_m) - \langle P \rangle]^2 \ll s_{yy}, \quad (\text{A.21})$$

follows immediately from the previous equation.

With the definitions and simplifications from above, σ_{N_S} can be calculated explicitly:

$$\begin{aligned}
 \sigma_{N_S} &\stackrel{\text{Eq. (A.20)}}{\approx} \sqrt{\frac{s_{yy}}{(m_2 - m_1 - 2)s_{xx}}} = \sqrt{\frac{\sum_{m=m_1}^{m_2} \{\Delta N(E_m) + N_S [P(E_m) - \langle P \rangle]\}^2}{(m_2 - m_1 - 2) \sum_{m=m_1}^{m_2} [P(E_m) - \langle P \rangle]^2}} \\
 &= \sqrt{\frac{\sum_{m=m_1}^{m_2} \Delta N(E_m)^2 + 2\Delta N(E_m)N_S [P(E_m) - \langle P \rangle] + N_S^2 [P(E_m) - \langle P \rangle]^2}{(m_2 - m_1 - 2) \sum_{m=m_1}^{m_2} [P(E_m) - \langle P \rangle]^2}} \\
 &\approx \sqrt{\frac{\sum_{m=m_1}^{m_2} \Delta N(E_m)^2}{(m_2 - m_1 - 2) \sum_{m=m_1}^{m_2} [P(E_m) - \langle P \rangle]^2}} \tag{A.22} \\
 &\stackrel{\text{Eq. (A.4)}}{=} \sqrt{\frac{(m_2 - m_1) \langle \sigma_N \rangle^2}{(m_2 - m_1 - 2) \sum_{m=m_1}^{m_2} [P(E_m) - \langle P \rangle]^2}} \\
 &\stackrel{(m_2 - m_1) \gg 2}{\approx} \frac{\bar{\sigma}_N}{\sqrt{\sum_{m=m_1}^{m_2} [P(E_m) - \langle P \rangle]^2}}
 \end{aligned}$$

In the fourth equality in Eq. (A.22), the numerator is significantly simplified: The term proportional to N_S vanishes due to the following general property of the average value:

$$\sum_{m=m_1}^{m_2} [P(E_m) - \langle P \rangle] = 0. \tag{A.23}$$

The term proportional to N_S^2 can be neglected due to Eq. (A.21). In the next-to last step, the fact that all residuals are approximately equal in the given energy range was used to simplify the sum over m , and the notation $\langle \sigma_N \rangle$ was introduced for the average standard deviation of a bin content in the region of interest. In the last approximate equality in Eq. (A.22), it was assumed that the number of bins over which the line shape is spread is large enough, so that the difference by 2 in the denominator can be neglected. In summary, an equation was derived that relates σ_{N_S} , the fit uncertainty of the peak area which will be an input for Eqs. (4.19) and (4.20), to the statistical fluctuations of the background via a known line-shape model.

A.1. Evaluation for Theuerkauf Lineshape Model

The sum in the denominator of Eq. (A.22) will be evaluated in the following for the so-called Theuerkauf line-shape model $P_T(E_m)$ which is used by the nuclear spectrum analysis tools tv [208, 209] and hdtv [210, 211]¹:

$$P_T(E_m, \mu, \sigma, t_l, t_r) = N_T(\sigma, t_l, t_r) \quad (\text{A.24})$$

$$\begin{aligned} & \times \begin{cases} \exp\left\{\frac{t_l[(E_m - \mu) + t_l/2]}{\sigma^2}\right\} & \text{if } E_m - \mu < t_l \\ \exp\left\{\frac{-t_r[(E_m - \mu) - t_r/2]}{\sigma^2}\right\} & \text{if } E_m - \mu > t_r \\ \exp\left\{\frac{(E_m - \mu)^2}{\sigma^2}\right\} & \text{else} \end{cases} \\ N_T(\sigma, t_l, t_r) & \equiv \left[\sigma^2 \frac{\exp(-t_l^2/2\sigma^2)}{t_l} + \sigma^2 \frac{\exp(-t_r^2/2\sigma^2)}{t_r} \right. \\ & \left. + \sqrt{\frac{\pi}{2}} \sigma \operatorname{erf}(t_l \sigma / \sqrt{2}) + \sqrt{\frac{\pi}{2}} \sigma \operatorname{erf}(t_r \sigma / \sqrt{2}) \right]^{-1} \end{aligned} \quad (\text{A.25})$$

The Theuerkauf model is a continuous stepwise-defined distribution which consists of a left tail that increases exponentially, a central normal-distributed part, and a right tail that decreases exponentially. Left tails of peaks are mostly caused by incomplete charge collection or particles escaping from the detection volume (see chapter 12.III in [129]), while right tails can be caused by pileup (see Sec. 4.3.3 and chapter 17.VII in [129]). The central normal distribution provides the parameters μ (mean value, here: peak position) and σ (standard deviation, here: detector resolution). The (positive) distance to the left (right) of the peak position, where the normal distribution turns into an exponential increase (decay), is denoted as t_l (t_r). Equation (A.25) defines the normalization factor which depends on σ , t_l , and t_r . A normal distribution can be obtained by taking the limit

¹A more general version of the Theuerkauf model exists, which includes an arctan-shaped background contribution. It models incomplete charge collection in the detector crystal, which leads to a quasi-constant increase of the background to the left of a peak (denoted 'long-term tail' in chapter 12.IV of [129]). Note that this effect appears in addition to the left tail which is included in Eq. (A.24). The step is neglected here since the peak, and therefore the influence of its long-term tail, was assumed to be small compared to the background.

where t_l and t_r are infinite:

$$\lim_{t_l, t_r \rightarrow \infty} P_T(E_m) = \underbrace{\frac{1}{\sqrt{2\pi}\sigma}}_{\lim_{t_l, t_r \rightarrow \infty} N_T(\sigma, t_l, t_r)} \exp\left[-\frac{(E_m - \mu)^2}{2\sigma^2}\right] \quad (\text{A.26})$$

In the limit of a large number of bins and a large fit range ΔE , the calculation of the denominator in Eq. (A.22) can be performed in the continuum and $\langle P \rangle$ can be set to zero:

$$\begin{aligned} & \sum_{m=m_1}^{m_2} [P_T(E_m) - \langle P \rangle]^2 \\ & \xrightarrow{(m_2-m_1) \gg 1} \frac{1}{\Delta E_N} \int_{\mu-\Delta E/2}^{\mu+\Delta E/2} [P_T(E) - \langle P \rangle]^2 dE \\ & \xrightarrow{\Delta E \rightarrow \infty} \frac{1}{\Delta E_N} \int_{-\infty}^{\infty} P_T(E, \mu, \sigma)^2 dE \\ & = N_T^2 \Delta E_N \left\{ \exp\left(\frac{t_l^2 - 2t_l\mu}{\sigma^2}\right) \int_{-\infty}^{-t_l} \exp\left(\frac{2t_l E}{\sigma^2}\right) dE \right. \\ & \quad + \int_{-t_l}^{t_r} \exp\left[-\frac{(E-\mu)^2}{\sigma^2}\right] dE \\ & \quad \left. + \exp\left(\frac{t_r^2 + 2t_r\mu}{\sigma^2}\right) \int_{t_r}^{\infty} \exp\left(\frac{-2t_r E}{\sigma^2}\right) dE \right\} \quad (\text{A.27}) \\ & = N_T(\sigma, t_l, t_r)^2 \Delta E_N \left\{ \exp\left(\frac{-t_l^2 - 2t_l\mu}{\sigma^2}\right) \frac{\sigma^2}{2t_l} \right. \\ & \quad + \frac{\sqrt{\pi}\sigma}{2} \left[\operatorname{erf}\left(\frac{\mu + t_l}{\sigma}\right) + \operatorname{erf}\left(\frac{t_r - \mu}{\sigma}\right) \right] \\ & \quad \left. + \exp\left(\frac{-t_r^2 - 2t_r\mu}{\sigma^2}\right) \frac{\sigma^2}{2t_r} \right\}. \end{aligned}$$

Note that an additional factor of ΔE_N^2 needs to be multiplied to the continuous Theuerkauf model in the third equality to fulfil Eq. (A.2). Equation (A.27) is

the most general form for non-infinite t_l and t_r . Taking the limit of a normal distribution as in Eq. (A.26), one ends up with the simple expression:

$$\lim_{t_l, t_r \rightarrow \infty} \sum_{m=m_1}^{m_2} [P_T(E_m) - \langle P \rangle]^2 \stackrel{\text{Eq. (A.27)}}{=} \frac{\Delta E_N}{2\sqrt{\pi}\sigma} \quad (\text{A.28})$$

$$(\text{A.29})$$

Using the result of Eq. (A.28) in Eq. (A.22) yields:

$$\sigma_{N_s} = \langle \sigma_N \rangle \sqrt{2\sqrt{\pi} \frac{\sigma}{\Delta E_N}} \approx 1.88 \times \langle \sigma_N \rangle \sqrt{\frac{\sigma}{\Delta E_N}} \quad (\text{A.30})$$

This is in good agreement with the value of $\sigma_{N_s}^{\text{DIN}}$, which can be obtained from the DIN recommendation [207] in Eq. (4.21) (using $c_{\text{DIN}} = 1.2$):

$$\begin{aligned} \sigma_{N_s}^{\text{DIN}} &= \sqrt{2}\sigma_{N_b}^{\text{DIN}} = \sqrt{2}\langle \sigma_N \rangle \sqrt{\frac{1.2 \times \text{FWHM}}{\Delta E_N}} = \sqrt{2}\langle \sigma_N \rangle \sqrt{\frac{1.2 \times 2\sqrt{2\ln(2)}\sigma}{\Delta E_N}} \quad (\text{A.31}) \\ &\approx 2.38 \times \langle \sigma_N \rangle \sqrt{\frac{\sigma}{\Delta E_N}} \end{aligned}$$

In Eq. (A.31), the relation $\text{FWHM} = 2\sqrt{2\ln(2)}\sigma$ for a normal distribution has been used.



B. Schematic Detector Setups

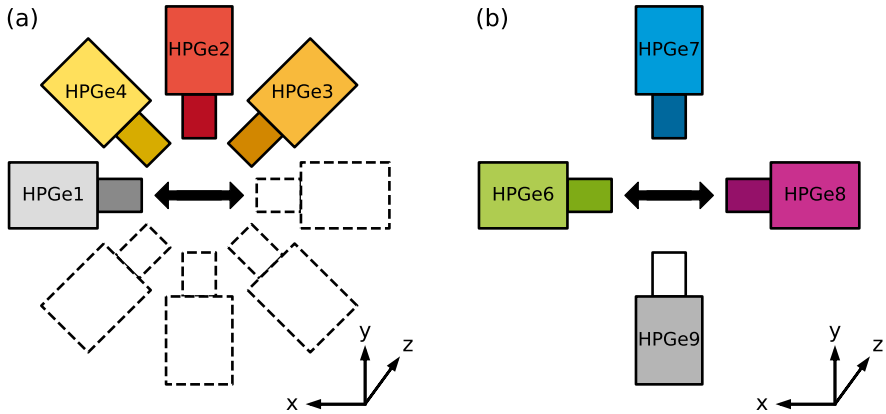


Figure B.1.: Schematic detector arrangement in the γ^3 setup (a) and the polarimetry setup (b). This represents the first configuration, used from run 707 to run 726 (for an overview of the runs, see Tab. 3.1). See also the second configuration in Fig. B.2. The coordinate system is defined at the bottom right of each part of the figures. In terms of these coordinates, detectors at intermediate angles of $\varphi = 45^\circ, 135^\circ, 225^\circ$ and 315° were mounted at a backward angle of $\theta = 135^\circ$. The polarization axis of the HI γ S gamma-ray coincides with the x -axis, as indicated by the central two-sided arrow, and the direction of propagation of the beam is in the positive z -axis. The detector colors are identical to the colors of the colored residual bands in the spectra of Sec. D. In (a), additional detectors in the γ^3 setup, which were not used in this work, are shown as empty shapes with dashed lines.

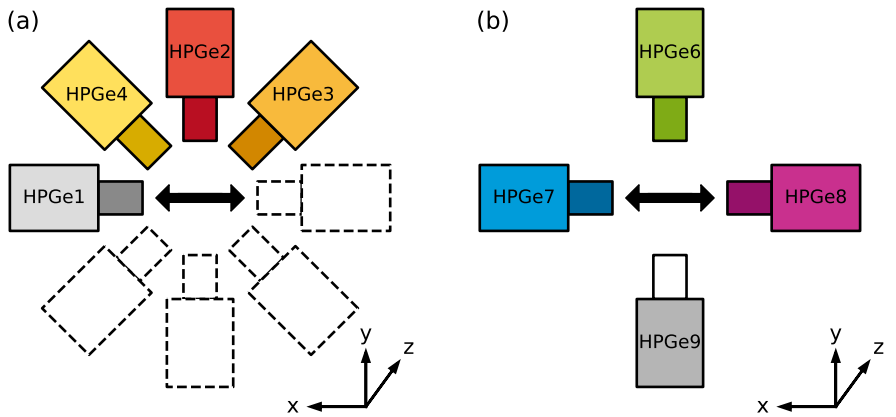


Figure B.2.: Schematic detector arrangement in the γ^3 setup (a) and the polarimetry setup (b). This represents the second configuration, used from run 727 to run 770. The arrangement of the detectors in the γ^3 setup is identical to the first configuration. See also the description of the first configuration in Fig. B.1.

C. List of Gamma Energies

Table C.1.: Reference list of ^{82}Kr photon energies which are relevant in the $^{82}\text{Kr}/^{82}\text{Se}$ experiment. The photon energies are sorted by the initially excited states from which they are emitted. A new initial state is indicated by a line without an ID number in which the level's excitation energy and quantum numbers are shown. It may be followed by labelled photon energies of transitions to the given lower-lying states. The IDs in the first column are used as labels for the spectra of this appendix (Sec. D).

ID	Energy (keV)	Initial state	Final state	Reference
K0	776.526(8) 776.511(10)	2_1^+	0_1^+	[138]
K1	1474.900(8) 1474.895(10)	2_2^+	0_1^+	[138]
K1_0	698.361(10)		2_1^+	[138]
K2_0	1487.70(5) 711.09(7)	0_2^+	2_1^+	[138]
K3	3254.36(24) 3254.36(24)	1_1^-	0_1^+	
K3_0	2477.84(24)		2_1^+	

Table C.1.: (Continued).

K3_1	1779.46(24)		2_2^+	
K3_2	1766.66(25)		0_2^+	
	3770.4(8)	1_1^+		
K4	3770.4(8)		0_1^+	
K4_0	2993.9(8)		2_1^+	
K4_1	2295.5(8)		2_2^+	
K4_2	2282.7(8)		0_2^+	
	3815.25(7)	1_2^+		
K5	3815.25(7)		0_1^+	[138]
K5_0	3038.72(7)		2_1^+	[138]
K5_1	2340.35(7)		2_2^+	
K5_2	2327.55(9)		0_2^+	
	3918.7(5)	1_2^-		
K6	3918.7(5)		0_1^+	[138]
K6_0	3142.1(5)		2_1^+	
K6_1	2443.8(5)		2_2^+	
K6_2	2431.0(5)		0_2^+	
	3958.05(14)	1_3^+		
K7	3958.05(14)		0_1^+	[138]
K7_0	3181.52(14)		2_1^+	
K7_1	2483.15(14)		2_2^+	
K7_2	2470.35(15)		0_2^+	
	4055.8(5)	1_4^+		
K8	4055.8(5)		0_1^+	
K8_0	3279.2(5)		2_1^+	
K8_1	2580.9(5)		2_2^+	
K8_2	2568.1(5)		0_2^+	

Table C.2.: Reference list of ^{82}Se photon energies which are relevant in the $^{82}\text{Kr}/^{82}\text{Se}$ experiment. See also the description of Tab. C.1.

ID	Energy (keV)	Initial state	Final state	Reference
S0	654.71(16) 654.7(5)	2_1^+	0_1^+	[138]
S1_0	1410.22(17) 755.60(10)	0_2^+	2_1^+	[138]
S2	1731.51(10) 1731.50(10)	2_2^+	0_1^+	[138]
S2_0	1076.40(10)		2_1^+	[138]
S3	2494.7(5) 2494.8(5)	1	0_1^+	[137]
S3_0	1840.1(5)		2_1^+	[137]
S4	2980.56(10) 2980.56(10)	1_1^+	0_1^+	[137]
S4_0	2325.87(9)		2_1^+	[137]
S4_1	1570.34(20)		0_2^+	
S4_2	1249.05(14)		2_2^+	
S5	3034.1(4) 3034.1(4)	2_3^+	0_1^+	[137]
S5_0	2379.4(4)		2_1^+	[137]
S5_1	1623.9(4)		0_2^+	
S5_2	1302.6(4)		2_2^+	
S6	3244.64(14) 3244.64(14)	1_2^+	0_1^+	
S6_0	2589.93(21)		2_1^+	
S6_1	1834.42(22)		0_2^+	

Table C.2.: (Continued).

S6_2	1513.13(17)		2_2^+
	3342.89(17)	1_1^-	
S7	3342.89(17)		0_1^+
S7_0	2688.17(16)		2_1^+
S7_1	1932.67(24)		0_2^+
S7_2	1611.38(20)		2_2^+
	3632.0(4)	1_3^+	
S8	3632.0(4)		0_1^+
S8_0	2977.3(4)		2_1^+
S8_1	2221.8(4)		0_2^+
S8_2	1900.5(4)		2_2^+
	3806.63(18)	1_2^-	
S9	3806.63(18)		0_1^+
S9_0	3151.50(10)		2_1^+
S9_1	2396.41(24)		0_2^+
S9_2	2075.12(20)		2_2^+
	3823.90(26)	1_4^+	
S10	3823.90(26)		0_1^+
S10_0	3168.66(8)		2_1^+
S10_1	2413.68(31)		0_2^+
S10_2	2091.79(12)		2_2^+
	4061.9(5)	1_3^-	
S11	4061.9(5)		0_1^+
S11_0	3407.13(24)		2_1^+
S11_1	2651.7(5)		0_2^+
S11_2	2330.4(5)		2_2^+

Table C.3.: Reference list of background photons which are relevant in the $^{82}\text{Kr}/^{82}\text{Se}$ experiment. Compared to the lists of NRF photons in this section (see, e.g., Tab. C.1), this one only shows photon energies and the process in which they have most probably been created.

ID	Energy (keV)	Origin	Reference
0	328.16(7)	unknown	
1	338.48(15)	unknown	
2	352.10(16)	unknown	
3	409.85(22)	unknown	
4	443.42(9)	unknown	
5	463.09(8)	unknown	
6	510.9989461(31)	$e^+ - e^-$ annihilation	[2]
7	583.1870(20)	Decay $^{208}\text{Tl} \rightarrow ^{208}\text{Pb}$	[215]
8	609.316(4)	Decay $^{214}\text{Bi} \rightarrow ^{214}\text{Po}$	[186]
9	665.447(9)	Decay $^{214}\text{Bi} \rightarrow ^{214}\text{Po}$	[186]
10	678.34(19)	unknown	
11	688.20(16)	unknown	
12	727.25(9)	unknown	
13	768.360(5)	Decay $^{214}\text{Bi} \rightarrow ^{214}\text{Po}$	[186]
14	778.43(16)	unknown	
15	786.35(14)	Decay $^{214}\text{Bi} \rightarrow ^{214}\text{Po}$	[186]
16	788.742(8)	Decay $^{138}\text{La} \rightarrow ^{138}\text{Ce}$	[173]
17	794.95(6)	unknown	
18	806.180(9)	Decay $^{214}\text{Bi} \rightarrow ^{214}\text{Po}$	[186]
19	810.63(14)	unknown	
20	835.73(7)	unknown	
21	860.557(4)	Decay $^{208}\text{Tl} \rightarrow ^{208}\text{Pb}$	[215]
22	866.94(20)	unknown	
23	911.204(4)	Decay $^{228}\text{Ac} \rightarrow ^{228}\text{Th}$	[252]
24	934.056(6)	Decay $^{214}\text{Bi} \rightarrow ^{214}\text{Po}$	[186]
25	963.86(15)	unknown	
26	968.974(17)	Decay $^{228}\text{Ac} \rightarrow ^{228}\text{Th}$	[252]

Table C.3.: (Continued).

27	977.19(10)	unknown	
28	1001.07(4)	unknown	
29	1021.997892(6)	$e^+ - e^-$ annihilation pileup	[2]
30	1085.42(18)	unknown	
31	1111.56(20)	unknown	
32	1120.249(6)	Decay $^{214}\text{Bi} \rightarrow ^{214}\text{Po}$	[186]
33	1155.210(8)	Decay $^{214}\text{Bi} \rightarrow ^{214}\text{Po}$	[186]
34	1238.122(7)	Decay $^{214}\text{Bi} \rightarrow ^{214}\text{Po}$	[186]
35	1280.976(10)	Decay $^{214}\text{Bi} \rightarrow ^{214}\text{Po}$	[186]
36	1377.669(8)	Decay $^{214}\text{Bi} \rightarrow ^{214}\text{Po}$	[186]
37	1385.310(13)	Decay $^{214}\text{Bi} \rightarrow ^{214}\text{Po}$	[186]
38	1401.515(12)	Decay $^{214}\text{Bi} \rightarrow ^{214}\text{Po}$	[186]
39	1407.988(11)	Decay $^{214}\text{Bi} \rightarrow ^{214}\text{Po}$	[186]
40	1435.795(10)	Decay $^{138}\text{La} \rightarrow ^{138}\text{Ba}$	[173]
41	1460.820(5)	Decay $^{40}\text{K} \rightarrow ^{40}\text{Ar}$	[214]
42	1495.90(6)	unknown	
43	1501.90(10)	unknown	
44	1509.210(10)	Decay $^{214}\text{Bi} \rightarrow ^{214}\text{Po}$	[186]
45	1523.70(27)	unknown	
46	1538.53(5)	Decay $^{214}\text{Bi} \rightarrow ^{214}\text{Po}$	[186]
47	1543.34(5)	Decay $^{214}\text{Bi} \rightarrow ^{214}\text{Po}$	[186]
48	1575.68(29)	unknown	
49	1583.204(15)	Decay $^{214}\text{Bi} \rightarrow ^{214}\text{Po}$	[186]
50	1588.190(30)	Decay $^{228}\text{Ac} \rightarrow ^{228}\text{Th}$	[252]
51	1594.75(7)	Decay $^{214}\text{Bi} \rightarrow ^{214}\text{Po}$	[186]
52	1599.37(5)	Decay $^{214}\text{Bi} \rightarrow ^{214}\text{Po}$	[186]
53	1620.73(4)	unknown	
54	1630.627(10)	Decay $^{228}\text{Ac} \rightarrow ^{228}\text{Th}$	[252]
55	1638.39(14)	unknown	
56	1661.274(16)	Decay $^{214}\text{Bi} \rightarrow ^{214}\text{Po}$	[186]
57	1684.012(20)	unknown	
58	1692.93(24)	unknown	
59	1729.595(11)	Decay $^{214}\text{Bi} \rightarrow ^{214}\text{Po}$	[186]
60	1764.491(10)	Decay $^{214}\text{Bi} \rightarrow ^{214}\text{Po}$	[186]

Table C.3.: (Continued).

61	1810.23(32)	unknown	
62	1838.36(4)	Decay $^{214}\text{Bi} \rightarrow ^{214}\text{Po}$	[186]
63	1847.429(16)	Decay $^{214}\text{Bi} \rightarrow ^{214}\text{Po}$	[186]
64	1963.62(12)	unknown	
65	2103.44(17)	unknown	
66	2086.64(31)	unknown	
67	2118.514(19)	Decay $^{214}\text{Bi} \rightarrow ^{214}\text{Po}$	[186]
68	2179.52(18)	unknown	
69	2204.059(22)	Decay $^{214}\text{Bi} \rightarrow ^{214}\text{Po}$	[186]
70	2230.78(35)	unknown	
71	2447.700(30)	Decay $^{214}\text{Bi} \rightarrow ^{214}\text{Po}$	[186]
72	2614.511(10)	Decay $^{208}\text{Tl} \rightarrow ^{208}\text{Pb}$	[215]
73	2690.4(4)	unknown	
74	2741.9(4)	unknown	
75	2761.5(4)	unknown	
76	2939.86(26)	unknown	

Table C.4.: Reference list of photon energies of ^{13}C which are relevant in the $^{82}\text{Kr}/^{82}\text{Se}$ experiment. See also the description of Tab. C.1.

ID	Energy (keV)	Initial state	Final state	Reference
C0	3684.507(19)	$3/2_1^-$	$1/2_1^-$	[253]
	3683.921(23)			

Table C.5.: Reference list of photon energies of ^{35}Cl which are relevant in the $^{82}\text{Kr}/^{82}\text{Se}$ experiment. See also the description of Tab. C.1.

Table C.5.: (Continued).

ID	Energy (keV)	Initial state	Final state	Reference
C5_0	1219.29(11)	$1/2_1^+$	$3/2_1^+$	[174]
	1219.30(20)			
C5_1	1763.04(7)	$5/2_1^+$	$3/2_1^+$	[174]
	1763.13(10)			
C5_2	2693.75(8)	$3/2_2^+$	$3/2_1^+$	[174]
	2693.60(10)			
C5_2_0	1474.80(30)		$1/2_1^+$	[174]
C5_2_1	930.90(20)		$5/2_1^+$	[174]
C5_3	3002.30(30)	$5/2_2^+$	$3/2_1^+$	[174]
	3002.4(4)			
C5_4	3918.49(17)	$3/2_3^+$	$3/2_1^+$	[174]
	3918.4(6)			
C5_4_0	2155.1(1.5)		$5/2_1^+$	[174]

Table C.6.: Reference list of photon energies of ^{37}Cl which are relevant in the $^{82}\text{Kr}/^{82}\text{Se}$ experiment. See also the description of Tab. C.1.

ID	Energy (keV)	Initial state	Final state	Reference
C7_0	3086.12(7)	$5/2_1^+$	$3/2_1^+$	[175]
	3086.20(20)			
C7_1	3741.19(10)	$5/2_1^-$	$3/2_1^+$	[175]
	3741.05(10)			

Table C.6.: (Continued).

Table C.7.: Reference list of photon energies of the ^{56}Co source which are relevant in the $^{82}\text{Kr}/^{82}\text{Se}$ experiment. See also the description of Tab. C.3.

ID	Energy (keV)	Origin	Reference
CO0	846.7700(20)		[177]
CO1	1037.843(4)		[177]
CO2	1175.101(4)		[177]
CO3	1238.2880(30)		[177]
CO4	1360.212(4)		[177]
CO5	1771.357(4)		[177]
CO6	2015.215(5)		[177]
CO7	2034.791(5)		[177]
CO8	2113.14(6)		[177]
CO9	2212.944(4)		[177]
CO10	2598.500(4)		[177]
CO11	3009.654(4)		[177]
CO12	3202.029(8)		[177]
CO13	3253.503(4)		[177]
CO14	3273.079(4)		[177]
CO15	3451.232(4)		[177]
CO16	3548.05(6)		[177]

Table C.8.: Reference list of photon energies of ^{56}Fe which are relevant in the $^{82}\text{Kr}/^{82}\text{Se}$ experiment. See also the description of Tab. C.1.

ID	Energy	Initial state	Final state	Reference
----	--------	---------------	-------------	-----------

Table C.8.: (Continued).

(keV)				
F0	846.7778(19)	2_1^+	0_1^+	[177]
	846.7638(19)			
F1	3369.95(7)	2_4^+	0_1^+	[177]
	3369.84(4)			
F1_0	2523.06(5)		2_1^+	[177]
F2	3448.41(6)	1_1^+	0_1^+	[177]
	3448.0(0)			
F2_0	2601.0(0)		2_1^+	[177]
F3	3600.21(7)	$(1, 2^+)$	0_1^+	[177]
	3600.0(0)			
F3_0	2753.0(0)		2_1^+	[177]

D. Spectra

This section presents the sum spectra of all detectors from all unique experimental runs. They are sorted by the photon-beam energy from low to high. Measurements at the same beam energy, but with empty targets, follow the actual experimental runs. At the very end of this section, a background measurement is shown.

The colors of the spectra in this section correspond to the colors in Sec. B. As described in Sec. 4.4, the continuous background in each spectrum was interpolated to determine the sensitivity limit. The interpolating curve is shown as a dashed line in each spectrum. The positions of all background lines and all NRF lines which could have been excited by the beam are shown. In particular, the transition energies of decays to the excited states 0_2^+ , 2_1^+ , and 2_2^+ are shown for ^{82}Kr and ^{82}Se . Sometimes, there was not enough space for all labels of transitions. In this case, background labels are simply not shown. The bottom panel of each spectrum shows the residual of the background-subtracted spectrum, compared to the sensitivity limits L_C and N_D from Sec. 4.4.1. It was normalized to the quantity N_D for better visibility.

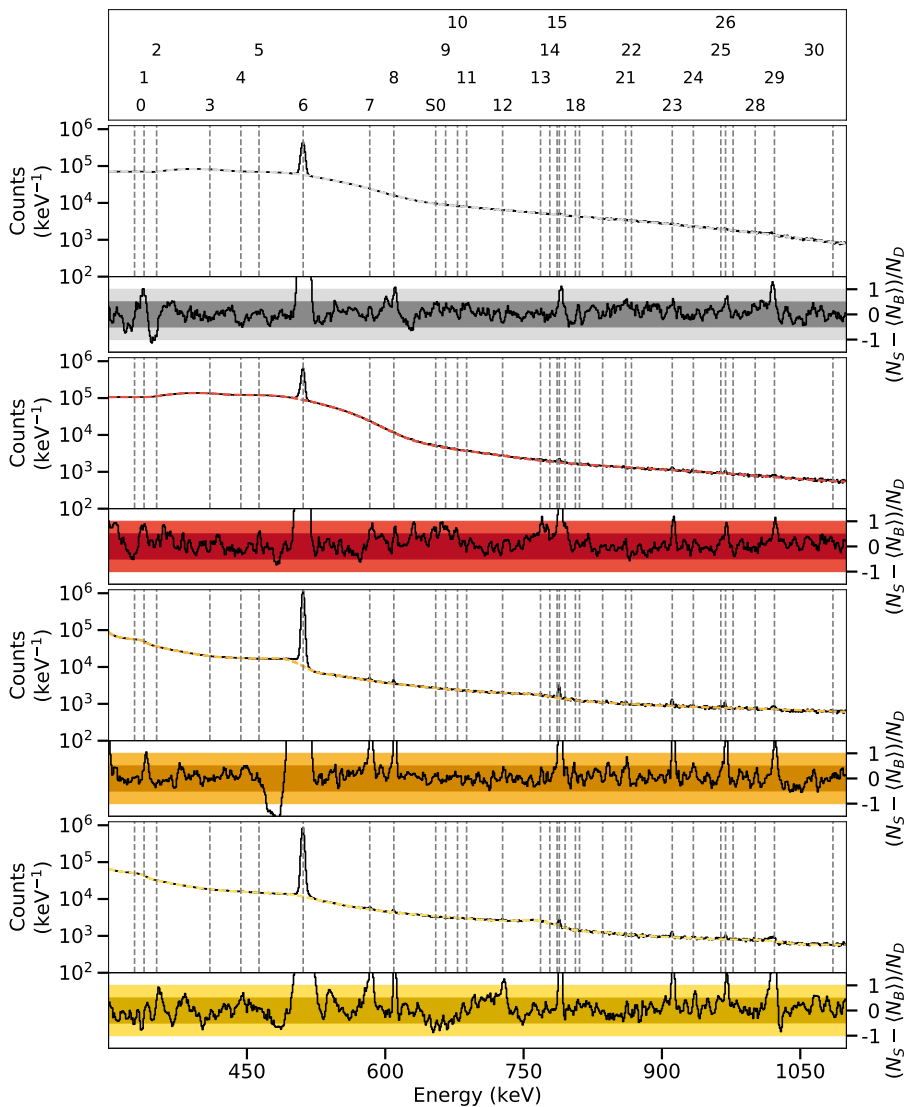


Figure D.1.: Spectra of the ^{82}Se target in the γ^3 setup at a beam energy of 2.40 MeV between 300 keV and 1100 keV.

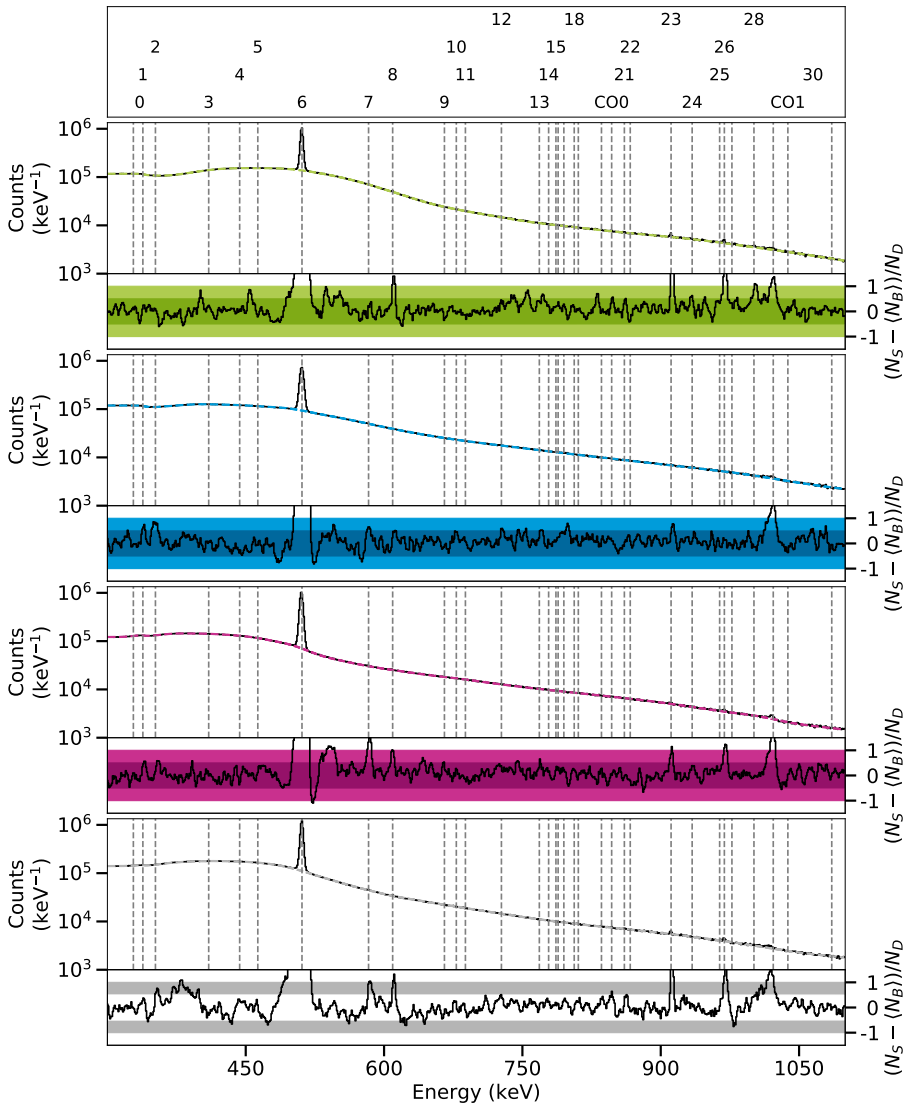


Figure D.2.: Spectra of the ^{82}Kr target in the polarimetry setup at a beam energy of 2.40 MeV between 300 keV and 1100 keV.

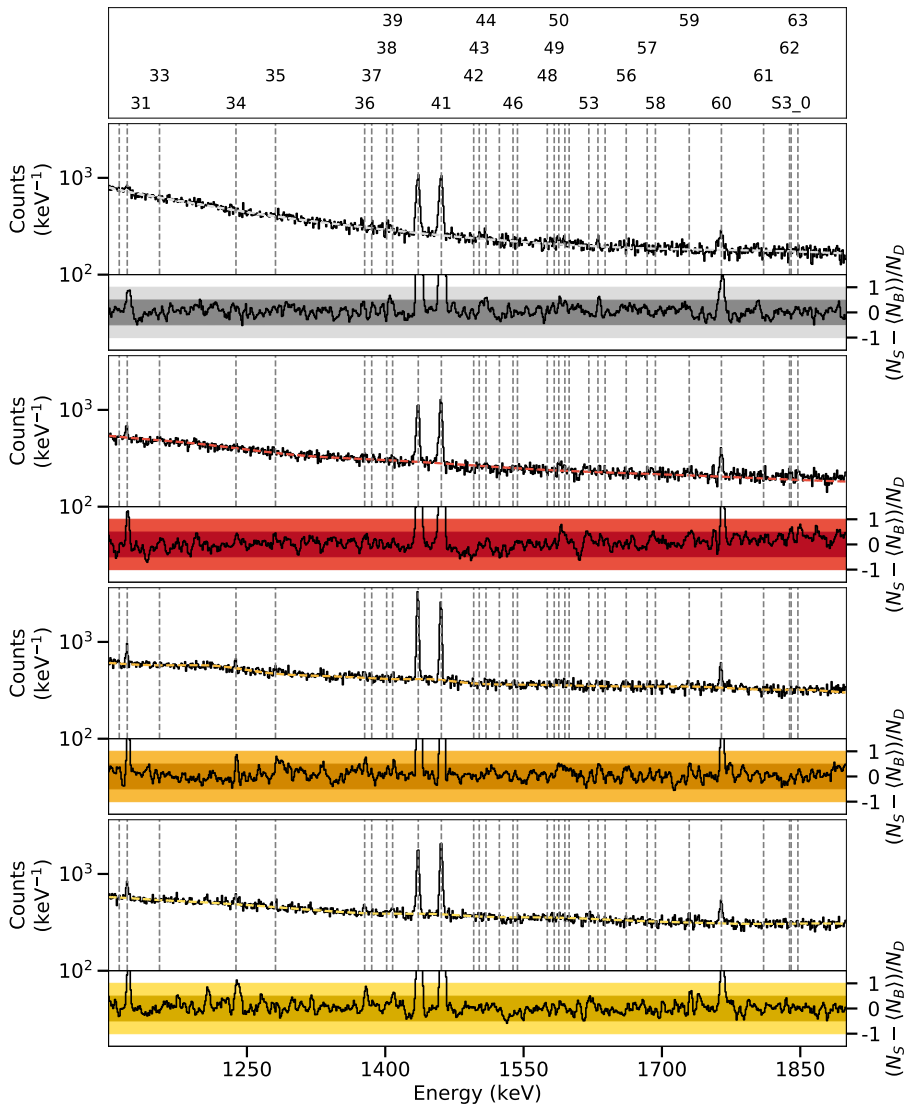


Figure D.3.: Spectra of the ^{82}Se target in the γ^3 setup at a beam energy of 2.40 MeV between 1100 keV and 1900 keV.

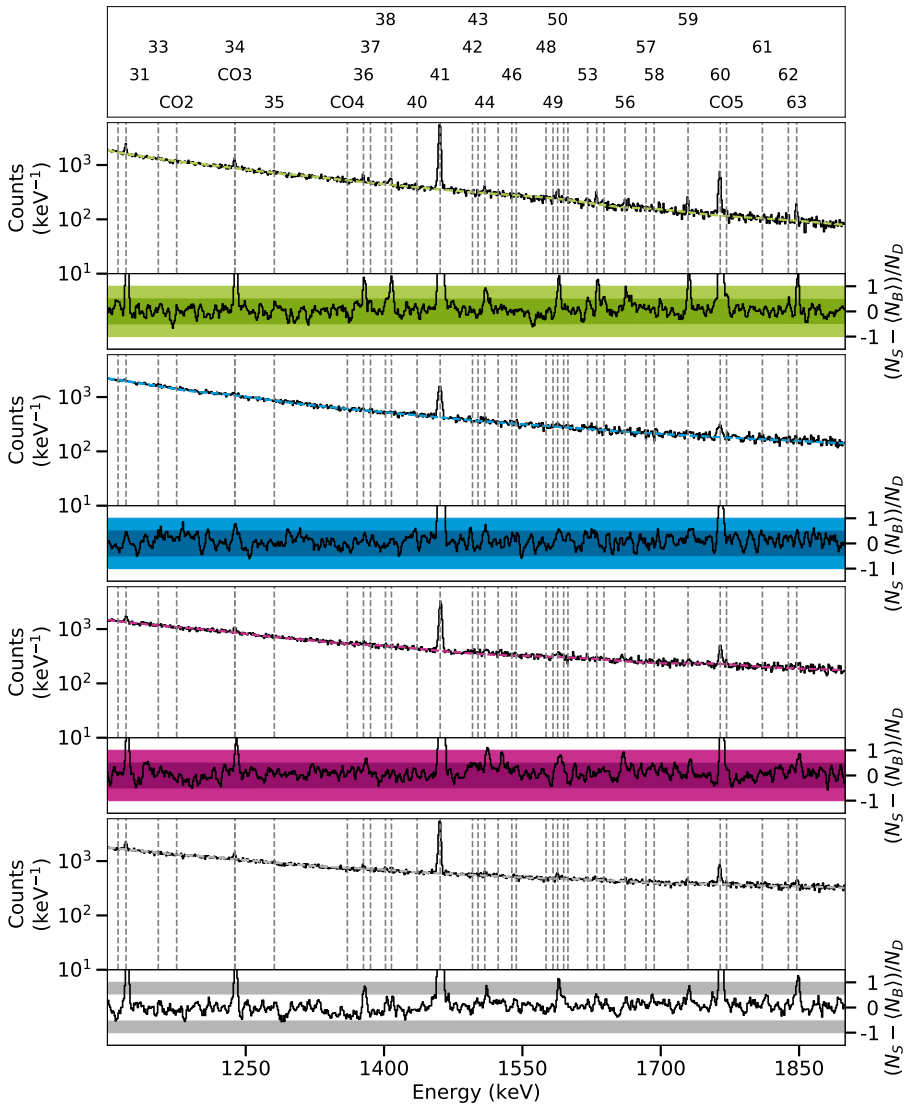


Figure D.4.: Spectra of the ^{82}Kr target in the polarimetry setup at a beam energy of 2.40 MeV between 1100 keV and 1900 keV.

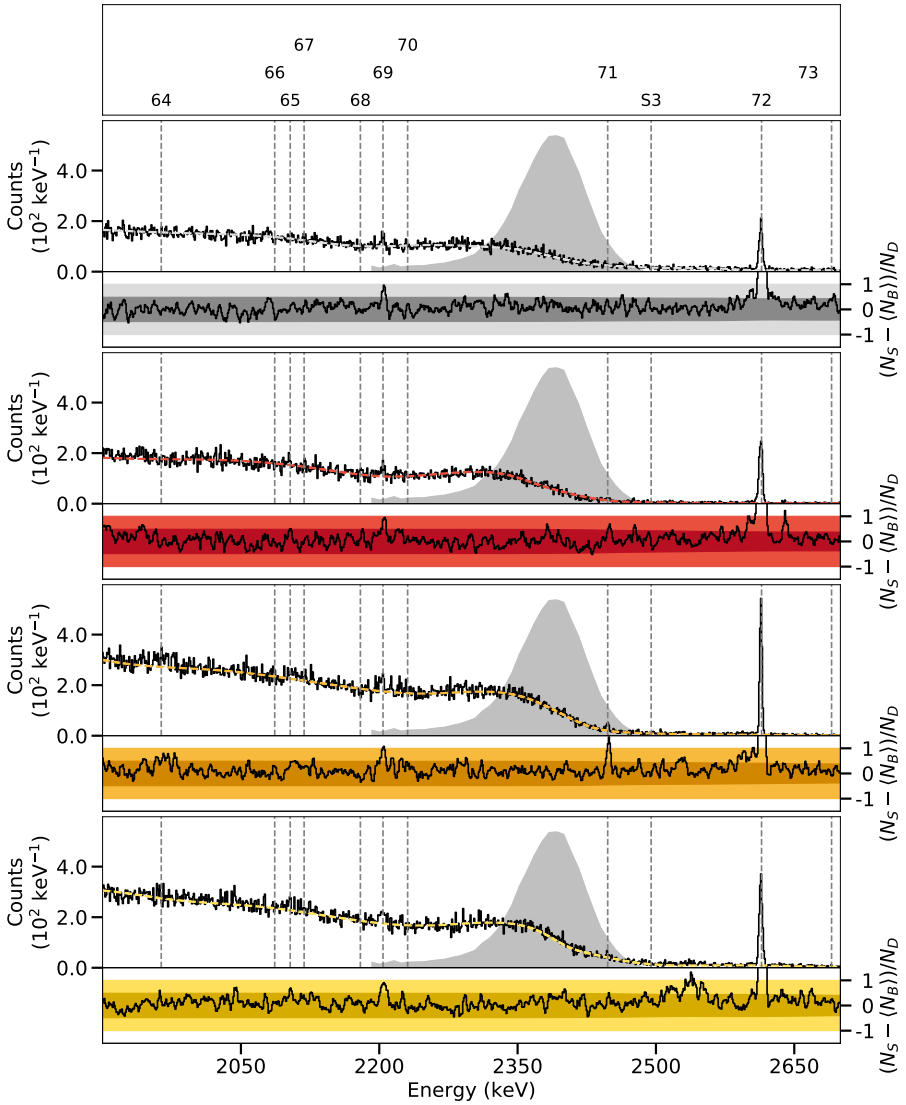


Figure D.5.: Spectra of the ^{82}Se target in the γ^3 setup at a beam energy of 2.40 MeV between 1900 keV and 2700 keV.

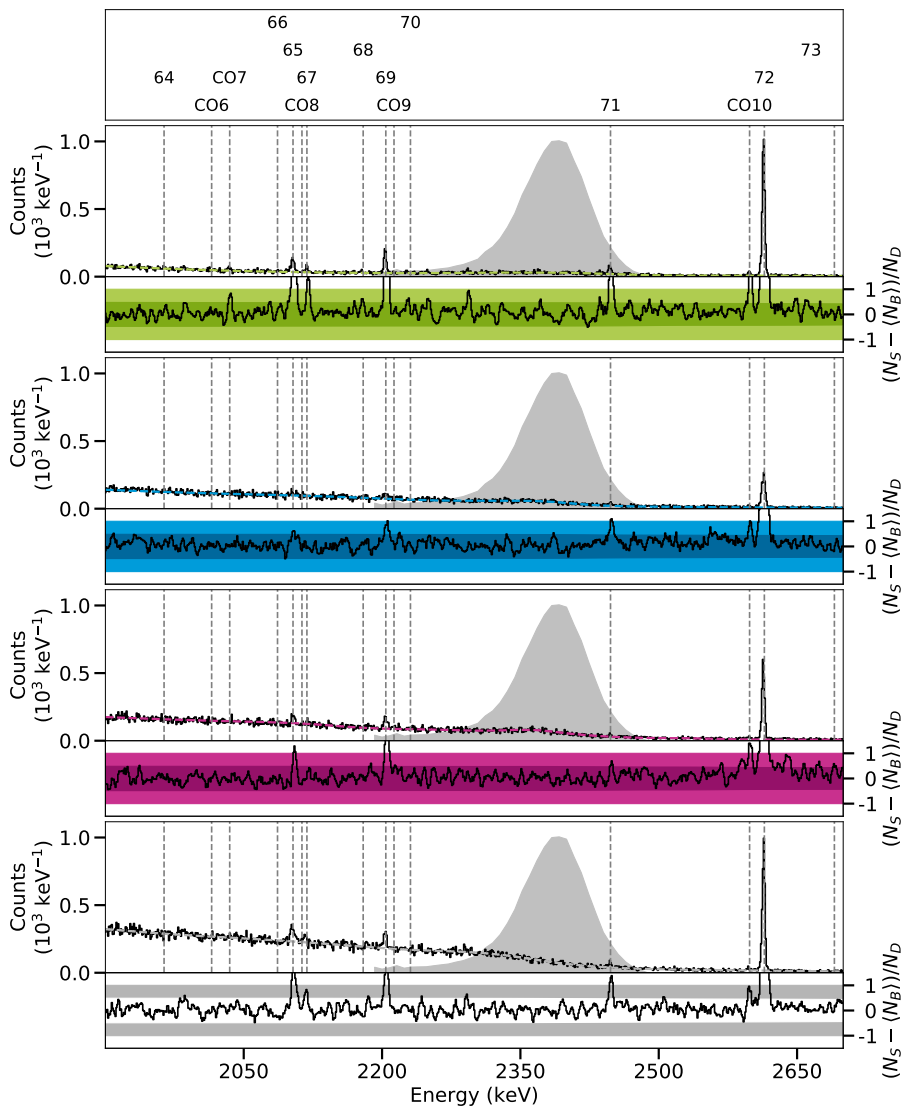


Figure D.6.: Spectra of the ^{82}Kr target in the polarimetry setup at a beam energy of 2.40 MeV between 1900 keV and 2700 keV.

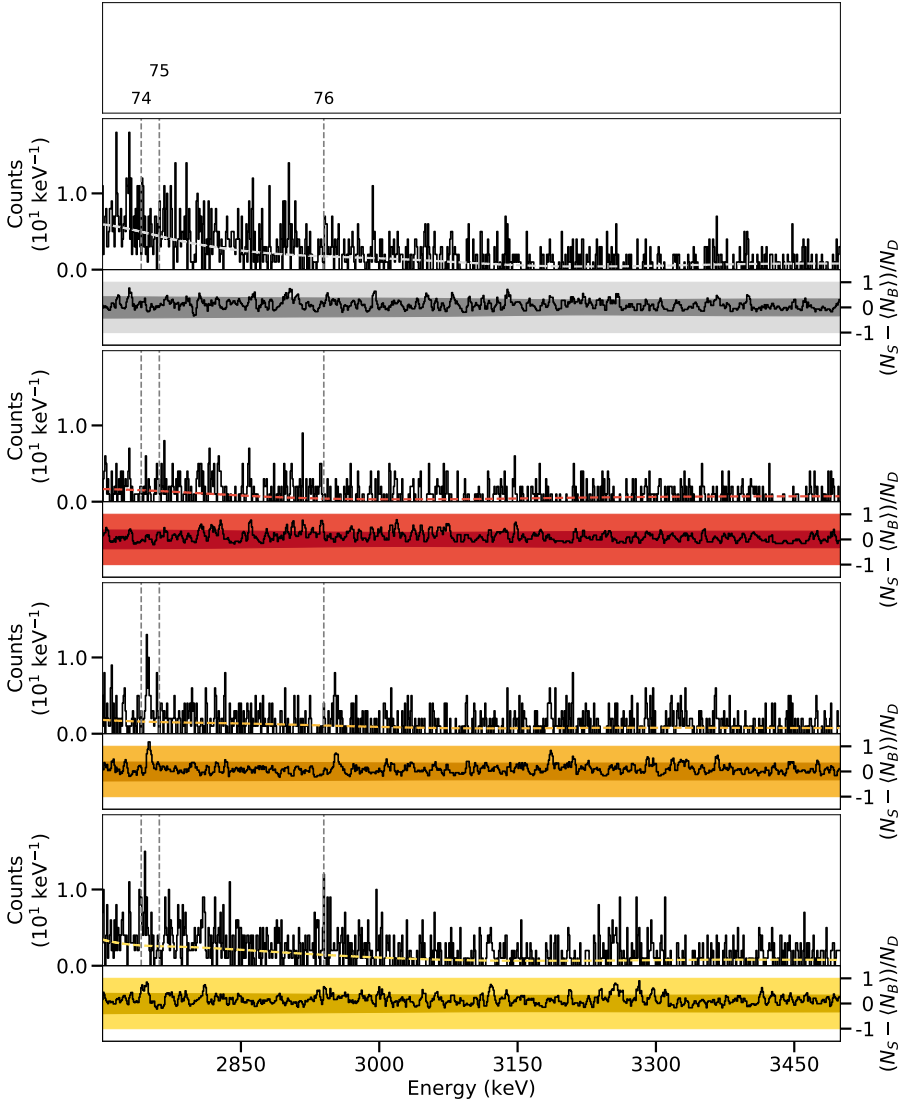


Figure D.7.: Spectra of the ^{82}Se target in the γ^3 setup at a beam energy of 2.40 MeV between 2700 keV and 3500 keV.

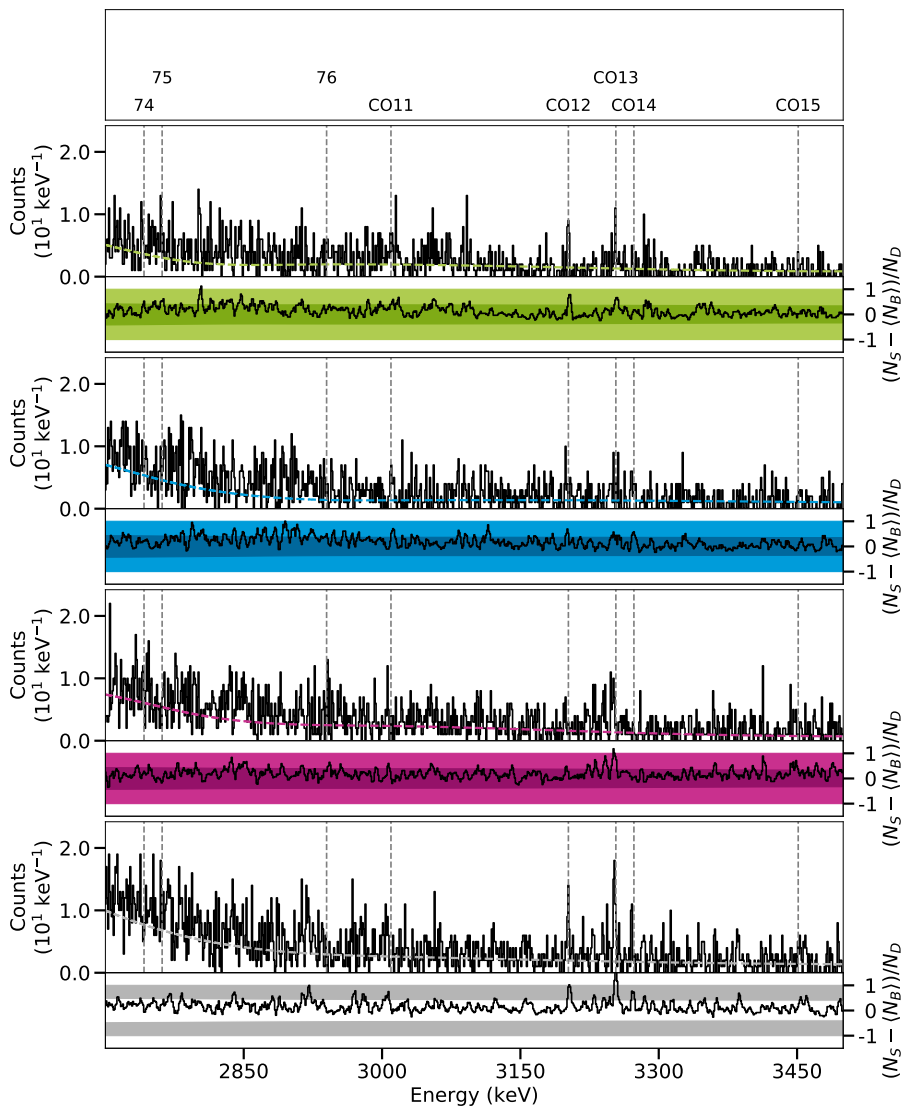


Figure D.8.: Spectra of the ^{82}Kr target in the polarimetry setup at a beam energy of 2.40 MeV between 2700 keV and 3500 keV.

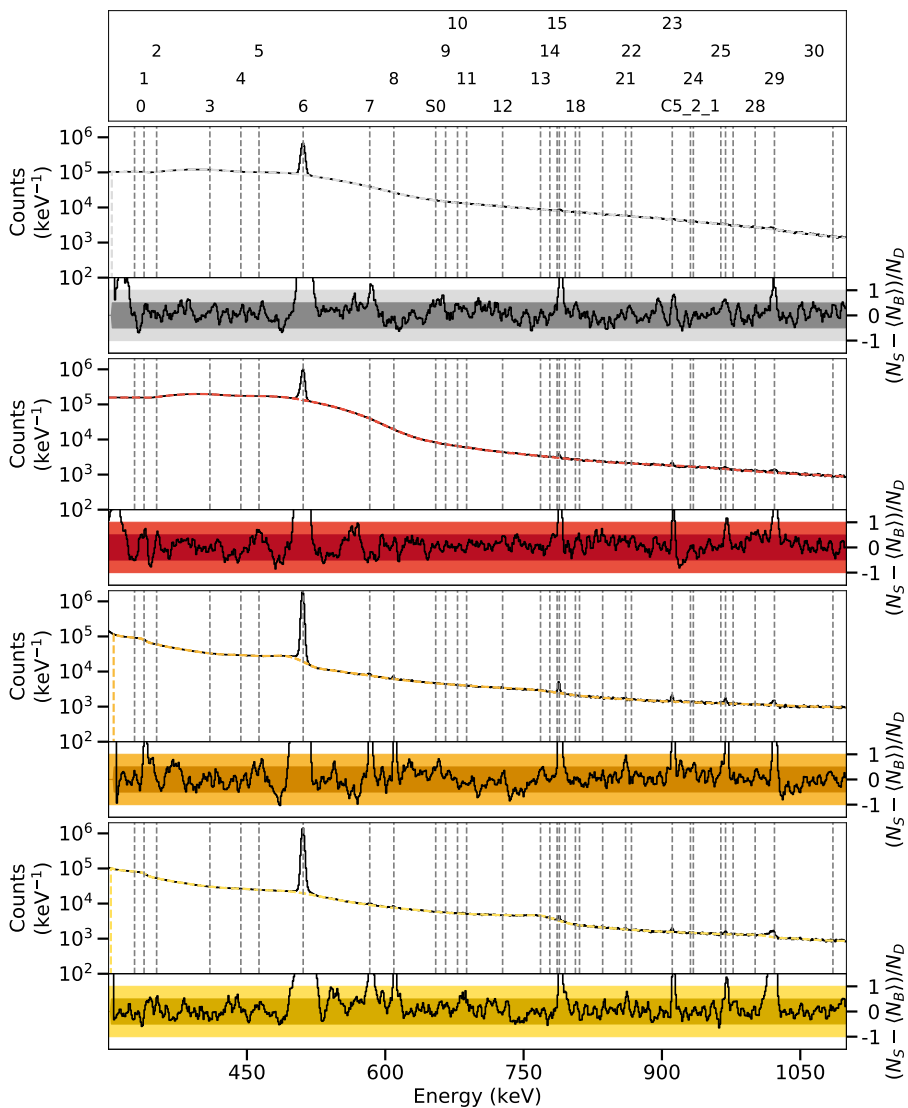


Figure D.9.: Spectra of the ^{82}Se target in the γ^3 setup at a beam energy of 2.50 MeV between 300 keV and 1100 keV.

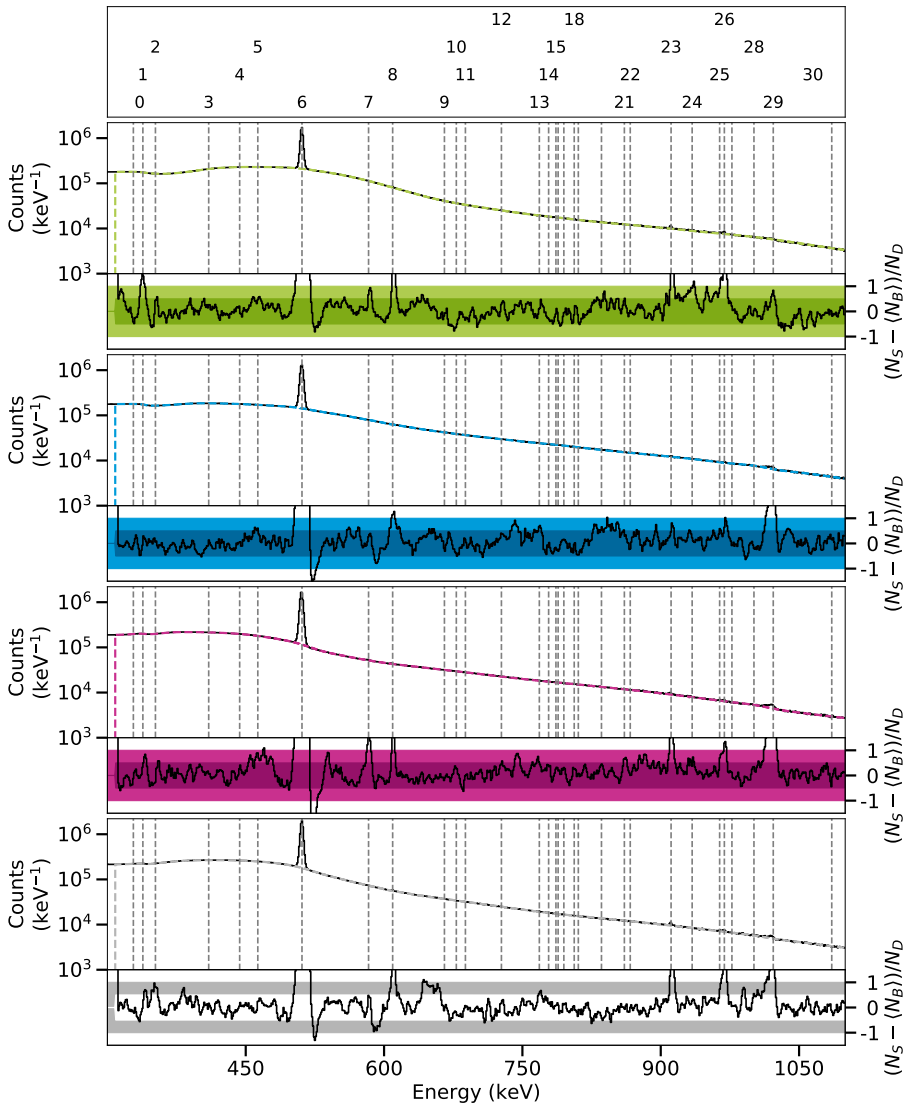


Figure D.10.: Spectra of the ^{82}Kr target in the polarimetry setup at a beam energy of 2.50 MeV between 300 keV and 1100 keV.

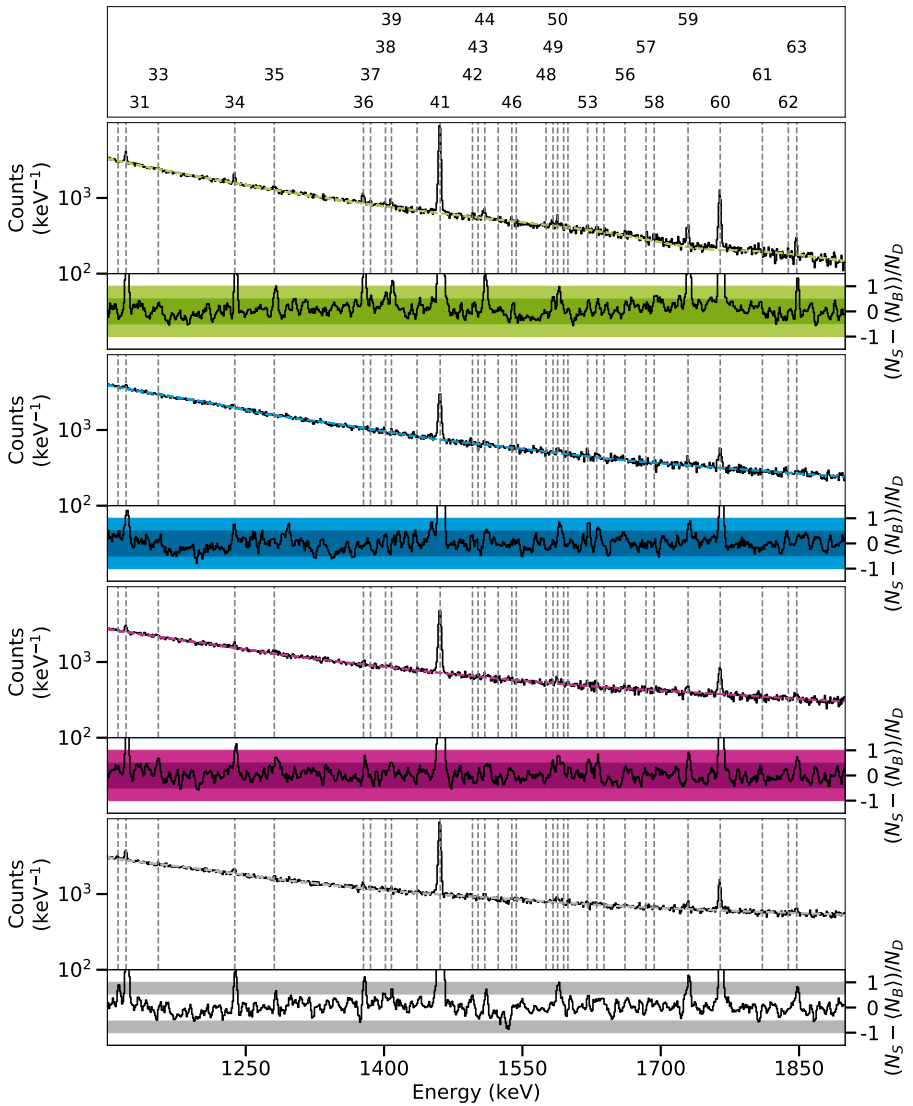


Figure D.12.: Spectra of the ^{82}Kr target in the polarimetry setup at a beam energy of 2.50 MeV between 1100 keV and 1900 keV.

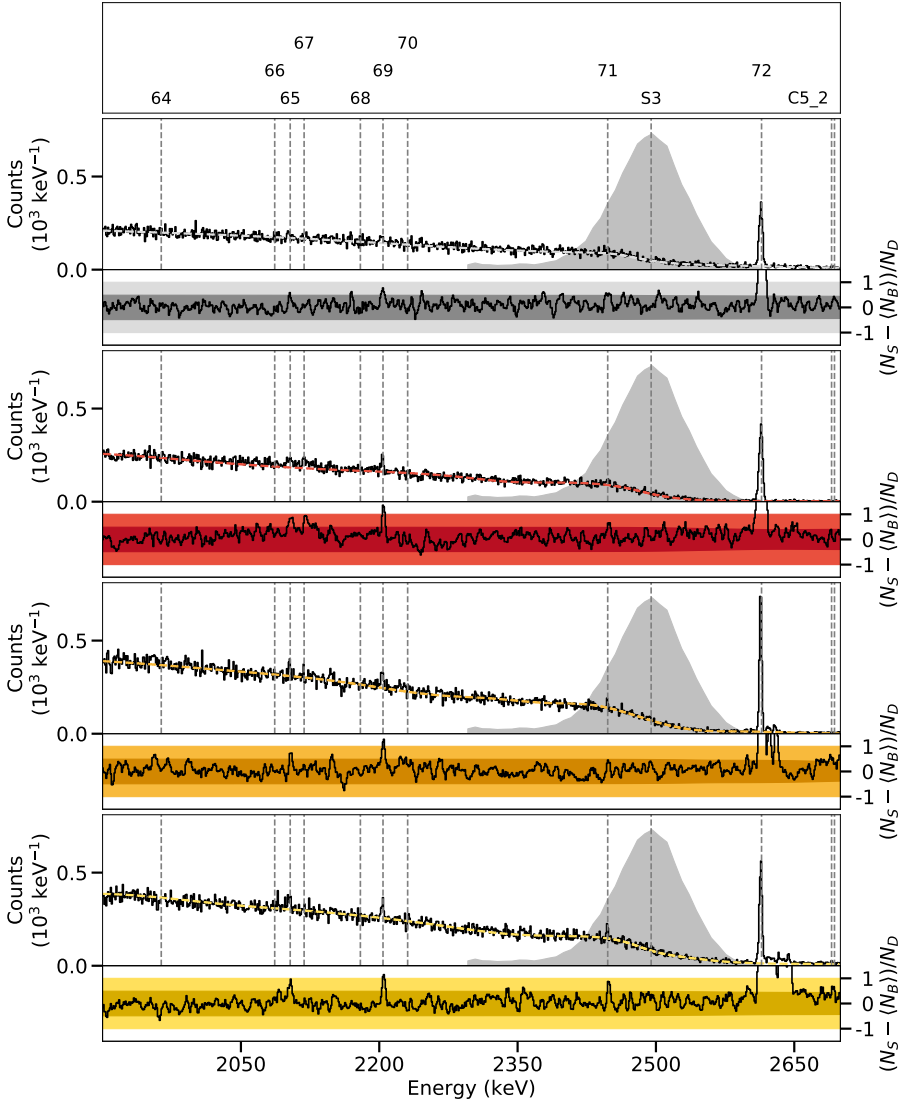


Figure D.13.: Spectra of the ^{82}Se target in the γ^3 setup at a beam energy of 2.50 MeV between 1900 keV and 2700 keV.

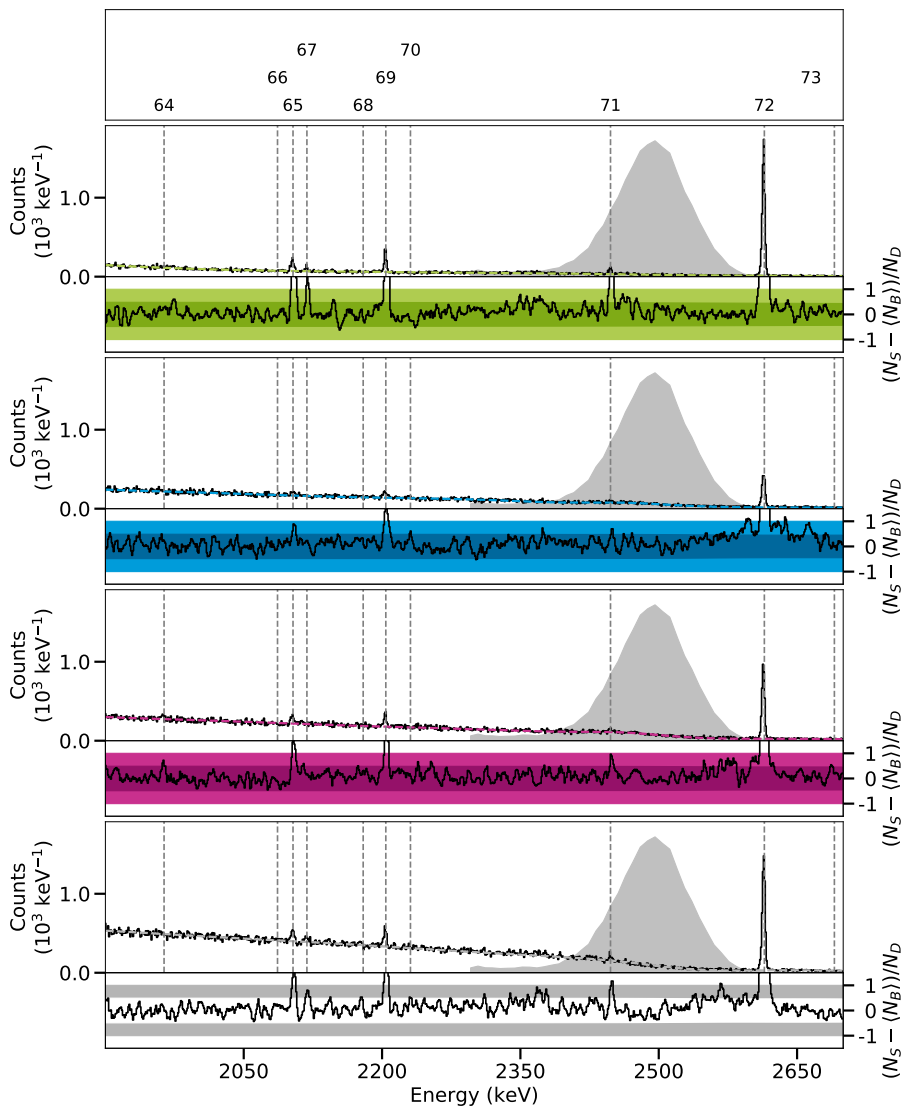


Figure D.14.: Spectra of the ^{82}Kr target in the polarimetry setup at a beam energy of 2.50 MeV between 1900 keV and 2700 keV.

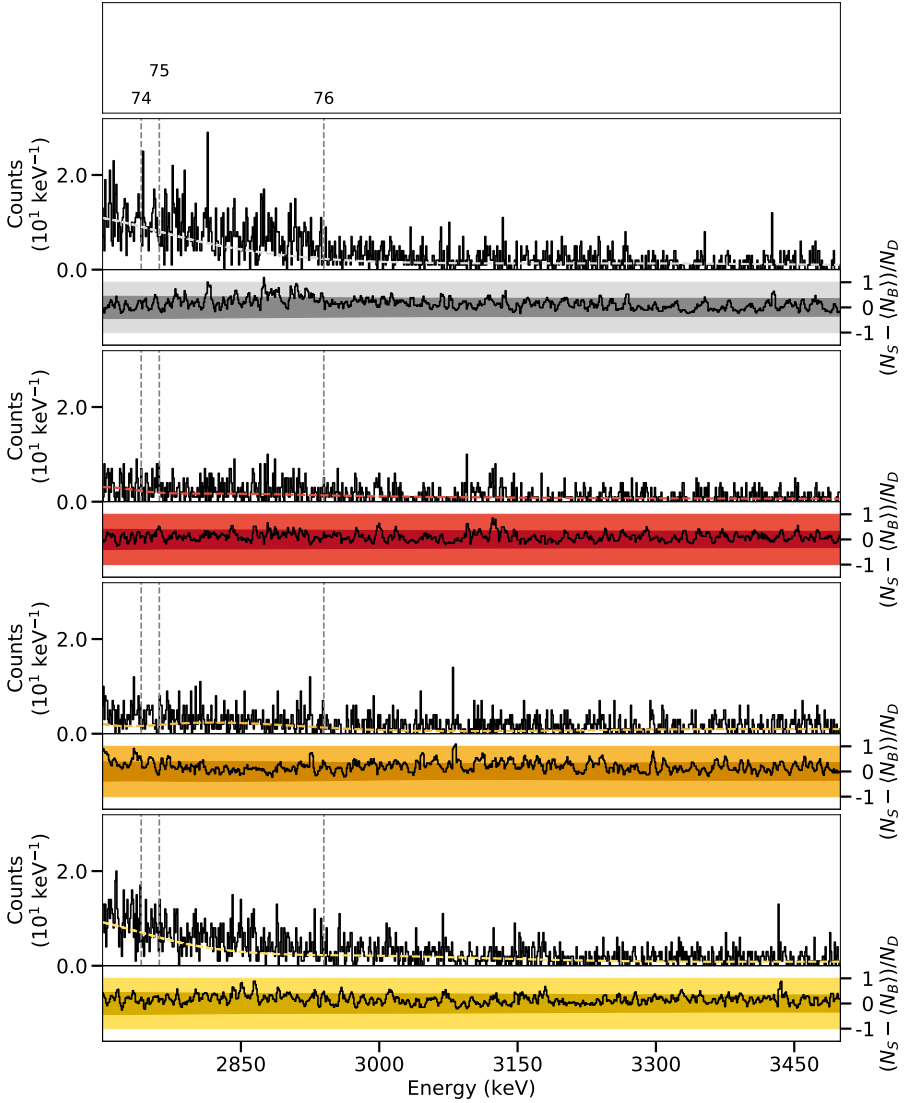


Figure D.15.: Spectra of the ^{82}Se target in the γ^3 setup at a beam energy of 2.50 MeV between 2700 keV and 3500 keV.

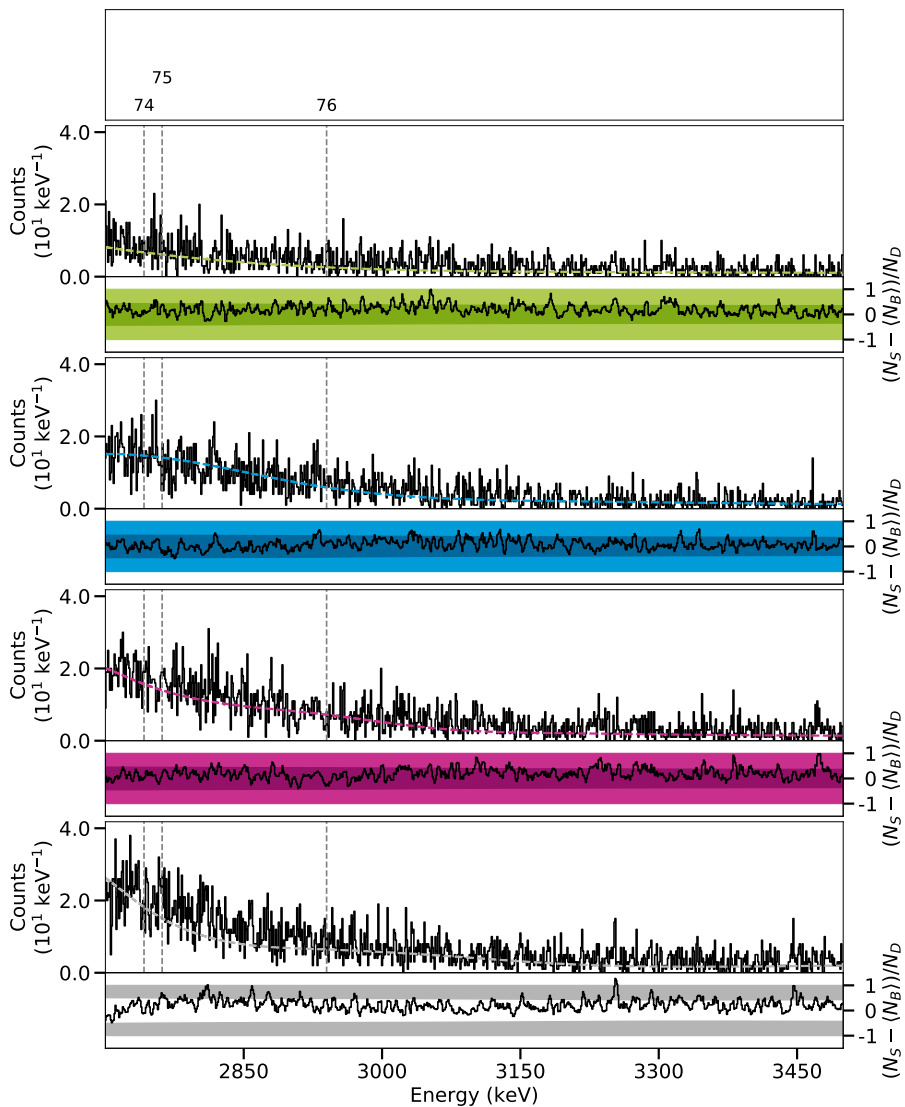


Figure D.16.: Spectra of the ^{82}Kr target in the polarimetry setup at a beam energy of 2.50 MeV between 2700 keV and 3500 keV.

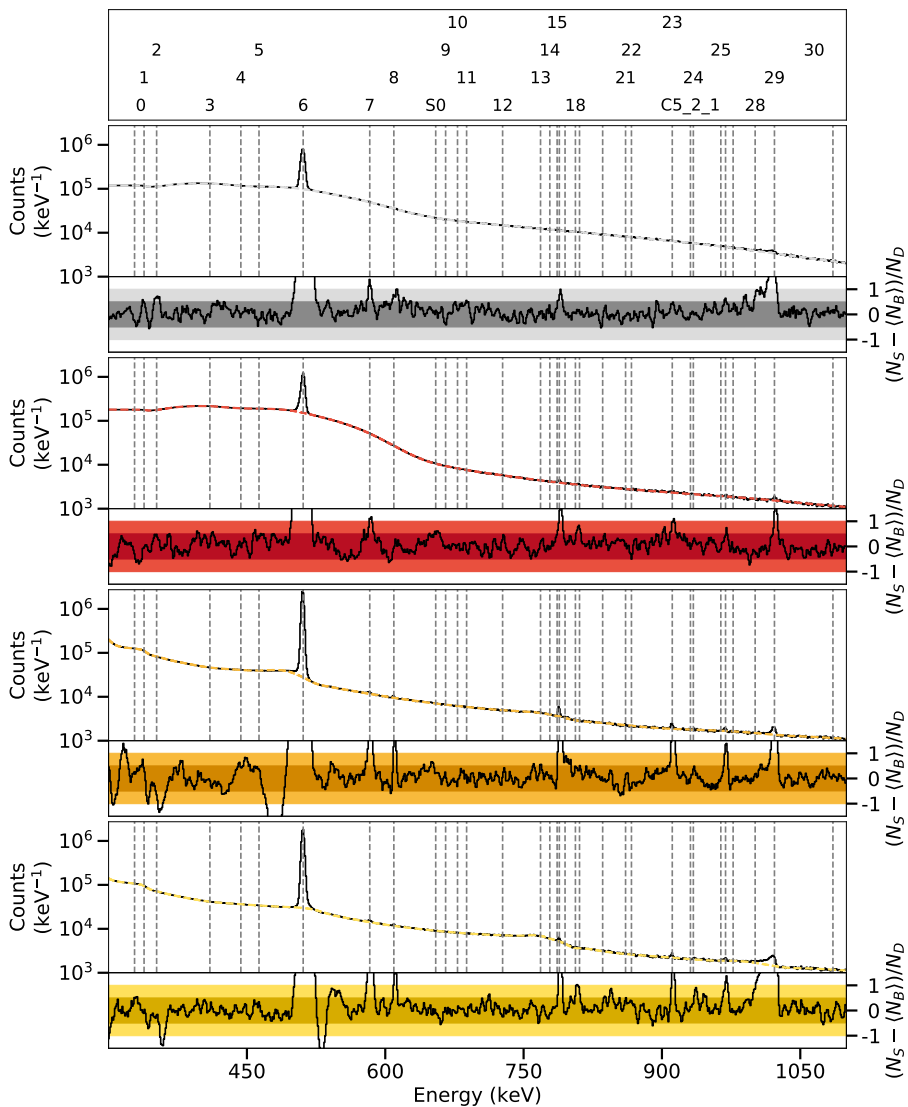


Figure D.17.: Spectra of the ^{82}Se target in the γ^3 setup at a beam energy of 2.65 MeV between 300 keV and 1100 keV.

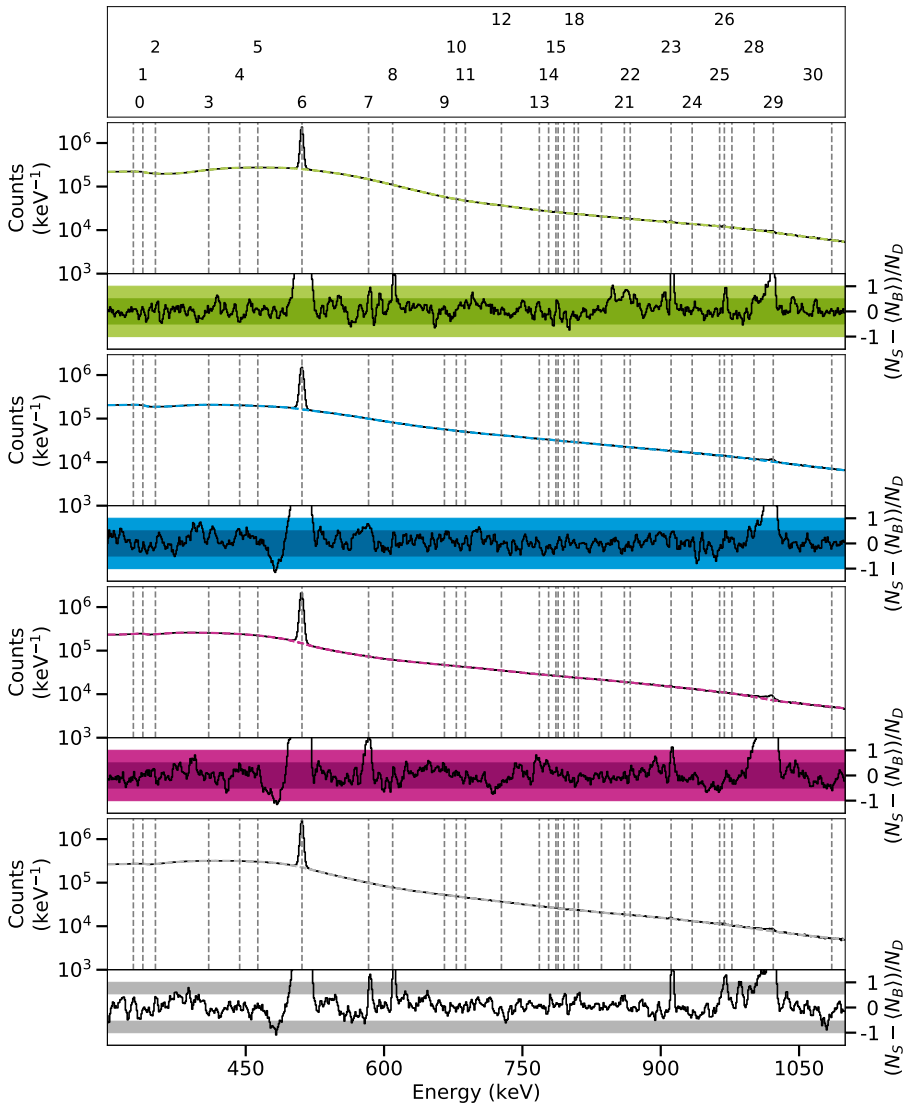


Figure D.18.: Spectra of the ^{82}Kr target in the polarimetry setup at a beam energy of 2.65 MeV between 300 keV and 1100 keV.

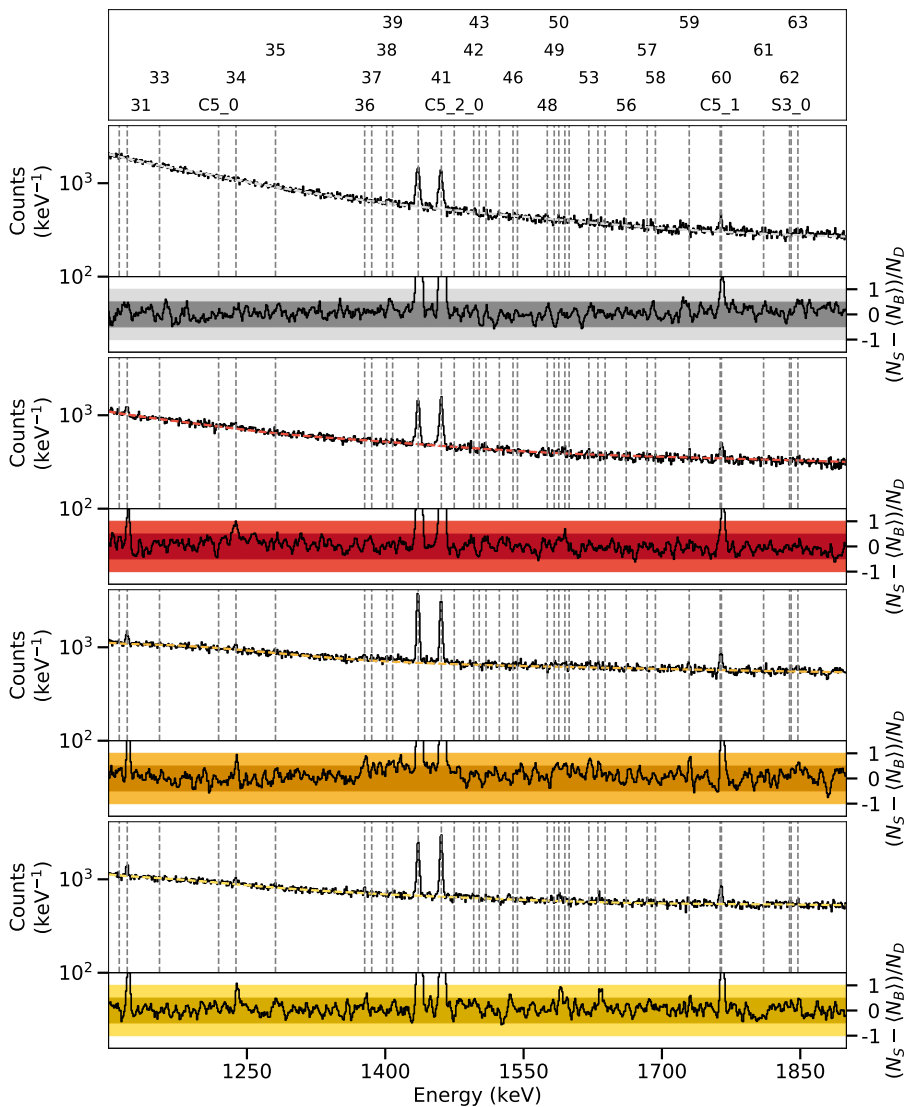


Figure D.19.: Spectra of the ^{82}Se target in the γ^3 setup at a beam energy of 2.65 MeV between 1100 keV and 1900 keV.

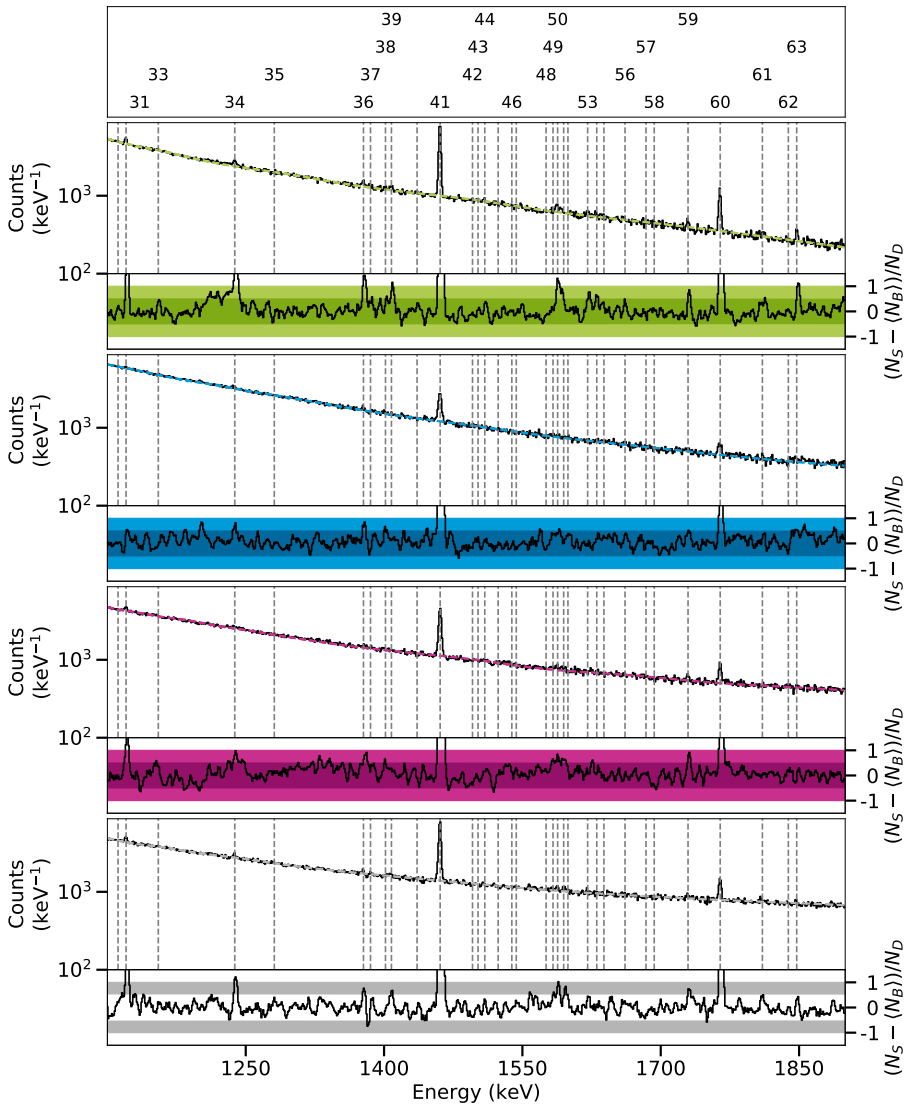


Figure D.20.: Spectra of the ^{82}Kr target in the polarimetry setup at a beam energy of 2.65 MeV between 1100 keV and 1900 keV.

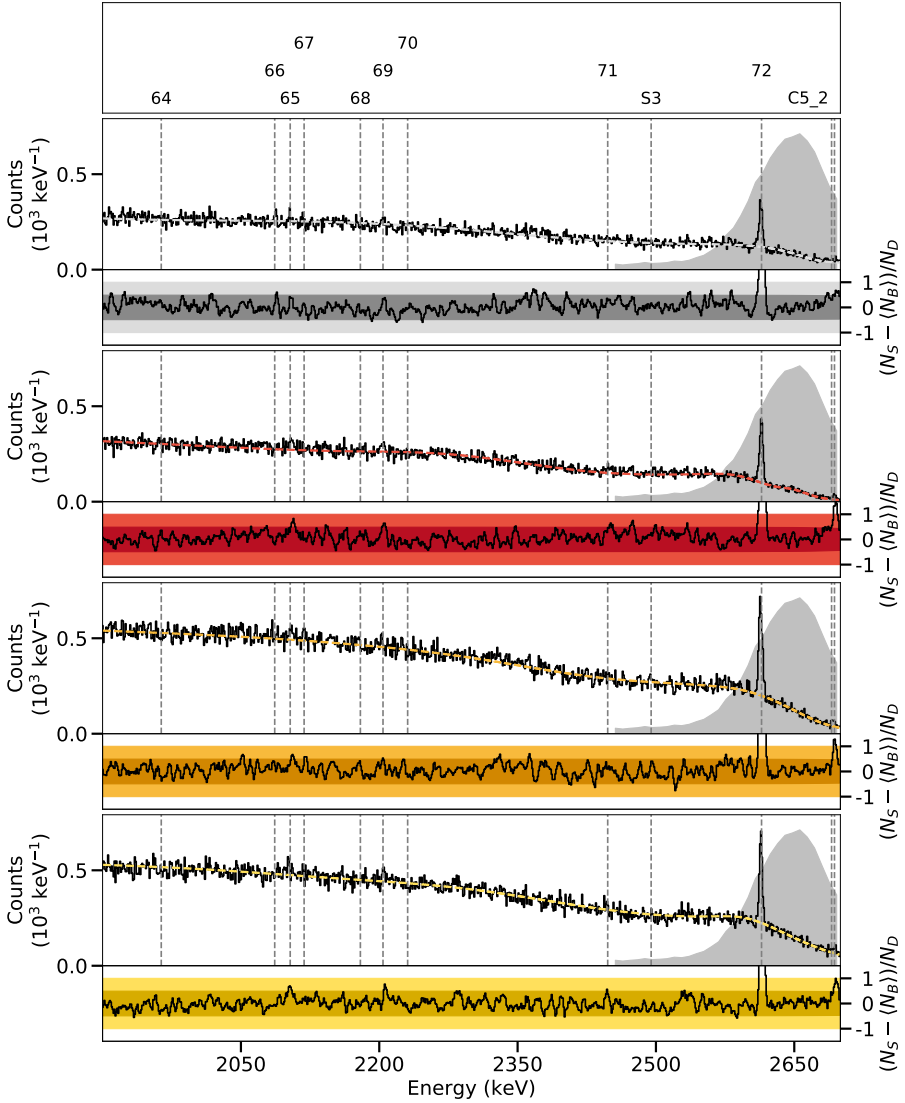


Figure D.21.: Spectra of the ^{82}Se target in the γ^3 setup at a beam energy of 2.65 MeV between 1900 keV and 2700 keV.

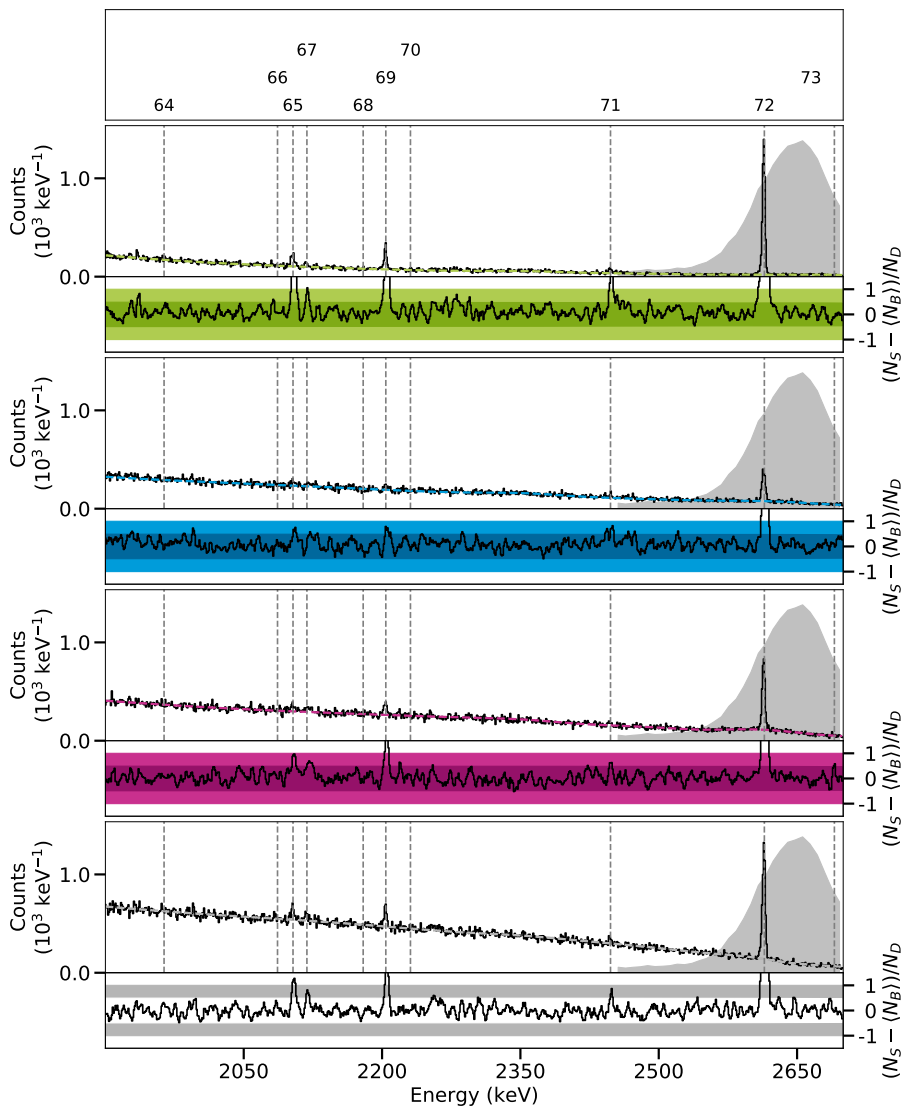


Figure D.22.: Spectra of the ^{82}Kr target in the polarimetry setup at a beam energy of 2.65 MeV between 1900 keV and 2700 keV.

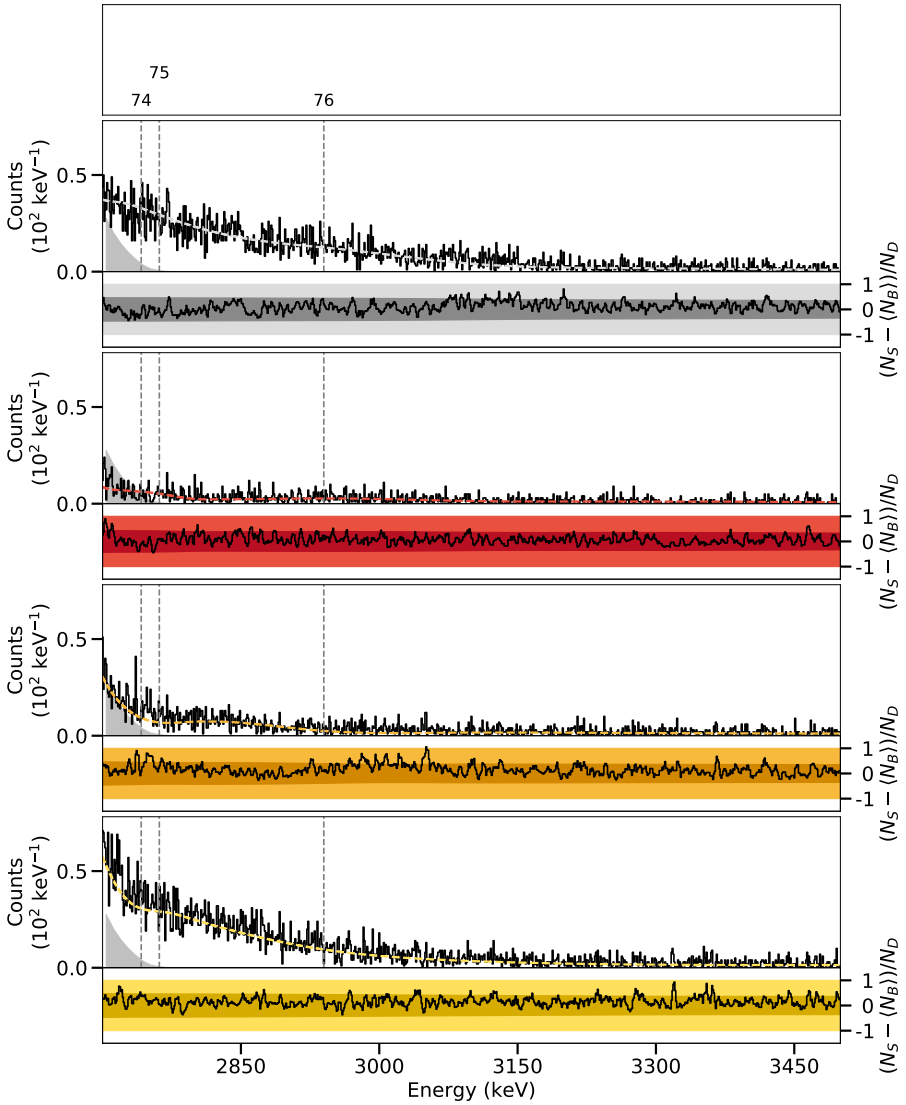


Figure D.23.: Spectra of the ^{82}Se target in the γ^3 setup at a beam energy of 2.65 MeV between 2700 keV and 3500 keV.

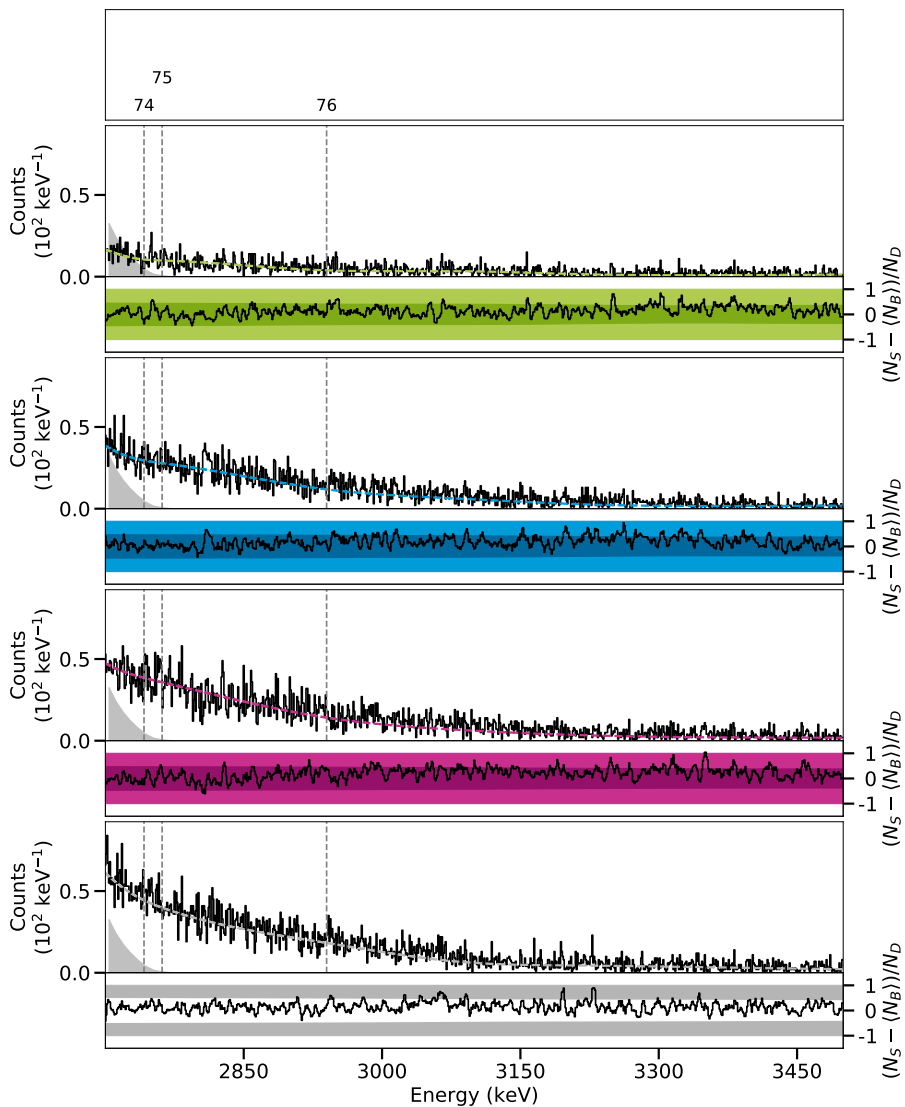


Figure D.24.: Spectra of the ^{82}Kr target in the polarimetry setup at a beam energy of 2.65 MeV between 2700 keV and 3500 keV.

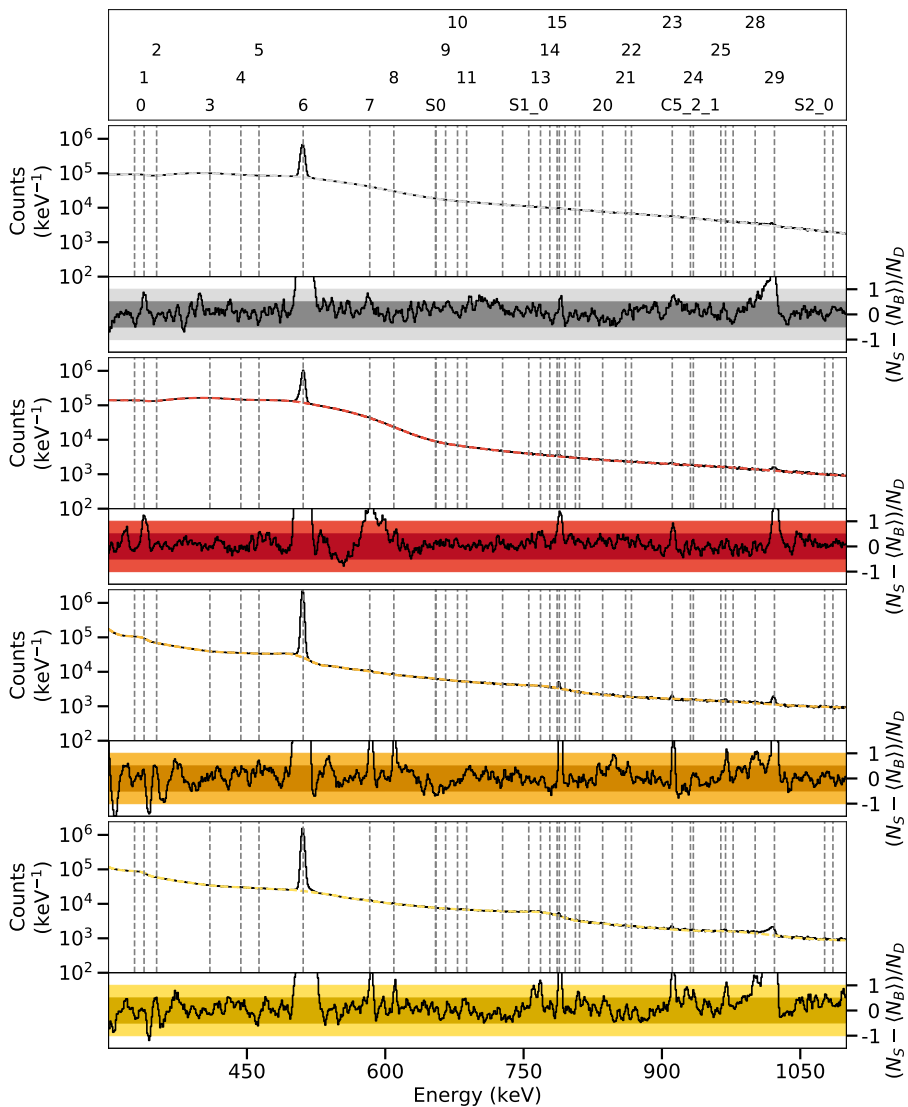


Figure D.25.: Spectra of the ^{82}Se target in the γ^3 setup at a beam energy of 2.80 MeV between 300 keV and 1100 keV.

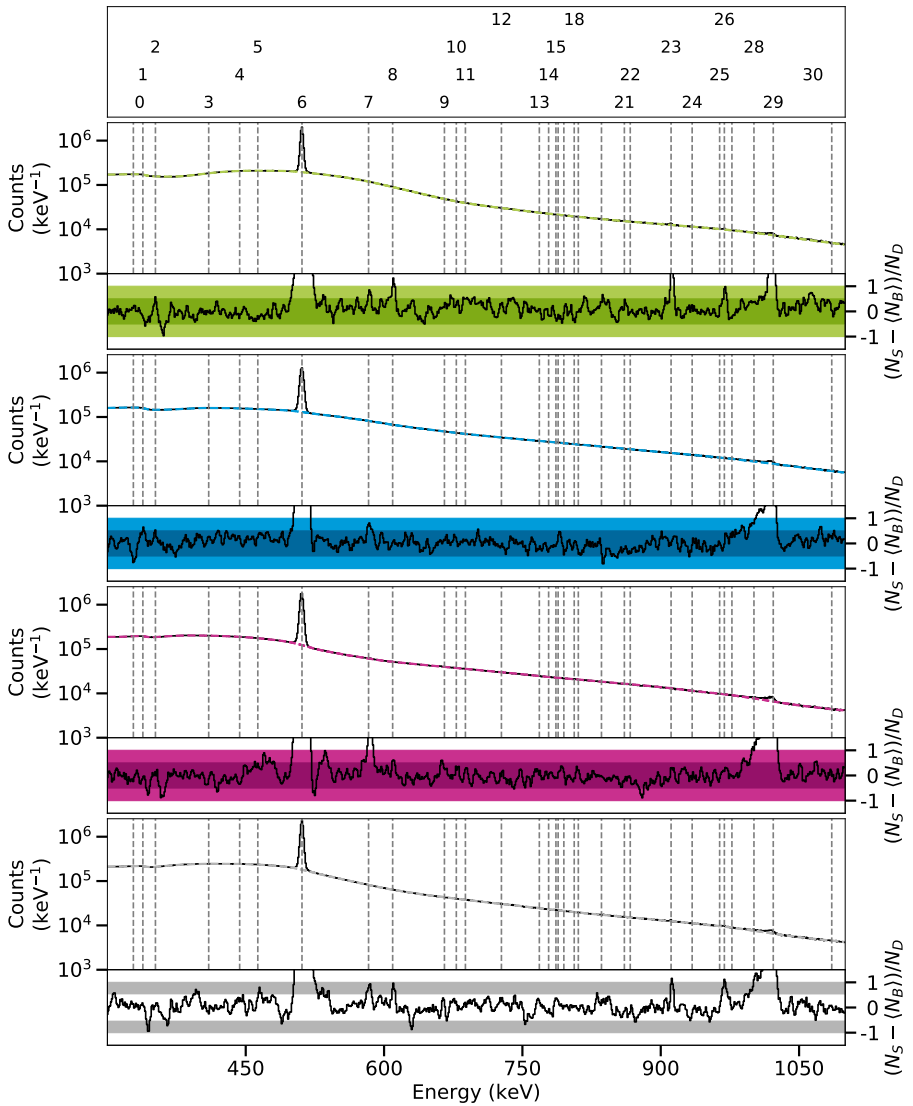


Figure D.26.: Spectra of the ^{82}Kr target in the polarimetry setup at a beam energy of 2.80 MeV between 300 keV and 1100 keV.

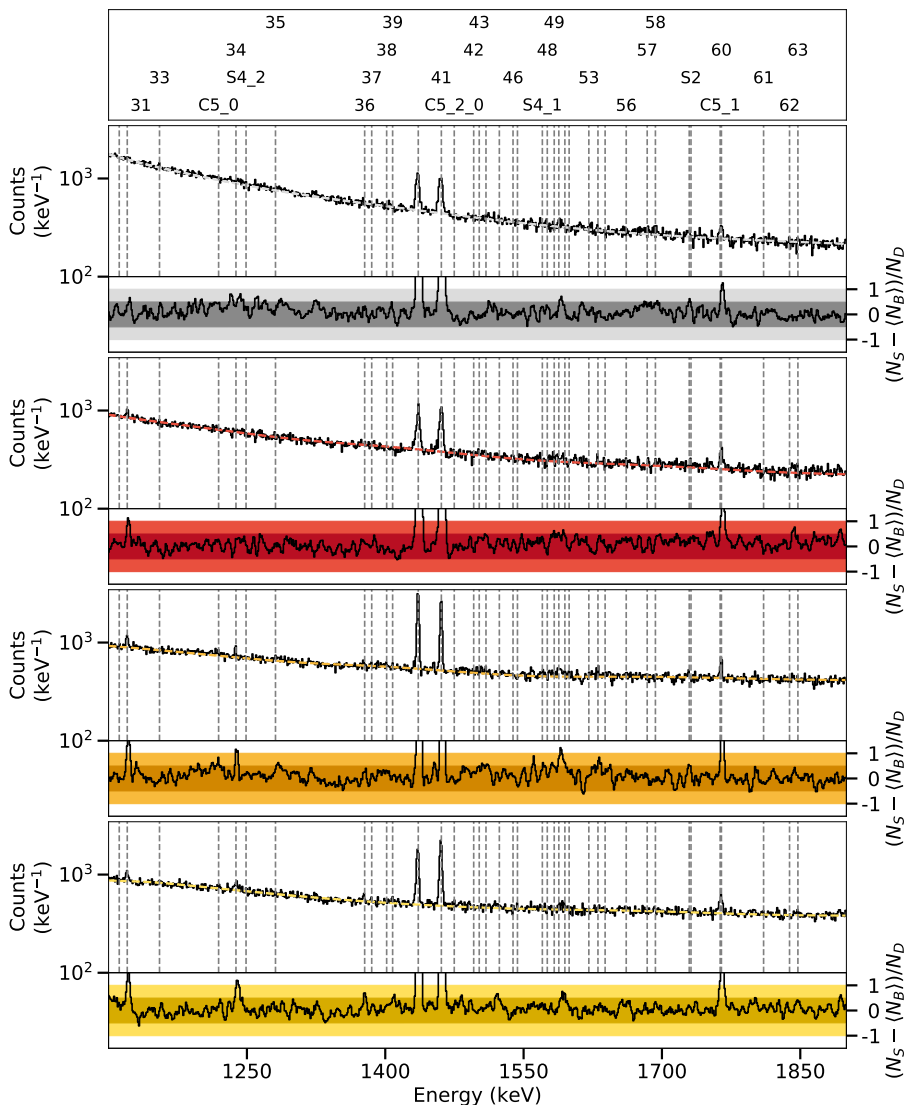


Figure D.27.: Spectra of the ^{82}Se target in the γ^3 setup at a beam energy of 2.80 MeV between 1100 keV and 1900 keV.

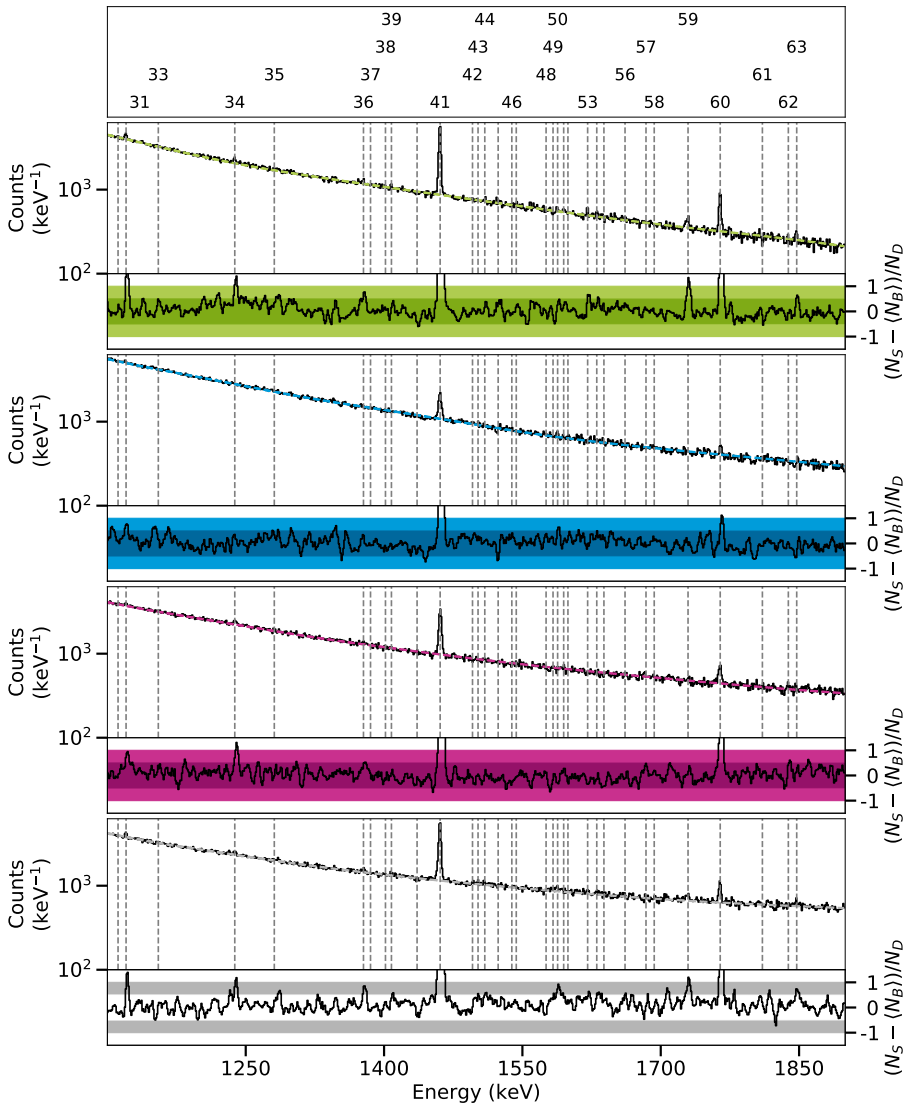


Figure D.28.: Spectra of the ^{82}Kr target in the polarimetry setup at a beam energy of 2.80 MeV between 1100 keV and 1900 keV.

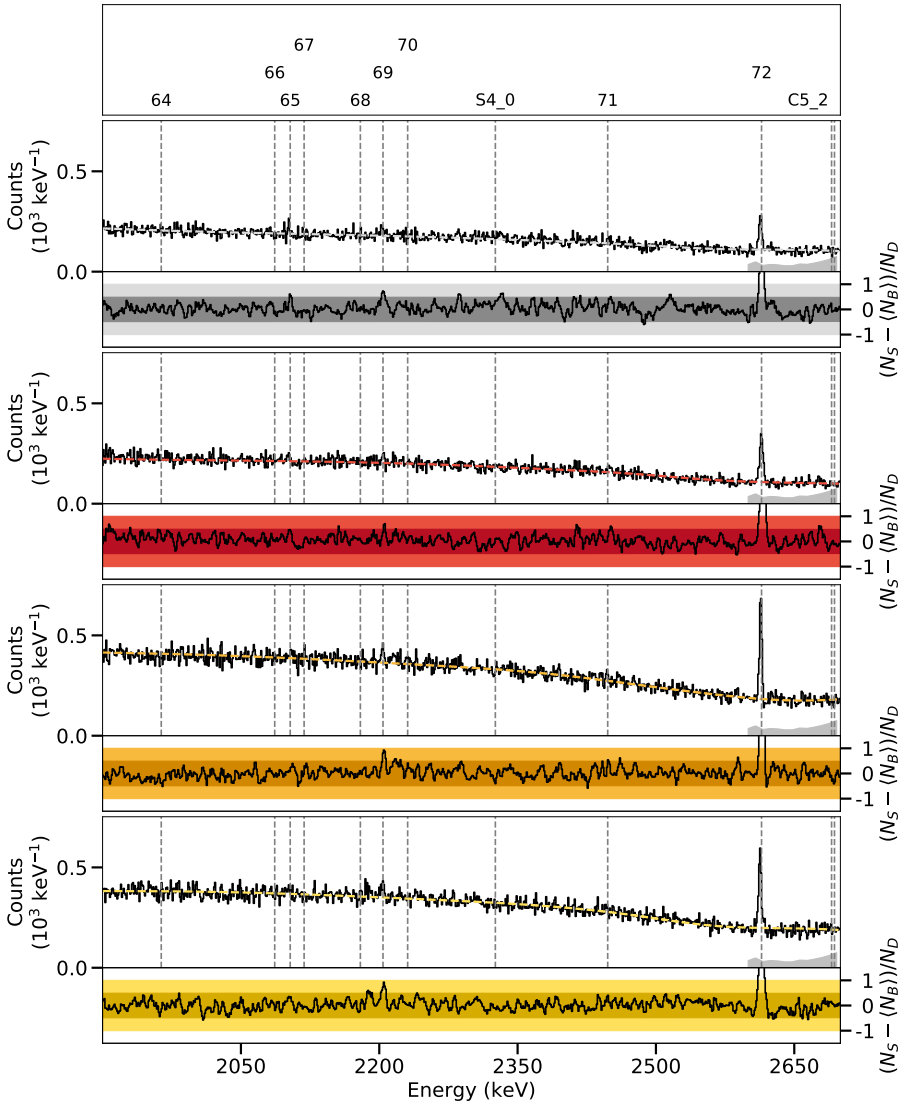


Figure D.29.: Spectra of the ^{82}Se target in the γ^3 setup at a beam energy of 2.80 MeV between 1900 keV and 2700 keV.

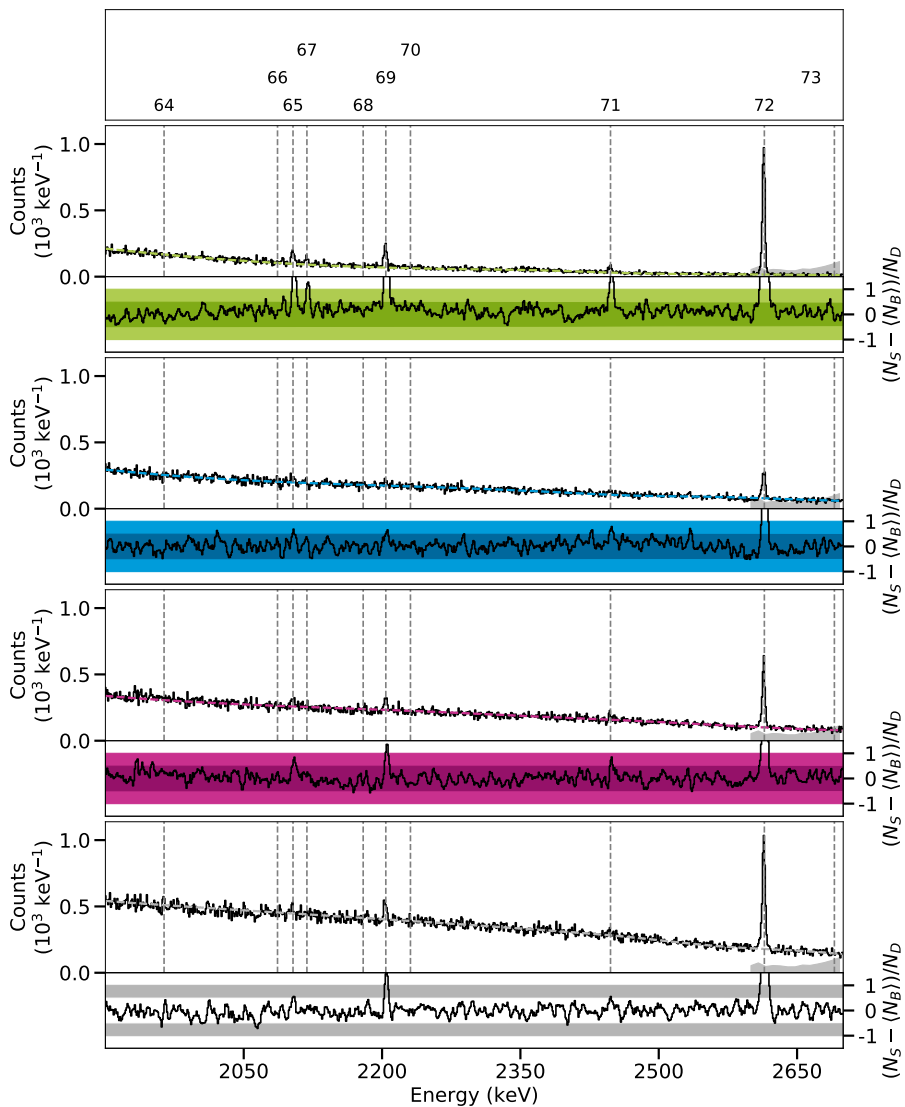


Figure D.30.: Spectra of the ^{82}Kr target in the polarimetry setup at a beam energy of 2.80 MeV between 1900 keV and 2700 keV.

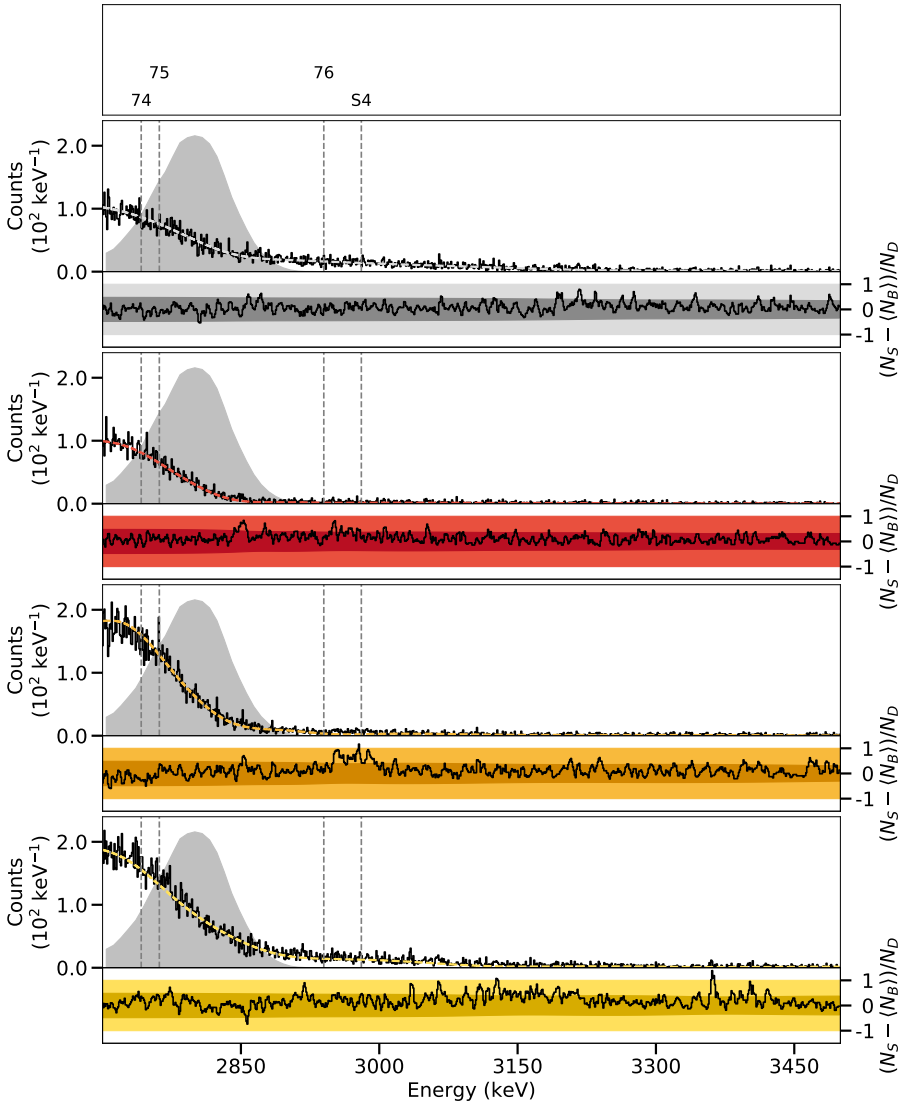


Figure D.31.: Spectra of the ^{82}Se target in the γ^3 setup at a beam energy of 2.80 MeV between 2700 keV and 3500 keV.

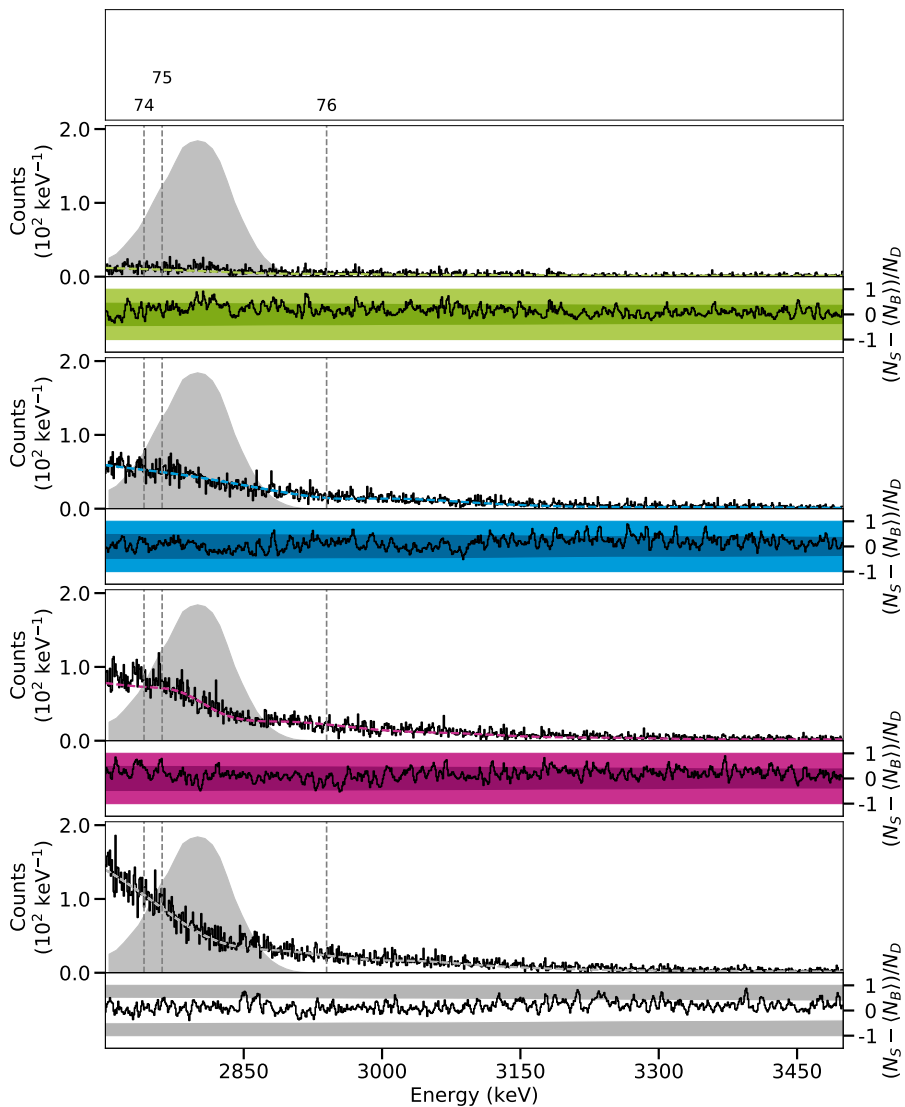


Figure D.32.: Spectra of the ^{82}Kr target in the polarimetry setup at a beam energy of 2.80 MeV between 2700 keV and 3500 keV.

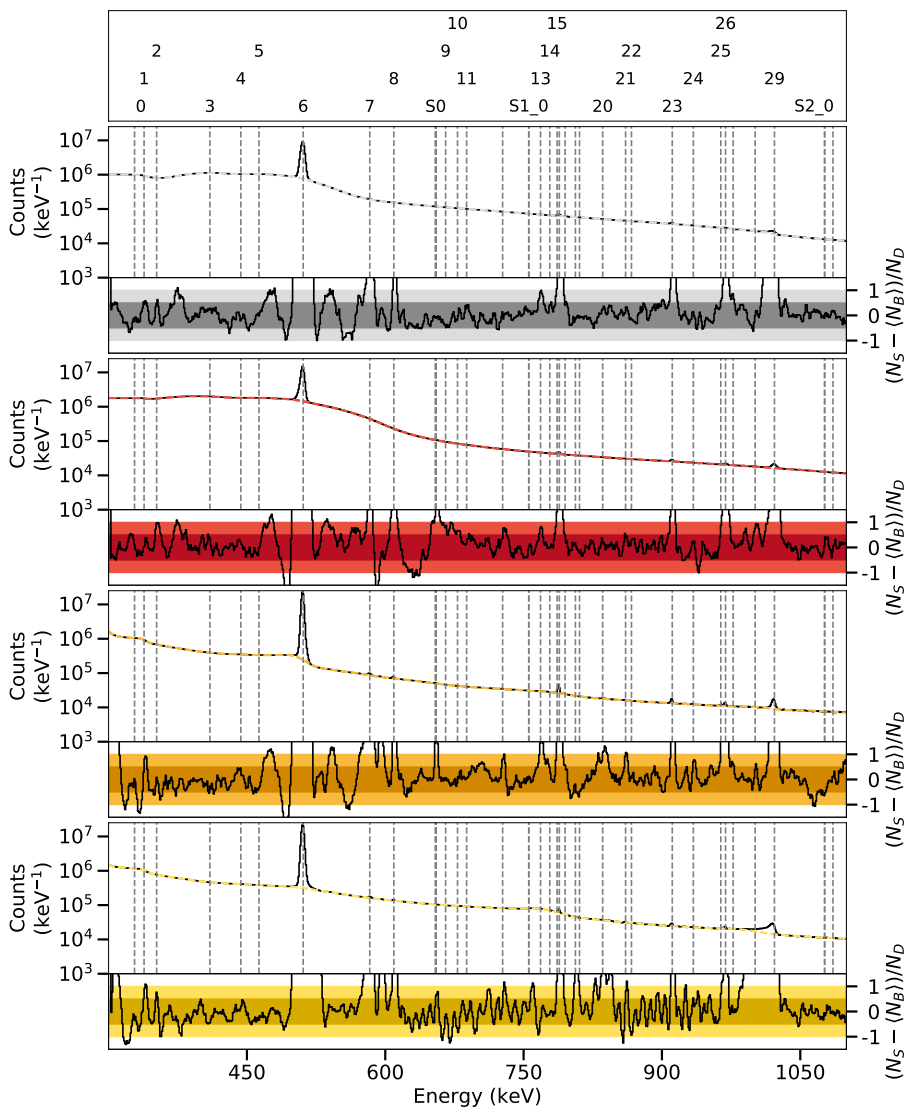


Figure D.33.: Spectra of the ^{82}Se target in the γ^3 setup at a beam energy of 2.98 MeV between 300 keV and 1100 keV.

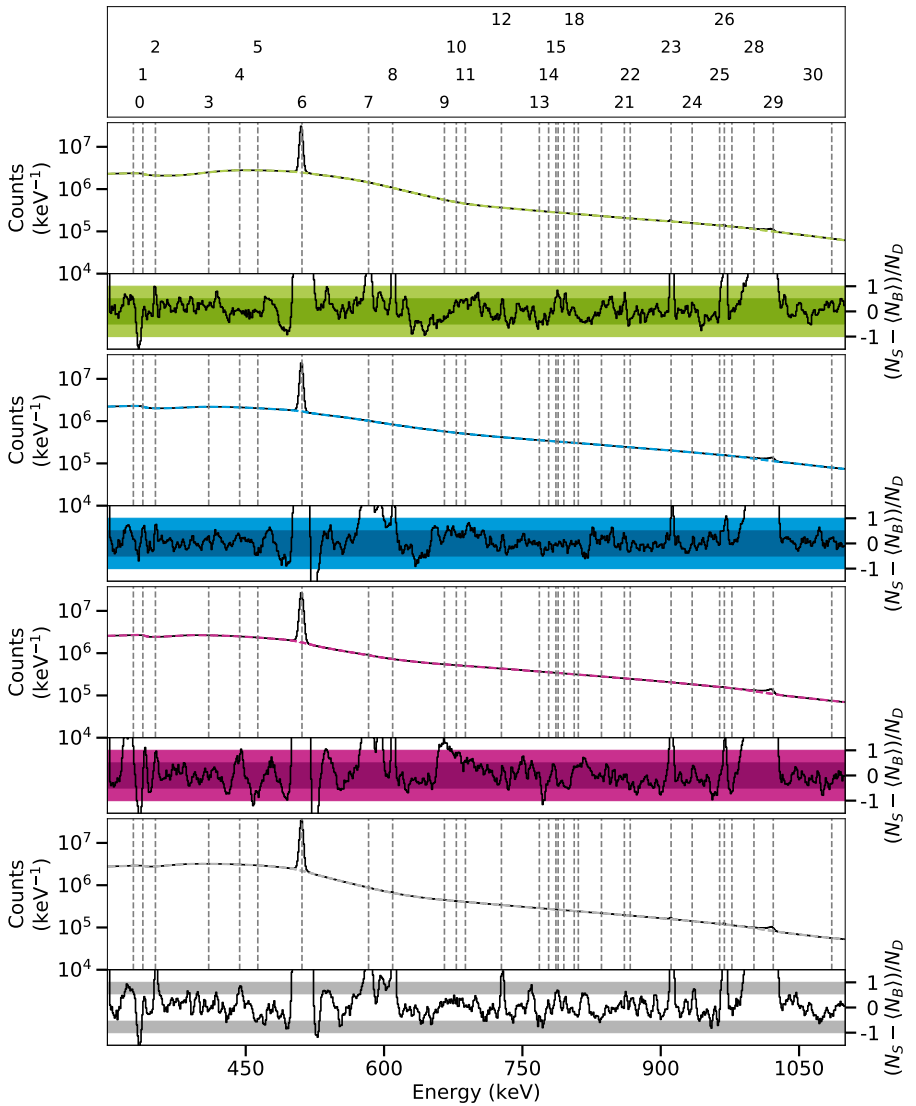


Figure D.34.: Spectra of the ^{82}Kr target in the polarimetry setup at a beam energy of 2.98 MeV between 300 keV and 1100 keV.

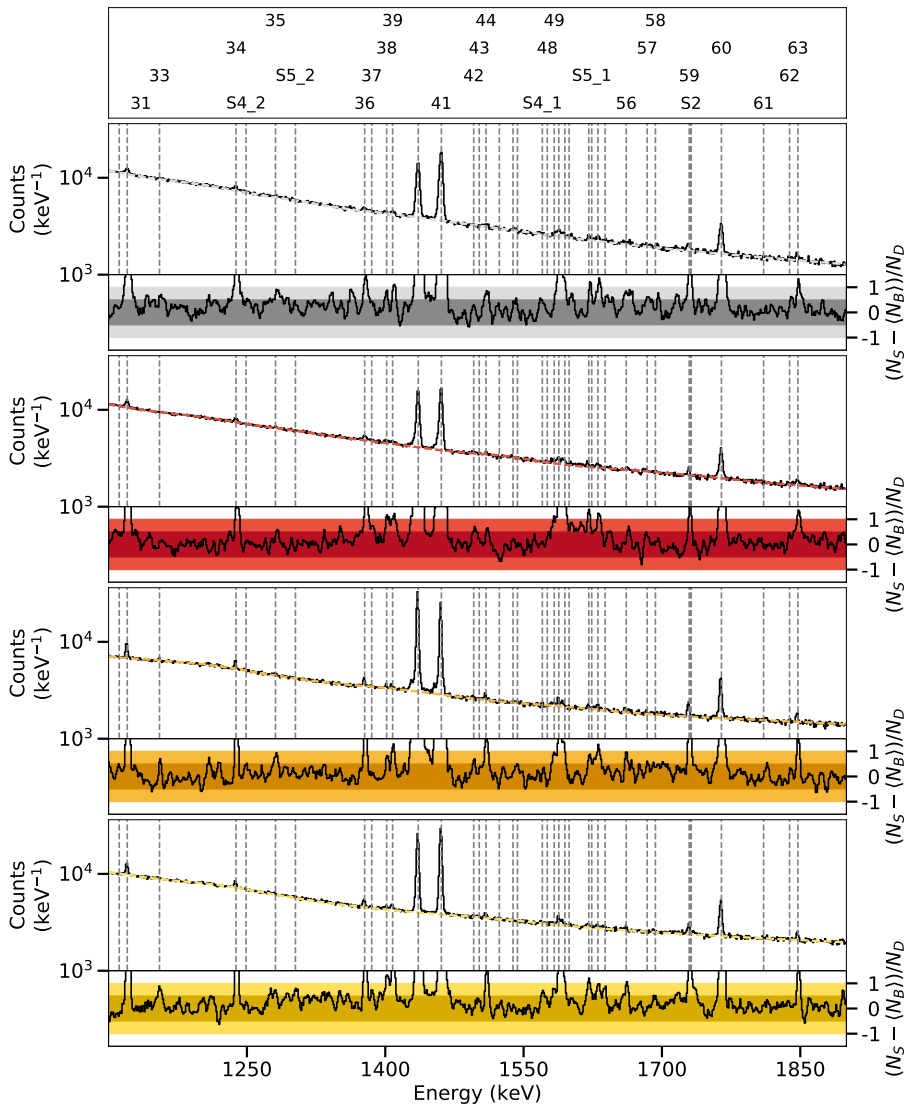


Figure D.35.: Spectra of the ⁸²Se target in the γ^3 setup at a beam energy of 2.98 MeV between 1100 keV and 1900 keV.

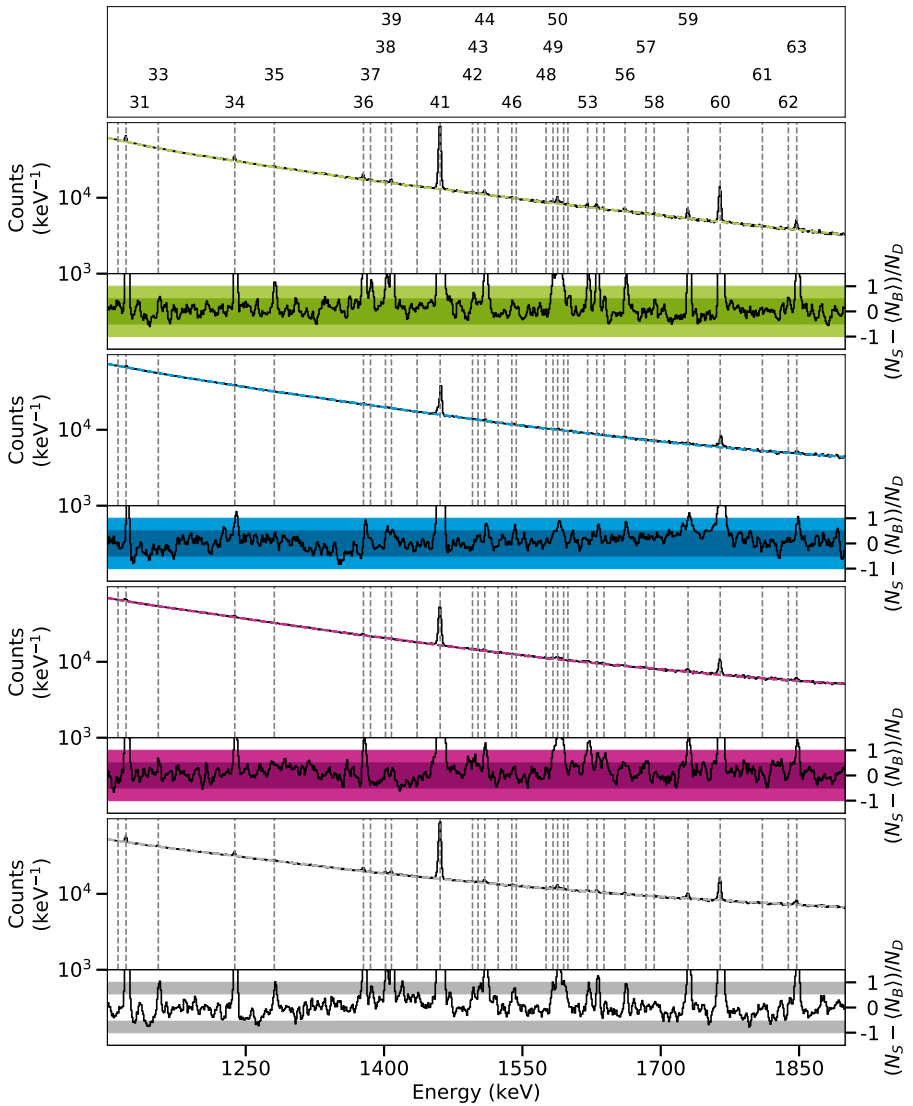


Figure D.36.: Spectra of the ^{82}Kr target in the polarimetry setup at a beam energy of 2.98 MeV between 1100 keV and 1900 keV.

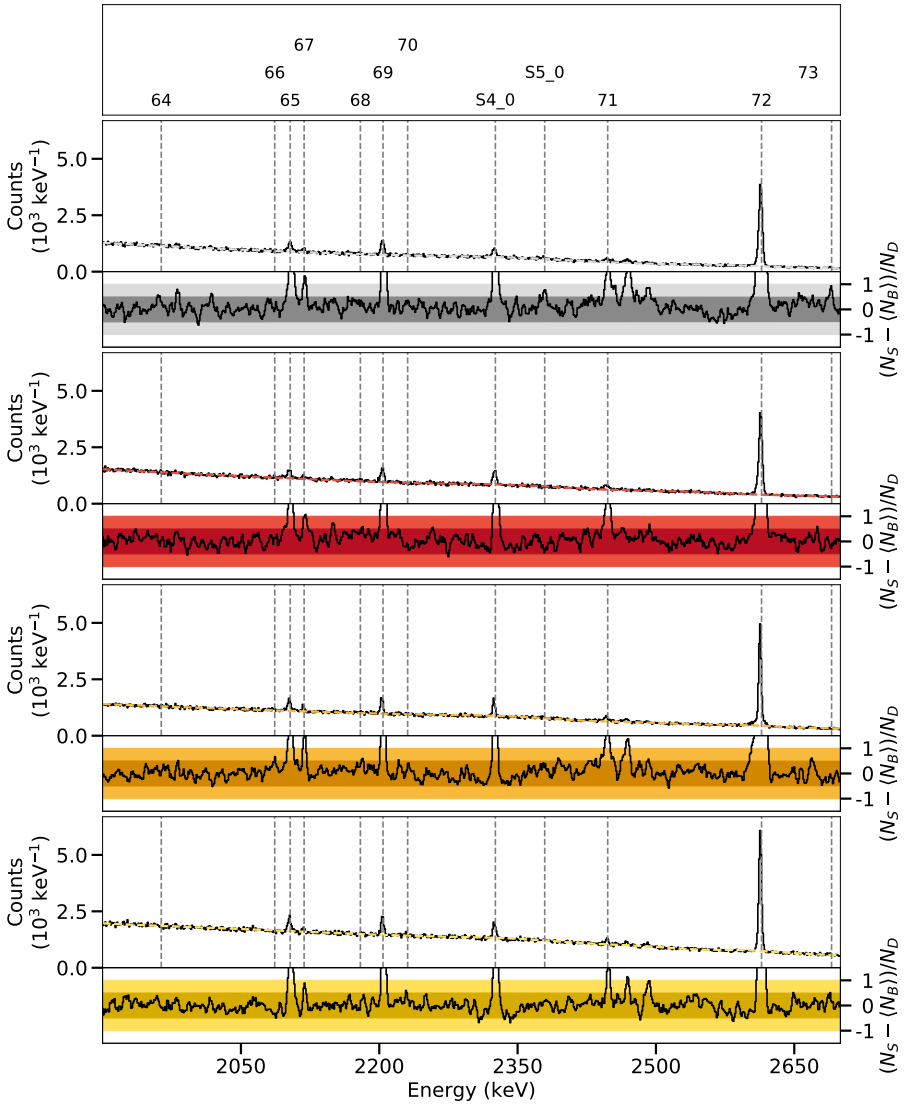


Figure D.37.: Spectra of the ^{82}Se target in the γ^3 setup at a beam energy of 2.98 MeV between 1900 keV and 2700 keV.

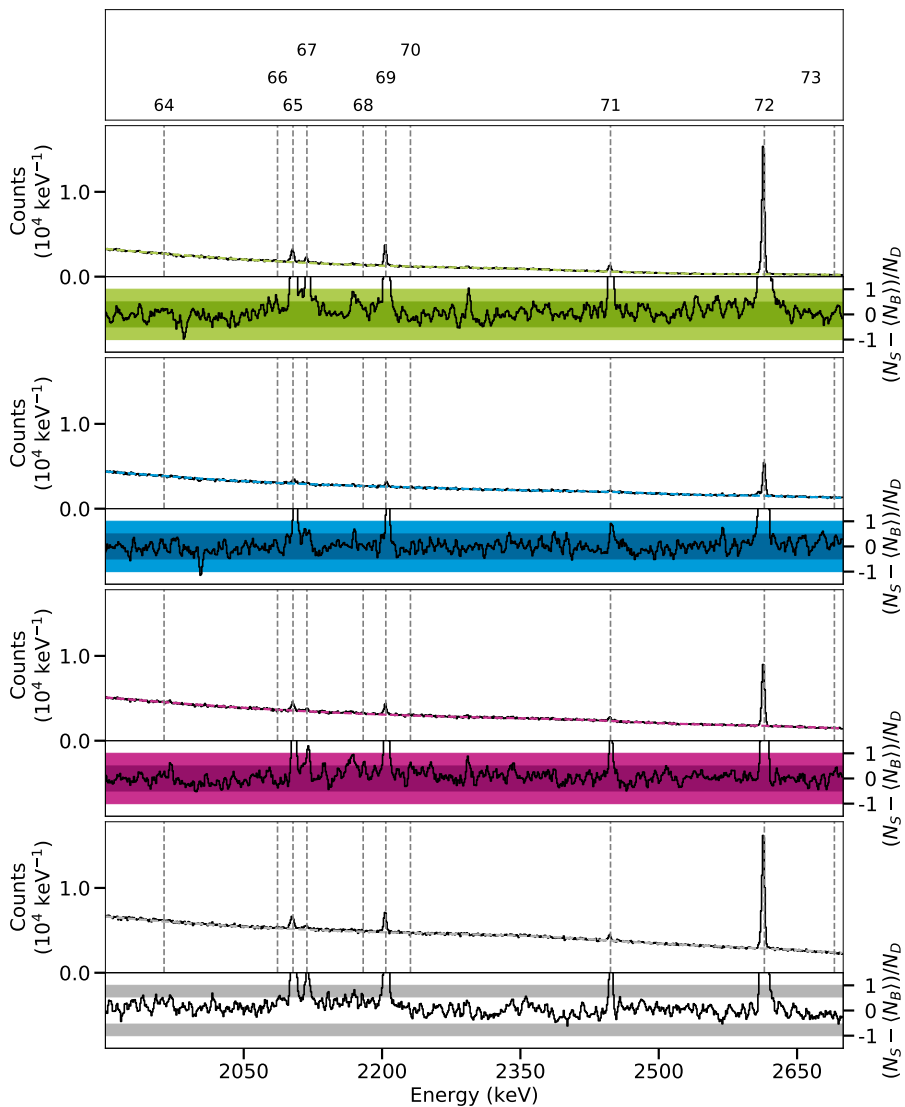


Figure D.38.: Spectra of the ^{82}Kr target in the polarimetry setup at a beam energy of 2.98 MeV between 1900 keV and 2700 keV.

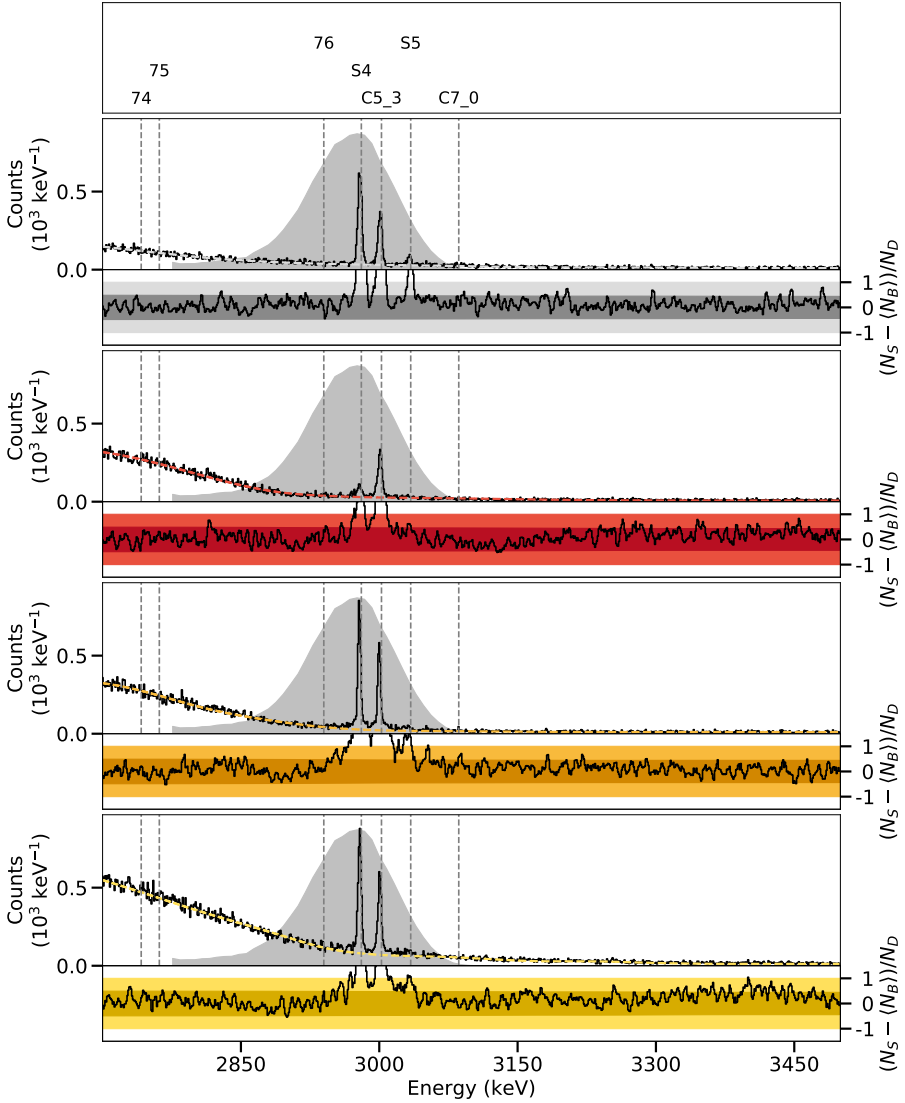


Figure D.39.: Spectra of the ^{82}Se target in the γ^3 setup at a beam energy of 2.98 MeV between 2700 keV and 3500 keV.

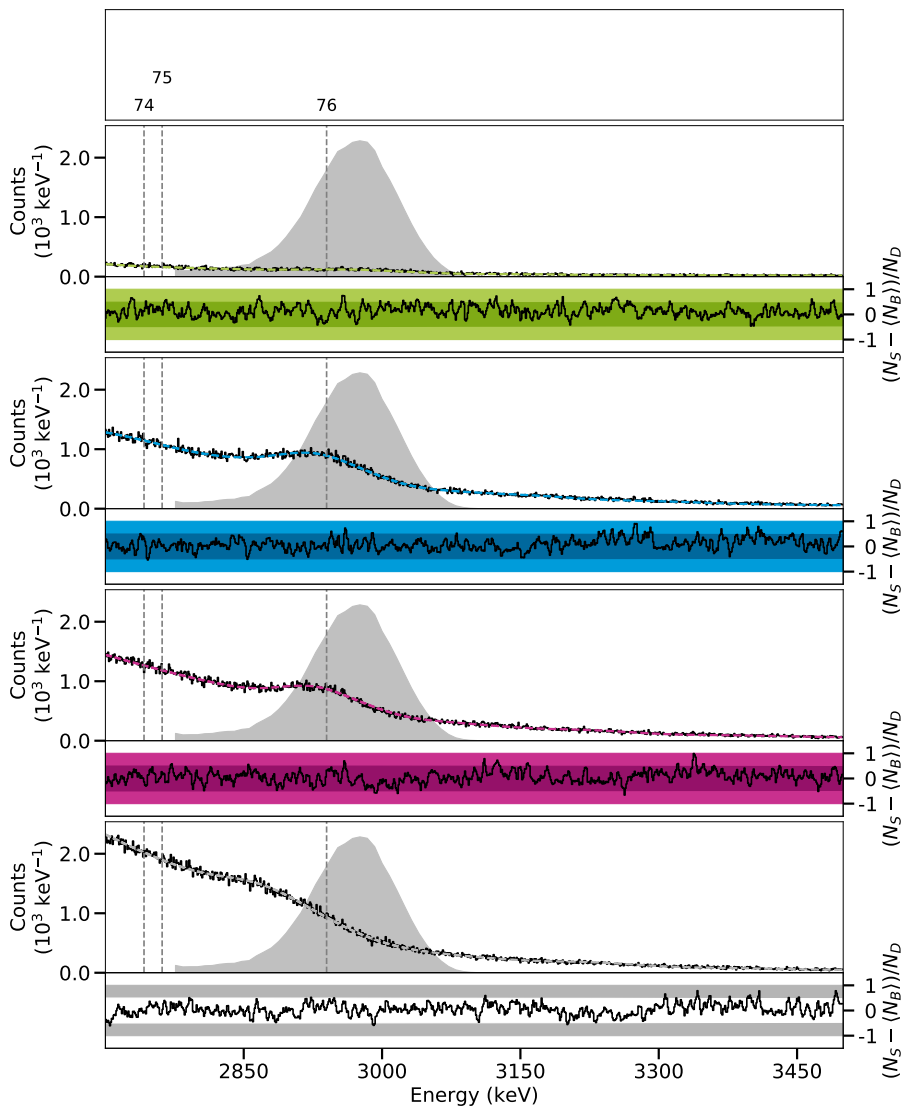


Figure D.40.: Spectra of the ^{82}Kr target in the polarimetry setup at a beam energy of 2.98 MeV between 2700 keV and 3500 keV.

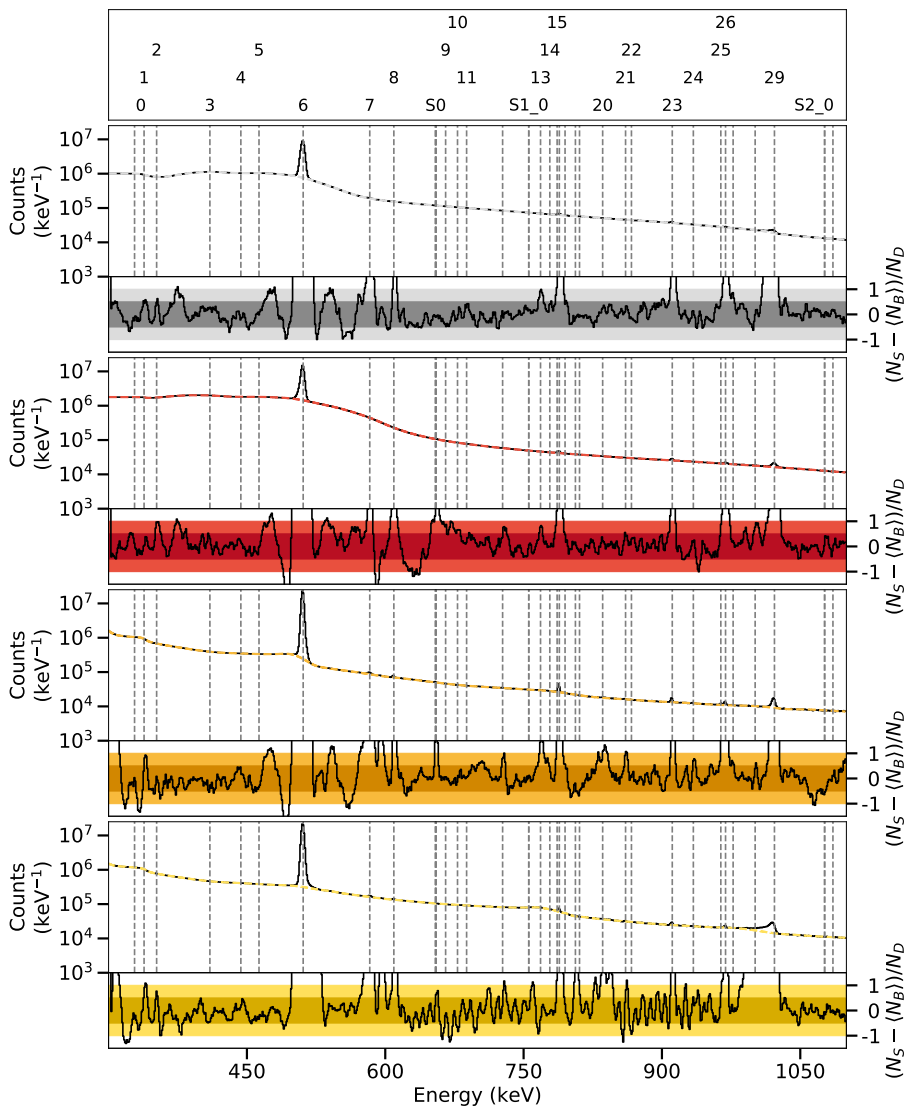


Figure D.41.: Spectra of the ^{82}Se target in the γ^3 setup at a beam energy of 2.98 MeV between 300 keV and 1100 keV.

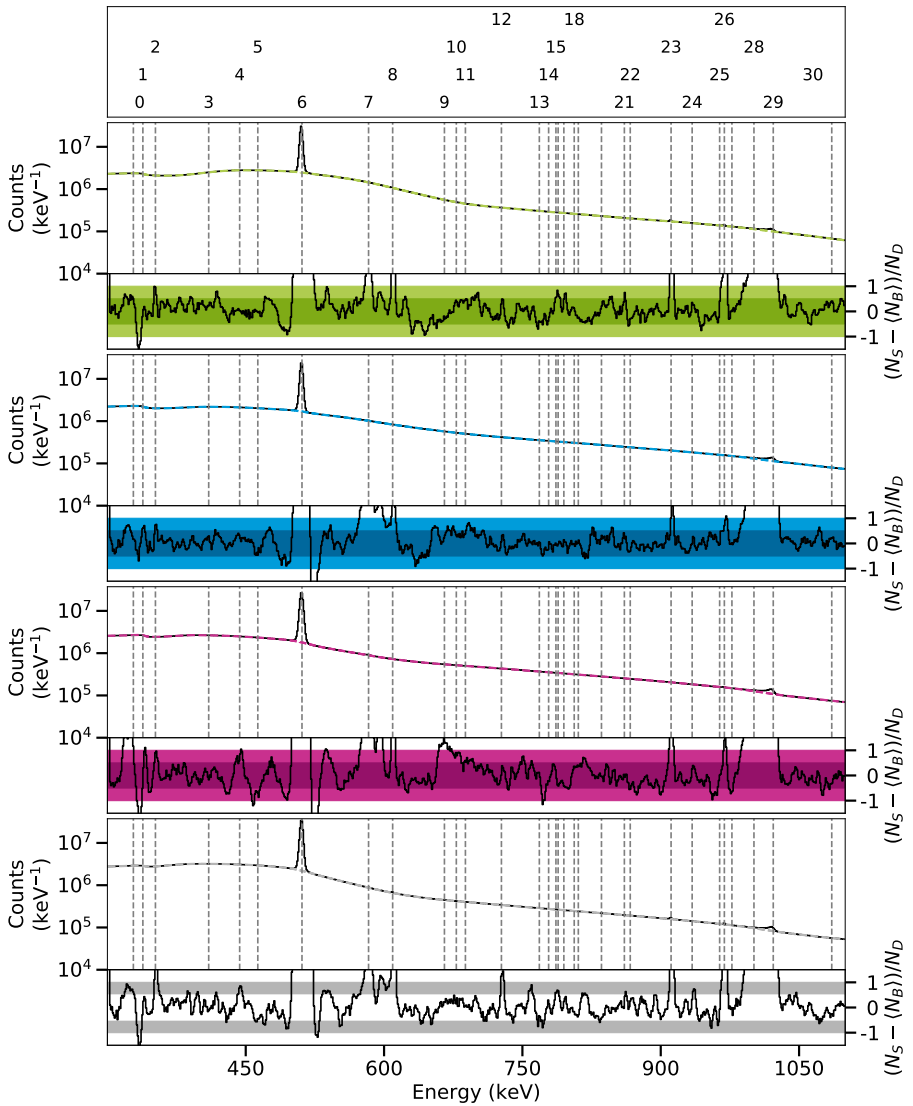


Figure D.42.: Spectra of the ^{82}Kr target in the polarimetry setup at a beam energy of 2.98 MeV between 300 keV and 1100 keV.

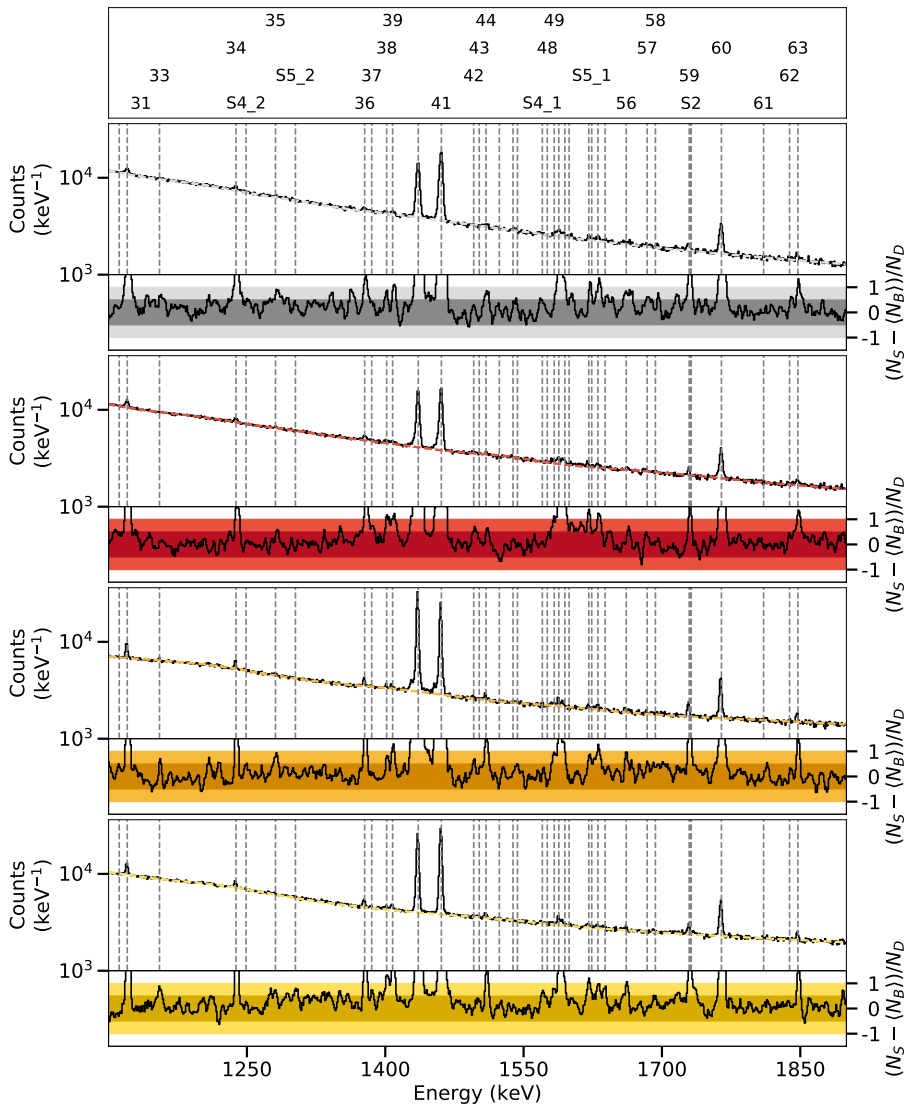


Figure D.43.: Spectra of the ^{82}Se target in the γ^3 setup at a beam energy of 2.98 MeV between 1100 keV and 1900 keV.

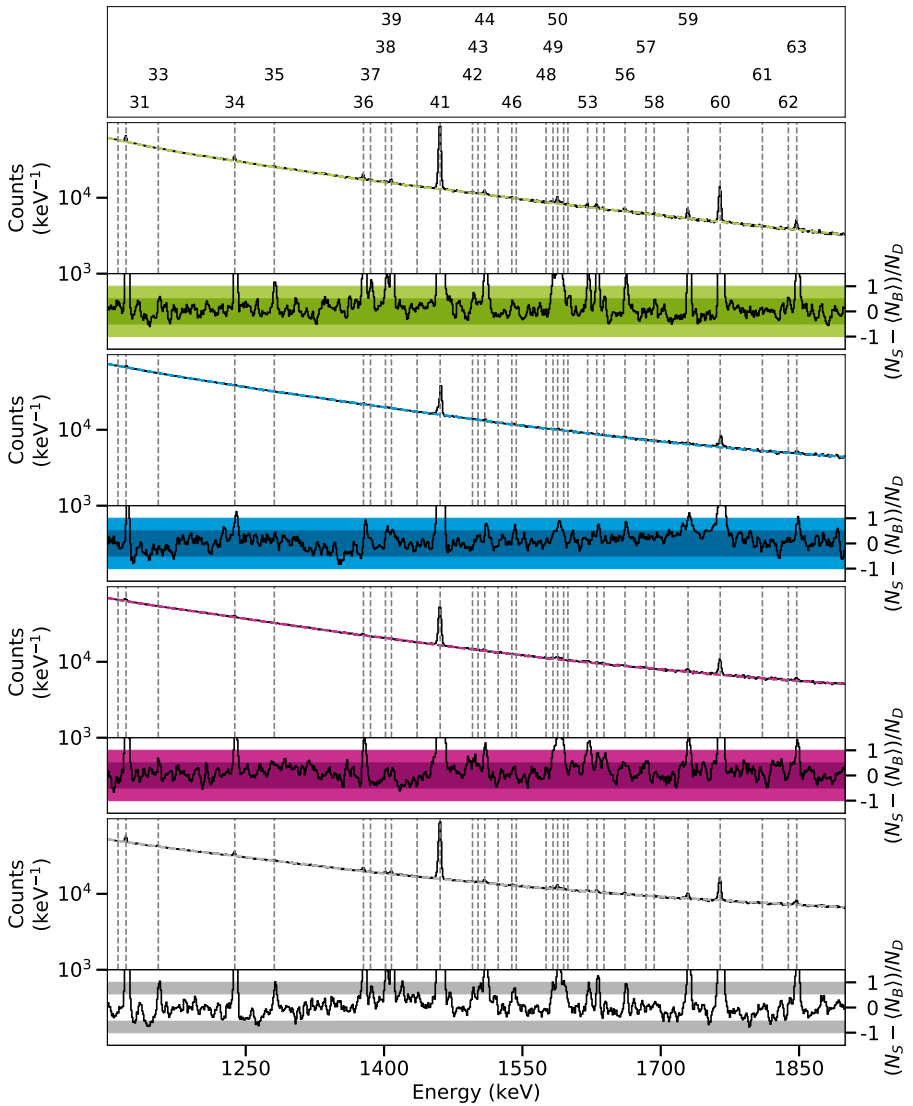


Figure D.44.: Spectra of the ^{82}Kr target in the polarimetry setup at a beam energy of 2.98 MeV between 1100 keV and 1900 keV.

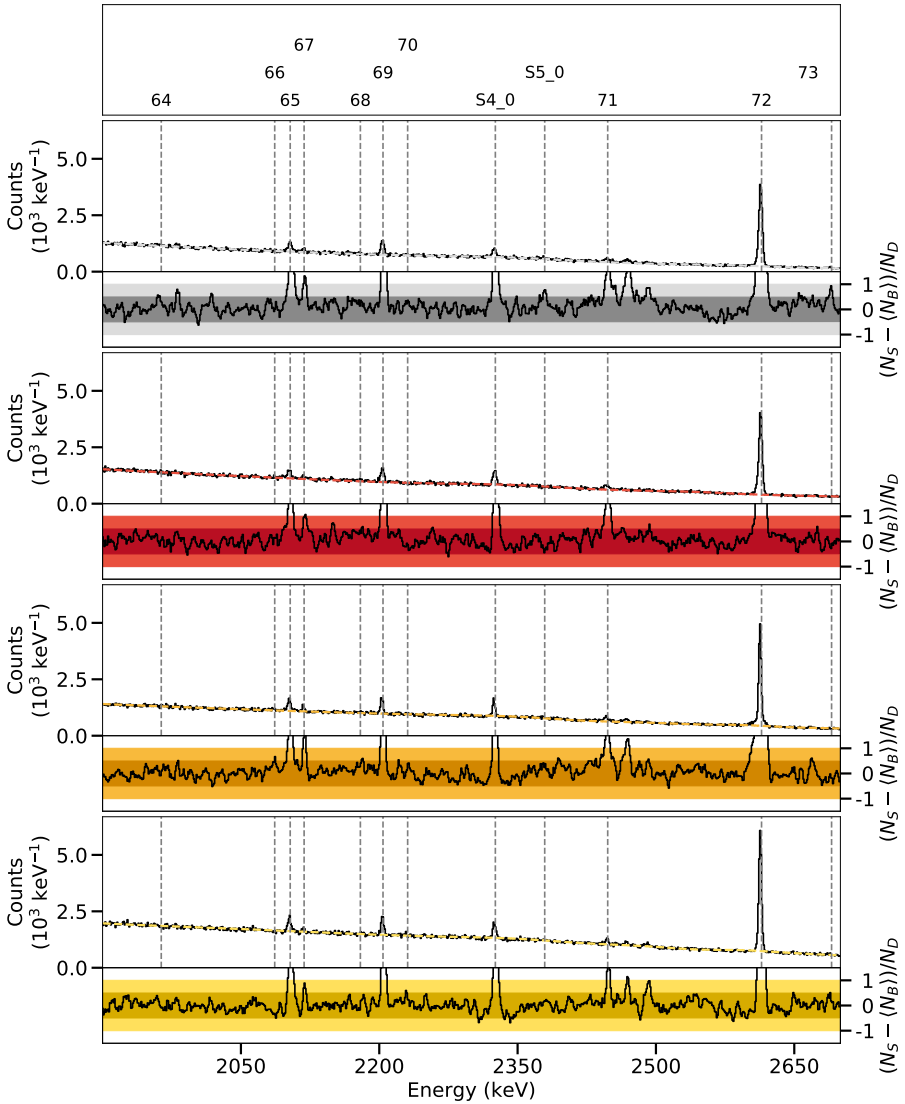


Figure D.45.: Spectra of the ^{82}Se target in the γ^3 setup at a beam energy of 2.98 MeV between 1900 keV and 2700 keV.

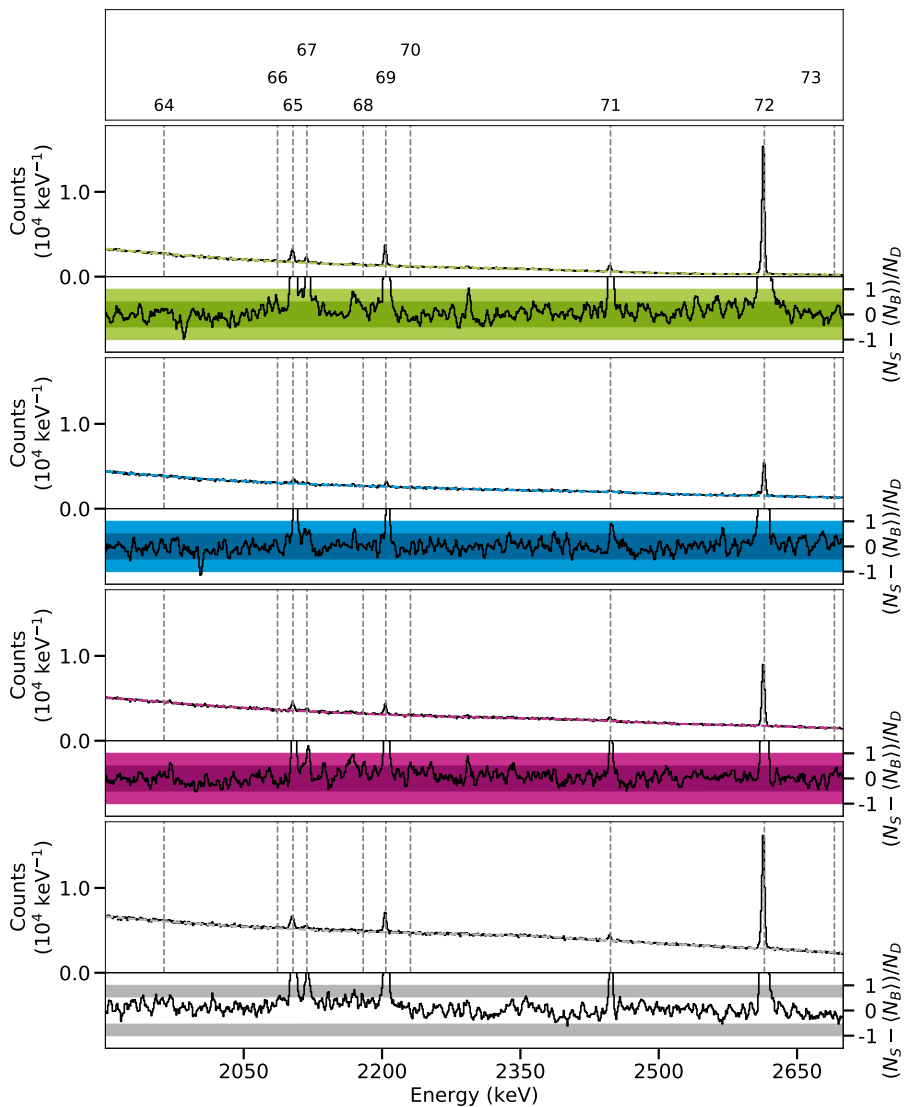


Figure D.46.: Spectra of the ^{82}Kr target in the polarimetry setup at a beam energy of 2.98 MeV between 1900 keV and 2700 keV.

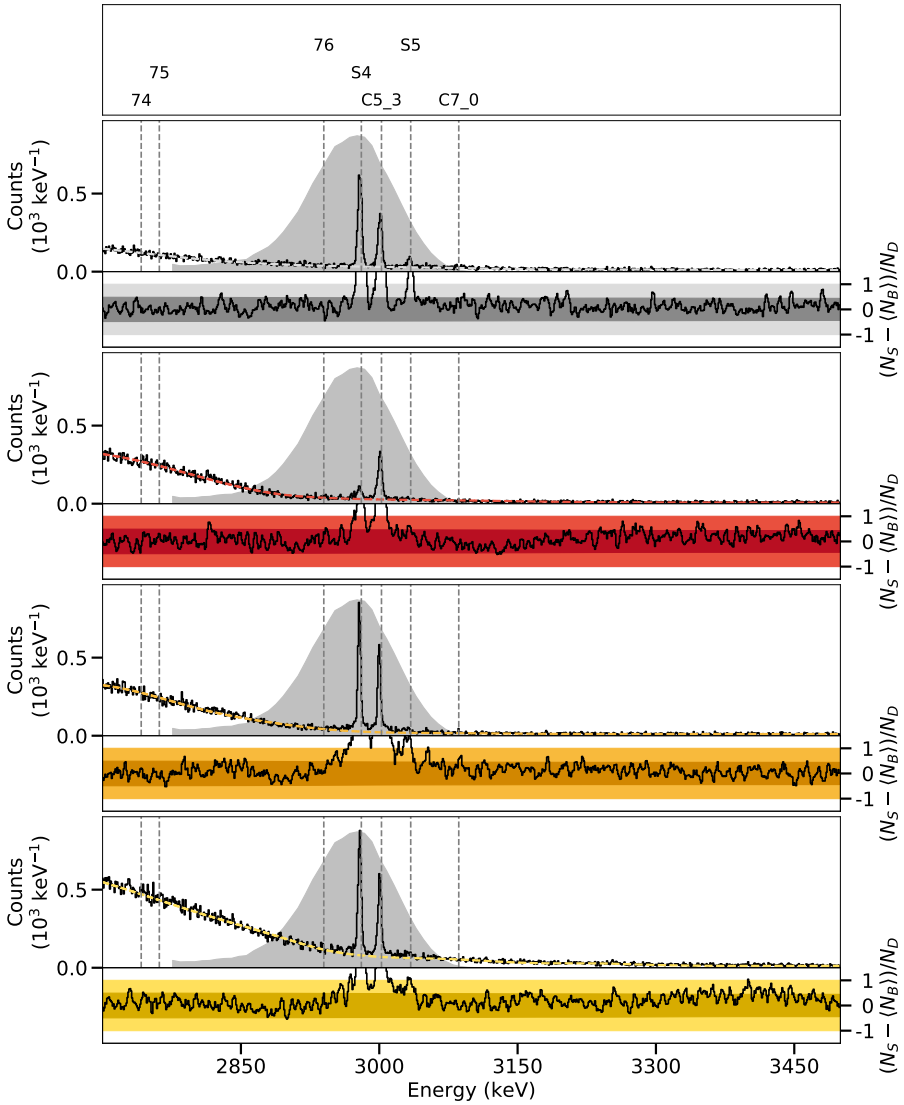


Figure D.47.: Spectra of the ^{82}Se target in the γ^3 setup at a beam energy of 2.98 MeV between 2700 keV and 3500 keV.

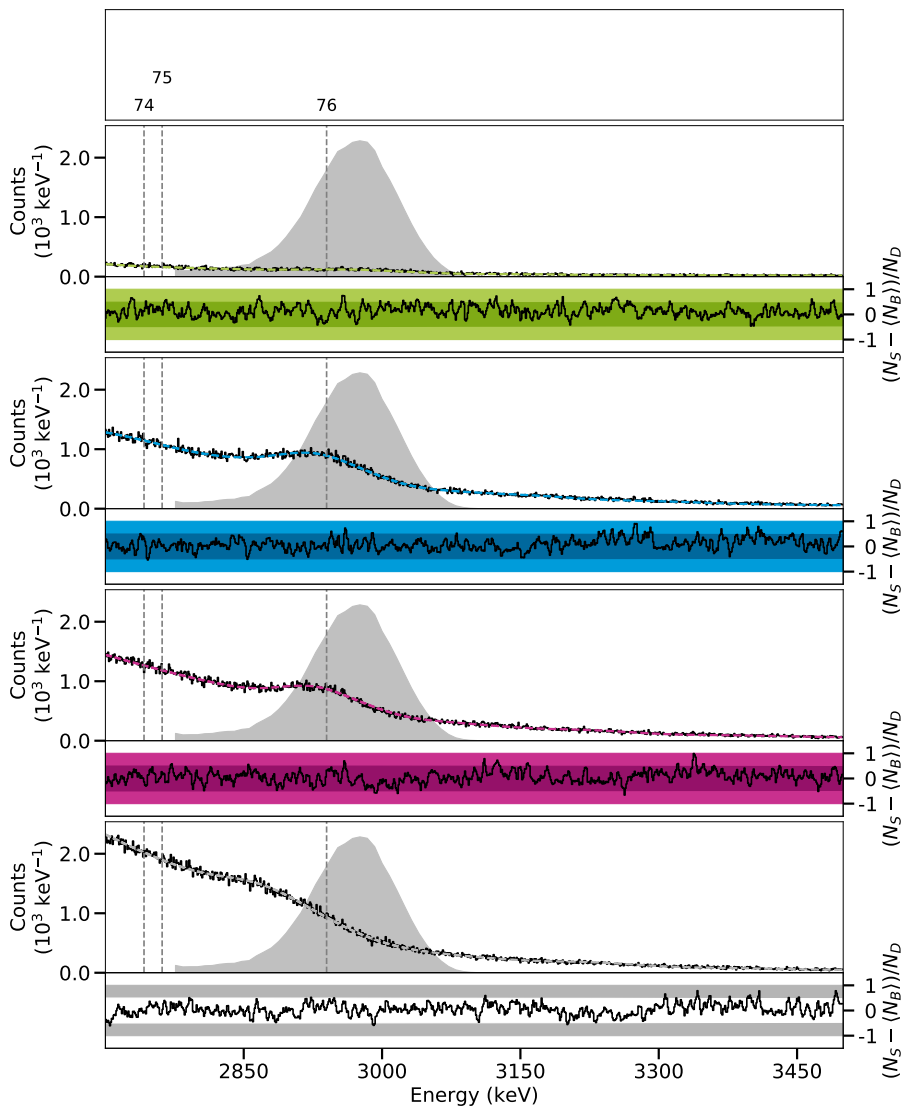


Figure D.48.: Spectra of the ^{82}Kr target in the polarimetry setup at a beam energy of 2.98 MeV between 2700 keV and 3500 keV.

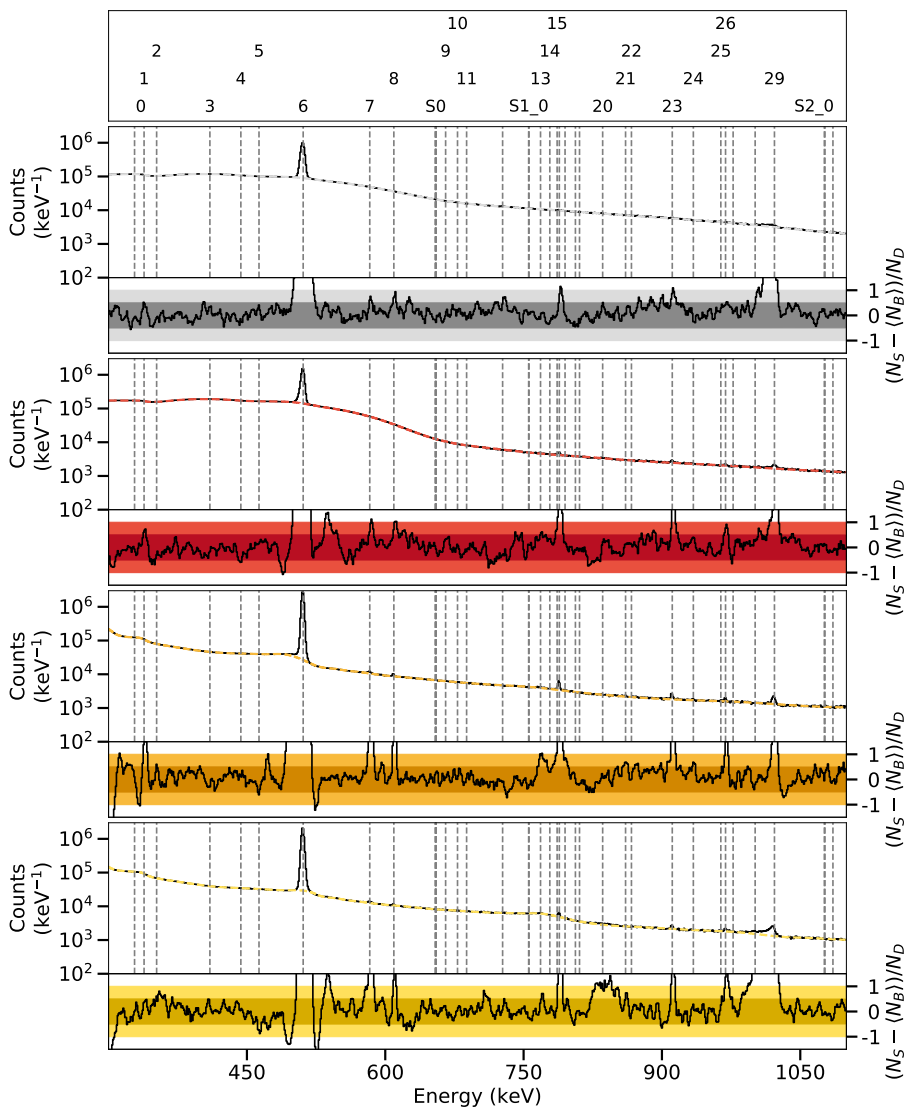


Figure D.49.: Spectra of the ^{82}Se target in the γ^3 setup at a beam energy of 3.10 MeV between 300 keV and 1100 keV.

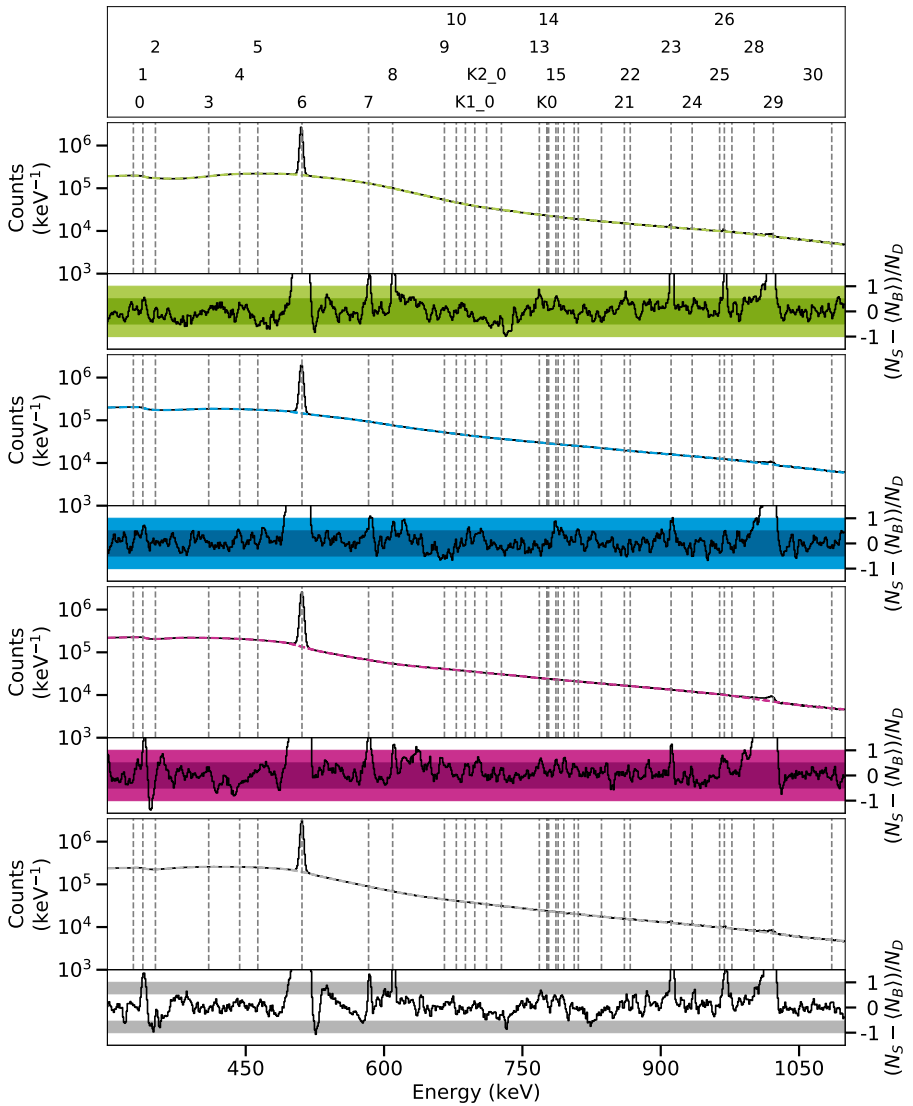


Figure D.50.: Spectra of the ^{82}Kr target in the polarimetry setup at a beam energy of 3.10 MeV between 300 keV and 1100 keV.

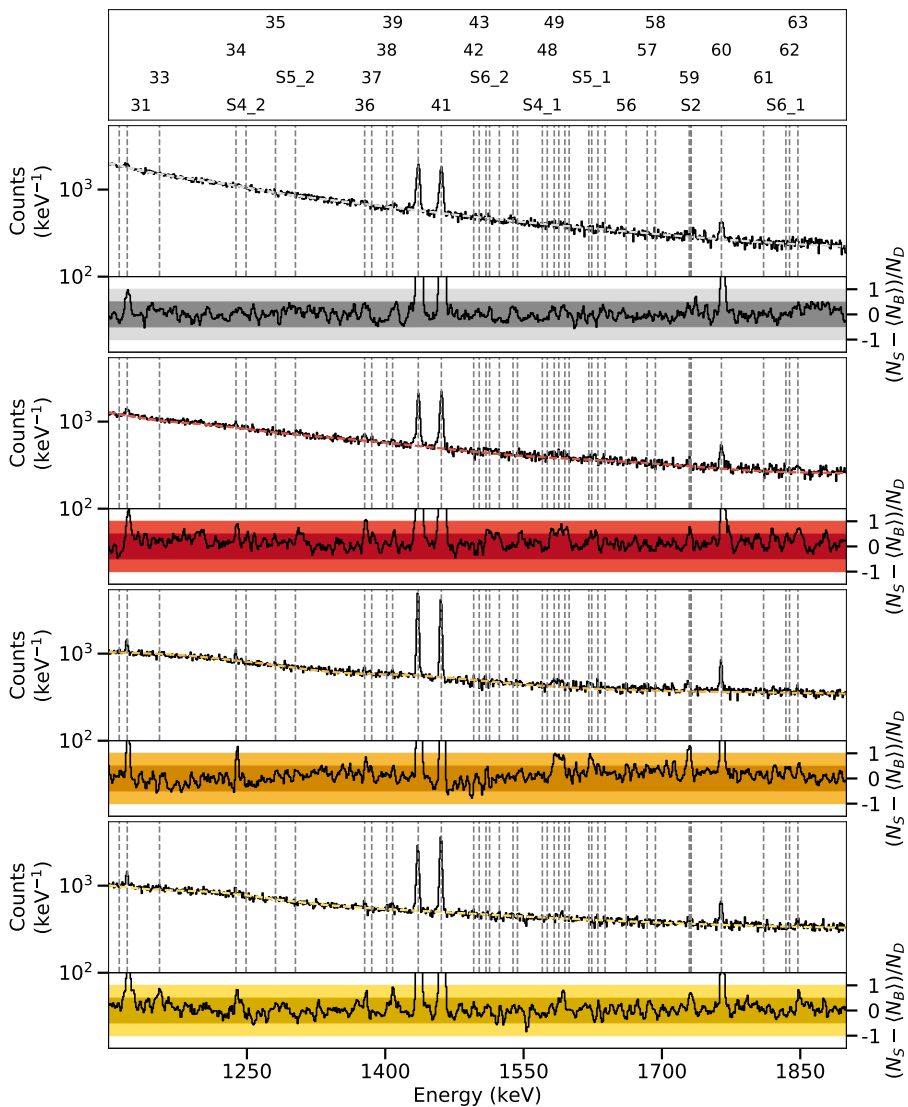


Figure D.51.: Spectra of the ^{82}Se target in the γ^3 setup at a beam energy of 3.10 MeV between 1100 keV and 1900 keV.

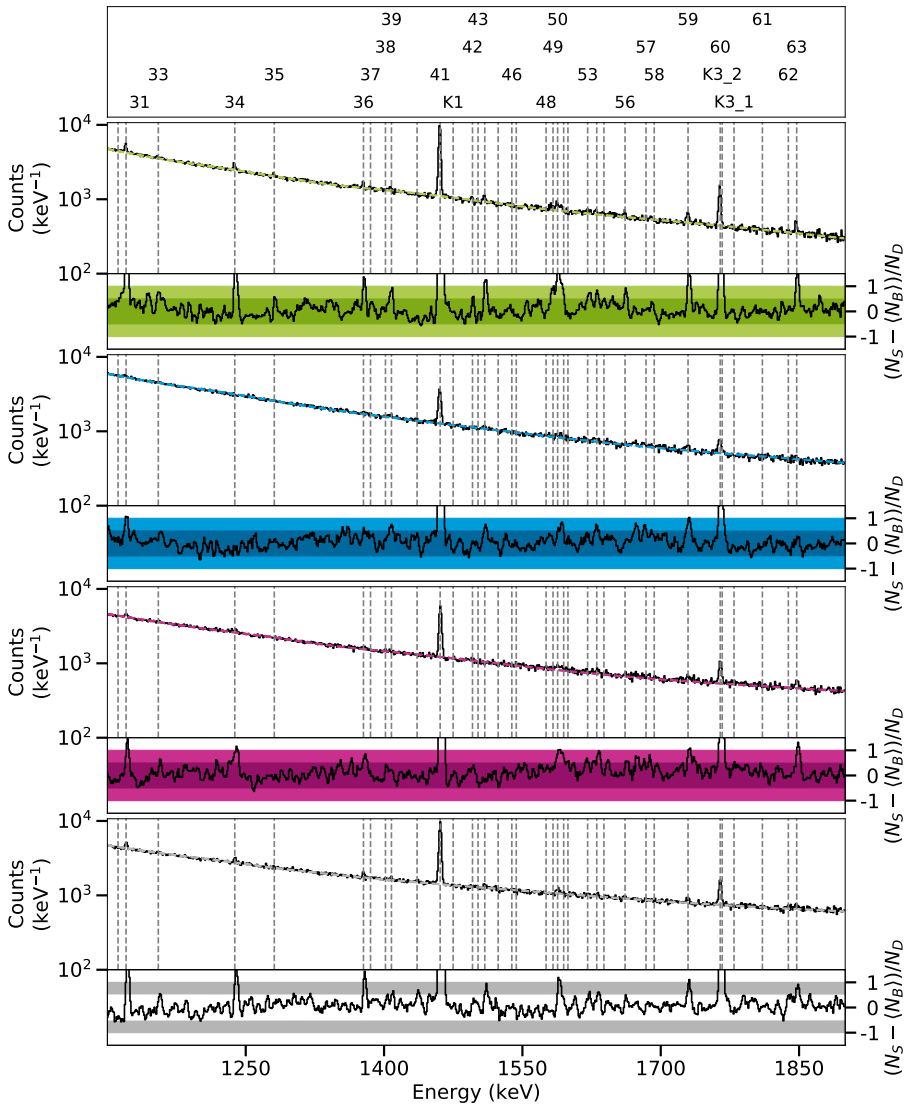


Figure D.52.: Spectra of the ^{82}Kr target in the polarimetry setup at a beam energy of 3.10 MeV between 1100 keV and 1900 keV.

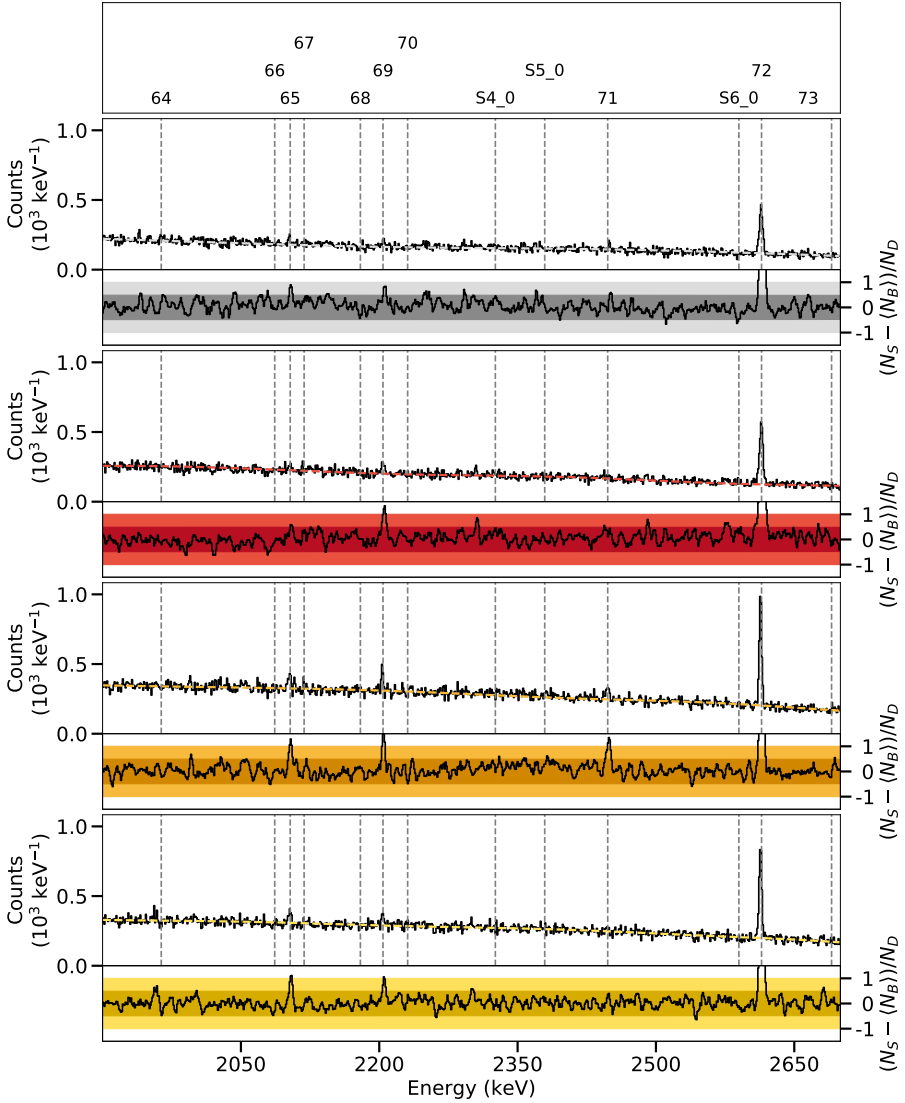


Figure D.53.: Spectra of the ^{82}Se target in the γ^3 setup at a beam energy of 3.10 MeV between 1900 keV and 2700 keV.

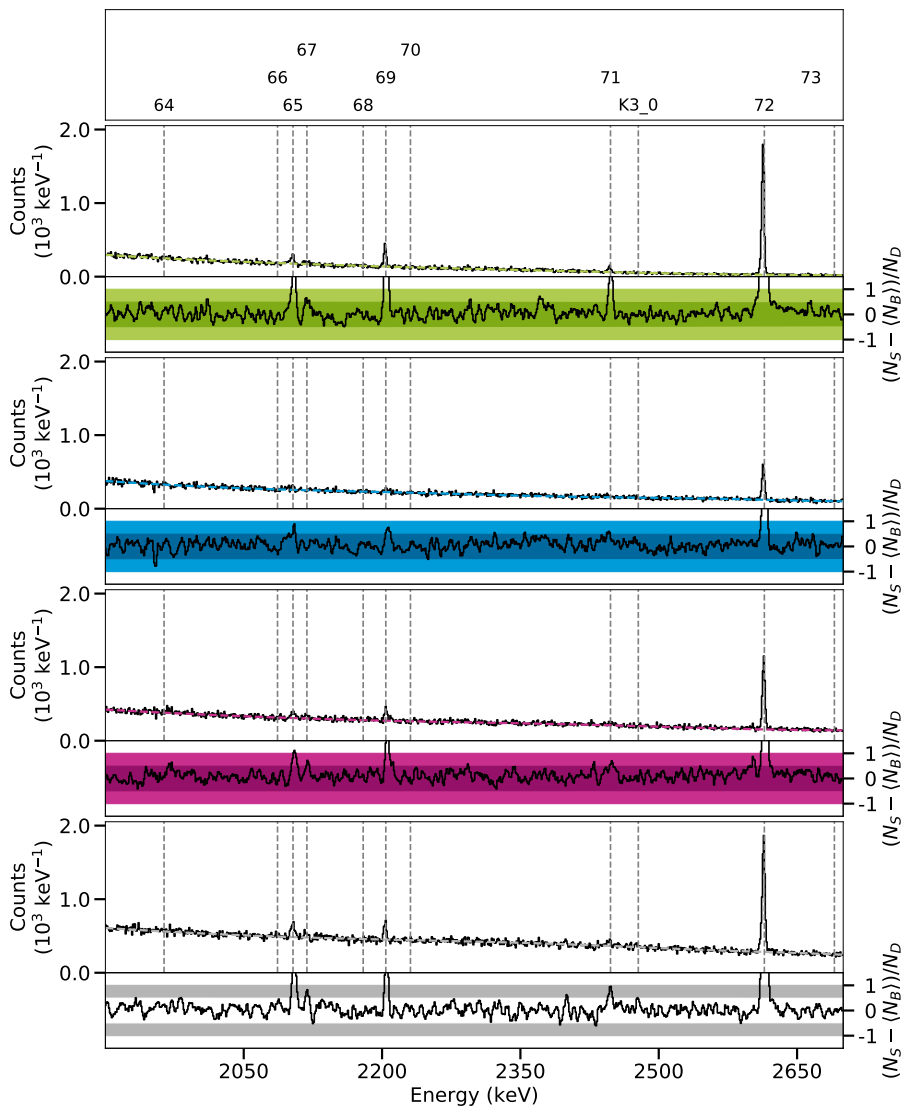


Figure D.54.: Spectra of the ^{82}Kr target in the polarimetry setup at a beam energy of 3.10 MeV between 1900 keV and 2700 keV.

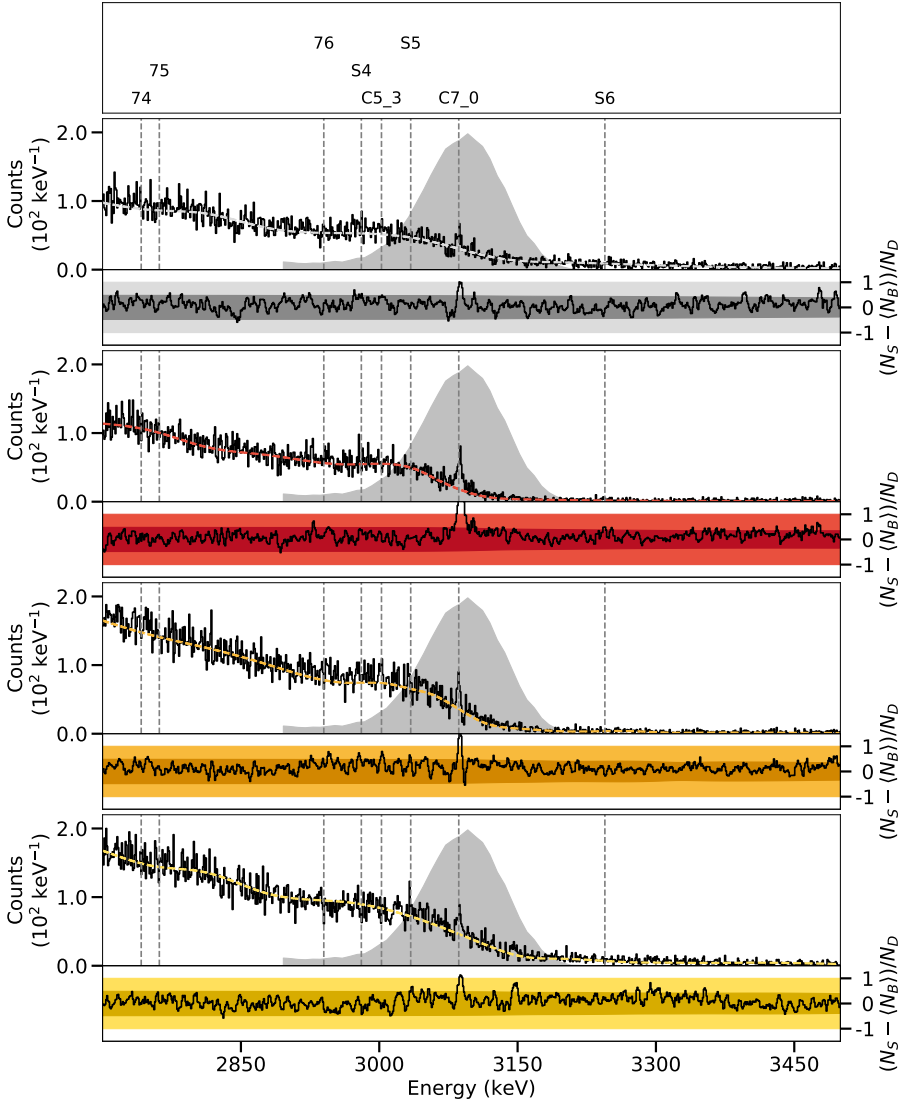


Figure D.55.: Spectra of the ^{82}Se target in the γ^3 setup at a beam energy of 3.10 MeV between 2700 keV and 3500 keV.

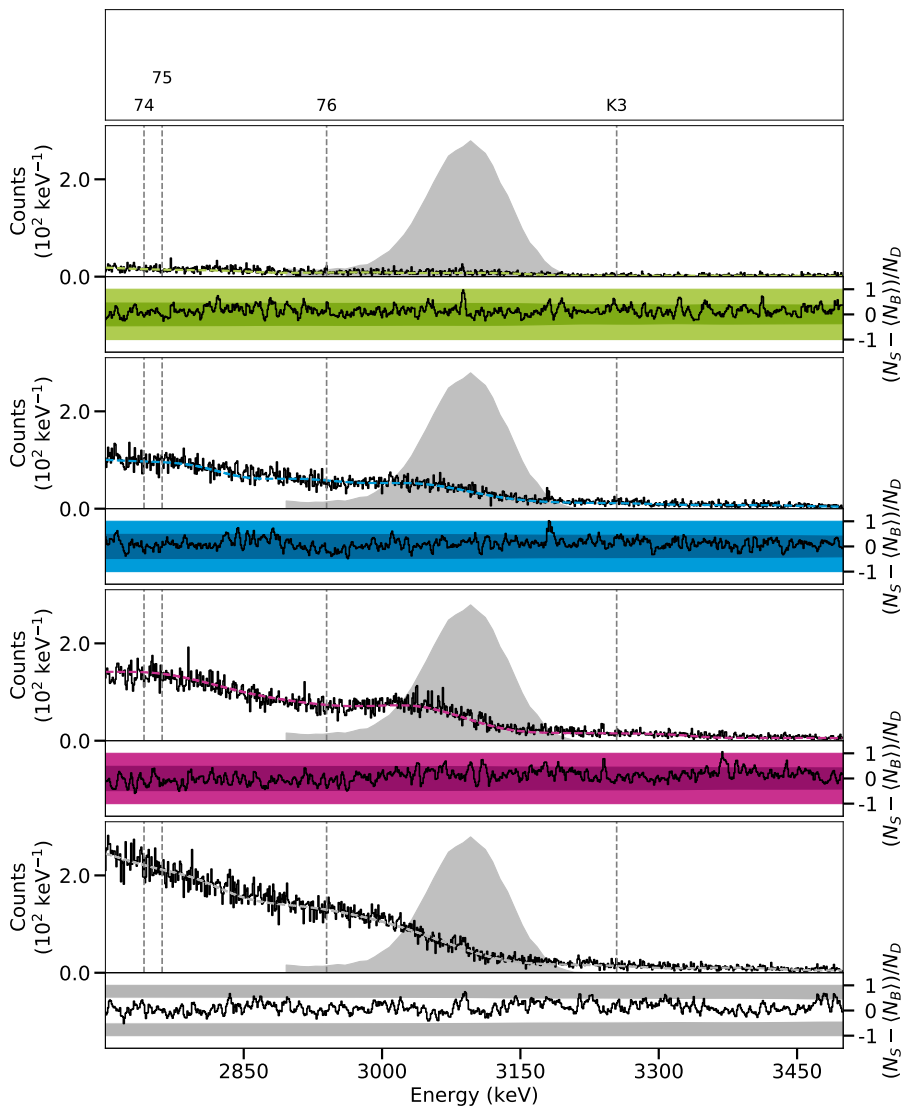


Figure D.56.: Spectra of the ^{82}Kr target in the polarimetry setup at a beam energy of 3.10 MeV between 2700 keV and 3500 keV.

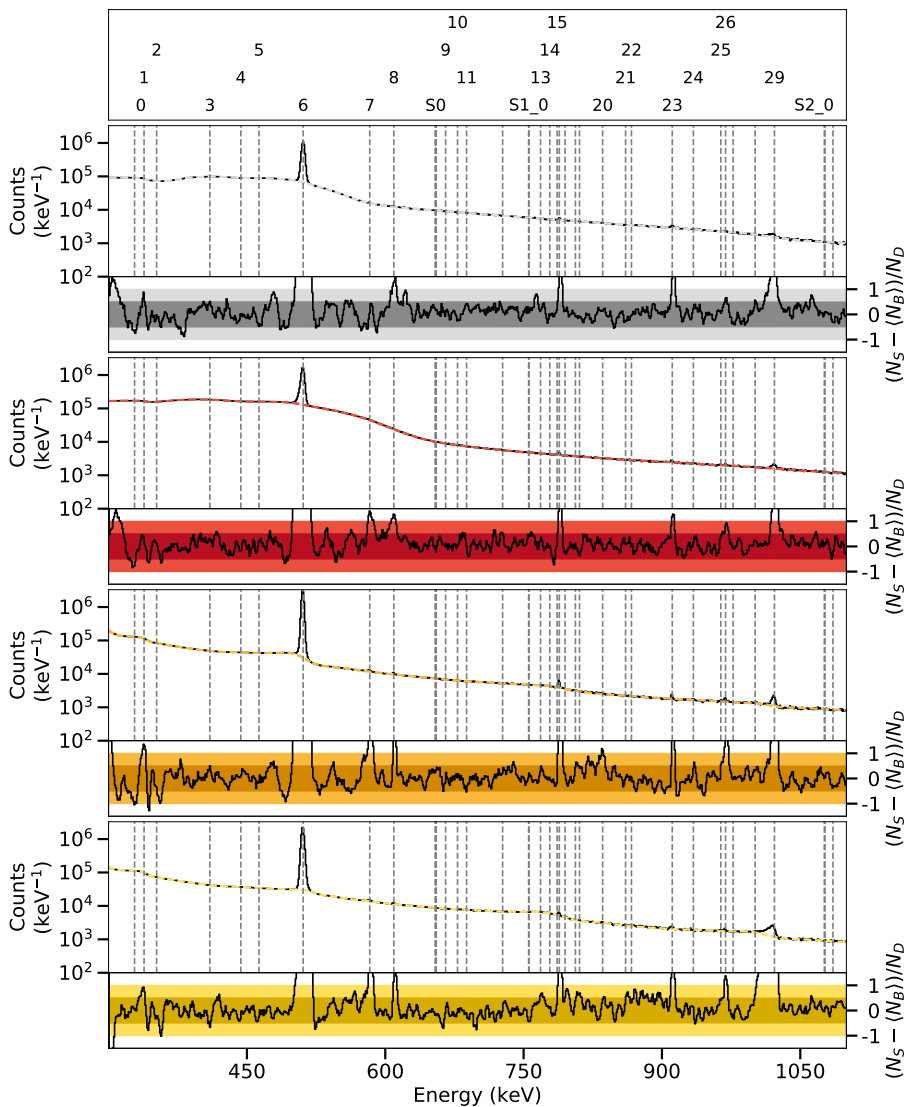


Figure D.57.: Spectra of the ^{82}Se target in the γ^3 setup at a beam energy of 3.20 MeV between 300 keV and 1100 keV.

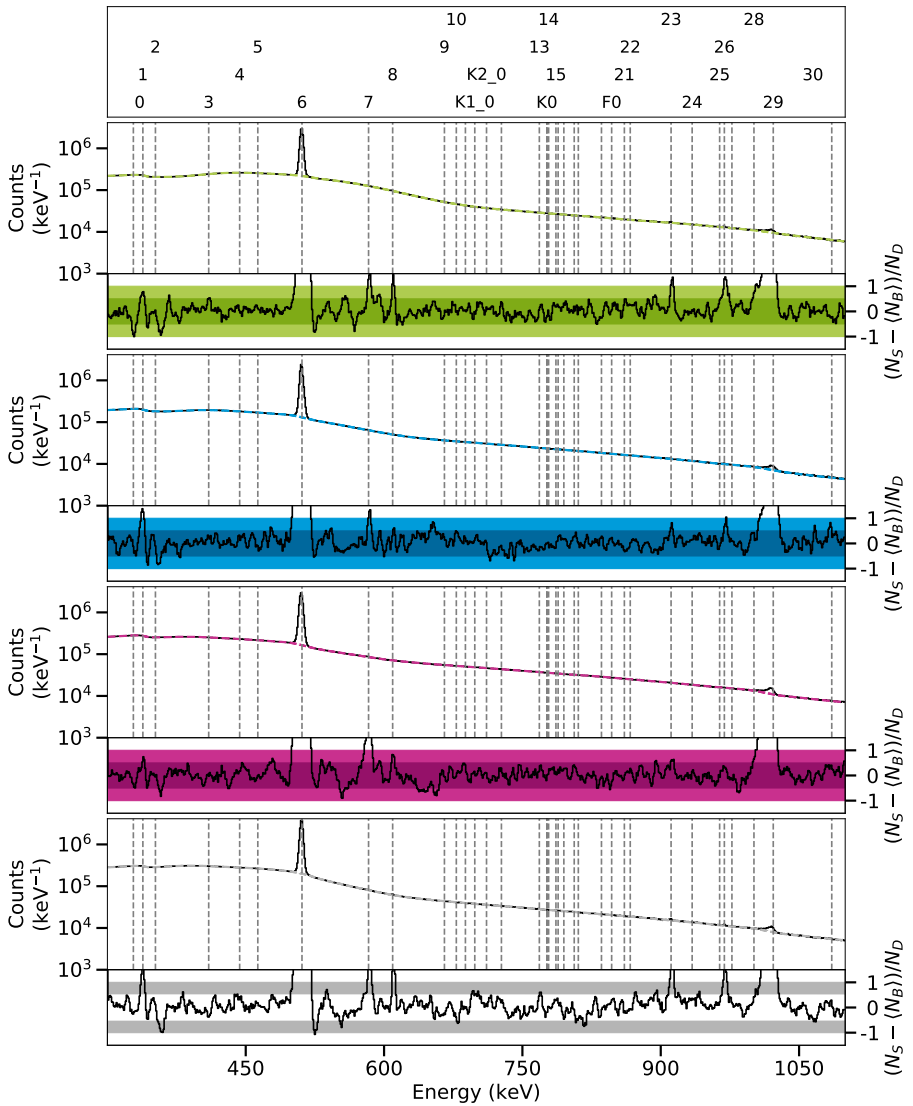


Figure D.58.: Spectra of the ^{82}Kr target in the polarimetry setup at a beam energy of 3.20 MeV between 300 keV and 1100 keV.

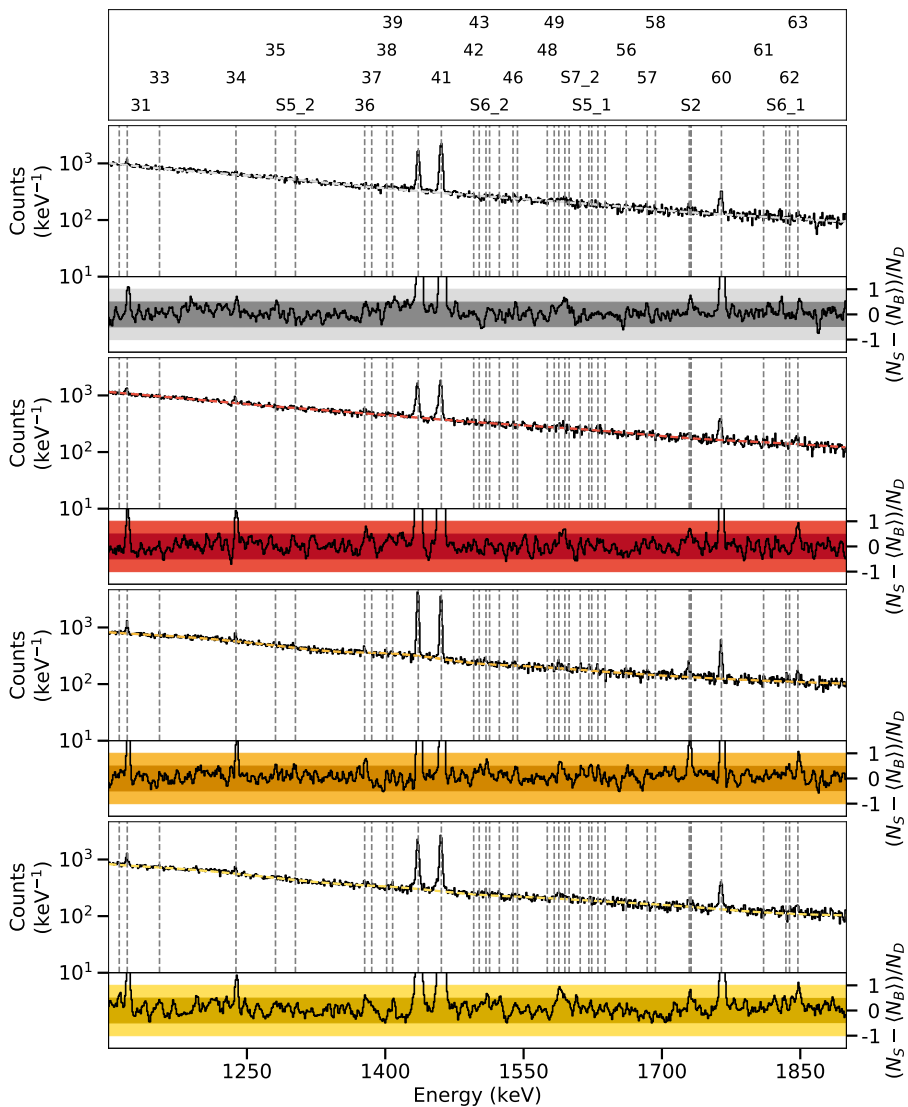


Figure D.59.: Spectra of the ^{82}Se target in the γ^3 setup at a beam energy of 3.20 MeV between 1100 keV and 1900 keV.

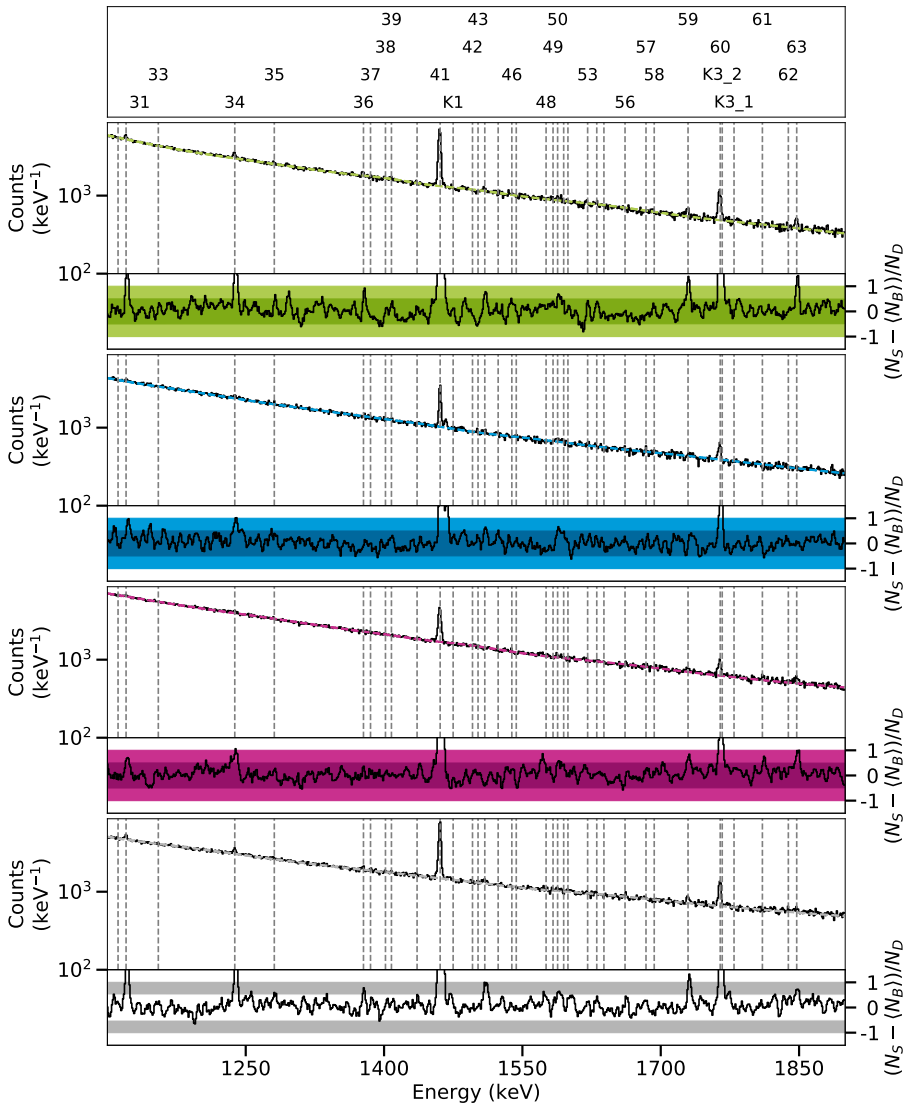


Figure D.60.: Spectra of the ^{82}Kr target in the polarimetry setup at a beam energy of 3.20 MeV between 1100 keV and 1900 keV.

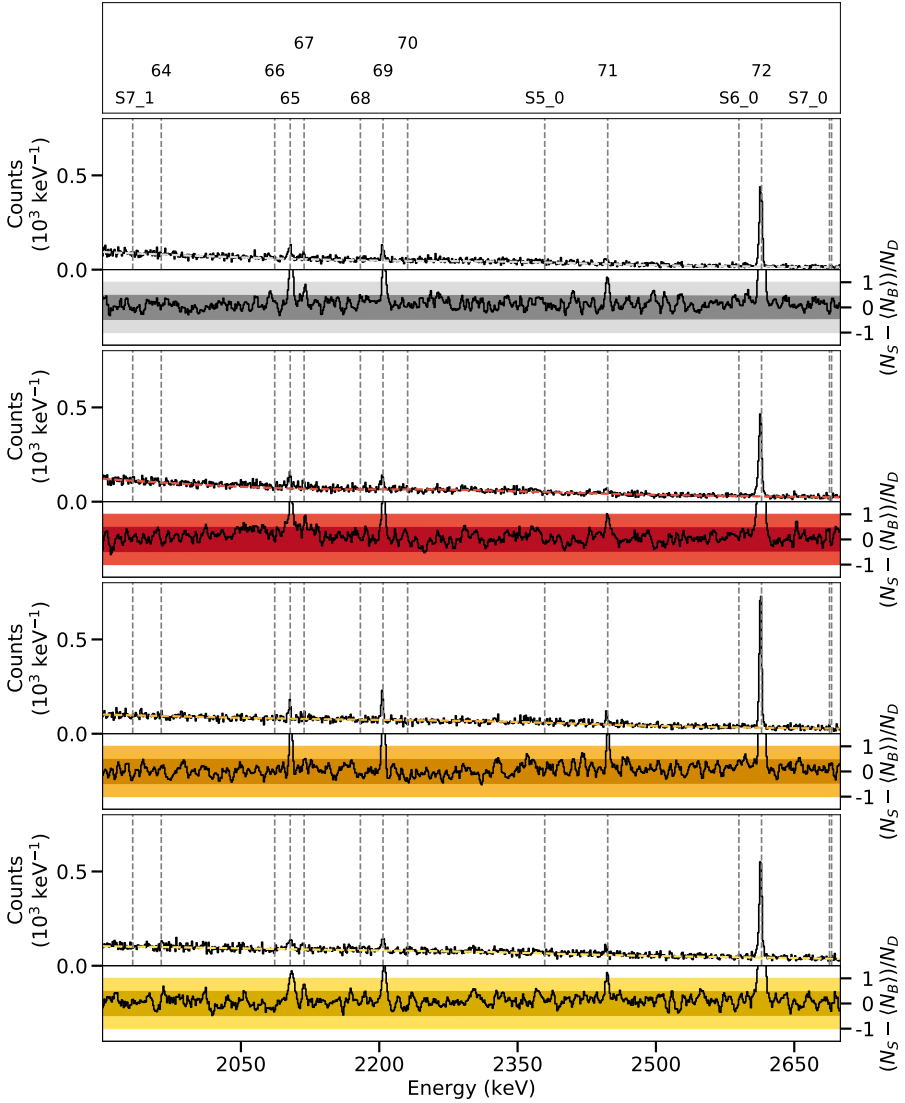


Figure D.61.: Spectra of the ^{82}Se target in the γ^3 setup at a beam energy of 3.20 MeV between 1900 keV and 2700 keV.

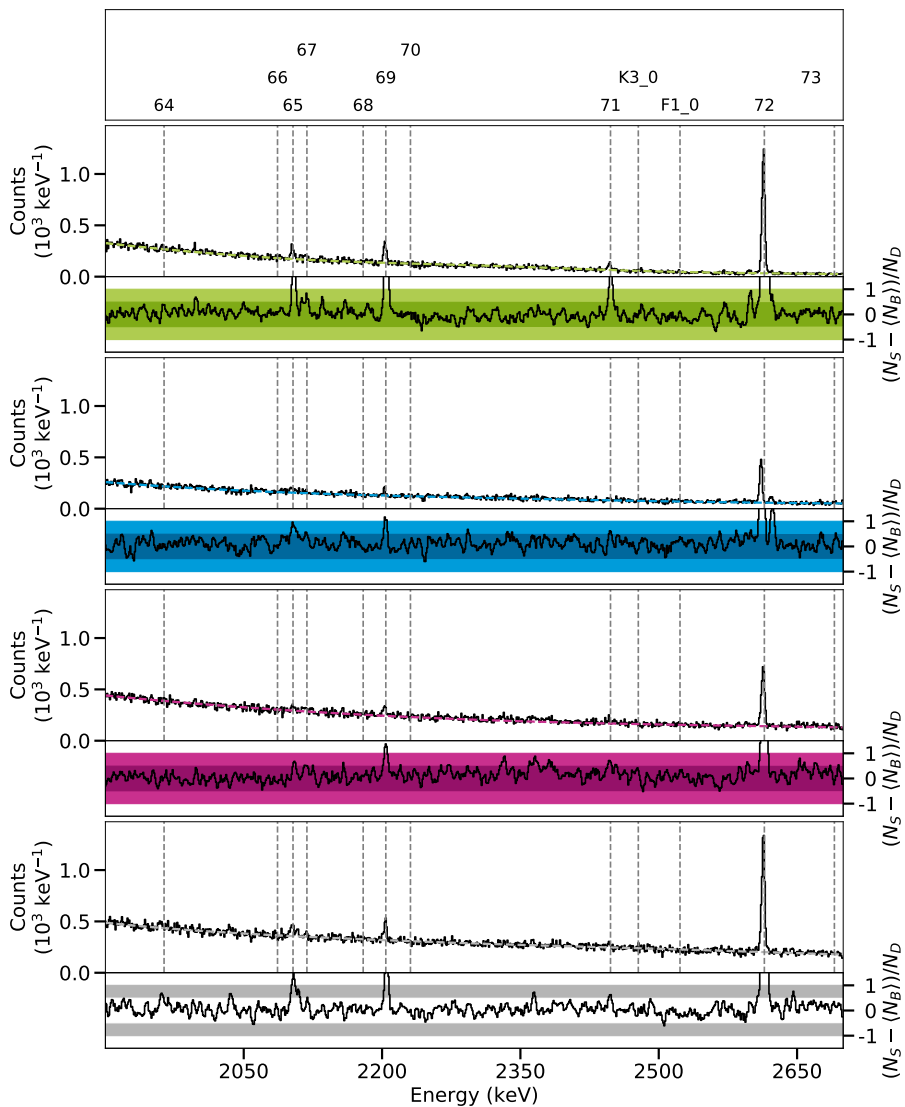


Figure D.62.: Spectra of the ^{82}Kr target in the polarimetry setup at a beam energy of 3.20 MeV between 1900 keV and 2700 keV.

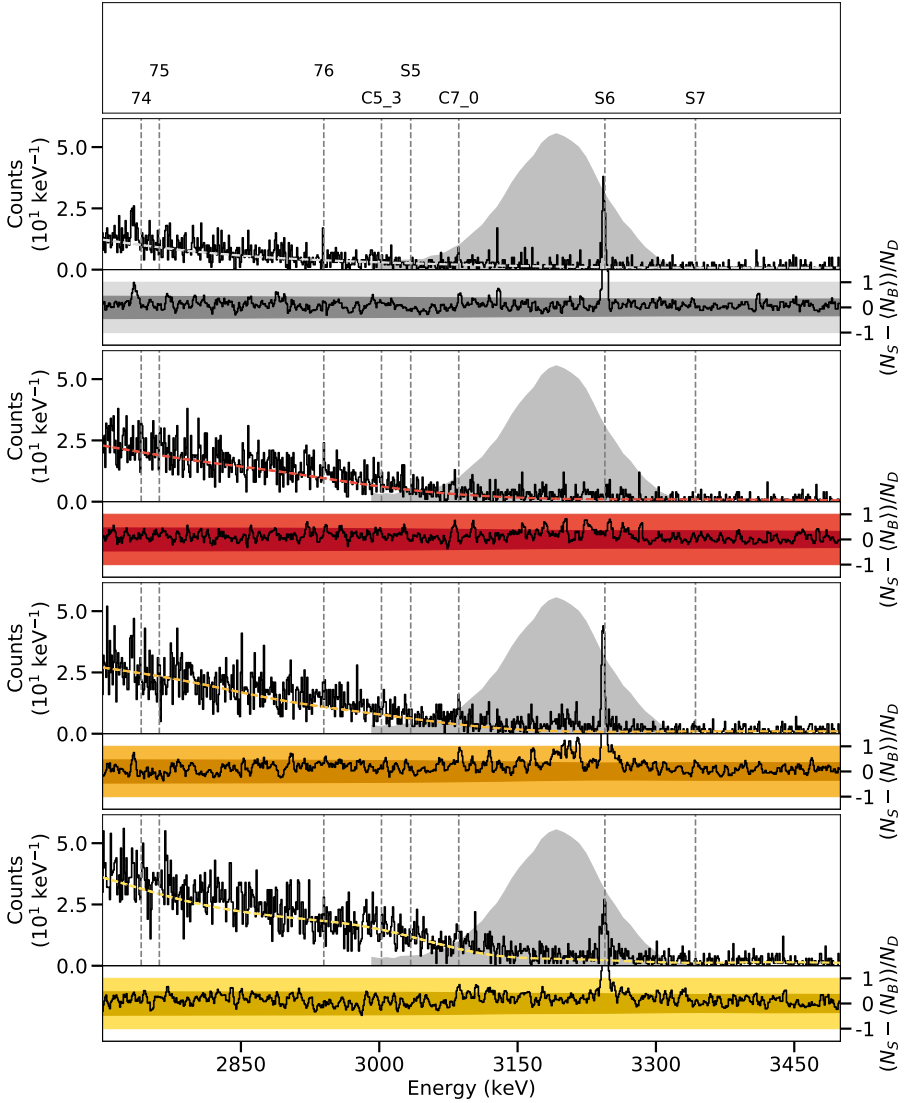


Figure D.63.: Spectra of the ^{82}Se target in the γ^3 setup at a beam energy of 3.20 MeV between 2700 keV and 3500 keV.

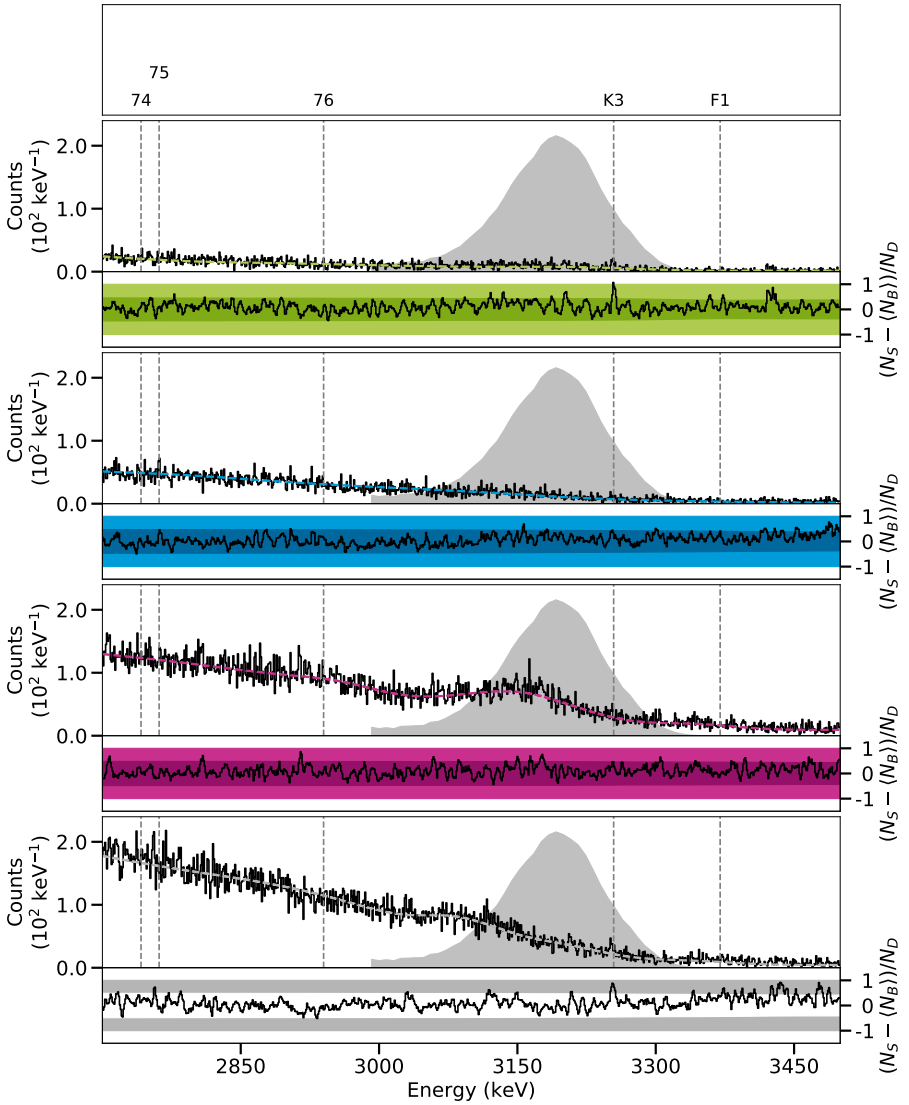


Figure D.64.: Spectra of the ^{82}Kr target in the polarimetry setup at a beam energy of 3.20 MeV between 2700 keV and 3500 keV.

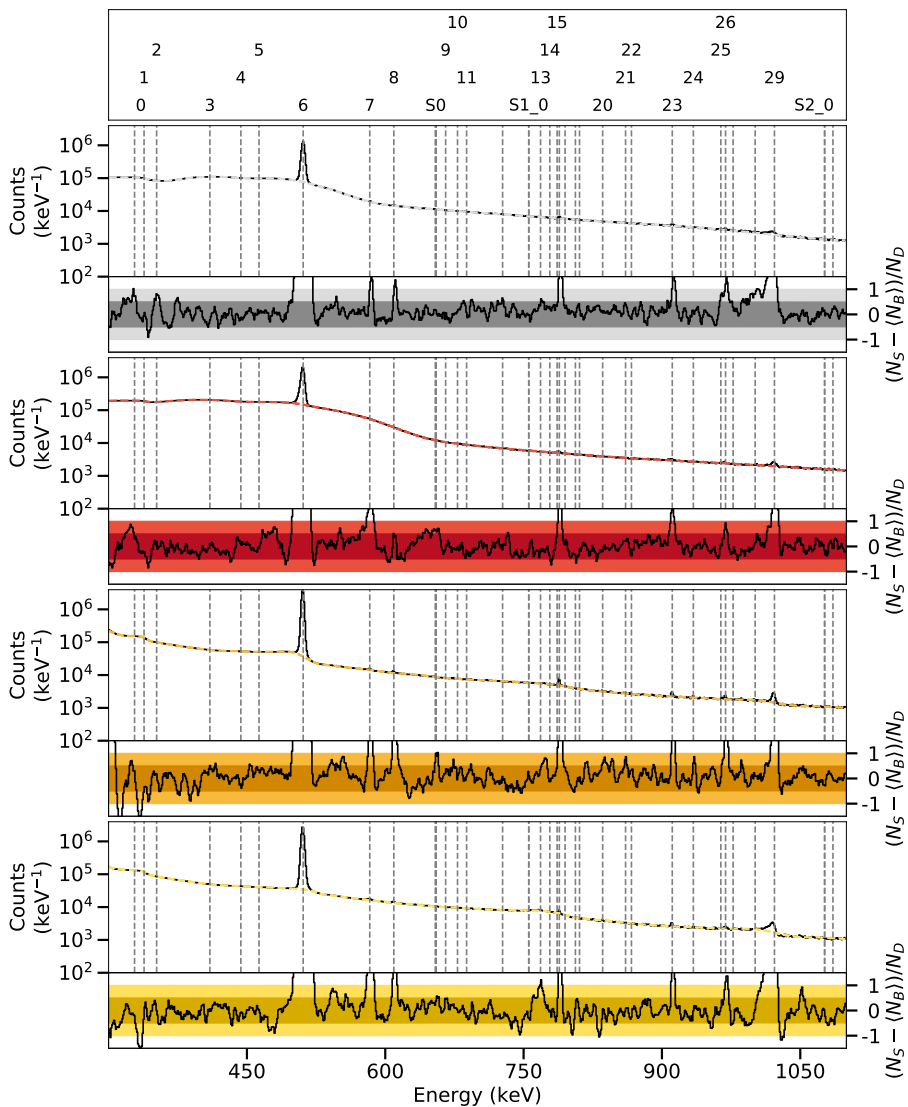


Figure D.65.: Spectra of the ^{82}Se target in the γ^3 setup at a beam energy of 3.35 MeV between 300 keV and 1100 keV.

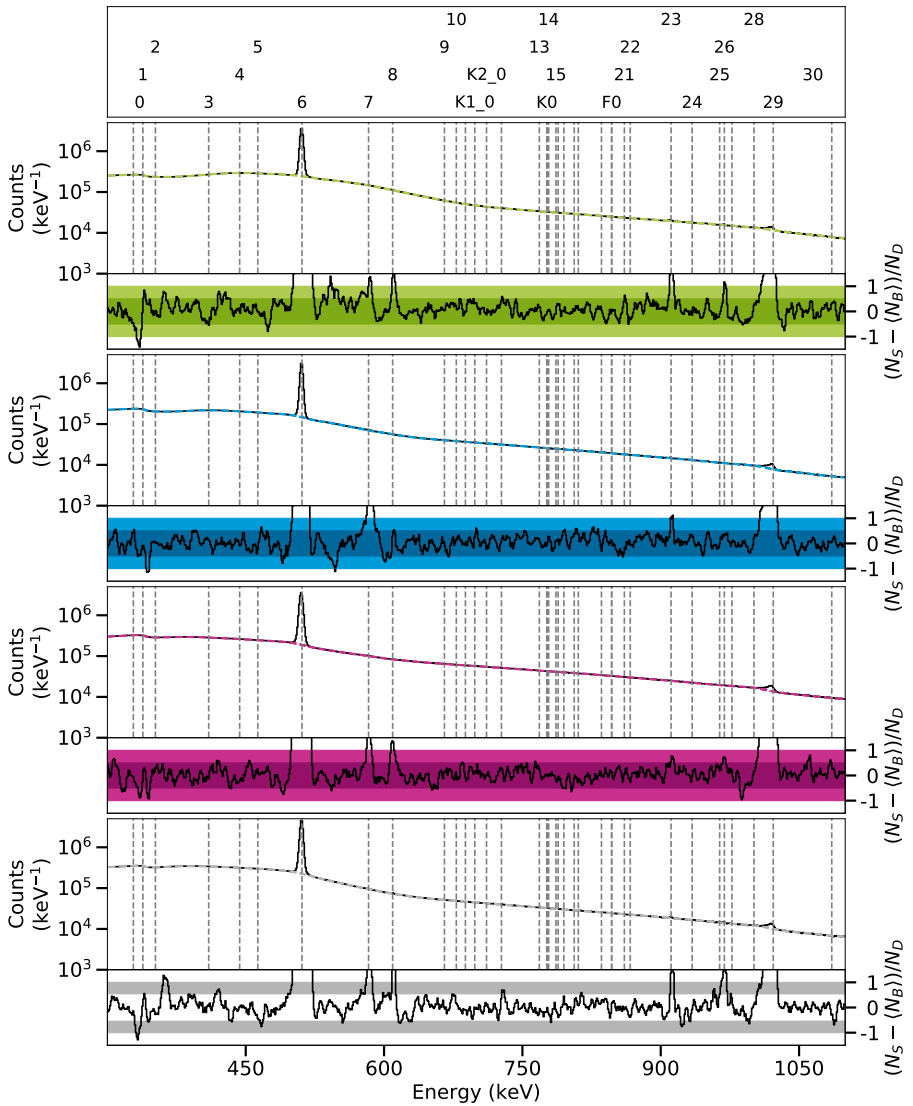


Figure D.66.: Spectra of the ^{82}Kr target in the polarimetry setup at a beam energy of 3.35 MeV between 300 keV and 1100 keV.

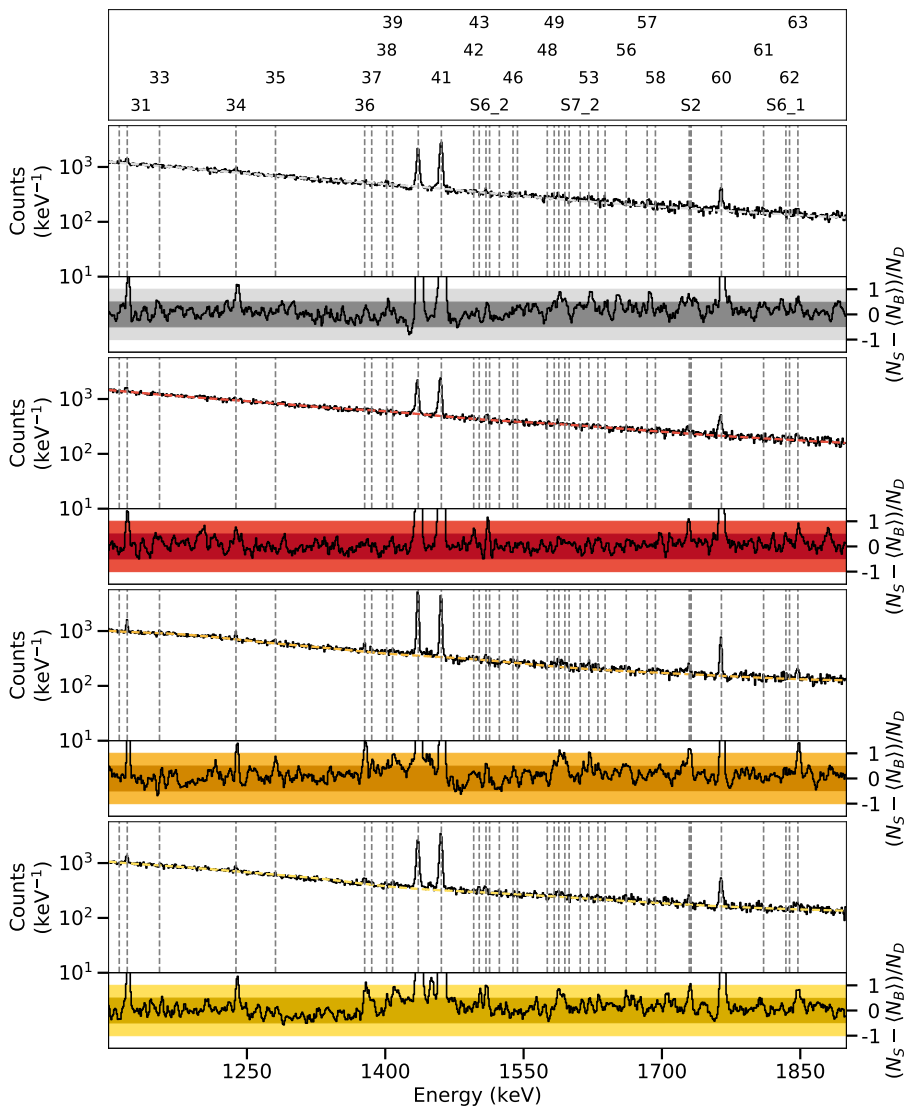


Figure D.67.: Spectra of the ^{82}Se target in the γ^3 setup at a beam energy of 3.35 MeV between 1100 keV and 1900 keV.

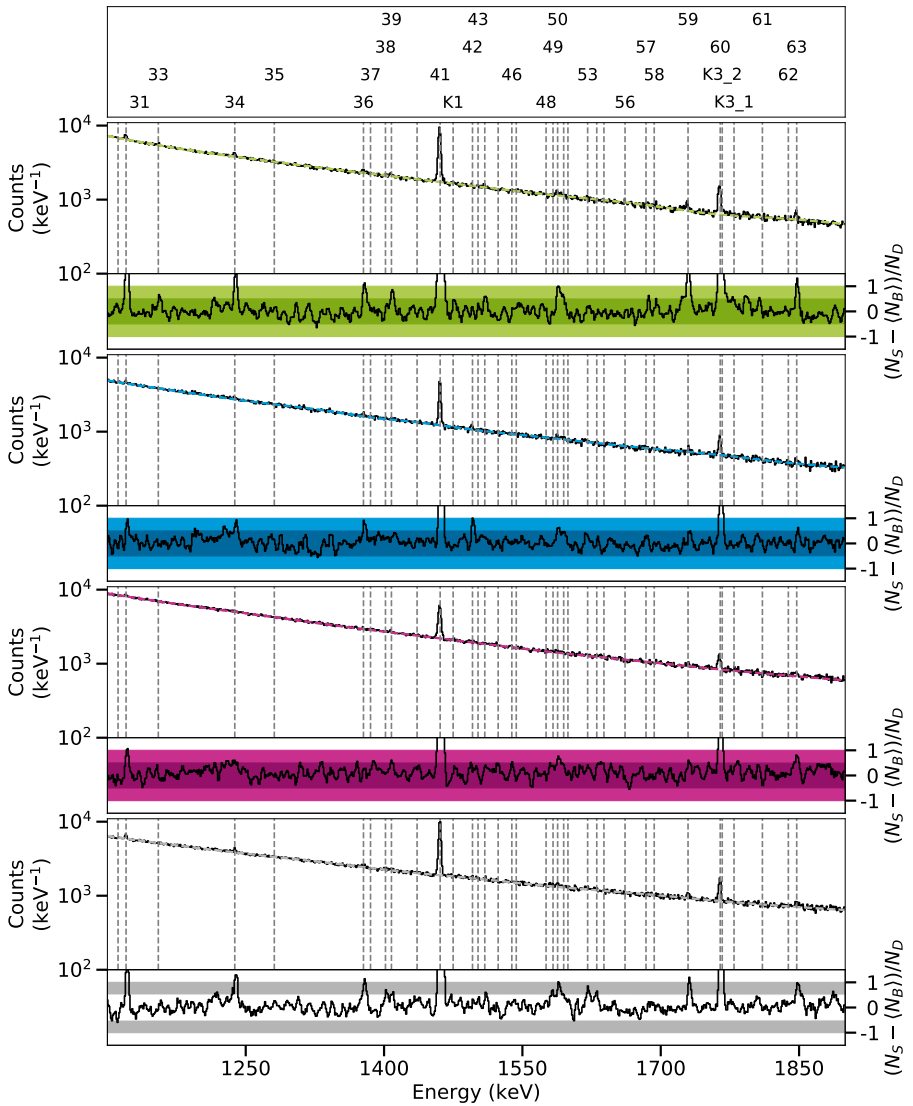


Figure D.68.: Spectra of the ^{82}Kr target in the polarimetry setup at a beam energy of 3.35 MeV between 1100 keV and 1900 keV.

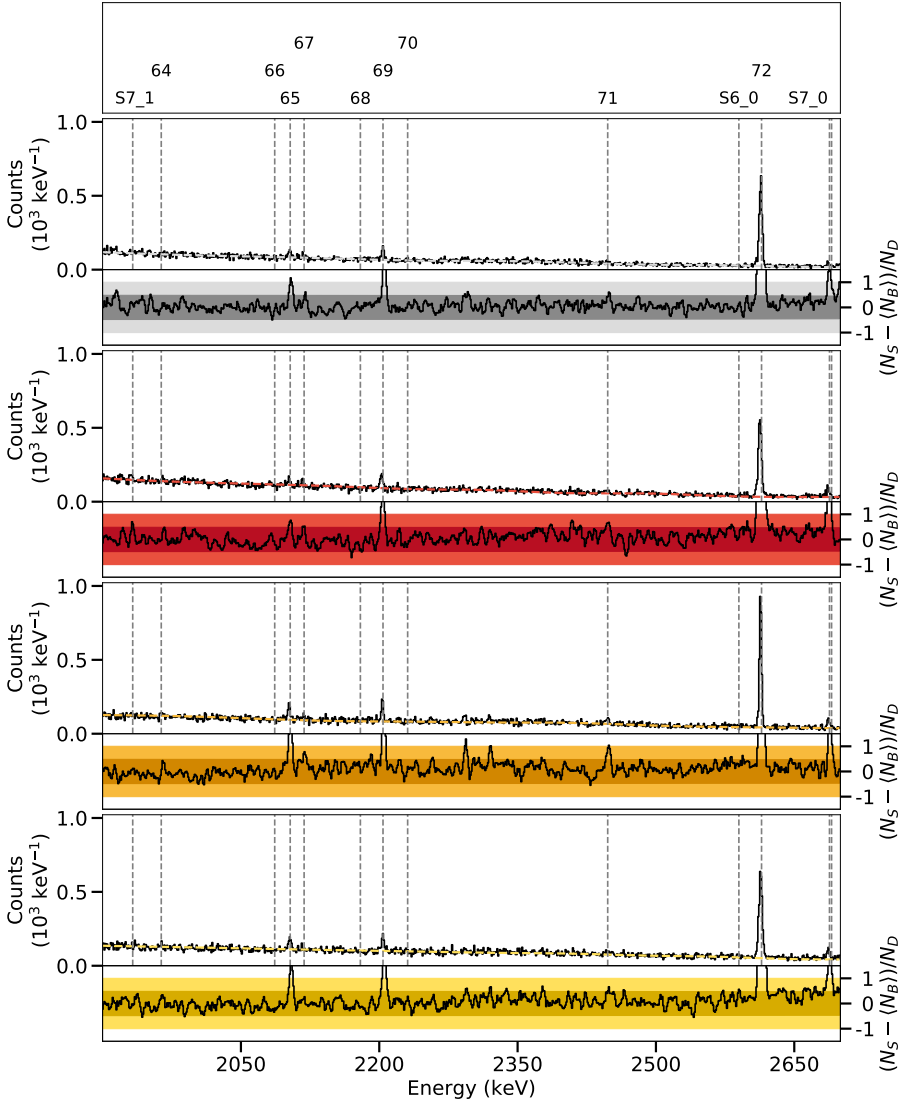


Figure D.69.: Spectra of the ^{82}Se target in the γ^3 setup at a beam energy of 3.35 MeV between 1900 keV and 2700 keV.

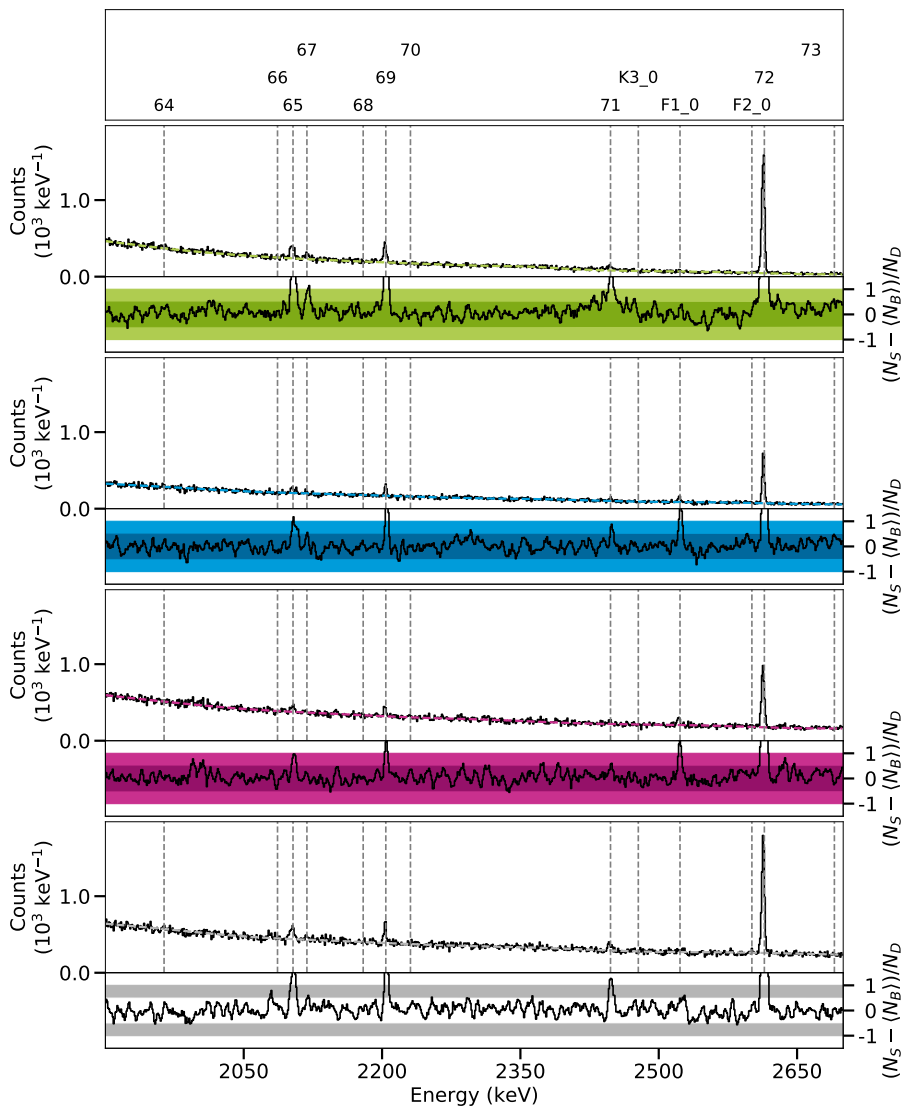


Figure D.70.: Spectra of the ^{82}Kr target in the polarimetry setup at a beam energy of 3.35 MeV between 1900 keV and 2700 keV.

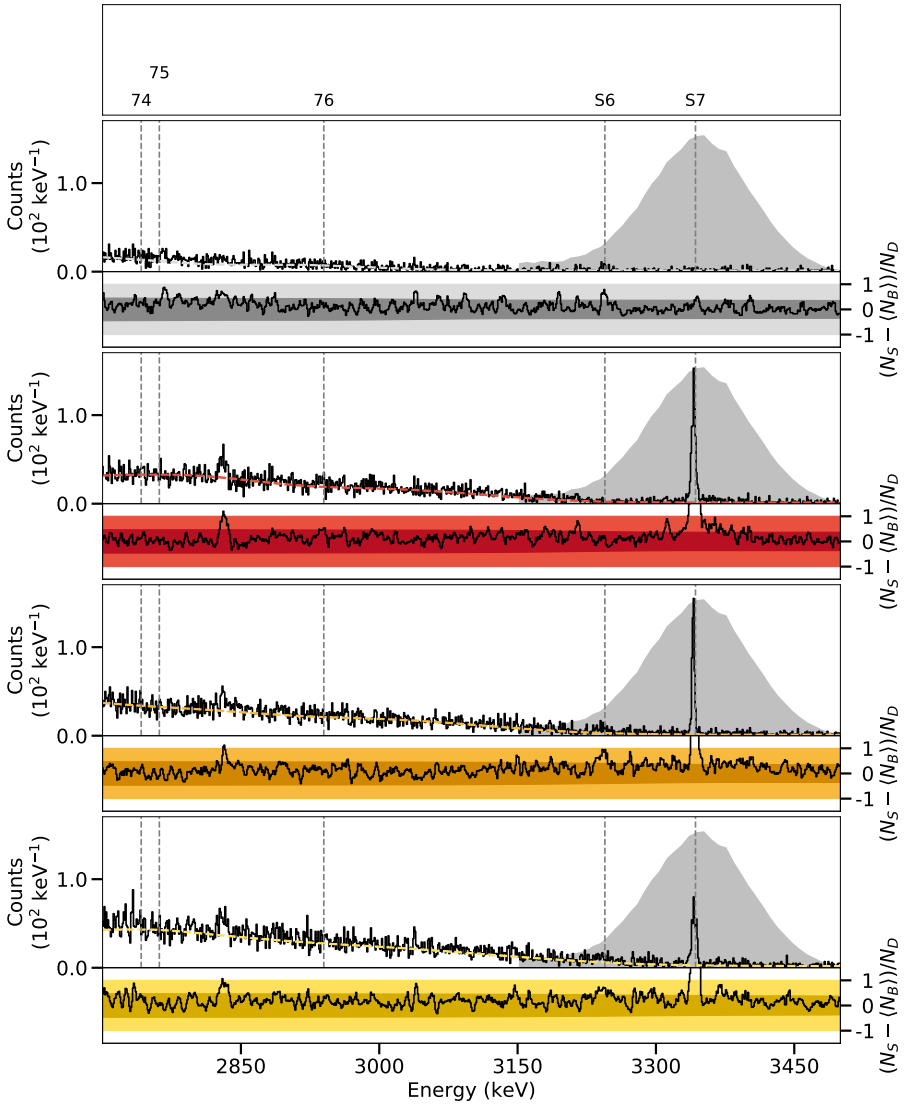


Figure D.71.: Spectra of the ^{82}Se target in the γ^3 setup at a beam energy of 3.35 MeV between 2700 keV and 3500 keV.

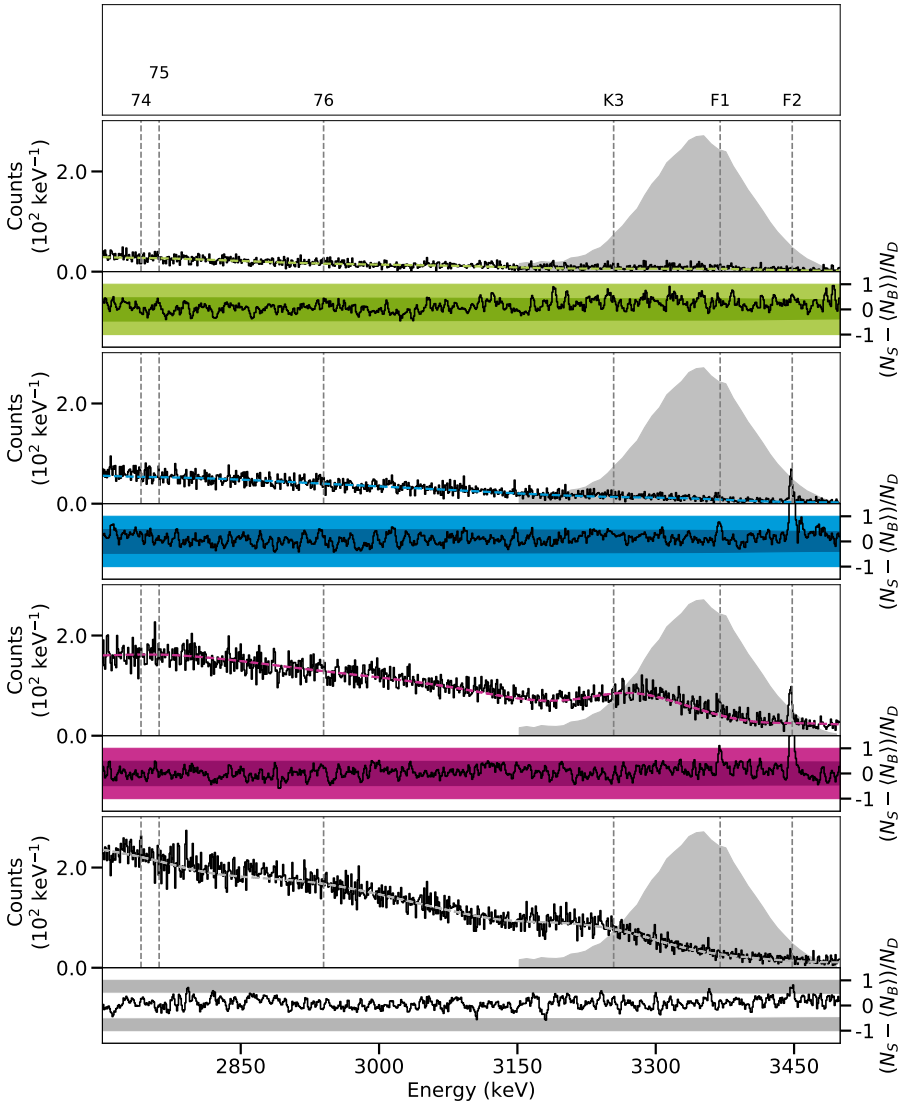


Figure D.72.: Spectra of the ^{82}Kr target in the polarimetry setup at a beam energy of 3.35 MeV between 2700 keV and 3500 keV.

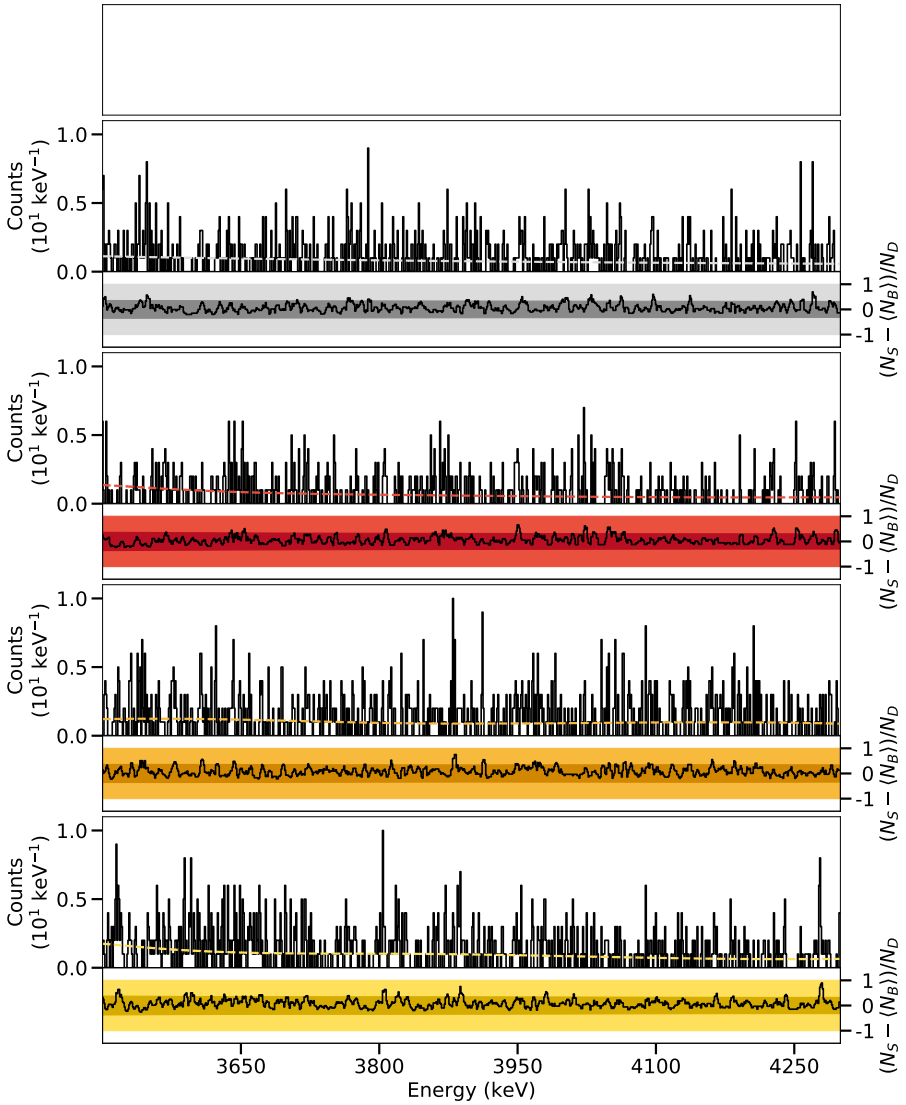


Figure D.73.: Spectra of the ^{82}Se target in the γ^3 setup at a beam energy of 3.35 MeV between 3500 keV and 4300 keV.

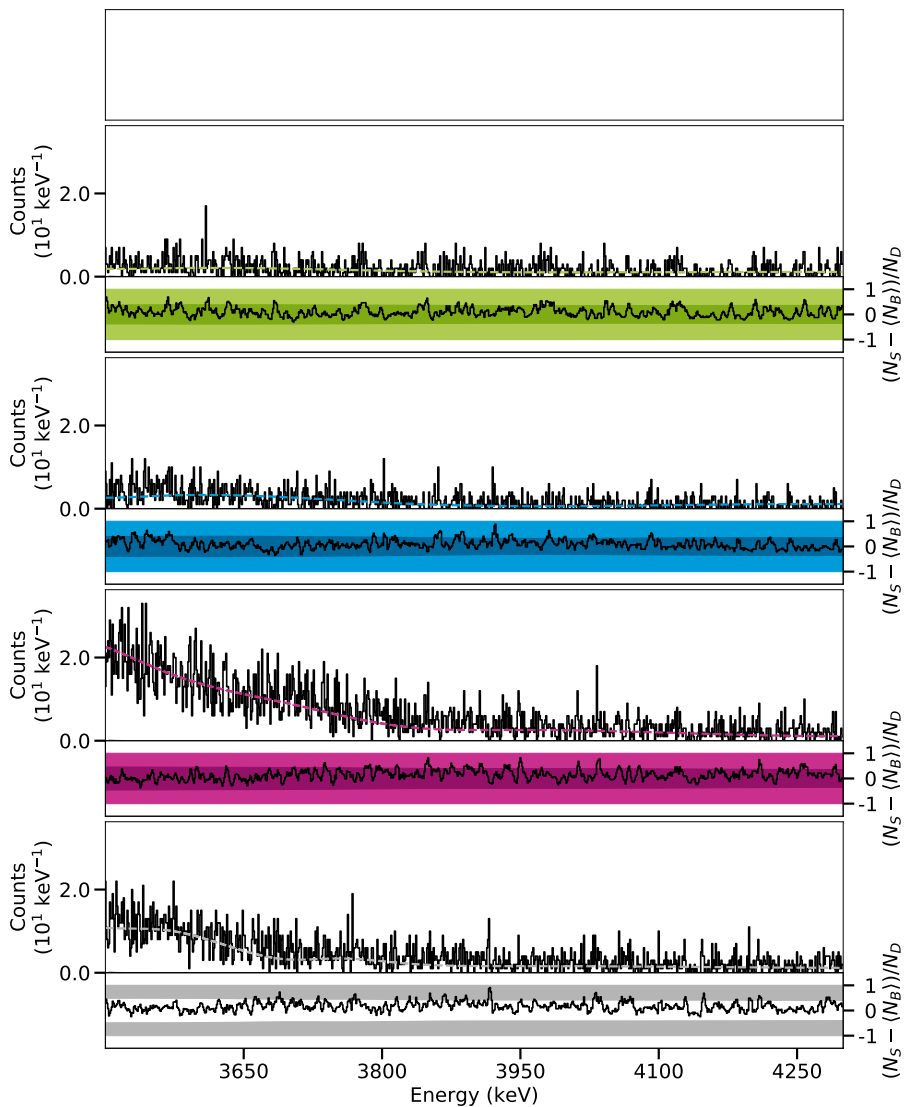


Figure D.74.: Spectra of the ^{82}Kr target in the polarimetry setup at a beam energy of 3.35 MeV between 3500 keV and 4300 keV.

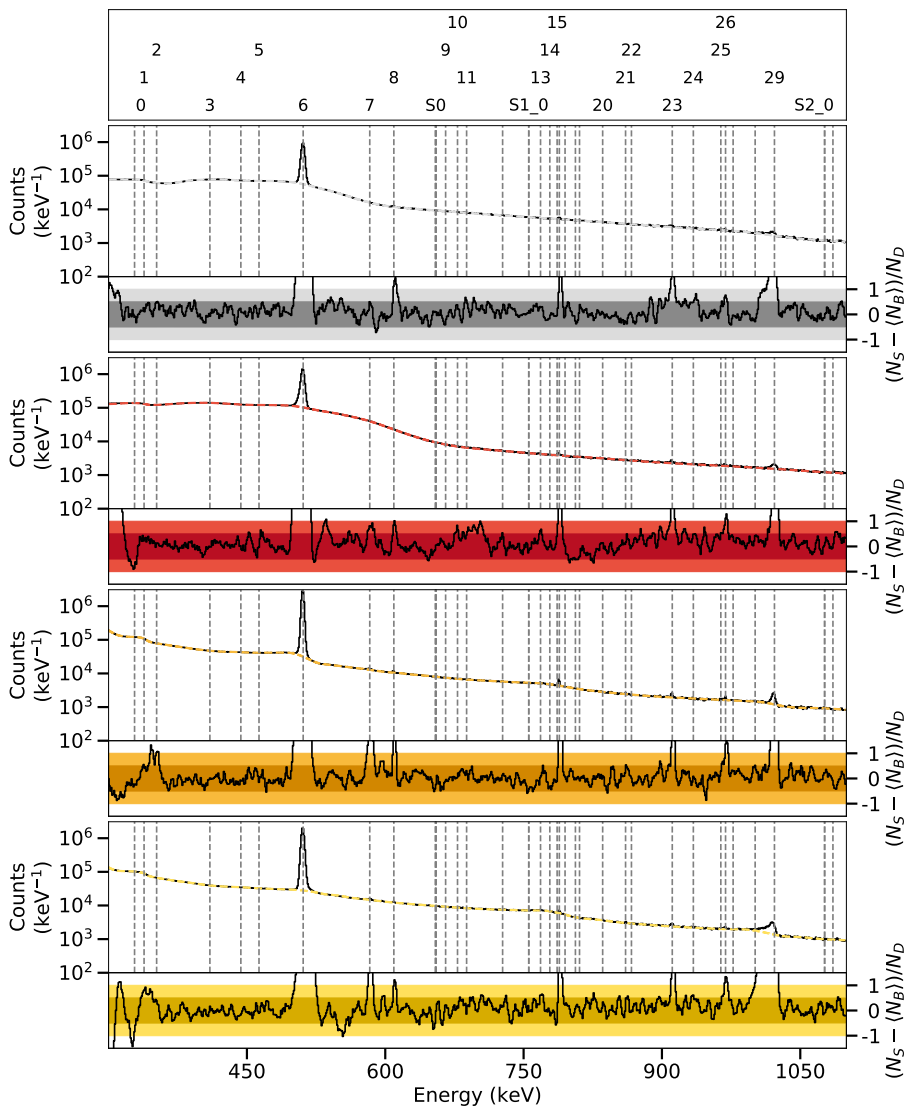


Figure D.75.: Spectra of the ^{82}Se target in the γ^3 setup at a beam energy of 3.50 MeV between 300 keV and 1100 keV.

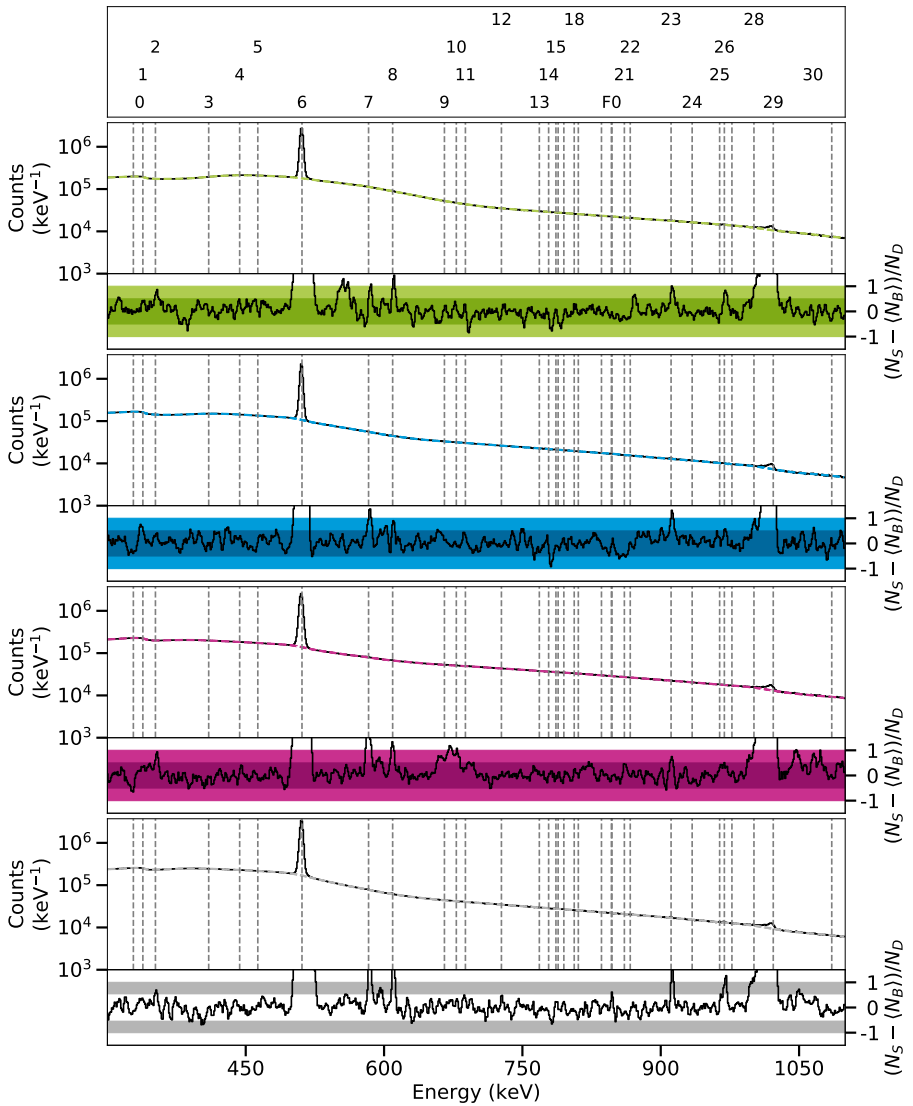


Figure D.76.: Spectra of the ^{82}Kr target in the polarimetry setup at a beam energy of 3.50 MeV between 300 keV and 1100 keV.

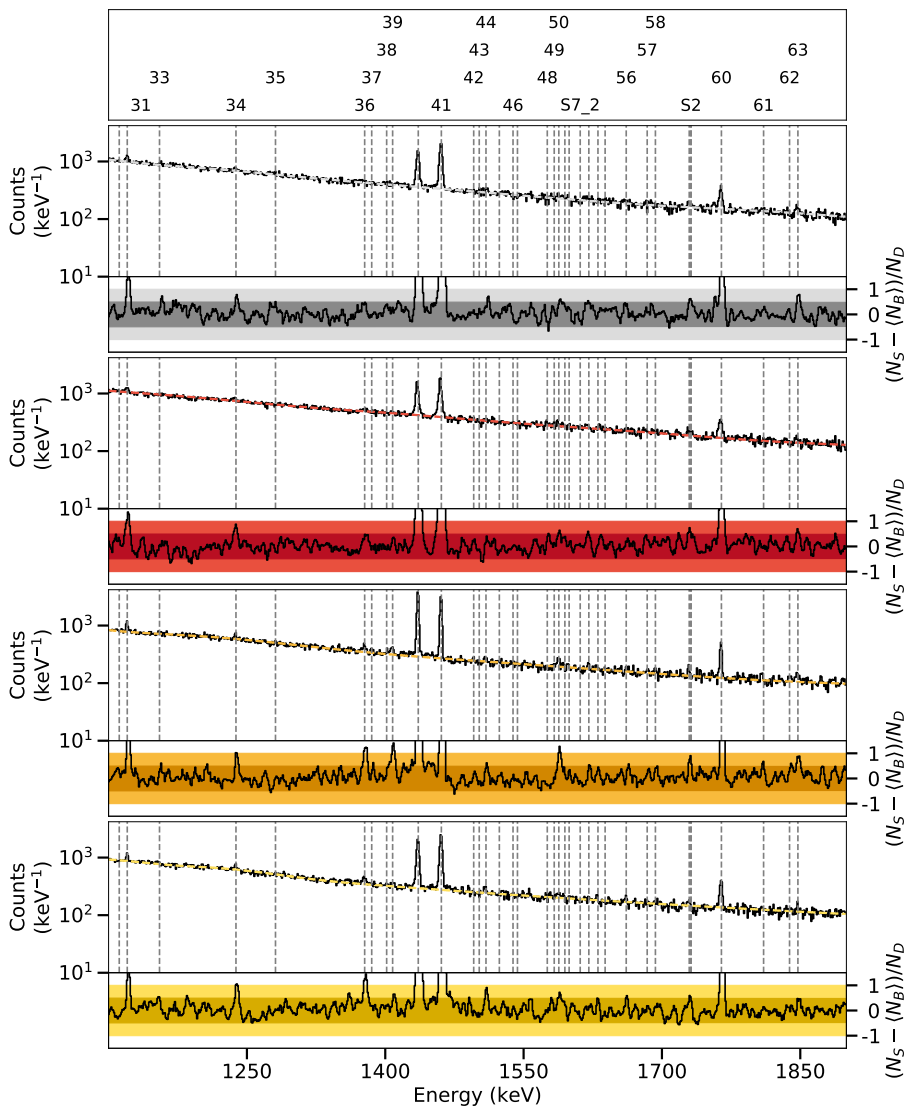


Figure D.77.: Spectra of the ^{82}Se target in the γ^3 setup at a beam energy of 3.50 MeV between 1100 keV and 1900 keV.

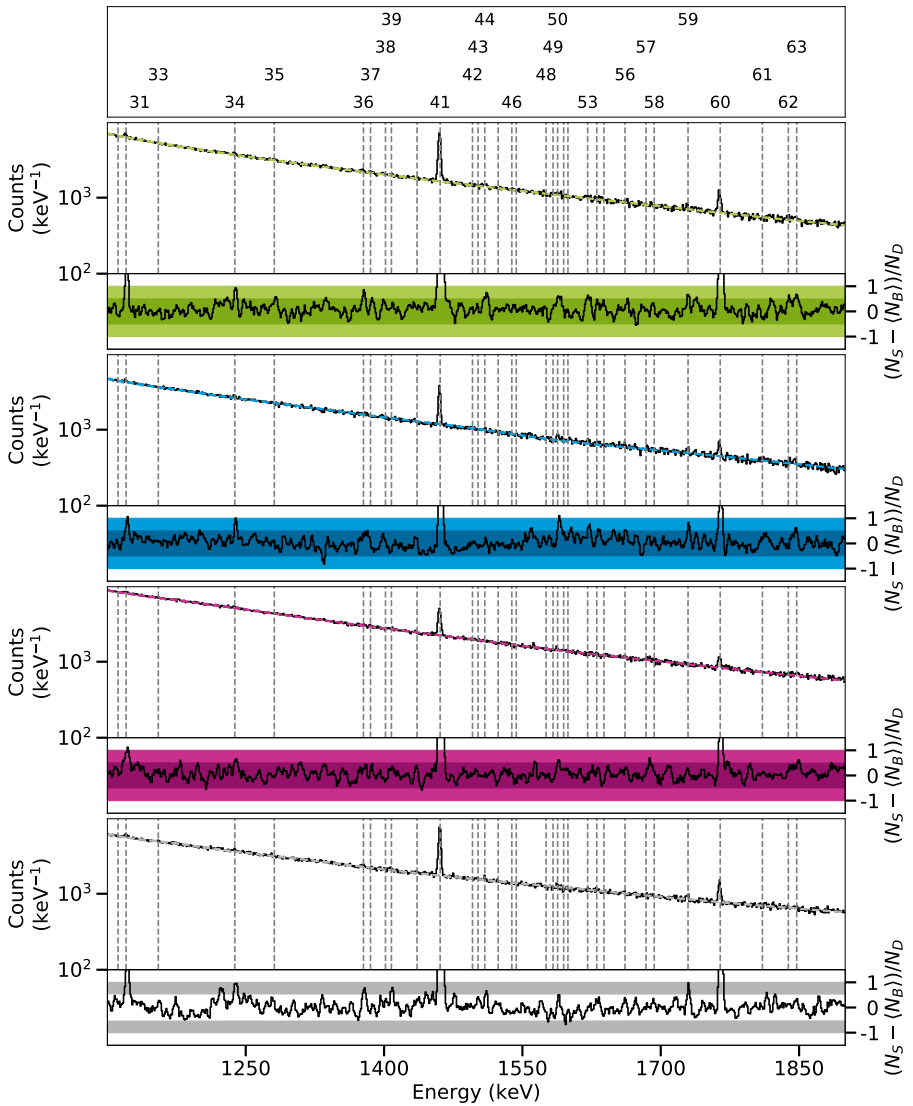


Figure D.78.: Spectra of the ^{82}Kr target in the polarimetry setup at a beam energy of 3.50 MeV between 1100 keV and 1900 keV.

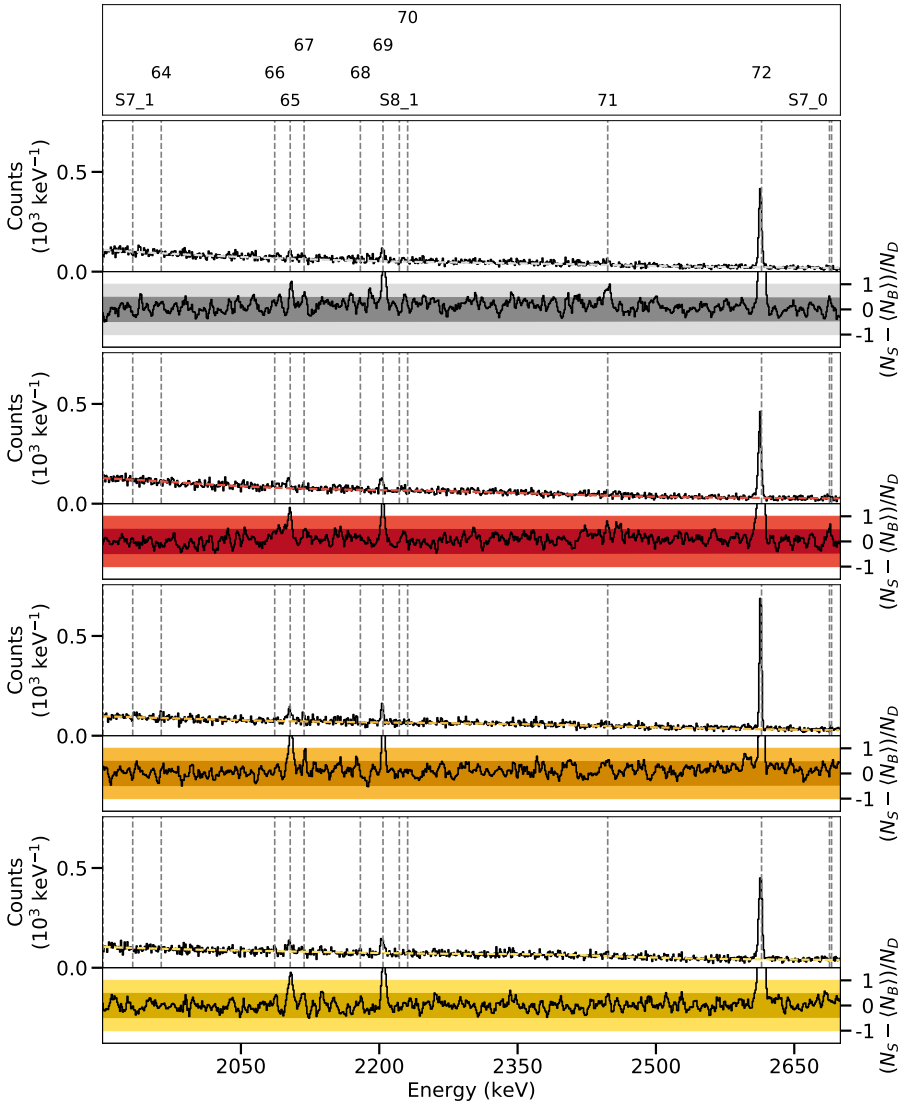


Figure D.79.: Spectra of the ^{82}Se target in the γ^3 setup at a beam energy of 3.50 MeV between 1900 keV and 2700 keV.

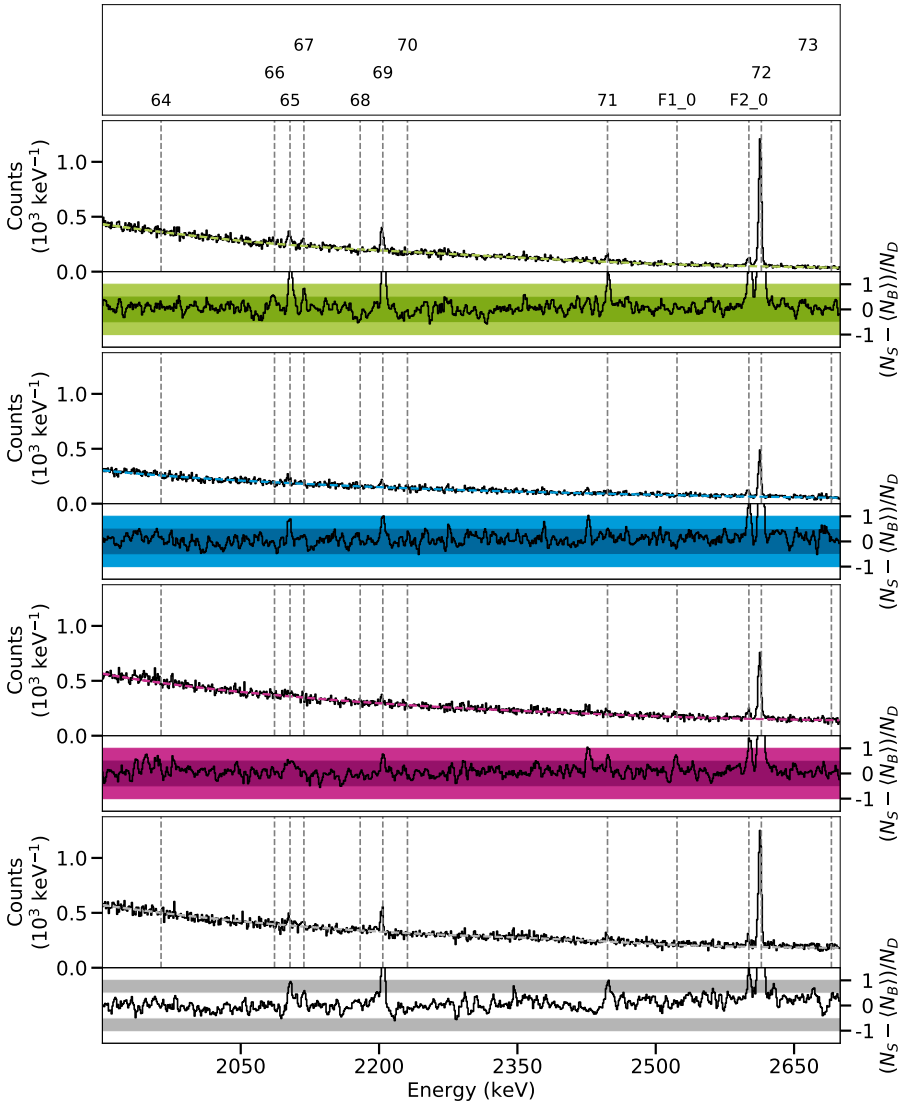


Figure D.80.: Spectra of the ^{82}Kr target in the polarimetry setup at a beam energy of 3.50 MeV between 1900 keV and 2700 keV.

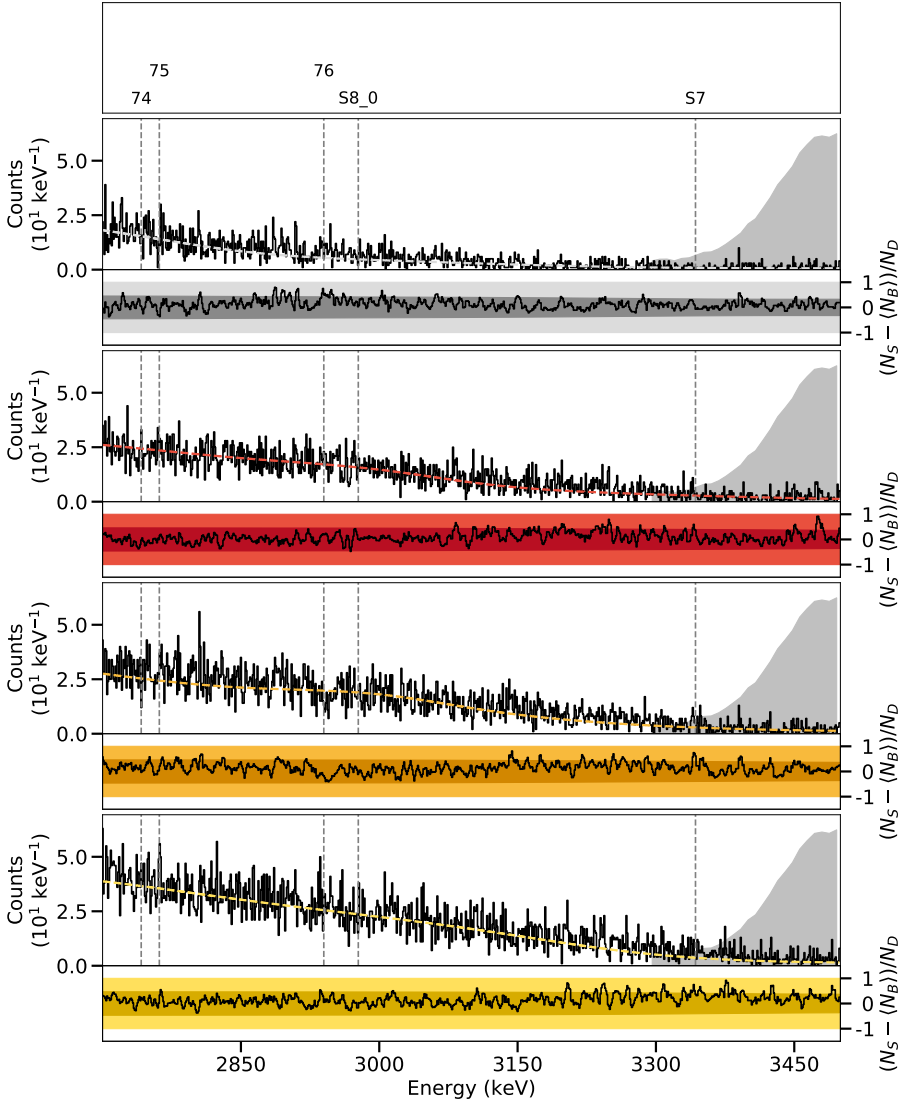


Figure D.81.: Spectra of the ^{82}Se target in the γ^3 setup at a beam energy of 3.50 MeV between 2700 keV and 3500 keV.

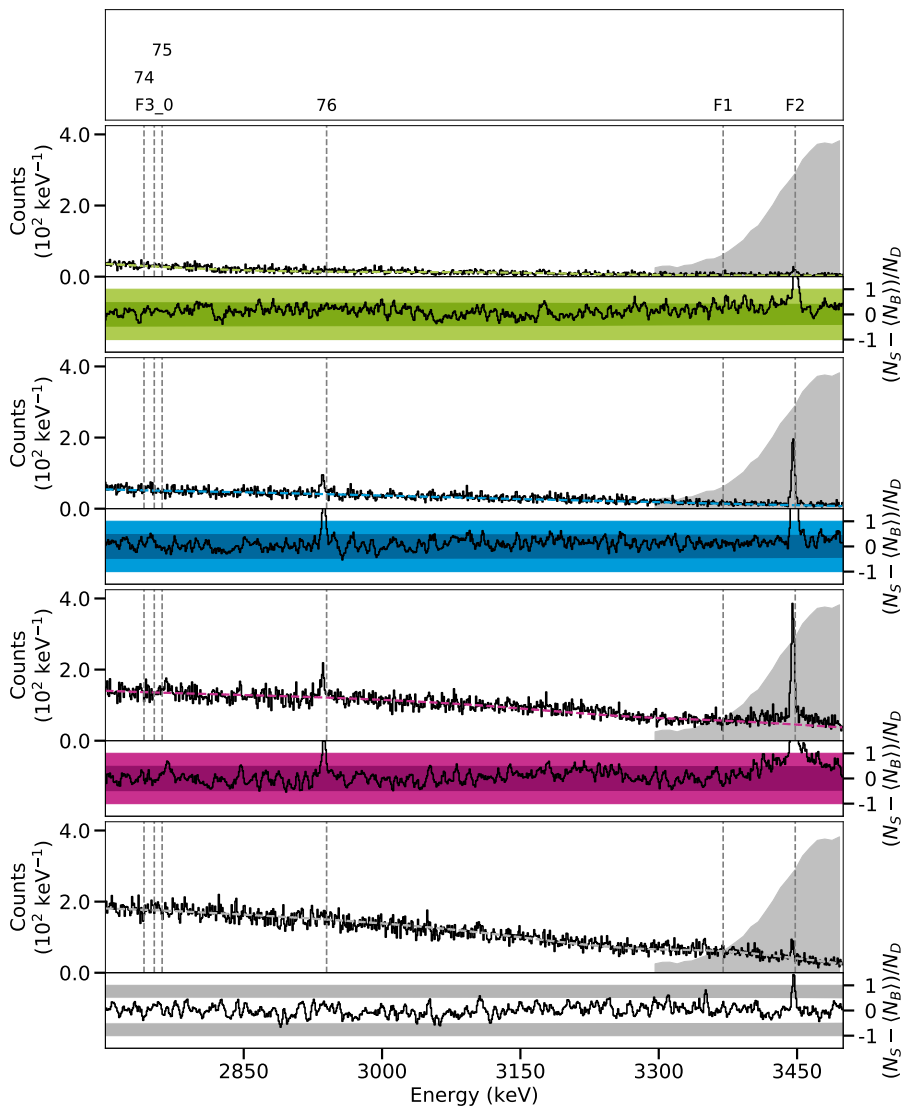


Figure D.82.: Spectra of the ^{82}Kr target in the polarimetry setup at a beam energy of 3.50 MeV between 2700 keV and 3500 keV.

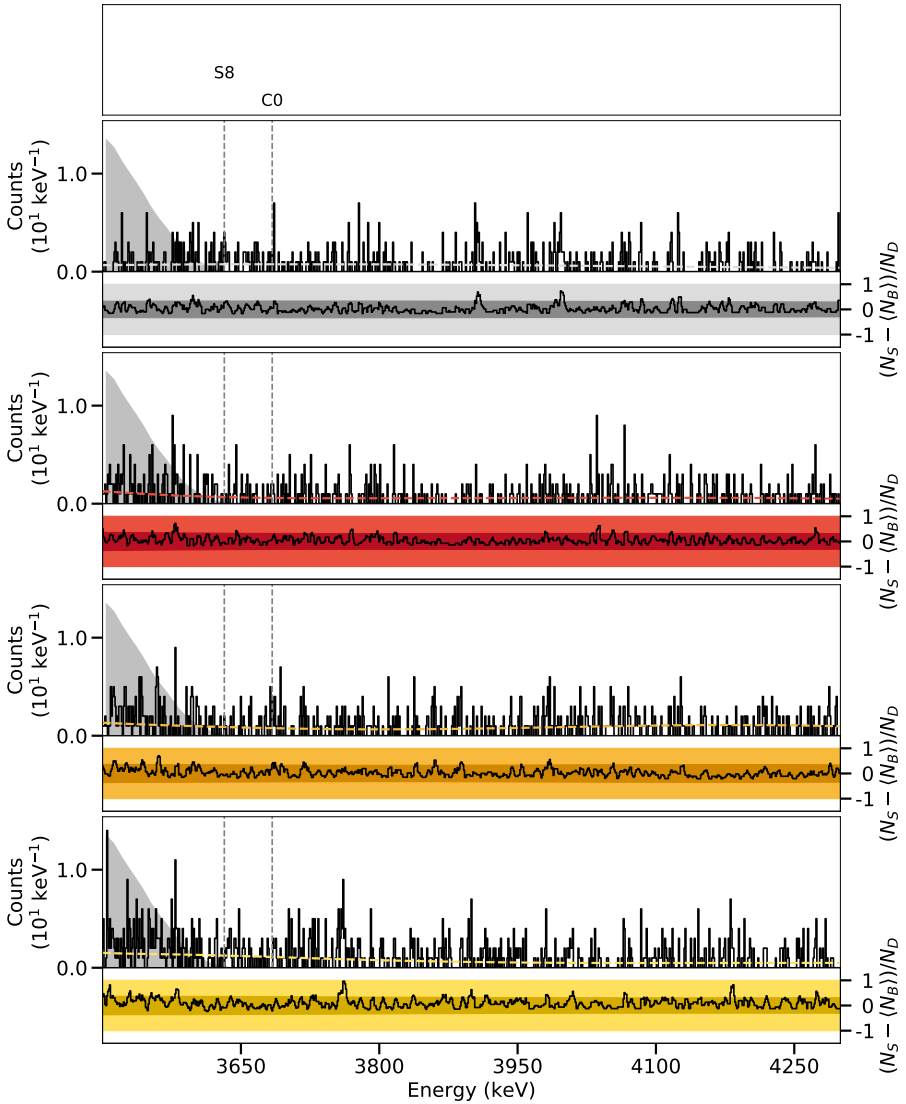


Figure D.83.: Spectra of the ^{82}Se target in the γ^3 setup at a beam energy of 3.50 MeV between 3500 keV and 4300 keV.

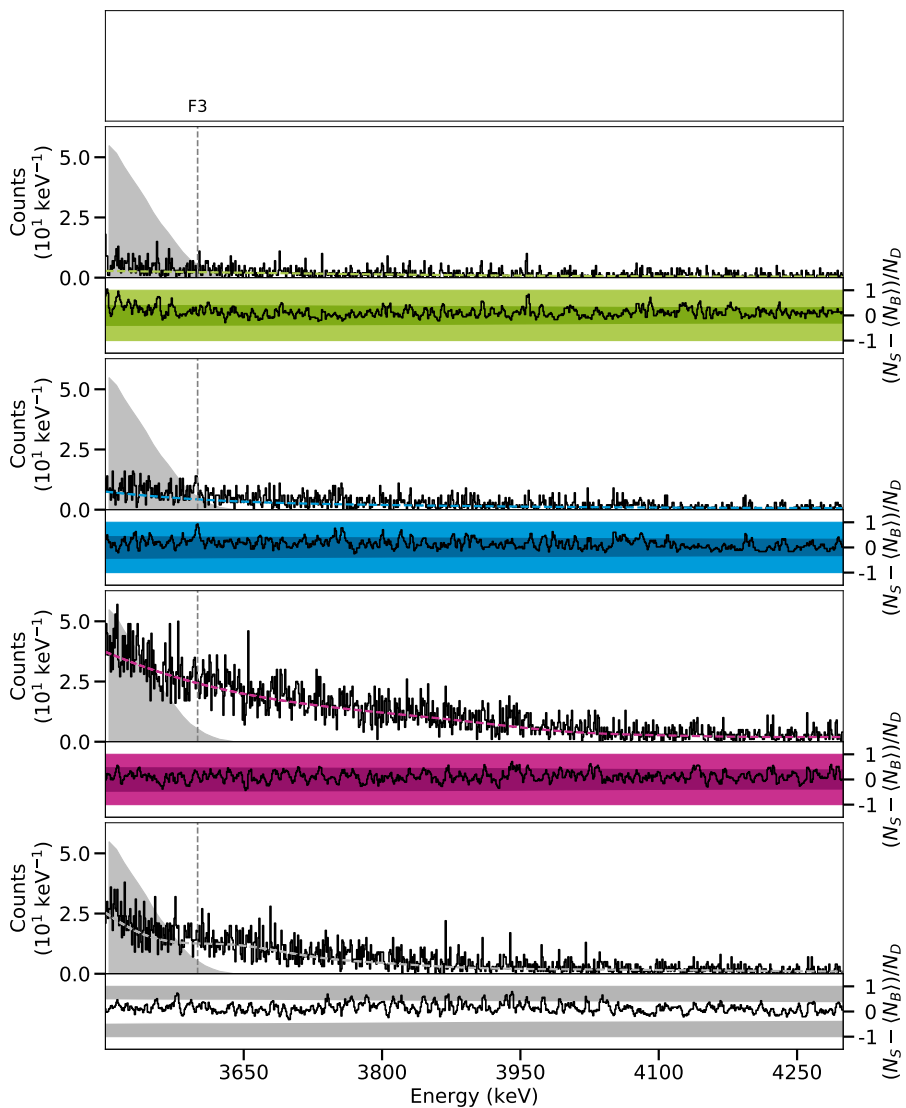


Figure D.84.: Spectra of the ^{82}Kr target in the polarimetry setup at a beam energy of 3.50 MeV between 3500 keV and 4300 keV.

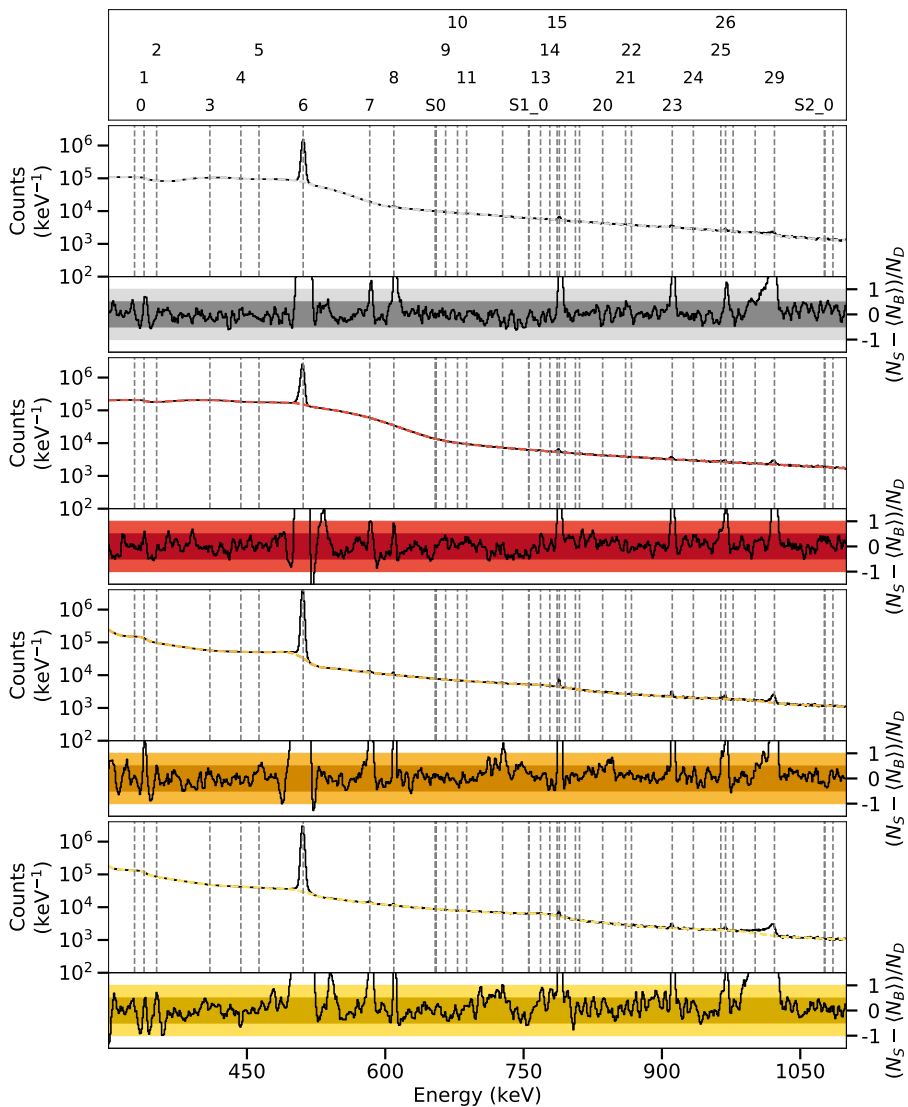


Figure D.85.: Spectra of the ^{82}Se target in the γ^3 setup at a beam energy of 3.65 MeV between 300 keV and 1100 keV.

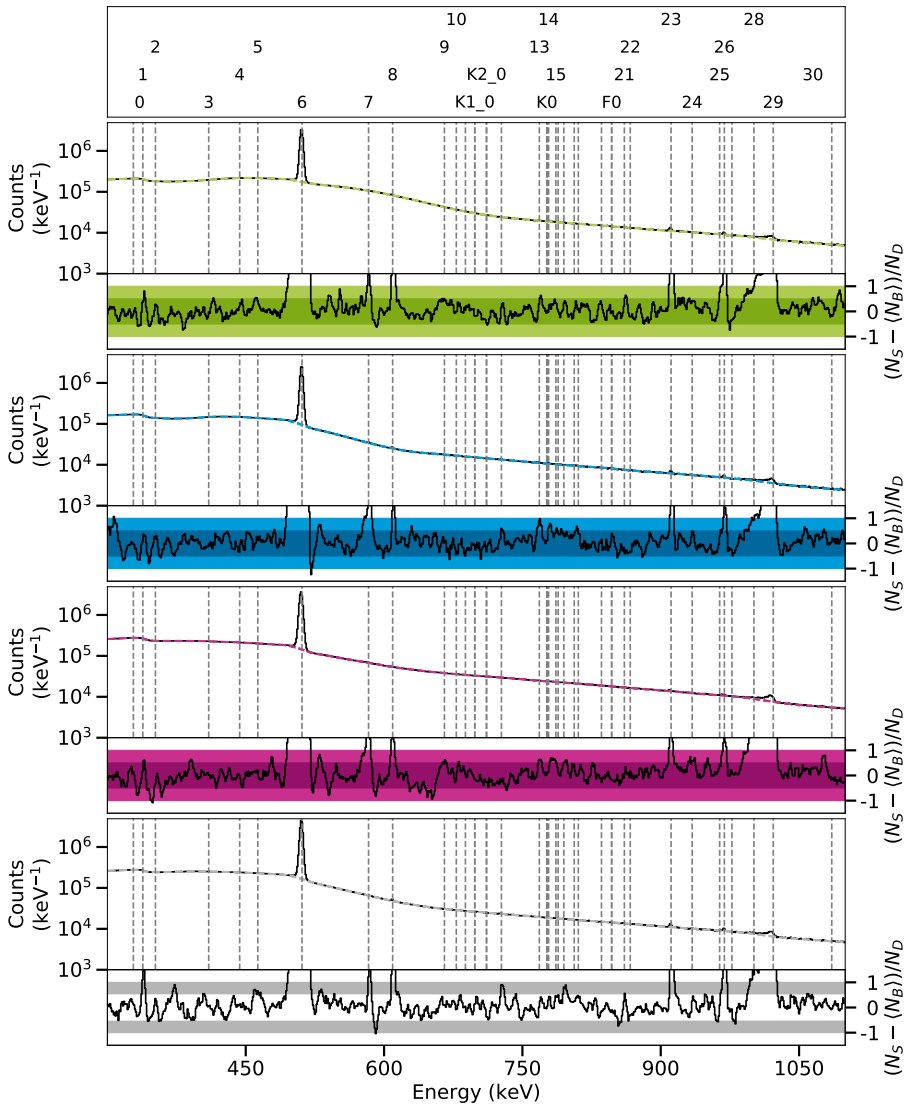


Figure D.86.: Spectra of the ^{82}Kr target in the polarimetry setup at a beam energy of 3.65 MeV between 300 keV and 1100 keV.

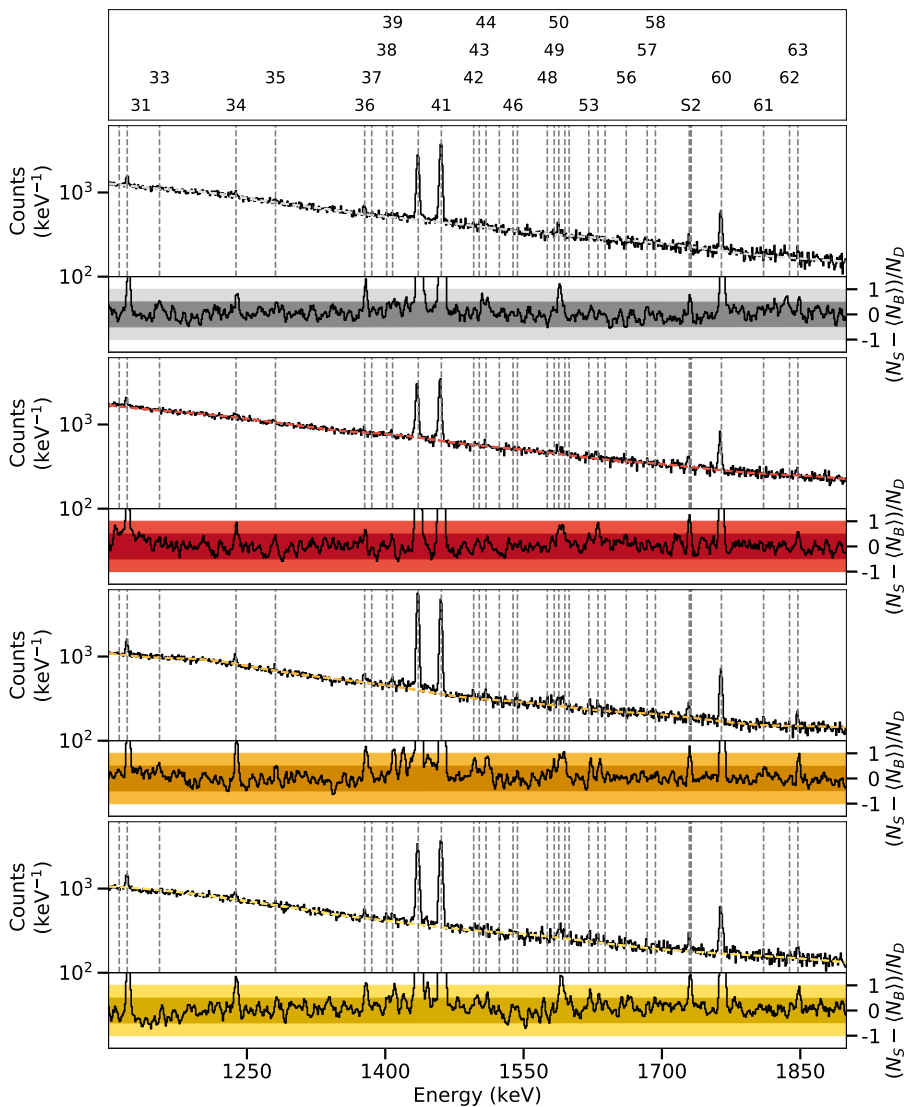


Figure D.87.: Spectra of the ^{82}Se target in the γ^3 setup at a beam energy of 3.65 MeV between 1100 keV and 1900 keV.

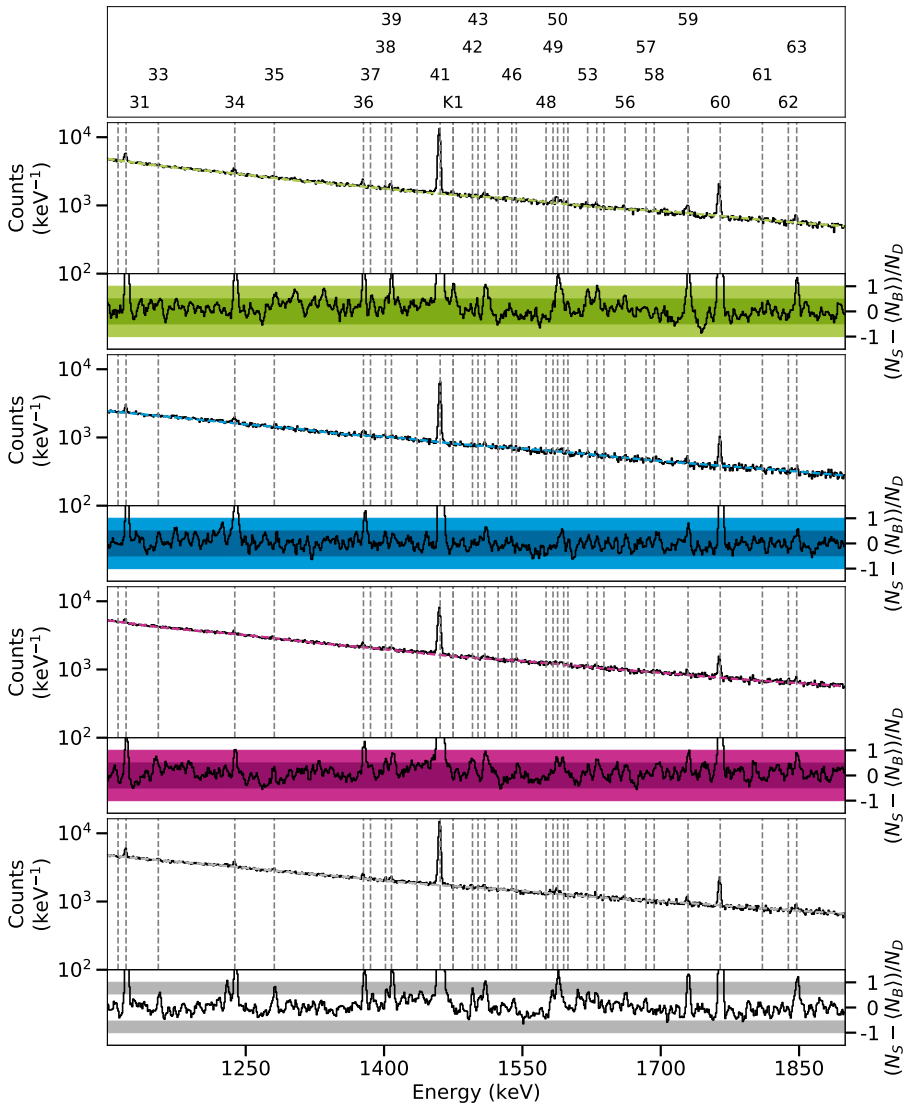


Figure D.88.: Spectra of the ^{82}Kr target in the polarimetry setup at a beam energy of 3.65 MeV between 1100 keV and 1900 keV.

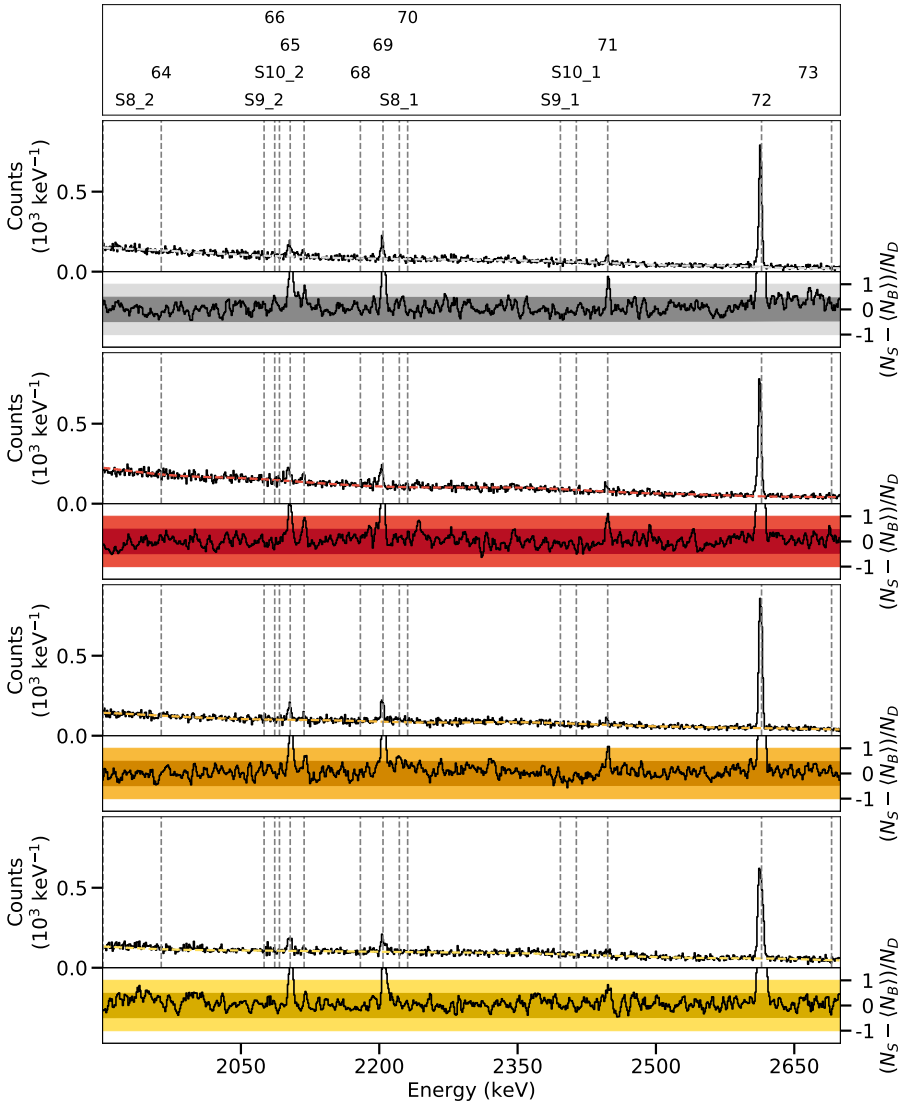


Figure D.89.: Spectra of the ^{82}Se target in the γ^3 setup at a beam energy of 3.65 MeV between 1900 keV and 2700 keV.

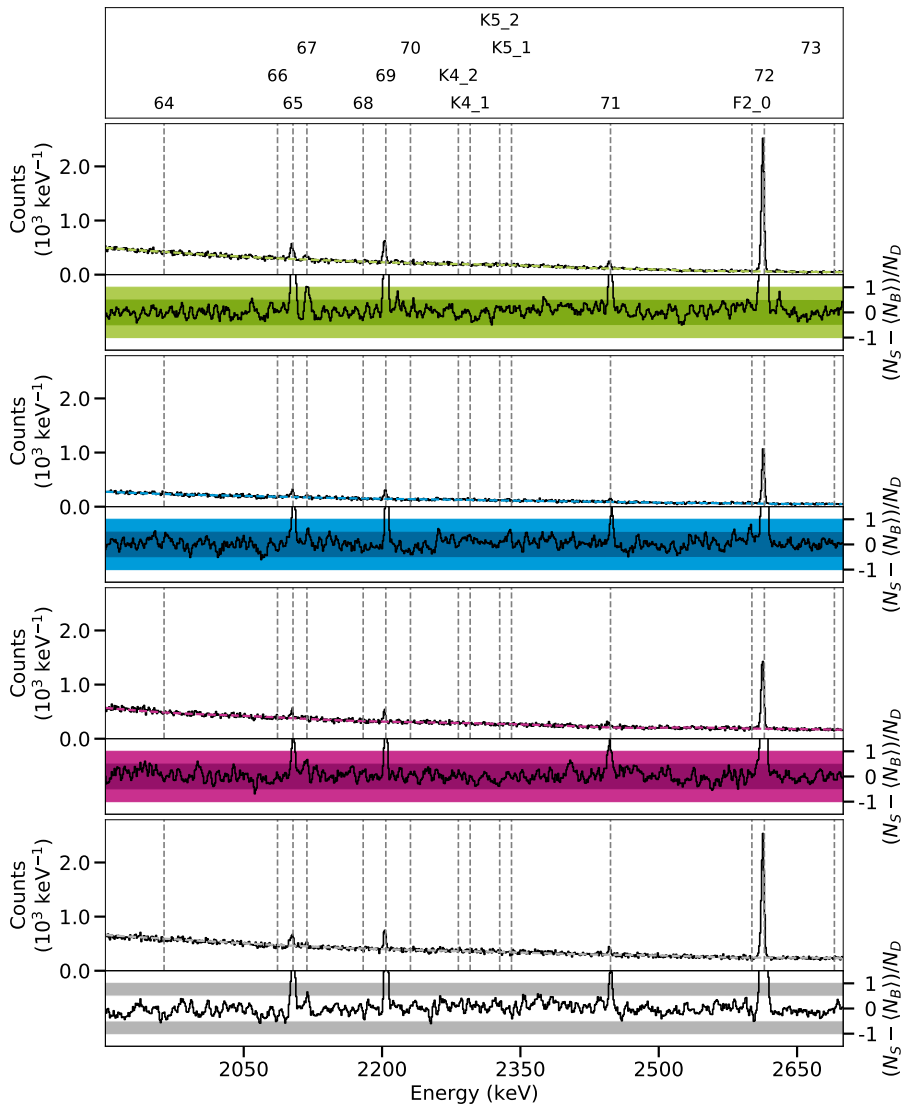


Figure D.90.: Spectra of the ^{82}Kr target in the polarimetry setup at a beam energy of 3.65 MeV between 1900 keV and 2700 keV.

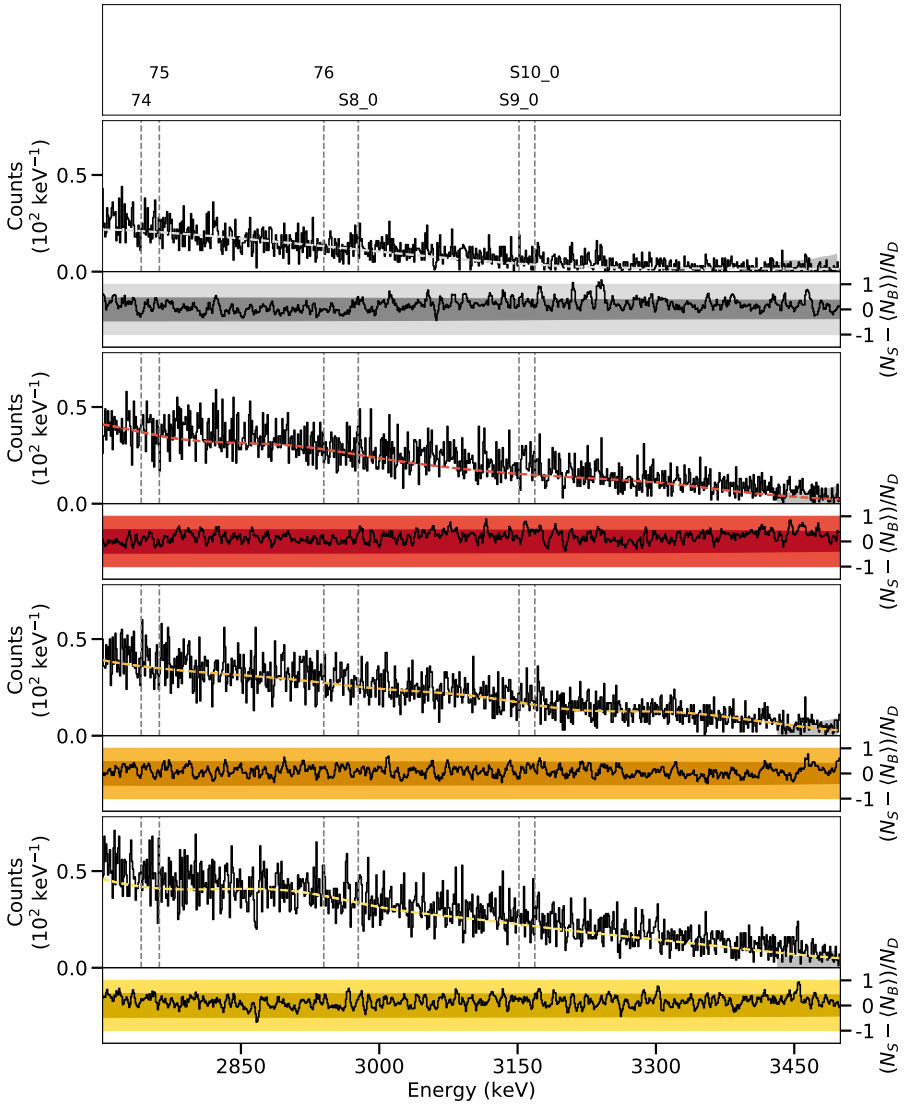


Figure D.91.: Spectra of the ^{82}Se target in the γ^3 setup at a beam energy of 3.65 MeV between 2700 keV and 3500 keV.

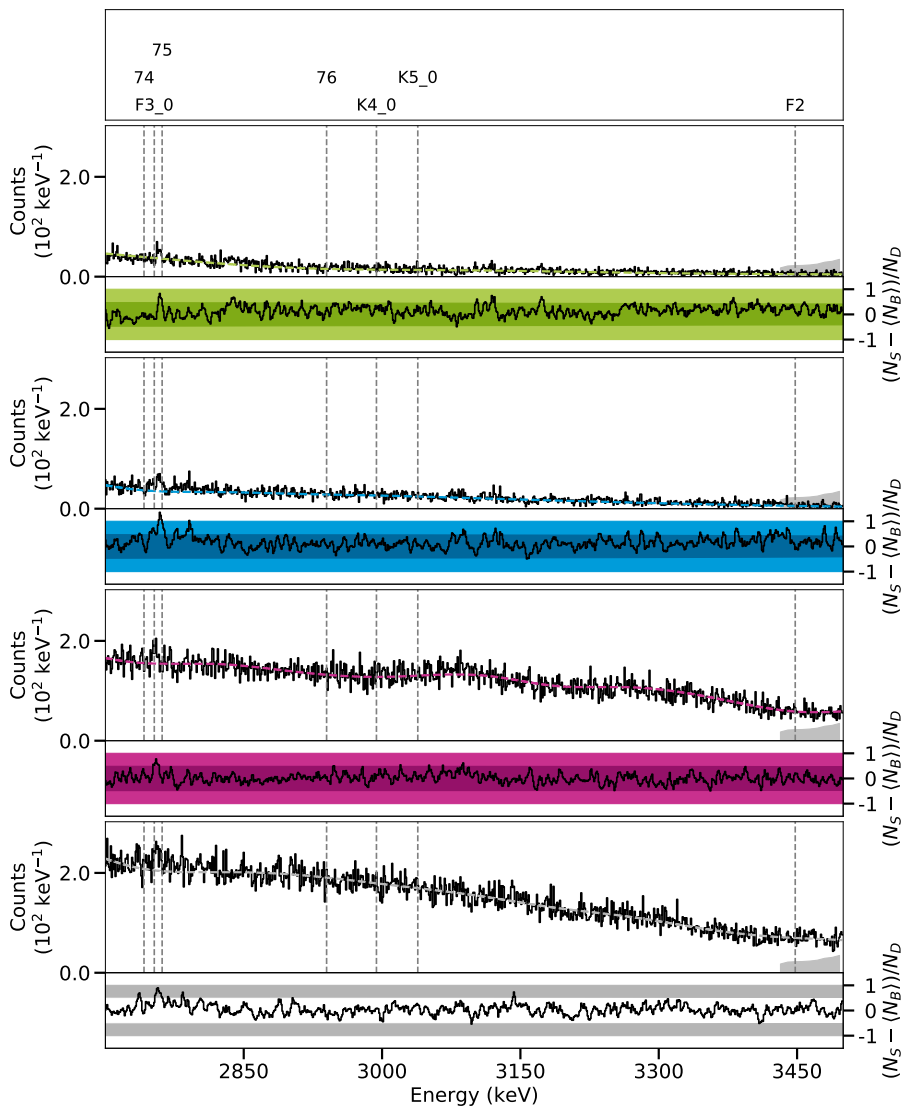


Figure D.92.: Spectra of the ^{82}Kr target in the polarimetry setup at a beam energy of 3.65 MeV between 2700 keV and 3500 keV.

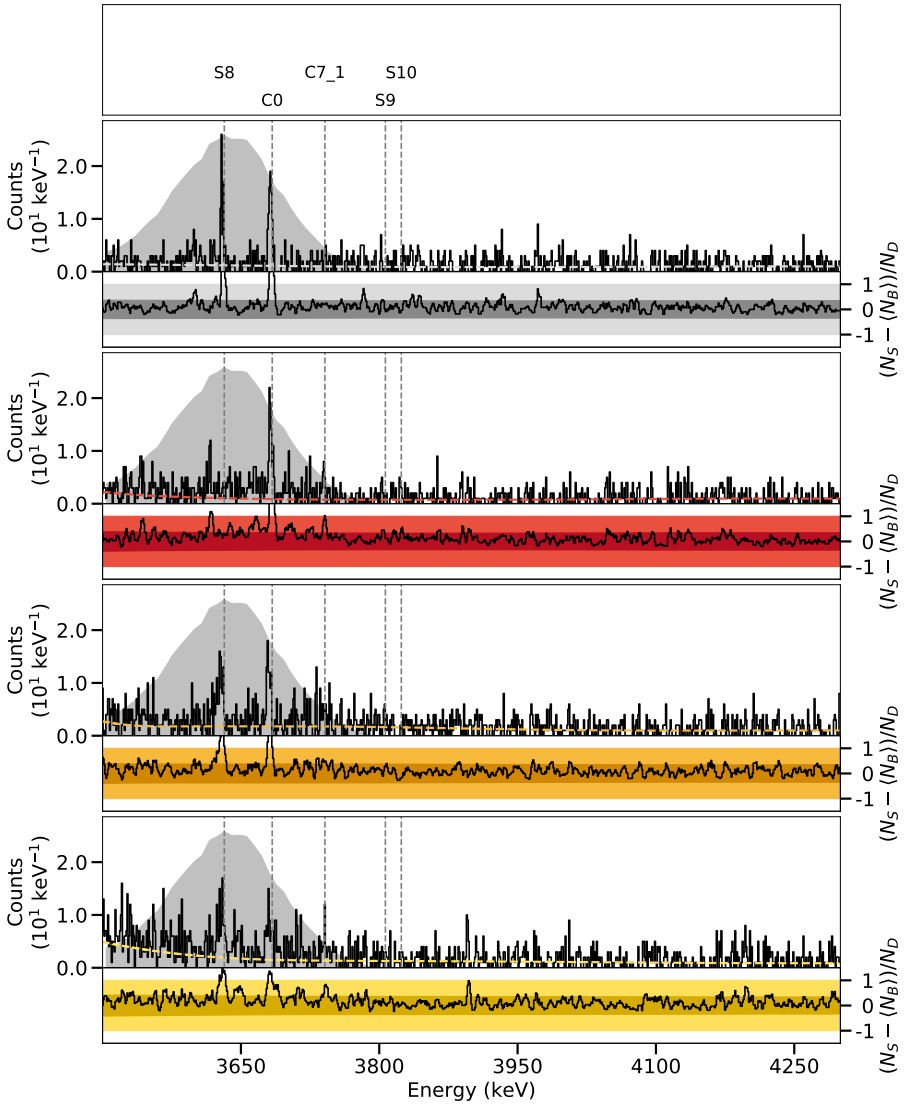


Figure D.93.: Spectra of the ^{82}Se target in the γ^3 setup at a beam energy of 3.65 MeV between 3500 keV and 4300 keV.

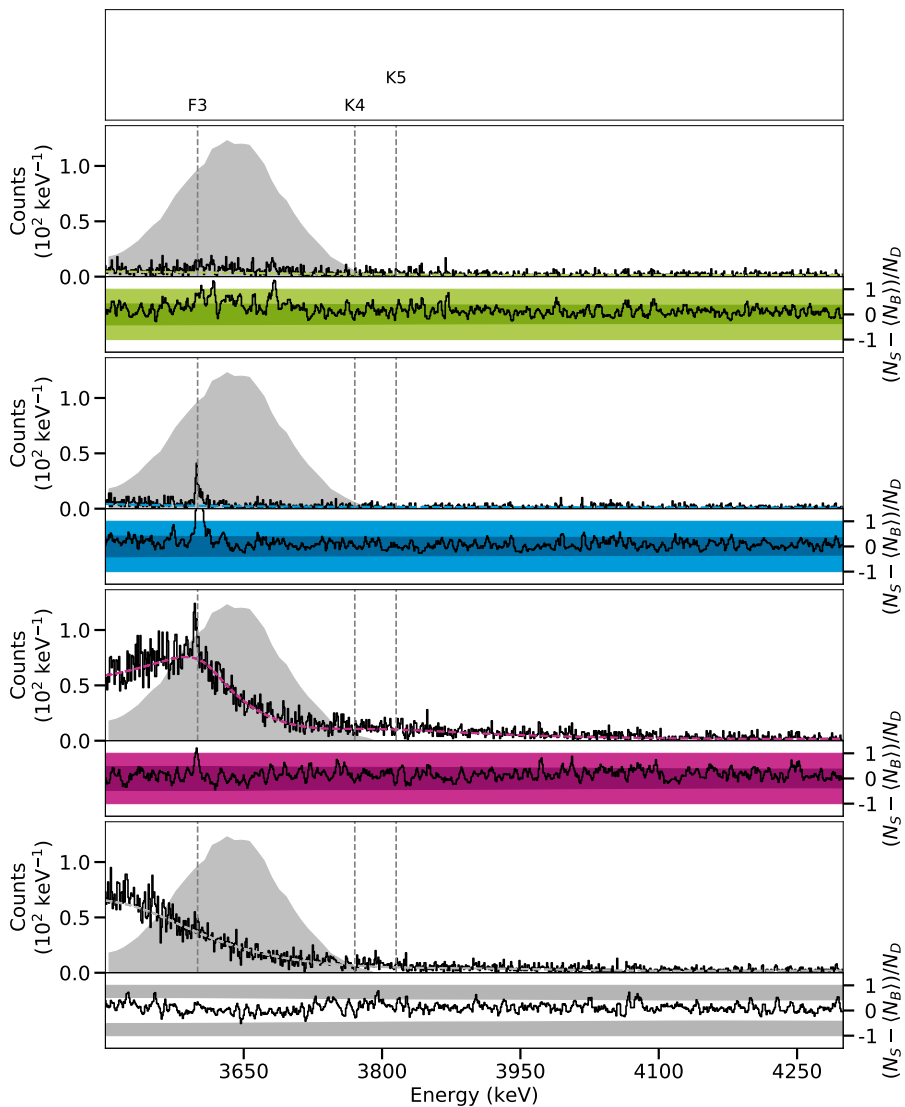


Figure D.94.: Spectra of the ^{82}Kr target in the polarimetry setup at a beam energy of 3.65 MeV between 3500 keV and 4300 keV.

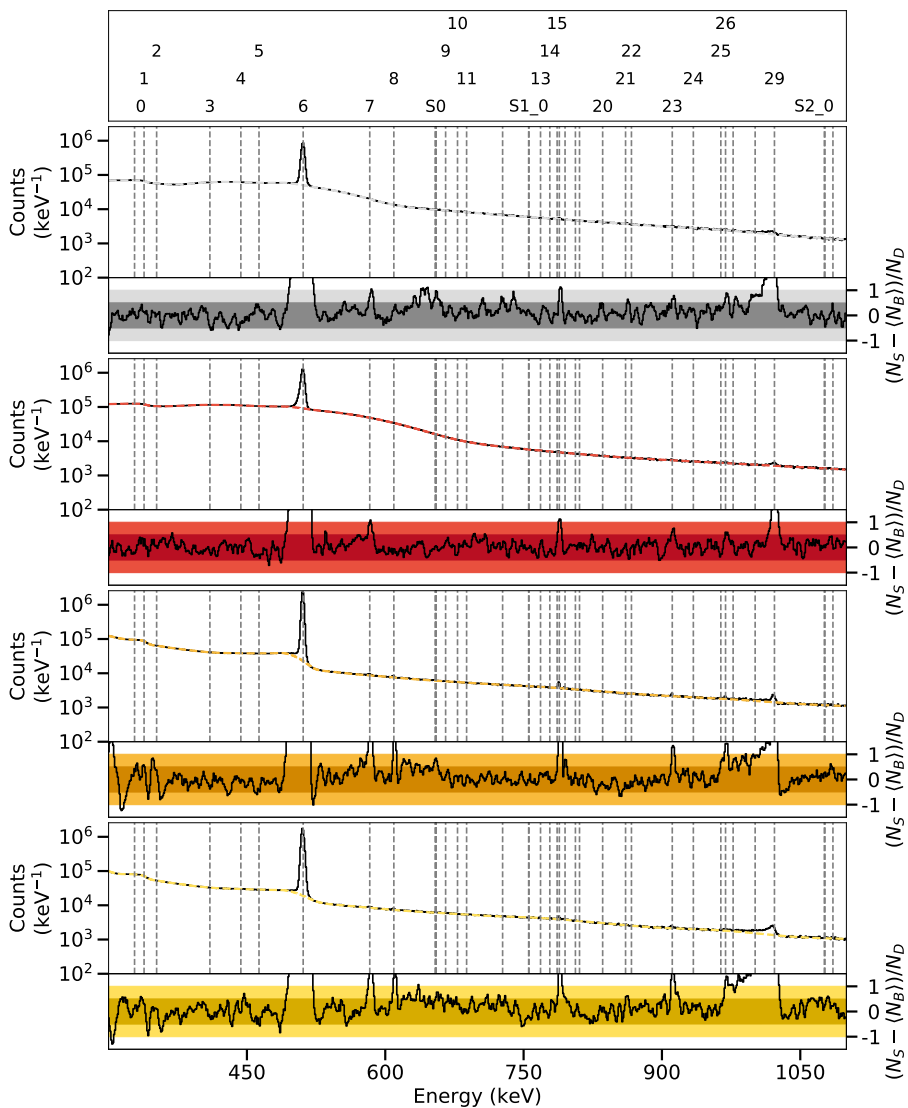


Figure D.95.: Spectra of the ^{82}Se target in the γ^3 setup at a beam energy of 3.80 MeV between 300 keV and 1100 keV.

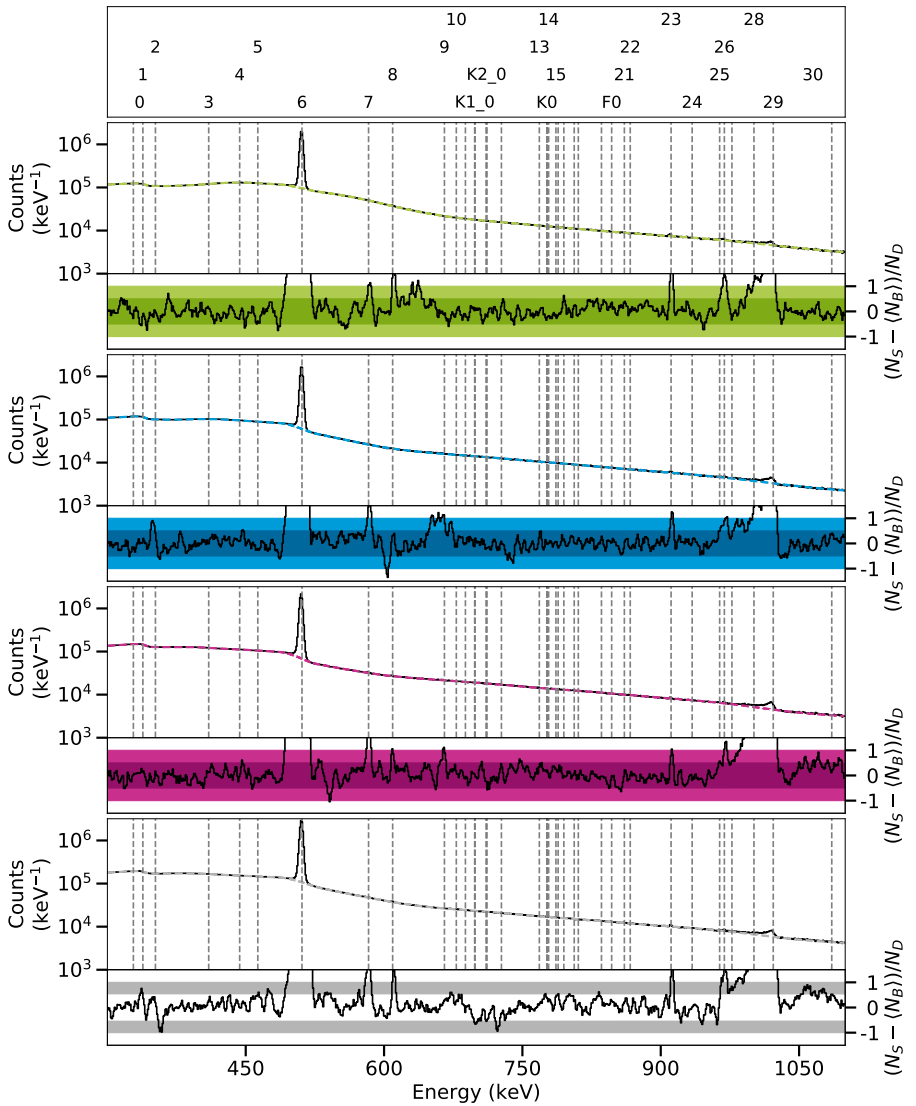


Figure D.96.: Spectra of the empty krypton target in the polarimetry setup at a beam energy of 3.80 MeV between 300 keV and 1100 keV.

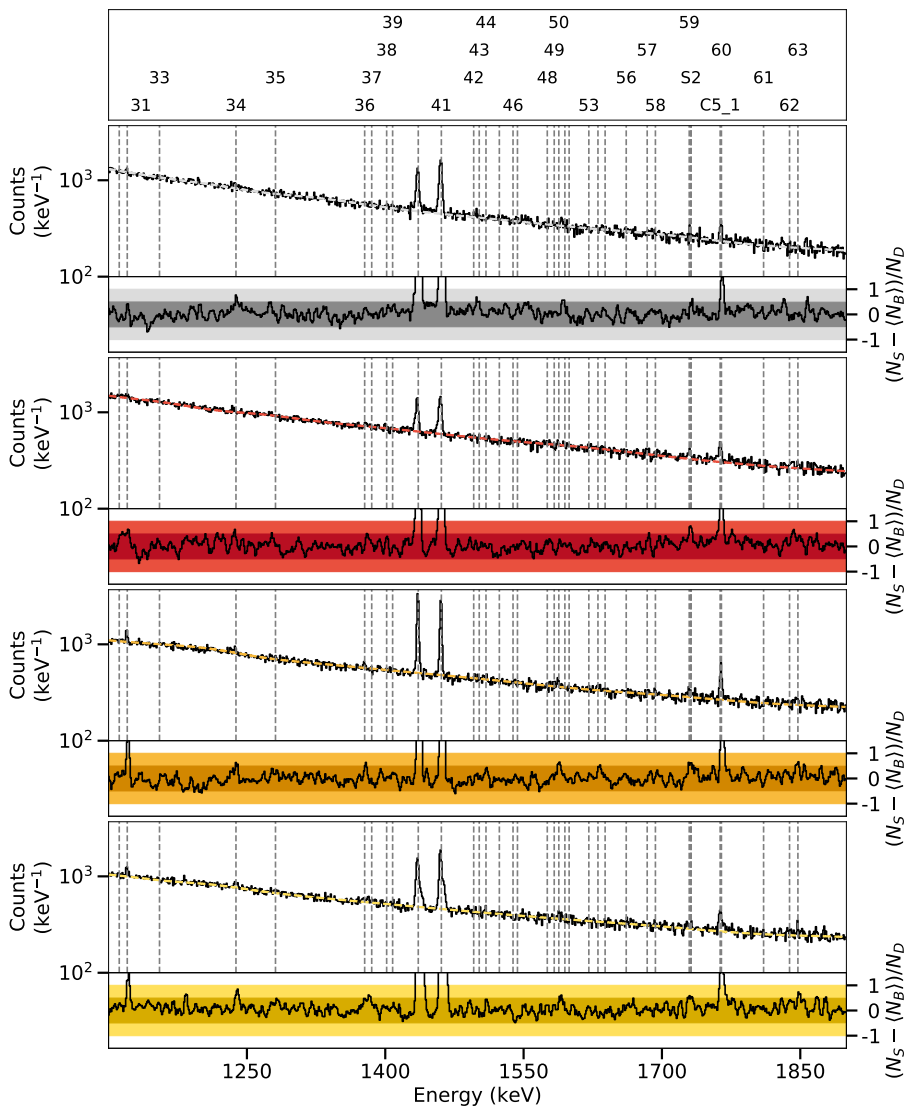


Figure D.97.: Spectra of the ^{82}Se target in the γ^3 setup at a beam energy of 3.80 MeV between 1100 keV and 1900 keV.

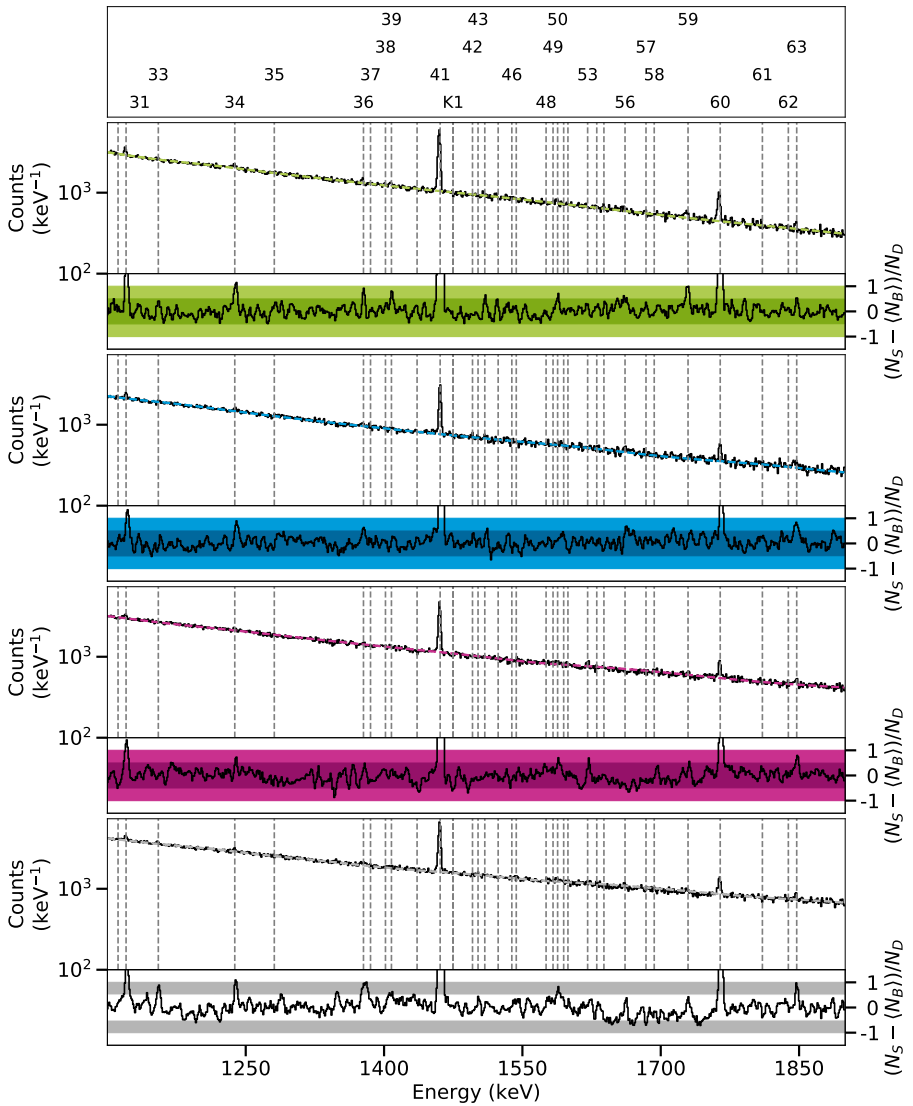


Figure D.98.: Spectra of the empty krypton target in the polarimetry setup at a beam energy of 3.80 MeV between 1100 keV and 1900 keV.

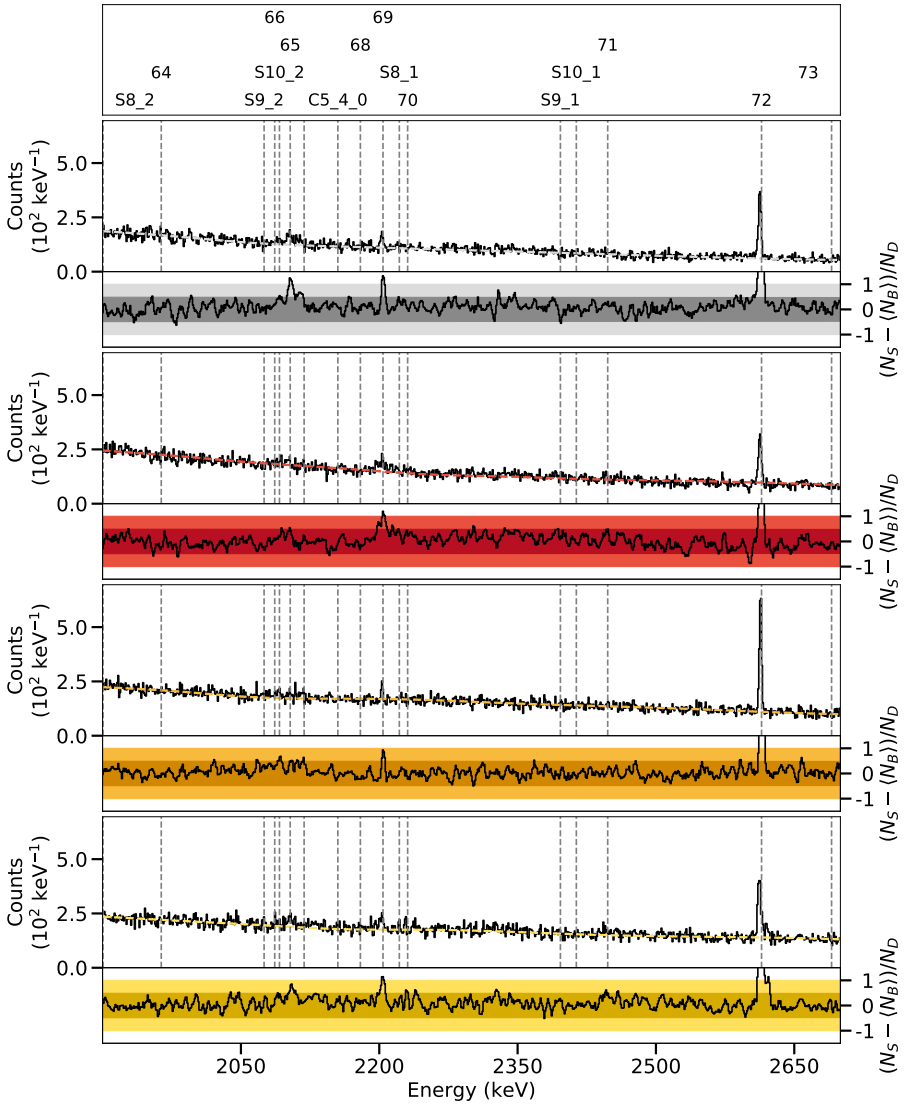


Figure D.99.: Spectra of the ^{82}Se target in the γ^3 setup at a beam energy of 3.80 MeV between 1900 keV and 2700 keV.

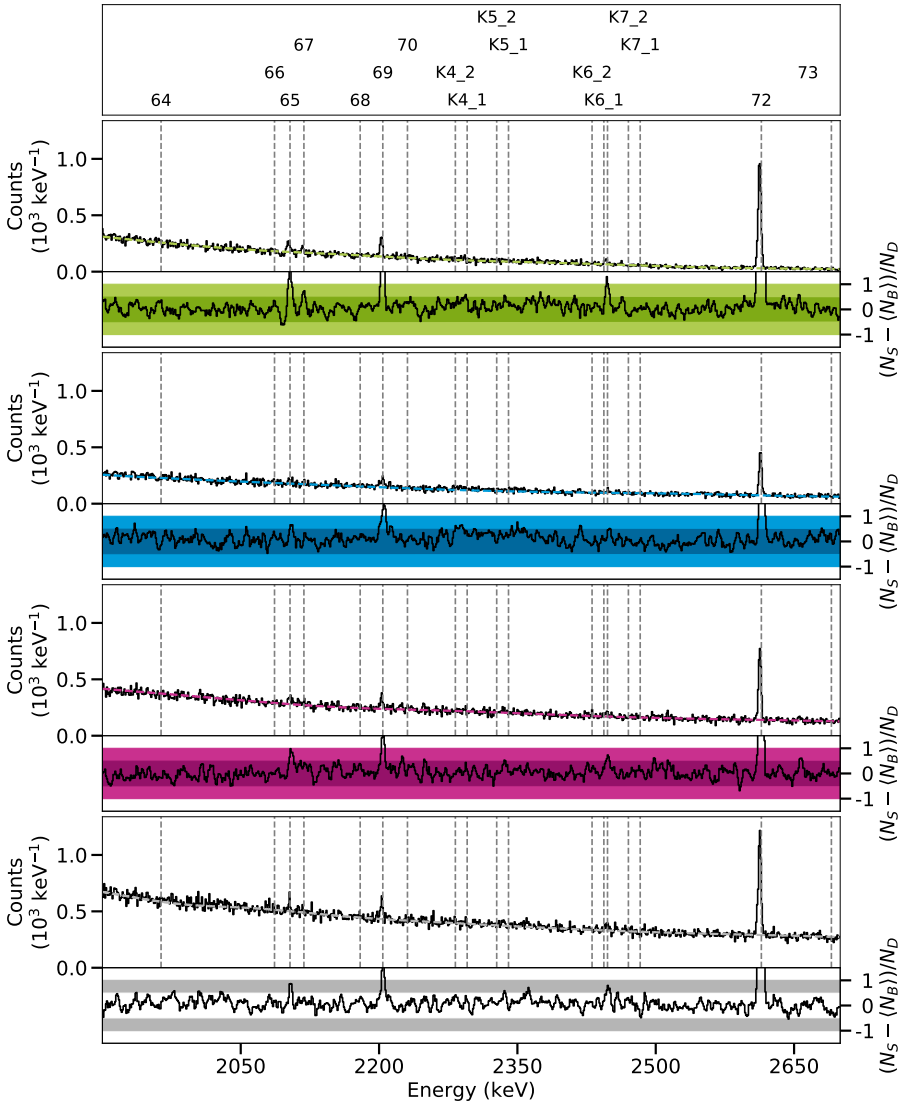


Figure D.100.: Spectra of the empty krypton target in the polarimetry setup at a beam energy of 3.80 MeV between 1900 keV and 2700 keV.

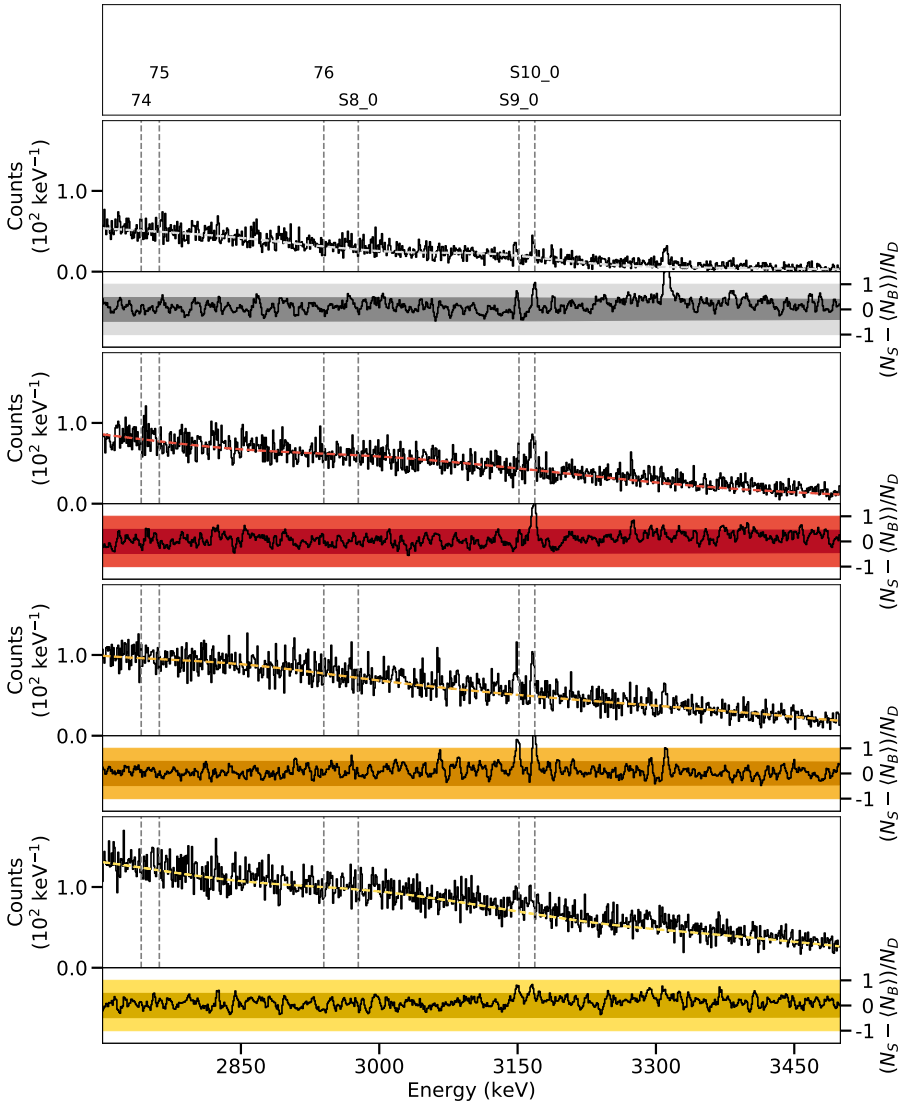


Figure D.101.: Spectra of the ^{82}Se target in the γ^3 setup at a beam energy of 3.80 MeV between 2700 keV and 3500 keV.

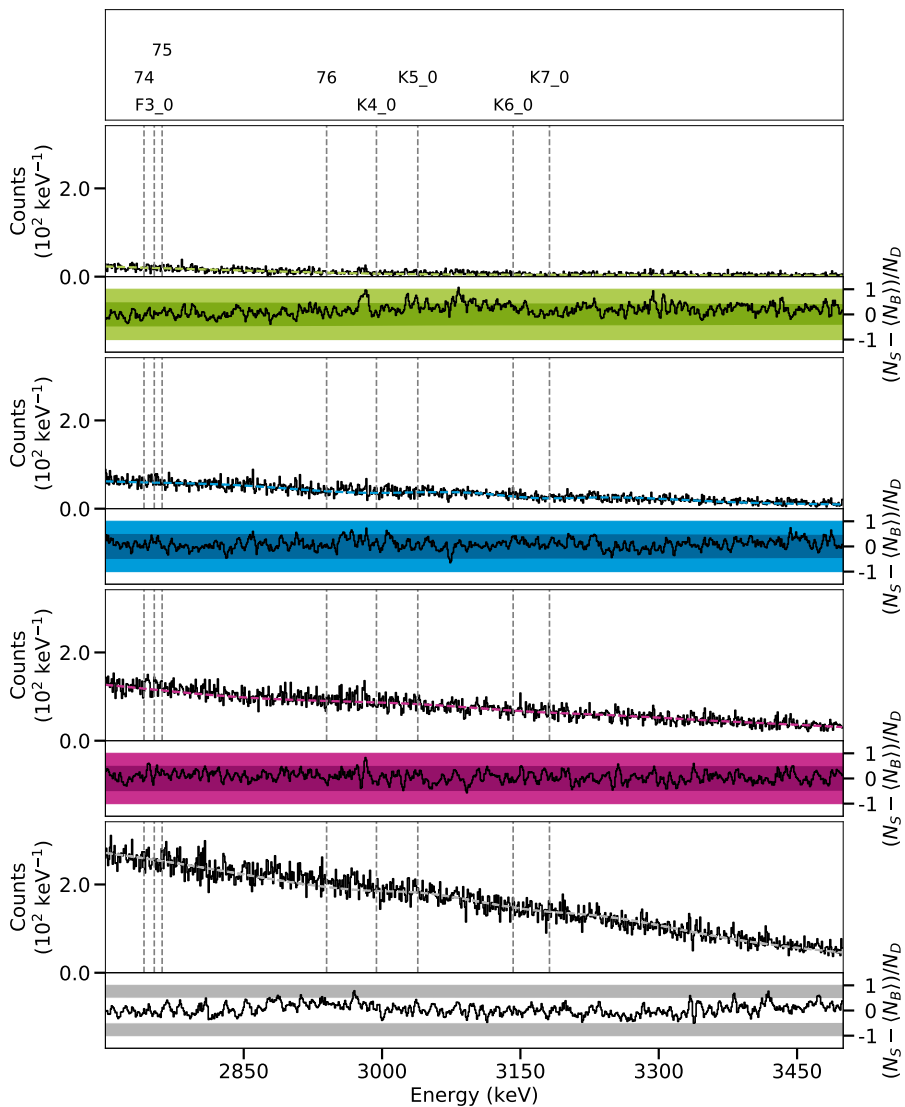


Figure D.102.: Spectra of the empty krypton target in the polarimetry setup at a beam energy of 3.80 MeV between 2700 keV and 3500 keV.

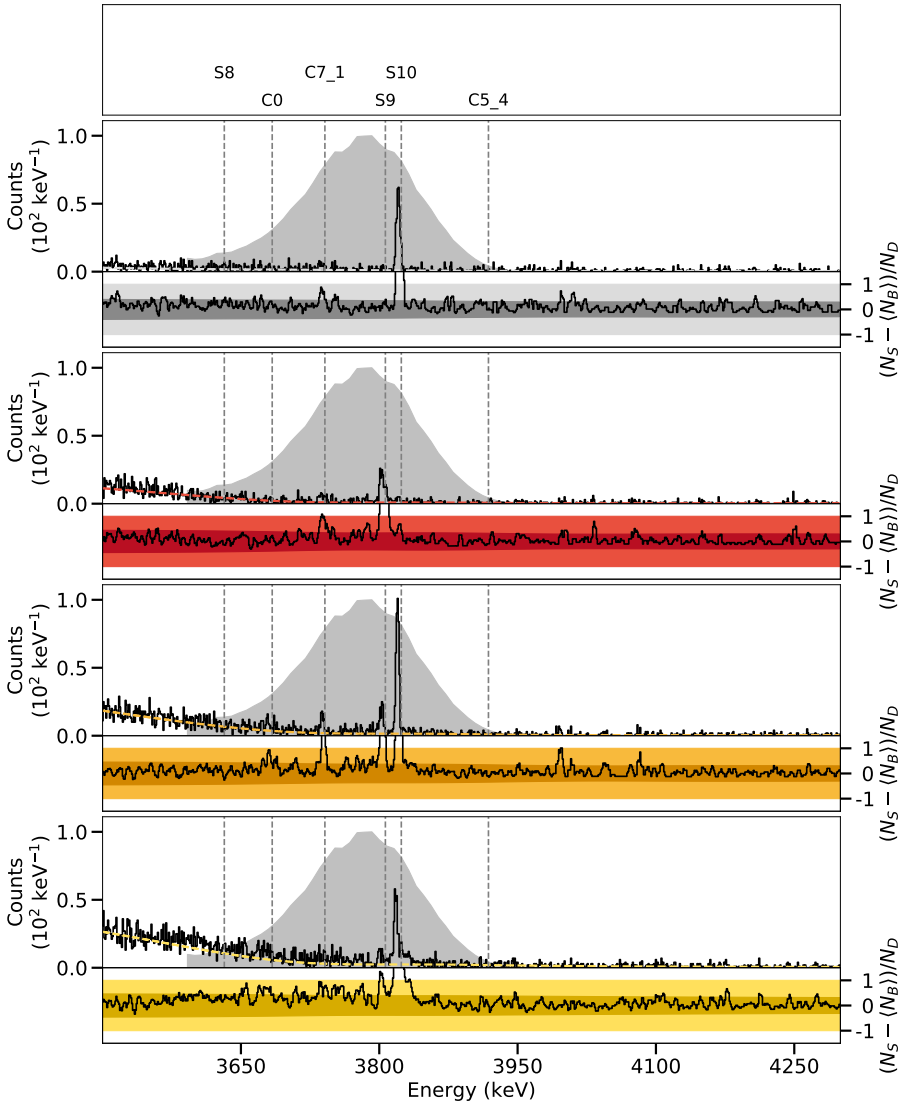


Figure D.103.: Spectra of the ^{82}Se target in the γ^3 setup at a beam energy of 3.80 MeV between 3500 keV and 4300 keV.

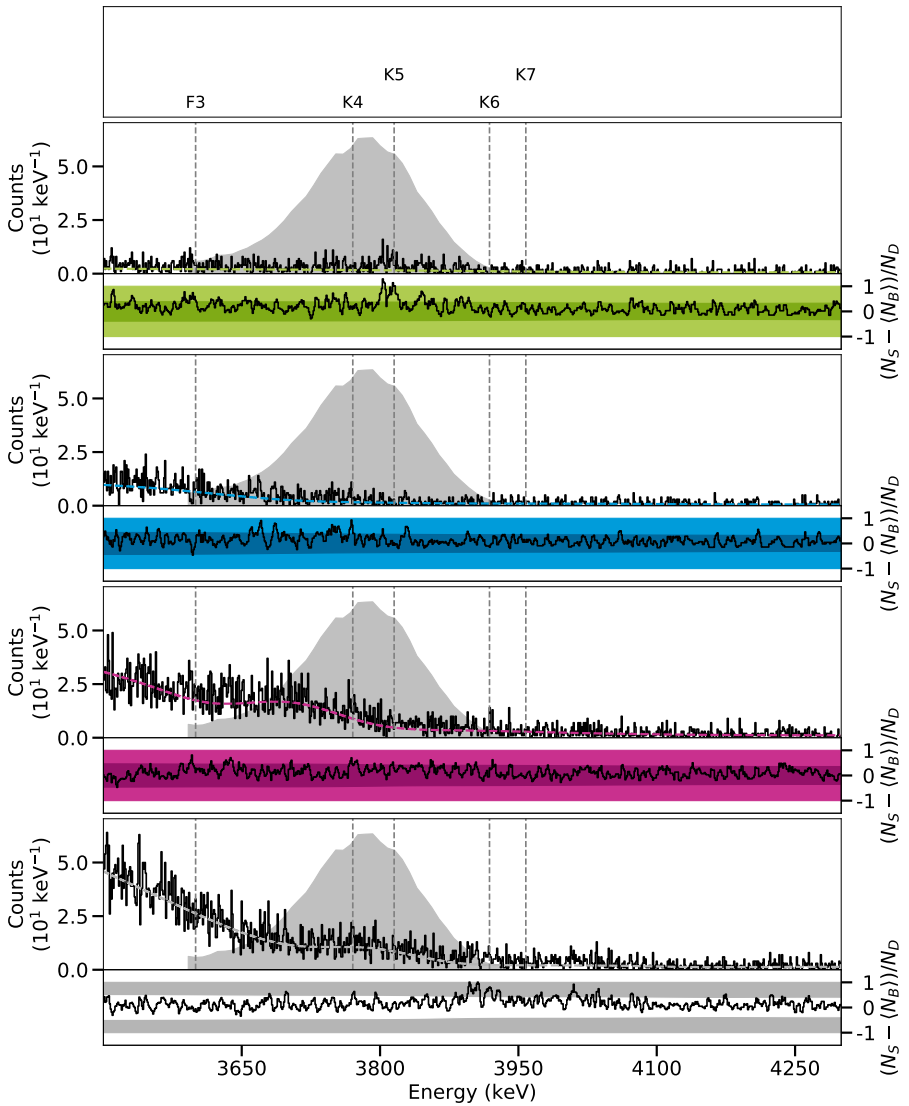


Figure D.104.: Spectra of the empty krypton target in the polarimetry setup at a beam energy of 3.80 MeV between 3500 keV and 4300 keV.

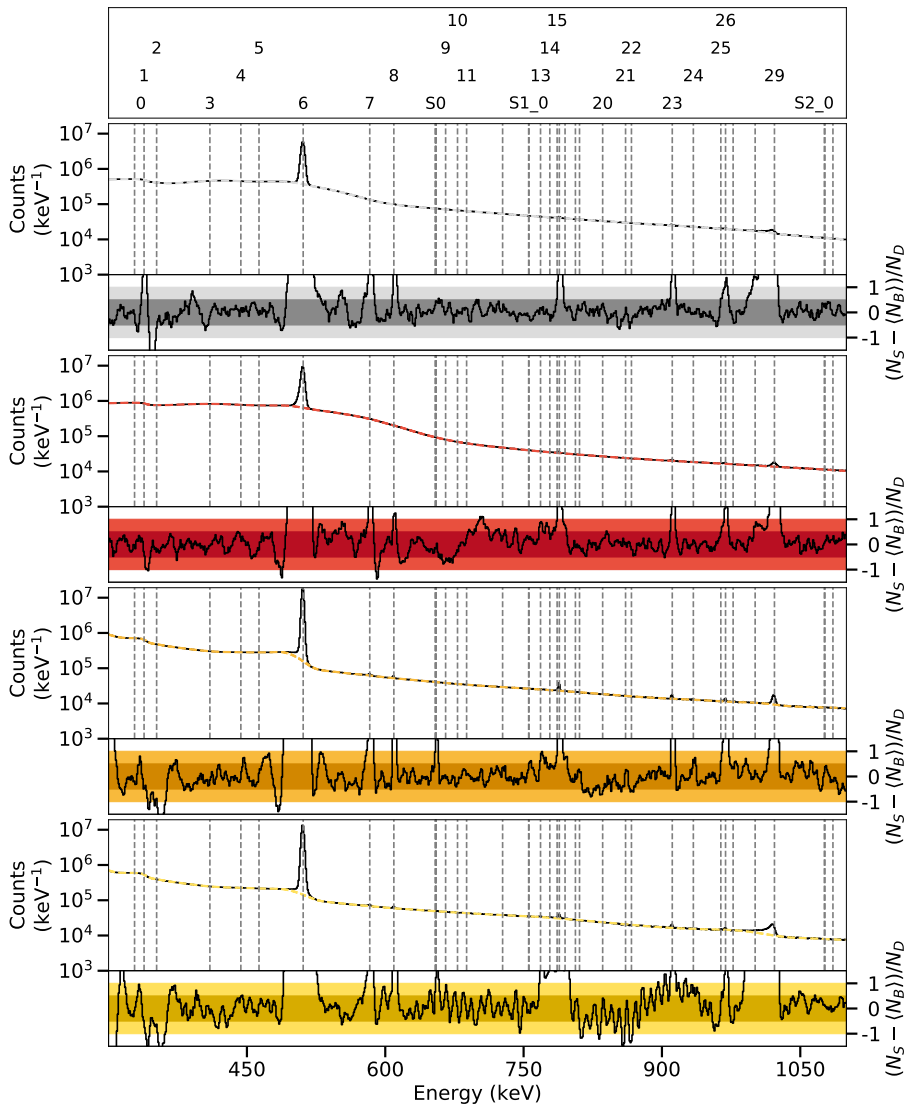


Figure D.105.: Spectra of the ^{82}Se target in the γ^3 setup at a beam energy of 3.82 MeV between 300 keV and 1100 keV.

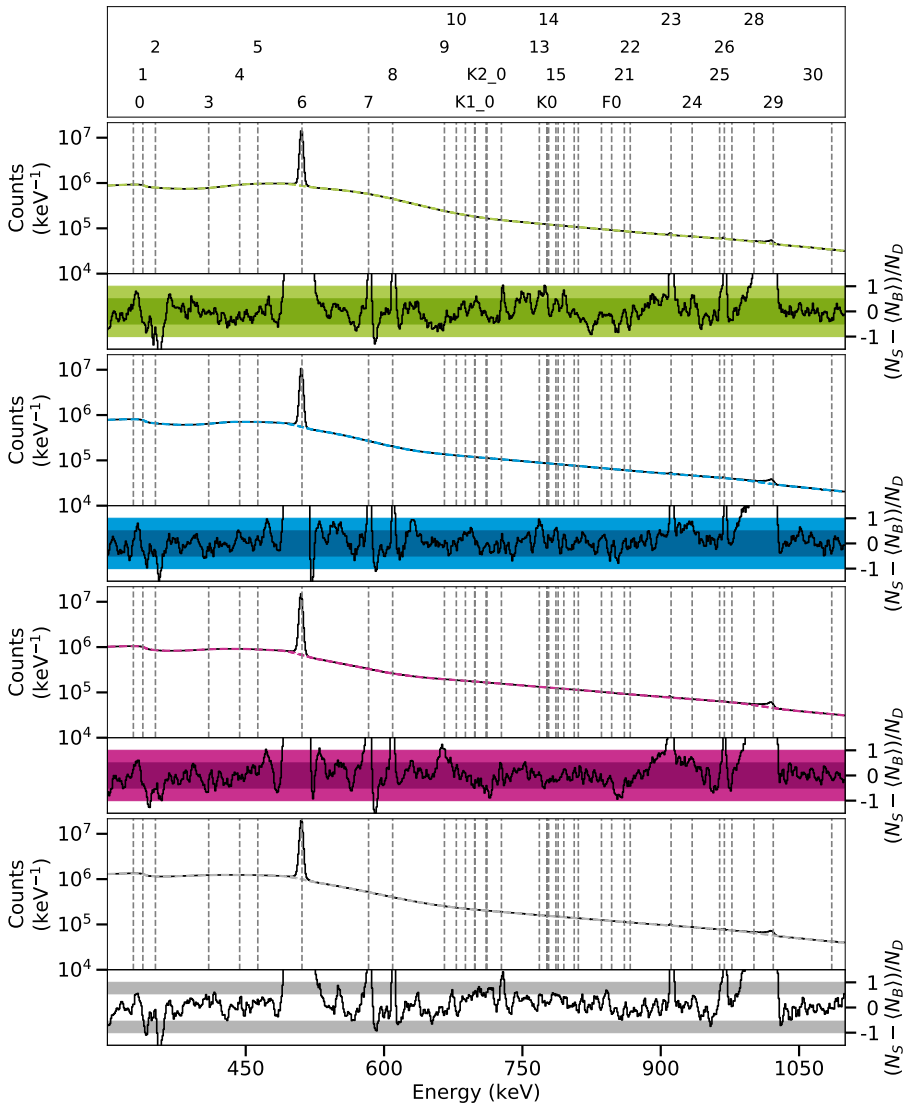


Figure D.106.: Spectra of the ^{82}Kr target in the polarimetry setup at a beam energy of 3.82 MeV between 300 keV and 1100 keV.

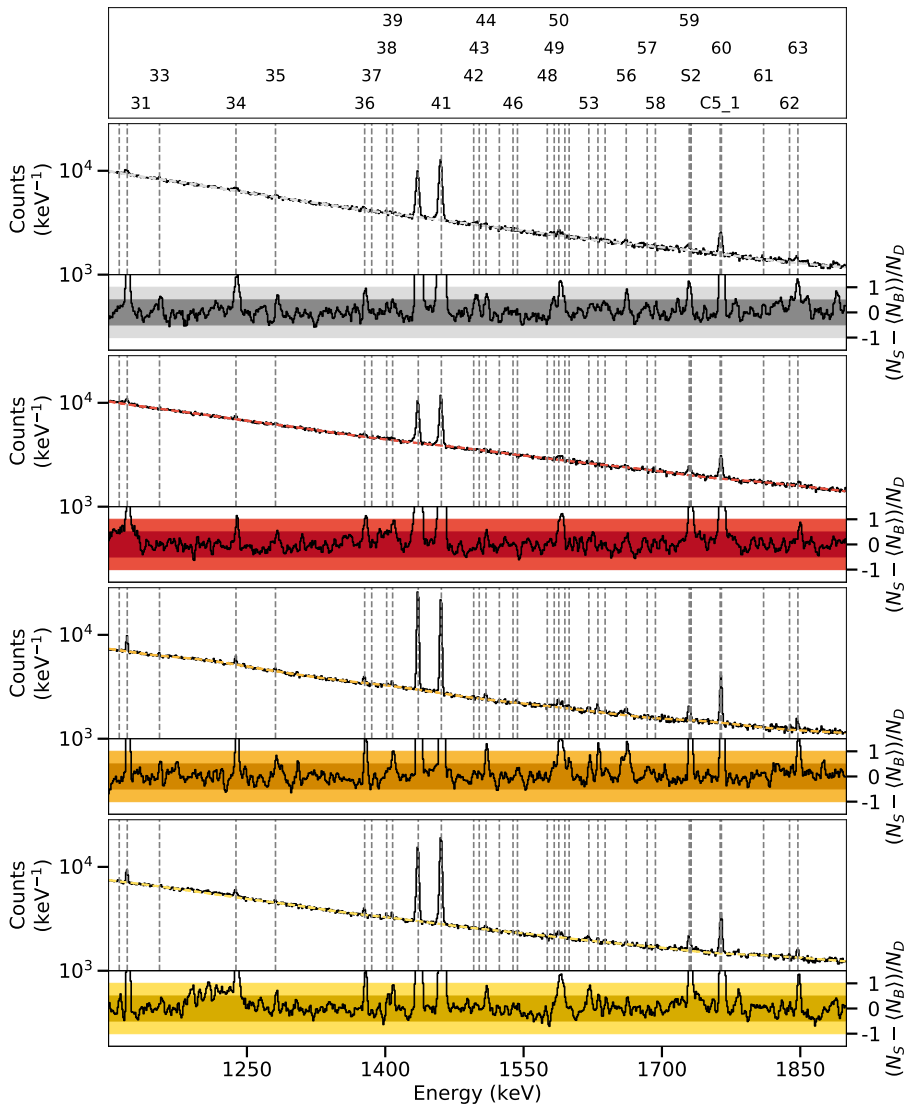


Figure D.107.: Spectra of the ^{82}Se target in the γ^3 setup at a beam energy of 3.82 MeV between 1100 keV and 1900 keV.

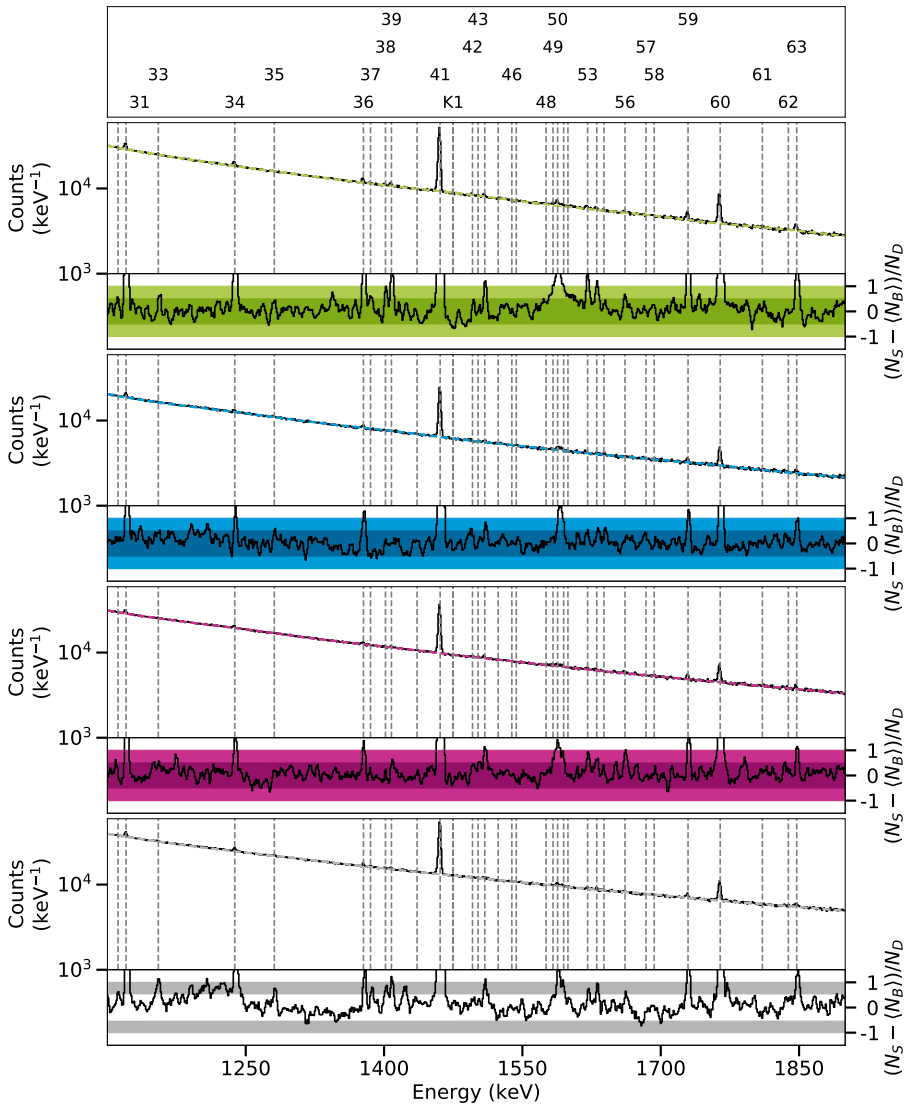


Figure D.108.: Spectra of the ^{82}Kr target in the polarimetry setup at a beam energy of 3.82 MeV between 1100 keV and 1900 keV.

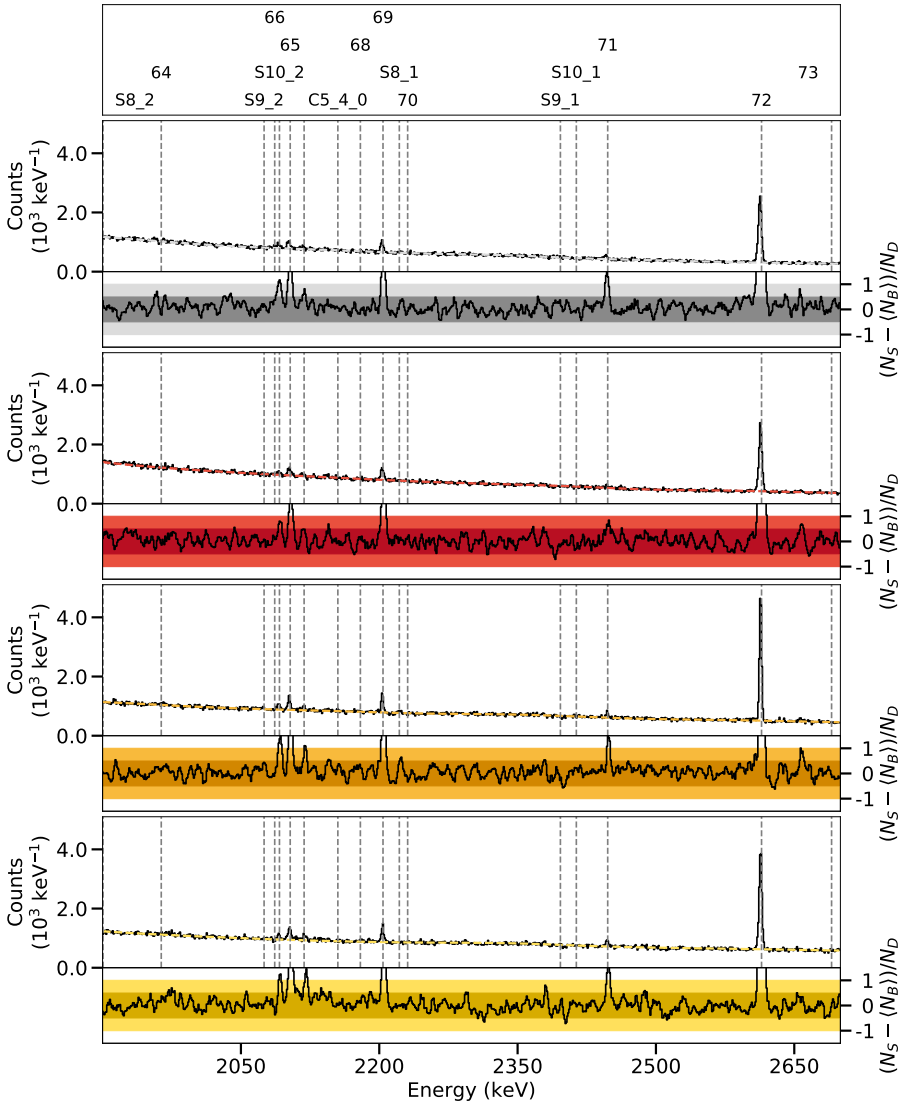


Figure D.109.: Spectra of the ^{82}Se target in the γ^3 setup at a beam energy of 3.82 MeV between 1900 keV and 2700 keV.

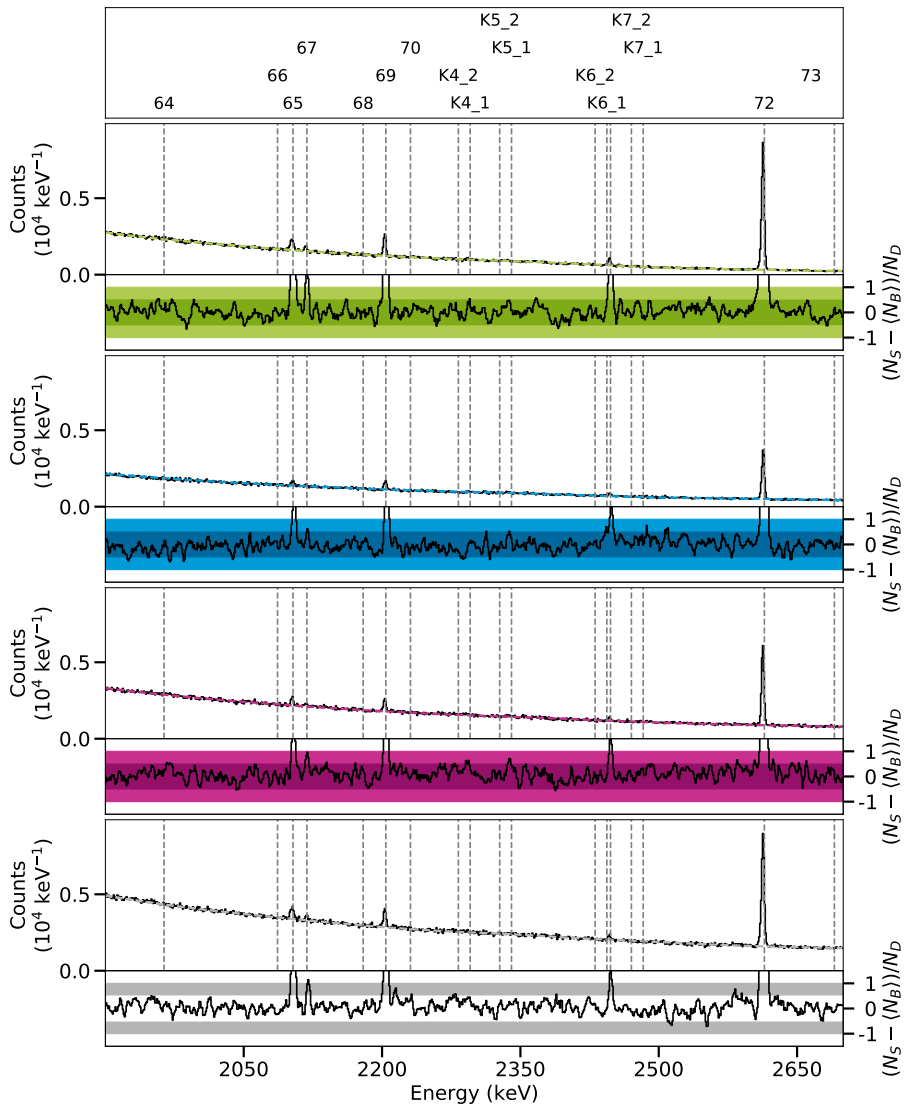


Figure D.110.: Spectra of the ^{82}Kr target in the polarimetry setup at a beam energy of 3.82 MeV between 1900 keV and 2700 keV.

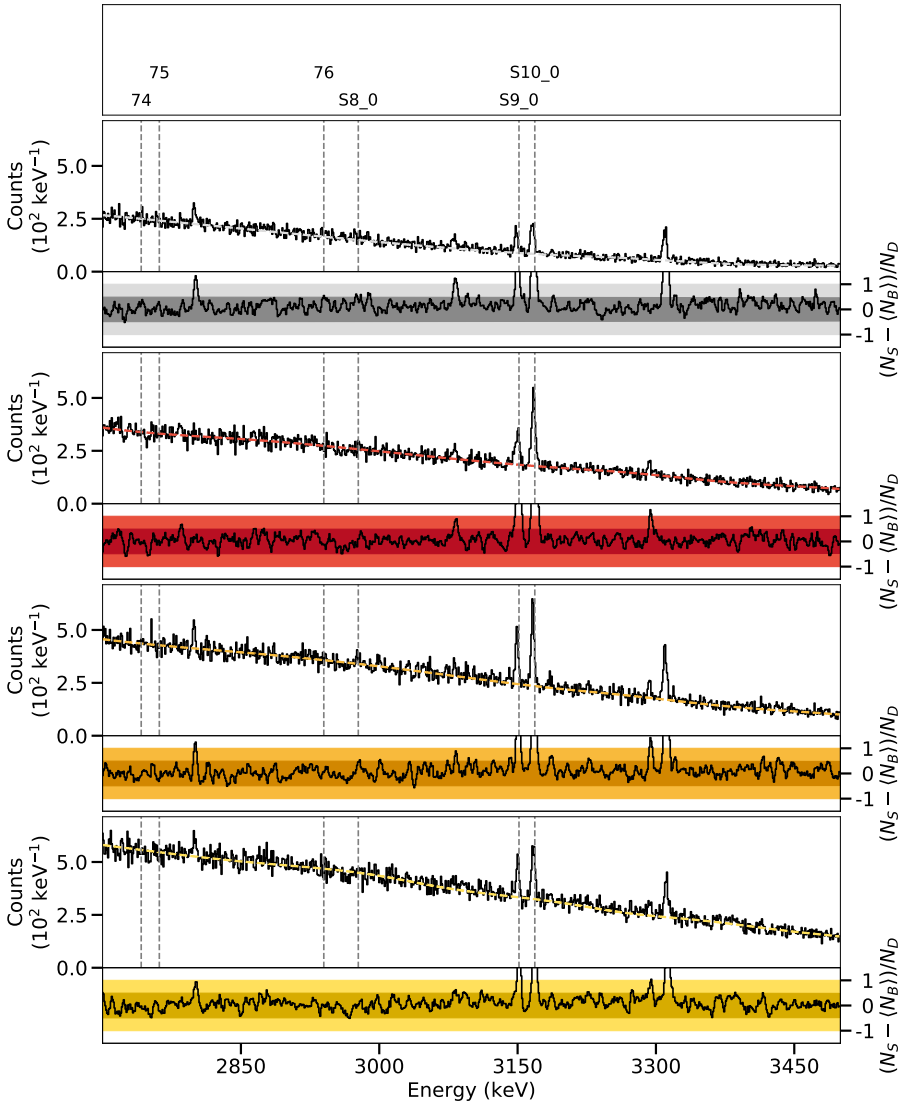


Figure D.111.: Spectra of the ^{82}Se target in the γ^3 setup at a beam energy of 3.82 MeV between 2700 keV and 3500 keV.

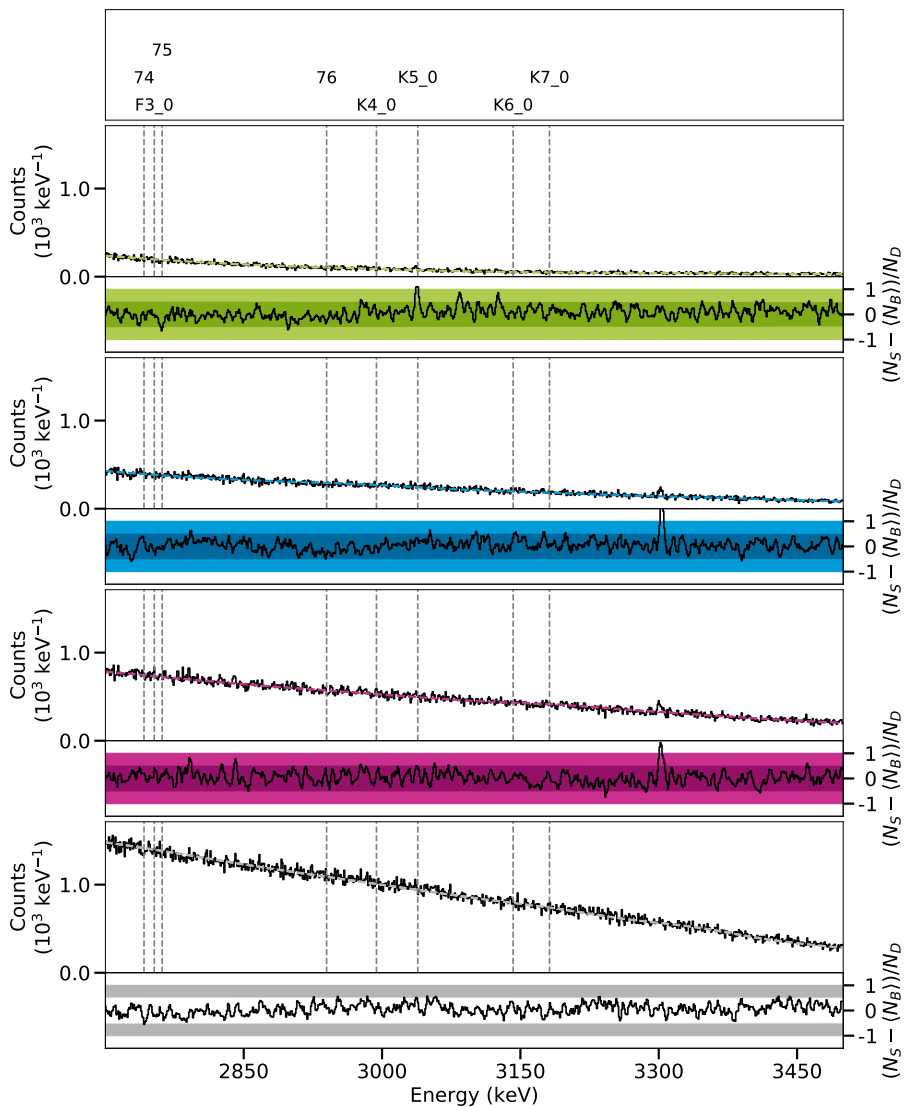


Figure D.112.: Spectra of the ^{82}Kr target in the polarimetry setup at a beam energy of 3.82 MeV between 2700 keV and 3500 keV.

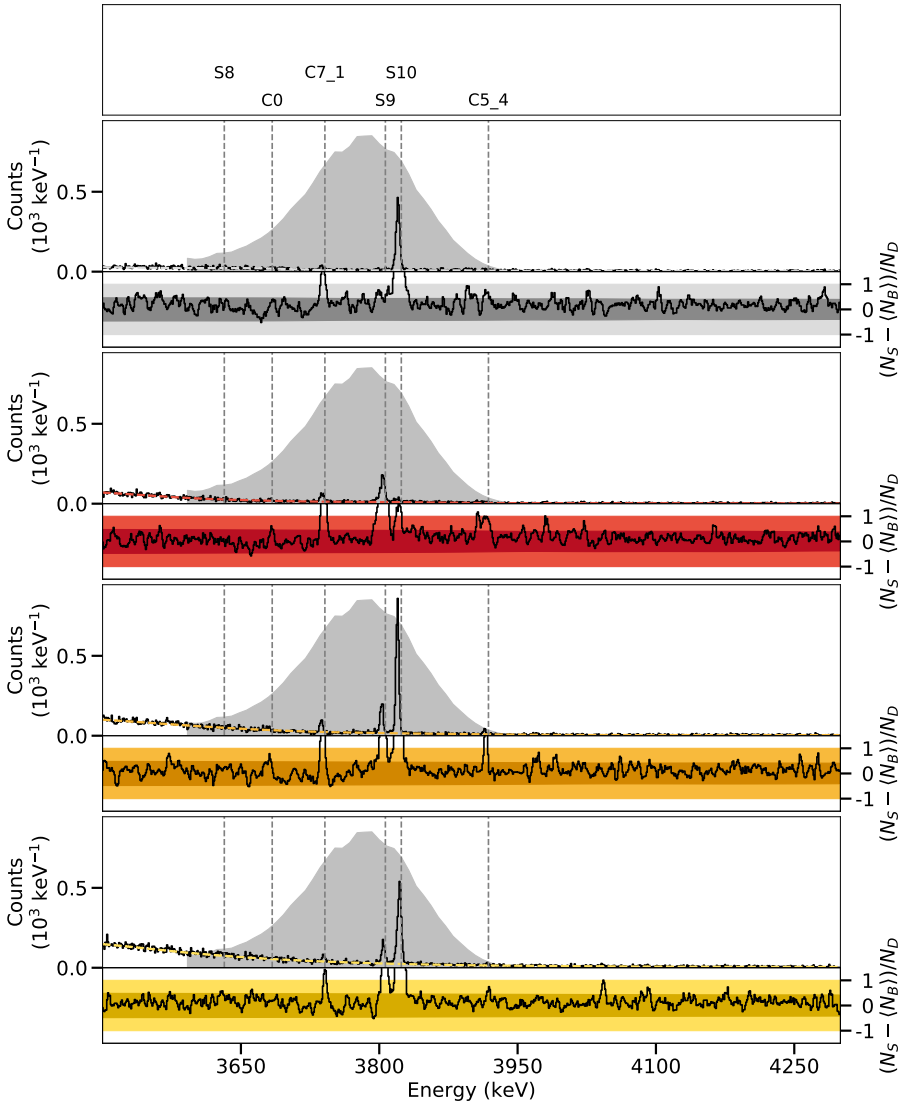


Figure D.113.: Spectra of the ^{82}Se target in the γ^3 setup at a beam energy of 3.82 MeV between 3500 keV and 4300 keV.

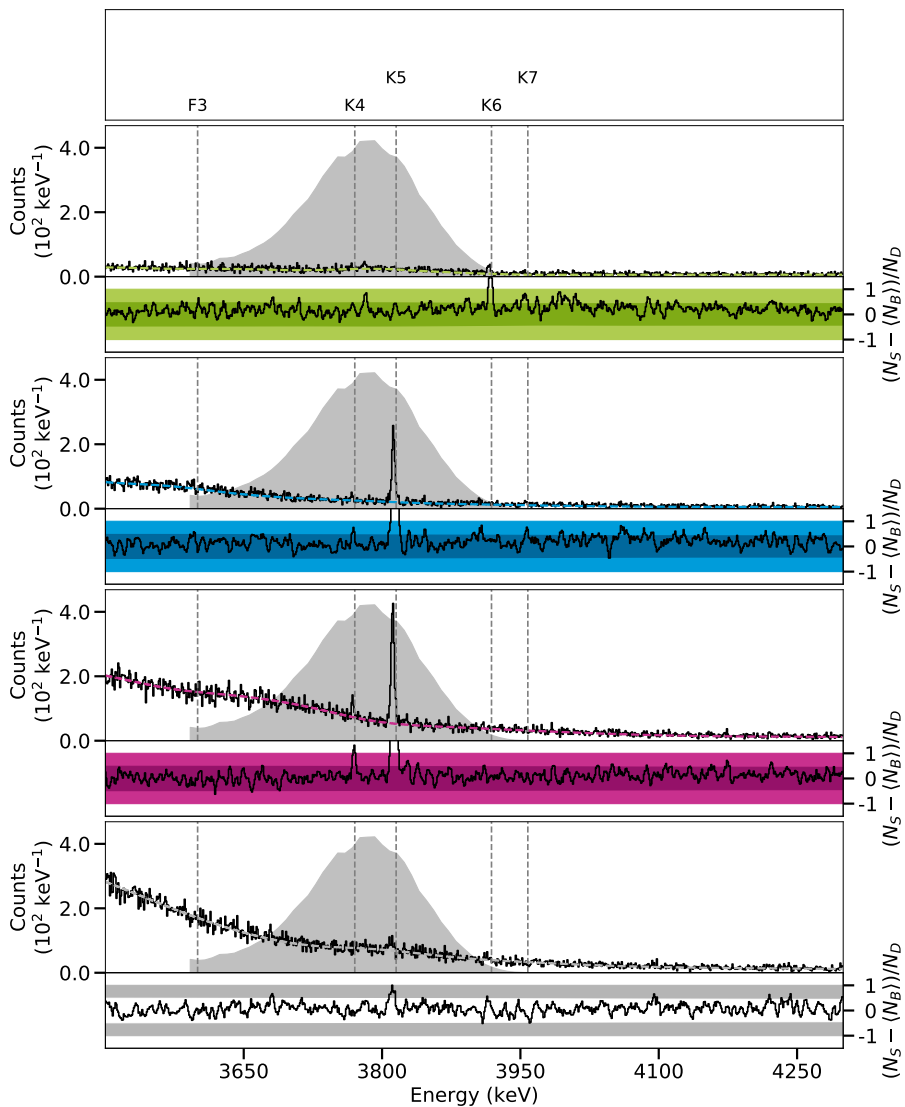


Figure D.114.: Spectra of the ^{82}Kr target in the polarimetry setup at a beam energy of 3.82 MeV between 3500 keV and 4300 keV.

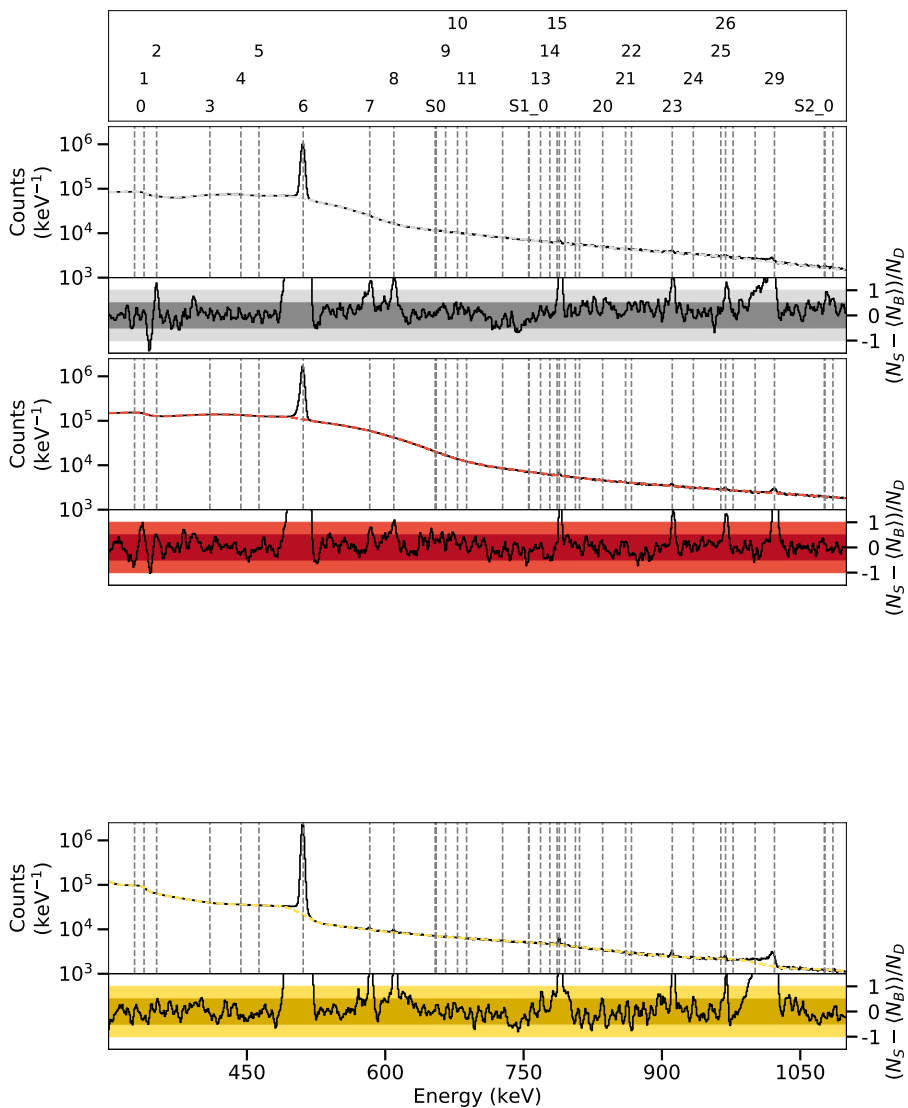


Figure D.115.: Spectra of the ^{82}Se target in the γ^3 setup at a beam energy of 3.95 MeV between 300 keV and 1100 keV.

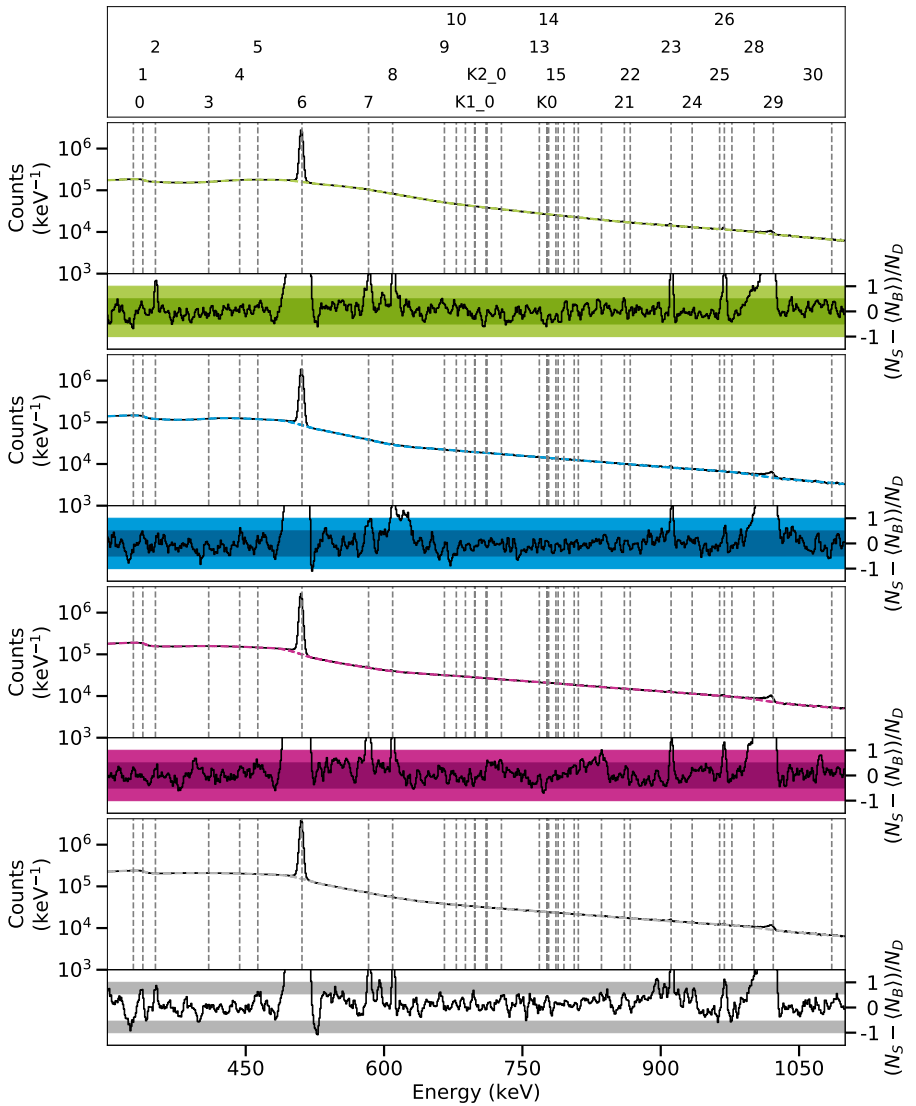


Figure D.116.: Spectra of the ^{82}Kr target in the polarimetry setup at a beam energy of 3.95 MeV between 300 keV and 1100 keV.

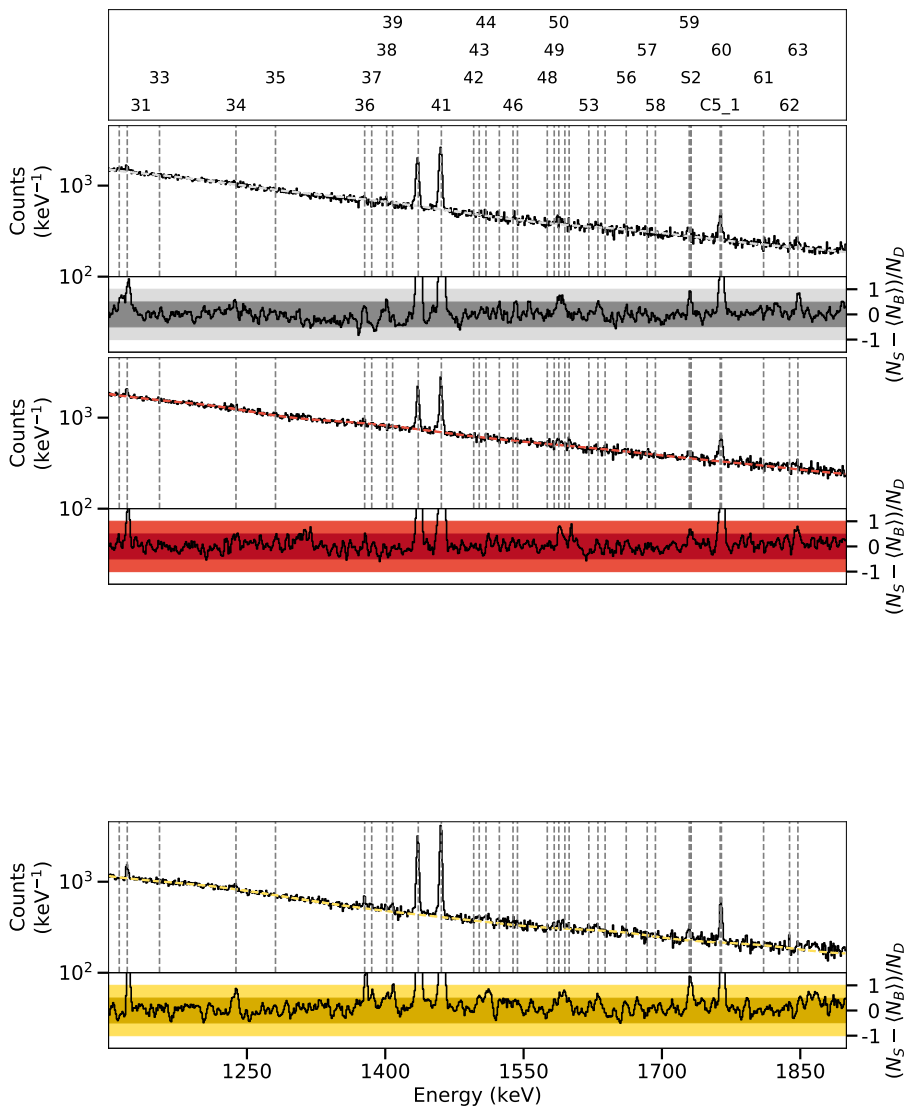


Figure D.117.: Spectra of the ^{82}Se target in the γ^3 setup at a beam energy of 3.95 MeV between 1100 keV and 1900 keV.

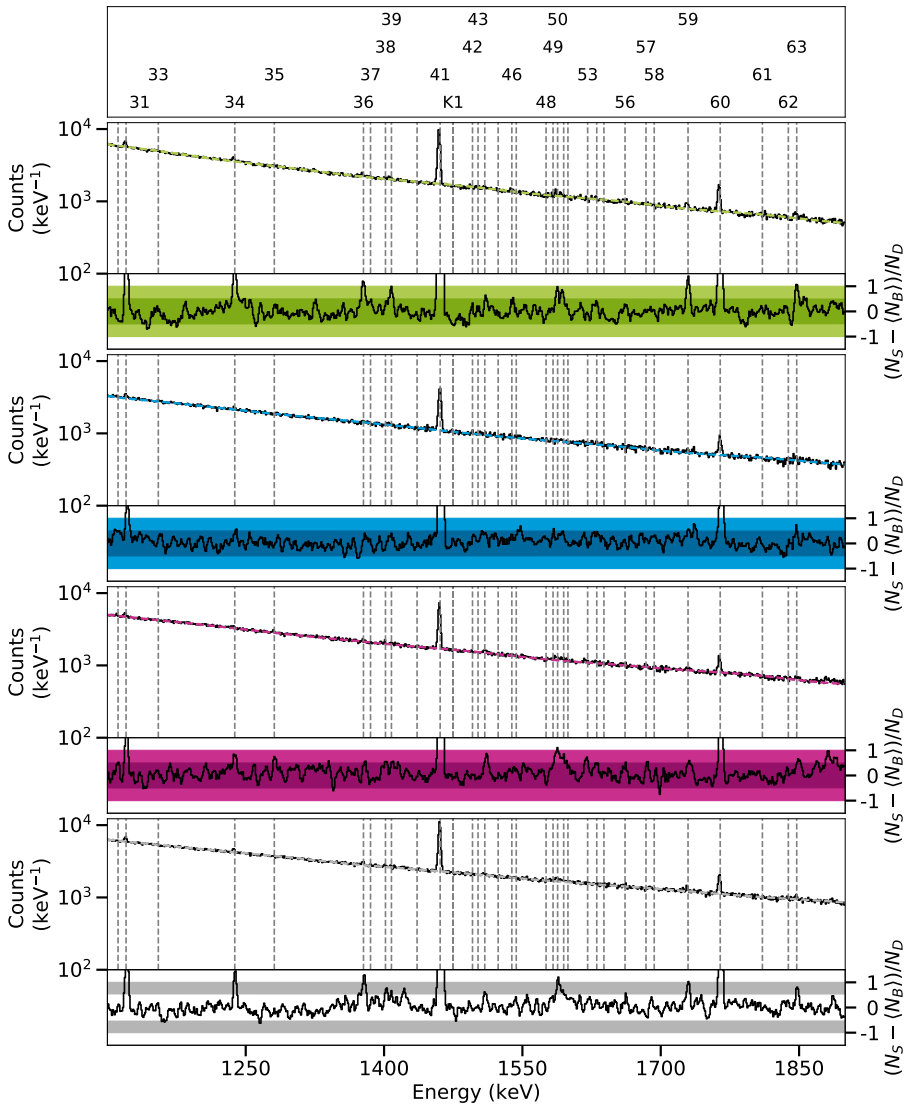


Figure D.118.: Spectra of the ^{82}Kr target in the polarimetry setup at a beam energy of 3.95 MeV between 1100 keV and 1900 keV.

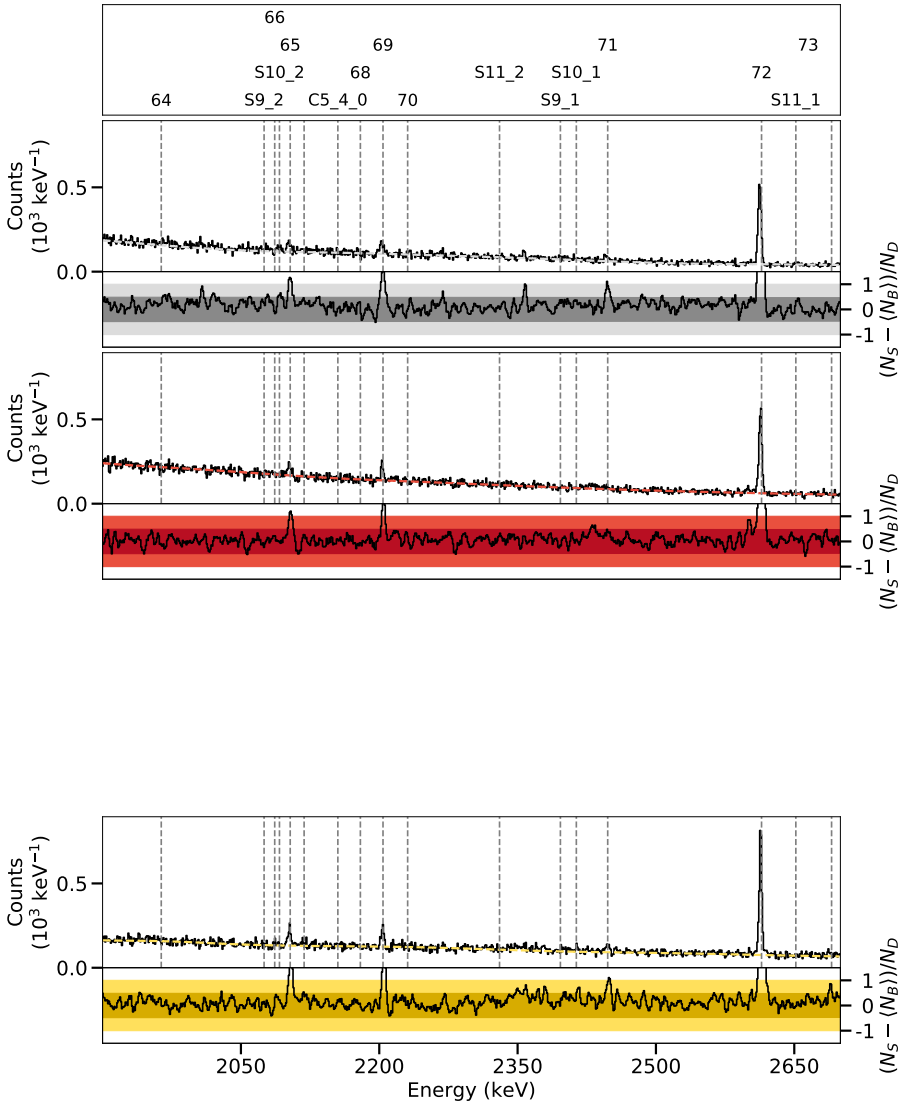


Figure D.119.: Spectra of the ^{82}Se target in the γ^3 setup at a beam energy of 3.95 MeV between 1900 keV and 2700 keV.

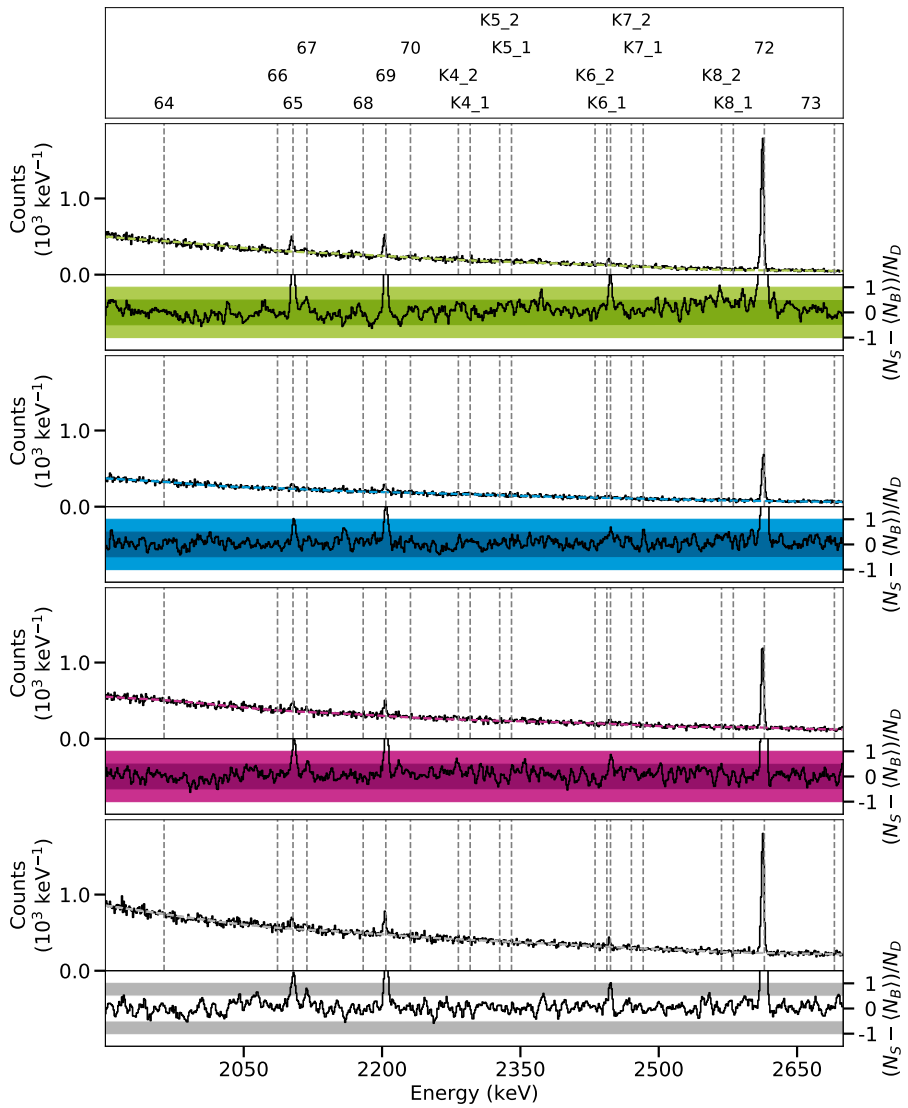


Figure D.120.: Spectra of the ^{82}Kr target in the polarimetry setup at a beam energy of 3.95 MeV between 1900 keV and 2700 keV.

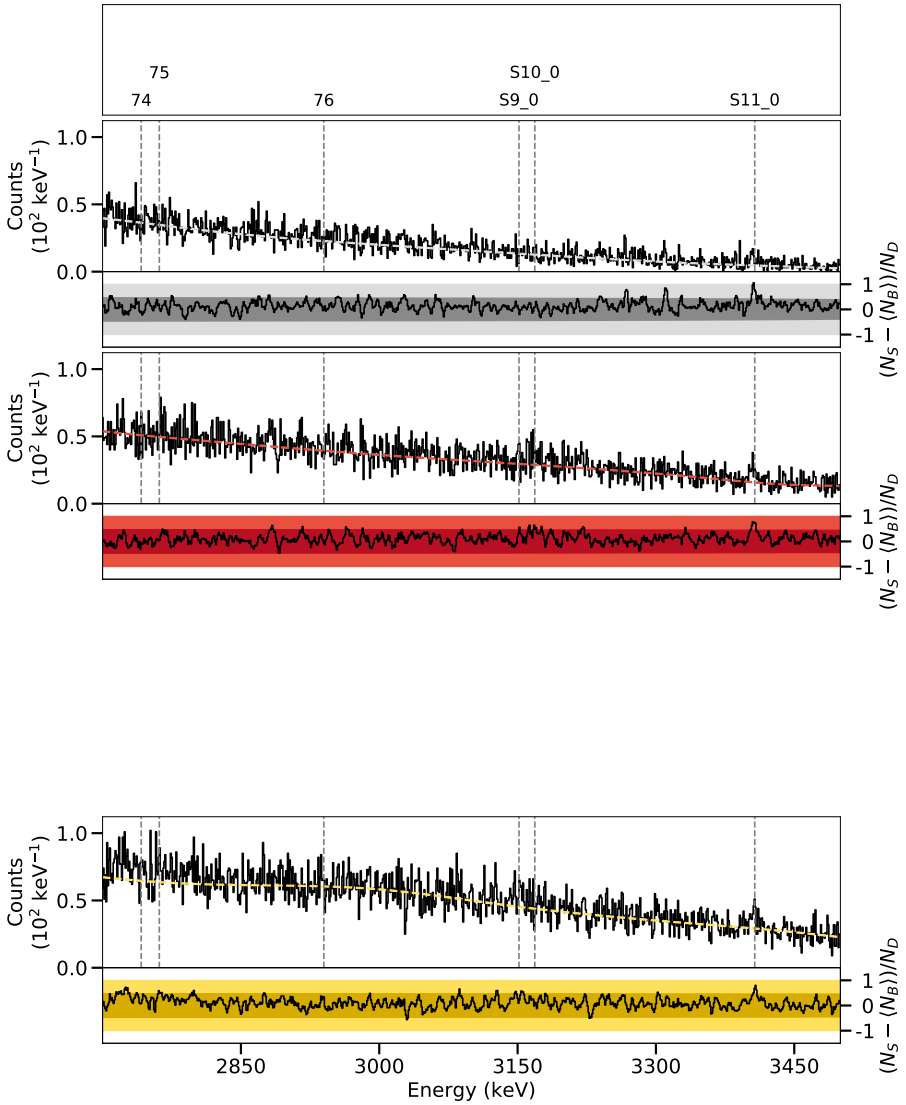


Figure D.121.: Spectra of the ^{82}Se target in the γ^3 setup at a beam energy of 3.95 MeV between 2700 keV and 3500 keV.

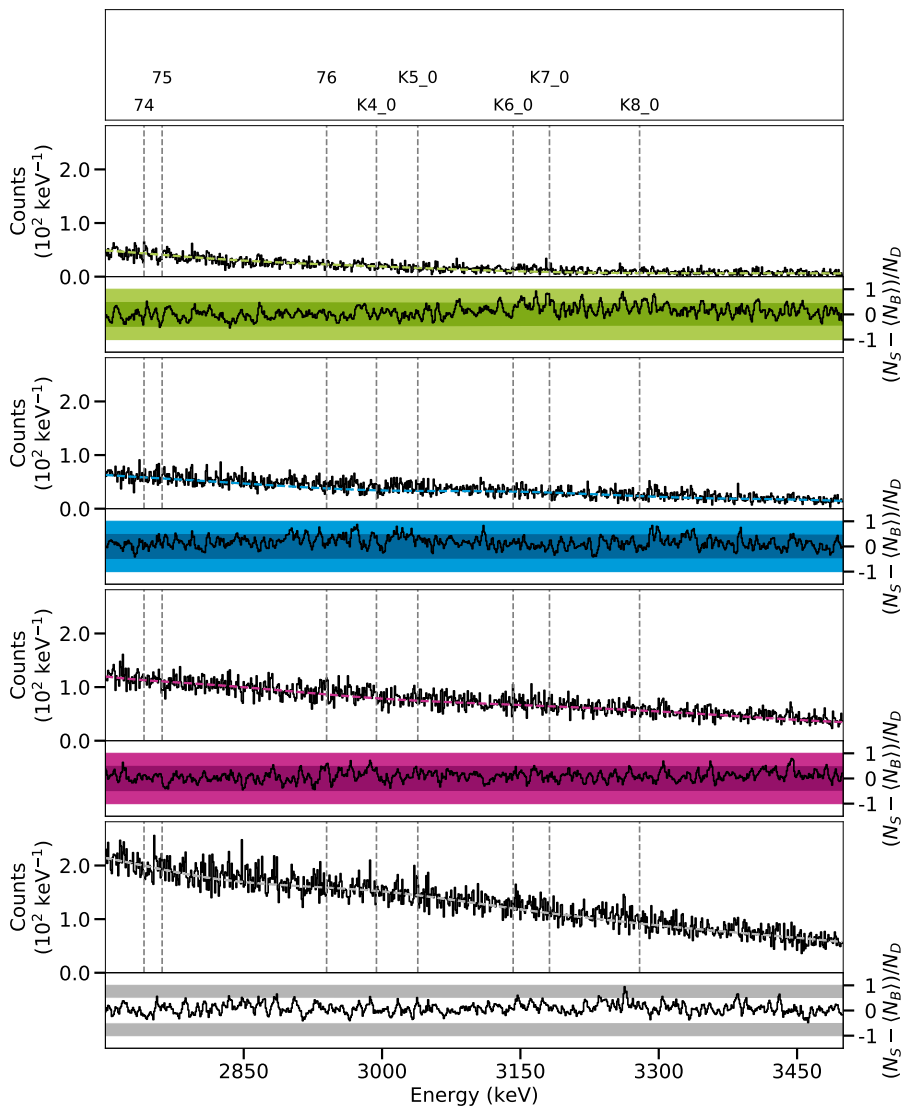


Figure D.122.: Spectra of the ^{82}Kr target in the polarimetry setup at a beam energy of 3.95 MeV between 2700 keV and 3500 keV.

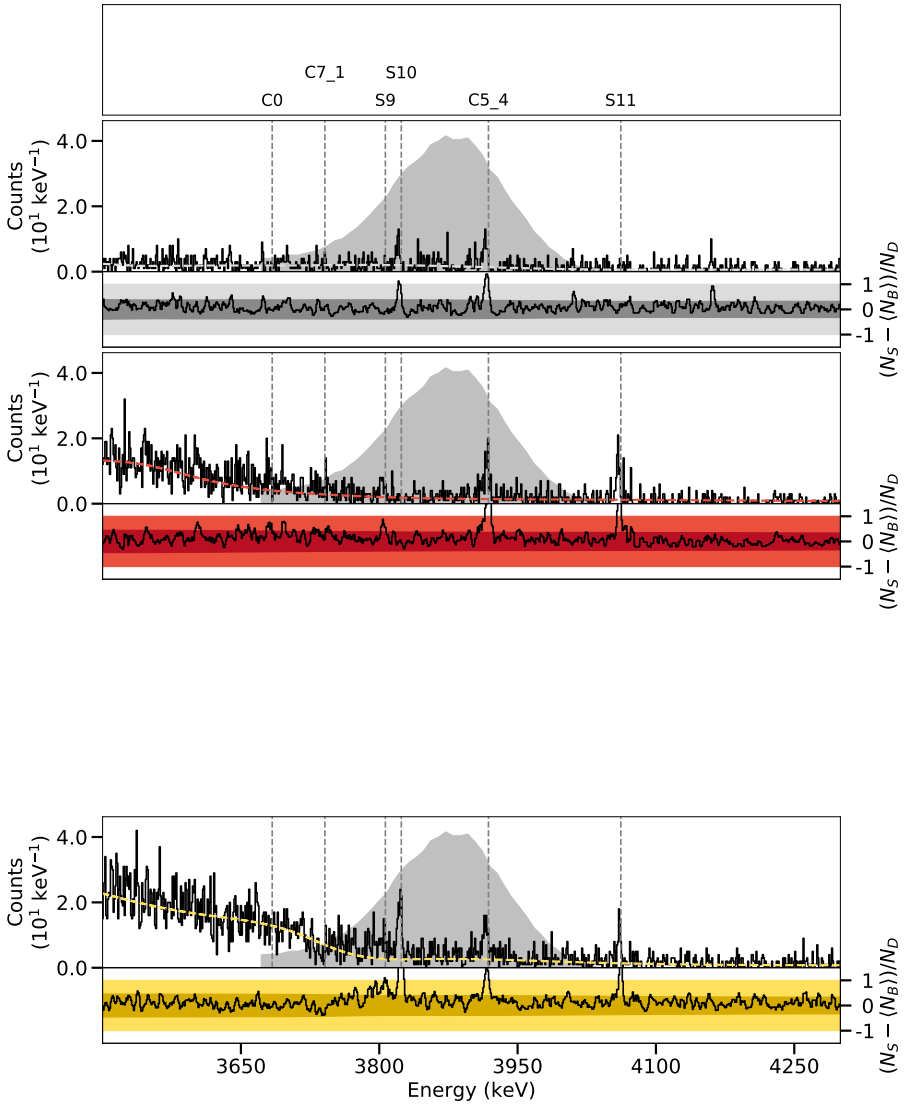


Figure D.123.: Spectra of the ^{82}Se target in the γ^3 setup at a beam energy of 3.95 MeV between 3500 keV and 4300 keV.

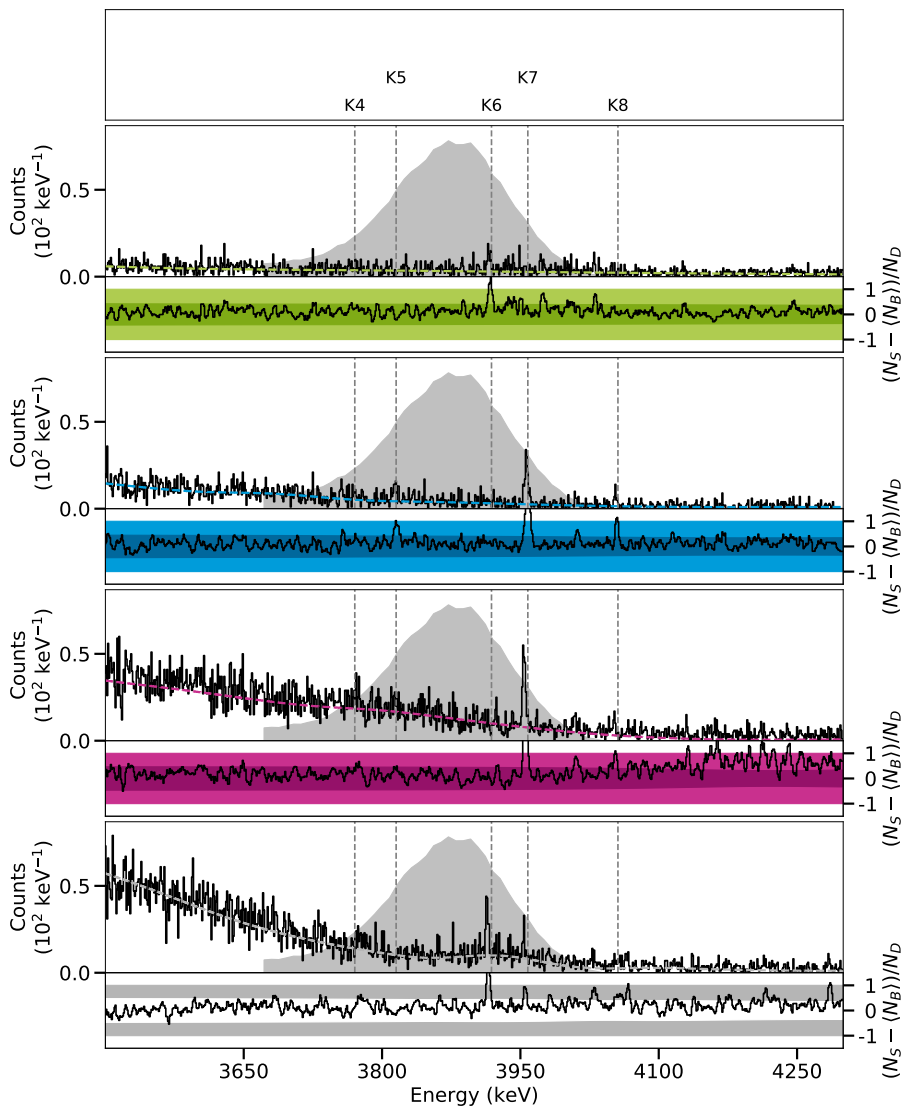


Figure D.124.: Spectra of the ^{82}Kr target in the polarimetry setup at a beam energy of 3.95 MeV between 3500 keV and 4300 keV.

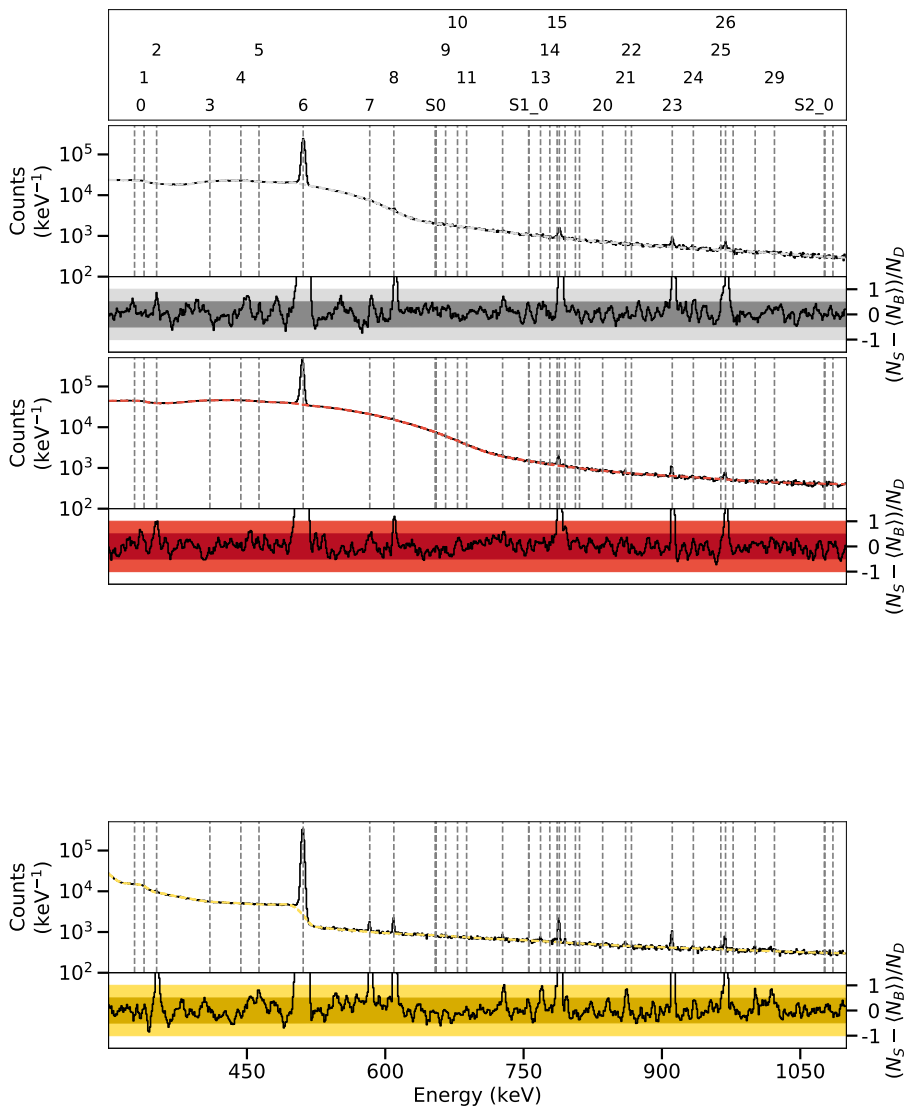


Figure D.125.: Spectra of the empty selenium target in the γ^3 setup at a beam energy of 3.95 MeV between 300 keV and 1100 keV.

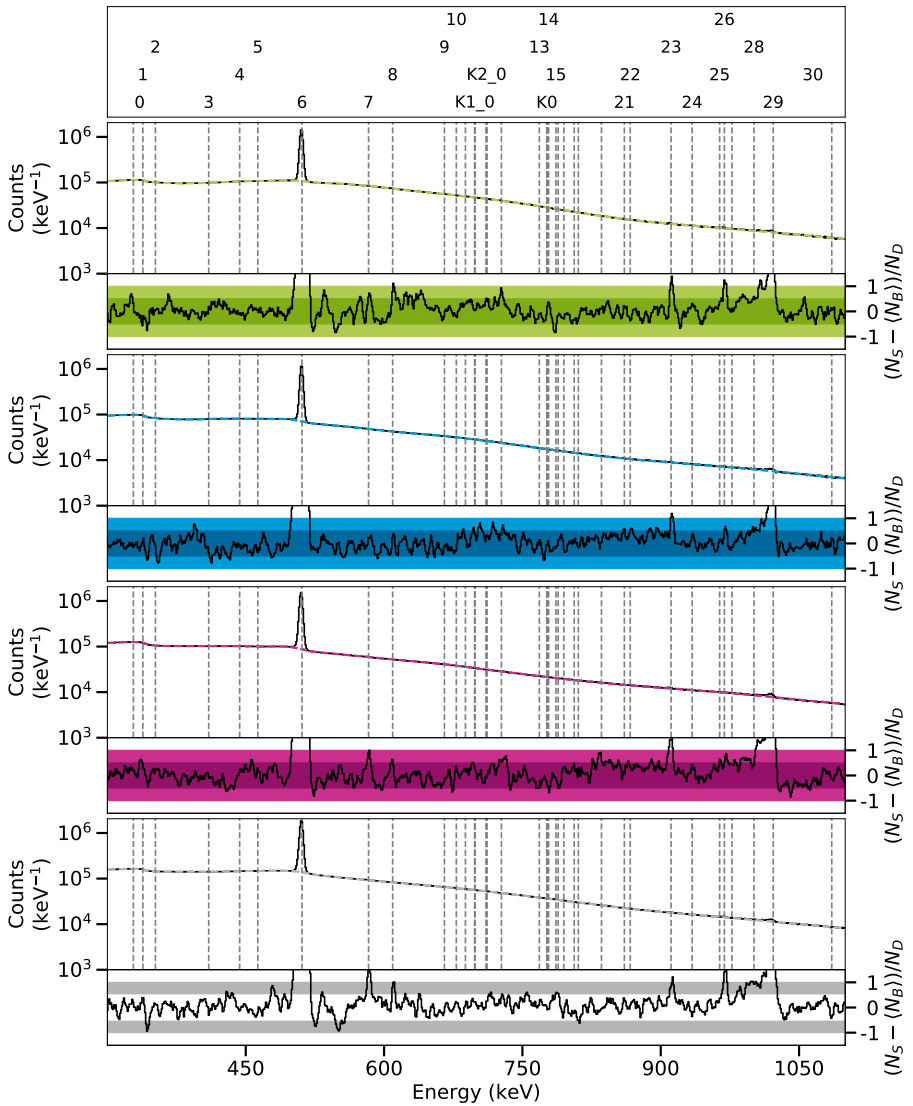


Figure D.126.: Spectra of the empty krypton target in the polarimetry setup at a beam energy of 3.95 MeV between 300 keV and 1100 keV.

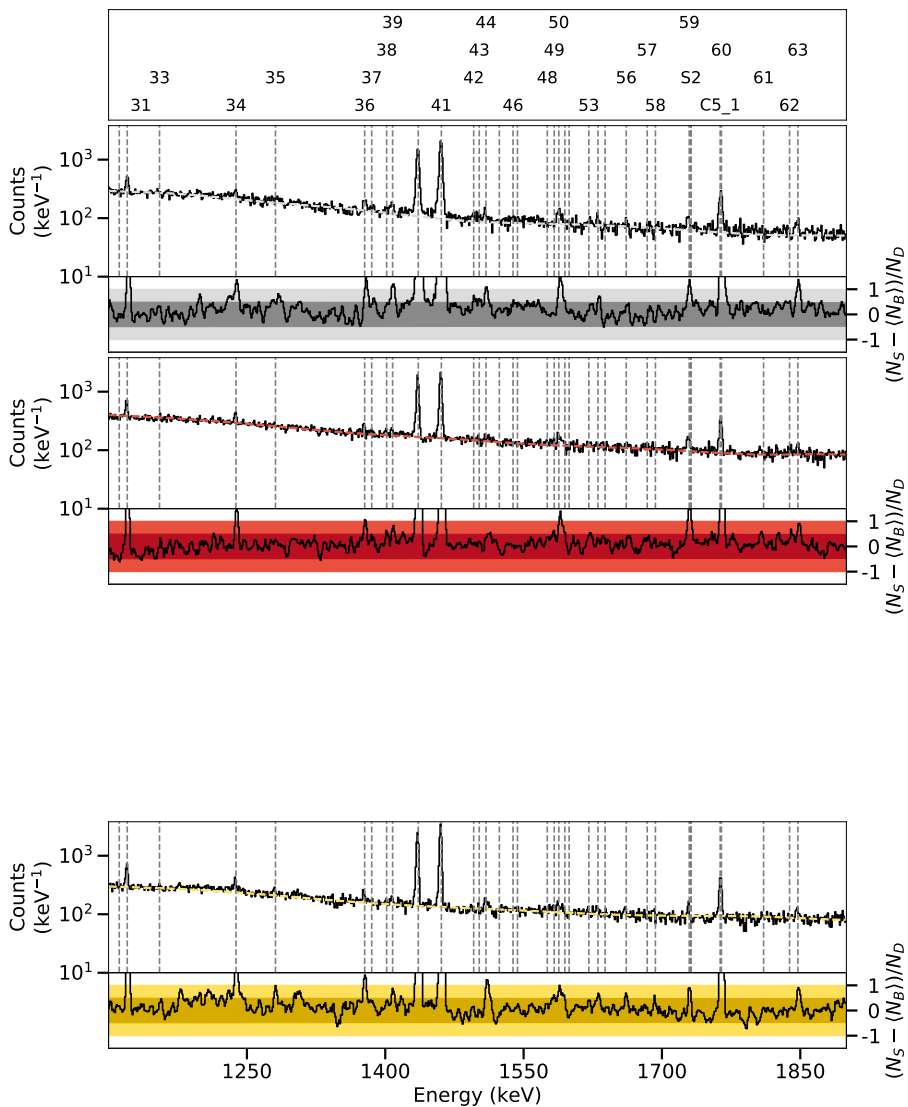


Figure D.127.: Spectra of the empty selenium target in the γ^3 setup at a beam energy of 3.95 MeV between 1100 keV and 1900 keV.

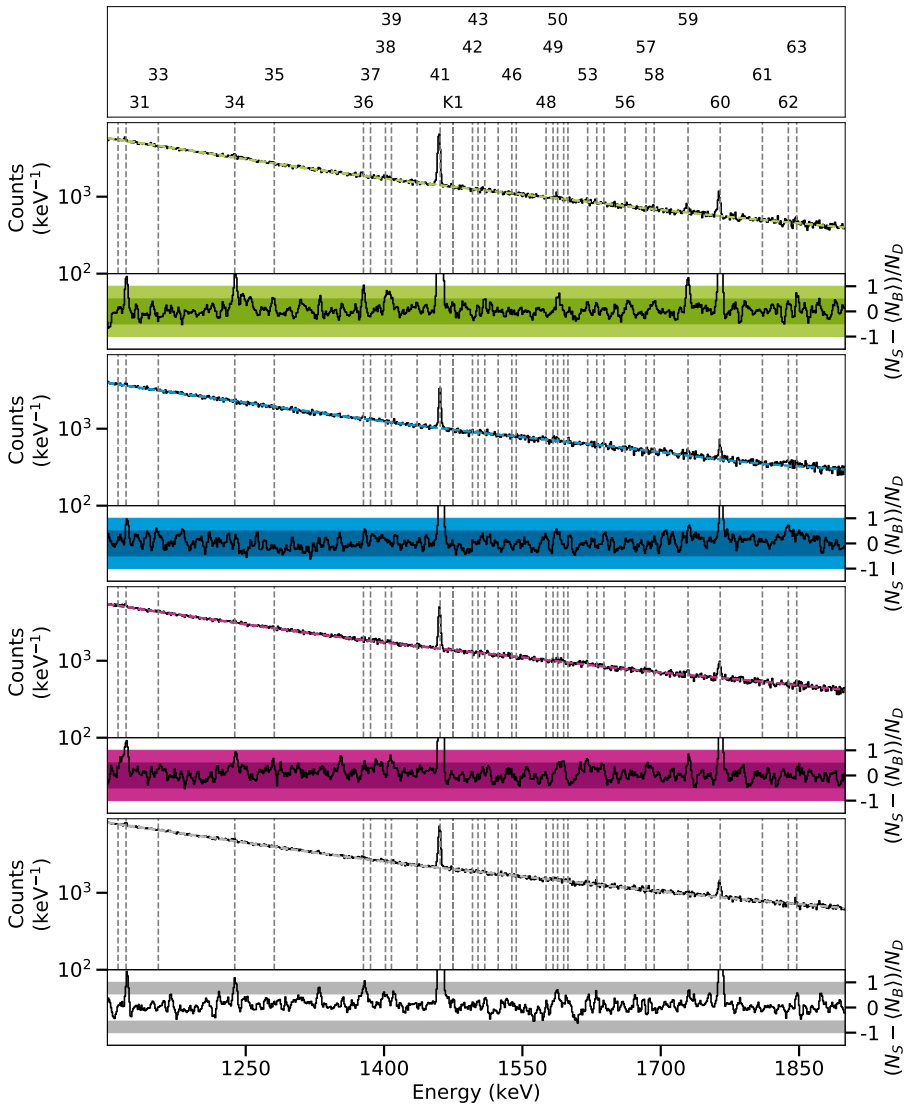


Figure D.128.: Spectra of the empty krypton target in the polarimetry setup at a beam energy of 3.95 MeV between 1100 keV and 1900 keV.

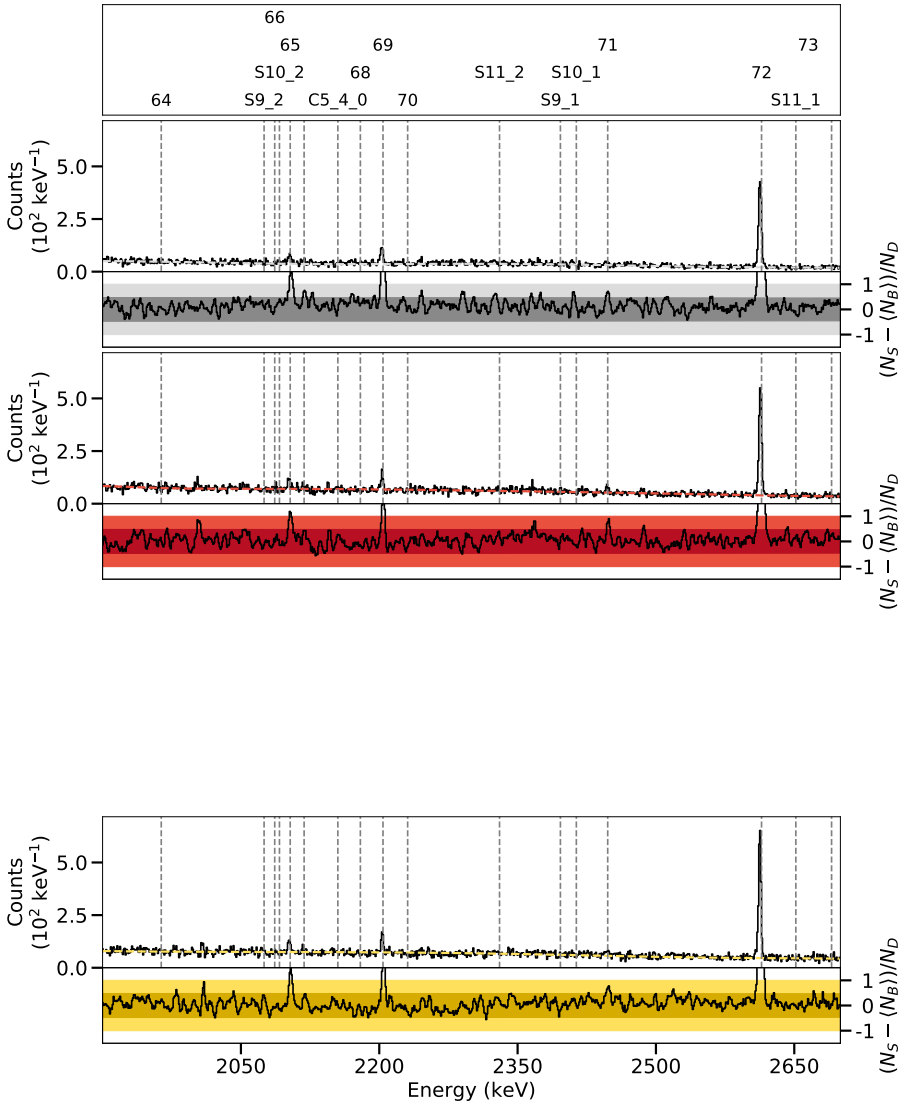


Figure D.129.: Spectra of the empty selenium target in the γ^3 setup at a beam energy of 3.95 MeV between 1900 keV and 2700 keV.

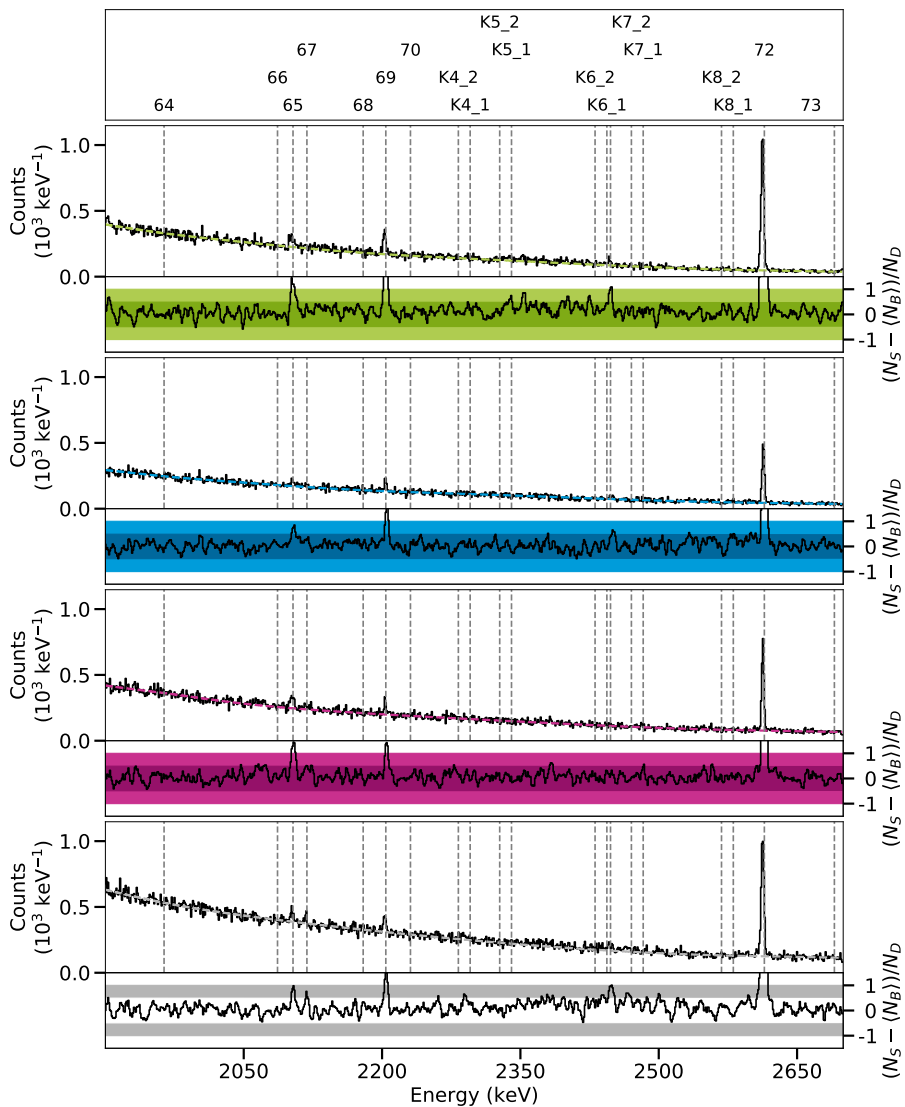


Figure D.130.: Spectra of the empty krypton target in the polarimetry setup at a beam energy of 3.95 MeV between 1900 keV and 2700 keV.

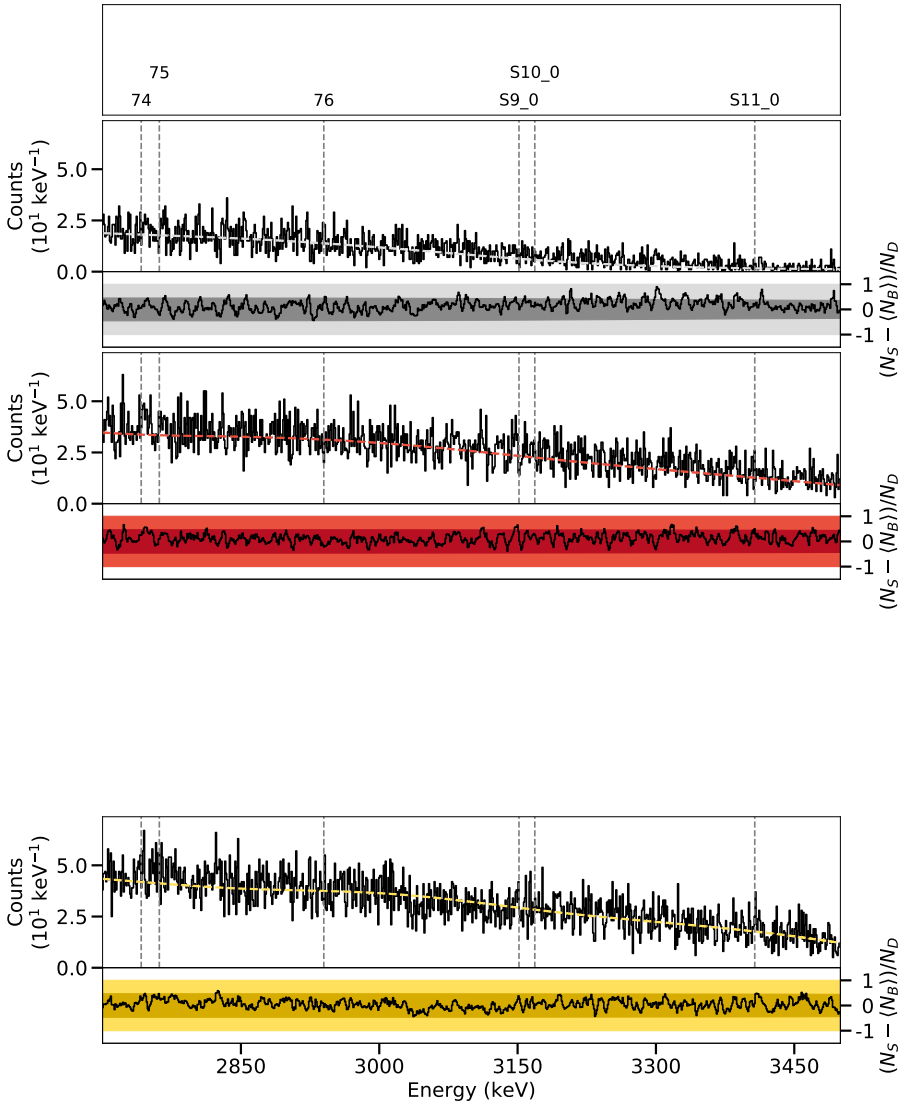


Figure D.131.: Spectra of the empty selenium target in the γ^3 setup at a beam energy of 3.95 MeV between 2700 keV and 3500 keV.

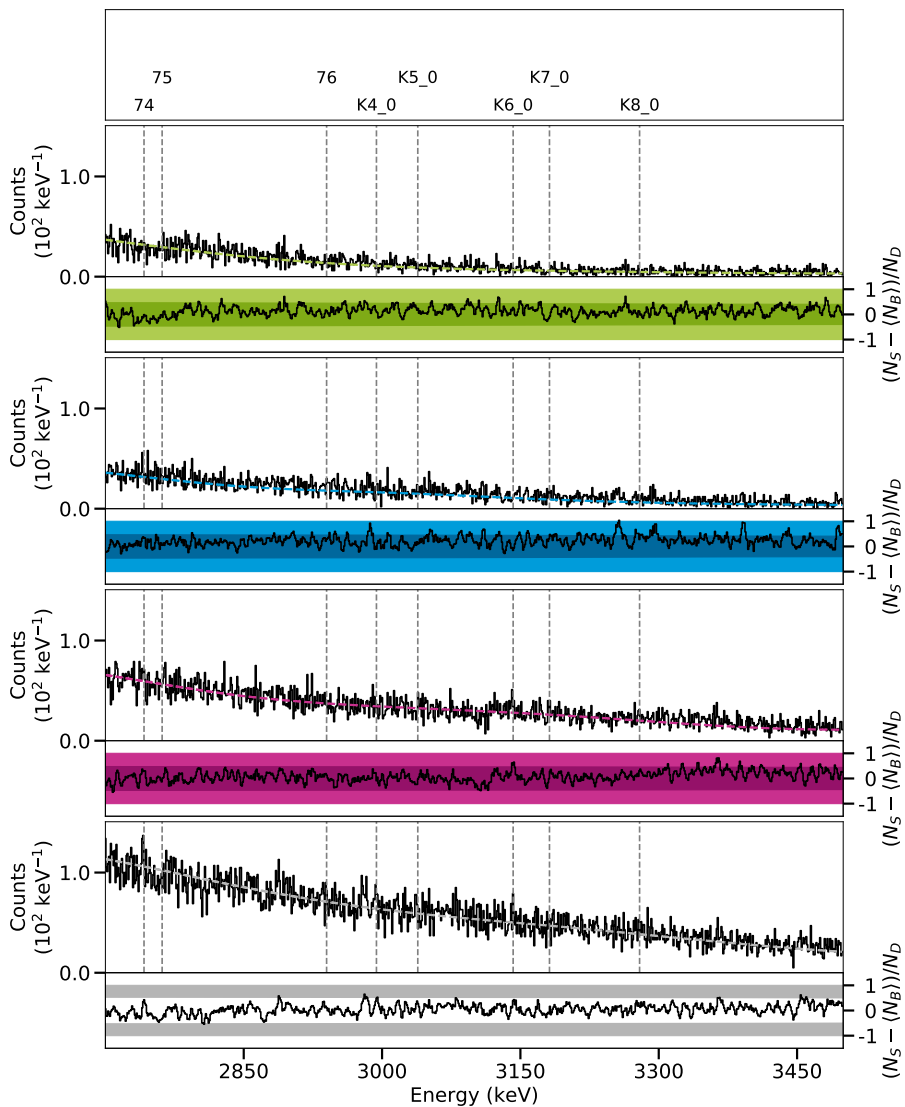


Figure D.132.: Spectra of the empty krypton target in the polarimetry setup at a beam energy of 3.95 MeV between 2700 keV and 3500 keV.

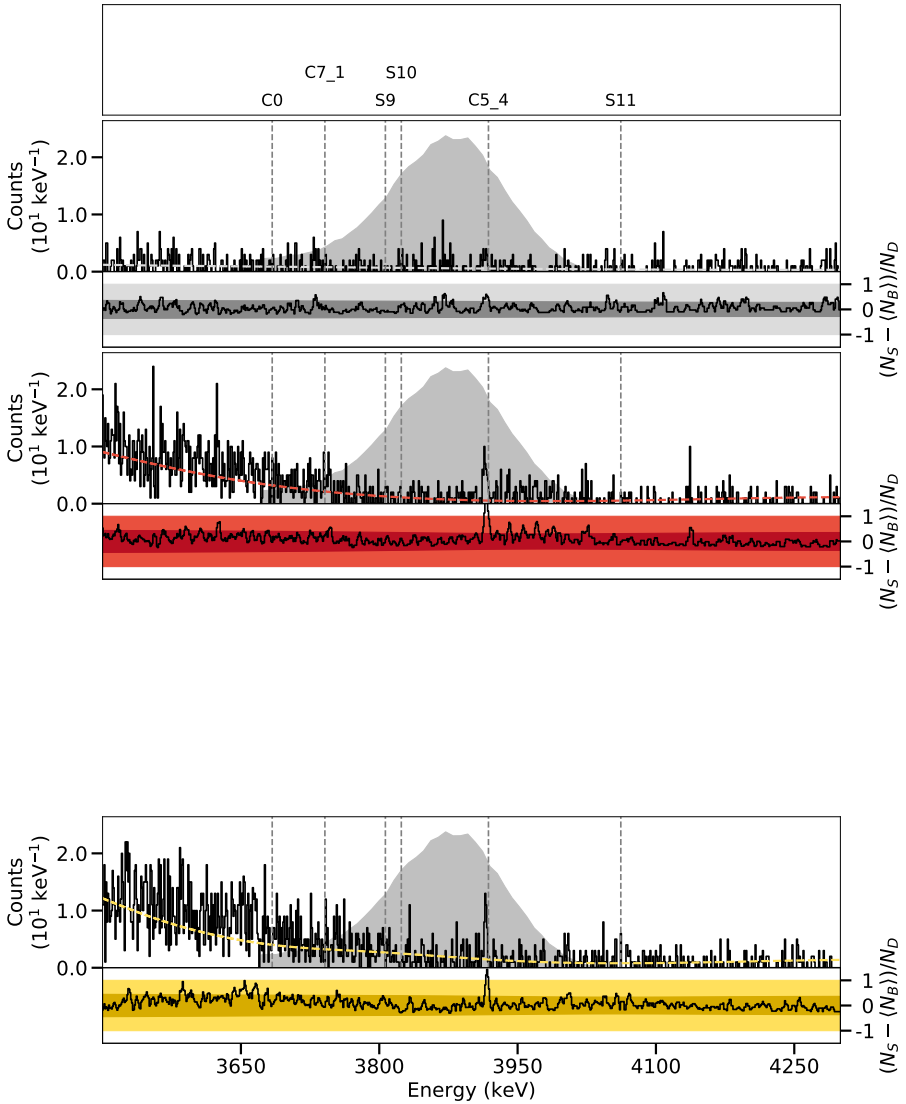


Figure D.133.: Spectra of the empty selenium target in the γ^3 setup at a beam energy of 3.95 MeV between 3500 keV and 4300 keV.

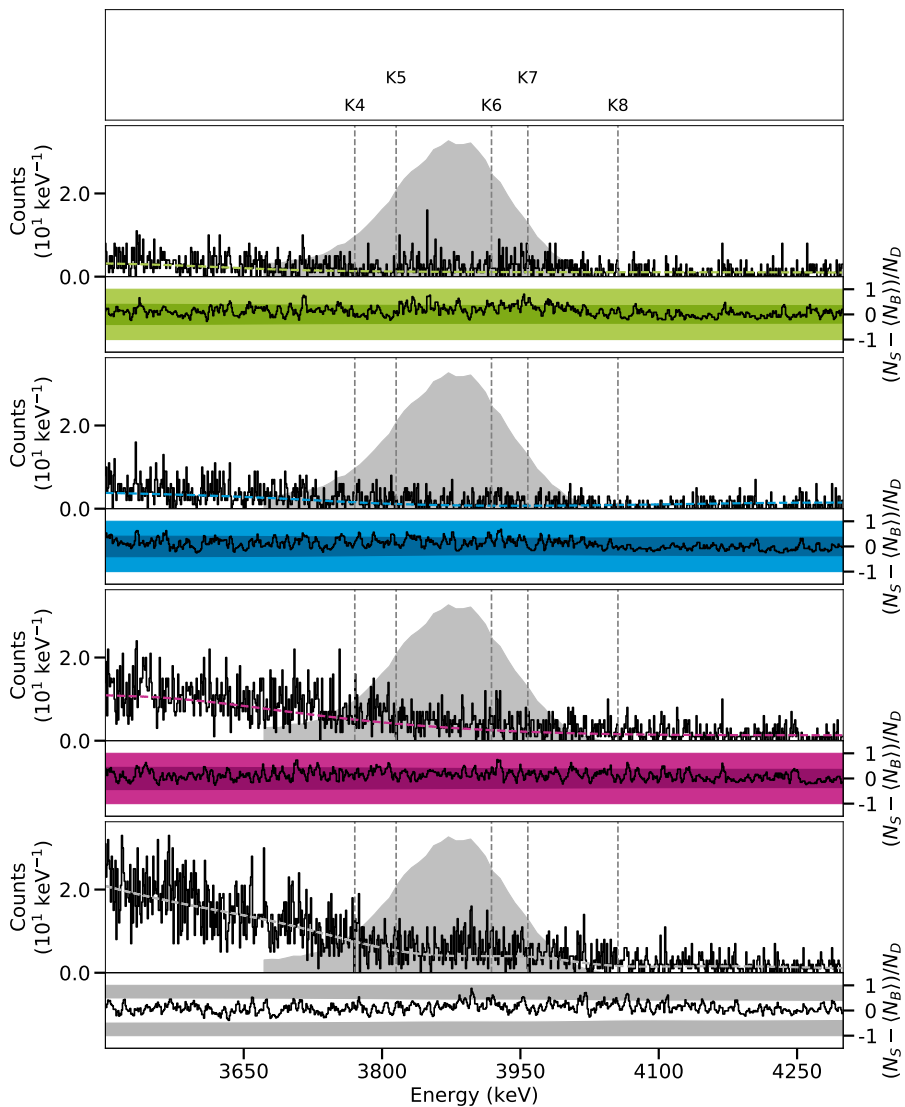


Figure D.134.: Spectra of the empty krypton target in the polarimetry setup at a beam energy of 3.95 MeV between 3500 keV and 4300 keV.

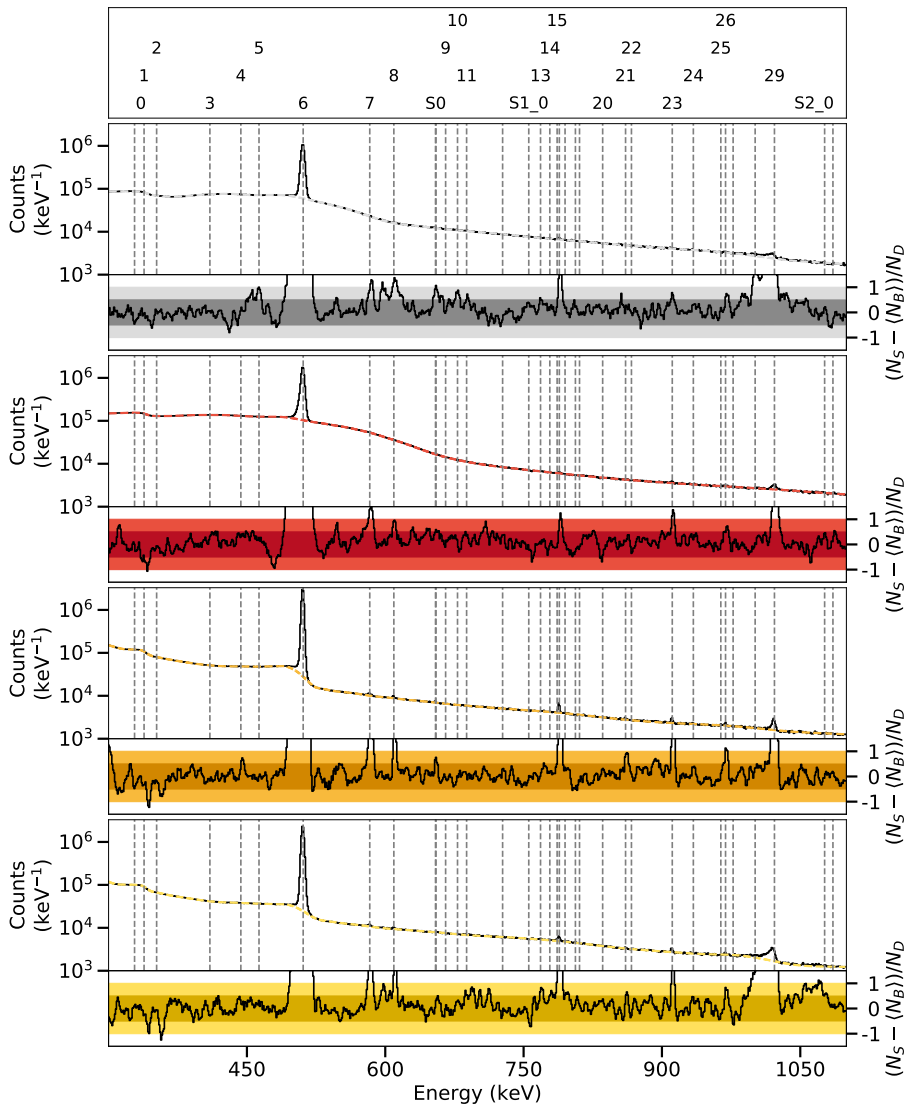


Figure D.135.: Spectra of the ^{82}Se target in the γ^3 setup at a beam energy of 4.10 MeV between 300 keV and 1100 keV.

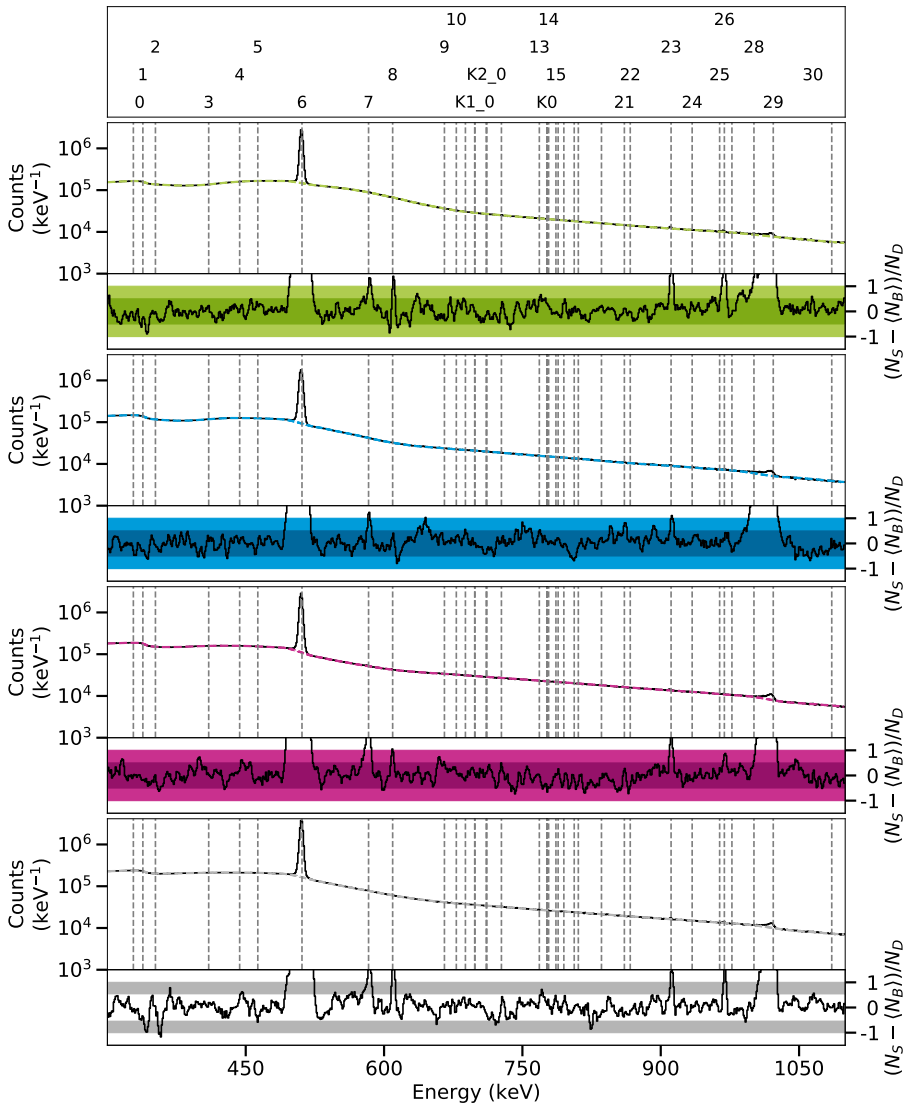


Figure D.136.: Spectra of the ^{82}Kr target in the polarimetry setup at a beam energy of 4.10 MeV between 300 keV and 1100 keV.

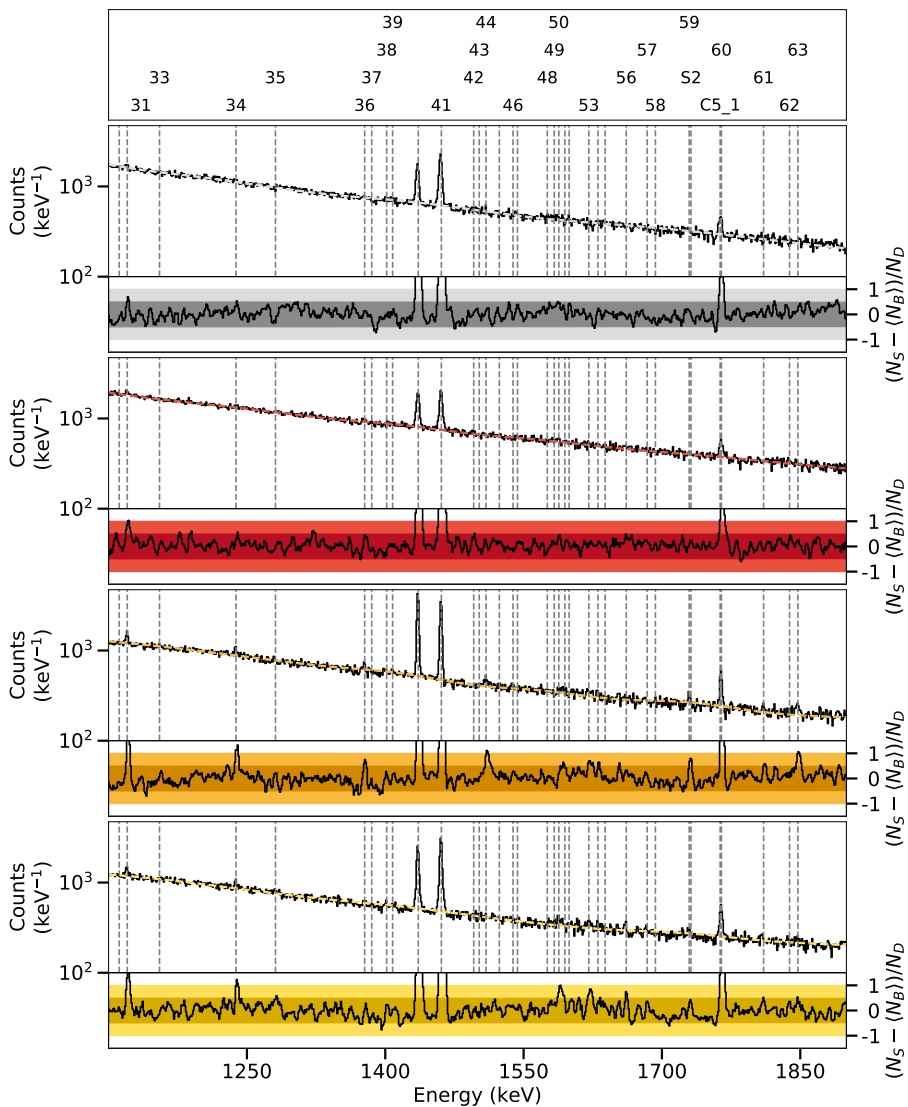


Figure D.137.: Spectra of the ^{82}Se target in the γ^3 setup at a beam energy of 4.10 MeV between 1100 keV and 1900 keV.

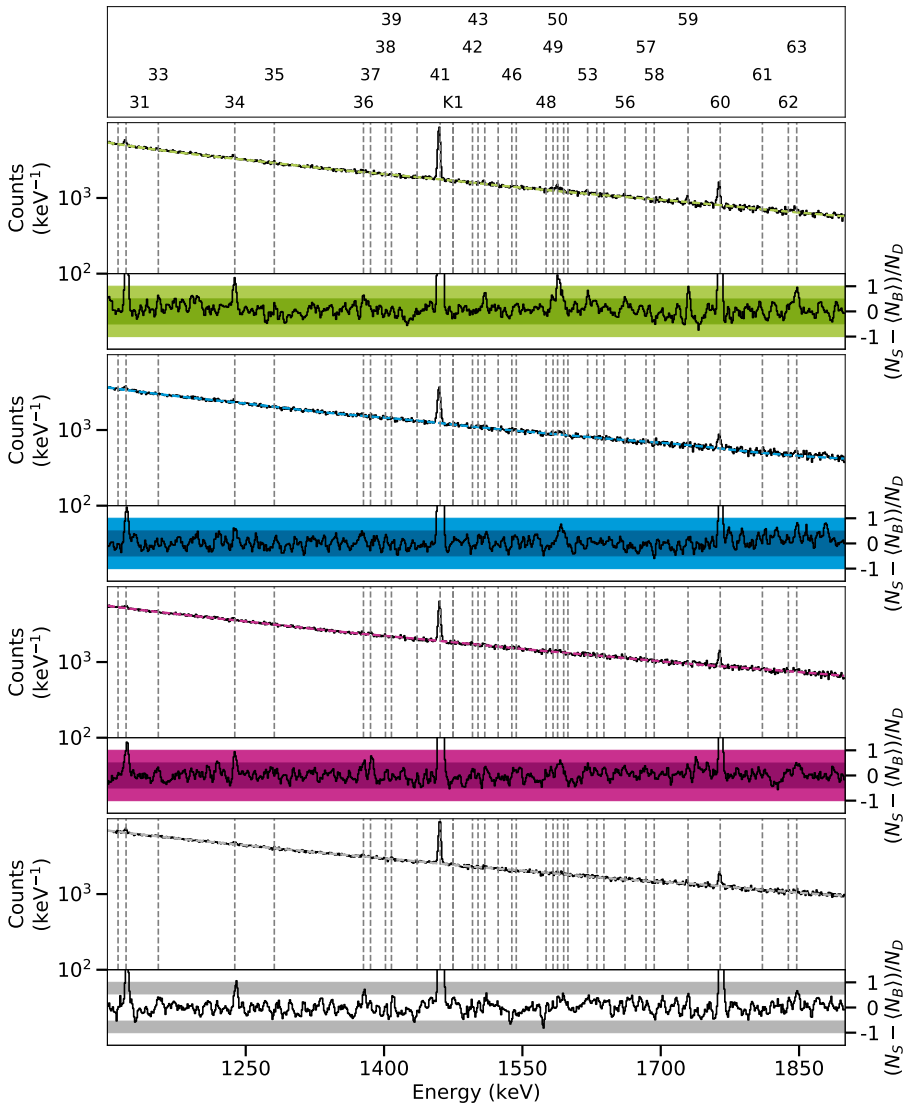


Figure D.138.: Spectra of the ^{82}Kr target in the polarimetry setup at a beam energy of 4.10 MeV between 1100 keV and 1900 keV.

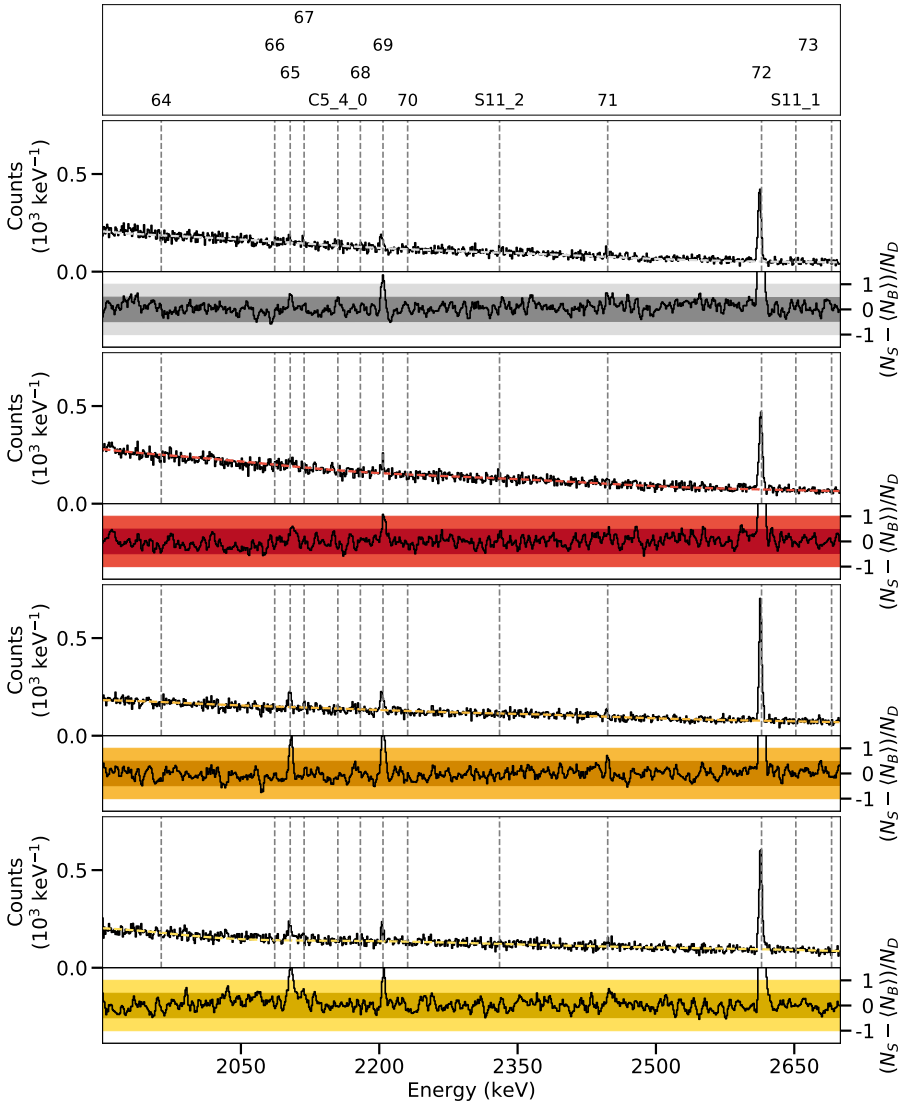


Figure D.139.: Spectra of the ^{82}Se target in the γ^3 setup at a beam energy of 4.10 MeV between 1900 keV and 2700 keV.

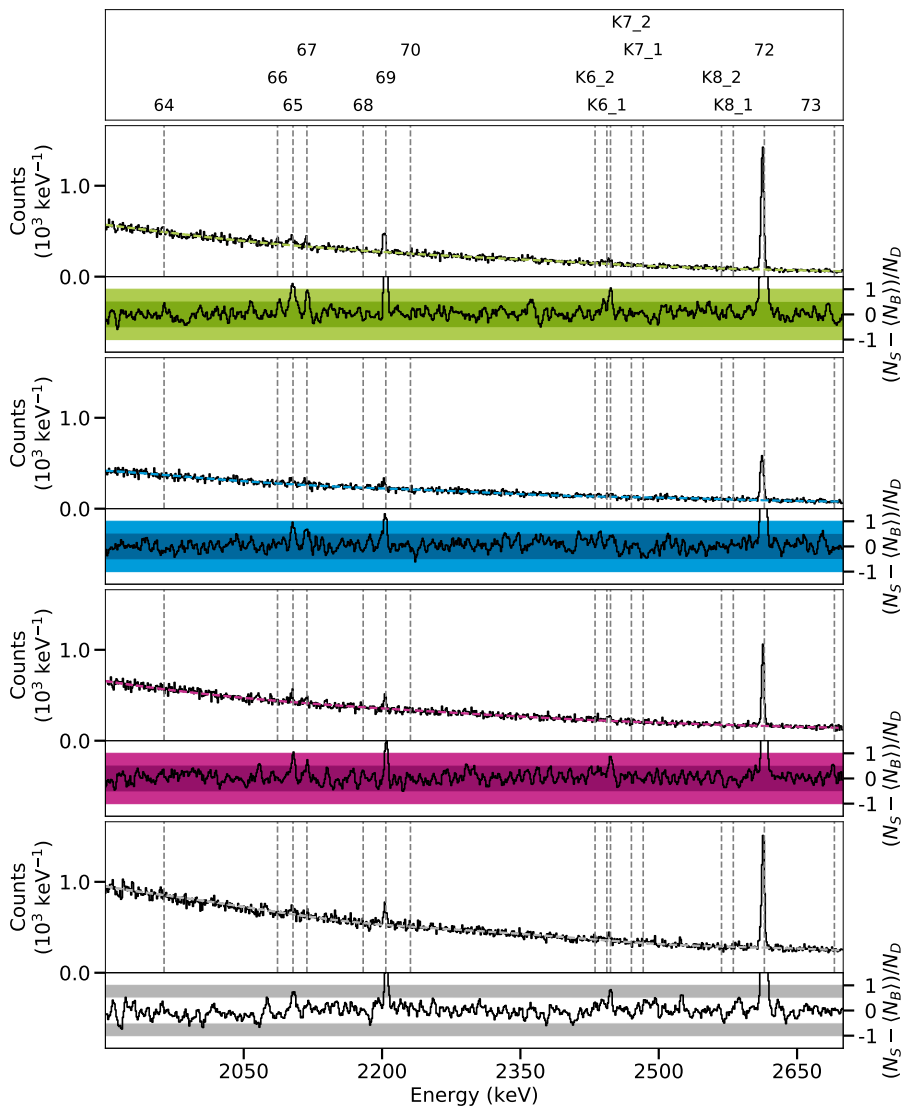


Figure D.140.: Spectra of the ^{82}Kr target in the polarimetry setup at a beam energy of 4.10 MeV between 1900 keV and 2700 keV.

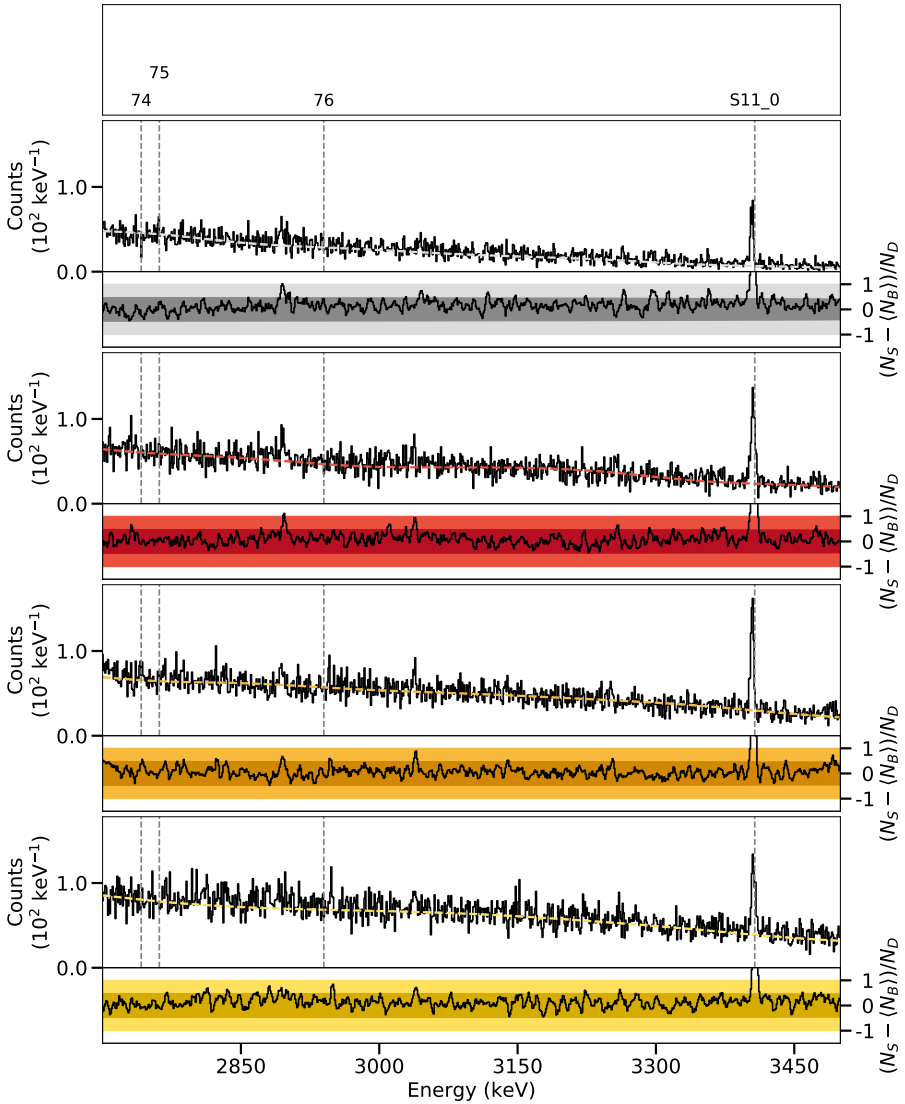


Figure D.141.: Spectra of the ^{82}Se target in the γ^3 setup at a beam energy of 4.10 MeV between 2700 keV and 3500 keV.

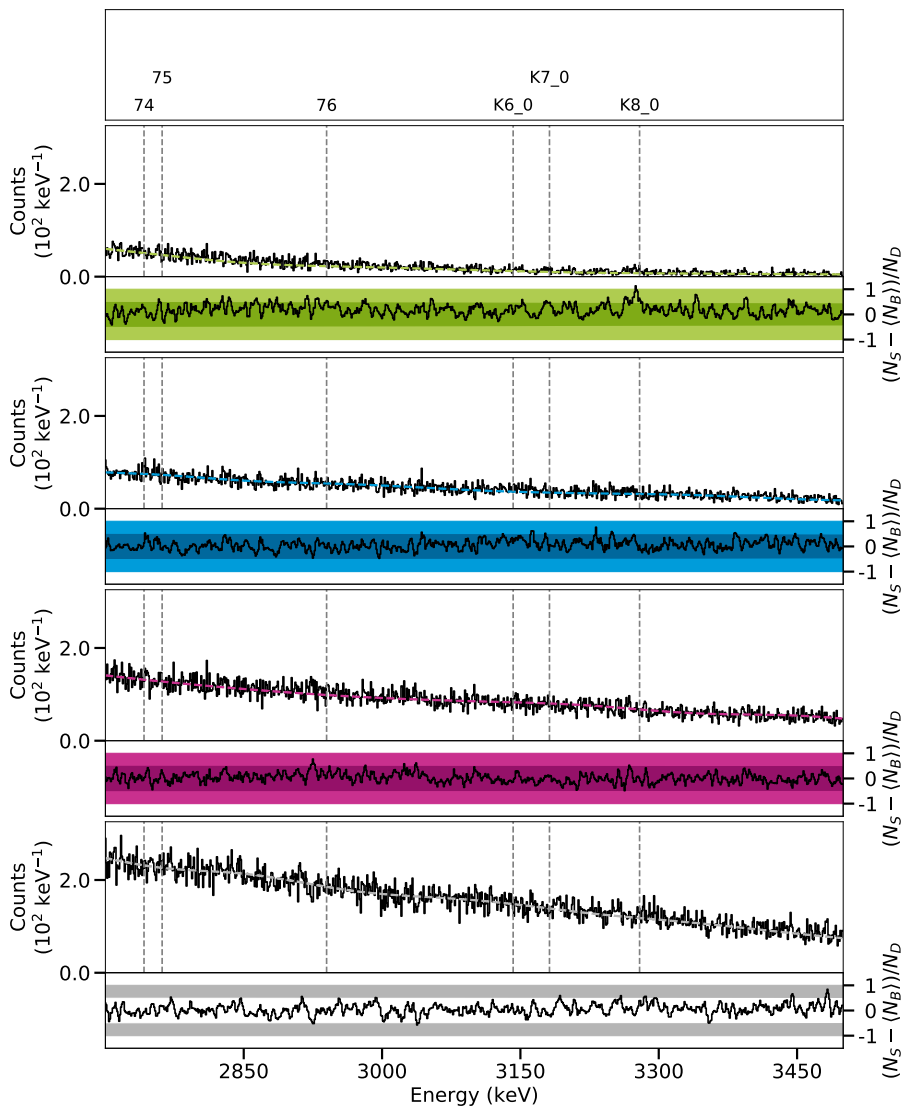


Figure D.142.: Spectra of the ^{82}Kr target in the polarimetry setup at a beam energy of 4.10 MeV between 2700 keV and 3500 keV.

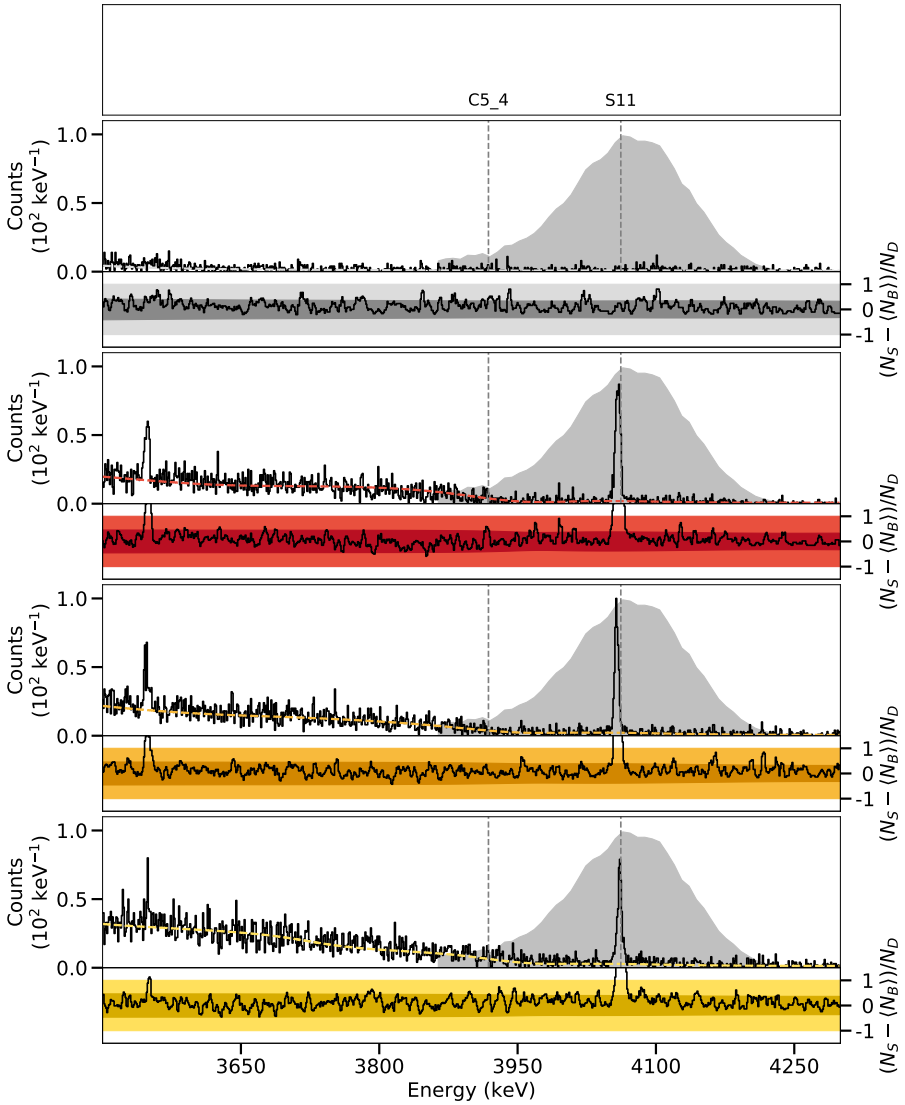


Figure D.143.: Spectra of the ^{82}Se target in the γ^3 setup at a beam energy of 4.10 MeV between 3500 keV and 4300 keV.

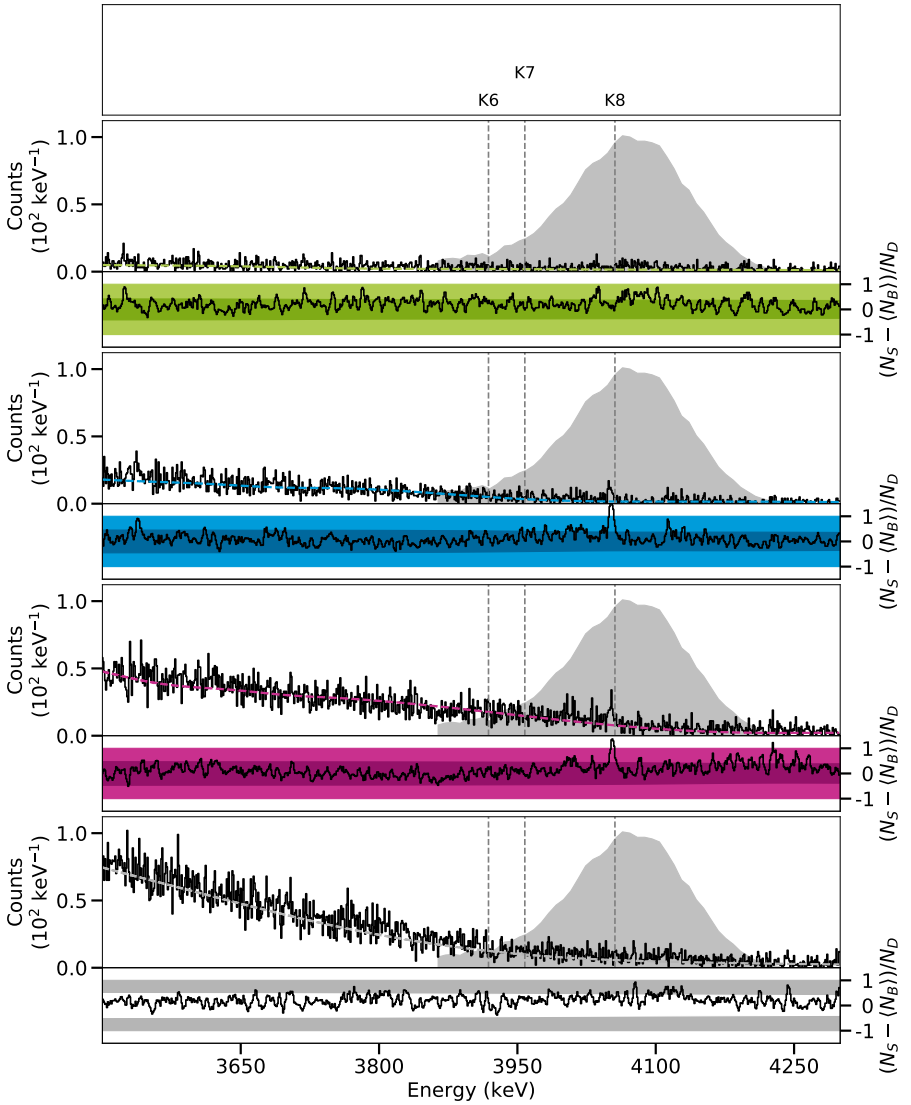


Figure D.144.: Spectra of the ^{82}Kr target in the polarimetry setup at a beam energy of 4.10 MeV between 3500 keV and 4300 keV.

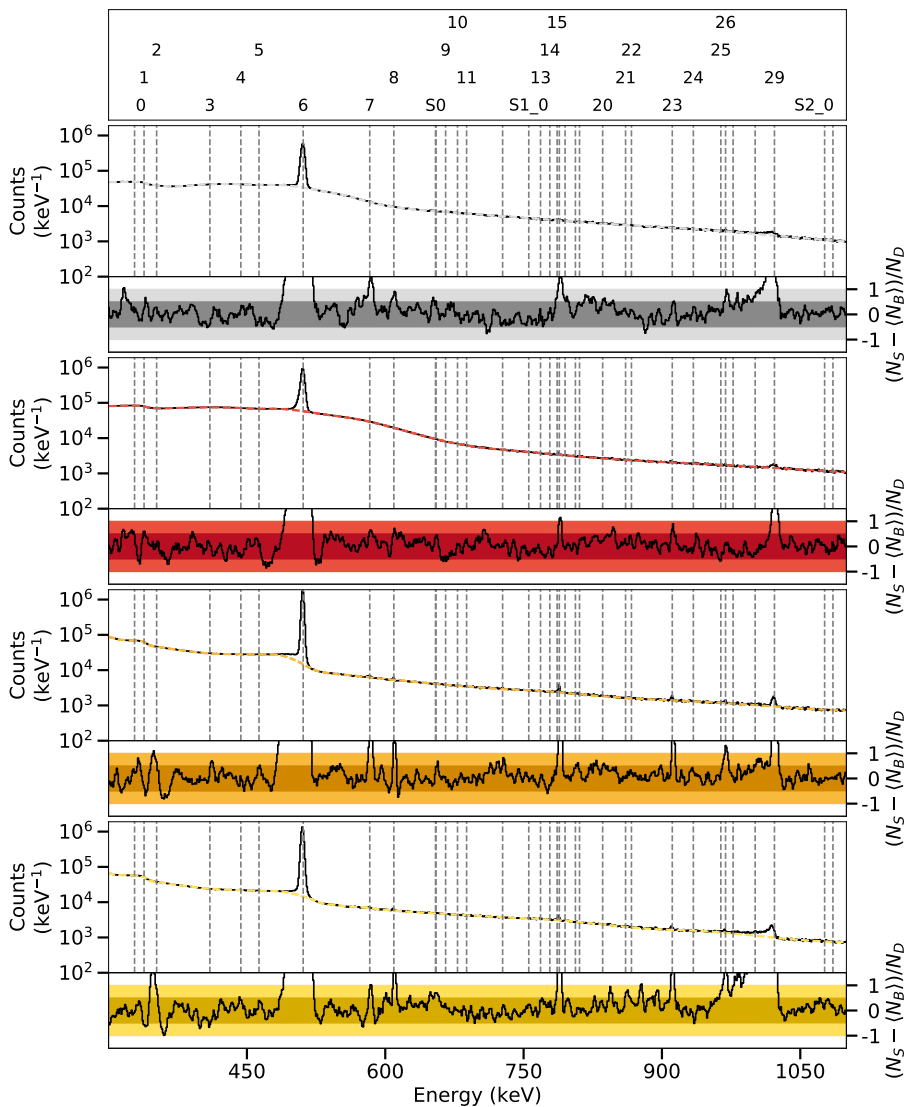


Figure D.145.: Spectra of the ^{82}Se target in the γ^3 setup at a beam energy of 4.10 MeV between 300 keV and 1100 keV.

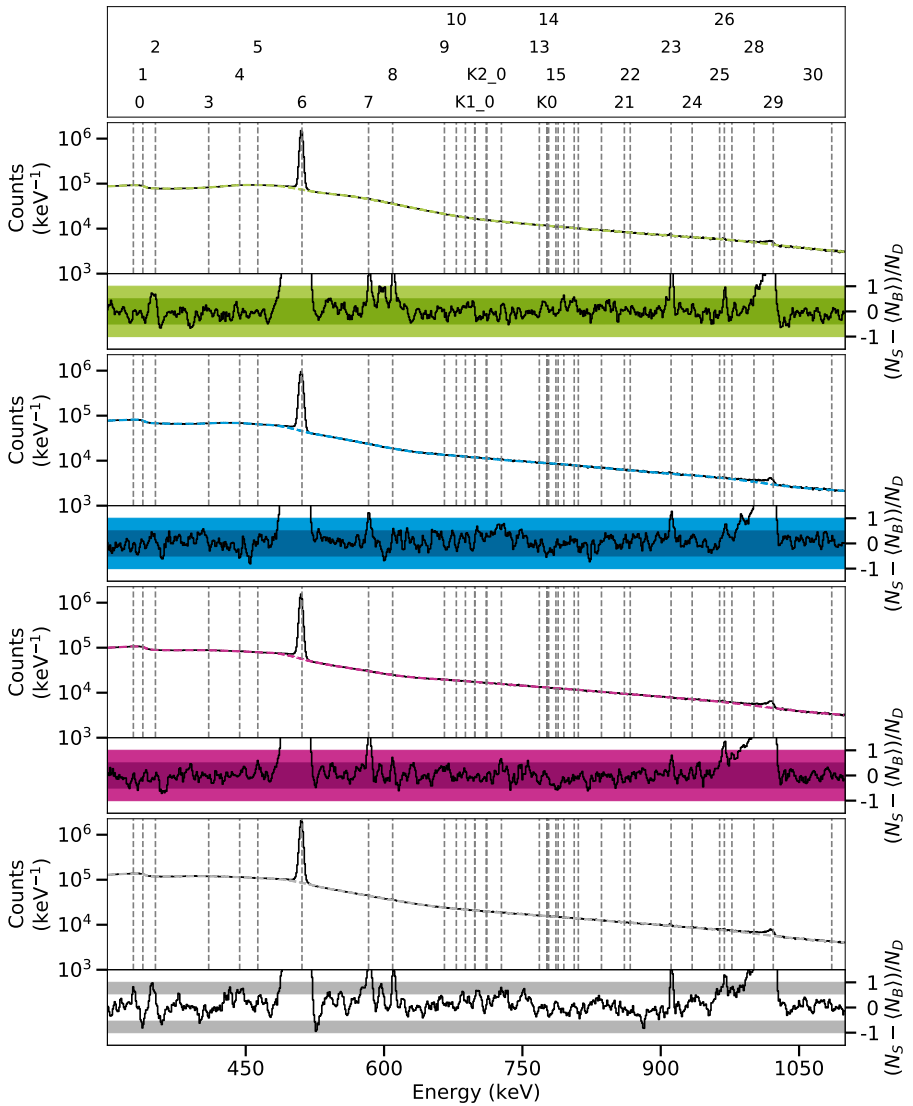


Figure D.146.: Spectra of the empty krypton target in the polarimetry setup at a beam energy of 4.10 MeV between 300 keV and 1100 keV.

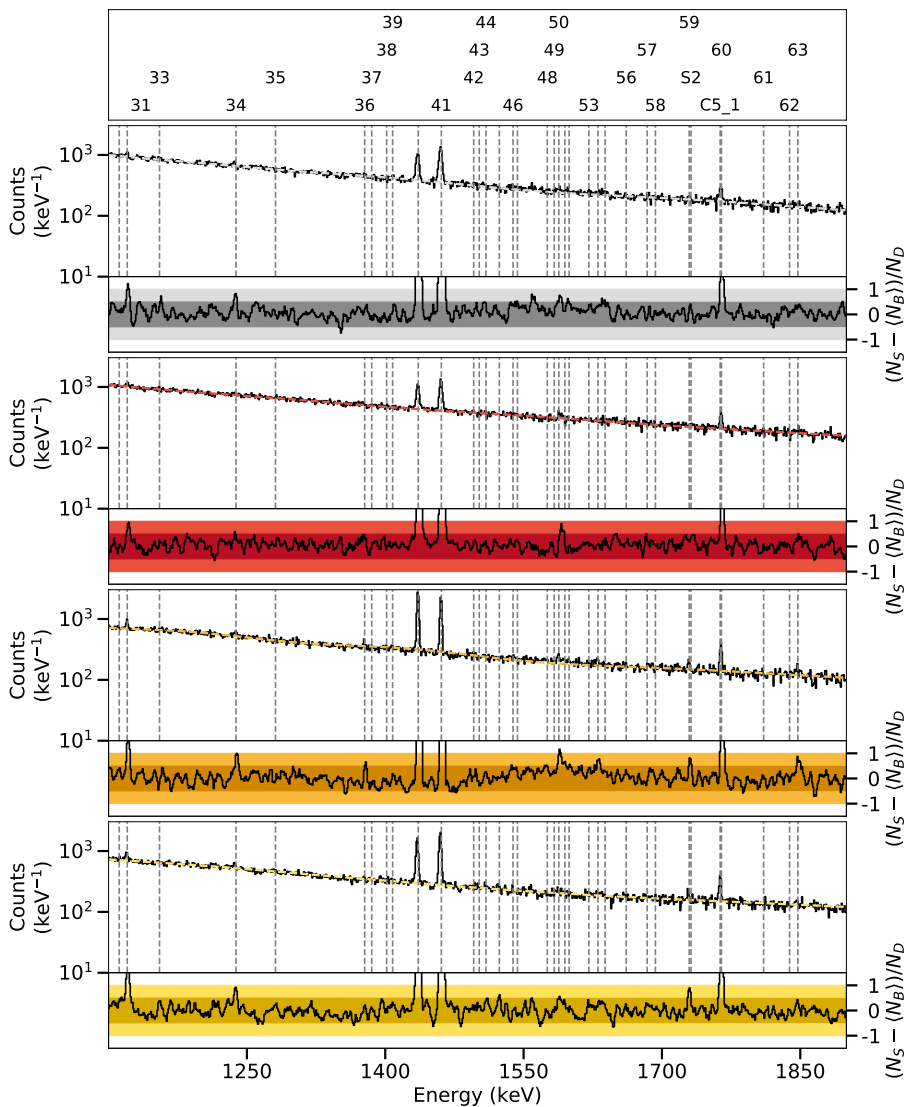


Figure D.147.: Spectra of the ^{82}Se target in the γ^3 setup at a beam energy of 4.10 MeV between 1100 keV and 1900 keV.

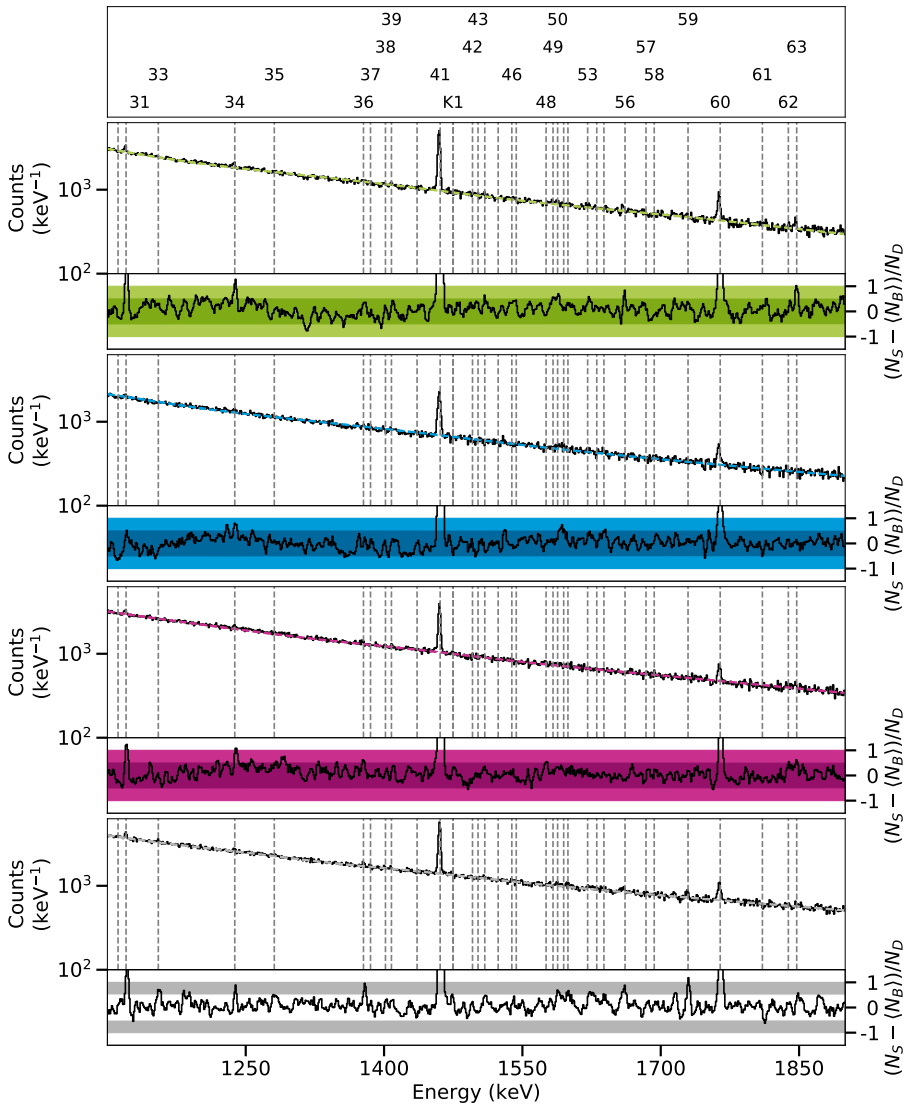


Figure D.148.: Spectra of the empty krypton target in the polarimetry setup at a beam energy of 4.10 MeV between 1100 keV and 1900 keV.

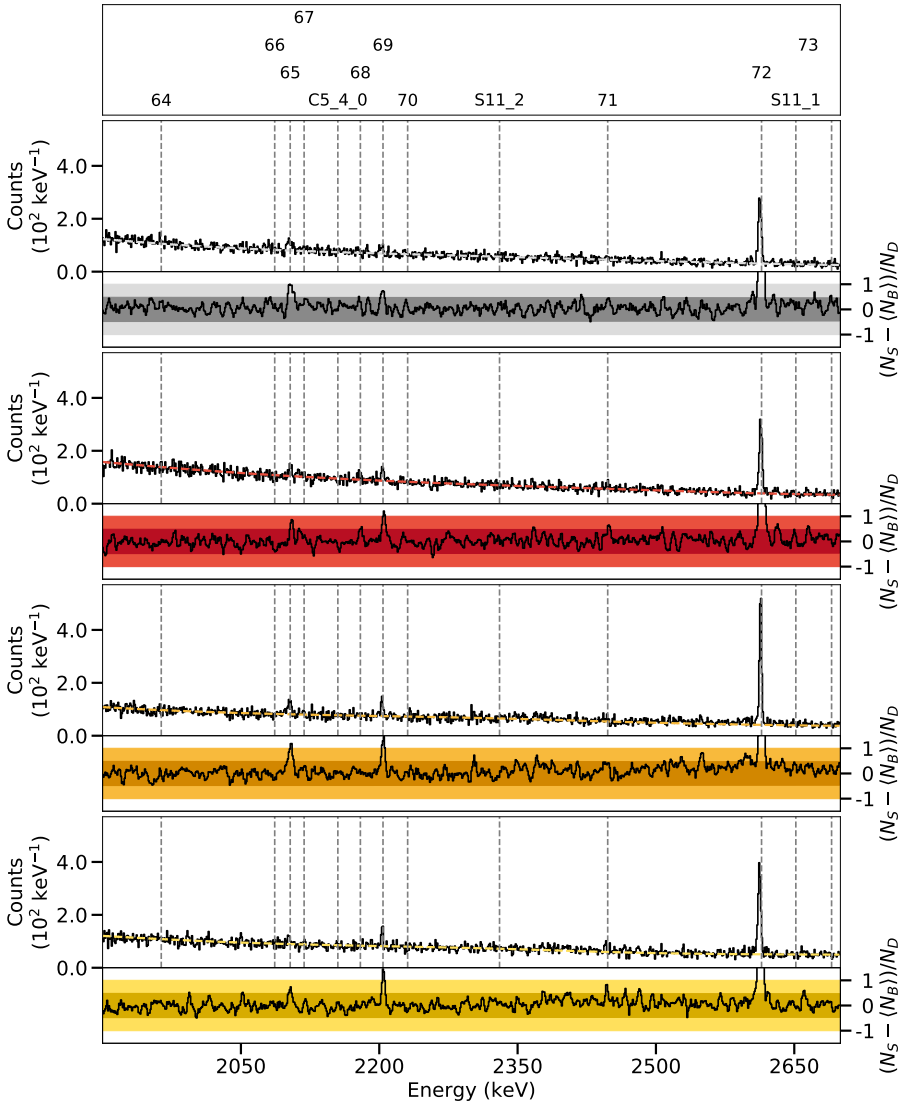


Figure D.149.: Spectra of the ^{82}Se target in the γ^3 setup at a beam energy of 4.10 MeV between 1900 keV and 2700 keV.

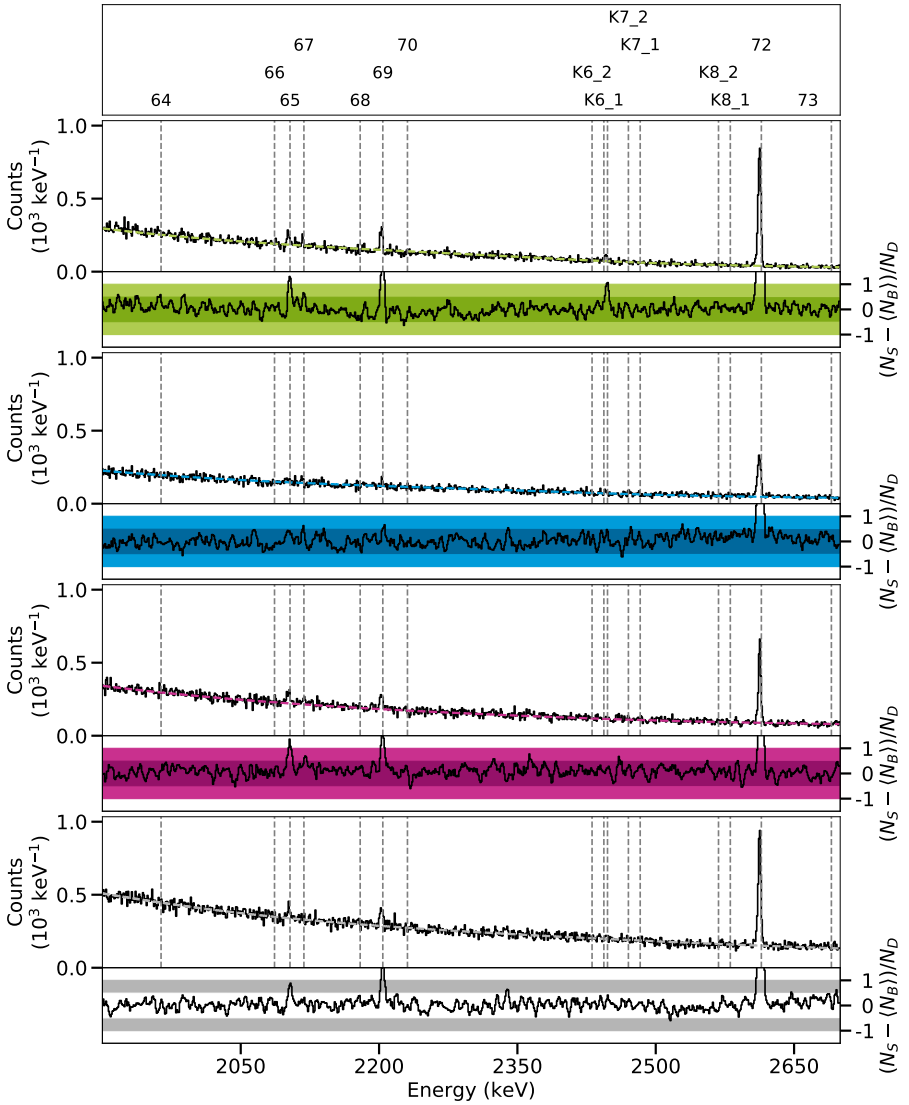


Figure D.150.: Spectra of the empty krypton target in the polarimetry setup at a beam energy of 4.10 MeV between 1900 keV and 2700 keV.

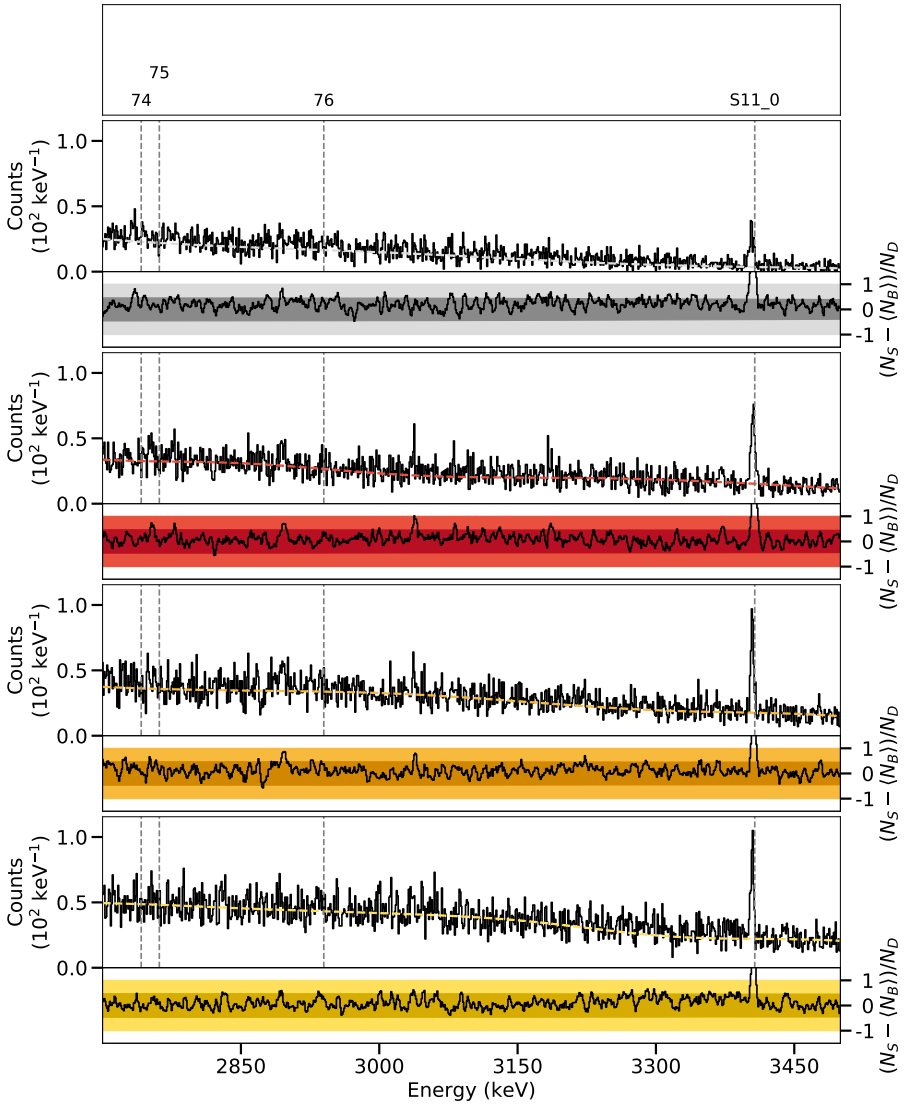


Figure D.151.: Spectra of the ^{82}Se target in the γ^3 setup at a beam energy of 4.10 MeV between 2700 keV and 3500 keV.

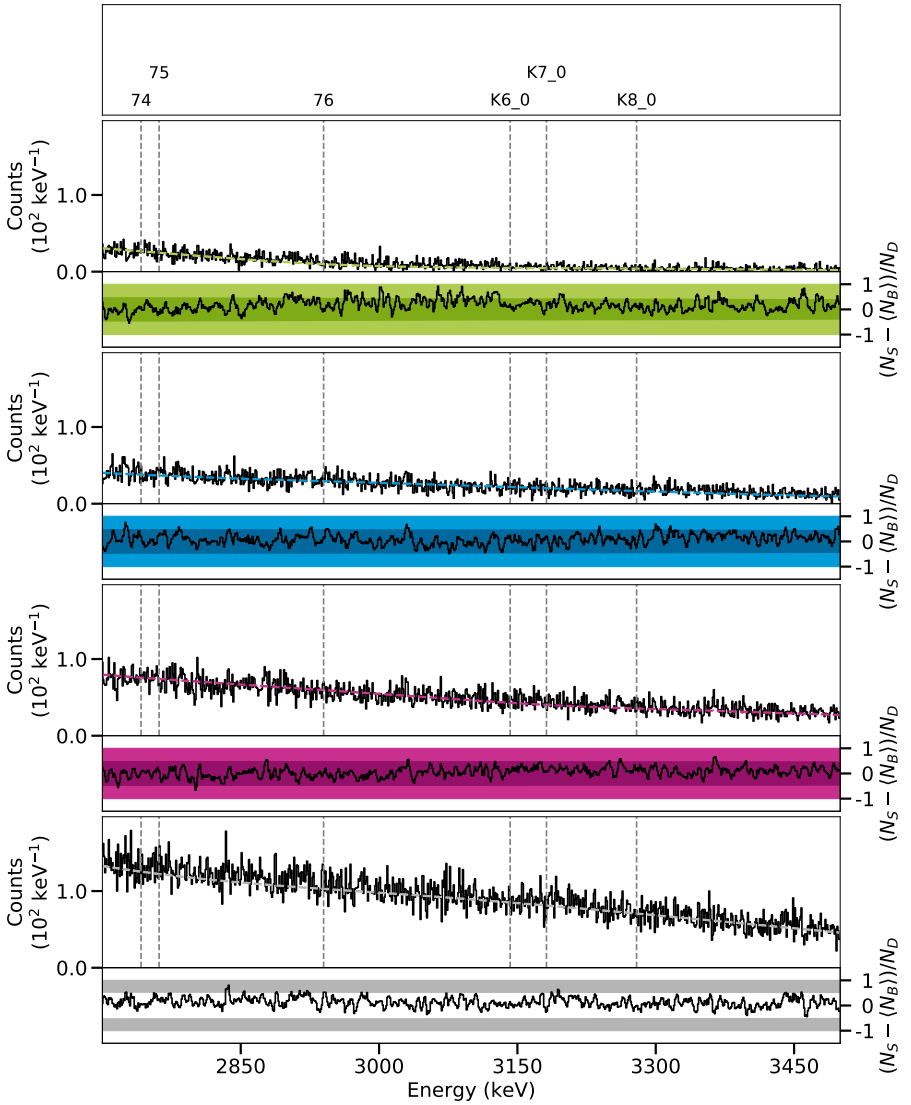


Figure D.152.: Spectra of the empty krypton target in the polarimetry setup at a beam energy of 4.10 MeV between 2700 keV and 3500 keV.

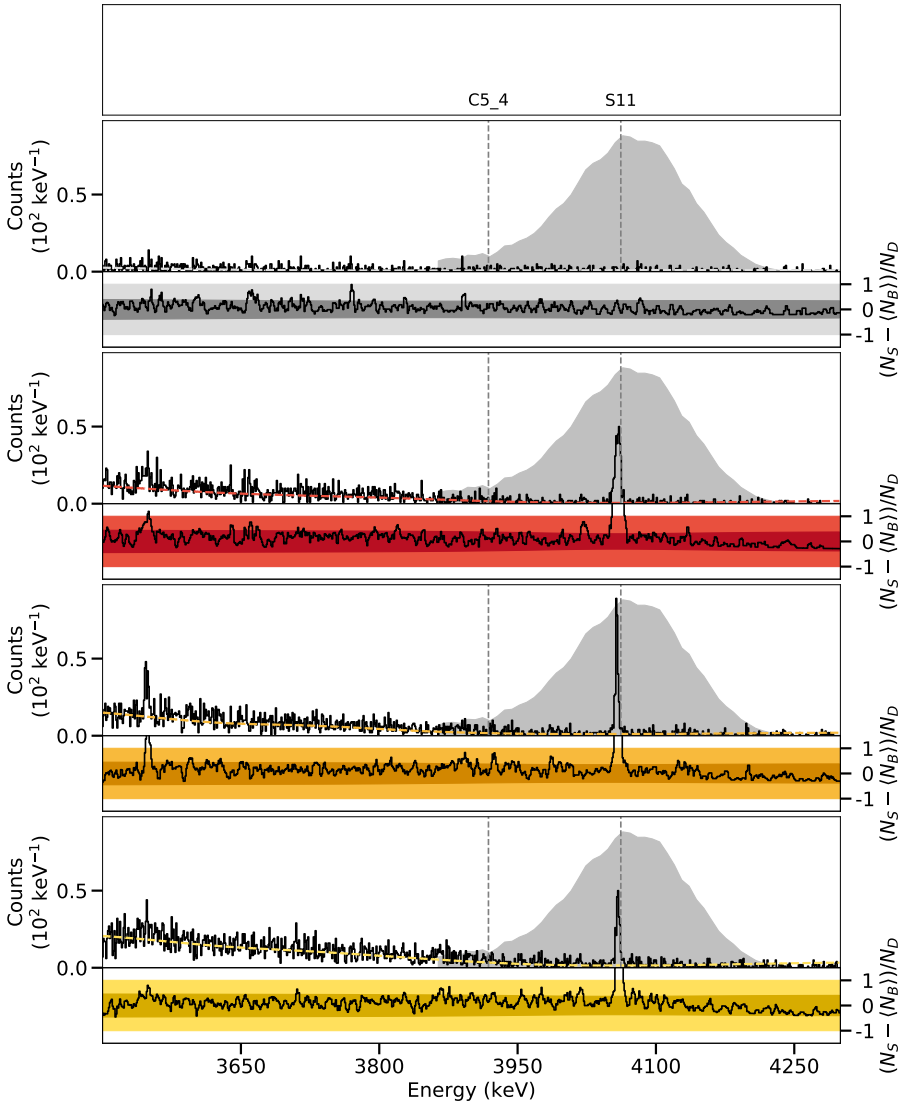


Figure D.153.: Spectra of the ^{82}Se target in the γ^3 setup at a beam energy of 4.10 MeV between 3500 keV and 4300 keV.

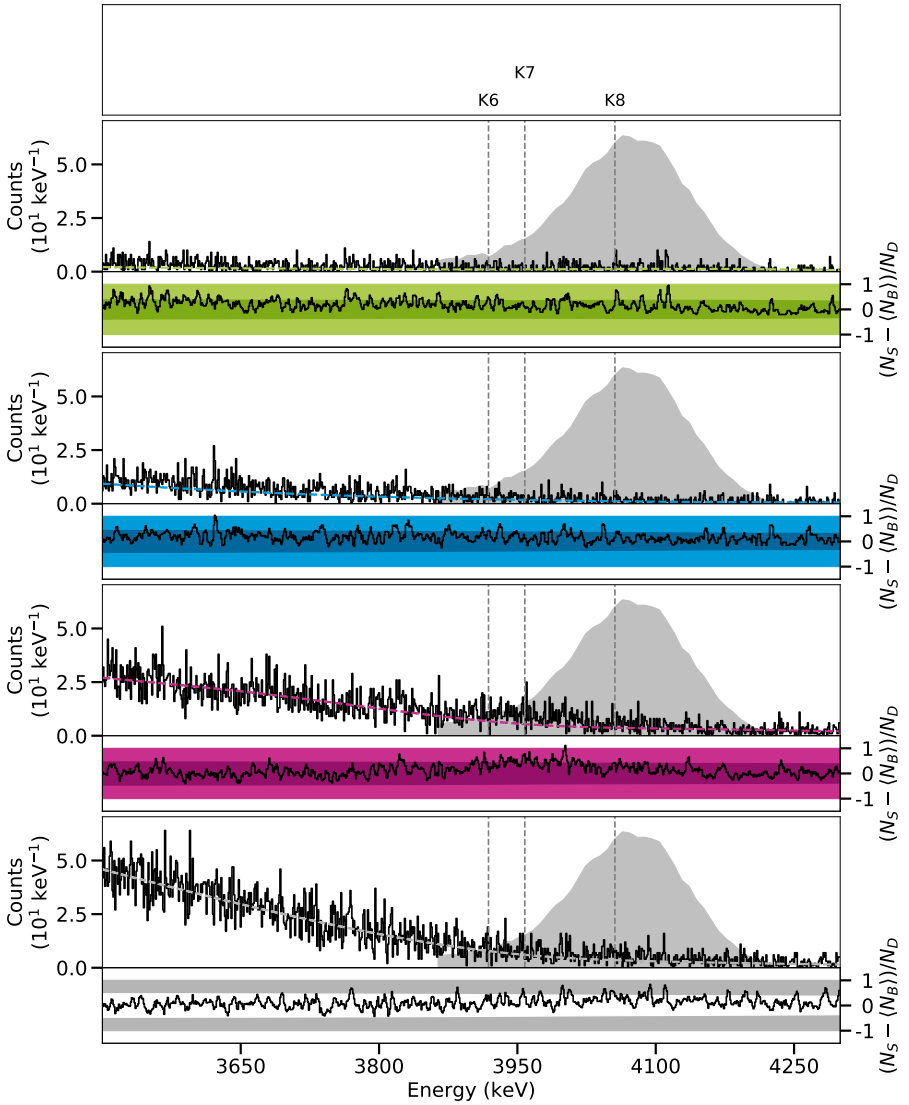


Figure D.154.: Spectra of the empty krypton target in the polarimetry setup at a beam energy of 4.10 MeV between 3500 keV and 4300 keV.

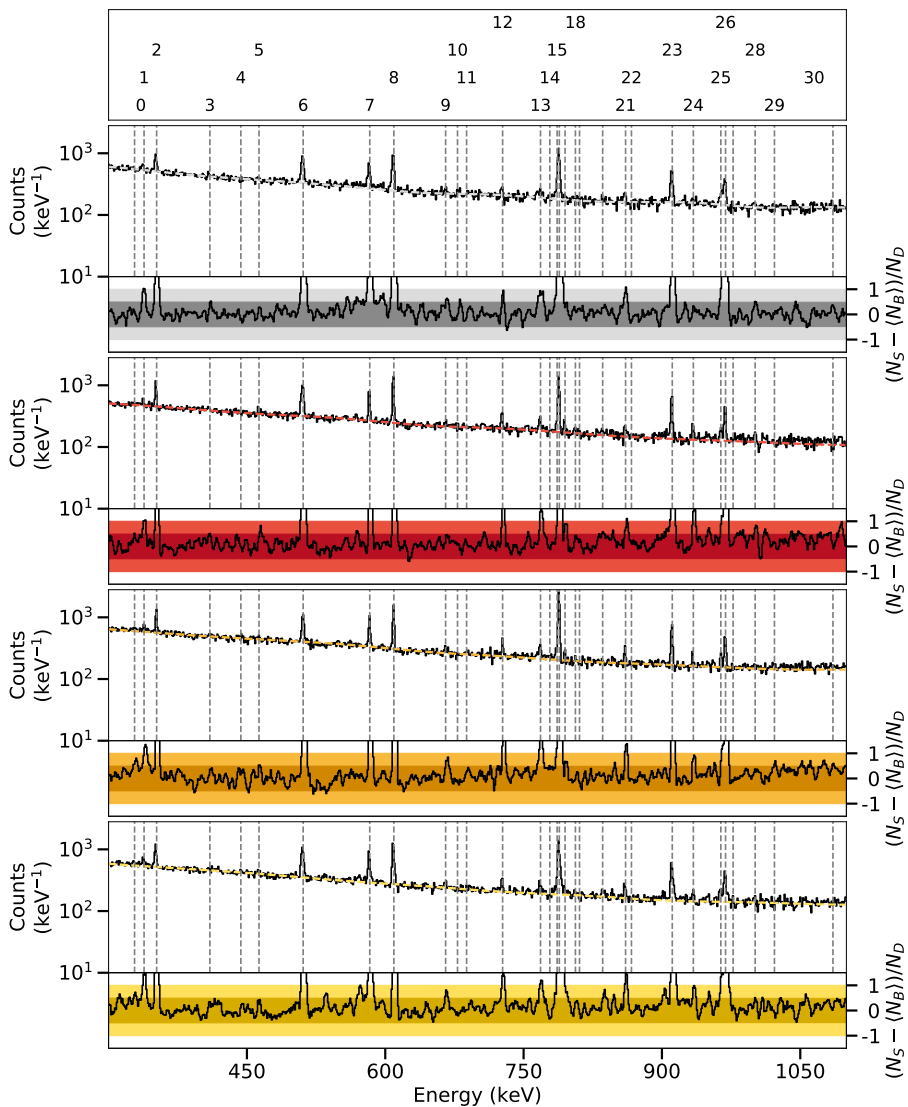


Figure D.155.: Spectrum of the background at the γ^3 setup between 300 keV and 1100 keV (Run 742).

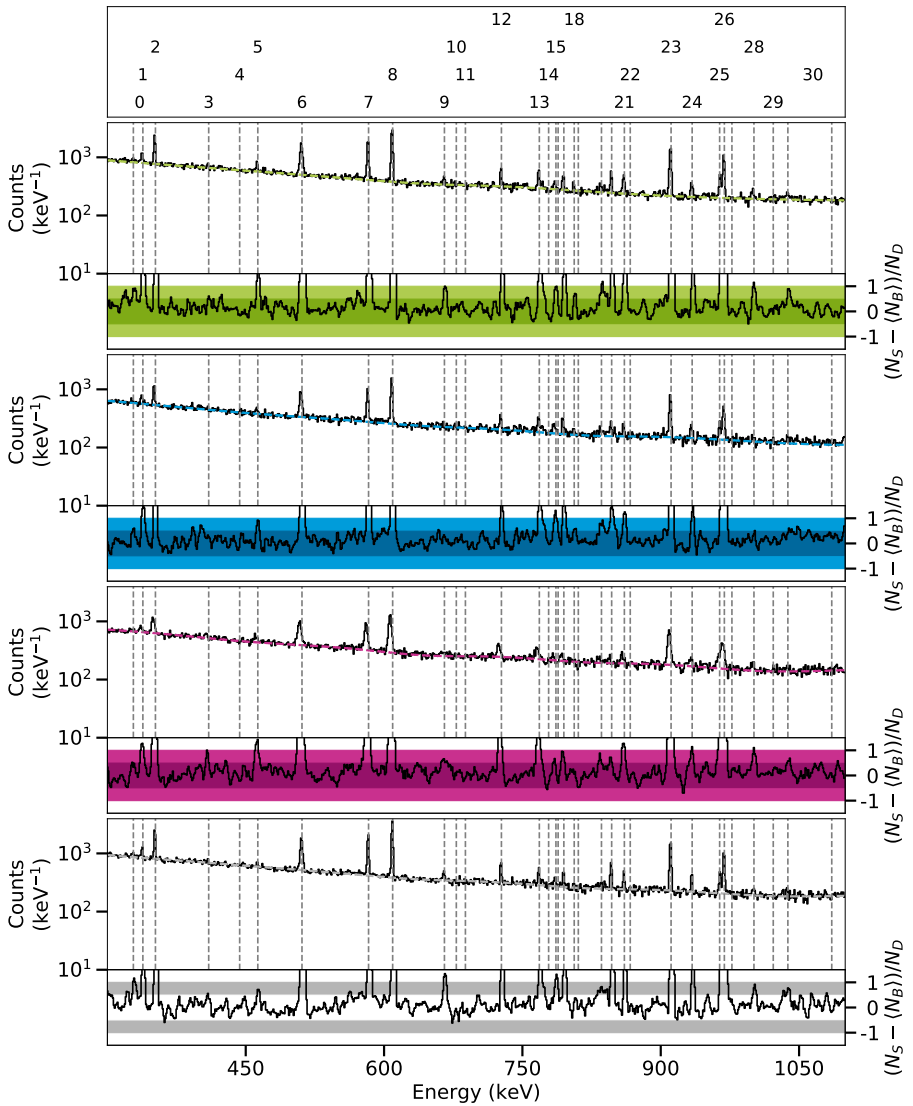


Figure D.156.: Spectrum of the background at the polarimetry setup between 300 keV and 1100 keV (Run 742).

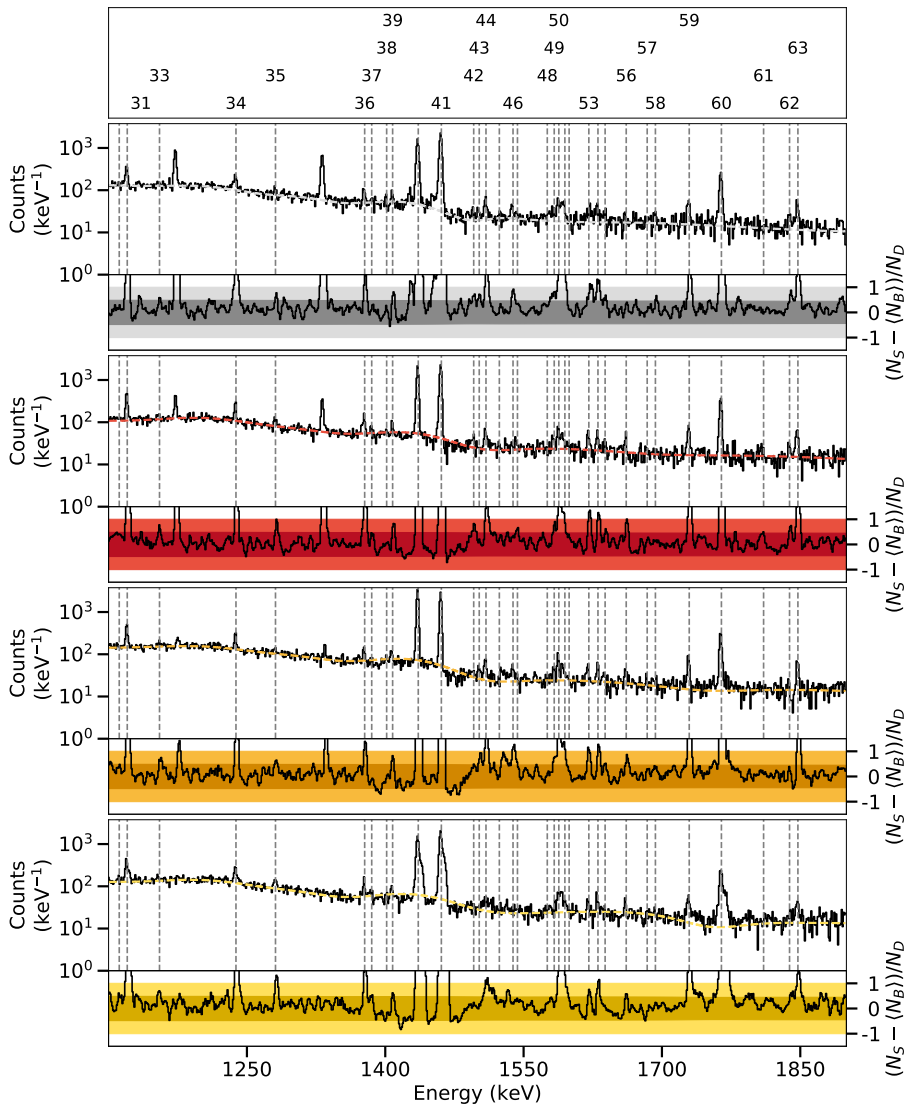


Figure D.157.: Spectrum of the background at the γ^3 setup between 1100 keV and 1900 keV (Run 742).

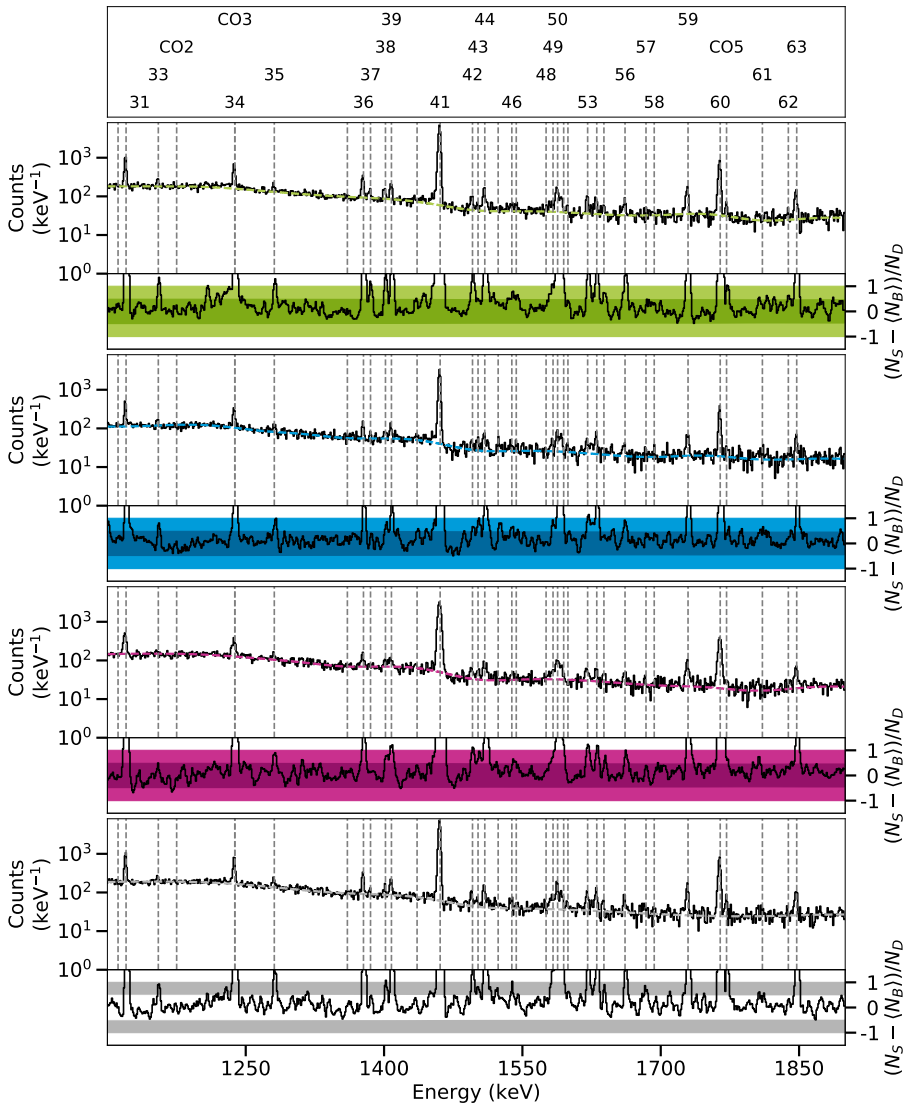


Figure D.158.: Spectrum of the background at the polarimetry setup between 1100 keV and 1900 keV (Run 742).

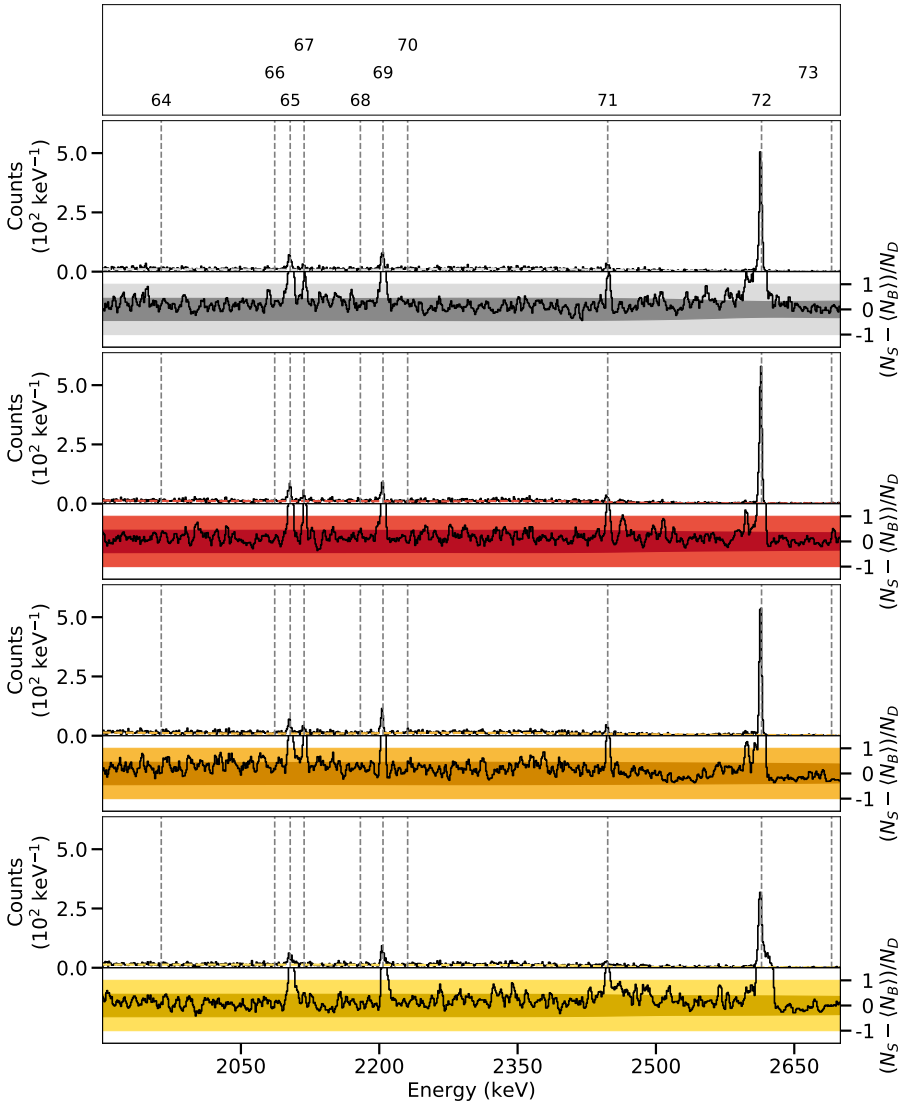


Figure D.159.: Spectrum of the background at the γ^3 setup between 1900 keV and 2700 keV (Run 742).

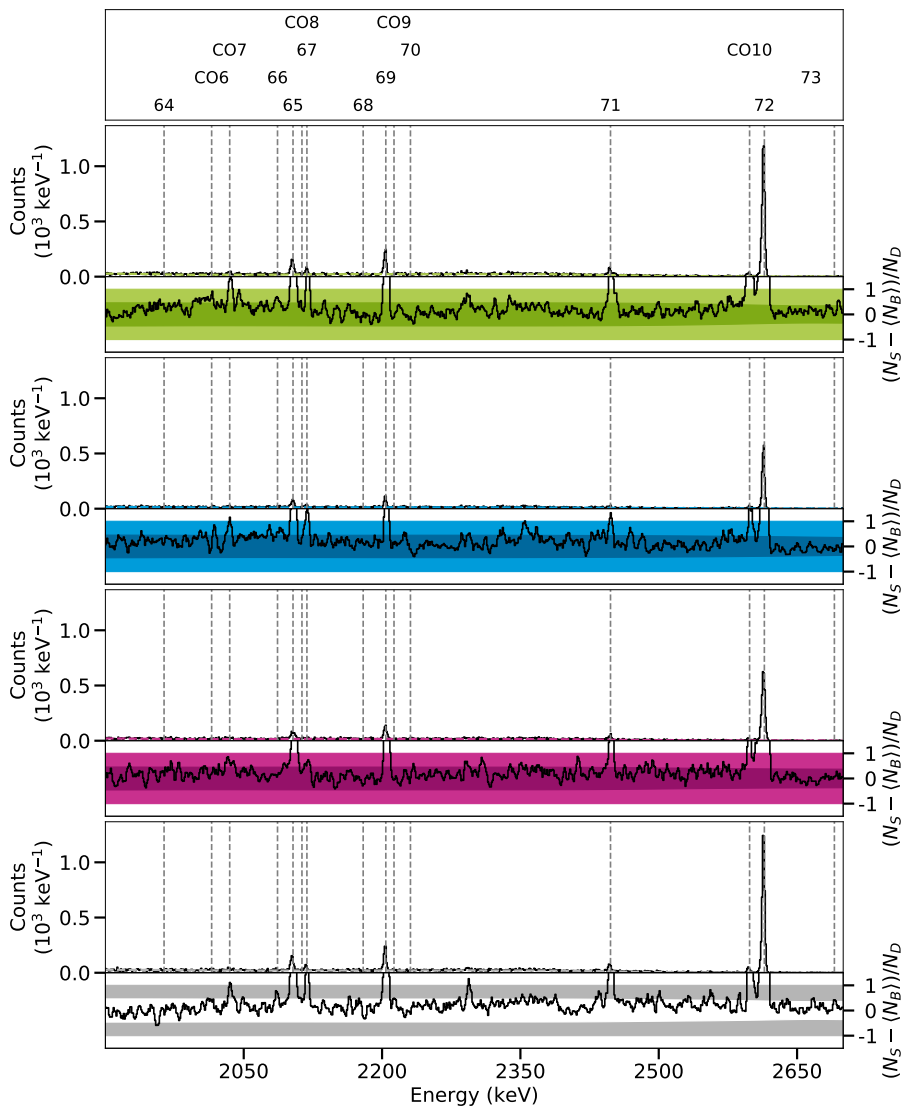


Figure D.160.: Spectrum of the background at the polarimetry setup between 1900 keV and 2700 keV (Run 742).

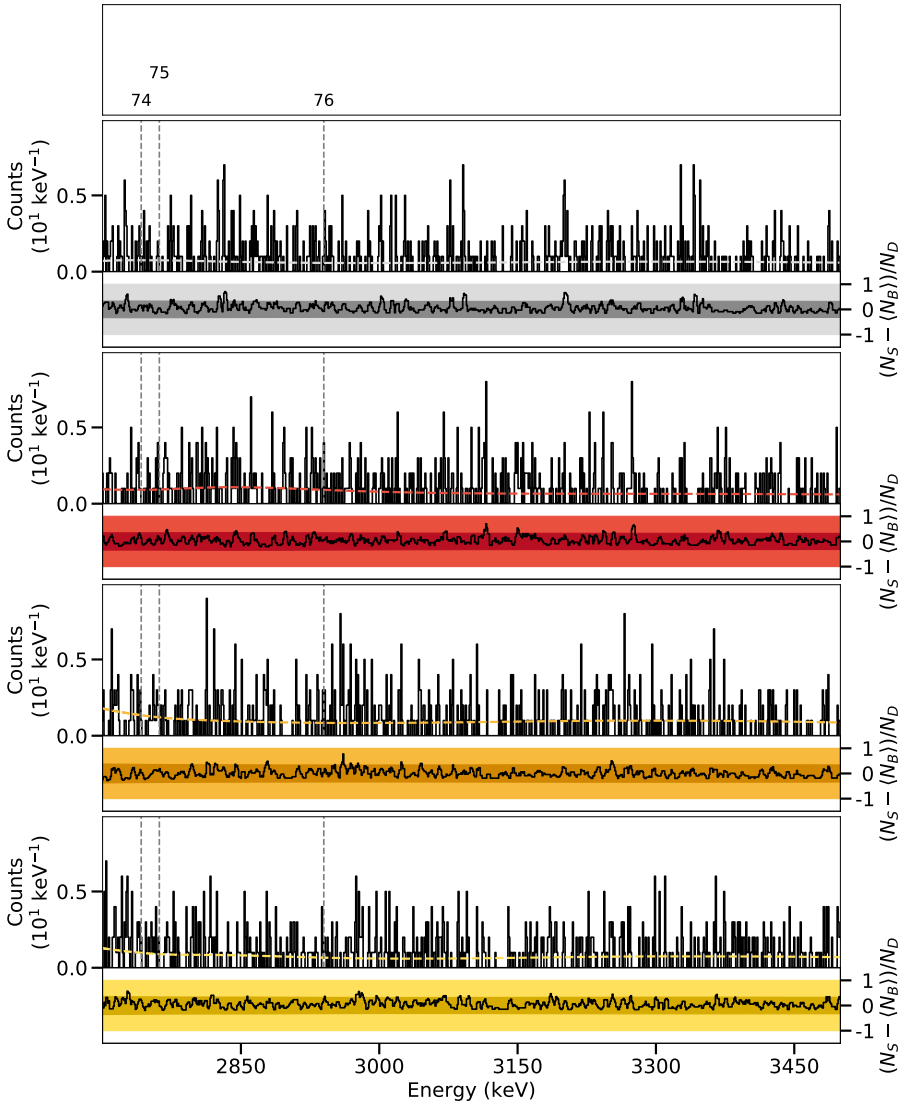


Figure D.161.: Spectrum of the background at the γ^3 setup between 2700 keV and 3500 keV (Run 742).

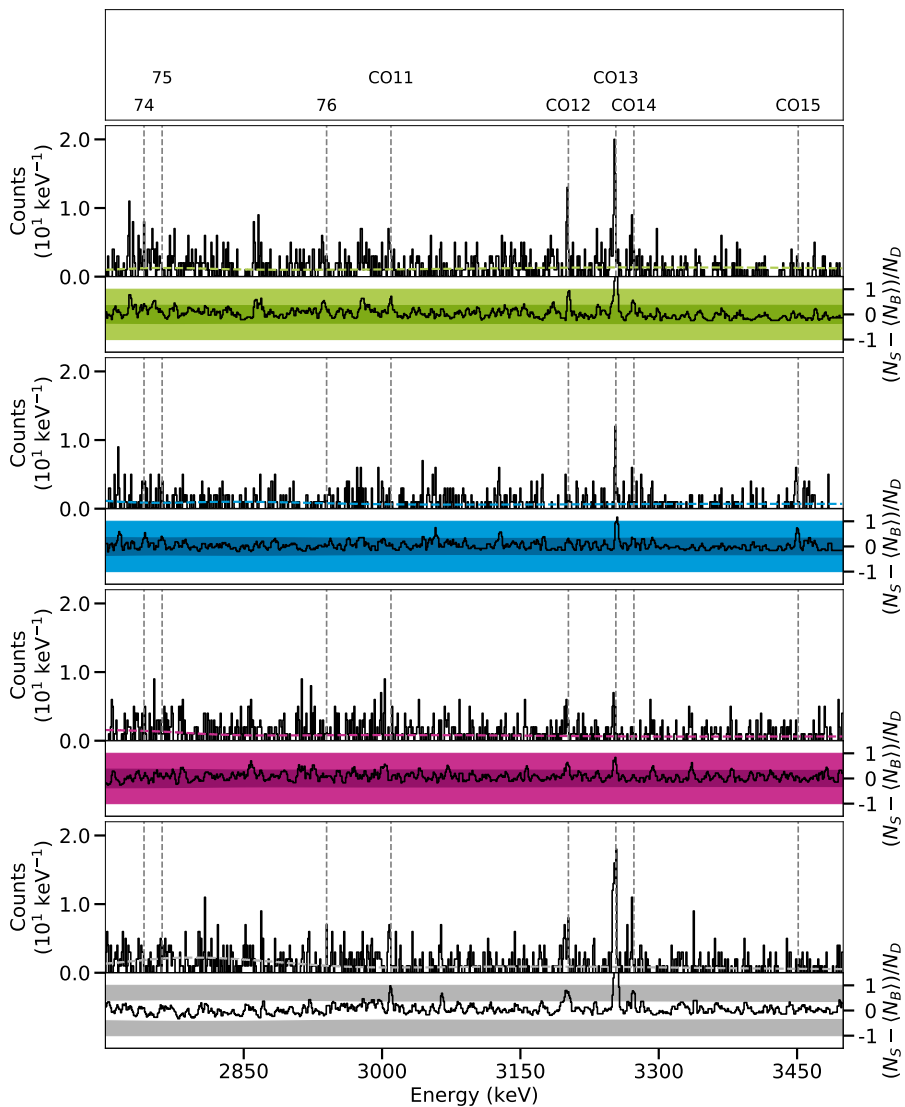


Figure D.162.: Spectrum of the background at the polarimetry setup between 2700 keV and 3500 keV (Run 742).

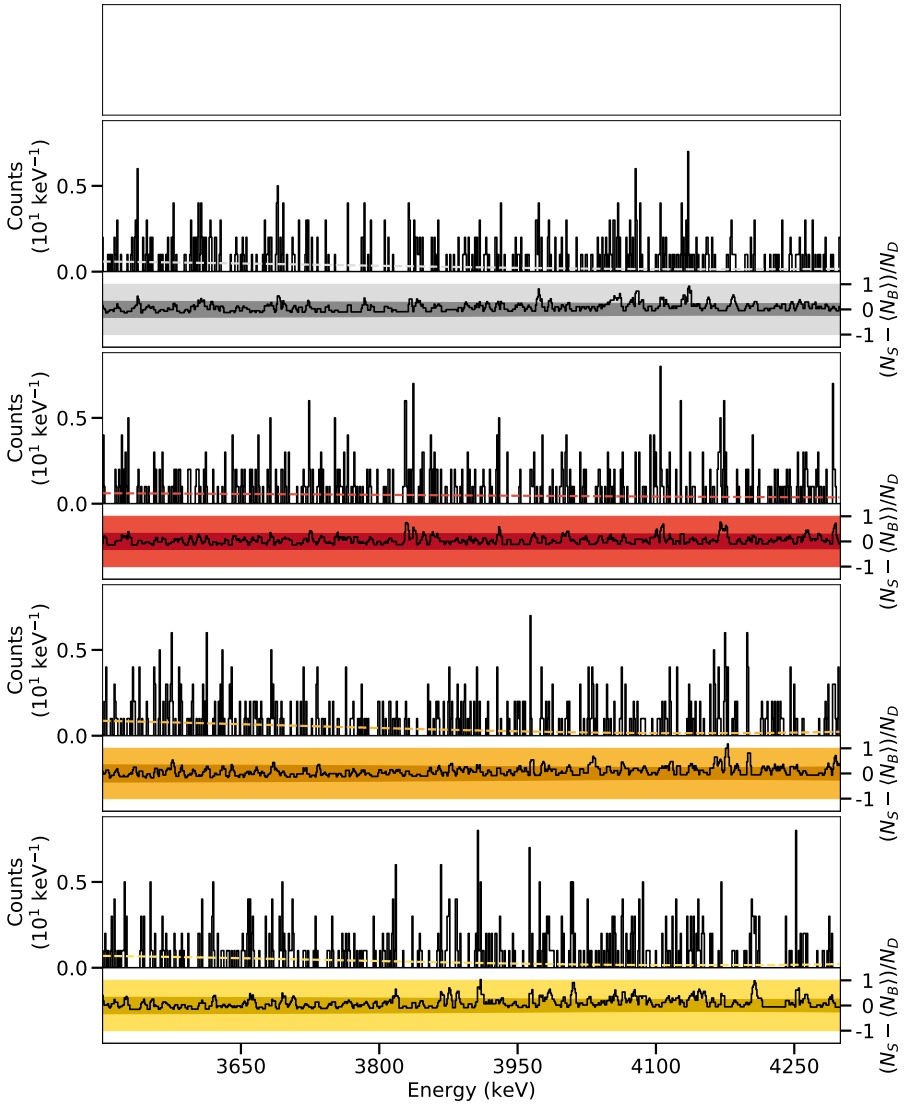


Figure D.163.: Spectrum of the background at the γ^3 setup between 3500 keV and 4300 keV (Run 742).

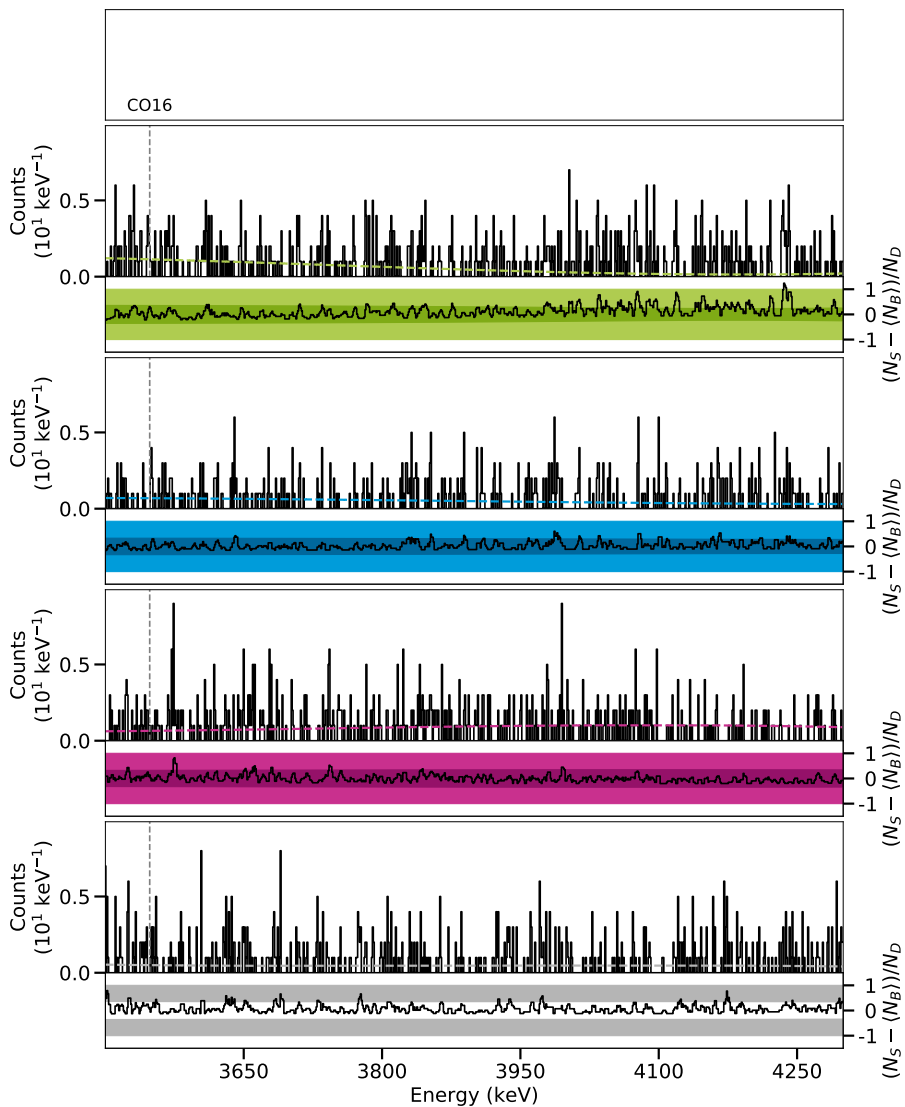


Figure D.164.: Spectrum of the background at the polarimetry setup between 3500 keV and 4300 keV (Run 742).

Bibliography

- [1] J. K. Tuli, *The Evaluated Nuclear Structure Data File. A Manual for Preparation of Data Sets*. International Atomic Energy Agency (IAEA) (2001).
- [2] M. Tanabashi et al., (Particle Data Group), “Review of Particle Physics”, *Phys. Rev. D* **98**, 030001 (2018).
- [3] BIPM, *Le Système international d’unités / The International System of Units*, 9th ed. (Bureau international des poids et mesures, 2019).
- [4] B. Märkisch et al., “Measurement of the Weak Axial-Vector Coupling Constant in the Decay of Free Neutrons Using a Pulsed Cold Neutron Beam”, *Phys. Rev. Lett.* **122**, 242501 (2019).
- [5] E. Caurier, G. Martínez-Pinedo, F. Nowacki, A. Poves, and A. P. Zuker, “The shell model as a unified view of nuclear structure”, *Rev. Mod. Phys.* **77**, 427 (2005).
- [6] P. J. Mohr, D. B. Newell, B. N. Taylor, and E. Tiesinga, “Data and analysis for the CODATA 2017 special fundamental constants adjustment”, *Metrologia* **55**, 125 (2018).
- [7] W. J. Huang, G. Audi, Meng Wang, F. G. Kondev, S. Naimi, and Xing Xu, “The AME2016 atomic mass evaluation (I). Evaluation of input data; and adjustment procedures”, *Chinese Phys. C* **41**, 030002 (2017).
- [8] S. Agostinelli et al., “GEANT4-a simulation toolkit”, *Nucl. Instrum. Meth. A* **506**, 250 (2003).
- [9] J. Allison et al., “Geant4 developments and applications”, *IEEE T. Nucl. Sci.* **53**, 270 (2006).
- [10] J. Allison et al., “Recent developments in GEANT4”, *Nucl. Instrum. Meth. A* **835**, 186 (2016).

-
- [11] C. F. Gauss, “Intensitas vis magneticae terrestres ad mensuram absolutam revocata”, in *Werke: Fünfter Band* (Springer Verlag, 1877), pp. 293–304.
- [12] K. S. Krane, R. M. Steffen, and R. M. Wheeler, “Directional correlations of gamma radiations emitted from nuclear states oriented by nuclear reactions or cryogenic methods”, *At. Data Nucl. Data* **11**, 351 (1973).
- [13] J. M. Blatt and V. F. Weisskopf, *Theoretical Nuclear Physics*, 1st ed. (Springer Verlag, 1979).
- [14] A. S. Barabash, “Average and recommended half-life values for two-neutrino double beta decay”, *Nucl. Phys. A* **935**, 52 (2015).
- [15] B. A. Watson, T. T. Bardin, J. A. Becker, and T. R. Fisher, “Two-Photon Decay of the 6.05-MeV State of ^{16}O ”, *Phys. Rev. Lett.* **35**, 1333 (1975).
- [16] J. Schirmer, D. Habs, R. Kroth, N. Kwong, D. Schwalm, M. Zirnbauer, and C. Broude, “Double Gamma Decay in ^{40}Ca and ^{90}Zr ”, *Phys. Rev. Lett.* **53**, 1897 (1984).
- [17] J. Kramp, D. Habs, R. Kroth, M. Music, J. Schirmer, D. Schwalm, and C. Broude, “Nuclear two-photon decay in $0^+ \rightarrow 0^+$ transitions”, *Nucl. Phys. A* **474**, 412 (1987).
- [18] C. Walz, H. Scheit, N. Pietralla, T. Aumann, R. Lefol, and V. Yu. Ponomarev, “Observation of the competitive double-gamma nuclear decay”, *Nature* **526**, 406 (2015).
- [19] E. Aprile et al., “Observation of two-neutrino double electron capture in ^{124}Xe with XENON1T”, *Nature* **568**, 532 (2019).
- [20] D. Štefánik, R. Dvornický, F. Šimkovic, and P. Vogel, “Reexamining the light neutrino exchange mechanism of the $0\nu\beta\beta$ decay with left- and right-handed leptonic and hadronic currents”, *Phys. Rev. C* **92**, 055502 (2015).
- [21] J. Engel and J. Menéndez, “Status and future of nuclear matrix elements for neutrinoless double-beta decay: a review”, *Rep. Prog. Phys.* **80**, 046301 (2017).
- [22] E. A. Coello Pérez, J. Menéndez, and A. Schwenk, “Two-neutrino double electron capture on ^{124}Xe based on an effective theory and the nuclear shell model”, *Phys. Lett. B* **797**, 134885 (2019).

-
- [23] A. Messiah, *Quantum Mechanics*, Vol. 1 (North-Holland Publishing Company, 1961).
- [24] F. Cappuzzello et al., “The NUMEN project: NUclear Matrix Elements for Neutrinoless double beta decay”, *Eur. Phys. J. A* **54**, 72 (2018).
- [25] N. Shimizu, J. Menéndez, and K. Yako, “Double Gamow-Teller Transitions and its Relation to Neutrinoless $\beta\beta$ Decay”, *Phys. Rev. Lett.* **120**, 142502 (2018).
- [26] M. K. Gaillard, P. D. Grannis, and F. J. Sciulli, “The standard model of particle physics”, *Rev. Mod. Phys.* **71**, S96 (1999).
- [27] J. D. Vergados, H. Ejiri, and F. Šimkovic, “Theory of neutrinoless double-beta decay”, *Rep. Prog. Phys.* **75**, 106301 (2012).
- [28] F. T. Avignone III, S. R. Elliott, and J. Engel, “Double beta decay, Majorana neutrinos, and neutrino mass”, *Rev. Mod. Phys.* **80**, 481 (2008).
- [29] M. Goeppert-Mayer, “Double Beta-Disintegration”, *Phys. Rev.* **48**, 512 (1935).
- [30] G. Racah, “Sulla Simmetria Tra Particelle e Antiparticelle”, *Nuovo Cimento* **14**, 322 (1937).
- [31] E. Majorana, “Teoria simmetrica dell’elettrone e del positrone”, *Nuovo Cimento* **14**, 171 (1937).
- [32] E. Fermi, “Versuch einer Theorie der β -Strahlen. I”, *Z. Phys.* **88**, 161 (1934).
- [33] W. H. Furry, “On Transition Probabilities in Double Beta-Disintegration”, *Phys. Rev.* **56**, 1184 (1939).
- [34] K. S. Krane, *Introductory Nuclear Physics* (John Wiley & Sons, Inc., 1988).
- [35] C. F. v. Weizsäcker, “Zur Theorie der Kernmassen”, *Zeitschrift für Physik* **96**, 431 (1935).
- [36] M. Doi, T. Kotani, and E. Takasugi, “Double Beta Decay and Majorana Neutrino”, *Prog. Theor. Phys. Supp.* **83**, 1 (1985).
- [37] J. Kotila and F. Iachello, “Phase-space factors for double- β decay”, *Phys. Rev. C* **85**, 034316 (2012).
- [38] S. Stoica and M. Mirea, “New calculations for phase space factors involved in double- β decay”, *Phys. Rev. C* **88**, 037303 (2013).

-
- [39] J. D. Vergados, “The Neutrino mass and family, Lepton and Baryon number non-conservation in gauge theories”, *Phys. Rep.* **133**, 1 (1986).
- [40] M. J. Dolinski, A. W. Poon, and W. Rodejohann, “Neutrinoless Double-Beta Decay: Status and Prospects”, *Annu. Rev. Nucl. Part. S.* **69**, 219 (2019).
- [41] S. Umehara et al., “Neutrino-less double- β decay of ^{48}Ca studied by $\text{CaF}_2(\text{Eu})$ scintillators”, *Phys. Rev. C* **78**, 058501 (2008).
- [42] R. Arnold et al., (NEMO-3 Collaboration), “Measurement of the double-beta decay half-life and search for the neutrinoless double-beta decay of ^{48}Ca with the NEMO-3 detector”, *Phys. Rev. D* **93**, 112008 (2016).
- [43] T. Iida et al., “The CANDLES experiment for the study of Ca-48 double beta decay”, *Nucl. Part. Phys. P.* **273-275**, 37th International Conference on High Energy Physics (ICHEP), 2633 (2016).
- [44] M. Agostini et al., (GERDA Collaboration), “Probing Majorana neutrinos with double- β decay”, *Science* **365**, 1445 (2019).
- [45] S. I. Alvis et al., (MAJORANA Collaboration), “Search for neutrinoless double- β decay in ^{76}Ge with 26 kg yr of exposure from the Majorana Demonstrator”, *Phys. Rev. C* **100**, 025501 (2019).
- [46] O. Azzolini et al., “Final Result of CUPID-0 Phase-I in the Search for the ^{82}Se Neutrinoless Double- β Decay”, *Phys. Rev. Lett.* **123**, 032501 (2019).
- [47] A. S. Barabash et al., (NEMO Collaboration), “Investigation of double-beta decay with the NEMO-3 detector”, *Phys. Atom. Nucl.* **74**, 312 (2011).
- [48] R. Arnold et al., (NEMO-3 Collaboration), “Final results on ^{82}Se double beta decay to the ground state of ^{82}Kr from the NEMO-3 experiment”, *Eur. Phys. J. C* **78**, 821 (2018).
- [49] J. Argyriades et al., (NEMO-3 Collaboration), “Measurement of the two neutrino double beta decay half-life of Zr-96 with the NEMO-3 detector”, *Nucl. Phys. A* **847**, 168 (2010).
- [50] R. Arnold et al., (NEMO-3 Collaboration), “Results of the search for neutrinoless double- β decay in ^{100}Mo with the NEMO-3 experiment”, *Phys. Rev. D* **92**, 072011 (2015).
- [51] V. Alenkov et al., “First results from the AMoRE-Pilot neutrinoless double beta decay experiment”, *Eur. Phys. J. C* **79**, 791 (2019).

-
- [52] A. S. Barabash et al., “Final results of the Aurora experiment to study 2β decay of ^{116}Cd with enriched $^{116}\text{CdWO}_4$ crystal scintillators”, Phys. Rev. D **98**, 092007 (2018).
- [53] R. Arnold et al., (NEMO-3 Collaboration), “Measurement of the $2\nu\beta\beta$ decay half-life and search for the $0\nu\beta\beta$ decay of ^{116}Cd with the NEMO-3 detector”, Phys. Rev. D **95**, 012007 (2017).
- [54] C. Arnaboldi et al., “A calorimetric search on double beta decay of ^{130}Te ”, Phys. Lett. B **557**, 167 (2003).
- [55] C. Alduino et al., (CUORE Collaboration), “First Results from CUORE: A Search for Lepton Number Violation via $0\nu\beta\beta$ Decay of ^{130}Te ”, Phys. Rev. Lett. **120**, 132501 (2018).
- [56] A. Gando et al., (KamLAND-Zen Collaboration), “Search for Majorana Neutrinos Near the Inverted Mass Hierarchy Region with KamLAND-Zen”, Phys. Rev. Lett. **117**, 082503 (2016).
- [57] G. Anton et al., (EXO-200 Collaboration), “Search for Neutrinoless Double- β Decay with the Complete EXO-200 Dataset”, Phys. Rev. Lett. **123**, 161802 (2019).
- [58] R. Arnold et al., (NEMO-3 Collaboration), “Measurement of the $2\nu\beta\beta$ decay half-life of ^{150}Nd and a search for $0\nu\beta\beta$ decay processes with the full exposure from the NEMO-3 detector”, Phys. Rev. D **94**, 072003 (2016).
- [59] I. Talmi, *Simple Models of Complex Nuclei, The Shell Model and Interacting Boson Model* (Harwood Academic Publishers, 1993).
- [60] Q. Chen et al., “Measurement of the neutron-neutron scattering length using the π^-d capture reaction”, Phys. Rev. C **77**, 054002 (2008).
- [61] V. Huhn, L. Wätzold, Ch. Weber, A. Siepe, W. von Witsch, H. Witała, and W. Glöckle, “New Attempt to Determine the $n-n$ Scattering Length with the $^2\text{H}(n, np)n$ Reaction”, Phys. Rev. Lett. **85**, 1190 (2000).
- [62] J. R. Bergervoet, P. C. van Campen, W. A. van der Sanden, and J. J. de Swart, “Phase shift analysis of 0–30 MeV pp scattering data”, Phys. Rev. C **38**, 15 (1988).
- [63] H.-W. Hammer and S. König, “Constraints on a possible dineutron state from pionless EFT”, Phys. Lett. B **736**, 208 (2014).

-
- [64] A. Bohr and B. R. Mottelson, *Nuclear Structure*, Vol. 2 (W. A. Benjamin, Inc., 1975).
- [65] R. F. Casten, *Nuclear Structure From A Simple Perspective* (Oxford University Press, 1990).
- [66] A. de Shalit and I. Talmi, *Nuclear Shell Theory* (Dover Publications, Inc., 2004).
- [67] R. A. Sen'kov and M. Horoi, "Neutrinoless double- β decay of ^{48}Ca in the shell model: Closure versus nonclosure approximation", *Phys. Rev. C* **88**, 064312 (2013).
- [68] R. A. Sen'kov, M. Horoi, and B. A. Brown, "Neutrinoless double- β decay of ^{82}Se in the shell model: Beyond the closure approximation", *Phys. Rev. C* **89**, 054304 (2014).
- [69] R. F. Casten, "Shape phase transitions and critical-point phenomena in atomic nuclei", *Nat. Phys.* **2**, 811 (2006).
- [70] J. Jolie, P. Cejnar, R. F. Casten, S. Heinze, A. Linnemann, and V. Werner, "Triple Point of Nuclear Deformations", *Phys. Rev. Lett.* **89**, 182502 (2002).
- [71] D. Warner, "A triple point in nuclei", *Nature* **420**, 614 (2002).
- [72] D. Bonatsos, E. A. McCutchan, R. F. Casten, and R. J. Casperson, "Simple Empirical Order Parameter for a First-Order Quantum Phase Transition in Atomic Nuclei", *Phys. Rev. Lett.* **100**, 142501 (2008).
- [73] P. Cejnar, J. Jolie, and R. F. Casten, "Quantum phase transitions in the shapes of atomic nuclei", *Rev. Mod. Phys.* **82**, 2155 (2010).
- [74] T. R. Rodríguez and G. Martínez-Pinedo, "Energy Density Functional Study of Nuclear Matrix Elements for Neutrinoless $\beta\beta$ Decay", *Phys. Rev. Lett.* **105**, 252503 (2010).
- [75] T. R. Rodríguez and G. Martínez-Pinedo, "Neutrinoless double beta decay studied with configuration mixing methods", *Prog. Part. Nucl. Phys.* **66**, 436 (2011).
- [76] J. Dechargé and D. Gogny, "Hartree-Fock-Bogolyubov calculations with the $D1$ effective interaction on spherical nuclei", *Phys. Rev. C* **21**, 1568 (1980).
- [77] J. F. Berger, M. Girod, and D. Gogny, "Microscopic analysis of collective dynamics in low energy fission", *Nucl. Phys. A* **428**, 23 (1984).

-
- [78] N. L. Vaquero, T. R. Rodríguez, and J. L. Egido, “Shape and Pairing Fluctuation Effects on Neutrinoless Double Beta Decay Nuclear Matrix Elements”, *Phys. Rev. Lett.* **111**, 142501 (2013).
- [79] J. M. Yao, L. S. Song, K. Hagino, P. Ring, and J. Meng, “Systematic study of nuclear matrix elements in neutrinoless double- β decay with a beyond-mean-field covariant density functional theory”, *Phys. Rev. C* **91**, 024316 (2015).
- [80] J. M. Yao and J. Engel, “Octupole correlations in low-lying states of ^{150}Nd and ^{150}Sm and their impact on neutrinoless double- β decay”, *Phys. Rev. C* **94**, 014306 (2016).
- [81] J. Hyvärinen and J. Suhonen, “Nuclear matrix elements for $0\nu\beta\beta$ decays with light or heavy Majorana-neutrino exchange”, *Phys. Rev. C* **91**, 024613 (2015).
- [82] F. Šimkovic, V. Rodin, A. Faessler, and P. Vogel, “ $0\nu\beta\beta$ and $2\nu\beta\beta$ nuclear matrix elements, quasiparticle random-phase approximation, and isospin symmetry restoration”, *Phys. Rev. C* **87**, 045501 (2013).
- [83] D.-L. Fang, A. Faessler, and F. Simkovic, “Partial restoration of isospin symmetry for neutrinoless double β decay in the deformed nuclear system of ^{150}Nd ”, *Phys. Rev. C* **92**, 044301 (2015).
- [84] M. T. Mustonen and J. Engel, “Large-scale calculations of the double- β decay of ^{76}Ge , ^{130}Te , ^{136}Xe , and ^{150}Nd in the deformed self-consistent Skyrme quasiparticle random-phase approximation”, *Phys. Rev. C* **87**, 064302 (2013).
- [85] J. Barea, J. Kotila, and F. Iachello, “ $0\nu\beta\beta$ and $2\nu\beta\beta$ nuclear matrix elements in the interacting boson model with isospin restoration”, *Phys. Rev. C* **91**, 034304 (2015).
- [86] M. Horoi and A. Neacsu, “Shell model predictions for ^{124}Sn double- β decay”, *Phys. Rev. C* **93**, 024308 (2016).
- [87] J. Menéndez, A. Poves, E. Caurier, and F. Nowacki, “Disassembling the nuclear matrix elements of the neutrinoless $\beta\beta$ decay”, *Nucl. Phys. A* **818**, 139 (2009).
- [88] Y. Iwata, N. Shimizu, T. Otsuka, Y. Utsuno, J. Menéndez, M. Honma, and T. Abe, “Large-Scale Shell-Model Analysis of the Neutrinoless $\beta\beta$ Decay of ^{48}Ca ”, *Phys. Rev. Lett.* **116**, 112502 (2016).

-
- [89] K. Heyde, P. von Neumann-Cosel, and A. Richter, “Magnetic Dipole Excitations in Nuclei: Elementary Modes of Nucleonic Motion”, *Rev. Mod. Phys.* **82**, 2365 (2010).
- [90] I. S. Towner, “Quenching of spin matrix elements in nuclei”, *Phys. Rep.* **155**, 263 (1987).
- [91] E. Epelbaum, H.-W. Hammer, and U.-G. Meißner, “Modern theory of nuclear forces”, *Rev. Mod. Phys.* **81**, 1773 (2009).
- [92] P. Gysbers et al., “Discrepancy between experiment and theoretical β -decay rates resolved from first principles”, *Nat. Phys.* **15**, 428 (2019).
- [93] T. D. Morris, J. Simonis, S. R. Stroberg, C. Stumpf, G. Hagen, J. D. Holt, G. R. Jansen, T. Papenbrock, R. Roth, and A. Schwenk, “Structure of the Lightest Tin Isotopes”, *Phys. Rev. Lett.* **120**, 152503 (2018).
- [94] G. Hagen, T. Papenbrock, M. Hjorth-Jensen, and D. J. Dean, “Coupled-cluster computations of atomic nuclei”, *Rep. Prog. Phys.* **77**, 096302 (2014).
- [95] H. Hergert, S. K. Bogner, T. D. Morris, A. Schwenk, and K. Tsukiyama, “The In-Medium Similarity Renormalization Group: A novel ab initio method for nuclei”, *Physics Reports* **621**, 165 (2016).
- [96] R. F. Garcia Ruiz et al., “Unexpectedly large charge radii of neutron-rich calcium isotopes”, *Nat. Phys.* **12**, 594 (2016).
- [97] J. Birkhan et al., “Electric Dipole Polarizability of ^{48}Ca and Implications for the Neutron Skin”, *Phys. Rev. Lett.* **118**, 252501 (2017).
- [98] International Atomic Energy Agency (IAEA), *Live Chart of Nuclides*, <https://www-nds.iaea.org/relnsd/vcharthtml/VChartHTML.html> (visited on 2020-01-20).
- [99] M. Goeppert Mayer, “On Closed Shells in Nuclei. II”, *Phys. Rev.* **75**, 1969 (1949).
- [100] O. Haxel, J. H. D. Jensen, and H. E. Suess, “On the “Magic Numbers” in Nuclear Structure”, *Phys. Rev.* **75**, 1766 (1949).
- [101] M. Honma, T. Otsuka, T. Mizusaki, and M. Hjorth-Jensen, “New effective interaction for $f_5p g_9$ -shell nuclei”, *Phys. Rev. C* **80**, 064323 (2009).
- [102] J. P. Schiffer et al., “Nuclear Structure Relevant to Neutrinoless Double β Decay: ^{76}Ge and ^{76}Se ”, *Phys. Rev. Lett.* **100**, 112501 (2008).

-
- [103] B. P. Kay et al., “Nuclear structure relevant to neutrinoless double β decay: The valence protons in ^{76}Ge and ^{76}Se ”, *Phys. Rev. C* **79**, 021301 (2009).
- [104] S. Mukhopadhyay, B. P. Crider, B. A. Brown, S. F. Ashley, A. Chakraborty, A. Kumar, M. T. McEllistrem, E. E. Peters, F. M. Prados-Estévez, and S. W. Yates, “Nuclear structure of ^{76}Ge from inelastic neutron scattering measurements and shell model calculations”, *Phys. Rev. C* **95**, 014327 (2017).
- [105] S. Mukhopadhyay, B. P. Crider, B. A. Brown, A. Chakraborty, A. Kumar, M. T. McEllistrem, E. E. Peters, F. M. Prados-Estévez, and S. W. Yates, “Inelastic neutron scattering studies of ^{76}Se ”, *Phys. Rev. C* **99**, 014313 (2019).
- [106] A. D. Ayangeakaa et al., “Evidence for Rigid Triaxial Deformation in ^{76}Ge from a Model-Independent Analysis”, *Phys. Rev. Lett.* **123**, 102501 (2019).
- [107] O. Azzolini et al., “CUPID-0: A double-readout cryogenic detector for Double Beta Decay search”, *Nucl. Instrum. Meth. A*, 162441 (2019).
- [108] G. Wang et al., (CUPID Interest Group), *CUPID: CUORE (Cryogenic Underground Observatory for Rare Events) Upgrade with Particle Identification*, arXiv:1504.03599, 2015, <https://arxiv.org/abs/1504.03599>.
- [109] G. Wang et al., (CUPID Interest Group), *R&D towards CUPID (CUORE Upgrade with Particle Identification)*, arXiv:1504.03612, 2015, <https://arxiv.org/abs/1504.03612>.
- [110] J. Beller et al., “Constraint on $0\nu\beta\beta$ Matrix Elements from a Novel Decay Channel of the Scissors Mode: The Case of ^{154}Gd ”, *Phys. Rev. Lett.* **111**, 172501 (2013).
- [111] O. Scholten, “The Interacting Boson Approximation Model and Applications”, Dissertation (Rijksuniversiteit te Groningen, 1980).
- [112] R. Krücken et al., “ $B(E2)$ Values in ^{150}Nd and the Critical Point Symmetry X(5)”, *Phys. Rev. Lett.* **88**, 232501 (2002).
- [113] F. Iachello, “Analytic Description of Critical Point Nuclei in a Spherical-Axially Deformed Shape Phase Transition”, *Phys. Rev. Lett.* **87**, 052502 (2001).
- [114] A. Barabash et al., *Summary of the Workshop on: Nuclear matrix elements for neutrinoless double beta decay*, edited by K. Zuber, arXiv:nucl-ex/0511009, 2005, <https://arxiv.org/abs/nucl-ex/0511009>.

-
- [115] H. Ejiri, “Nuclear spin isospin responses for low-energy neutrinos”, *Phys. Rep.* **338**, 265 (2000).
- [116] K. Wimmer, “Nucleon transfer reactions with radioactive beams”, *J. Phys. G* **45**, 033002 (2018).
- [117] M. Kortelainen and J. Suhonen, “Nuclear muon capture as a powerful probe of double-beta decays in light nuclei”, *J. Phys. G* **30**, 2003 (2004).
- [118] C. Volpe, “Neutrino–nucleus interactions as a probe to constrain double-beta decay predictions”, *J. Phys. G* **31**, 903 (2005).
- [119] U. Kneissl, H. Pitz, and A. Zilges, “Investigation of Nuclear Structure by Resonance Fluorescence Scattering”, *Prog. Part. Nucl. Phys.* **37**, 349 (1996).
- [120] F. R. Metzger, “Resonance Fluorescence in Nuclei”, *Prog. Nucl. Phys.* **7**, 53 (1959).
- [121] W. Heitler, *The Quantum Theory of Radiation*, 3rd ed. (Dover Publications, Inc., 1984).
- [122] H. Überall, *Electron Scattering From Complex Nuclei, Part A* (Academic Press, 1972).
- [123] K. Alder, A. Bohr, T. Huus, B. Mottelson, and A. Winther, “Study of Nuclear Structure by Electromagnetic Excitation with Accelerated Ions”, *Rev. Mod. Phys.* **28**, 432 (1956).
- [124] D. S. Onley, T. A. Griffy, and J. T. Reynolds, “Partial-Wave Analysis of the Inelastic Scattering of Electrons by Nuclei. II. Application to the Liquid Drop Model”, *Phys. Rev.* **129**, 1689 (1963).
- [125] C. A. Bertulani and A. M. Nathan, “Excitation and photon decay of giant resonances from high-energy collisions of heavy ions”, *Nucl. Phys. A* **554**, 158 (1993).
- [126] N. Pietralla, “The Institute of Nuclear Physics at the TU Darmstadt”, *Nucl. Phys. News* **28**, 4 (2018).
- [127] DFELL/TUNL, *HIGS flux performance table for high-flux, quasi-CW operation*, 2.4 (2017).
- [128] J. H. Hubbell and S. M. Seltzer, “Tables of X-Ray Mass Attenuation Coefficients and Mass Energy-Absorption Coefficients”, *NISTIR* **126**, 5632 (2004).

-
- [129] G. F. Knoll, *Radiation Detection and Measurement*, 3rd ed. (John Wiley & Sons, Inc., 1999).
- [130] A. Krumbholz et al., “Low-energy electric dipole response in ^{120}Sn ”, *Phys. Lett. B* **744**, 7 (2015).
- [131] U. Gayer, T. Beck, M. Bhike, J. Isaak, N. Pietralla, P. C. Ries, D. Savran, M. Schilling, W. Tornow, and V. Werner, “Experimental $M1$ response of ^{40}Ar as a benchmark for neutrino-nucleus scattering calculations”, *Phys. Rev. C* **100**, 034305 (2019).
- [132] C. Romig et al., “Direct determination of ground-state transition widths of low-lying dipole states in ^{140}Ce with the self-absorption technique”, *Phys. Lett. B* **744**, 369 (2015).
- [133] C. T. Angell, R. Hajima, T. Shizuma, B. Ludewigt, and B. J. Quiter, “Branching and Fragmentation of Dipole Strength in ^{181}Ta in the Region of the Scissors Mode”, *Phys. Rev. Lett.* **117**, 142501 (2016).
- [134] D. Savran, T. Aumann, and A. Zilges, “Experimental studies of the Pygmy Dipole Resonance”, *Prog. Part. Nucl. Phys.* **70**, 210 (2013).
- [135] H. H. Pitz et al., “Low-energy photon scattering off $^{142,146,148,150}\text{Nd}$: An investigation in the mass region of a nuclear shape transition”, *Nucl. Phys. A* **509**, 587 (1990).
- [136] W. Ziegler, N. Huxel, P. von Neumann-Cosel, C. Rangacharyulu, A. Richter, C. Spieler, C. D. Coster, and K. Heyde, “Low-energy dipole-strength distributions in $^{148,150,152,154}\text{Sm}$ ”, *Nucl. Phys. A* **564**, 366 (1993).
- [137] V. Werner, “Suche nach gemischtsymmetrischen Zuständen in den Kernen ^{96}Mo und ^{82}Se und Untersuchung der Deformation schwerer Kerne”, Diplomarbeit (Institut für Kernphysik, Universität zu Köln, 2000).
- [138] J. Tuli and E. Browne, “Nuclear Data Sheets for $A = 82$ ”, *Nucl. Data Sheets* **157**, 260 (2019).
- [139] S. K. Basu and A. A. Sonzogni, “Nuclear Data Sheets for $A = 150$ ”, *Nucl. Data Sheets* **114**, 435 (2013).
- [140] F. Iachello and A. Arima, *The interacting boson model*, 1st ed. (Cambridge University Press, 1987).

-
- [141] L. Coraggio, A. Covello, A. Gargano, N. Itaco, and T. Kuo, “Shell-model calculations and realistic effective interactions”, *Prog. Part. Nucl. Phys.* **62**, 135 (2009).
- [142] E. Epelbaum, “Four-nucleon force in chiral effective field theory”, *Phys. Lett. B* **639**, 456 (2006).
- [143] S. Schulz, “Four-Nucleon Forces in Ab Initio Nuclear Structure”, Dissertation (Technische Universität, Darmstadt, 2018), <http://tuprints.ulb.tu-darmstadt.de/7384/>.
- [144] R. F. Casten, P. O. Lipas, D. D. Warner, T. Otsuka, K. Heyde, and J. P. Draayer, *Algebraic Approaches to Nuclear Structure*, edited by R. F. Casten (Harwood Academic Publishers, 1993).
- [145] B. A. Brown, “The nuclear shell model towards the drip lines”, *Prog. Part. Nucl. Phys.* **47**, 517 (2001).
- [146] S. Sels et al., “Shape staggering of midshell mercury isotopes from in-source laser spectroscopy compared with density-functional-theory and Monte Carlo shell-model calculations”, *Phys. Rev. C* **99**, 044306 (2019).
- [147] T. Otsuka, Y. Tsunoda, T. Abe, N. Shimizu, and P. Van Duppen, “Underlying structure of collective bands and self-organization in quantum systems”, *Phys. Rev. Lett.* **123**, 222502 (2019).
- [148] T. Otsuka, M. Honma, T. Mizusaki, N. Shimizu, and Y. Utsuno, “Monte Carlo shell model for atomic nuclei”, *Prog. Part. Nucl. Phys.* **47**, 319 (2001).
- [149] T. Otsuka, A. Arima, and F. Iachello, “Nuclear shell model and interacting bosons”, *Nucl. Phys. A* **309**, 1 (1978).
- [150] F. Iachello and I. Talmi, “Shell-model foundations of the interacting boson model”, *Rev. Mod. Phys.* **59**, 339 (1987).
- [151] D. J. Dean and M. Hjorth-Jensen, “Pairing in nuclear systems: from neutron stars to finite nuclei”, *Rev. Mod. Phys.* **75**, 607 (2003).
- [152] N. Pietralla, P. von Brentano, R. F. Casten, T. Otsuka, and N. V. Zamfir, “Distribution of Low-Lying Quadrupole Phonon Strength in Nuclei”, *Phys. Rev. Lett.* **73**, 2962 (1994).
- [153] S. Pittel, P. D. Duval, and B. R. Barrett, “The microscopic Interacting Boson Model for nondegenerate orbits”, *Ann. Phys.-New York* **144**, 168 (1982).

-
- [154] F. Iachello, “Dynamic Symmetries at the Critical Point”, *Phys. Rev. Lett.* **85**, 3580 (2000).
- [155] S. Frauendorf and A. O. Macchiavelli, “Overview of neutron–proton pairing”, *Prog. Part. Nucl. Phys.* **78**, 24 (2014).
- [156] T. Otsuka and Y. Nobuaki, “User’s manual of the program NPBOS”, JAERI-M 85-094, 55 (1985), http://inis.iaea.org/search/search.aspx?orig_q=RN:17033326.
- [157] P. O. Lipas, P. von Brentano, and A. Gelberg, “Proton-neutron symmetry in boson models of nuclear structure”, *Rep. Prog. Phys.* **53**, 1355 (1990).
- [158] F. Scholtz, G. Kyrchev, and A. Faessler, “Exact and analytic solutions of the generalized bohr-mottelson model for spherical nuclei”, *Nucl. Phys. A* **491**, 91 (1989).
- [159] N. Pietralla, P. von Brentano, and A. F. Lisetskiy, “Experiments on multiphonon states with proton–neutron mixed symmetry in vibrational nuclei”, *Prog. Part. Nucl. Phys.* **60**, 225 (2008).
- [160] D. D. Warner and R. F. Casten, “Revised Formulation of the Phenomenological Interacting Boson Approximation”, *Phys. Rev. Lett.* **48**, 1385 (1982).
- [161] P. Lipas, P. Toivonen, and D. Warner, “IBA consistent-Q formalism extended to the vibrational region”, *Phys. Lett. B* **155**, 295 (1985).
- [162] N. Pietralla, P. von Brentano, R.-D. Herzberg, U. Kneissl, J. Margraf, H. Maser, H. H. Pitz, and A. Zilges, “Correlation between low-lying M1 and E2 strength in heavy rare earth nuclei”, *Phys. Rev. C* **52**, R2317 (1995).
- [163] G. Rusev et al., “Decay of 1^+ States as a New Probe of the Structure of 0^+ Shape Isomers”, *Phys. Rev. Lett.* **95**, 062501 (2005).
- [164] J. Beller, “Systematische Untersuchung exotischer Zerfallskanäle der Scherenmode in Gadoliniumisotopen”, Dissertation (Technische Universität, Darmstadt, 2014), <http://tuprints.ulb.tu-darmstadt.de/3859/>.
- [165] U. Gayer et al., “Nuclear structure of ^{82}Kr and ^{82}Se relevant for neutrinoless double-beta decay”, *EPJ Web Conf.* **194**, 02004 (2018).
- [166] T. Beck et al., “E2 decay strength of the M1 scissors mode of ^{156}Gd and its first excited rotational state”, *Phys. Rev. Lett.* **118**, 212502 (2017).

-
- [167] *Electronic logbook of the γ^3 collaboration for the 2015-2017 campaigns*, https://elog.ikp.physik.tu-darmstadt.de/gamma3_2015-2017 (visited on 2020-01-20).
- [168] H. R. Weller, M. W. Ahmed, H. Gao, W. Tornow, Y. Wu, M. Gai, and R. Miskimen, “Research opportunities at the upgraded HI γ S facility”, *Prog. Part. Nucl. Phys.* **62**, 257 (2009).
- [169] C. Sun, “Characterizations and Diagnostics of Compton Light Source”, Dissertation (Duke University, Durham, NC, 2009), <https://hdl.handle.net/10161/1579>.
- [170] B. Löher et al., “The high-efficiency γ -ray spectroscopy setup γ^3 at HI γ S”, *Nucl. Instrum. Meth. A* **723**, 136 (2013).
- [171] Mirion Technologies, *GENIE™ 2000 Basic Spectroscopy Software*, (Note: This is not the actual version of GENIE that was used in the experiments, but a more recent one.) (2016).
- [172] J. H. Kelley, J. E. Purcell, and C. G. Sheu, “Energy levels of light nuclei A = 12”, *Nucl. Phys. A* **968**, 71 (2017).
- [173] J. Chen, “Nuclear Data Sheets for A = 138”, *Nucl. Data Sheets* **146**, 1 (2017).
- [174] J. Chen, J. Cameron, and B. Singh, “Nuclear Data Sheets for A = 35”, *Nucl. Data Sheets* **112**, 2715 (2011).
- [175] J. Cameron, J. Chen, B. Singh, and N. Nica, “Nuclear Data Sheets for A = 37”, *Nucl. Data Sheets* **113**, 365 (2012).
- [176] G. Rupp, D. Petrich, F. Käppeler, J. Kaltenbaek, B. Leugers, and R. Reifarth, “High pressure gas spheres for neutron and photon experiments”, *Nucl. Instrum. Meth. A* **608**, 152 (2009).
- [177] H. Junde, H. Su, and Y. Dong, “Nuclear Data Sheets for A = 56”, *Nucl. Data Sheets* **112**, 1513 (2011).
- [178] J. Kleemann, “Zerfallsverhalten der Scherenmode in der $0\nu\beta\beta$ -Tochter ^{150}Sm ”, BSc Thesis (Technische Universität Darmstadt, 2016).
- [179] J. Kleemann, “Decay Characteristics of the Scissors Mode of the $0\nu\beta\beta$ -Decay Mother ^{150}Nd ”, MSc Thesis (Technische Universität Darmstadt, 2018).

-
- [180] BIPM, IEC, IFCC, ILAC, ISO, IUPAP and OIML 2008, *Evaluation of measurement data - Supplement 1 to the "Guide to the expression of uncertainty in measurement" - Propagation of distributions using a Monte Carlo method*. (Joint Committee for Guides in Metrology, JCGM 100:2008, 2008).
- [181] BIPM, IEC, IFCC, ILAC, ISO, IUPAP and OIML 2008, *Evaluation of measurement data - Guide to the expression of uncertainty in measurement* (Joint Committee for Guides in Metrology, JCGM 100:2008, 2008).
- [182] R. Brun and F. Rademakers, "ROOT — An object oriented data analysis framework", Nucl. Instrum. Meth. A **389**, 81 (1997), <https://root.cern.ch/>.
- [183] D. W. Scott, *Multivariate Density Estimation: Theory, Practice, and Visualization* (John Wiley & Sons, Inc., 1992).
- [184] P. Virtanen et al., *SciPy 1.0-Fundamental Algorithms for Scientific Computing in Python*, arXiv:1907.10121, 2019, <https://arxiv.org/abs/1907.10121>.
- [185] P. T. Boggs, R. H. Byrd, and R. B. Schnabel, "A Stable and Efficient Algorithm for Nonlinear Orthogonal Distance Regression", SIAM J. Sci. Stat. Comp. **8**, 1052 (1987).
- [186] S.-C. Wu, "Nuclear Data Sheets for A = 214", Nucl. Data Sheets **110**, 681 (2009).
- [187] G. R. Gilmore, *Practical Gamma-ray Spectrometry*, 2nd ed. (John Wiley & Sons, Ltd., 2008).
- [188] S. van der Walt, S. C. Colbert, and G. Varoquaux, "The NumPy Array: A Structure for Efficient Numerical Computation", Comput. Sci. Eng. **13**, 22 (2011).
- [189] T. E. Oliphant, *Guide to NumPy*, 2nd ed. (CreateSpace Independent Publishing Platform, 2015).
- [190] J. D. Hunter, "Matplotlib: A 2D Graphics Environment", Comput. Sci. Eng. **9**, 90 (2007).
- [191] T. Tantau, "Graph Drawing in TikZ", J. Graph. Alg. App. **17**, 495 (2013).
- [192] U. Friman-Gayer, J. Kleemann, and O. Papst, "GEANT4 simulation of the Upstream Target Room (UTR) at the HI γ S facility", (2019) 10.5281/zenodo.3430154.

-
- [193] J. Wilhelmy et al., “Investigation of $J = 1$ states and their γ -decay behavior in ^{52}Cr ”, Phys. Rev. C **98**, 034315 (2018).
- [194] D. Savran and J. Isaak, “Self-absorption with quasi-monochromatic photon beams”, Nucl. Instrum. Meth. A **899**, 28 (2018).
- [195] R. Massarczyk et al., “Role of electric and magnetic dipole strength functions in the $^{114}\text{Cd}(\gamma, \gamma')$ and $^{113}\text{Cd}(n, \gamma)$ reactions”, Phys. Rev. C **93**, 014301 (2016).
- [196] Krishichayan, S. W. Finch, C. R. Howell, A. P. Tonchev, and W. Tornow, “Monoenergetic photon-induced fission cross-section ratio measurements for ^{235}U , ^{238}U , and ^{239}Pu from 9.0 to 17.0 MeV”, Phys. Rev. C **98**, 014608 (2018).
- [197] M. Tamkas et al., “Low-lying dipole strength in the well-deformed nucleus ^{156}Gd ”, Nucl. Phys. A **987**, 79 (2019).
- [198] T. Shizuma et al., “Dipole strength distribution in ^{206}Pb for the evaluation of the neutron capture cross section of ^{205}Pb ”, Phys. Rev. C **98**, 064317 (2018).
- [199] M. Omer and R. Hajima, “Including Delbrück scattering in GEANT4”, Nucl. Instrum. Meth. B **405**, 43 (2017).
- [200] M. N. Lakshmanan, B. P. Harrawood, G. Rusev, G. A. Agasthya, and A. J. Kapadia, “Simulations of nuclear resonance fluorescence in GEANT4”, Nucl. Instrum. Meth. A **763**, 89 (2014).
- [201] J. R. Vavrek, B. S. Henderson, and A. Danagoulian, “Validation of Geant4’s G4NRF module against nuclear resonance fluorescence data from ^{238}U and ^{27}Al ”, Nucl. Instrum. Meth. B **459**, 188 (2019).
- [202] C. P. Robert and G. Casella, *Monte Carlo Statistical Methods* (Springer, 1999).
- [203] V. T. Jordanov and G. F. Knoll, “Digital synthesis of pulse shapes in real time for high resolution radiation spectroscopy”, Nucl. Instrum. Meth. A **345**, 337 (1994).
- [204] D. Cano-Ott, J. L. Tain, A. Gadea, B. Rubio, L. Batist, M. Karny, and E. Roeckl, “Pulse pileup correction of large NaI(Tl) total absorption spectra using the true pulse shape”, Nucl. Instrum. Meth. A **430**, 488 (1999).

-
- [205] C. T. Angell, “Pulse pileup correction in the presence of a large low-energy background”, *J. Nucl. Sci. Technol.* **52**, 426 (2015).
- [206] L. A. Currie, “Limits for qualitative detection and quantitative determination. Application to radiochemistry”, *Anal. Chem.* **40**, 586 (1968).
- [207] *Nachweisgrenze und Erkennungsgrenze bei Kernstrahlungsmessungen (DIN 25482, Teil 2)*, Standard (Deutsches Institut für Normung e.V., 1992).
- [208] J. Theuerkauf, S. Esser, S. Krink, M. Luig, N. Nicolay, O. Stuch, and H. Wolters, *Program Tv*, Institut für Kernphysik, Universität zu Köln (1993).
- [209] A. Fitzler, *Tv User-Manual*, Institut für Kernphysik, Universität zu Köln (2000).
- [210] J. Mayer, E. Hoemann, O. Papst, N. Warr, N. Braun, T. Kotthaus, and R. Schulze, *HDTV - Nuclear Spectrum Analysis Tool*, version 18.04, <https://gitlab.ikp.uni-koeln.de/staging/hdtv> (visited on 2019-01-20).
- [211] O. Papst and U. Friman-Gayer, *Development version of: HDTV - Nuclear Spectrum Analysis Tool*, <https://github.com/op3/hdtv> (visited on 2019-01-20).
- [212] N. W. Ashcroft and N. D. Mermin, *Solid State Physics* (Harcourt College Publishers, 1976).
- [213] N. Pietralla, “Tiefliegende Kernanregungen: Die Yrastzustände und die Scherenmode”, Dissertation (Institut für Kernphysik, Universität zu Köln, 1996).
- [214] J. Chen, “Nuclear Data Sheets for $A = 40$ ”, *Nucl. Data Sheets* **140**, 1 (2017).
- [215] M. J. Martin, “Nuclear Data Sheets for $A = 208$ ”, *Nucl. Data Sheets* **108**, 1583 (2007).
- [216] W. Ritz, “Über eine neue Methode zur Lösung gewisser Variationsprobleme der mathematischen Physik”, *J. reine angew. Math.* **135**, 1 (1909).
- [217] E. O. Brigham, *The Fast Fourier Transform and its Applications* (Prentice-Hall, Inc., 1988).
- [218] S. P. Tsai, E. R. Mucciolo, and O. Helene, “Relocation of multichannel spectra”, *Nucl. Instrum. Meth. A* **345**, 538 (1994).

-
- [219] M. J. Martin, “Nuclear Data Sheets for A = 152”, Nucl. Data Sheets **114**, 1497 (2013).
- [220] B. Jäckel, W. Westmeier, and P. Patzelt, “On the photopeak efficiency of germanium gamma-ray detectors”, Nucl. Instrum. Meth. A **261**, 543 (1987).
- [221] G. A. P. Cirrone, G. Cuttone, F. D. Rosa, L. Pandola, F. Romano, and Q. Zhang, “Validation of the Geant4 electromagnetic photon cross-sections for elements and compounds”, Nucl. Instrum. Meth. A **618**, 315 (2010).
- [222] K. Debertin and R. G. Helmer, *Gamma- and X-ray Spectrometry with Semiconductor Detectors* (North Holland, 1988).
- [223] H. W. Koch and J. W. Motz, “Bremsstrahlung Cross-Section Formulas and Related Data”, Rev. Mod. Phys. **31**, 920 (1959).
- [224] C. Nair et al., “Photoactivation experiment on ^{197}Au and its implications for the dipole strength in heavy nuclei”, Phys. Rev. C **78**, 055802 (2008).
- [225] L. Pandola, C. Andenna, and B. Caccia, “Validation of the Geant4 simulation of bremsstrahlung from thick targets below 3MeV”, Nucl. Instrum. Meth. B **350**, 41 (2015).
- [226] K. Sonnabend et al., “The Darmstadt High-Intensity Photon Setup (DHIPS) at the S-DALINAC”, Nucl. Instrum. Meth. A **640**, 6 (2011).
- [227] O. Papst, “Dipole strength distribution of the deformed nucleus ^{164}Dy ”, MSc Thesis (Technische Universität Darmstadt, 2019).
- [228] O. Papst et al., “Low-energy dipole strength of ^{164}Dy ”, in preparation.
- [229] B. Löher, “Probing the decay characteristics of the Pygmy Dipole Resonance in the semi-magic nucleus ^{140}Ce with gamma-gamma coincidence measurements”, Dissertation (Johannes Gutenberg-Universität, Mainz, 2014), <http://nbn-resolving.org/urn:nbn:de:hebis:77-38195>.
- [230] R. Gold, “An iterative unfolding method for response matrices”, ANL Technical Report **6984**, 4634295 (1964).
- [231] M. Morháč, J. Kliman, V. Matoušek, M. Veselský, and I. Turzo, “Efficient one- and two-dimensional gold deconvolution and its application to γ -ray spectra decomposition”, Nucl. Instrum. Meth. A **401**, 385 (1997).
- [232] U. Friman-Gayer, *horst: histogram original reconstruction spectrum tool*, <https://github.com/uga-uga/Horst> (visited on 2019-01-20).

-
- [233] C. Sun, J. Li, G. Rusev, A. P. Tonchev, and Y. K. Wu, “Energy and energy spread measurements of an electron beam by Compton scattering method”, *Phys. Rev. Accel. Beams* **12**, 062801 (2009).
- [234] C. Sun and Y. K. Wu, “Theoretical and simulation studies of characteristics of a Compton light source”, *Phys. Rev. Accel. Beams* **14**, 044701 (2011).
- [235] C. Sun, Y. K. Wu, G. Rusev, and A. P. Tonchev, “End-to-end spectrum reconstruction method for analyzing Compton gamma-ray beams”, *Nucl. Instrum. Meth. A* **605**, 312 (2009).
- [236] R. D. Deslattes, E. G. Kessler, P. Indelicato, L. de Billy, E. Lindroth, and J. Anton, “X-ray transition energies: new approach to a comprehensive evaluation”, *Rev. Mod. Phys.* **75**, 35 (2003).
- [237] J. H. Hubbell, “Electron–positron pair production by photons: A historical overview”, *Radiat. Phys. Chem.* **75**, 614 (2006).
- [238] M. Jentschel, W. Urban, P. Mutti, P. Courtois, G. S. Simpson, and R. Frahm, “Measurements of the pair production cross section close to the threshold energy”, *Phys. Rev. C* **84**, 052501 (2011).
- [239] C. Romig, “Investigation of Nuclear Structure with Relative Self-Absorption Measurements”, Dissertation (Technische Universität, Darmstadt, 2015), <http://tuprints.ulb.tu-darmstadt.de/4446/>.
- [240] L. D. Landau and E. M. Lifshitz, *Course of Theoretical Physics*, 2nd ed., Vol. 6, Fluid Mechanics (Pergamon Press, 1987).
- [241] A. Tari, *The Specific Heat of Matter at Low Temperatures* (Imperial College Press, 2003).
- [242] F. Paxton, “Solid Angle Calculation for a Circular Disk”, *Rev. Sci. Instrum.* **30**, 254 (1959).
- [243] N. Pietralla et al., “Parity Measurements of Nuclear Levels Using a Free-Electron-Laser Generated γ -Ray Beam”, *Phys. Rev. Lett.* **88**, 012502 (2001).
- [244] G. Rusev, A. P. Tonchev, R. Schwengner, C. Sun, W. Tornow, and Y. K. Wu, “Multipole mixing ratios of transitions in ^{11}B ”, *Phys. Rev. C* **79**, 047601 (2009).
- [245] K. S. Krane, “Solid-angle correction factors for coaxial Ge(Li) detectors”, *Nucl. Instrum. Meth.* **98**, 205 (1972).

-
- [246] B. A. Brown and W. D. M. Rae, “The Shell-Model Code NuShellX@MSU”, Nucl. Data Sheets **120**, 115 (2014).
- [247] J. Barea and F. Iachello, “Neutrinoless double- β decay in the microscopic interacting boson model”, Phys. Rev. C **79**, 044301 (2009).
- [248] J. Barea, J. Kotila, and F. Iachello, “Nuclear matrix elements for double- β decay”, Phys. Rev. C **87**, 014315 (2013).
- [249] J. Kotila, “Updated calculations of nuclear matrix elements for $0\nu\beta\beta$ decay between ^{150}Nd and ^{150}Sm .”, private communication.
- [250] F. S. Acton, *Analysis of Straight-Line Data* (John Wiley & Sons, Inc., 1959).
- [251] E. W. Weisstein, *Least Squares Fitting*, MathWorld - A Wolfram Web Resource, <https://mathworld.wolfram.com/LeastSquaresFitting.html> (visited on 2020-01-20).
- [252] K. Abusaleem, “Nuclear Data Sheets for $A = 228$ ”, Nucl. Data Sheets **116**, 163 (2014).
- [253] F. Ajzenberg-Selove, “Energy levels of light nuclei $A = 13-15$ ”, Nucl. Phys. A **523**, 1 (1991).

Acknowledgements

In the following list, I would like to express my gratitude to individuals who have significantly influenced the present work.

I would like to thank ...

- ... my supervisor **Prof. Dr. Dr. h.c. Norbert Pietralla** for accepting me in his group during my undergraduate studies and offering me the exciting PhD project which resulted in this thesis. Furthermore, I would like to thank him for giving me several opportunities to expand my knowledge at several summer schools and workshops, and to connect with scientists from all over the world at various conferences. At last, I thank him for transferring some of his enormous passion for (nuclear) physics on me and for his enthusiasm when discussing any professional topic. I hope that I have been worth all the support he has given me over the last ≈ 6 years.

'Think outside the box!'

Prof. Pietralla's almost-shouted encouragement for me and several colleagues to be creative.

- ... my mentor **Dr. Volker Werner** for guidance and help during my project work, but also for letting me pursue my own interests. Volker found a good balance between the latter and pushing me towards my career goals (for example with the infamous 'Simulationsverbot'), which always made it a pleasure to work with him. I would also like to thank him for his great patience in reading manuscript drafts and listening to rehearsal talks. Last but not least, his practical advice on the life as a scientist was invaluable to me.

-
- ... the **Doctores Johann Isaak, Bastian Löher**, and **Deniz Savran** for their help with the experiments themselves at HI γ S and the analysis of the data. As the supervisors of the γ^3 setup, they have taken the experiments at HI γ S to a new level of sophistication, and I profited a lot from discussions with them. Incidentally, we also had a lot of fun at these experiments.
 - ... the previous generation of the nuclear resonance fluorescence (NRF) group, the **Doctores Jacob Beller, Christopher Romig**, and **Markus Zweidinger**, for teaching me the basics of NRF and the large variety of nuclear structure phenomena which are investigated in our group. In particular, I would like to advertise Christopher's PhD thesis which contains a thorough introduction to the NRF- and the self-absorption method.
 - ... **Prof. Dr. Marcus Scheck** from the University of the West of Scotland, for the introduction to the NRF method during my late undergraduate studies, which provided a solid foundation for all subsequent studies. Furthermore, I would like to thank him for the careful reading of manuscripts and for his valuable advice.
 - ... the current doctoral researchers of the NRF group, **Tobias Beck, Marcel Berger, Jörn Kleemann, Oliver Papst**, and **Philipp C. Ries** for their help and encouragement, and for the enjoyable atmosphere at work. Our frequent constructive discussion have helped to deepen my understanding and make my data analysis more consistent and transparent.
 - ... **Johannes Wiederhold** for his support during the long evening sessions at the Institut für Kernphysik, TU Darmstadt (IKP) when we were both writing our theses. His careful proofreading and his expertise in L^AT_EX and python/Matplotlib have significantly improved the quality of this thesis.
 - ... **Dr. Jonny Birkhan** for his help with the evaluation of experimental data and statistics.
 - ... **Prof. em. Dr. Werner Tornow** from Duke University and the Triangle Universities Nuclear Laboratory (TUNL), with his inexhaustible passion for experiments, for help during our campaigns at HI γ S and his careful reading of manuscript drafts. In this context, I would also like to thank his (former) group members **Megha Bhike, Krishichayan**, and **Sean Finch** for their support of the experiments.

- ... the **accelerator crew at HIγS** for providing excellent experimental conditions.
- ... **Dr. Ronald Schwengner** and **Andreas Hartmann** from the Helmholtz-Zentrum Dresden-Rossendorf (HZDR), for their friendly help with the preparation of the ^{82}Kr target, which unexpectedly turned into an action movie-like rush over the HZDR campus.
- ... **Michael Weinert** from the Universität zu Köln for help with the experimental setup.
- ... **Jenni Kotila, PhD** from the University of Jyväskylä for providing the theoretical calculations in the interacting boson model, which established the connection between the nuclear structure investigated in this work and the motivation of $0\nu\beta\beta$ decay.
- ... **Prof. Dr. Wilfried Nörtershäuser** for agreeing, on relatively short notice, to be the second reviewer.
- ... **Sonja Friman** for her careful proofreading and helpful comments despite her occupation with work on her own dissertation.

In addition to the directly thesis-related acknowledgements, I would like to thank the following individuals:

- My present or former colleagues at the IKP: **Axel F., Bernhard M., Christian S., Christopher B., Dima S., Esra A., Felix S., Gerhart S., Katharina I., Kristian K., Lars J., Laura M., Marc L., Marco K., Marius P., Matthias N., Max H., Michael T., Michaela H., Radostina Z., Ralph K., Robert S., Thomas M., Tobias K.** All of them, together with my aforementioned colleagues, have made the time at the IKP an unforgettable experience.
- My friends in Darmstadt $\pm\epsilon$ for a great time in my undergraduate-, graduate-, and doctoral studies. Although they actually helped more in diverting me from the aforementioned studies, I consider myself very lucky to have become acquainted with such an extraordinary group of people.
- My parents **Cornelia** and **Hubert Gayer** and my grandparents, for unconditional support throughout my life. Although they come from a non-academic background, they value education and reason very highly and allow me to

pursue my own interests, for which I am deeply grateful. I hope I have made them proud.

- My brother **Toni Gayer** for his profound influence on my humor and tastes, and his matter-of-fact attitude which keeps me from living in an ivory tower.
- My adorable wife **Sonja Friman** for her loving support and her patience at any time. It feels wonderful to have her at my side.

Funding

- This work was supported by the Deutsche Forschungsgemeinschaft (DFG) under grant No. SFB 1245 (Project ID 279384907) with the title 'Nuclei: From Fundamental Interactions to Structure and Stars'.
- The Helmholtz Graduate School for Hadron and Ion Research (HGS-HIRE) of the Helmholtz Association is acknowledged for support during my doctoral studies.

Academic CV

Udo Friman-Gayer (né Gayer)

Personal Information

Date of Birth November 7, 1990
Place of Birth Miltenberg, BY, DE
Nationality German

Education

since 04/2016 Doctoral candidate
Institut für Kernphysik (IKP)
Technische Universität (TU) Darmstadt
11/2013 - 03/2016 Master of Science in Physics
IKP, TU Darmstadt
10/2010 - 11/2013 Bachelor of Science in Physics
IKP, TU Darmstadt
09/2001 - 06/2010 Abitur
Karl Ernst Gymnasium Amorbach

Publications

- [1] H. Pai et al., “Magnetic dipole excitations of ^{50}Cr ”, Phys. Rev. C **93**, 014318 (2016).
- [2] T. Beck et al., “ $E2$ decay strength of the $M1$ scissors mode of ^{156}Gd and its first excited rotational state”, Phys. Rev. Lett. **118**, 212502 (2017).

-
-
- [3] J. Wilhelmy et al., “Investigation of $J = 1$ states and their γ -decay behavior in ^{52}Cr ”, Phys. Rev. C **98**, 034315 (2018).
 - [4] B. Dietz, B. A. Brown, U. Gayer, N. Pietralla, V. Yu. Ponomarev, A. Richter, P. C. Ries, and V. Werner, “Chaos and regularity in the spectra of the low-lying dipole excitations of $^{50,52,54}\text{Cr}$ ”, Phys. Rev. C **98**, 054314 (2018).
 - [5] J. Isaak et al., “The concept of nuclear photon strength functions: A model-independent approach via $(\vec{\gamma}, \gamma' \gamma'')$ reactions”, Phys. Lett. B **788**, 225 (2019).
 - [6] M. Tamkas et al., “Low-lying dipole strength in the well-deformed nucleus ^{156}Gd ”, Nucl. Phys. A **987**, 79 (2019).
 - [7] P. C. Ries et al., “Valence-shell dependence of the pygmy dipole resonance: $E1$ strength difference in $^{50,54}\text{Cr}$ ”, Phys. Rev. C **100**, 021301 (2019).
 - [8] U. Gayer, T. Beck, M. Bhike, J. Isaak, N. Pietralla, P. C. Ries, D. Savran, M. Schilling, W. Tornow, and V. Werner, “Experimental $M1$ response of ^{40}Ar as a benchmark for neutrino-nucleus scattering calculations”, Phys. Rev. C **100**, 034305 (2019).

Conference Proceedings

- [1] M. Zweidinger, T. Beck, J. Beller, U. Gayer, L. Mertes, H. Pai, N. Pietralla, P. C. Ries, C. Romig, and V. Werner, “Contemporary research with nuclear resonance fluorescence at the S-DALINAC”, AIP Conf. Proc. **1645**, 259 (2015).
- [2] C. Romig et al., “Direct Determination of Ground-State Transition Widths and Natural Level Widths with the Method of Relative Self Absorption”, EPJ Web Conf. **93**, 01035 (2015).
- [3] T. Beck et al., “Quadrupole decay strength of the $M1$ scissors mode”, AIP Conf. Proc. **1681**, 040007 (2015).
- [4] M. Scheck et al., “ β Decay as a New Probe for the Low-energy $E1$ Strength”, Acta Phys. Pol. B **48**, 547 (2017).
- [5] J. Isaak et al., “Study of photon strength functions via $(\vec{\gamma}, \gamma' \gamma'')$ reactions at the γ^3 -setup”, EPJ Web Conf. **178**, 03006 (2018).

-
- [6] N. Pietralla, C. Kremer, T. Beck, W. Witt, U. Gayer, P. von Neumann-Cosel, and V. Werner, “Shell Evolution and E2 Collectivity: New Spectroscopic Information”, EPJ Web Conf. **178**, 02007 (2018).
- [7] V. Werner et al., “Shape mixing in $0\nu\beta\beta$ candidates”, J. Phys. Conf. Ser. **1056**, 012061 (2018).
- [8] U. Gayer et al., “Nuclear structure of ^{82}Kr and ^{82}Se relevant for neutrinoless double-beta decay”, EPJ Web Conf. **194**, 02004 (2018).
- [9] P. C. Ries et al., “Investigation of the Pygmy Dipole Resonance Across the Shell Closure in Chromium Isotopes”, in Basic Concepts in Nuclear Physics: Theory, Experiments and Applications (2019), pp. 233–234.